

# JOURNAL OF THE ELECTROCHEMICAL SOCIETY

ELECTROCHEMICAL  
SCIENCE AND TECHNOLOGY

SOLID-STATE  
SCIENCE AND TECHNOLOGY

REVIEWS AND NEWS  
Call for Papers—  
Montreal, Canada, Meeting



VOL. 128, NO. 11

NOVEMBER 1981

JESOAN 128 (11) 2257-2492, 481C-508C





## FUTURE MEETINGS

### MONTREAL, CANADA—MAY 9-14, 1982—HEADQUARTERS AT THE QUEEN ELIZABETH

The detailed Call for Papers published in the July-November 1981 issues of **This Journal**. Final program published in the March 1982 issue of **This Journal**.

Planned symposia for the Montreal Meeting will include the following Divisions, Groups, Subcommittee, and subjects:

**Corrosion**—General Session; **Corrosion/Energy Technology/Dielectrics and Insulation/Electrothermics and Metallurgy**—Corrosion Problems in Nuclear and Fusion Technologies; **Dielectrics and Insulation/Corrosion/Electronics/Electrothermics and Metallurgy/Energy Technology**—Materials and New Processing Technologies for Photovoltaics; **Dielectrics and Insulation/Electronics/American Ceramics Society**—Applications of Glasses and Ceramics in Device Technology; **Dielectrics and Insulation/Electronics/New Technology Subcommittee**—Inorganic Resist Systems; **Electronics**—Micromachining and Micromechanics, Molecular Beam Epitaxy, Luminescence in Amorphous Materials, Phosphor Depreciation, Phosphor Screening, Luminescence General Session; **Electronics/Dielectrics and Insulation**—Growth of Single Crystals on Amorphous Substrates, Tutorial on Semiconductor Technology, Joint General Session, Joint Recent News Papers Session; **Electrothermics and Metallurgy**—Electrochemistry of Pyrometallurgical Processes, Transport Phenomena in Metals; **Electrothermics and Metallurgy/Corrosion**—Electrochemical Techniques for High Temperature Corrosion Studies; **Electrothermics and Metallurgy/Dielectrics and Insulation/Electronics**—Tenth International Conference on Electron and Ion Beam Science and Technology; **Energy Technology**—Ion Insertion Phenomena, Photobiological Energy Conversion and Storage Processes, General Session; **Energy Technology/Battery**—Energy Systems for Developing Countries; **Energy Technology/Battery/Physical Electrochemistry**—Platinum Electrocatalysts: Efficient Utilization and Alternatives, Molten Carbonate Fuel Cell Technology; **Industrial Electrolytic**—Electrochemical Process and Plant Design; **Industrial Electrolytic/Battery/Energy Technology**—Transport Processes in Electrochemical Systems; **Industrial Electrolytic/Energy Technology**—Hydrogen Production and Storage; **Organic and Biological Electrochemistry**—Electrochemistry for the Study and Control of Cell and Tissue Growth and Repair, Redox Mechanisms and Interfacial Properties of Molecules of Biological Importance, General Session; **Organic and Biological Electrochemistry/Industrial Electrolytic**—Industrial Electro-Organic Chemistry; **Organic and Biological Electrochemistry/Physical Electrochemistry/Dielectrics and Insulation**—Polymer Film Electrodes; **Physical Electrochemistry**—Double Layer Phenomena, General Session; and **Physical Electrochemistry/Battery/Energy Technology**—Solid Electrolytes.

### DETROIT, MICHIGAN—OCTOBER 17-22, 1982—HEADQUARTERS AT THE DETROIT PLAZA

The detailed Call for Papers published in the December 1981-May 1982 issues of **This Journal**. Final program published in the August 1982 issue of **This Journal**.

Planned symposia for the Detroit Meeting include the following Divisions, Group, Subcommittee, and subjects: **Battery**—Economic Trade Off Consideration on Batteries for Electric Vehicles, Long Term Batteries, Near Term Batteries, Thin Film Batteries, General Session; **Battery/Energy Technology/New Technology Subcommittee**—Reliability and Failure Analysis of Battery Arrays; **Corrosion**—Automotive Corrosion, General Session; **Corrosion/Electrodeposition**—New Materials for Electrical Contacts; **Corrosion/Energy Technology**—Corrosion in Fossil Fuel Systems; **Dielectrics and Insulation/Electronics**—Automotive Reliability of Solid-State Devices; **Electrodeposition**—Electrodeposition in Automotive Applications, General Session; **Electronics/Dielectrics and Insulation**—VLSI Technology, Joint General Session, Joint Recent News Papers Session; **Electrothermics and Metallurgy**—Emission Control—Catalysts, The Metallurgy and Chemistry of Silica Reduction, Thermal Management of Batteries; **Electrothermics and Metallurgy/Corrosion**—Materials Aspects of Turbine Technologies; **Energy Technology**—Extraction of Minerals from the Ocean, Novel Experimental Techniques in Electrochemical Energy Technologies, Surface Charge Measurement, Control and Modification for Industrial Processes, General Session; **Energy Technology/Battery**—Porous Electrodes; **Energy Technology/Battery/Corrosion/Physical Electrochemistry**—Advanced Electrolytes for Energy Systems; **Energy Technology/Battery/Physical Electrochemistry**—Intercalation Electrodes; **Industrial Electrolytic**—Optimization of Industrial Electrochemical Processes, General Session; **Physical Electrochemistry**—General Session; **Physical Electrochemistry/Battery**—Thermal Batteries; and **Physical Electrochemistry/Battery/Corrosion**—Reactions in High Temperature Batteries and Fuel Cells.

### SAN FRANCISCO, CALIFORNIA—MAY 8-13, 1983—HEADQUARTERS AT THE ST. FRANCIS HOTEL

The detailed Call for Papers published in the July-November 1982 issues of **This Journal**. Final program published in the March 1983 issue of **This Journal**.

Planned symposia for the San Francisco Meeting include the following Divisions, Group, Subcommittee, and subjects: **Battery**—Cell Design and Optimization, Cell Testing and Reliability, Nonaqueous Systems for Energy Conversion, Primary Cells, Reactive Metal/Air Batteries, Secondary Cells, General Session; **Corrosion**—General Session; **Dielectrics and Insulation/Electronics**—Dielectric Isolation, Packaging of Electronic Devices, Plasma Etching and Deposition; **Dielectrics and Insulation/Electrothermics and Metallurgy**—High Temperature Adhesives; **Electronics/Dielectrics and Insulation**—Joint General Session, Joint Recent News Papers Session; **Electrothermics and Metallurgy**—Materials Processing in Space, The Science and Technology of Nucleation and Growth of Particles from the Gas Phase; **Electrothermics and Metallurgy/Corrosion/Dielectrics and Insulation**—Protective Coatings; **Electrothermics and Metallurgy/Physical Electrochemistry/Battery/Energy Technology**—New Solid Electrolytes for Energy Conversion; **Energy Technology**—Electrochemical Methods for Treating Nuclear Waste, Novel Photoelectrochemical Synthetic Routes, Oxygen Cathodes in Aqueous Systems, General Session; **Energy Technology/Battery**—Conducting Organic Polymers in Energy Conversion; **Industrial Electrolytic**—Anode and Cathode Materials, Science and Engineering of Membranes and Separation; **Physical Electrochemistry**—Electrode Processes, Fourth International Symposium on Molten Salts, General Session; **Physical Electrochemistry/Corrosion**—In Situ Nonelectrochemical Techniques for the Study of Electrode Reactions; and **New Technology Subcommittee/Electronics**—Computer Controlled Manufacturing/Industrial Robotics.

# THE ELECTROCHEMICAL SOCIETY BOOKS IN PRINT

## Society Proceedings Series

The following softbound proceedings volumes are sponsored and published by The Electrochemical Society, Inc., 10 South Main Street, Pennington, N.J. 08534-2896. Orders filled at the list price given, subject to availability. Enclose payment with order.

- Electron and Ion Beam Science and Technology**, Fourth International Conference. R. Bakish, Editor. A 1970 symposium. 680 pages, **\$7.50**.
- Fundamentals of Electrochemical Machining**. C. L. Faust, Editor. A 1970 symposium. 365 pages, **\$4.50**.
- Electron and Ion Beam Science and Technology**, Fifth International Conference. R. Bakish, Editor. A 1972 symposium. 420 pages, **\$5.50**.
- Electrochemical Contributions to Environmental Protection**. T. R. Beck, O. B. Cecil, C. G. Enke, J. McCallum, and S. T. Wlodek, Editors. A 1972 symposium. 173 pages, **\$4.00**.
- Oxide-Electrolyte Interfaces**. R. S. Alwitt, Editor. A 1972 symposium. 312 pages, **\$9.00**.
- Electrochemical Bioscience and Bioengineering**. H. T. Silverman, I. F. Miller, and A. J. Salkind, Editors. A 1973 symposium. 268 pages, **\$8.00**.
- Chlorine Bicentennial Symposium**. T. C. Jeffery, P. A. Danna, and H. S. Holden, Editors. A 1974 symposium. 404 pages, **\$11.00**.
- Metal-Slag-Gas Reactions and Processes**. Z. A. Foroulis and W. W. Smeltzer, Editors. A 1975 symposium. 1032 pages, **\$20.00**.
- Chemistry and Physics of Aqueous Gas Solutions**. W. A. Adams, G. Greer, J. E. Desnoyers, G. Atkinson, G. S. Kell, K. B. Oldham, and J. Walkley, Editors. A 1975 symposium. 522 pages, **\$11.00**.
- Thermal and Photostimulated Currents in Insulators**. D. M. Smyth, Editor. A 1975 symposium. 215 pages, **\$7.00**.
- Electron and Ion Beam Science and Technology**, Seventh International Conference. R. Bakish, Editor. A 1976 symposium. 632 pages, **\$18.00**.
- International Symposium on Molten Salts**. J. P. Pemsler, J. Braunstein, K. Nobe, D. R. Morris, and N. E. Richards, Editors. A 1976 symposium. 632 pages, **\$16.00**.
- Properties of High Temperature Alloys**. Z. A. Foroulis and F. S. Pettit, Editors. A 1976 symposium. 851 pages, **\$12.00**.
- Semiconductor Silicon 1977**. H. R. Huff and E. Sirtl, Editors. A 1977 symposium. 1100 pages, **\$15.00**.
- A History of The Electrochemical Society**. The first 75 years. R. M. Burns with E. G. Enck. 160 pages, **\$5.00**.
- Semiconductor-Liquid Junction Solar Cells**. A. Heller, Editor. A 1977 symposium. 340 pages, **\$10.00**.
- Lead-Levelling**. N. P. Yao and J. R. Selman, Editors. A 1977 symposium. 412 pages, **\$13.00**.
- High Temperature Metal Halide Chemistry**. D. L. Hildenbrand and D. D. Cubicciotti, Editors. A 1977 symposium. 678 pages, **\$17.00**.
- Thin Film Phenomena—Interfaces and Interactions**. J. E. E. Baglin and J. M. Poate, Editors. A 1977 symposium. 525 pages, **\$14.00**.
- Semiconductor Characterization Techniques**. P. A. Barnes and G. A. Rozgonyi, Editors. A 1978 symposium. 532 pages, **\$16.00**.
- Industrial Water Electrolysis**. S. Srinivasan, F. J. Salzano, and A. R. Landgrebe, Editors. A 1978 symposium. 297 pages, **\$12.00**.
- Selected Topics in the History of Electrochemistry**. George Dubbner and J. H. Westbrook, Editors. A 1977 symposium. 523 pages, **\$11.00**.
- The Electrocatalysis of Fuel Cell Reactions**. W. E. O'Grady, S. Srinivasan, and R. F. Dudley, Editors. A 1978 workshop sponsored by the Division of Fossil Fuel Utilization, United States Department of Energy. 228 pages, **\$8.00**.
- Chemical Vapor Deposition**, Seventh International Conference. T. O. Sedgwick and H. Lydtin, Editors. A 1979 symposium. 658 pages, **\$16.00**.
- Laser and Electron Beam Processing of Electronic Materials**. C. L. Anderson, G. K. Celler, and G. A. Rozgonyi, Editors. A 1979 symposium. 560 pages, **\$13.00**.
- Thin Film Interfaces and Interactions**. J. E. E. Baglin and J. M. Poate, Editors. A 1979 symposium. 536 pages, **\$16.00**.
- Electrode Processes**. S. Bruckenstein, J. D. E. McIntyre, B. Miller, and E. Yeager, Editors. A 1979 symposium. 500 pages, **\$21.00**.
- Power Sources for Biomedical Implantable Applications and Ambient Temperature Lithium Batteries**. B. B. Owens and N. Margalit, Editors. A 1979 symposium. 652 pages, **\$18.00**.
- Electronic and Optical Properties of Polycrystalline or Impure Semiconductors and Novel Silicon Growth Methods**. K. V. Ravi and B. O'Mara, Editors. A 1980 symposium. 280 pages, **\$15.00**.
- Electron and Ion Beam Science and Technology**, Ninth International Conference. R. Bakish, Editor. A 1980 symposium. 672 pages, **\$28.00**.
- Lithium Nonaqueous Battery Electrochemistry**. E. B. Yeager, B. Schumm, Jr., G. Blomgren, D. R. Blankenship, V. Leger, and J. Akridge, Editors. A 1980 workshop. 328 pages, **\$18.00**.
- Plasma Processing**. R. G. Frieser and C. J. Mogab, Editors. A 1980 symposium. 360 pages, **\$20.00**.
- Ion Exchange: Transport and Interfacial Properties**. R. S. Yeo and R. P. Buck, Editors. A 1980 symposium. 396 pages, **\$15.00**.
- Materials and New Processing Technologies for Photovoltaics**. J. A. Amick, E. Sirtl, P. Rai-Choudhury, and J. P. Dismukes, Editors. A 1980 symposium. 368 pages, **\$14.00**.
- Lithium Batteries**. H. V. Venkatesetty, Editor. A 1980 symposium. 516 pages, **\$26.00**.
- Semiconductor Silicon 1981**. H. R. Huff, R. J. Kriegler, and Y. Takeishi, Editors. A 1981 symposium. 1064 pages, **\$25.00**.
- Electrocrystallization**. R. Weil and R. G. Barradas, Editors. A 1981 symposium. 352 pages, **\$13.00**.
- Chemical Vapor Deposition**, Eighth International Conference. J. M. Blocher, Jr., G. E. Vuillard, and G. Wahl, Editors. A 1981 symposium. 836 pages, **\$30.00**.
- Corrosion and Corrosion Protection**. R. P. Frankenthal and F. Mansfeld, Editors. A 1981 symposium. 304 pages, **\$10.00**.
- Third International Symposium on Molten Salts**. G. Mamanov, M. Blander, and G. P. Smith, Editors. A 1981 symposium. 600 pages, **\$23.00**.



November 1981

## ELECTROCHEMICAL SCIENCE AND TECHNOLOGY

### EDITOR

Norman Hackerman  
Jackie Bourne, Assistant to the Editor

### DIVISIONAL AND GROUP EDITORS

#### BATTERY

R. J. Brodd  
Elton J. Cairns  
G. F. Nordblom

C. Joseph Venuto  
J. L. Weininger

#### CORROSION

J. R. Ambrose  
J. W. Faust, Jr.  
R. P. Frankenthal  
Jerome Kruger  
D. D. MacDonald

Florian Mansfeld  
E. McCafferty  
Ken Nobe  
W. H. Smyrl

#### DIELECTRICS AND INSULATION

Robert S. Alwitt  
Rudolf G. Frieser  
Dennis Hess

T. W. Hickmott  
George L. Schnable

#### ELECTRODEPOSITION

Ugo Bertocci  
Huk Y. Cheh

Y. Oknaka  
Mordechai Schlesinger

#### ELECTRONICS

Ephraim Banks  
D. M. Brown  
Ted F. Cizak  
George R. Cronin  
John A. DeLuca  
Murray Gershenzon  
James S. Harris  
Simon Larach  
David L. Nelson

Ernest Paskell  
Bertram Schwartz  
Frederic W. Schwetmann  
Thomas O. Sedgwick  
Melvin Tecotzky  
C. C. Wang  
P. Wang  
J. M. Woodall

#### ELECTROTHERMICS AND METALLURGY

William A. Adams  
Joan B. Berkowitz  
Lee P. Hunt  
V. K. Kapur

R. A. Rapp  
David A. Shores  
Gene F. Wakefield  
Jack H. Westbrook

#### High Temperature Science and Technology

Leo Brewer  
Daniel Cubicciotti

E. D. Cater

#### ENERGY TECHNOLOGY GROUP

S. Srinivasan

Lee F. Donaghey

#### INDUSTRIAL ELECTROLYTIC

Richard C. Alkire

Scott Lynn

#### ORGANIC AND BIOLOGICAL ELECTROCHEMISTRY

Martin Blank  
M. Dale Hawley

Stanley Wawzonek

#### PHYSICAL ELECTROCHEMISTRY

M. J. Dignam  
Gregory C. Farrington  
David S. Ginley  
Gleb Mamantov  
Barry Miller  
Robert A. Osteryoung

David K. Roe  
C. W. Tobias  
F. G. Will  
Ronald H. Wilson  
M. S. Wrighton

News Editor—Jack H. Westbrook

Book Review Editor—Julius Klerer

### JOURNAL OF THE ELECTROCHEMICAL SOCIETY

(USPS 284-140)  
ISSN 0013-4651

The JOURNAL OF THE ELECTROCHEMICAL SOCIETY (USPS 284-140) is published monthly by The Electrochemical Society, Inc. at 215 Canal St., Manchester, N.H. 03108. The address for the Executive Offices, Editorial and Advertising Office, and Circulation Department of The Electrochemical Society, Inc., is 10 South Main St., Pennington, N.J. 08534-2896. Subscription to members as part of membership service; subscription to nonmembers \$80.00 plus \$5.00 for postage outside U.S. and Canada. Single copies \$4.00 to members, \$7.00 to nonmembers. © Copyright 1981 by The Electrochemical Society, Inc. Second Class Postage paid at Pennington, New Jersey and at additional mailing offices.

POSTMASTER: Send address changes to THE ELECTROCHEMICAL SOCIETY, INC., 10 South Main St., Pennington, N.J. 08534-2896.

### TECHNICAL PAPERS

- |  |  |
|--|--|
| J. Ahmad<br>T. H. Nguyen<br>R. T. Foley<br>... 2257                            | Evaluation of Organic Acids as Fuel Cell Electrolytes  |
| B. E. Conway<br>D. M. Novak<br>... 2262  | Electrochemical Reactivity of Strong Sulfuric Acid: Some Unusual Behavior at Pt Electrodes   |
| G. T. Burstein<br>R. C. Newman<br>... 2270                                     | Reactions of Scratched Copper Electrodes in Aqueous Solutions  |
| G. Mengoli<br>P. Bianco<br>S. Daolio<br>M. T. Munari<br>... 2276               | Protective Coatings by Anodic Coupling Polymerization of o-Allylphenol   |
| M. G. Chu<br>J. McBreen<br>G. Adzic<br>... 2281                                | Substrate Effects on Zinc Deposition from Zincate Solutions<br>I. Deposition on Cu, Au, Cd, and Zn   |
| J. McBreen<br>M. G. Chu<br>G. Adzic<br>... 2287                                | Substrate Effects on Zinc Deposition from Zincate Solutions<br>II. Deposition on Pb, Ti, Sn, and In  |
| A. K. Agrawal<br>A. E. Austin<br>... 2292                                      | Electrodeposition of Silicon from Solutions of Silicon Halides in Aprotic Solvents   |
| H. J. Pearson<br>G. T. Burstein<br>R. C. Newman<br>... 2297                    | Resistance to Flow of Current to Scratched Electrodes  |
| J. H. Kennedy<br>S. M. Stuber<br>... 2303                                      | Conductivity of Beta-Alumina Highly Doped with Iron  |
| F. R. Foulkes<br>J. W. Smith<br>R. Kalia<br>D. W. Kirk<br>... 2307             | Effects of Cadmium Impurities on the Electrowinning of Zinc  |
| F. Hine<br>M. Yasuda<br>K. Fujita<br>... 2314                                  | Effects of the Brine Impurities on the Cell Performance of the Diaphragm-Type Chlor-Alkali Cell  |
| B. MacDougall<br>M. J. Graham<br>... 2321                                      | Growth of Thick Anodic Oxide Films on Nickel in Borate Buffer Solution   |
| G. Hodes<br>J. Manassen<br>D. Cahen<br>... 2325                                | Effect of Surface Etching and Morphology on the Stability of CdSe/S <sub>z</sub> Photoelectrochemical Cells  |
| D. S. Newman<br>R. R. Rhinebarger<br>D. Siconolfi<br>O. A. Banjoko<br>... 2331 | The Relationship of Transport Properties and <sup>1</sup> H-NMR Spectra to the Structure of Molten Methylpyridinium Halides  |
| C. L. Gardner<br>D. T. Fouchard<br>W. R. Fawcett<br>... 2337                   | The Kinetics and Mechanism of the Electroreduction of Sulfur Dioxide in Nonaqueous Media<br>I. Reduction in Solutions of Tetraethylammonium Perchlorate in N,N-Dimethylformamide |
| C. L. Gardner<br>D. T. Fouchard<br>W. R. Fawcett<br>... 2345                   | The Kinetics and Mechanism of the Electroreduction of Sulfur Dioxide in Nonaqueous Media<br>II. Effects of Electrolyte and Solvent on the Mechanism of Reduction                 |
| I. Uchida<br>H. Urushibata<br>S. Toshima<br>... 2351                           | Electrocatalysis for Chlorine Electrode Reaction on RuO <sub>2</sub> Electrode in NaAlCl <sub>4</sub> Melt   |
| M. E. Langmuir<br>P. Hoenig<br>R. D. Rauh<br>... 2357                          | Electrochemical Photovoltaic Cells Based on n-GaAs in Propylene Carbonate  |

# ELECTROCHEMICAL SOCIETY

Vol. 128 • No. 11

R. Noufi  
D. Tench  
L. F. Warren  
... 2363

Photoelectrochemical Evaluation of the n-CdSe/Methanol/  
Ferro-Ferricyanide System

## TECHNICAL NOTES

F. M. Donahue  
... 2366

Kinetics of Electroless Copper Plating  
V. Mass Transport at Cylindrical Surfaces

R. Driver  
... 2367

Electrodeposition of Palladium on Iron and Steel for Elec-  
trochemical Hydrogen Permeation Studies

J. R. Wilson  
S.-M. Park  
... 2369

Dependence of Flatband Potentials of n-TiO<sub>2</sub> on Electro-  
lytes and Electrolyte Concentrations

J. H. Kennedy  
M. Anderman  
R. Shinar  
... 2371

Photoactivity of Polycrystalline  $\alpha$ -Fe<sub>2</sub>O<sub>3</sub> Electrodes Doped  
with Group IVA Elements

## SOLID-STATE SCIENCE AND TECHNOLOGY

### TECHNICAL PAPERS

F. Yamamoto  
S. Yamakawa  
M. Wagatsuma  
... 2374

Environmental Stability and Failure Mechanisms of Chro-  
mated Lead/Tin Alloy Joints Bonded with an Ethylene-  
Acrylic Acid Copolymer  
I. Acidic Conditions

F. Yamamoto  
S. Yamakawa  
S. Tsuru  
... 2379

Environmental Stability and Failure Mechanisms of Chro-  
mated Lead/Tin Alloy Joints Bonded with an Ethylene-  
Acrylic Acid Copolymer  
II. Alkaline Conditions

J. L. Stakebake  
... 2383

Kinetics for the Reaction of Hydrogen with a Plutonium-1  
Weight Percent Gallium Alloy Powder

F. T. J. Smith  
S. L. Lyu  
... 2388

Effects of Heat-Treatment on Indium-Tin Oxide Films

K. Carl  
J. A. M. Dikhoff  
W. Eckenbach  
H. G. Junginger  
... 2395

On the Limits of the Filter Concept for Color TV Screens

S. Inoue  
N. Toyokura  
T. Nakamura  
H. Ishikawa  
... 2402

Phosphorus-Doped Molybdenum Silicide Films for LSI Ap-  
plications

J. S. Blakemore  
R. S. Mand  
E. H. Wishnow  
... 2410

Shaping of Bulk Semiconductor Samples by Photolithog-  
raphy and Chemical Etching

L. M. Ephrath  
D. J. DiMaria  
F. L. Pesavento  
... 2415

Parameter Dependence of RIE Induced Radiation Damage  
in Silicon Dioxide

D. V. Morgan  
H. Ohno  
C. E. C. Wood  
L. F. Eastman  
J. D. Berry  
... 2419

Ion Beam Analysis of Molecular Beam Epitaxy InAlAs/  
InGaAs Layer Structures

A. K. Ray  
A. Reisman  
... 2424

Plasma Oxide FET Devices

Y. Iida  
K. Mori  
... 2429

A Modified SEM Type EB Direct Writing System and Its  
Application on MOS LSI Fabrication

K. Suzuki  
J. Matsui  
T. Ono  
Y. Saito  
... 2434

MOS Device Fabrication Using X-Ray Lithography

## DIVISION AND GROUP OFFICERS

### Battery Division

John Pierson, Chairman  
Theodore Katan, Vice-Chairman  
Gene Gagnon, Secretary-Treasurer  
General Motors Corp.  
Research Laboratories, Dept. 37  
12 Mile and Mounds Rds.  
Warren, Mich. 48090

### Corrosion Division

Robert P. Frankenthal, Chairman  
Florian Mansfeld, Vice-Chairman  
Robert A. Rapp, Secretary-Treasurer  
Dept. of Metallurgical Engineering  
Ohio State University  
116 West 19th Ave.  
Columbus, Oh. 43210

### Dielectrics and Insulation Division

James A. Amick, Chairman  
Werner Kern, Vice-Chairman  
John L. Maurer IV, Treasurer  
Laura E. Rothman, Secretary  
IBM Corp.  
Zip 48A  
Hopewell Junction, N.Y. 12533

### Electrodeposition Division

Richard Sard, Chairman  
Thomas Franklin, Vice-Chairman  
Lubomyr Romankiw, Secretary-Treasurer  
IBM T. J. Watson Research Center  
P.O. Box 218  
Yorktown Heights, N.Y. 10598

### Electronics Division

Ronald E. Enstrom, Chairman  
Edward H. Nicollan, Vice-Chairman  
(Semiconductors)  
Martin R. Royce, Vice-Chairman (Luminescence)  
F. N. Schwetzmann, Vice-Chairman (New Electronic  
Technologies)  
Patricia L. Castro, Treasurer  
Carlton M. Osburn, Secretary  
IBM T. J. Watson Research Center  
P.O. Box 218  
Yorktown Heights, N.Y. 10598

### Electrothermics and Metallurgy Division

William A. Adams, Jr., Chairman  
Lee P. Hunt, Senior Vice-Chairman  
Wayne Worrell, Junior Vice-Chairman  
Frederick S. Pettit, Secretary-Treasurer  
University of Pittsburgh  
848 Benedum Hall  
Pittsburgh, Pa. 15261

### Energy Technology Group

James McBreen, Chairman  
Arthur J. Nozik, Vice-Chairman  
A. J. Appleby, Secretary  
Electric Power Research Institute  
P.O. Box 10412  
Palo Alto, Calif. 94303

### Industrial Electrolytic Division

Leonard Nanis, Chairman  
Morris Grotheer, Vice-Chairman  
Robert Karpiuk, Secretary-Treasurer  
Dow Chemical Co.  
Functional Products and Systems  
2020 Dow Center  
Midland, Mich. 48640

### Organic and Biological Electrochemistry Division

John H. Wagenknecht, Chairman  
Martin Blank, Vice-Chairman  
Petr Zuman, Secretary-Treasurer  
Dept. of Chemistry  
Clarkson College of Technology  
Potsdam, N.Y. 13676

### Physical Electrochemistry Division

Elton J. Cairns, Chairman  
Robert A. Osteryoung, Vice-Chairman  
Larry R. Faulkner, Secretary-Treasurer  
Dept. of Chemistry  
University of Illinois  
Urbana, Ill. 61801



## SOCIETY OFFICERS AND STAFF

**Ralph J. Brodd, President**  
INCO Electro Energy  
5 Penn Center Plaza  
Philadelphia, Pa. 19103

**Frederick J. Strieter, Vice-President**  
Texas Instruments, Inc.  
7814 Fallmeadow Lane  
Dallas, Texas 75240

**J. Bruce Wagner, Vice-President**  
Center for Solid State Science  
Arizona State University  
Tempe, Ariz. 85281

**Paul C. Milner, Vice-President**  
Bell Laboratories  
Room 1D-259  
Murray Hill, N.J. 07974

**Forrest A. Trumbore, Secretary**  
Bell Laboratories  
Room 1E-208  
Murray Hill, N.J. 07974

**John L. Griffin, Treasurer**  
Research Laboratories  
General Motors Corporation  
General Motors Technical Center  
Warren, Mich. 48090

**V. H. Branneky, Executive Secretary**  
The Electrochemical Society, Inc.  
10 South Main Street  
Pennington, N.J. 08534-2896

**Donna Kimberlin, Administrative Assistant**  
The Electrochemical Society, Inc.  
10 South Main Street  
Pennington, N.J. 08534-2896

### PUBLICATION STAFF

Sarah A. Kilfoyle, **Publication Editor**  
Annette R. Van Deusen, **Assistant Publication Editor**

### PUBLICATION COMMITTEE

Forrest A. Trumbore  
Norman Hackerman  
Newton Schwartz  
Glenn W. Cullen  
Rudolf Keller  
Halina S. Wroblowa  
Robert P. Frankenthal  
Rudolf G. Frieser

Manuscripts submitted to the JOURNAL should be sent in triplicate to the Editorial Office at 10 South Main Street, Pennington, N.J. 08534-2896. They should conform to the revised "Instructions to Authors" available from Society Headquarters. Manuscripts so submitted, as well as papers presented before a Society technical meeting, become the property of the Society and may not be published elsewhere in whole or in part without written permission of the Society. Address such requests to the Editor.

The Electrochemical Society does not maintain a supply of reprints of papers appearing in its JOURNAL. A photoprint copy of any particular paper may be obtained from University Microfilms, Inc., 300 N. Zeeb St., Ann Arbor, Mich. 48106.

Inquiries regarding positive microfilm copies of issues should be addressed to University Microfilms, Inc., 300 N. Zeeb St., Ann Arbor, Mich. 48106.

Walter J. Johnson, Inc., 355 Chestnut St., Norwood, N.J. 07648, have reprint rights to out-of-print volumes of the JOURNAL, and also have available for sale back volumes and single issues with the exception of the last two calendar years.

The JOURNAL OF THE ELECTROCHEMICAL SOCIETY combines the JOURNAL and TRANSACTIONS OF THE ELECTROCHEMICAL SOCIETY. Statements and opinions given in articles and papers in the JOURNAL OF THE ELECTROCHEMICAL SOCIETY are those of the contributors, and The Electrochemical Society, Inc. assumes no responsibility for them.

Claims for a missing issue should be reported within 60 days of normal delivery date to the Circulation Dept., The Electrochemical Society, Inc., 10 South Main Street, Pennington, N.J. 08534-2896.

Notice of a change in address should be sent to the Circulation Dept., The Electrochemical Society, Inc., 10 South Main Street, Pennington, N.J. 08534-2896. Include the mailing label or the number from the mailing label from your previous issue of the JOURNAL to ensure proper identification.

## SOLID-STATE SCIENCE (Cont.)

**E. D. Bourret**  
**J. J. Favier**  
**O. Bourrel**  
... 2437

Measurement of the Diffusion Coefficient of Gallium in Molten Germanium

**F. Morin**  
... 2439

A Mathematical Assessment of Chemical Diffusion Measurements in Transition Metal Oxides

**G. Bernard**  
**G. Constant**  
**R. Feurer**  
... 2447

Comparison Between C.V.T. of Titanium Diboride by Different Transport Agents: Experimental Results and Application of Two Thermodynamic Models

**S. Kashu**  
**K. Watanabe**  
**M. Nagase**  
**C. Hayashi**  
**Y. Yoneda**  
... 2453

Vacuum Plasma Electron Beam Melting of Reactive and Refractory Metals and Their Alloys

**A. K. Ray**  
**A. Reisman**  
... 2460

The Formation of SiO<sub>2</sub> in an RF Generated Oxygen Plasma I. The Pressure Range Below 10 mTorr

**A. Reisman**  
**A. K. Ray**  
... 2466

The Formation of SiO<sub>2</sub> in an RF Generated Oxygen Plasma II. The Pressure Range Above 10 mTorr

**S. A. Shrivashankar**  
**R. Aragon**  
**H. R. Harrison**  
**C. J. Sandberg**  
**J. M. Honig**  
... 2472

Preparation and Electrical Properties of V<sub>2</sub>O<sub>5</sub> Single Crystals of Controlled Stoichiometry

**F. P. Koffyberg**  
**F. A. Benko**  
... 2476

p-Type NiO as a Photoelectrolysis Cathode

**D. Walton**  
**B. Ely**  
**G. Elliott**  
... 2479

Investigations into the Electrochromism of Lutetium and Ytterbium Diphthalocyanines

## TECHNICAL NOTE

**L. Ozawa**  
... 2484

Excitation into Charge Transfer Band of Y<sub>2</sub>O<sub>3</sub>:S:Eu

## ACCELERATED BRIEF COMMUNICATIONS

**T. A. Ramanarayanan**  
... 2487

Determination of the Measurable Low P<sub>O<sub>2</sub></sub> Limits of Oxygen Ion-Conducting Solid Electrolytes

**W. Siripala**  
**M. Tomkiewicz**  
... 2491

Direct Observation of Surface States at the TiO<sub>2</sub> Electrolyte Interface

## REVIEWS AND NEWS

### NEWS

... 485C



## Evaluation of Organic Acids as Fuel Cell Electrolytes

J. Ahmad,\* T. H. Nguyen,\* and R. T. Foley\*

Department of Chemistry, The American University, Washington, D.C. 20016

### ABSTRACT

The electrochemical behavior of methanesulfonic acid, ethanesulfonic acid, and sulfoacetic acid as fuel cell electrolytes was studied in a half-cell at various temperatures. The rate of the electro-oxidation of hydrogen at 115°C was very high in methanesulfonic acid. The rate of the electro-oxidation of propane in all three acids was low even at 135°C. Further, there is evidence for adsorption of these acids on the platinum electrode. It was concluded that anhydrous sulfonic acids are not good electrolytes; water solutions are required. Sulfonic acids containing unprotected carbon-hydrogen bonds are adsorbed on platinum and probably decompose during electrolysis. A completely substituted (fluorinated) sulfonic acid would be the preferred electrolyte.

This research was directed toward the investigation of improved fuel cell electrolytes suitable for the low temperature (under 200°C) fuel cell. A comprehensive review of the fuel cell electrolyte problem has been made (1). All of the inorganic acids, phosphoric, sulfuric, hydrochloric, perchloric, and hydrofluoric, as well as the "super acids," are deficient in one or more physical, chemical, or electrochemical property when evaluated in terms of the established characteristics of the "ideal" electrolyte (2). The desired properties of a fuel cell electrolyte are: (i) good ionic conduction; (ii) proper vapor pressure and viscosity characteristics; (iii) a good medium for the oxidation of the fuel; (iv) a good solvent for the active materials and for material transport; (v) chemically and electrochemically stable over the operating temperature range; (vi) noncorrosive to fuel cell container materials; (vii) proper surface tension characteristics (should not wet Teflon bonded electrodes or foam excessively when bubbled with gases).

The shortcomings of inorganic systems have suggested organic acids as alternatives, mainly because it was felt that the ability to alter the structure of an organic molecule allowed for a flexibility not available with inorganic systems. One important property, lacking, for example, in phosphoric acid, was the ability to support the electro-oxidation of propane. For future advancement in the fuel cell field, the development of a direct hydrocarbon-air fuel cell has a high priority.

The first organic acid studied in any depth and also giving promising results was trifluoromethanesulfonic acid used as its monohydrate (3-6). The important finding in this work was to demonstrate convincingly that the development of new improved electrolytes was a route, alternative to electrocatalysis, which could lead to improved fuel cell performance.

A review of the literature and an examination of the physical and chemical properties of certain organic sulfonic acids, namely, methanesulfonic, ethanesulfonic, and sulfoacetic, indicated that these acids warranted further investigation. The specific objective of the pres-

ent research was to evaluate these acids electrochemically, particularly their ability as electrolytes to support the electro-oxidation of hydrogen and propane.

### Experimental

*Preparation, purification, and analysis of electrolytes.*—Methanesulfonic acid, ethanesulfonic acid, and sulfoacetic acid, were evaluated as fuel cell electrolytes, and sulfuric acid and trifluoromethanesulfonic acid monohydrate were used as "reference" electrolytes. Some physical properties of the three acids compared to those of phosphoric acid, sulfuric acid, and trifluoromethanesulfonic acid monohydrate are given in Table I.

The methanesulfonic acid was Eastman 95% practical grade distilled twice under vacuum. The double-distilled acid was further cleaned by maintaining a fuel cell electrode at 0.5V for about 15 hr in the three-compartment cell in which the experiment was to be performed. The methanesulfonic acid was analyzed at three stages to follow the possible oxidation or reduction of the compound: (i) the as-supplied, 95% practical grade; (ii) the double-distilled material; and (iii) the 80% (water) solution of the double-distilled acid which was electrolyzed at 0.9V and 100°C for 20 hr. The analyses were conducted by obtaining nuclear magnetic resonance spectra and gas chromatograms. Analysis by infrared absorption was found to lack sufficient sensitivity. A Varian Associates A60 analytical NMR spectrometer was used for the proton analysis and a Bruker WP-80, <sup>13</sup>C NMR spectrometer, for the carbon analysis. Deuterium oxide (D<sub>2</sub>O) was used as a solvent and tetramethylsilane as an external standard. The tetramethylsilane peak was set at 0.00 ppm after properly phasing and maximizing the resolution and the spectra were run over a 1000 Hz range using a 250 sec sweep time. The gas chromatograms were obtained with a Hewlett-Packard 5830A Gas Chromatograph with a 18850A recorder. A 1% solution of the acid in ether was injected into the column (a 3% OV-225 column). A flame ionization detector was used to obtain a chromatogram of the acid. The experiment was programmed from 50° to 150°C with a 10% per min heating rate.

\* Electrochemical Society Active Member.

Key words: fuel cells, electrolytes, electro-oxidation.



Table I. Physical properties of fuel cell electrolytes

Compound	Melt- ing point	Boiling point	Solubility in water	Specific conduct- ance at 40°C ( $\Omega^{-1} \text{ cm}^{-1}$ )	Contact angle on Teflon (degrees)
Methanesulfonic acid, $\text{CH}_3\text{SO}_3\text{H}$	19-20	167/10 mm	Miscible in all proportions	0.019 (98 w/o)	93.59 (100%)
Ethanesulfonic acid, $\text{CH}_3\text{CH}_2\text{SO}_3\text{H}$	-17	123/1 mm	Very soluble	0.009 at 25°C (98 w/o)	
Sulfoacetic acid, $\text{HO}_2\text{S-CH}_2\text{-COOH}$	84-86	245d	Very soluble	0.464 (58% $\text{H}_2\text{O}$ solution)	90.15° (58% $\text{H}_2\text{O}$ solu- tion)
Phosphoric acid, $\text{H}_3\text{PO}_4$	42.35	$\frac{1}{2} \text{ H}_2\text{O}$ , 213	Very soluble	0.1381 (85% $\text{H}_2\text{O}$ solution)	>90 (58% $\text{H}_2\text{O}$ solution)
Sulfuric acid, $\text{H}_2\text{SO}_4$	10.36	338 (98.3%)	Miscible in all proportions	0.790 (50% $\text{H}_2\text{O}$ solution)	>90 (50% $\text{H}_2\text{O}$ solution)
Trifluoromethanesul- fonic acid, monohy- drate $\text{CF}_3\text{SO}_3\text{H} \cdot \text{H}_2\text{O}$	33.8	217-219	Miscible in all proportions	0.01122 (100% (40% $\text{H}_2\text{O}$ solution)	72.83 (100%)

The ethanesulfonic acid was supplied by Aldrich and Company, vacuum distilled to remove impurities, and further cleaned in the cell by electrolyzing at 0.5V with a cleaning electrode for about 15 hr.

The sulfoacetic acid was supplied by Eastman as black crystals in semi-solid form and 98% purity. The acid could be further purified by forming the Pb salt with  $\text{PbCO}_3$  and freeing the acid by precipitating PbS. However, the traces of sulfide that remained in solution poisoned the Pt electrode during the electrochemical experiments. The sulfoacetic acid of 98% purity was used in the electrochemical experiments described below.

**Electrochemical techniques.**—Two types of experiments were performed: (i) polarization studies with argon, hydrogen, and propane in the three electrolytes. The electrical apparatus, the three-compartment cell, the reference system, and the method of pretreatment of the gases have been described in previous publications (2). All potentials reported are *vs.* the dynamic hydrogen electrode (7); (ii) cyclic voltammetry experiments with apparatus and techniques previously described (6).

### Results and Discussion

**Methanesulfonic acid.**—In preliminary experiments the systems were calibrated with polarization curves obtained by the electro-oxidation of  $\text{H}_2$  in trifluoromethanesulfonic acid monohydrate over the temperature range of 80°–135°C and cyclic voltammetric scans in 4N sulfuric acid and in trifluoromethanesulfonic acid monohydrate. The results obtained from experiments with the monohydrate were similar to those previously reported in this laboratory (3) and the voltammetric sweeps in sulfuric acid were identical to those reported in the literature (8).

The polarization curves for argon, propane, and hydrogen in an 80%  $\text{CH}_3\text{SO}_3\text{H}$  solution at 115° and 135°C are given in Fig. 1. For hydrogen oxidation clear-cut limiting currents were observed, 78.8 and 108  $\mu\text{A}/\text{cm}^2$  at 115° and 135°C, respectively. There was no definite Tafel region in the hydrogen polarization curve. The oxidation currents for argon and propane increased with overvoltage. At an overvoltage of 0.3V the currents for Ar were 0.64 and 1.6  $\mu\text{A}/\text{cm}^2$  at 115° and 135°C, respectively, while for propane values of 5.5 and 7.5  $\mu\text{A}/\text{cm}^2$  were obtained. Above 0.65V the current density for Ar and propane increased rapidly and reached peak currents, or limiting currents at about 0.90V *vs.* DHE. At 135°C the peak currents were almost the same for both Ar and propane, suggesting that the oxidation current of the electrolyte, *per se*, exceeded that due to the electro-oxidation of propane.

The inspection of the cyclic voltammograms of the acid taken over a range of temperatures revealed some significant characteristics. At room temperature and up to 80°C, the hydrogen, double layer, and oxygen film

regions were well defined and separated in the positive going part of the curve. At 90°C a strong oxidizing peak at 1200 mV and a shoulder-like peak at 760 mV started to appear; at higher temperature (115° and 135°C) those peaks increased and the hydrogen structure began to lose its fine structure. But the most dramatic change was that, in the cathodic scan, the current crossed into the anodic current domain directly following the reduction of the Pt oxide. This must be characteristic of the presence of an electroactive species. Cyclic voltammograms at 26° and 115°C in Fig. 2 illustrate this behavior. To further study this phenomena, a background voltammogram with 4N  $\text{H}_2\text{SO}_4$  was run and then a few drops of methanesulfonic acid was added to the cell. A typical cyclic voltammogram for 4N  $\text{H}_2\text{SO}_4$  was obtained at 80°C (Fig. 3). After addition of a few drops of methanesulfonic acid it was observed that there was no change in the background

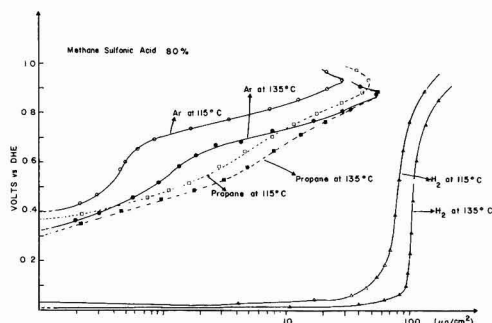


Fig. 1. Polarization curves for argon, propane, and hydrogen in an 80%  $\text{CH}_3\text{SO}_3\text{H}$  solution at 115° and 135°C.

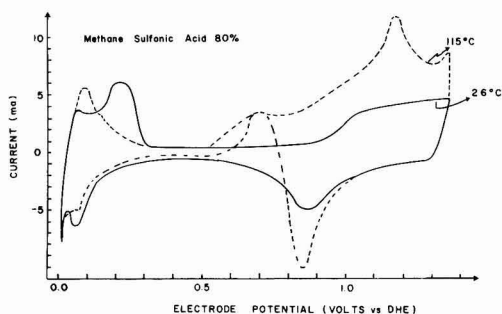


Fig. 2. Cyclic voltammograms in 80% solution of methanesulfonic acid at 26° and 115°C.

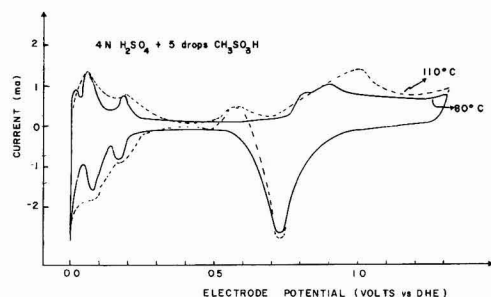


Fig. 3. Cyclic voltammogram in 4N  $\text{H}_2\text{SO}_4$  to which was added a few drops of  $\text{CH}_3\text{SO}_3\text{H}$ .

curve. However, when the solution was heated up to  $110^\circ\text{C}$ , the effect of methanesulfonic acid became apparent. A strong oxidizing peak at  $1.02\text{V}$  was then observed and in the reverse scan to the cathodic side, the current crossed over to the anodic area after the reduction of the platinum oxide.

From these observations, it is then concluded that methanesulfonic acid is dissociatively adsorbed



At sufficiently large potential, the radical is desorbed and contributes to the high oxidation current. Then, in the reverse scan, after the reduction of the oxide layer on Pt, a product of the higher potential electrolysis reaction is oxidized on the oxide-free platinum surface.

To explain some of these electrochemical results, the methanesulfonic acid was analyzed using  $^1\text{H}$  NMR,  $^{13}\text{C}$  NMR, and gas chromatography techniques, the last being most informative.

The  $^1\text{H}$  NMR spectra were recorded employing as-supplied, double-distilled, and electrolyzed samples. In these spectra two peaks were obtained: peak I, attributed to the  $-\text{CH}_3$  group and peak II, attributed to the combined effect of the sulfonic group and solvent. The position of peak II changes from sample to sample and the shift is tabulated in Table II. The presence of  $\text{H}_2\text{O}$  in the sample tends to shift the spectrum to a lower ppm value so the shift of peak II to  $5.2$  ppm is interpreted as the presence of a new structure.

The  $^{13}\text{C}$  NMR spectra were not particularly informative but seemed to indicate an impurity in all three samples.

These NMR spectra were run at  $60^\circ\text{C}$  (proton) and at room temperature (carbon). The gas chromatography analyzed the acid samples at elevated temperature (up to  $150^\circ\text{C}$ ). The chromatograms obtained from the double-distilled sample of methanesulfonic acid and the acid that had been electrolyzed at  $0.9\text{V}$  and  $100^\circ\text{C}$  for 20 hr are displayed in Fig. 4 and 5, respectively. It is apparent that the electrolysis at  $100^\circ\text{C}$  was effective in producing several fragments or new compounds. These analyses suggest that methanesulfonic acid is unstable at  $100^\circ\text{C}$  and  $0.9\text{V}$ .

Table II. The positions of the absorption peaks in the  $^1\text{H}$  NMR spectra of methanesulfonic acid samples

Spectrum	*Position of peak I (ppm)	*Position of peak II (ppm)
As-supplied sample	1.5	4.8
Double-distilled sample	1.5	4.55
Electrolyzed sample	1.5	5.2

\* These positions are over a  $1000$  Hz range using a  $250$  sec sweep time.

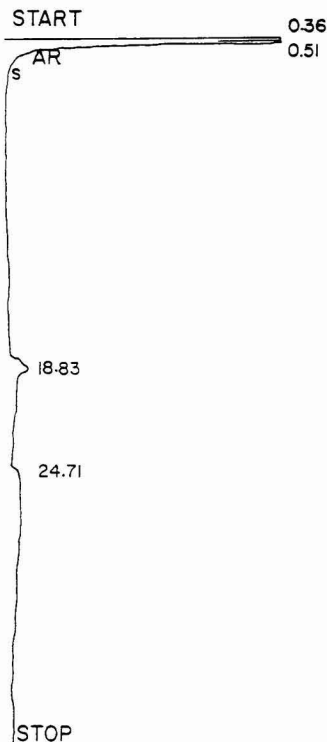


Fig. 4. Chromatogram obtained with a double-distilled sample of methanesulfonic acid.

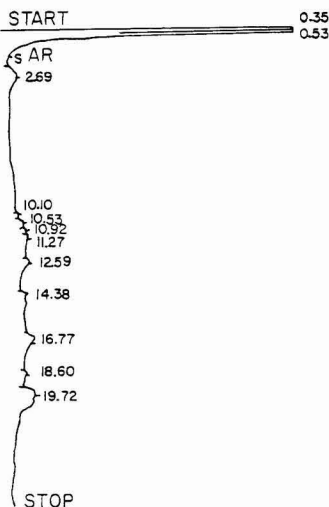


Fig. 5. Chromatograms obtained with a sample of methanesulfonic acid that had been electrolyzed at  $0.9\text{V}$  for 20 hr at  $100^\circ\text{C}$ .

**Ethanesulfonic acid.**—Polarization curves were obtained with Ar, propane, and  $\text{H}_2$  in a 50% acid- $\text{H}_2\text{O}$  solution of ethanesulfonic acid. At  $115^\circ\text{C}$ , the limiting-current for hydrogen was  $27.6 \mu\text{A}/\text{cm}^2$ , about half of the current obtained with methanesulfonic acid. Also, the polarization curve did not show a distinct Tafel region (Fig. 6). For propane and Ar, there were no



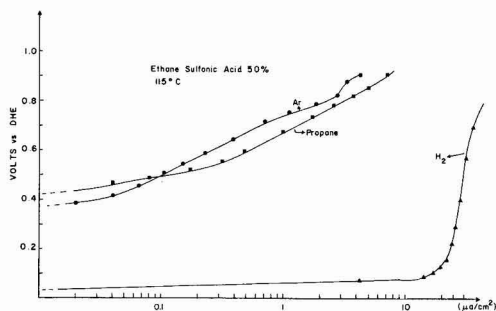


Fig. 6. Polarization curves for argon, propane, and  $H_2$  in 50% solution of ethanesulfonic acid at  $115^\circ C$ .

clear-cut limiting currents but the current density for propane was slightly higher than for Ar. At an overvoltage of 0.3V the current density for propane was  $1.2 \mu A \cdot cm^{-2}$  compared to  $0.65 \mu A \cdot cm^{-2}$  for Ar.

The cyclic voltammogram of the 50% acid solution at different temperature is shown in Fig. 7. It is interesting to note that at room temperature, ethanesulfonic acid exhibited electrochemical behavior similar to that of methanesulfonic acid at higher temperatures. This suggests that ethanesulfonic acid is strongly adsorbed on the platinum electrode surface. As we increased the temperature, it is observed that: (i) the oxidation peak-current increases; (ii) the Pt-oxide reduction current slightly decreases; (iii) the electro-oxidation current of the electroactive species increased; and (iv) the definition of the hydrogen peaks decreases and almost completely disappears above  $85^\circ C$ . From those observations, it is concluded that ethanesulfonic acid is strongly adsorbed on the Pt surface and at sufficiently high temperature, inhibits the hydrogen and oxidation reactions. This behavior appears to be characteristic of a platinum electrode in strong concentrated acidic electrolytes.

**Sulfoacetic acid.**—The polarization curves for argon, propane, and hydrogen in a 50% acid solution are shown in Fig. 8. The current density for hydrogen oxidation at an overvoltage of 0.3V was  $38 \mu A/cm^2$  at  $115^\circ C$ . The polarization curves for argon and propane did not exhibit a limiting current density but it can be remarked that the current obtained with propane was almost the same as with argon. The voltammogram for the acid shown in Fig. 9 did not show any special behavior. It did not appear that sulfoacetic acid is adsorbed on the Pt electrode from the study of the

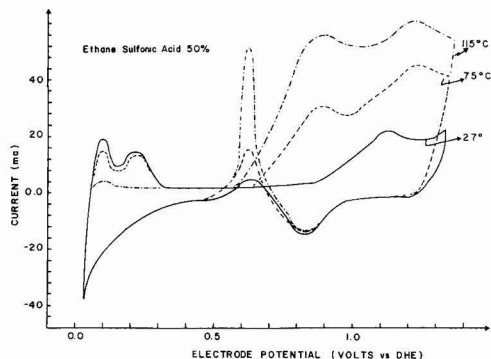


Fig. 7. Cyclic voltammogram in 50% solution of ethanesulfonic acid at  $27^\circ$ ,  $75^\circ$ , and  $115^\circ C$ .

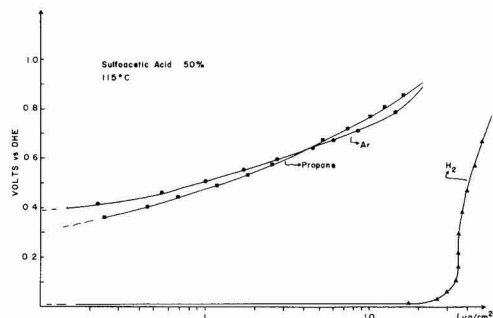


Fig. 8. Polarization curves for argon, propane, and  $H_2$  in 50% sulfoacetic acid solution at  $115^\circ C$ .

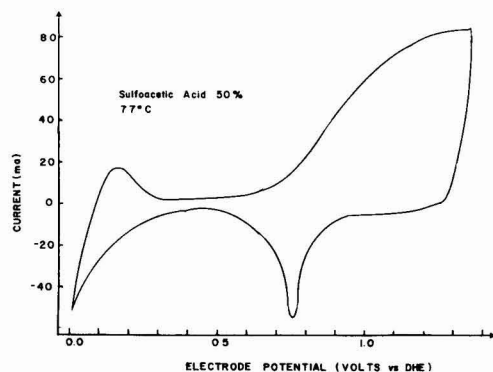


Fig. 9. Cyclic voltammogram in 50% solution of sulfoacetic acid at  $77^\circ C$ .

cyclic voltammogram at different temperature. However, it must be remarked that the commercially available sulfoacetic acid appears to be of uncertain quality to use as an electrolyte and no suitable method of purification has been worked out despite considerable effort to recrystallize the compound using conventional organic chemistry methods.

### Conclusions

The three electrolytes are compared by tabulating the current densities achieved with hydrogen, argon, and propane in Table III.

Certain conclusions may be drawn with regard to the three sulfonic acids. The polarization studies indicate that an electrolytic solution, 80% in methanesulfonic acid and 20% in  $H_2O$  supports high current densities with  $H_2$ , but shows little promise with propane. The results obtained with  $H_2$  agree with results obtained by Rebert *et al.* (9) in a study with platin-

Table III. Summary of current density values obtained in different electrolytes

Electrolyte	Current densities ( $\mu A/cm^2$ ) at 0.3V over potential					
	Hydrogen		Propane		Argon	
	$115^\circ C$	$135^\circ C$	$115^\circ C$	$135^\circ C$	$115^\circ C$	$135^\circ C$
Methanesulfonic acid, $CH_3SO_3H$	78.8	108	5.5	7.5	0.64	1.6
Ethanesulfonic acid, $C_2H_5SO_3H$	27.6		1.2		0.65	
Sulfoacetic acid, $HO_2SCH_2COOH$	38		3.3		6.4	
Trifluoromethanesulfonic acid, monohydrate $CF_3SO_3H \cdot H_2O$	122	296				

ized-platinum rotating disk electrodes. They found that at the same potential and comparable rotation speeds, methanesulfonic acid supports currents that are more than an order of magnitude higher than those obtainable in phosphoric acid. They did not study propane. The practical grade (95%) methanesulfonic acid darkens during electrolysis probably due to further decomposition. The cyclic voltammetry studies indicate that methanesulfonic acid is decomposed at elevated temperatures and high potentials. Analysis of this acid by NMR and gas chromatography also indicates that this acid decomposes into different fragments or forms new compounds during electrolysis, particularly at temperatures 100°C or above.

The polarization studies with ethanesulfonic acid indicate that this acid as an electrolyte does not support high current densities either with  $H_2$  or propane. Ethanesulfonic acid is also completely adsorbed on the Pt electrode. For these reasons this compound does not appear to be a promising fuel cell electrolyte.

From these results it is concluded that sulfonic acids, such as  $CH_3SO_3H$  or  $CH_3-CH_2-SO_3H$ , containing terminal methyl groups unprotected by fluorination, are strongly adsorbed on the platinum surface and decompose relatively easily during electrolysis. It now appears necessary that the sulfonic acid electrolytes to be evaluated in future studies should be properly substituted to protect the molecule against electrolytic oxidation or reduction.

During the course of the investigation it became apparent that it would be necessary to work with aqueous solutions rather than the anhydrous acids. The anhydrous acids are poor ionic conductors—the conduction process is achieved with hydrated protons. Further, there is evidence that many of these compounds are thermally unstable at temperatures over 100°C.

The commercially available sulfoacetic acid appears to be of uncertain quality to use as an electrolyte and no suitable method of purification has been worked out. Furthermore, the acid is chemically unstable in the 80°–115°C range.

#### Acknowledgment

The support of the U.S. Army Mobility Equipment Research and Development Command, Fort Belvoir, Virginia under Contract DAAK70-77-C-0080 is gratefully acknowledged.

Manuscript received June 8, 1981.

Any discussion of this paper will appear in a Discussion Section to be published in the June 1982 JOURNAL. All discussions for the June 1982 Discussion Section should be submitted by Feb. 1, 1982.

#### REFERENCES

1. R. T. Foley, "On the Properties of a Fuel Cell Electrolyte," Final Technical Report, July 10, 1978–January 15, 1979, Contract No. DAAK70-78-C-0128.
2. A. A. Adams and R. T. Foley, "Research on Electrochemical Energy Conversion Systems," Report No. 7, Final Technical Report on Contract No. DAAK02-72-C-0084, December 1975.
3. A. A. Adams and H. J. Barger, *This Journal*, **121**, 987 (1974).
4. A. A. Adams, R. T. Foley, and H. J. Barger, *ibid.*, **124**, 1228 (1977).
5. A. A. Adams and R. T. Foley, *ibid.*, **126**, 775 (1979).
6. T. Sarada, R. D. Granata, and R. T. Foley, *ibid.*, **125**, 1899 (1978).
7. J. Giner, *ibid.*, **111**, 376 (1964).
8. W. Bold and M. Breiter, *Electrochim. Acta*, **5**, 1223 (1964).
9. N. Rebert, B. G. Ateya, T. Poweigha, and L. G. Austin, *This Journal*, **127**, 2641 (1980).

# Electrochemical Reactivity of Strong Sulfuric Acid: Some Unusual Behavior at Pt Electrodes

B. E. Conway\* and D. M. Novak\*<sup>1</sup>

Chemistry Department, University of Ottawa, Ottawa, Ontario, Canada K1N 6N5

## ABSTRACT

In very strong, 98%, sulfuric acid cyclic-voltammetry experiments at Pt reveal unusual reduction and oxidation processes as distinct from those associated with electrodeposition and ionization of atomic H, and surface oxide formation and reduction, which are familiar in dilute aqueous solutions of H<sub>2</sub>SO<sub>4</sub> at Pt. No reduction processes are observed on a less electrocatalytic metal, Au, under the same conditions. Holding the potential of a Pt electrode near the H<sup>+</sup>/H<sub>2</sub> potential ( $E_H$ ) in 98% H<sub>2</sub>SO<sub>4</sub> gives rise to reduction of the acid, producing a species that is immediately chemisorbed and becomes oxidized in the adsorbed state in a following anodic potential sweep over the "surface oxide formation" potential region. In the succeeding cathodic sweep, a large cathodic current peak follows surface oxide reduction. By means of chemical simulation experiments, it is shown that the reduction behavior is accounted for first by formation of SO<sub>2</sub> or HSO<sub>3</sub><sup>-</sup> at potentials near  $E_H$ , followed by oxidation to a species, possibly adsorbed dithionate (S<sub>2</sub>O<sub>6</sub><sup>2-</sup>), or some other chemisorbed sulfur-oxygen species, in a following anodic sweep. This oxidation process cannot be from SO<sub>2</sub> or HSO<sub>3</sub><sup>-</sup> back to H<sub>2</sub>SO<sub>4</sub> or HSO<sub>4</sub><sup>-</sup> since, in the next cathodic sweep, a re-reduction occurs in a well-defined peak, a little positive to  $E_H$ . Experiments at a rotated Pt disk electrode enable distinctions to be made between processes associated with strongly bound chemisorbed species and other species that can be spun off into solution, giving diminished currents in successive cyclic voltammograms. Additions of small quantities of water diminish the reduction reaction observed in 98% H<sub>2</sub>SO<sub>4</sub>.

In the course of experiments (1) on the surface oxidation of Pt in nonaqueous media containing traces of water, we investigated the behavior of Pt electrodes in very strong 98% sulfuric acid. Some unusual and interesting bulk and surface electrochemical processes are found which are not observed in ordinary aqueous solutions of H<sub>2</sub>SO<sub>4</sub>. At the 98% level of concentration of H<sub>2</sub>SO<sub>4</sub>, the medium is essentially a nonaqueous solution with H<sub>3</sub>O<sup>+</sup> and HSO<sub>4</sub><sup>-</sup> ions as the electrolyte at about 1.1M concentration. Some higher, condensed sulfuric acid species, e.g., H<sub>2</sub>S<sub>2</sub>O<sub>7</sub>, are also present in traces (2).

Studies in very strong acid media are of interest in fuel-cell technology where acids such as H<sub>3</sub>PO<sub>4</sub> and CF<sub>3</sub>SO<sub>3</sub>H are used at ca. 85% concentrations, often at elevated temperatures.

As far as we are aware, no previous studies of the electrochemical surface reactivity of pure H<sub>2</sub>SO<sub>4</sub> to give chemisorbed decomposition products at electrode interfaces have been reported except in the work of Arvia *et al.* (3) who investigated electrochemical surface processes at Ir in 96% H<sub>2</sub>SO<sub>4</sub>. In this work, however, only the usual surface reactions of Ir are revealed with H adsorption and surface oxide formation regions being observed in the normal way, but with displacement of these two processes to more negative and more positive potentials, respectively, due to HSO<sub>4</sub><sup>-</sup> ion adsorption, as is known in more dilute solutions at Pt with SO<sub>4</sub><sup>2-</sup> (4) and HSO<sub>4</sub><sup>-</sup> ion (5), depending on concentration and pH.

An interesting study was also made by Arvia *et al.* (6) on the electrochemistry of fuming sulfuric acid containing various concentrations of SO<sub>3</sub> and small quantities of SO<sub>2</sub>, and comparatively on 97.4% H<sub>2</sub>SO<sub>4</sub> in the same paper. Most of this work was concerned with the steady-state current-potential behavior arising from reduction of SO<sub>3</sub> at stationary and rotated Pt electrodes, which gives rise to SO<sub>2</sub> and some S.

Also, the cathodic evolution of H<sub>2</sub> and the anodic decomposition to O<sub>2</sub> and persulfuric acid was investigated. The question of adsorbed species that might be involved in the reactions was not treated in this work. In work by Lal *et al.* (7-10) and by Loučka (11-13), however, adsorbed species from SO<sub>2</sub> solutions and S layers formed from H<sub>2</sub>S and SO<sub>2</sub> were recognized and investigated. As we discuss later, some of these results are relevant to the interpretation of the experiments in the present work.

Arvia *et al.*, in a series of papers (14), have also reported underpotential deposition of H and surface oxidation of Pt and Ir in KHSO<sub>4</sub> and NaHSO<sub>4</sub>/KHSO<sub>4</sub> melts.

In the present paper, we report some unusual reduction and oxidation processes at Pt in 98% H<sub>2</sub>SO<sub>4</sub> at ordinary temperatures, studied by means of the linear potentiodynamic sweep method and related procedures. Attempts to identify the principal intermediates involved were made by means of chemical simulation experiments using likely species such as SO<sub>2</sub>, dithionite, and dithionate.

## Experimental

**Method.**—A conventional system for applying single and repetitive linear potential sweeps to an electrode was used, employing the equipment and procedure referred to in previous publications (5, 15, 16). In the cyclic-voltammetry mode, the system enables a series of sweeps in an anodic or cathodic direction to be made to successively more positive or more negative potentials, respectively, using the triggering capability for sweep reversal at a constant sweep rate which is provided by a Servomex LF 141 function generator operating on a Wenking potentiostat. This system also allows the potential to be held conveniently at a controlled fixed value (potential "holding" experiment) for recorded times before a following anodic or cathodic sweep is initiated. This type of apparatus enabled current-density (*i*) vs. potential (*V*) profiles to be recorded, as described previously by us

\* Electrochemical Society Active Member.

<sup>1</sup> Present address: Research Laboratories, Eldorado Nuclear Limited, Tunney's Pasture, Ottawa, Canada.



(1, 5, 16) and by other authors, e.g., Ref. (15). Most experiments were conducted at 298 K at a Pt disk electrode (Pine Instrument Company) that could be rotated when desired. Some comparative experiments were made at a high purity grade Au wire.

**H<sub>2</sub>SO<sub>4</sub> electrolyte.**—B.D.H. Aristar pure (98%) H<sub>2</sub>SO<sub>4</sub> was used as the electrolyte, initially without dilution. This is the acid which gives, at ordinary concentrations (0.5 ~ 1M), the best clean aqueous solution of H<sub>2</sub>SO<sub>4</sub> for cyclic-voltammetry experiments at Pt, as we have described in earlier papers (5, 16). In some experiments, where controlled small additions of water are made, pyrodistilled water (16) was used.

**Cell.**—A small 3-compartment cell capable of being fitted to a rotating disk electrode system was used, as described previously (1). It was provided with a compartment in which either a reversible H<sub>2</sub>/H<sup>+</sup> electrode or an ( $\alpha + \beta$ )PdH electrode was situated.

**Reference electrodes.**—A platinized-Pt hydrogen electrode was employed as the reference electrode directly in the strong H<sub>2</sub>SO<sub>4</sub>. In the 98% H<sub>2</sub>SO<sub>4</sub>, the potentials are not true reversible potentials but rather steady mixed potentials due to the slow electrocatalytic reduction reaction involving H<sub>2</sub>SO<sub>4</sub> which is the subject of this paper. Very satisfactorily steady potentials ( $\pm < 1$  mV) could, however, be maintained over an hour or so. In some experiments the ( $\alpha + \beta$ )PdH reference electrode was used. Potentials on all graphs to be shown below are on the scale of the H<sub>2</sub>/H<sup>+</sup> electrode in the same solution as that in which the working Pt or Au (see below) electrodes were studied. This scale is designated for convenience by E<sub>H</sub>.

**Potential programs.**—The potential-time programs shown in Fig. 1 were applied to the working Pt electrode in 98% H<sub>2</sub>SO<sub>4</sub> in order to investigate the nature of the observed electrochemical reactivity of H<sub>2</sub>SO<sub>4</sub> and to distinguish the currents from those arising in the normal way [cf. (5, 15, 16)] from underpotential deposition of H, or OH and O species; the potentials employed were adjusted on the function generator and the potentiostat and read with an accuracy of 1 mV on a high impedance digital millivoltmeter. At all times, the latter instrument was used to monitor numerically the various potentials involved at sweep

reversal and in constant potential holding experiments (see below).

(i) **Cyclic-voltammetry at 70 mV sec<sup>-1</sup>.**—Cyclic-voltammetry experiments were first made by means of a repetitive symmetrical triangular sweep, referred to as program (i) (Fig. 1). Several potential limits to the cathodic and anodic sweeps were employed and are defined on the experimental *i* vs. *V* profiles shown in Fig. 2a and b and Fig. 3a and b. Experiments in this mode established the normal *i* vs. *V* profiles for the surface processes at Pt in 98% H<sub>2</sub>SO<sub>4</sub>, as shown in Fig. 2 and 3.

(ii) **Cyclic-voltammetry experiments over progressively decreasing ranges of potential.**—These were made by reversing the sweep at successively increas-

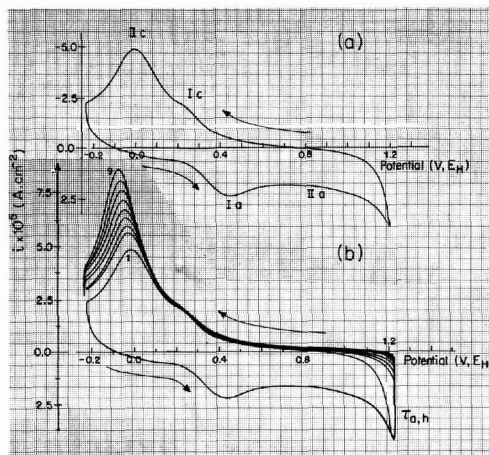


Fig. 2. (a) Cyclic-voltammetry *i* vs. *V* profiles for Pt in 98% H<sub>2</sub>SO<sub>4</sub> at 70 mV sec<sup>-1</sup> at 298 K, [program (i)]. Designations of principal anodic and cathodic processes are shown. (b) As in Fig. 2 (a) but with holding the potential constant at the positive end of the anodic sweep giving rise to growth of the surface oxide at Pt (70 mV sec<sup>-1</sup>, 298 K). Curves 1 to 9 for  $\tau_{h,a} = 0, 5, 10, 15, 20, 60, 120, 240,$  and 360 sec.

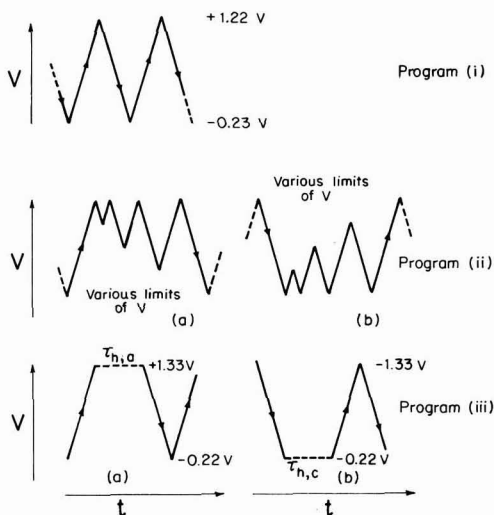


Fig. 1. Potential programs

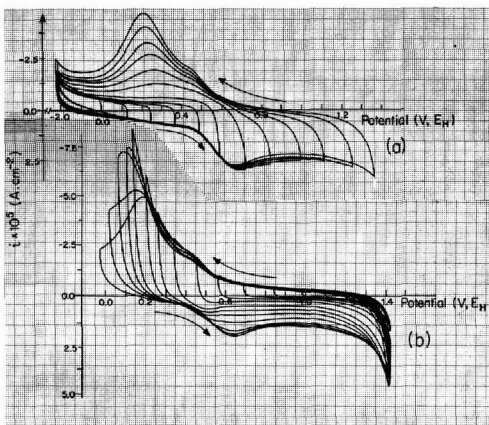


Fig. 3. (a) Cyclic-voltammetry *i* vs. *V* profiles for Pt in 98% H<sub>2</sub>SO<sub>4</sub> at 70 mV sec<sup>-1</sup> at 298 K showing the effects of reversing the direction of potential sweep at successively more positive potentials in the anodic sweep direction [program (iib)]. (b) As in Fig. 3 (a), but showing the effects of reversing the direction of potential sweep at successively less positive potentials in the cathodic sweep direction [program (iia)].

ing potentials in the anodic or successively decreasing potentials in the cathodic sweep directions. These procedures are illustrated in Fig. 1 and are referred to as programs (iib) and (iia), respectively. These procedures give information on what processes observed in, e.g., a cathodic sweep (where a current peak arises) are conjugate to processes in the prior anodic sweep, or vice-versa, as shown in Fig. 3a and b. The changing potential limits in the programs (iia) and (iib) are evident from the potentials of reversal of the series of curves shown in Fig. 3a, b.

(iii) *Potential holding experiments.*—Holding the potential at either the end of an anodic sweep for a time  $\tau_{h,a}$  [program (iia)] or at the end of a cathodic sweep for a time,  $\tau_{h,c}$  [program (iib)] followed by initiation of a further cathodic or anodic sweep, respectively, enabled the formation and reactivity of products of slow processes to be followed. It was in these experiments, with cathodic holding of the potential near ( $-0.2V E_H$ ) the steady-state hydrogen electrode potential (see above), that the unusual reactivity of  $H_2SO_4$  was observed. The potentials at which cathodic or anodic holding for times  $\tau_h$  was maintained are shown later in the respective figures.

After each change of conditions, e.g., potential holding, the electrode was allowed to return to the reproducible state generated initially as in section (i) above by repetitive anodic/cathodic cycling [program (i)] until the initial *i vs. V* curve, corresponding to the cyclic-voltammetry profile shown in Fig. 2, was recovered. This *i vs. V* profile, under continuous cycling, was exactly reproducible from one experiment to another and between different Pt electrodes with normalization to the same real area. It was also virtually identical with the initial anodic and cathodic *i vs. V* profile observed when an electrode, precycled in 1M aq  $H_2SO_4$ , was transferred to the 98%  $H_2SO_4$ .

*Real electrode area.*—The real area of the disk Pt electrode used in most of the experiments was determined, in the usual way, from the charge for desorption of the underpotential deposited H layer measured separately in 0.05M aq  $H_2SO_4$ , using the figure  $2.10 C m^{-2}$  for the H monolayer at Pt [cf. (17)]. After several days' experiments in the 98%  $H_2SO_4$ , the real area of the electrode determined by the H accommodation remained unchanged within 0.5%.

*Experiments at Au.*—In order to establish how specific the observed  $H_2SO_4$  reduction was to Pt, comparative experiments were carried out on a noble metal less electrocatalytic than Pt, viz., Au.

*Reflectance experiments.*—In order to see if chemisorbed intermediate species which arise, as shown later, in the reduction of  $H_2SO_4$  can be distinguished from other, e.g., surface oxide, species on the electrode, relative reflectivities ( $\Delta R/R$ ) were measured in the cyclic-voltammetry experiments using the apparatus and procedures previously described (18).

## Results and Discussion

*Phenomenology of the effects.*—Cyclic-voltammetry and potential-holding experiments: programs (i) and (iii).—The unusual electrochemical reactivity of  $H_2SO_4$  at Pt arises in the cathodic holding experiments, (iib). However, it is first necessary to show the normal behavior of a Pt electrode in 98%  $H_2SO_4$  under conditions where the unusual reactions either do not take place significantly in the time scale of an anodic/cathodic sweep at 25 mV  $sec^{-1}$  or at all, if the potential range in the sweep is adjusted appropriately.

Figure 2a shows the *i vs. V* profiles for a Pt electrode in 98%  $H_2SO_4$  over the potential range  $-0.244$  to  $+1.210V E_H$  and with cycling over successively diminished ranges of potential in the anodic (Fig. 3a)

or cathodic (Fig. 3b) sweeps. These figures define the general behavior of Pt in the 98%  $H_2SO_4$  without any further added water. Characteristic regions of the *i vs. V* profile are designated by Ia, IIa, Ic, IIc, etc., where "a" and "c" denote anodic and cathodic processes, respectively.

Under the above conditions, the observed currents are predominantly for surface processes since the reduced current densities, *i/s*, (viz., the apparent pseudocapacitance per unit area) are almost constant with changing sweep rate, *s*, after a given holding period,  $\tau_{h,c}$ .

The *i vs. V* profiles for Pt in 98%  $H_2SO_4$  under the conditions of Fig. 2 and 3 differ substantially from those well known (5, 15, 16) for Pt in dilute ( $\sim 0.05M$ ) aqueous  $H_2SO_4$ . Principally, no region of underpotential deposition of H is seen, i.e., before  $H_2$  is evolved at the most negative end of a cathodic potential sweep. This is presumably due to strong adsorption of  $H_2SO_4$  molecules and  $HSO_4^-$  ions and to the changed nature of the solvent. The regions Ia, IIa (Fig. 2a) of the anodic sweep, which are presumably attributable in the usual way to surface oxidation (since, e.g., the charge in the reduction peak increases logarithmically with time of holding at the positive end of the anodic sweep and the hysteresis between formation and reduction regions increases with time of anodic holding), are broad and almost structureless, showing less well-resolved states than are observed in a dilute aqueous solution (15, 16) of  $H_2SO_4$ .

An oxide reduction region, which appears to be conjugate with the broad surface oxidation region, Ia, IIa, shows a peak (IIc) and a shoulder (Ic). A similar behavior is only resolved in more dilute  $H_2SO_4$  solutions under special low temperature conditions (19) or with weakly adsorbed anions, e.g.,  $ClO_4^-$ . That the currents in the region Ia,c and IIa,c correspond to surface processes is indicated by approximate constancy (to 5%) of the charges under the curves in experiments conducted at various sweep rates.

Application of the potential holding program (iia) at the positive end of an anodic sweep gives the results shown in Fig. 2b. Only growth of the surface oxide occurs, as indicated by the increasing reduction charges with time,  $\tau_{h,a}$ , in the cathodic sweep which increase logarithmically in  $\tau_{h,a}$ . This is the normal kind of behavior, e.g., as observed (20, 21) in dilute solutions at Pt.

It is under the cathodic holding program (iib) that the unusual behavior of  $H_2SO_4$  is observed. When the potential is held at the negative end of a cathodic sweep at  $-0.244V E_H$  for various times,  $\tau_{h,c}$ , an increasing anodic current appears initially over the surface oxide region in a following anodic sweep (Fig. 4). With increasing  $\tau_{h,c}$ , the currents in following anodic sweeps after the holding period: (a) initially increase but eventually reach a saturation limit; (b) are independent of solution mass-transfer rate at a rotated electrode [see the following section]; also, (c) a component of anodic current in these anodic sweeps appears at a lower than usual (Fig. 2) anodic potential, giving a shoulder. IIIa, (Fig. 4), on the anodic *i vs. V* profiles after holding for more than 20 sec.

As this shoulder current appears and increases with increasing  $\tau_{h,c}$ , the oxide reduction current profile (Ic, IIc) diminishes and a new cathodic current peak (IIIC) appears and progressively increases with increasing  $\tau_{h,c}$ , eventually reaching saturation. This behavior is illustrated in the succession of *i vs. V* profiles shown in Fig. 4 for various times of holding.

The dependence of the extra anodic currents which appear over the oxide formation region and of the new cathodic currents which appear in the cathodic sweep, and also of the oxide reduction charges, on time of cathodic holding,  $\tau_{h,c}$ , is shown as integrated charges in

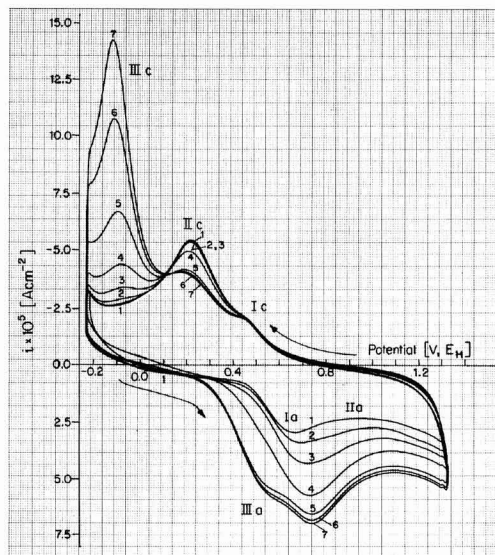


Fig. 4. A series of anodic followed by cathodic cyclic-voltammetry curves for Pt in 98% H<sub>2</sub>SO<sub>4</sub> at 298 K after various times  $\tau_{h,c}$  of holding the potential constant at  $-0.244E$ . Sweep rate 70 mV sec<sup>-1</sup>; times  $\tau_{h,c}$ : curve 1, 0; curve 2, 5; curve 3, 10; curve 4, 15; curve 5, 20; curve 6, 40; and curve 7, 80 sec.

Fig. 5. There appears to be some induction period in the formation of whatever species (see later) that gives rise to the extra cathodic peak in the cathodic sweep which follows the first anodic sweep after holding. All the charges derived from integration of the currents over various regions of the  $i$  vs.  $V$  profiles correspond, in order of magnitude (see Fig. 5), to values

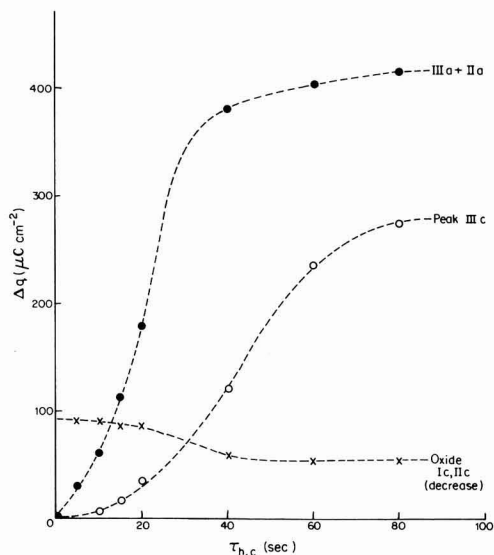


Fig. 5. Charges in  $\mu\text{C cm}^{-2}$  for the three principal time-dependent processes in the curves of Fig. 4 as a function of cathodic holding time  $\tau_{h,c}$  sec.  $\circ$  Charges for process IIIc;  $\bullet$  charges for processes in the region IIIa + IIa; and  $\times$  charges in the surface oxide reduction region Ic, IIc.

for monolayer processes, suggesting the role of chemisorption in the reactions involved.

If, after the experiment at a series of successively increasing cathodic holding times, the electrode is allowed to be freely cycled [cyclic-voltammetry mode (i)], the new cathodic peak IIIc gradually diminishes, the currents over the surface oxidation region diminish, and the surface oxide reduction region eventually recovers to its initial charge and peak currents. As this recovery takes place (slowly, as shown in Fig. 6), an isopotential point (22) is observed between the series of decreasing current peaks at 0.05V for process IIIc and the series of increasing surface oxide reduction currents Ic and IIc. This suggests that there is a coupling between the processes, Ic, IIc, and the reduction process, IIIc, probably through adsorption and occupancy of surface sites on the Pt electrode by two species.

**Behavior at the rotated Pt electrode.**—If the experiments corresponding to the results shown in Fig. 4 and 6 are performed at a rotating Pt disk electrode (1000 ~ 3000 rpm), the initial ( $\tau_{h,c} = 0$ )  $i$  vs.  $V$  profile shown in Fig. 2a remains unchanged. If, however, the cathodic holding experiment is carried out under rotation conditions, the development of the enhanced anodic and new cathodic currents in following sweeps (as shown in Fig. 4) is retarded, but eventually, as  $\tau_{h,c} \rightarrow 90$  sec (Fig. 7) the same (saturation) anodic current profiles are attained as in the static solution with  $\tau_{h,c} \simeq 45$  sec (curve for IIa + IIIa in Fig. 5). This result suggests that (a) the immediate product of reduction becomes spun-off into solution, but (see below) may become re-adsorbed after its formation; and (b) the primary reduction process involves H<sub>2</sub>SO<sub>4</sub> rather than another species such as H<sub>2</sub>S<sub>2</sub>O<sub>7</sub> (2) at low concentration, since electrode rotation retards rather than enhances the reduction process; thus, if the reduction effects observed in 98% H<sub>2</sub>SO<sub>4</sub> were, in fact, due to a small concentration of electroactive H<sub>2</sub>S<sub>2</sub>O<sub>7</sub>, rotation would tend to enhance rather than diminish the observed reduction effects, due to the expected facilitation of mass transfer of H<sub>2</sub>S<sub>2</sub>O<sub>7</sub> molecular to the electrode surface under rotation conditions.

An experiment in which the cathodic holding is conducted at a stationary Pt disk electrode, but the

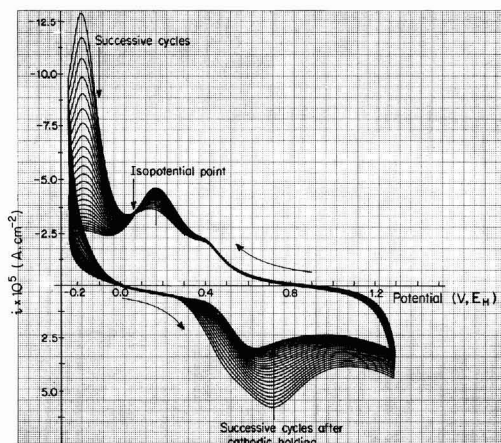


Fig. 6. "Recovery" of initial cyclic-voltammetry  $i$  vs.  $V$  profile [Fig. 3(a)] after a series of 25 repetitive potential sweeps at 70 mV sec<sup>-1</sup>, following a period  $\tau_{h,c}$  of holding the potential at  $-0.244E_H$ . Time scale of the succession of the 25 curves is determined by the sweep rate of 70 mV sec<sup>-1</sup> and the potential range of 1.54V.

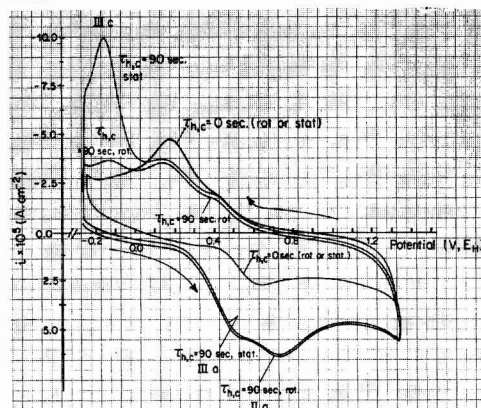


Fig. 7. Cyclic-voltammetry  $i$  vs.  $V$  profiles for a Pt disk electrode in 98%  $\text{H}_2\text{SO}_4$  at  $70 \text{ mV sec}^{-1}$  after 0 and 90 sec cathodic holding, with ("rot") and without ("stat") electrode rotation at 3000 rpm. Current-density profiles in regions IIIa, IIa are independent of electrode rotation.

following anodic sweep is taken with or without rotation at 3000 rpm, shows (Fig. 7) that the profiles of the extra anodic currents that pass at the rotated electrode on the anodic sweep immediately following the reduction during the time  $\tau_{h,c}$  are identical with those observed at the stationary electrode under otherwise the same conditions. This suggests that, although the immediate product (say "X") of reduction in the cathodic holding experiment may be a species weakly adsorbed and hence able to be spun away into solution (as indicated by the result referred to in the previous paragraph), eventually a strongly bound species (say "Y") becomes, and remains, chemisorbed up to a saturation limit (Fig. 4 and 5) at the Pt electrode during the subsequent anodic sweep.

If, however, after cathodic holding for 80 sec without rotation, free potential cycling is allowed to occur as in Fig. 6, but now with electrode rotation, the cathodic peak currents marked IIIc and the extra anodic currents (marked IIIa and IIa) which overlap with the original surface oxide formation region Ia + IIa, rapidly decay (as shown in Fig. 7) almost to the level of currents in the initial  $i$  vs.  $V$  profile (cf. Fig. 1a) without holding. This shows that while the species (Y, say) which originates from the species X produced in the cathodic holding treatment is a chemisorbed species, it can, however, following oxidation on the surface in processes Ia + IIa + IIIa (Fig. 4), be spun away into the bulk solution after reduction and slow desorption in the next cathodic sweep, so that currents in subsequent cathodic and anodic sweeps progressively diminish; Y itself and its products of oxidation in IIIa and IIa are bound species unaffected by mass-transfer conditions (Fig. 7).

The reduction process in IIIc appears to be associated with a species that arises from IIc and is loosely bound on the surface since electrode rotation eliminates most of the reduction current in this region almost from its commencement in the IIIc region (Fig. 7), yet the remainder of the anodic and cathodic  $i$  vs.  $V$  profile is independent of rotation, e.g., after  $\tau_{h,c} = 90 \text{ sec}$ . However, under successive cycling conditions (Fig. 6) after  $\tau_{h,c} = 90 \text{ sec}$  with no rotation, it then takes ca. 20 cycles (ca. 400 sec) for the peak current at IIIc to decay to the level in Fig. 7 after 1 cycle with rotation, so that the species being reduced at the surface in IIIc remains in some loose attachment to the Pt sufficient for reoxidation immediately in the following anodic sweep with little loss of the level

of currents over the regions IIIa, and Ia (Fig. 4). (Possibly a polymeric form of S or a polysulfide is involved.) The latter result indicates clearly that the species generated at the end of the cathodic sweep through the IIIc region (e.g., the top curve, Fig. 6) is the same as that formed in the initial holding period for  $\tau_{h,c} \text{ sec}$ .

**Possible mechanism of the effects: elucidation by chemical simulation experiments.**—The results of Fig. 4, 5, and 6 suggest that a product, X, derived from the sulfuric acid is first formed by reduction near the  $\text{H}_2/\text{H}^+$  steady potential. Some of X, probably in a further reduced chemisorbed state Y (see below), then becomes oxidized to a species  $\text{Y}_0$  in the following anodic sweep. The reduction of  $\text{H}_2\text{SO}_4$  to form detectable X and Y, as indicated by its subsequent oxidation to  $\text{Y}_0$  and the following reduction of  $\text{Y}_0$  in the next cathodic sweep, is quite slow, requiring ca. 20 sec for formation of a detectable adsorbed intermediate at 298 K.

In the next cathodic sweep, following formation of  $\text{Y}_0$  by oxidation of Y derived from X,  $\text{Y}_0$  is reduced to a species "Z", giving (Fig. 4) the substantial peak IIIc on the cathodic  $i$  vs.  $V$  profile near the  $\text{H}_2/\text{H}^+$  potential. The reduction current giving Z depends on how much X, and hence Y (and thus  $\text{Y}_0$  from Y), were produced in the cathodic holding.

The observation of the reduction peak IIIc producing Z, after oxidation of X and Y to  $\text{Y}_0$  species in the previous anodic sweep, means that the process of oxidation of X or Y is not re-formation of  $\text{H}_2\text{SO}_4$  or  $\text{H}_2\text{SO}_4^-$  ion (i.e.,  $\text{Y}_0$  is not one of these species) since  $\text{H}_2\text{SO}_4$  (or  $\text{HSO}_4^-$ ) itself is not rapidly reduced in a single cathodic sweep, as follows from the behavior in Fig. 2, and from the fact that the primary reduction process which takes place during cathodic holding is quite slow.

Consideration of the chemistry of 98%  $\text{H}_2\text{SO}_4$  suggests that the first reduction product X is likely to be  $\text{SO}_2$  or  $\text{HSO}_3^-$  produced either from  $\text{H}_2\text{SO}_4$  molecules or any dissolved  $\text{SO}_3$  present [cf. Ref. (6)]. However, the latter possibility is quite unlikely since the concentration of  $\text{SO}_3$  in 98%  $\text{H}_2\text{SO}_4$  (ca. 1M in  $\text{H}_2\text{O}$ ) is known to be vanishingly small (2). The effects are unlikely to be due to other adventitious impurities since we have found previously (16) with this B.D.H. acid, and in the present work, that its solutions in pyrodistilled water give excellent cyclic voltammograms for Pt without any impurity problems. This is also indicated by the behavior of Au (see later) in this acid.

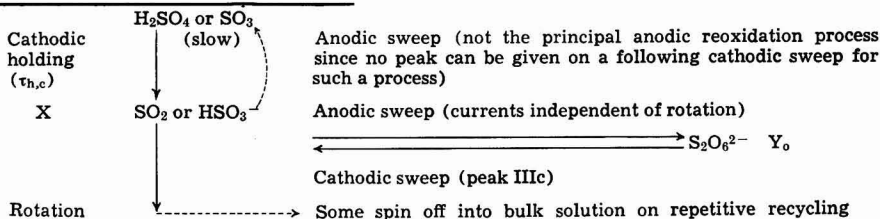
Since only monolayer magnitudes of intermediates in the  $\text{H}_2\text{SO}_4$  reduction are produced in the experiments (e.g., see Fig. 5), direct chemical analyses and characterizations were not feasible, especially in excess of 98%  $\text{H}_2\text{SO}_4$ . However, chemical simulations of the behavior of several likely intermediates, by addition of known sulfur compounds in trace amounts, were found to be profitable for the purpose of indicating some of the initial processes that take place.

First, in order to test the possibility that X is  $\text{SO}_2$  (or  $\text{HSO}_3^-$ ), a small amount of  $\text{SO}_2$  was added (as  $\text{SO}_3^{2-}$  in a crystal of  $\text{Na}_2\text{SO}_3$ ) to the 98%  $\text{H}_2\text{SO}_4$  in which the potential of the Pt electrode was being cycled as in Fig. 2a (full potential range). Immediately the characteristics of Fig. 4 were developed, including quantitatively the finer details. Therefore, the initial reduction of  $\text{H}_2\text{SO}_4$  is evidently to  $\text{SO}_2$  or  $\text{HSO}_3^-$ . However, it is known [e.g., Ref. (7)] that  $\text{SO}_2$  itself can be reduced at Pt to sulfur species in lower oxidation states, e.g.,  $\text{H}_2\text{S}$  or S. This could explain the initial effects of electrode rotation in the cathodic holding experiment; thus,  $\text{SO}_2$  (X) is first produced and some can be spun away, but some more strongly bound reduced species Y, such as one-site



and two-site chemisorbed S and corresponding SO species (7, 8) are eventually built up on the surface from the  $\text{SO}_2$  and give rise the anodic saturation

(23):  $2\text{SO}_3^{2-} \rightarrow \text{S}_2\text{O}_6^{2-} + 2e$ . This suggests an alternative pathway for the reduction and reoxidation processes observed in 98%  $\text{H}_2\text{SO}_4$  at Pt, as follows:



currents for partial reoxidation of these species in regions IIa + IIIa (Fig. 4, 5, and 7) when  $\tau_{th,c}$  is sufficiently long (90 sec). The subsequent oxidation of these strongly bound species, or of the  $\text{SO}_2$  initially produced, in the anodic sweep following the time  $\tau_{th,c}$  cannot be back to  $\text{H}_2\text{SO}_4$  or  $\text{SO}_3$ , otherwise no further facile reduction of  $\text{Y}_0$  to Z in the next cathodic sweep would be observed, as we mentioned earlier.

There is some induction time in the development of the species (Y) that is oxidized in the anodic sweeps after cathodic holding and after this induction time an extra anodic current shoulder (IIIa) appears on the anodic sweep. It is when this shoulder is developed that the re-reduction peak, IIIc, on the subsequent cathodic sweep is developed (Fig. 4). The efficiency of the production of Y and  $\text{Y}_0$  from X depends on the mass-transport conditions and these determine the induction time.

The chemistry of the oxy- and thio-oxy-acids of sulfur is very complex (23) and a number of possibilities exists for the identity of the species Y and  $\text{Y}_0$ . Generally speaking, there are two types of species that may be involved: (a) thio-oxy-acid or anion species that may be produced in an adsorbed state on the electrode, but correspond stoichiometrically to known molecules or ions; or (b) chemisorbed species, not necessarily known molecules, derived from reduction of  $\text{SO}_2$  (produced initially from the  $\text{H}_2\text{SO}_4$ ) and from the reoxidation of these species on the electrode surface, e.g., Ref. (7, 8). First, we shall deal with possibilities of type (a).

The experiment with added  $\text{SO}_2$  as  $\text{SO}_3^{2-}$  gives the unambiguous conclusion that the initial product (X) of electrochemical reduction of  $\text{H}_2\text{SO}_4$  at Pt is  $\text{SO}_2$  or  $\text{HSO}_3^-$ . Products of further reduction could be dithionite (X', see below), and of subsequent reoxidation in the following anodic sweep, they could be  $\text{SO}_2$  (or  $\text{HSO}_3^-$ ) or dithionate ( $\text{S}_2\text{O}_6^{2-}$ ), or the corresponding acids or acid anions. Sulfoxyate or sulfoxylic acid,  $\text{S}(\text{OH})_2$ , is unlikely to be the species  $\text{Y}_0$ , as the S in this compound is in a lower valence state than that of S in  $\text{SO}_2$  or  $\text{HSO}_3^-$  and is very unstable (23).

A first possibility for consideration is that, initially, after short periods of cathodic holding,  $\text{SO}_2$  can, in fact, be to some extent reoxidized back to  $\text{H}_2\text{SO}_4$  (or  $\text{SO}_3$ ) in an anodic sweep, but, during longer times of reduction,  $\tau_{th,c}$ ,  $\text{SO}_2$  can be reduced further to dithionite ion,  $\text{S}_2\text{O}_4^{2-}$ . This could be then reoxidized on the following anodic sweep to the species  $\text{Y}_0$  that can be re-reduced in the cathodic peak IIIc. Thus  $\text{Y}_0$  would be  $\text{SO}_2$  and Z  $\text{S}_2\text{O}_4^{2-}$  again.

A chemical simulation experiment with addition of dithionite (as  $\text{Na}_2\text{S}_2\text{O}_4$ ) was unproductive as the  $\text{S}_2\text{O}_4^{2-}$ , or the corresponding acid, is immediately decomposed by 98%  $\text{H}_2\text{SO}_4$  to  $\text{SO}_2$ , and some  $\text{H}_2\text{S}$  and colloidal S. Only the characteristics of added  $\text{SO}_2$  are observed.  $\text{S}_2\text{O}_4^{2-}$  appears therefore to be too unstable to be a likely intermediate giving rise to Y as  $\text{SO}_2$ .

The electrolytic oxidation of  $\text{SO}_2$  or  $\text{SO}_3^{2-}$  to dithionate, however, is reported in the early literature

Here it is supposed that the species  $\text{Y}_0$  (which cannot be  $\text{H}_2\text{SO}_4$  or  $\text{SO}_3$ ) is  $\text{S}_2\text{O}_6^{2-}$ , formed in the anodic sweep over regions Ia and IIa from X ( $\text{SO}_2$  or  $\text{HSO}_3^-$ ), and that  $\text{S}_2\text{O}_6^{2-}$  can be reduced with facility back to  $\text{SO}_2$  or  $\text{HSO}_3^-$  in the cathodic sweep (peak IIIc), following its formation from  $\text{SO}_2$  or  $\text{HSO}_3^-$ .

A further simulation experiment was performed in which  $\text{S}_2\text{O}_6^{2-}$  (as the  $\text{Na}^+$  salt) was added at the beginning of the surface oxidation region (Ia) in an anodic sweep. No enhancement of anodic currents is observed under these conditions, but on the following cathodic sweep, the cathodic current peak IIIc near the  $\text{H}_2$  reference potential is observed, as in the experiments with slow reduction of the  $\text{H}_2\text{SO}_4$  (Fig. 4) in the absence of an added compound. A subsequent anodic/cathodic cycle gave a substantial increase in this cathodic peak; the behavior of added  $\text{S}_2\text{O}_6^{2-}$  is illustrated in Fig. 8.

These observations are consistent with  $\text{Y}_0$  being an adsorbed form of  $\text{S}_2\text{O}_6^{2-}$  (or  $\text{HS}_2\text{O}_6^-$  or dithionic acid) since if  $\text{Y}_0$  is  $\text{S}_2\text{O}_6^{2-}$  and it is added at the beginning of the surface oxidation region, no extra anodic currents should be observed; this is as found. Moreover, if  $\text{Y}_0$  is  $\text{S}_2\text{O}_6^{2-}$  formed from the  $\text{SO}_2$  or  $\text{HSO}_3^-$  produced in the reduction experiments in  $\text{H}_2\text{SO}_4$ , then it could be reduced back to  $\text{SO}_2$  or  $\text{HSO}_3^-$  (or some other species such as  $\text{H}_2\text{S}$ ) in the cathodic peak sweep (peak IIIc); this is observed in the simulation experiment (Fig. 8).

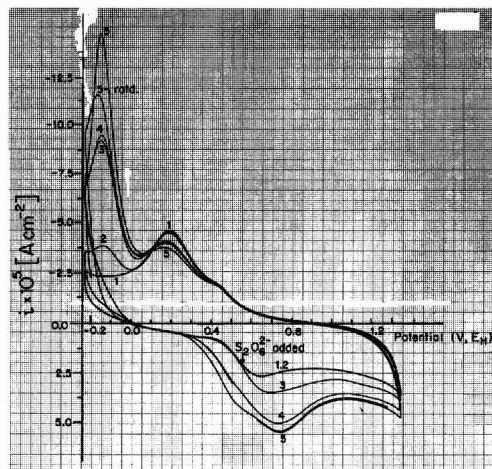


Fig. 8. Cyclic voltammograms at  $70 \text{ mV sec}^{-1}$  for Pt in 98%  $\text{H}_2\text{SO}_4$  with dithionate added on the anodic sweep at  $0.48 \text{ V } E_H$ . Curve 1, initial anodic sweep  $i$  vs.  $V$  profile without holding and without addition of  $\text{S}_2\text{O}_6^{2-}$ . Curve 2 (beyond  $0.48 \text{ V}$ ), after addition of  $10^{-4} \text{ mol S}_2\text{O}_6^{2-}$  (no change). Curves 3, 4, 5  $i$  vs.  $V$  profiles for successive potential sweeps after completion of 1, 2 following addition of the dithionate.



It should be noted that most of the thio-oxy-acids of S, and their anions, are unstable in acid medium but  $S_2O_6^{2-}$  is known to be the least unstable (23). It does, however, decompose in  $H_2SO_4$  with evolution of  $SO_2$ , as was observed in the present experiments. Since this  $SO_2$  could form  $Y_0$  on the anodic sweep, whatever  $Y_0$  is, another simulation experiment was carried out by cycling the electrode only over the potential range up to the onset of surface oxidation (0.48V) (Fig. 8), i.e., over the range where  $Y_0$  could be reduced on a following cathodic sweep, but where no oxidation peaks for any species such as  $SO_2$  formed from some decomposition of added  $S_2O_6^{2-}$  would be observed.  $S_2O_6^{2-}$  was added and again gave, under these conditions, a reduction peak on the cathodic cycle, similar to that observed in the experiments on reduction of  $H_2SO_4$  or with added  $SO_2$  or  $HSO_3^-$ .

These results suggest that the intermediate  $Y_0$  could be  $S_2O_6^{2-}$  (or  $HS_2O_6^-$  or dithionic acid) or, more likely,  $S_2O_6^{2-}$  in an adsorbed state. We next consider (b), chemisorbed species.

**Possible chemisorbed species.**—Not all the features of the reduction behavior of  $H_2SO_4$  can be accounted for simply in terms of plausible, "stable" chemical intermediates such as dithionite or dithionate species, even if they are chemisorbed. It has already been mentioned that the lack of an effect of electrode rotation rate on the anodic  $i$  vs.  $V$  profile observed after reduction of the  $H_2SO_4$  to  $SO_2$  for times  $\tau_{ch}$  indicates that a species in a chemisorbed state is derived from  $SO_2$  (X) and saturation coverage can be attained as measured by the subsequent oxidation current profile (IIIa + IIa). This opens up a number of possibilities for the identity of species  $Y_0$ , or Z, other than in terms of known chemical intermediates of the kind considered above.

Some insight into the nature of the chemisorbed species that evidently might be involved in the reduction of  $H_2SO_4$  can be gained from the work of Lal *et al.* (7-10) and of Loučka (11-13) who studied chemisorbed S-containing species at Pt, derived from  $H_2S$  and  $SO_2$  in aqueous medium. Both Loučka (11, 13) and Lal *et al.* (7, 8) concluded that an oxygenated S species arose in chemisorption from either  $SO_2$  or  $H_2S$  solutions (9) at Pt when the Pt surface was subjected to an anodic sweep. Bridged and linear "Pt-S-O" species (valencies and bonding not defined) were proposed, based on cyclic-voltammetry experiments on 0.5M aq  $H_2SO_4$  solutions containing  $SO_2$  and  $H_2S$ . Doubly and singly bound S and  $S_2$  species produced in successive reduction stages from  $SO_2$  were also postulated. Species such as "Pt-S-O" would be qualitatively consistent with the observation that the reduction peaks in the "surface oxide" region, observed in the present work, are related in some coupled way to the reduction process IIIc nearer the H region, as indicated by the isopotential point (Fig. 6). When the species X and some derived oxidized form  $Y_0$  is produced on the electrode, the bound surface oxide reduction charge on the following cathodic sweep is diminished, but the charge associated with the "re-reduction" process at IIIc is increased. The process IIIc can evidently produce a product which is desorbed as indicated by the experiments at a rotated electrode (Fig. 7). This product is unlikely to be regenerated  $SO_2$  since the results show that at potentials near the cathodic side of the peak IIIc,  $SO_2$  is strongly adsorbed. Possibly the step IIIc involves reduction of the previously adsorbed species to  $H_2S$ . At the moment the nature of the various chemisorbed species remains speculative.

An attempt was made by means of relative reflectivity measurements to distinguish qualitatively between the surface oxide species generated in the regions Ia, IIa, and the species associated with the extra

currents observed in this region and IIIa (Fig. 4) after cathodic holding. Thus the surface oxide monolayer formed at Pt normally gives an increasingly negative ( $\Delta R/R$ ) signal with increasing positive potential.

Figure 9 shows how ( $\Delta R/R$ ) varies with potential in anodic and cathodic sweeps following cathodic holding. The potential range is the same as that in Fig. 4, so that both the regions where extra anodic currents pass in IIIa, + Ia + IIa, and the region where the cathodic peak IIIc arises are covered in this diagram.

Figure 9 shows that the general shape of the ( $\Delta R/R$ ) vs.  $V$  relations remains the same while the chemisorbed reactive species produced on cathodic holding is removed by successive anodic/cathodic cycling, but the intensity of the ( $\Delta R/R$ ) signal falls

as less of the species remains on the electrode. In the anodic direction, the reflectivity features of surface oxidation are not lost despite the development of extra oxidation charge ( $\sim 4.20$  C m $^{-2}$ , Fig. 5) over the surface oxide formation region. This suggests [cf. Ref. (7, 8, 11, 13)] that the adsorbed species generated by cathodic holding and oxidized in the following sweep, is in a state intimately connected with the development of the surface oxide film as we have implied earlier in discussing the cyclic voltammograms and the isopotential point observed therein.

**Relation to surface oxide formation and reduction.**—The diminution of the surface oxide reduction peak as larger extents of reduction of  $H_2SO_4$  are allowed to take place (Fig. 4) during cathodic holding, probably arises because the surface oxide participates, during the anodic sweep after holding, in the oxidation of  $SO_2$  or of a reduced and/or chemisorbed (7-13, 24) form, to  $S_2O_6^{2-}$  or to other adsorbed species such as -S-O (9), so that less oxide is formed during the time of that anodic sweep. The experiment where cathodic holding was carried out at the stationary and

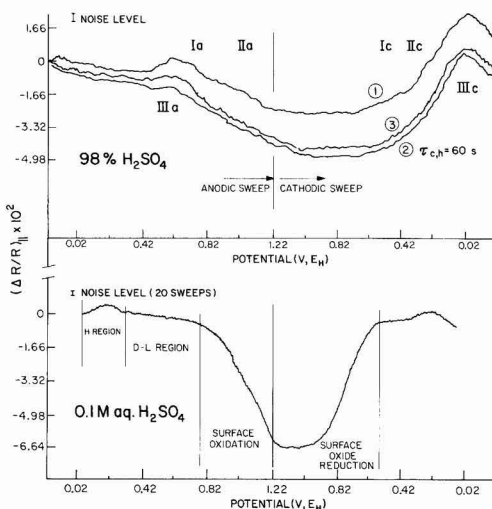


Fig. 9. Relative reflectivity ( $\Delta R/R$ ) profiles for Pt in 98%  $H_2SO_4$  as a function of potential (sweep rate 70 mV sec $^{-1}$ , 298 K) at Pt in the presence of the adsorbed species generated by cathodic holding for 60 sec and in its absence during a repetitive sweep or during its decline after holding. Designations as in Fig. 2(a). Curve 1, behavior on repetitive cycling, as in Fig. 2(a); curve 2, after 60 sec holding at cathodic end of sweep, one cycle; curve 3, third cycle after the 60 sec cathodic holding; lower curve for 0.1M aq  $H_2SO_4$  for comparison.

rotated electrode, showing that rotation had no effect on anodic currents observed on the subsequent anodic sweep, implies that  $\text{S}_2\text{O}_8^{2-}$  or S-O-species are being formed in an adsorbed state, thus competing with formation of some of the surface oxide that would otherwise have been produced on the anodic sweep as in Fig. 2 without any reduction of  $\text{H}_2\text{SO}_4$ . The complete absence of an observable up region for H at Pt (Fig. 2a) indicates that strong adsorption of  $\text{H}_2\text{SO}_4$  molecules and/or  $\text{HSO}_4^-$  ions is occurring as well.

The conclusions concerning  $\text{S}_2\text{O}_8^{2-}$  or S-O-adsorption are supported by the behavior observed when the potential is held constant for some time at the end of the anodic sweep, following slow reduction of  $\text{H}_2\text{SO}_4$  during cathodic holding: then a normal quantity (cf. Fig. 2) of surface oxide becomes again observable. It was also concluded by Geronov *et al.* (25), that reduction of  $\text{SO}_2$  at Pt, in this case in  $\text{CH}_3\text{CN}$ , leads to formation of an adsorbed species that rapidly transforms into a passivating film of dithionate (*sic*; probably dithionite in their case).

**Role of water.**—Following the work described above in "98%"  $\text{H}_2\text{SO}_4$ , some experiments were performed with controlled additions of water to give concentrations of 0.275, 0.55, and 1.10M of added  $\text{H}_2\text{O}$  in the 98%  $\text{H}_2\text{SO}_4$ . As shown in the series of  $i$  vs.  $V$  profiles in Fig. 10, addition of water allows some up of H to arise before significant  $\text{H}_2$  evolution currents appear. Also, in the presence of added water, cathodic holding, followed by an anodic sweep, produces less of the reduced and reoxidizable species as the water content is increased. Eventually normal behavior of an aqueous  $\text{H}_2\text{SO}_4$  solution is recognized where reduction effects are insignificant.

Since, with relatively small additions of water, the reduction reaction is considerably diminished, yet the concentration of  $\text{H}_2\text{SO}_4$  is still ca. 17M, this behavior suggests that the reduction to  $\text{SO}_2$  and another intermediate does not take place from molecular  $\text{H}_2\text{SO}_4$  but possibly from the small concentration<sup>2</sup> of  $\text{H}_2\text{S}_2\text{O}_7$  that is present at equilibrium with  $\text{H}_2\text{SO}_4$  molecules (2). The added water of course, even at the highest concentration of 1.1M could only produce 1.1M of extra  $\text{H}_3\text{O}^+$  and  $\text{HSO}_4^-$  ions, i.e., ca. 5.8 mol percent, so that most of the  $\text{H}_2\text{SO}_4$  remains as un-ionized molecules.

**Behavior at Au.**—In order to examine if the reduction of  $\text{H}_2\text{SO}_4$ , or  $\text{H}_2\text{S}_2\text{O}_7$  contained in it, is a simple electron-transfer process or one requiring chemisorption and electrocatalysis, the behavior of a gold electrode in 98%  $\text{H}_2\text{SO}_4$  was examined comparatively. An excellent cyclic-voltammetry profile is obtained at Au, with no evidence of impurity effects [cf. Ref. (5, 16)], confirming the high degree of purity of B.D.H. Aristar  $\text{H}_2\text{SO}_4$ . The general features of this curve for Au are similar to those for Au in aqueous  $\text{H}_2\text{SO}_4$ . Cathodic holding for up to 2 min at the same potential as at Pt revealed absolutely no indication of any reduction of the  $\text{H}_2\text{SO}_4$ . The subsequent anodic and cathodic sweeps were identical with those under repetitive cycling conditions. Under the same conditions as at Pt, addition of  $\text{SO}_2$  (as  $\text{SO}_3^{2-}$ ) also gave no reaction currents, either in anodic or cathodic sweeps. This is contrary to what has been found in aqueous solutions (24) and the absence of such an effect here must be attributed presumably to the strong adsorption of  $\text{H}_2\text{SO}_4$  [cf. Ref. (5)] at Au and the different effective cathodic range of potentials therefore involved. Adsorption and reactivity of S (as  $\text{S}^{2-}$ ) at Au are also known (26).

It is therefore to be concluded that the reaction of  $\text{H}_2\text{SO}_4$  reduction observed at Pt is associated with the

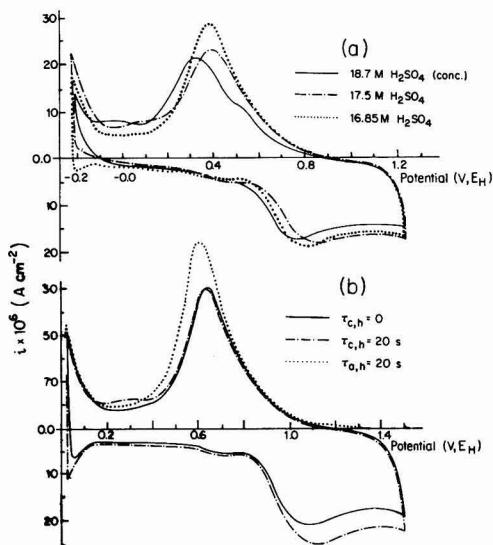


Fig. 10. Cyclic-voltammetry  $i$  vs.  $V$  profiles for Pt in 98%  $\text{H}_2\text{SO}_4$  with small additions of extra water. Sweep rate  $58 \text{ mV sec}^{-1}$ ;  $298 \text{ K}$ . (a) Anodic/cathodic cyclic-voltammograms without cathodic holding. (b) Behavior after cathodic holding for 20 sec or, separately, anodic holding for 20 sec. Concentrations of  $\text{H}_2\text{SO}_4$ , after additions of water, as indicated.

catalytic and adsorptive properties of this metal and that  $\text{H}_2\text{SO}_4$ , or  $\text{H}_2\text{S}_2\text{O}_7$ , is not easily reduced in an electron-transfer process not involving chemisorption and electrocatalysis.

### Conclusions

98%  $\text{H}_2\text{SO}_4$  can be reduced at Pt electrodes near the steady potential of a hydrogen electrode in the same solution. Chemical simulation experiments demonstrate that the identity of the initial product of the observed slow reduction of  $\text{H}_2\text{SO}_4$  is  $\text{SO}_2$  or  $\text{HSO}_3^-$ . A chemisorbed species derived from  $\text{SO}_2$  is oxidized in a following anodic sweep not back to  $\text{H}_2\text{SO}_4$  or  $\text{SO}_3$  but to an adsorbed intermediate  $\text{Y}_0$  that is reduced back to a species that is relatively easily desorbed into solution at the end of a subsequent sweep near the  $\text{H}_2/\text{H}^+$  steady potential. Simulation experiments show that it is possible that the species ( $\text{Y}_0$ ) derived from  $\text{SO}_2$  is dithionate or dithionic acid, probably stabilized in some state by adsorption at the Pt electrode. It is most likely that chemisorbed intermediates, derived from  $\text{SO}_2$ , or from the added  $\text{S}_2\text{O}_8^{2-}$ , which are not normal stable compounds, are involved.

No reduction of 98%  $\text{H}_2\text{SO}_4$  or electroactivity of  $\text{SO}_2$  (or  $\text{HSO}_3^-$ ) is observed at Au under the same conditions as at Pt. By comparison, therefore, the observation of reactions which take place at Pt indicate that an electrode surface, where electrosorption and electrocatalysis can occur, is required for the initial stage of reduction of  $\text{H}_2\text{SO}_4$  to  $\text{SO}_2$ .

### Acknowledgments

Grateful acknowledgment is made to the Natural Sciences and Engineering Research Council of Canada for support of this work. One of us (D.M.N.) acknowledges a Leave of Absence for Specialization from the Laboratory of Physicochemical Separations, Centre for Marine Research, Ruder Boskovic Institute, Zagreb, Yugoslavia. We thank Mr. J. C. Ku in our laboratory for carrying out the reflectivity experiments.

<sup>2</sup> However, the rotation experiments mentioned on p. 2265 on behavior at the rotated Pt electrode would not support this conclusion unless the rotation effect is more connected with spin-off of  $\text{SO}_2$  restricting further reduction and/or chemisorption to Y.

Manuscript submitted Sept. 12, 1980; revised manuscript received May 12, 1981.

Any discussion of this paper will appear in a Discussion Section to be published in the June 1982 JOURNAL. All discussions for the June 1982 Discussion Section should be submitted by Feb. 1, 1982.

Publication costs of this article were assisted by the University of Ottawa.

#### REFERENCES

1. B. E. Conway and D. M. Novak, *J. Phys. Chem.*, **81**, 1459 (1977); see also B. E. Conway and D. M. Novak, *J. Electroanal. Chem. Interfacial Electrochem.*, **99**, 133 (1979).
2. R. J. Gillespie and E. A. Robinson, in "Non-Aqueous Solvent Systems," T. C. Waddington, Editor, Chap. 4, Academic Press, New York (1965).
3. J. O. Zerbino, N. R. de Tacconi, and A. J. Arvia, *This Journal*, **125**, 1266 (1978).
4. N. A. Balashova and V. E. Kazarinov, *Elektrokhimiya*, **1**, 514 (1965); *Dokl. Acad. Nauk SSSR*, **157**, 1174 (1964).
5. B. E. Conway, H. Angerstein-Kozłowska, B. Barnett, and J. Mozota, *J. Electroanal. Chem. Interfacial Electrochem.*, **100**, 417 (1979).
6. J. S. W. Carrozza, H. A. Garrera, and A. J. Arvia, *Electrochim. Acta*, **14**, 205 (1969); **13**, 771 (1968).
7. A. Q. Contractor and H. Lal, *J. Electroanal. Chem. Interfacial Electrochem.*, **93**, 99 (1978).
8. A. Q. Contractor and H. Lal, *ibid.*, **96**, 175 (1979).
9. R. Jayaram, A. Q. Contractor, and H. Lal, *ibid.*, **87**, 225 (1978).
10. A. Q. Contractor and H. Lal, *ibid.*, **103**, 103 (1979).
11. T. Loučka, *ibid.*, **31**, 319 (1971).
12. T. Loučka, *ibid.*, **36**, 366, 369 (1972).
13. T. Loučka, *ibid.*, **44**, 221 (1973).
14. J. O. Zerbino, N. R. Tacconi, A. J. Calandra, and A. J. Arvia, *ibid.*, **77**, 379 (1977); A. J. Calandra, N. R. de Tacconi, and A. J. Arvia, *ibid.*, **49**, 145 (1974); N. R. de Tacconi, A. J. Calandra, and A. J. Arvia, *ibid.*, **51**, 25 (1975); N. R. de Tacconi, A. J. Calandra, and A. J. Arvia, *ibid.*, **57**, 267, 325 (1974). See also F. Colom, A. de la Plaza, and R. Gancedo, *Anal. Quim.*, **71**, 985 (1975).
15. E.g., see F. G. Will and C. A. Knorr, *Z. Elektrochem.*, **64**, 258 (1960).
16. B. E. Conway, W. B. A. Sharp, H. Angerstein-Kozłowska, and E. E. Criddle, *Anal. Chem.*, **45**, 1331 (1973).
17. M. W. Breiter, *Z. Elektrochem.*, **60**, 37, 119 (1956); see also S. B. Brummer, J. I. Ford, and M. J. Turner, *J. Phys. Chem.*, **69**, 3424 (1965).
18. S. Gottesfeld and B. E. Conway, *J. Chem. Soc., Faraday Trans. 1*, **69**, 1090 (1973).
19. H. Angerstein-Kozłowska, B. E. Conway, and W. B. A. Sharp, *J. Electroanal. Chem. Interfacial Electrochem.*, **43**, 1 (1973).
20. D. Gilroy and B. E. Conway, *Can. J. Chem.*, **46**, 875 (1968).
21. P. Stonehart, H. A. Kozłowska, and B. E. Conway, *Proc. R. Soc. London, Ser. A*, **310**, 541 (1969).
22. D. F. Untereker and S. Bruckenstein, *Anal. Chem.*, **44**, 1009 (1974).
23. H. Remy, "Treatise on Inorganic Chemistry," pp. 720-726, Elsevier Publishing Co., Amsterdam (1956).
24. Z. Samec and J. Weber, *Electrochim. Acta*, **20**, 402 (1975).
25. Y. Geronov, R. V. Moshtev, and B. Puresheva, *J. Electroanal. Chem. Interfacial Electrochem.*, **108**, 335 (1980).
26. D. G. Wierse, M. M. Lohengrel, and J. W. Schultze, *ibid.*, **92**, 121 (1978).

## Reactions of Scratched Copper Electrodes in Aqueous Solutions

G. T. Burstein\* and R. C. Newman<sup>†</sup>

Department of Metallurgy and Materials Science, University of Cambridge, Cambridge CB2 3QZ, England

#### ABSTRACT

The behavior of copper electrodes scratched under potential control in aqueous electrolytes is presented. In alkaline solution the metal surface shows the presence of two distinct types of oxidized monolayer, ascribed to  $\text{CuOH}$  and  $\text{Cu}_2\text{O}$ , each formed over a unique potential range well below the reversible potential for bulk  $\text{Cu}_2\text{O}$  formation. The  $\text{Cu}_2\text{O}$  monolayer is a necessary precursor to passivation of the metal, and in sulfuric acid solution only the  $\text{CuOH}$  monolayer is observed. This monolayer acts as an intermediate layer in both the dissolution and passivation processes and probably also exists during steady-state hydrogen evolution. Addition of ammonia to alkaline electrolytes modifies the  $\text{CuOH}$  monolayer, probably by incorporation of  $\text{NH}_3$ , rendering formation of  $\text{Cu}_2\text{O}$  more difficult.

Determination of the kinetics of reaction between scratched metal electrodes and aqueous electrolytes gives quantitative information on fast electron transfer steps (1-6). The scratched iron electrode (1) reacts very rapidly to form an  $\text{Fe(I)}$  species adsorbed to complete coverage to the metal surface. Given the nominal composition of  $\text{FeOH}$ , this monolayer is affected by some anions in the electrolyte such as  $\text{Cl}^-$  and  $\text{H}_2\text{PO}_4^-$  (2). Silver has been shown to react anodically with the formation of single adsorbed monolayers of  $\text{AgOH}$  and  $\text{Ag}_2\text{O}$  (3, 4). These monolayers are formed at po-

tentials well below the reversible potential for bulk  $\text{Ag}_2\text{O}$  formation and the behavior is in complete accord with results obtained from fast potential sweeping and potential pulsing experiments on polished silver surfaces (3). Thus, at least in the case of silver, these underpotential reactions are not uniquely a property of the heavily cold-worked scratch surface. Further, at pH 14, scratched silver shows a small potential range in which no oxidation reaction occurs: Under these conditions it is possible to determine the zero charge potential of the unreacted metal surface (3, 7).

The fast electron transfer reactions that occur from scratched surfaces have been used to interpret the rate of stress-corrosion cracking in some systems (5, 6, 8). The relevance of bare surface reaction kinetics

\* Electrochemical Society Active Member.

<sup>†</sup> Present address: Brookhaven National Laboratory, Upton, New York 11973.

Key words: copper anode, copper polarization, scraped copper, underpotential monolayers.

to mechanically assisted corrosion processes such as stress-corrosion cracking and corrosion fatigue has prompted investigation of dissolution and passivation processes on dynamically strained wire electrodes (9); however, the ill-defined rate of bare surface generation in this type of experiment renders difficult the quantification of this type of result.

The ohmic potential drop to potentiostatically controlled scratched electrodes in relatively resistive solutions has been calculated (10): This type of calculation is necessary because of the very large current densities that flow from the freshly generated metal surface. It is worthy of note that when pure copper is scratched in solutions containing  $\text{NO}_2^-$  in open circuit, reduction of the anion to  $\text{NH}_3$  occurs (11, 12).

In the present paper we examine the behavior of potentiostatically controlled scratched copper electrodes and describe the effects of ammonia on the reactions that occur.

### Experimental

Rotating disk electrodes (8 mm diam) were prepared from pure Cu (Johnson-Matthey, 99.999%) by mounting into Perspex and sealing with Araldite. The technique used to scratch potentiostatically controlled rotating disk electrode was described previously (1-6). The diamond stylus tracked with a weight of  $\sim 2\text{g}$ , creating a shallow scratch  $\sim 3\text{ }\mu\text{m}$  deep and  $40\text{ }\mu\text{m}$  wide at a rotation rate of 100 Hz and a linear scratching velocity of  $\sim 2\text{ msec}^{-1}$ . The contact times of the stylus varied from 0.2 to  $\sim 1\text{ msec}$ . By using the slope of the rising current transient during the actual scratching process to calculate the bare surface current density  $i_s$ , the resulting value is independent of the contact time of the stylus and also independent of any small irregularities occurring in the scratch width. Thus

$$i_s = \frac{1}{2\pi\omega y} \frac{dI}{dt}$$

where  $dI$  is the change in current on the electrode in time  $dt$  due to scratching,  $r$  is the distance of the scratch from the center of rotation,  $\omega$  is the rotation rate of the disk, and  $y$  the scratch width. The maximum scratch depth is small compared with its width and is thus ignored. The total charge density  $q_s$  required to bring the scratch back to a steady state was also measured; this was calculated from the total area under the current transient, and is given by

$$q_s = \frac{1}{2\pi\omega y t_c} \int_0^\infty I dt$$

where  $t_c$  is the contact time of the stylus. The quantity  $2\pi\omega y t_c$  is the area of the scratch surface. Where re-equilibration of the scratch surface took longer than 5 msec, the  $q_s$  values quoted are for 5 msec after initial contact of the stylus.

The potential of the working electrode was measured relative to a saturated calomel electrode via a Luggin capillary probe positioned  $\sim 40\text{ mm}$  below the working electrode. All potentials are presented relative to the normal hydrogen electrode and have been corrected for the liquid junction potential between the working and reference electrolytes. Corrections have also been made for the ohmic potential drop in the electrolyte due to the current from the scratch using calculations and measurements of the resistance to flow of current to narrow strip electrodes (10).

The counterelectrode was a circular platinum foil, 30 mm diam, containing a small concentric hole through which the Luggin capillary probe emerged. Electrolytes were prepared from analytical grade reagents and doubly distilled water and were purged with de-oxygenated nitrogen before and during experiments. Ammoniacal electrolytes were made up to a constant

concentration of  $(\text{NH}_3 + \text{NH}_4^+)$  at 1.0M, the latter being added as  $(\text{NH}_4)_2\text{SO}_4$ . Where necessary  $\text{Na}_2\text{SO}_4$  was added as supporting electrolyte to give approximately constant ionic strength. Measurements were made at a temperature of  $293 \pm 2\text{ K}$ . Potentials were controlled with a Wenking potentiostat (Type OPA 69). Current transients were recorded in a transient recorder (Datalab Type DL 905) and displayed on an oscilloscope or chart recorder.

### Results

Bare surface polarization curves and charge density curves for copper in 1.0M KOH are shown in Fig. 1. The anodic reaction is accelerated by orders of magnitude at all potentials above  $-900\text{ mV}$  (NHE) when compared with the steady-state current densities  $i_b$  (also shown in Fig. 1). At potentials more negative than  $-900\text{ mV}$  (NHE) the cathodic reaction, representing the evolution of hydrogen, is also greatly accelerated. Both anodic and cathodic branches of the bare surface polarization curves do indeed represent electron transfer reactions and are not accounted for by non-faradaic double layer charging processes, since the bare surface charge densities,  $q_s$ , are too large at all potentials to represent the latter process. Only in the region of the bare surface mixed potential  $E_{ms}$ , at  $E_{ms} \pm 25\text{ mV}$ , does  $q_s$  fall below  $100\text{ }\mu\text{C cm}^{-2}$ , accounted for quite clearly by the fact that the anodic and cathodic reactions occur at comparable rates over this small range.

Anodic current density plateaus occur between  $-800$  and  $-550\text{ mV}$  (NHE) and between  $-500$  and  $-350\text{ mV}$  (NHE). These correspond to plateaus in charge density  $q_s$ , at  $145 \pm 26$  and  $378 \pm 58\text{ }\mu\text{C cm}^{-2}$ , respectively; although the latter is rather poorly defined it is in quantitative agreement with that found for the

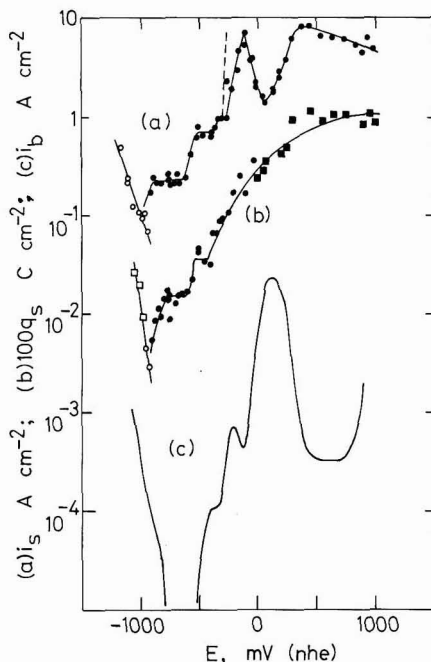


Fig. 1. Bare surface electrochemistry of copper in 1.0M KOH. (a)  $i_s$ . (b)  $q_s$  after complete re-equilibration ( $\bullet$ ), or 5 msec after first stylus contact ( $\blacksquare$ ). (c)  $i_b$  obtained from potential sweeping at  $10\text{ mV sec}^{-1}$ . Broken line denotes  $i_s$  corrected for ohmic drop (10). Black points anodic; white points cathodic.  $\omega = 100\text{ Hz}$ .

silver electrode in the same electrolyte (3) (see below). Between  $-120$  and  $+80$  mV (NHE)  $i_s$  decreases with increase in  $E$ . This potential range corresponds to a rise in the steady-state current density  $i_b$ , where copper dissolves anodically to give  $\text{CuO}_2^{2-}$  in solution prior to passivation of the metal by  $\text{CuO}$ . It should be noted that during this process  $q_s$  increases continuously. The maximum anodic current density observed on the scratch surface is  $8 \text{ A cm}^{-2}$ . Typical current transients obtained at different potentials in  $1.0 \text{ M KOH}$  are shown in Fig. 2.

Further bare surface polarization curves measured in nonammoniacal electrolytes are shown in Fig. 3-5. In  $1.0 \text{ M H}_2\text{SO}_4$  the maximum anodic current density,  $i_s$ , is  $1 \text{ A cm}^{-2}$ , and  $q_s$  shows a maximum at  $208 \pm 58 \mu\text{C cm}^{-2}$  covering the long potential range  $-250$  to  $+250$  mV (NHE). The second plateau in  $i_s$  and  $q_s$  does not occur in this electrolyte. Figures 4 and 5 also show plateau anodic charge densities in borate solutions.

Results obtained for ammoniacal electrolytes at three pH values are shown in Fig. 6-8. The diagrams show regions in which both  $i_s$  and  $q_s$  are independent of  $E$ . Regions of potential are also shown where  $i_s$  decreases with increase in  $E$ , although there is no parallel decrease in  $q_s$ . The potential range over which the latter effect occurs commences with the onset of anodic activity of the electrode as a whole, as can be seen by inspecting the appropriate values of  $i_b$  in Fig. 6-8. These features of the bare surface polarization curves are discussed below.

The bare surface mixed potentials  $E_{ms}$  are plotted in Fig. 9 as a function of pH, together with the reversible potentials for stable equilibrium reactions given by Pourbaix (13) for copper in noncomplexing solutions. Solution species are plotted at a concentration of  $10^{-6} \text{ M}$ . The values of  $E_{ms}$ , which represent potentials at which the rates of oxidation of copper and reduction of hydrogen on the scratch are equal, all lie well below the thermodynamic equilibrium potentials. The anodic reactions on the scratch are thus

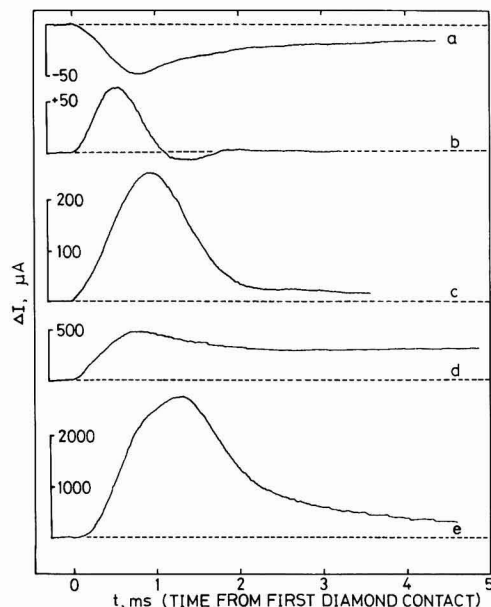


Fig. 2. Current transients obtained from scratching copper in  $1.0 \text{ M KOH}$  at the following potentials in mV (NHE): (a)  $-1060$ , (b)  $-760$ , (c)  $-385$ , (d)  $+65$ , (e)  $+540$ .

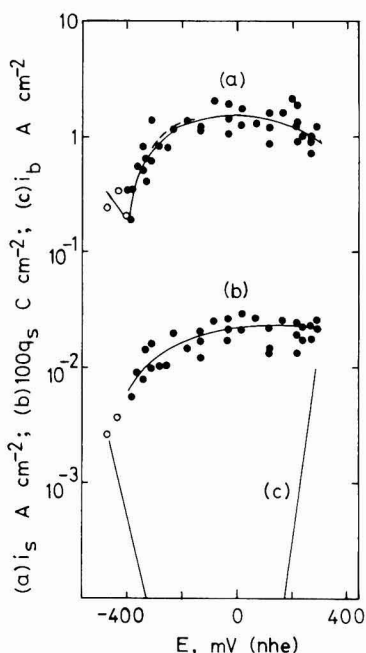


Fig. 3. Bare surface electrochemistry of copper in  $1.0 \text{ M H}_2\text{SO}_4$ . (a)  $i_s$ , (b)  $q_s$ , (c)  $i_b$ . Broken line denotes  $i_s$  corrected for ohmic drop (10). Black points anodic; white points cathodic.  $\omega = 100 \text{ Hz}$ .

occurring at an underpotential compared with the equilibrium potentials for bulk reactions. In the non-ammoniacal electrolytes two regions of pH dependence occur: For  $\text{pH} < 8$ ,  $\partial E_{ms}/\partial \text{pH} = -57 \text{ mV}$ , while for  $\text{pH} > 11$  the bare surface mixed potential is indepen-

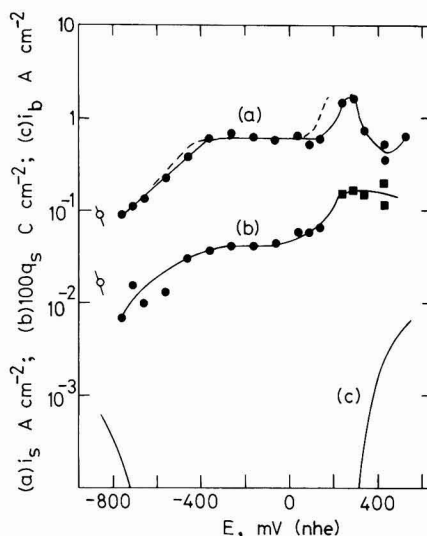


Fig. 4. Bare surface electrochemistry of copper in  $0.5 \text{ M Na}_2\text{SO}_4 + 0.05 \text{ M (H}_3\text{BO}_3 + \text{Na}_2\text{B}_4\text{O}_7)$ ,  $\text{pH} = 7.3$ . (a)  $i_s$ , (b)  $q_s$  after complete re-equilibration ( $\bullet$ ), or 5 msec after first stylus contact ( $\blacksquare$ ). (c)  $i_b$ . Broken line denotes  $i_s$  corrected for ohmic drop (10). Black points anodic; white points cathodic.  $\omega = 100 \text{ Hz}$ .



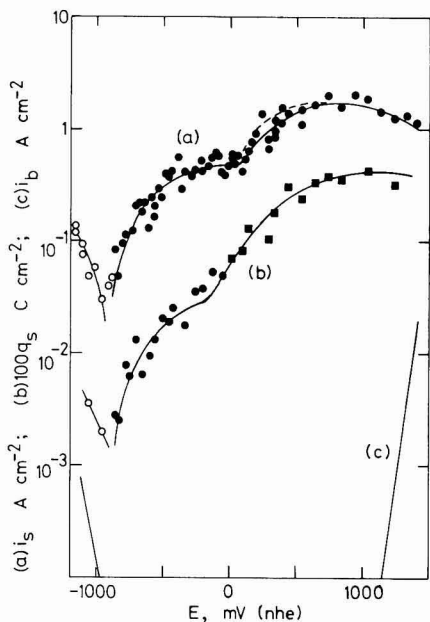


Fig. 5. Bare surface electrochemistry of copper in 0.5M  $K_2B_4O_7$ , pH = 9.8. (a)  $i_s$ , (b)  $q_s$  after complete re-equilibration (●) or 5 msec after first stylus contact (■). (c)  $i_b$ . Broken line denotes  $i_s$  corrected for ohmic drop (10). Black points anodic; white points cathodic.  $\omega = 100$  Hz.

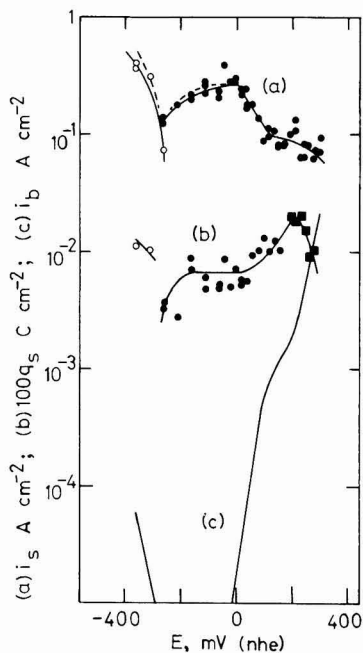


Fig. 6. Bare surface electrochemistry of copper in 1.0M  $(NH_3 + NH_4^+)$ , pH = 7.25. (a)  $i_s$ , (b)  $q_s$  after complete re-equilibration (●) or 5 msec after first stylus contact (■). (c)  $i_b$ . Broken line denotes  $i_s$  corrected for ohmic drop (10). Black points anodic; white points cathodic.  $\omega = 100$  Hz.

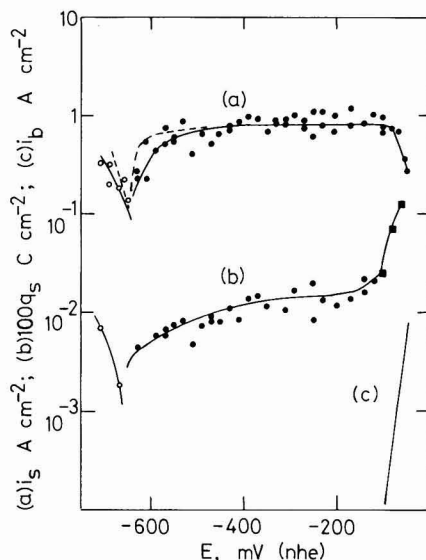


Fig. 7. Bare surface electrochemistry of copper in 1.0M  $(NH_3 + NH_4^+)$ , pH = 9.5. (a)  $i_s$ , (b)  $q_s$  after complete re-equilibration (●) or 5 msec after first stylus contact (■). (c)  $i_b$ . Broken line denotes  $i_s$  corrected for ohmic drop (10). Black points anodic; white points cathodic.  $\omega = 100$  Hz.

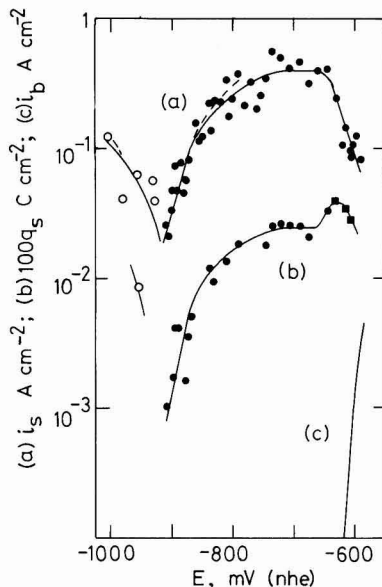


Fig. 8. Bare surface electrochemistry of copper in 1.0M  $NH_3 + 0.5M Na_2SO_4$ , pH = 11.6. (a)  $i_s$ , (b)  $q_s$  after complete re-equilibration (●) or 5 msec after first stylus contact (■). (c)  $i_b$ . Broken line denotes  $i_s$  corrected for ohmic drop (10). Black points anodic; white points cathodic.  $\omega = 100$  Hz.

dent of pH. In ammoniacal electrolytes the values of  $E_{ms}$  are more positive and give for pH < 10.  $\partial E_{ms}/\partial pH = 137$  mV, but this also tends toward pH independence at high pH.

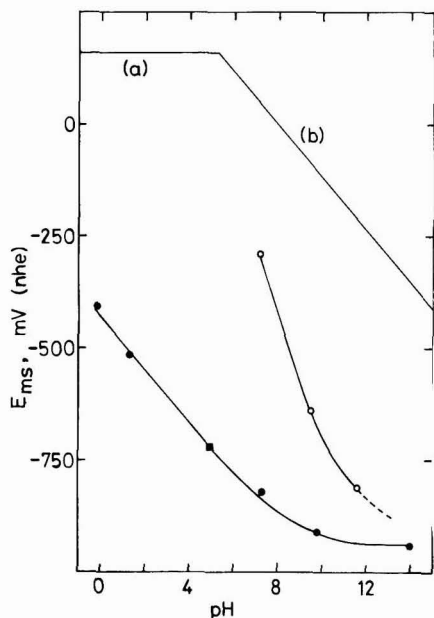


Fig. 9. Bare surface mixed potential  $E_{ms}$  of copper as a function of pH. Black points from nonammoniacal electrolytes; white points from ammoniacal electrolytes containing 1.0M  $(\text{NH}_3 + \text{NH}_4^+)$ . (■) from an acetate buffer solution containing 0.5M HOAc + 0.5M NaOAc. Also shown are the following equilibrium lines from Pourbaix (13): (a)  $\text{Cu} = \text{Cu}^{2+} + 2e^-$  with  $(\text{Cu}^{2+}) = 10^{-6}\text{M}$ , (b)  $2\text{Cu} + \text{H}_2\text{O} = \text{Cu}_2\text{O} + 2\text{H}^+ + 2e^-$ .

### Discussion

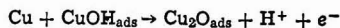
**Nonammoniacal electrolytes.**—In a previous paper we showed that the current and charge densities passed on scratched silver surfaces in 1.0M KOH were not significantly different from those obtained by potential pulsing or rapid potential sweeping experiments on unscratched silver surfaces. Two different adsorbed oxidized monolayers, designated AgOH and Ag<sub>2</sub>O, were proposed to account for anodic charge densities of  $\sim 150$  and  $\sim 300 \mu\text{C cm}^{-2}$ , respectively, obtained by all three techniques; these monolayers were shown to exist over two consecutive potential ranges, both well below the potentials at which anodic activity of the metal is expected (13). The fact that all three techniques showed similar behavior indicates that these observations are not influenced significantly by the highly defective nature of the surface produced by scratching. Figure 1 shows that copper behaves in a very similar way when scratched in 1.0M KOH, with two distinguishable plateaus in the anodic  $q_s$  vs.  $E$  curve (145 and  $378 \mu\text{C cm}^{-2}$ , respectively) at low potentials. It is not possible to compare these results obtained on scratched copper directly with those obtained from rapid potential sweeping or potential pulsing experiments owing to interference from the hydrogen electrode reaction. Thus no zero charge potential is observed for scratched copper [as was obtained for silver (3)] owing either to formation of adsorbed hydrogen or oxidation of Cu, or both, at all potentials around the bare surface mixed potential. The two plateau charge densities in the anodic region are ascribed to formation of single adsorbed monolayers of CuOH and Cu<sub>2</sub>O, respectively. One would expect a monolayer of Cu<sub>2</sub>O to contain approximately twice as many Cu<sup>+</sup> ions per unit area as CuOH, in line with comparisons of other oxide-hydroxide molar density ratios. Both of these monolayers occur at potentials well below the

equilibrium potentials required for multilayer oxide formation (13).

The full sequence of reactions exhibited by the scratched Cu electrode in 1.0M KOH is given in Table I. At  $-350$  mV (NHE)  $q_s$  rises above  $378 \mu\text{C cm}^{-2}$ , representing growth of a multilayer film of Cu<sub>2</sub>O, in full agreement with the value of  $E_o = -356$  mV (NHE) (13). Dissolution as  $\text{CuO}_2^{2-}$  also occurs and this contributes to the rise in  $i_b$ . Formation of Cu<sub>2</sub>O and CuO on the bare surface in Table I is described in terms of the net reactions, and the mechanisms are unknown. Thus for example the underpotential monolayer of Cu<sub>2</sub>O may occur in one step



or may form from the previously formed CuOH monolayer



The effects of scratching on the oxygen evolution reaction ( $E_o = +400$  mV (NHE)) are also unknown because of interference from the copper oxidation reactions.

The results obtained in 1.0M H<sub>2</sub>SO<sub>4</sub> (Fig. 3) differ from those shown in Fig. 2 in that  $q_s$  is almost constant at  $208 \mu\text{C cm}^{-2}$  over a large potential range. This charge density is consistent with, although slightly greater than that assigned to formation of a monolayer of CuOH in the alkaline solution, and the monolayer of Cu<sub>2</sub>O is not formed. In the borate electrolytes (Fig. 4 and 5) the higher charge density plateau, at  $300$  to  $400 \mu\text{C cm}^{-2}$ , is observed although plateaus at around  $150 \mu\text{C cm}^{-2}$  are obscure. The full analyses of these charges are given in Table II, together with those obtained from the ammoniacal electrolytes.

It is important to realize that in 1.0M H<sub>2</sub>SO<sub>4</sub> only the CuOH monolayer is formed. The monolayer of adsorbed Cu<sub>2</sub>O, which is apparent at potentials below the Cu/bulk Cu<sub>2</sub>O reversible potential in neutral and alkaline solutions, was not found in acid solution. Inspection of the  $i_b$  vs.  $E$  curve for the acid electrolyte (Fig. 3) shows that there is no tendency for the metal to passivate. Clearly, the first monolayer of Cu<sub>2</sub>O is a necessary precursor for passivation, whereas the adsorbed CuOH monolayer acts as an intermediate layer in both the dissolution and passivation processes. Indeed, the CuOH layer probably participates in the hydrogen evolution reaction as well, since Fig. 1-5 indicate that the layer is present at potentials where hydrogen evolution occurs in the steady state. It is for this reason, of course, that the hydrogen evolution reaction is accelerated on scratching. In the regions where  $i_s$  is cathodic in Fig. 1-5 values of  $q_s$  show that more than a monolayer of hydrogen is reduced on the scratch surface before a steady state is reestablished.

**Ammoniacal electrolytes.**—The introduction of 1.0M  $(\text{NH}_3 + \text{NH}_4^+)$  into neutral electrolytes (Fig. 6) profoundly affects the behavior of the scratched copper electrode. Values of  $q_s$  in the potential range  $-150$  to  $+50$  mV (NHE) were  $62 \mu\text{C cm}^{-2}$ , compared with  $388 \mu\text{C cm}^{-2}$  in the absence of ammonia (see Table II). The Cu<sub>2</sub>O monolayer is thus not formed in the ammoniacal solution. Indeed, the values of  $q_s$  are even smaller than that expected for a monolayer of CuOH, and it is clear that NH<sub>3</sub> must be incorporated into the monolayer lattice, so that the number of copper atoms required to form the oxidized monolayer is decreased. The proposed monolayer for ammoniacal electrolytes is  $\text{Cu}(\text{NH}_3)\text{OH}$ , in which the cation is now  $\text{Cu}(\text{NH}_3)^+$ , occupying a greater surface area per cation than Cu<sup>+</sup> for nonammoniacal electrolytes. The formation of the ammonia-containing monolayer might be expected to hinder further reaction to produce the Cu<sub>2</sub>O monolayer and thus impede passivation of the metal at higher po-

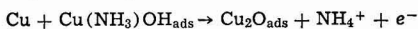
Table I. Reactions of scratched copper in 1.0M KOH and steady-state surface composition as a function of *E*

<i>E</i> , mV (NHE)	Bare surface reactions	Steady-state surface composition
< -900	$\text{H}_2\text{O} + e^- \rightarrow \text{H}_{\text{ads}} + \text{OH}^-$	$\theta_{\text{H}} \ll 1$ $\theta_{\text{CuOH}} = 1$ $\theta_{\text{CuO}} + \theta_{\text{Cu}_2\text{O}} = 1$
-900 to -550	$\text{Cu} + \text{OH}^- \rightarrow \text{CuOH}_{\text{ads}} + e^-$	$\theta_{\text{CuOH}} = 1$
-550 to -500	$\text{Cu} + \text{OH}^- \rightarrow \text{CuOH}_{\text{ads}} + e^-$ $2\text{Cu} + \text{OH}^- \rightarrow \text{Cu}_2\text{O}_{\text{ads}} + \text{H}^+ + 2e^-$	$\theta_{\text{Cu}_2\text{O}} = 1$
-500 to -350	$2\text{Cu} + \text{OH}^- \rightarrow \text{Cu}_2\text{O}_{\text{ads}} + \text{H}^+ + 2e^-$	$\text{Cu}_2\text{O}$ (multilayer)
-350 to -150	$2\text{Cu} + \text{OH}^- \rightarrow \text{Cu}_2\text{O}_{\text{ads}} + \text{H}^+ + 2e^-$	$\text{CuO}$ (multilayer)
> -150	$\text{Cu} + \text{OH}^- \rightarrow \text{CuO}_{\text{ads}} + \text{H}^+ + 2e^-$	

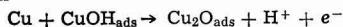
Table II. Analysis of plateau charge densities passed on a bare copper surface in several electrolytes. Error limits are standard deviations over the number of points given. The adsorbed surface monolayers give the proposed stoichiometries, each at complete monolayer coverage.

Electrolyte	pH	<i>E</i> , mV (NHE)	<i>q<sub>s</sub></i> (μC cm <sup>-2</sup> )	Number of points	Adsorbed surface monolayer
1.0M KOH	14	-800 to -600	145 ± 26	9	CuOH
1.0M KOH	14	-500 to -400	378 ± 58	4	Cu <sub>2</sub> O
0.5M K <sub>2</sub> B <sub>4</sub> O <sub>7</sub>	9.8	-250 to -200	352 ± 25	2	Cu <sub>2</sub> O
0.5M Na <sub>2</sub> SO <sub>4</sub> + 0.05M (H <sub>2</sub> BO <sub>3</sub> + Na <sub>2</sub> B <sub>4</sub> O <sub>7</sub> )	7.3	-450 to -50	388 ± 55	5	Cu <sub>2</sub> O
1.0M H <sub>2</sub> SO <sub>4</sub>	-0.16	-250 to +275	208 ± 58	26	CuOH
1.0M NH <sub>3</sub> + 0.5M Na <sub>2</sub> SO <sub>4</sub>	11.6	-490 to -350	233 ± 33	6	CuOH
1.0M (NH <sub>3</sub> + NH <sub>4</sub> <sup>+</sup> ) + SO <sub>4</sub> <sup>2-</sup>	9.5	-390 to -170	133 ± 32	10	CuOH + Cu(NH <sub>3</sub> )OH
1.0M (NH <sub>3</sub> + NH <sub>4</sub> <sup>+</sup> ) + SO <sub>4</sub> <sup>2-</sup>	7.25	-150 to +50	62 ± 15	12	Cu(NH <sub>3</sub> )OH

tentials, since the process



requires removal of NH<sub>4</sub><sup>+</sup> rather than H<sup>+</sup>, as in the reaction



This is reflected in the far higher steady-state dissolution current densities *i<sub>b</sub>* shown for ammoniacal electrolytes (compare Fig. 6-8 with Fig. 1, 4, and 5). In this respect it is noteworthy that the main product of steady-state anodic dissolution of Cu in these ammoniacal electrolytes is Cu(NH<sub>3</sub>)<sub>2</sub><sup>+</sup>, which is soluble to the extent of 0.05M in equilibrium with Cu<sub>2</sub>O (14).

For higher pH, on the other hand, the values of *q<sub>s</sub>* shown in Table II for ammoniacal electrolytes are higher; this is probably due to reversion of the monolayer to CuOH with increase in hydroxide concentration. This is also reflected in the *E<sub>ms</sub>* vs. pH curve (Fig. 9): at high pH *E<sub>ms</sub>* approaches the same constant value for both types of electrolytes. Values of the dissolution current density *i<sub>b</sub>*, however, are not a direct consequence of whether the initial monolayer is CuOH or Cu(NH<sub>3</sub>)OH, since formation of the monolayer is not the rate-determining step in the total dissolution process. Subsequent steps also clearly involve complexing ligands. This has already been described for the scratched iron electrode in chloride and bicarbonate electrolytes (2). Both Cl<sup>-</sup> and HCO<sub>3</sub><sup>-</sup> cause pitting of iron, but only Cl<sup>-</sup> enters the formation of the initial monolayer.

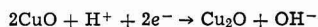
**Effects of electrolyte resistance.**—Many of the bare surface polarization curves shown in Fig. 1 and 3-8 exhibit regions in which *i<sub>s</sub>* decreases as *E* becomes more positive. The feature is shown most dramatically in Fig. 1 and 6-8 and is invariably associated with a rise in *i<sub>b</sub>*, representing an increasing rate of anodic dissolution of Cu from the unscratched surface. It is not seen in electrolytes in which Cu is passive (Fig. 4 and 5); nor is it seen in the sulfuric acid system. The effect is associated invariably with ohmic potential drops (10) which occur on and near the scratched surfaces owing to a combination of high electrolyte resistance and high anodic scratch current densities. The consequence of this is to superimpose on the anodic

current transient emanating from the scratch, a cathodic current transient resulting from a lowering of the electrode potential on an area surrounding the scratch when the electrode as a whole is dissolving or carries a readily reducible film. The effect may include two components: a decrease in the rate of steady-state anodic dissolution of the area surrounding the scratch, or electrochemical reduction of surface oxidized species. Thus for example, in Fig. 1 in the potential region in which steady-state dissolution as Cu(II) (in the form of CuO<sub>2</sub><sup>2-</sup>) occurs from the electrode as a whole, scratching the electrode causes a transient reduction in the rate of steady-state dissolution on an area surrounding the scratch, giving an apparent lowering of the value of *i<sub>s</sub>* with increasing *E*. The further possible effect of the ohmic potential drop is to reduce oxidized ions on the surface, for example by the following reactions:

on the scratch



on the surrounding surface



Either or both mechanisms may explain the effect as it is observed in 1.0M KOH (Fig. 1) since it occurs in a potential region [commencing at -150 mV (NHE)] where both CuO<sub>2</sub><sup>2-</sup> and CuO can form (13). The effect has also been observed for the scratched silver electrode (3) at potentials where AgO is reduced transiently to Ag<sub>2</sub>O on the area surrounding the scratch.

In 1.0M H<sub>2</sub>SO<sub>4</sub> (Fig. 3) the ohmic potential drop effect is not observed, despite overall dissolution of the electrode, since the ohmic resistance of the electrolyte is small, and the values of *i<sub>s</sub>* are themselves lower. In the ammoniacal environments, however, where the electrolyte resistance is high, the effect is clearly observed where the entire electrode is dissolving as Cu(NH<sub>3</sub>)<sub>2</sub><sup>+</sup>.

Previous work on scratched and rapidly strained brass electrodes in ammoniacal electrolytes (8, 15) has overlooked these effects and thus obtained values of *i<sub>b</sub>* which are too low. While the effect has not yet been fully quantified, it is clear that the electrode surface

area over which it extends is large compared with the scratch area since  $i_s$  is large compared with  $i_b$ . It follows that an increase in the ratio of the scratch area to the total electrode area would decrease the ohmic potential effect, and this has indeed been demonstrated by the use of lacquered and partially lacquered electrodes. Appropriate positioning of the Luggin capillary probe would also be of some benefit, but this is impracticable because (i) the proximity of the scratching stylus and (ii) the diameter of the probe tip which would have to be small compared with the scratch size.

### Conclusions

1. Scratching of Cu electrodes at constant potential results in greatly accelerated anodic oxidation and cathodic reduction current densities. Up to  $8 \text{ A cm}^{-2}$  of anodic reaction have been recorded.

2. Copper carries two surface oxidized monolayers at potentials very much more negative than the Cu/Cu<sub>2</sub>O reversible potential. These underpotential monolayers are designated as CuOH and Cu<sub>2</sub>O and account for anodic charge densities of  $\sim 150$  and  $300\text{--}400 \mu\text{C cm}^{-2}$  on the scratch surface, each occurring to complete coverage. The former exists at the lowest accessible anodic potentials on the scratch and probably even into the region where hydrogen evolution is the dominant electrode reaction.

3. The Cu<sub>2</sub>O monolayer occurs only in neutral and alkaline solutions and is a necessary precursor to passivation of the metal at higher potentials by a thicker film of Cu<sub>2</sub>O.

4. The steady-state anodic dissolution of Cu occurs through an adsorbed monolayer of CuOH at complete coverage. The steady-state evolution of hydrogen on Cu also occurs through this monolayer, at least at low cathodic overpotentials.

5. The presence of  $1.0 \text{ M } (\text{NH}_3 + \text{NH}_4^+)$  in the electrolyte results in formation of an adsorbed monolayer of  $\text{Cu}(\text{NH}_3)\text{OH}$  in the neutral pH range at potentials very much more negative than the Cu/Cu<sub>2</sub>O reversible potential. This monolayer is not readily converted to a Cu<sub>2</sub>O monolayer, and results in dissolution of the metal as  $\text{Cu}(\text{NH}_3)_2^+$  at higher anodic potentials.

6. The scratched copper electrode does not yield a potential of zero charge since electron transfer occurs at all potentials for all pH.

### Acknowledgment

We are grateful to the British Petroleum Company Limited for the award of a research studentship to R.C.N.

Manuscript submitted Nov. 19, 1980; revised manuscript received March 31, 1981.

Any discussion of this paper will appear in a Discussion Section to be published in the June 1982 JOURNAL. All discussions for the June 1982 Discussion Section should be submitted by Feb. 1, 1982.

### REFERENCES

1. G. T. Burstein and D. H. Davies, *This Journal*, **128**, 33 (1981).
2. G. T. Burstein and D. H. Davies, *Corros. Sci.*, **20**, 1143 (1980).
3. G. T. Burstein and R. C. Newman, *Electrochim. Acta*, **25**, 1009 (1980).
4. G. T. Burstein and R. C. Newman, *ibid.*, **26**, 1143 (1981).
5. F. P. Ford, G. T. Burstein, and T. P. Hoar, *This Journal*, **127**, 1325 (1980).
6. R. C. Newman and G. T. Burstein, *Corros. Sci.*, **21**, 119 (1981).
7. T. N. Andersen, J. L. Anderson, and H. Eyring, *J. Phys. Chem.*, **73**, 3562 (1969).
8. D. J. Lees and T. P. Hoar, *Corros. Sci.*, **20**, 761 (1980).
9. T. P. Hoar and J. C. Scully, *This Journal*, **111**, 348 (1964).
10. H. J. Pearson, G. T. Burstein, and R. C. Newman, *ibid.*, **128**, 2297 (1981).
11. S. P. Pednekar, A. K. Agrawal, H. E. Chaung, and R. W. Staehle, *ibid.*, **127**, 701 (1980).
12. R. C. Newman and G. T. Burstein, *ibid.*, **127**, 2527 (1980).
13. M. Pourbaix, "Atlas of Electrochemical Equilibria in Aqueous Solutions," p. 393, Pergamon/CEBELCOR, Oxford (1966).
14. T. P. Hoar and G. P. Rothwell, *Electrochim. Acta*, **15**, 1037 (1970).
15. J. J. Podesta, G. P. Rothwell, and T. P. Hoar, *Corros. Sci.*, **11**, 241 (1971).

## Protective Coatings by Anodic Coupling Polymerization of o-Allylphenol

Giuliano Mengoli, Paolo Bianco, Sergio Daolio, and Maria Teresa Munari

Istituto di Polarografia ed Elettrochimica Preparativa del C.N.R., Corso Stati Uniti 4, 35100 Padova, Italy

### ABSTRACT

The anodization of Fe sheets in hydroalcoholic solutions of o-allylphenol containing allylamine leads to *in situ* formation of coherent coatings. These coatings consist of thermosetting polyoxyphenylenes which after thermal curing have good adhesion and impart corrosion protection to the substrate. The anodization time and electric power consumption are comparable with those typical of a conventional electrophoretic coating.

A route for achieving the *in situ* formation of thick ( $10\text{--}20 \mu\text{m}$ ) polyoxyphenylene coatings, having possible applications for metal protection, has been recently outlined (1, 2). The process may be realized by anodizing, at the metal surface to be coated, hydroalcoholic solutions of phenol containing a suitable amine [allylamine gave the best performances (2)]. However, the data so far reported have shown that

the process is not yet competitive with other conventional "painting" techniques. In comparison with the electrophoretic deposition (3) of preformed polymers, the major handicaps were: extended electrolysis times; limited corrosion resistance of the coatings (from salt fog tests), and poor adhesion under stress (from conical mandrel and drawing tests).

The fact that the electrolysis time was too long was mainly related to the low useful electrolysis current

Key words: film, corrosion, organic, electrolysis.

(<10 mA/cm<sup>2</sup>). *In situ* phenol polymerization, in fact, did not tolerate high applied voltages,<sup>1</sup> because either passivation of the substrate occurred especially when Fe sheet anodes were coated, or rupture of the film being formed took place. The limited corrosion resistance and poor adhesion were likely related to the structure of the polymer. The polymer probably was, *ab initio*, exceedingly branched and cross-linked and thus could neither take appreciable advantage from thermal curing nor have elasticity enough to tolerate stresses and deformations. Through the utilization of *o*-allylphenol instead of phenol we now have overcome such handicaps.

The aim of this paper is to describe both the features of *o*-allylphenol/allylamine *in situ* polymerization on to Fe sheet anodes and the protective performances of the resulting coatings.

### Experimental

**Apparatus and procedure.**—The coating runs were performed in a single compartment cell described previously (1, 4) by applying a constant voltage between the sample of Fe sheet (anode) and a Pt coil (cathode) facing the sheet. Physical properties of the coated specimens were determined according to ASTM methods. The composition of the polymeric material, once recovered from the substrate, was investigated by instrumental analytical techniques, including pyrolysis coupled to mass spectroscopy (5) and thermogravimetry. Information on the molecular weights and their distribution was obtained by vapor pressure osmometry and gel permeation chromatography. Other experimental details are reported in either the tables or the captions of the figures.

**Chemicals.**—All compounds used in this study were commercially available reagent grade chemicals. The reaction medium consisted of water/alcohol mixtures. The preferred standard composition was: *o*-allylphenol 6 ml, allylamine 6 ml, cellosolve 2 ml, KOH 0.5g, all dissolved in a standard 100 ml of H<sub>2</sub>O/CH<sub>3</sub>OH (equal volumes). The Fe sheets [23.5 × 2.5 × 0.05 cm (1, 2)] were dipped in alkaline cleaning bath prior to coating.

### Results

**Characteristics of the electrolytic process.**—The formation of coatings on Fe sheet anodes from the *o*-allylphenol/allylamine system bears many similarities to systems based on phenol as described in preceding papers (1, 2). Thus, the coating material is produced by a yield not far from 2F/mol of monomer consumed. An oxidative coupling process is therefore strongly supported, whereas the engagement of the allyl group in an electrolytic polymerization must be discarded.

The formation of a coherent and homogeneous coating is indicated, during electrolysis, by a smooth continuous current decrease. Such current transients are qualitatively affected by experimental variables such as monomer and amine concentration, temperature, composition of the medium, and applied voltage.

However, it must be noted that the high voltages applied here (≥ 15V) do not cause the dramatic passivation phenomena observed elsewhere (1, 2). This behavior is illustrated in Fig. 1 and 2. Figure 1 shows the current transients obtained during the coating process for various applied voltages. In each case the sheets were uniformly coated: The high residual current tested at the highest voltage is due to the relatively low electrical resistance of the wet film. Figure 2 shows the current-potential curves obtained potentiodynamically on a rotating Fe microdisk. Anode insulation by filming is evident here only for very

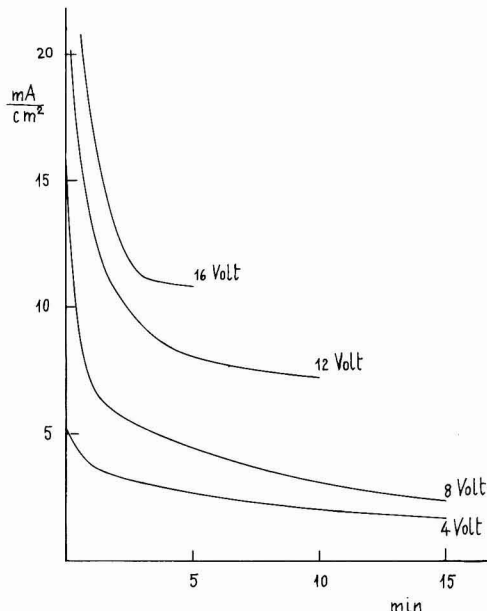


Fig. 1. Current transients during the anodization of Fe sheets in the standard composition (*o*-allylphenol 0.456 mol liter<sup>-1</sup>, allylamine 0.800 mol liter<sup>-1</sup>, cellosolve 0.200 mol liter<sup>-1</sup>, KOH 0.09 mol liter<sup>-1</sup>, in H<sub>2</sub>O/CH<sub>3</sub>OH at *t* = 25°C) for increasing applied voltages.

low potential sweep rates (i.e., long electrolysis times).

As mentioned before, the fact that the *o*-allylphenol/allylamine system tolerates far higher voltages than phenol-based systems is very important from a practical point of view, as faster coating operations are achieved. This may be deduced from the data of Table I. The decrease of coulombic yield taking place as the voltage is increased to 16V is quite acceptable considering that both coating thickness (mg/cm<sup>2</sup>) and deposition time become typical of a conventional electrophoretic process.<sup>2</sup>

**Molecular weights.**—In previous work, the coating material obtained from phenol, when dried, partially dissolved only in trifluoroacetic acid. By contrast the (uncured) products from allylphenol consist of a major fraction soluble in common organic solvents (acetone) and a minor insoluble fraction. The latter, which constitutes the inner layer in contact with the metal, may become important in some experimental conditions.

Table II shows how the experimental variables influence both  $\bar{M}_n$  and the ratio of soluble to insoluble fractions. Constancy (in the range 2000-3000) of  $\bar{M}_n$  obtained for different conditions indicates that the termination step is mainly determined by insolubility of the chains, which cannot thus undergo further anode oxidation. The higher  $\bar{M}_n$  resulting either at a high percentage of methanol (runs 8-9) or with ethanol and propanol instead of methanol (runs 20-21), therefore takes into account the increased solubility of the polymer in the medium, whereby chain precipitation takes place for higher degrees of polymerization. The inverse dependence of  $\bar{M}_n$  on monomer concentration which seems indicated by runs 1

<sup>1</sup> Not more than 3.5V could be generally applied to an electrolyzer having a cell constant ~20 cm, and for solutions having  $\chi = 3.8$  msec (1).

<sup>2</sup> The current passed is about ten times higher here than in electrophoresis, but power consumption ( $i \times t \times v$ ) is of the same order.



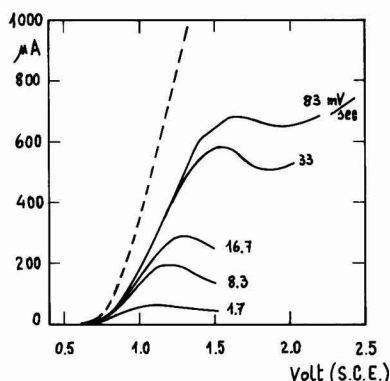


Fig. 2. Current-potential (vs. SCE) curves obtained from the standard composition by a rotating (1000 r/min) Fe microanode (area 0.03 cm<sup>2</sup>). The dashed line refers to the oxidation of the background system alone; the other curves refer to increasing sweep rates (mV sec<sup>-1</sup>).

and 5-7 is not surprising when considering that polymer chains are built up step by step at the anode and that the probability of oxidizing and coupling the same chains again increases with monomer dilution. The formation of the insoluble fraction seems to be favored by the highest temperatures, methanol concentrations, and electrolysis times, but depends inversely on the amine concentration (runs 17-19). Neither applied voltage nor charge transferred has any influence.

Molecular weight distributions were estimated, using polystyrene as a standard, by gel permeation chromatography, as shown in Fig. 3.

Table I. Features of electrolytic coating process for various voltages applied\*

Applied voltage (V)	Time (min)	Charge (C)	I initial (mA/cm <sup>2</sup> )	I final (mA/cm <sup>2</sup> )	Current yield (mg/C)
3.0	50	81	2.78	0.59	0.577
5.0	15	78	8.52	1.89	0.554
10.0	8	86	23.33	5.00	0.477
16.0	3	74	31.48	10.55	0.400

\* Conditions: o-allylphenol 0.456 mol liter<sup>-1</sup>; allylamine 0.800 mol liter<sup>-1</sup>; cellosolve 0.200 mol liter<sup>-1</sup>; H<sub>2</sub>O/CH<sub>3</sub>OH 50% by volume;  $t = 25^{\circ}\text{C}$ . The coating yield (mg/cm<sup>2</sup>) ranged from 1.7 (3V) to 1.3 (16V).

Table II. Features of the coating and molecular weight of the product for various experimental conditions

Run No.	Temp (°C)	Alcohol (%)	o-Allylphenol (mol/liter)	Allylamine (mol/liter)	Voltage (V)	Electr. time (min)	Coulombs	Yield (mg/C)	Insoluble (%)	$\bar{M}_n$ *
1	25	Methanol 50	0.456	0.800	4.0	65	100	0.60	17.7	2660
2	25	Methanol 50	0.456	0.800	8.0	18	100	0.52	10.0	2320
3	25	Methanol 50	0.456	0.800	12.0	9	100	0.42	10.0	2110
4	25	Methanol 50	0.456	0.800	16.0	4 30 sec	100	0.40	7.0	2420
5	25	Methanol 50	0.110	0.200	8.0	38	22	0.30	27.6	3030
6	25	Methanol 50	0.228	1.400	8.0	49	60	0.53	8.9	2630
7	25	Methanol 50	0.684	1.200	8.0	5	60	0.62	5.2	2030
8	25	Methanol 85	0.228	0.400	8.0	20	60	0.15	63.7	3220
9	25	Methanol 70	0.228	0.400	8.0	46	60	0.20	20.8	3050
10	25	Methanol 35	0.228	0.400	8.0	10	60	0.65	7.4	2160
11	45	Methanol 50	0.456	0.800	8.0	47	100	0.60	56.3	2520
12	35	Methanol 50	0.456	0.800	8.0	23	100	0.60	20.8	2670
13	13	Methanol 50	0.456	0.800	8.0	13	100	0.54	0.1	1630
14	25	Methanol 50	0.456	0.800	8.0	44	200	0.53	6.7	2260
15	25	Methanol 50	0.456	0.800	8.0	2	30	0.65	5.8	2000
16	25	Methanol 50	0.456	0.800	8.0	1	15	0.68	4.3	2360
17	25	Methanol 50	0.456	0.270	8.0	34	100	0.54	28.5	2700
18	25	Methanol 50	0.456	0.132	8.0	60	100	0.50	45.1	2500
19	25	Methanol 50	0.456	0.068	8.0	40	100	0.58	56.4	2500
20	25	Propanol 50	0.456	0.800	8.0	18	100	0.39	8.6	3750
21	25	Ethanol 50	0.456	0.800	8.0	27	100	0.49	5.0	3220

\* Determined by vapor pressure osmometry in acetone at 40°C.

**Reproducibility of coating performances.**—Figure 3 refers to samples selected from a series of 50 sheets, all coated one after the other, with the same 100 ml of standard solution. The good independence of molecular weights on the progressive number of the sheets constitutes a first test of reproducibility for the system.

Confirmation is provided by the constancy of the coulombic yield (mg/C  $\approx$  0.55) observed during the coating process for all these 50 sheets. However, in a limited volume of solution, repeated coating runs lead to a kinetic decline. This is shown in Fig. 4 where the coating yield (mg/cm<sup>2</sup>) obtained on each sheet after 30 min of electrolysis (i.e., average coating rate) is plotted vs. the progressive number of sheets. This behavior is determined by progressive impoverishment of the monomer from the solution (compare dashed curves a and b of Fig. 4). For the same voltage and electrolysis time, a concentration decrease in effect results in a reduced transfer of current. However, since from a practical point of view it is very easy to achieve automatic control of both monomer concentration in solution and thickness of coatings formed (by the coulombs passed), it may be concluded that system features<sup>3</sup> are such as to allow application in continuous processes.

**Protective features of the coatings.**—When withdrawn from the anodization bath, the coated sheets appear homogeneous and coherent, their color varying from pale yellow to brown yellow.

Wet film adhesion to the substrate is good enough to allow rinsing in running water before drying. When the samples are cured in an oven at 150°-155°C for 20-30 min a fine gloss is obtained. Thermal treatment further improves resistance toward chemicals and organic solvents as well as any other protective feature.

Table III shows the properties of samples obtained on varying either o-allylphenol/allylamine concentrations or electrolysis voltages. Each sample was prepared with the same current passed. The very good results of the conical mandrel and drawing tests, evidencing strong adhesion coupled to elasticity, are to be noted. Remarkable improvements are furthermore shown in the salt fog tests: The time scale of resistance to salt corrosion, especially for samples prepared by fast electrolysis (high voltages), is now more than an order of magnitude higher than the data

<sup>3</sup> The gas chromatographic analysis of the solutions after repeated coating operations performed on different days showed only dimers as by-products; however, these are easily engaged in the anodic coupling.

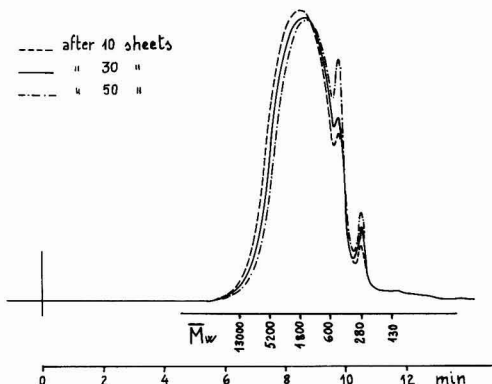


Fig. 3. Gel permeation of unpurified coating samples obtained from a solution utilized for repetitive coating runs. Progressive number of the sheet equal to: --- 10; — 30; - - - 50. Chromatographic conditions: column  $\mu$ m Styragel 500 A; solvent THF 1 ml/min; detector u.v. 254 nm.

previously reported (800 hr as against 24 hr (1) and 48 hr (2)).

Table IV shows the influence on physical properties of either the temperature of the electrolytic bath or the amount of current passed. An increase in temperature seems to increase the resistance to salt corrosion, while the number of coulombs passed (which controls the thickness of the polymer film) improves that resistance until the coating is between 10–15  $\mu$ m thick. As regards the influence of the medium on physical properties, it must be mentioned that in nearly methanolic solvent (85%) only thin films (1–2  $\mu$ m) are obtained, by a low current yield. During the electrolysis these films rapidly passivate the substrate, but when submitted to physical tests, neither give (making due allowance for their thinness) improved protection to the metal nor benefit from curing. The reason for this is discussed below.

**Composition of the coating material.**—The elemental compositions of either the soluble or the insoluble fractions are not far from the theoretical provisions of an allylsubstituted polyoxyphenylene, although some nitrogen is present (see Table V). With respect

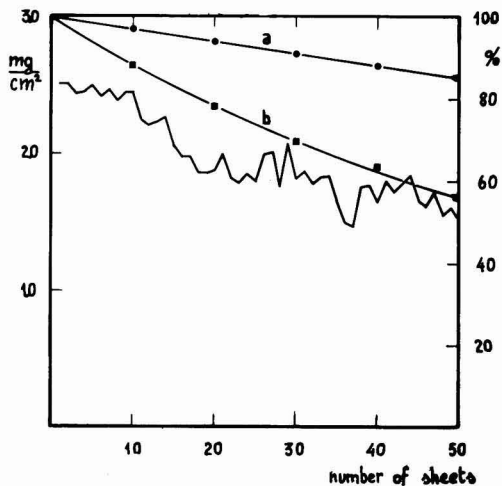


Fig. 4. Left-side scale: polymer yield ( $\text{mg}/\text{cm}^2$ ) obtained after a fixed electrolysis time as a function of the number of the samples coated. Right-side scale: curve a, volume decrease (%); curve b, o-allylphenol decrease (%).

to this fact it must be noted that the amount of nitrogen (which derives from the amine) is many times higher in the coatings obtained from phenol (2.5–6%). Similarity for both the soluble and insoluble fractions also exists in the infrared and mass spectroscopy patterns. The second technique, after pyrolysis of the samples at  $t \approx 260^\circ\text{C}$  and ionization by a 70 eV electron beam, mainly shows peaks of the structure:

	m/e	n
$\text{H}-\left[\text{C}_6\text{H}_4-\text{O}\right]_n-\text{CH}_2-\text{CH}=\text{CH}_2$	134	1
	266	2
	398	3
	530	4

The thermal curing reaction was examined by both infrared and thermogravimetry.

Table III. Physical properties of samples obtained for various o-allylphenol concentrations and applied voltages

	0.228 0.400	0.456 0.800	0.684 1.200	0.608 0.533
o-Allylphenol (mol/liter)				
Allylamine (mol/liter)				
Voltage (V)	8.0	4.0	8.0	8.0
Thickness ( $\mu\text{m}$ )	10	18	14	16
Cross cut adhesion	Very good	Very good	Very good	Very good
Microholes/ $\text{cm}^2$	0	0	0	0
Conical mandrel (ASTM test)	Very good	Very good	Good	Good
Drawing (ASTM test)	Very good	Very good	Good	Good
Hardness*	6H	6H	6H	6H
Salt fog resistance (h)**	200	150	180	220
U.V. resistance (h)	>300	>300	>300	>300

\* Determined by graphite standards.

\*\* ASTM method B117.

Table IV. Physical properties of samples obtained for various temperatures and coulombs

Temperature ( $^\circ\text{C}$ )	13	35	45	25	25	25	25	25
Coulombs	100	100	100	15	30	60	150	200
Thickness ( $\mu\text{m}$ )	14	18	15	2.5	4	9.5	25	30
Microholes/ $\text{cm}^2$	0	0	0	50	20	0	0	2
Hardness	6H	6H	6H	6H	6H	6H	6H	6H
Adhesion + elasticity	Very good	Very good	Very good	Very good	Very good	Very good	Good	Good
Salt fog resistance (h)	120	280	500	70	280	400	150	120

The anodization solution had the standard composition.

On comparing infrared spectra obtained from samples before and after thermal curing, the following variations may be outlined: (i) The uncured samples show three bands in the range 3000–2840  $\text{cm}^{-1}$ , typical of allyl C–H stretching, and a sharp band at 1640  $\text{cm}^{-1}$ , which may be ascribed to  $\text{—HC=CH}_2$  stretching; (ii) in the cured samples, the morphology of the bands between 3000–2840  $\text{cm}^{-1}$  changes, although the respective  $\nu$  do not. At the same time the band at 1640  $\text{cm}^{-1}$  becomes very feeble, and a new absorption appears between 1750–1650  $\text{cm}^{-1}$  (maximum at 1715  $\text{cm}^{-1}$ ), which may be ascribed to  $\text{C=O}$ .

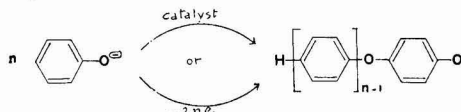
Different results are obtained from the thermogravimetric analysis when the experiments are performed in either nitrogen or air. Under  $\text{N}_2$  a slow weight loss takes place up to pyrolysis conditions: at 285°C an exothermic reaction occurs (by DTG). Under air, the weight of the samples increases from 140°C, the reaction reaching its maximum at 170°C; pyrolysis occurs at 230°C.

An oxidative cross-linking is thus strongly supported as the main curing process. It must also be noted that since the polymer has a  $T_g$  at 328 K, it passes through a viscous quasi-melting state in the oven before reacting with oxygen.

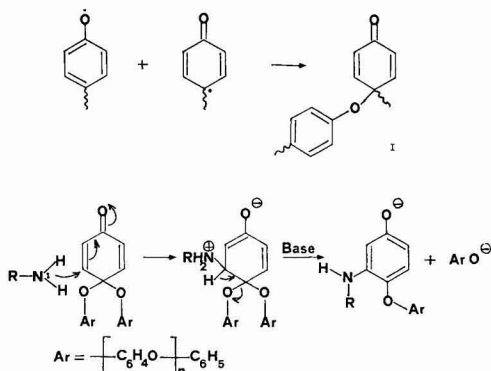
### Discussion

In order to explain the results shown by *o*-allylphenol, it seems useful to summarize the mechanism of *in situ* coating formation.

In the electrochemical coupling of phenoxide anions, the anode substitutes the copper salt amine complex catalyst (6)



For the chemical polymerization the exhausted (reduced) copper catalyst is continuously restored (oxidized) by oxygen; electrochemically the continuity of the oxidation is provided by the anodic potential. The polymerization reaction is not limited to head-to-tail coupling, but also involves the ortho positions: For this reason 2,6-dimethylphenol is usually used for obtaining technologically useful linear polymers (6). We have also shown (2) that during anodic coupling of phenol in the presence of amines,<sup>4</sup> a side reaction frequently takes place between quinol-ether polymeric (I) intermediates (6–8) and amine according to the following scheme



<sup>4</sup> The amine has a fundamental role as inhibitor of Fe oxidation in the anodic formation of polyoxyphenylene coatings onto Fe sheets (2).

Table V.

	Elemental analysis		
	C	H	N
Theoretical composition	81.2	6.7	—
Soluble fraction	79.2	5.31	0.70
Insoluble fraction	77.8	4.65	0.78

The reaction with amines is favored by the electron-attracting ortho substituents which increase the electrophilicity of quinol-ether meta positions. It is probable that other nucleophilic molecules or ions such as  $\text{OH}^-$  may attack the same positions. In this last case, the newly formed phenolic group might be engaged in the oxidative coupling, thus contributing strongly toward cross-linking. As regards *o*-allylphenol, the *o*-allyl group reduces the occurrence either of coupling in ortho or attack in meta by amine and  $\text{OH}^-$ . Branching and cross-linking are therefore strongly reduced with respect to phenol polymers. The linearity of the chains leads to two consequences: Uncured coatings have good solubility; and in the oven, before curing, the coating material may melt, thus achieving complete and homogeneous spreading onto the substrate.

However, the same should also hold for other alkyl substituted phenols, whereas we have observed the formation of poorly adhering coatings from, for instance, 2,6-dimethylphenol. The reason for the peculiar behavior of *o*-allylphenol is thus to be found in a strong interaction of the allyl group with the substrate, which causes adsorption of the monomer and bonding to the metal of the polymer as it is formed.

These considerations seem strongly supported by the following macroscopic evidence:

1. High voltages are tolerated during deposition. This fact is also related to the linearity of chains which, swollen by solution, do not cause excessive electric resistance.

2. There is strong adhesion of the polymeric material to the substrate. Such adhesion (which may also be related to the morphology of the chains as determined by the allyl group) cannot be due to some product of the oxidative cross-linking because films dried below 100°C adhere strongly. In addition the reactivity of the allyl group allows thermal curing, whereby the molecular complexity is increased so as to obtain good resistance to chemical and physical agents.

3. Furthermore, since polyoxyphenylene chains are cross-linked in this way through nonrigid bridges composed of several aliphatic carbon atoms, the cured coatings retain sufficient elasticity to cope with any stress or deformation of the substrate.

### Concluding Remarks

From the low electrical resistance of the wet films (Fig. 1) it may be deduced that "throwing power" is rather low. Indeed by varying some experimental conditions (e.g., by increasing either temperature or methanol percentage) throwing power may increase, but the benefits generally are lower than the disadvantages. From this point of view, therefore, *in situ* electropolymerization of allylphenol is at a disadvantage compared to classical electrophoretic coatings. Another hindrance to practical applications is the fact that inorganic pigments cannot be entrapped in the film during its *in situ* formation. Such pigments often contribute significantly to the life of the electrophoretic coatings.

The advantages of preparing the polyoxy-(allyl)-phenylene coatings by the electrolytic process presented in this paper are: (i) good corrosion resistance

of the coatings; (ii) simplicity of the electrolytic process; (iii) stability of the solutions (the electrophoretic bath instead is a metastable colloidal system); (iv) strong adhesion, which likely originates from interactions existing *ab initio* between monomer and substrate (for this same reason the substrate does not require, apart from cleanliness, any particular pretreatment); and (v) good ability of bonding organic overpaintings.

#### Acknowledgment

The authors are indebted to Mr. F. Furlanetto for experimental support. This work was done in collaboration with Centro Ricerche Fiat, 10043 Orbassano, Torino, Italy.

Manuscript submitted Oct. 21, 1980; revised manuscript received May 22, 1981.

Any discussion of this paper will appear in a Discussion Section to be published in the June 1982 JOURNAL.

All discussions for the June 1982 Discussion Section should be submitted by Feb. 1, 1982.

Publication costs of this article were assisted by the Istituto di Polarografia ed Elettrochimica Preparativa del C.N.R.

#### REFERENCES

1. G. Mengoli, S. Daolio, U. Giulio, and C. Folonari, *J. Appl. Electrochem.*, **9**, 483 (1979).
2. G. Mengoli, S. Daolio, and M. M. Musiani, *ibid.*, **10**, 459 (1980).
3. R. L. Yeats, "Electro-painting," Robert Draper Ltd., Teddington (1970).
4. G. Mengoli, *Adv. Polymer Sci.*, **33**, 1 (1979).
5. G. Mol, R. J. Gritter, and G. Adams, in "Applications of Polymer Spectroscopy," E. G. Brame, Jr., Editor, p. 257, Academic Press, New York (1978).
6. A. S. Hay, *Adv. Polymer Sci.*, **4**, 496 (1967).
7. G. D. Cooper and J. G. Bennett, *J. Org. Chem.*, **37**, 441 (1972).
8. G. D. Cooper, H. S. Blanchard, G. F. Endress, and H. L. Finkbeiner, *J. Am. Chem. Soc.*, **87**, 3996 (1965).

## Substrate Effects on Zinc Deposition from Zincate Solutions

### I. Deposition on Cu, Au, Cd and Zn

M. G. Chu,\* J. McBreen,\* and G. Adzic\*<sup>1</sup>

Brookhaven National Laboratory, Department of Energy and Environment, Upton, New York 11973

#### ABSTRACT

The deposition of zinc on Cu, Au, and Cd from alkaline zincate solutions has been investigated using cyclic voltammetry, potential pulse methods, x-ray diffraction, and scanning electron microscopy. Deposits on Zn were examined by scanning electron microscopy and x-ray diffraction. In the case of Au and Cu approximately a monolayer of zinc is formed in the underpotential deposition region prior to bulk deposition. The respective underpotential shifts of Au and Cu are 0.45 and 0.22V and are in good agreement with the difference in work function between zinc and the substrate. Electrodeposited zinc forms an undetermined surface brass phase on Cu and two alloys (Au<sub>2</sub>Zn and AuZn<sub>3</sub>) with Au. The deposits on all substrates are oriented preferentially parallel to the basal plane.

In a recent study of inorganic oxide additives in pasted zinc electrodes it was found that in many cases the oxide was reduced to the metal prior to deposition of zinc (1). Thus the effect the additives have on the zinc electrode could be due to a substrate effect. Accordingly, an investigation of zinc deposition on various substrates was carried out. Work on Ag substrates has been reported (2). In this case zinc deposition is a complex process involving underpotential deposition, alloy formation, and growth of bulk zinc.

Most morphological studies on zinc electrodeposition have been carried out on either Zn (3-9) or Cu (10-13) substrates. Detailed treatment of deposition habits on single crystal Zn has been carried out in both sulfate (10) and zincate (4, 9) electrolytes. In the latter case at low overvoltages (50 mV) layered deposits were found. There have been two detailed studies of zinc deposition on single crystal Cu from sulfate solution (10, 11). The zinc deposits are of the layered or ridge type with an orientation parallel to the basal plane. Oxley and Fleischman studied zinc

deposition on Zn, Cu, Ag, and Cd under conditions of activation control and diffusion control (14, 15). In the case of diffusion-controlled deposition the initiation period for dendrite growth appeared to be a function of the substrate. In the case of activation-controlled deposition the weight of nonadherent deposit for 27C of Zn/cm<sup>2</sup> varied with the substrate according to Cu > Zn > Ag > Cd. For an identical quantity of deposit under diffusion control the weight of nonadherent deposit decreased in the order Cu > Ag > Zn > Cd. Cadmium-plated current collectors have been used in zinc-ferrocyanide (16) and nickel-zinc batteries (17).

Despic (13) has investigated the deposition of zinc on Cu and Au in sulfate solutions. In both cases he found underpotential deposition of zinc and a low nucleation overvoltage for bulk deposition. Kolb, in his review (18), mentions underpotential deposition of zinc from sulfate solution on Au.

It is well known that copper turns to a gray color when coupled with zinc in alkaline solutions (19, 20). This apparently is due to alloy formation.

Even though it is known that the substrate greatly affects the adherency of zinc deposits in alkaline electrolyte and that in some cases there is evidence for

\* Electrochemical Society Active Member.

<sup>1</sup> Present address, Institute of Chemical Power Sources, ICTM, Beograd, Yugoslavia.

Key words: amalgam, battery, electrodeposition, nucleation.

alloy formation with the substrate, no systematic study has been carried out on the effects of various substrates on zinc deposition. The purpose of the present work was to elucidate the reasons for the substrate effect on the morphology and dissolution behavior of zinc deposits in alkaline electrolyte.

In the present study the deposition of zinc on polycrystalline substrates of Cu, Au, Cd, and Zn was investigated using cyclic voltammetry, potential pulse methods, scanning electron microscopy, and x-ray diffraction. The data were analyzed for evidence of underpotential deposition of zinc, alloy formation, and deposit morphology and orientation.

### Experimental

**Cell.**—The cell was the same as that used for deposition on Ag (2).

**Working electrode.**—Two types of working electrodes were used. One was a simple "flag" type sheet electrode ( $1 \times 1$  cm); the other was a machined disk electrode ( $0.686$  cm $^2$ ). The electrodes were polycrystalline and were at least 99.998% pure. The preparation of the electrodes is given below. No common electrode preparation method could be used because of the differences in the metallurgical and chemical properties of the metals.

**Copper.**—Copper sheet electrodes were first immersed in dilute  $\text{HNO}_3$  for a few seconds and then washed with triply distilled water. Copper disk electrodes were mounted in the holder and polished successively with 600 grit SiC paper, Microcut sheets (Buehler Limited), 5 and  $0.5 \mu\text{m}$  alumina. The electrodes were then washed with triply distilled water prior to incorporation into the cell.

**Gold.**—Gold sheets were degreased in acetone and washed with triply distilled water.

**Cadmium.**—Cadmium sheet electrodes were first immersed in a solution of 75% fuming nitric acid and 25% water for 5–10 sec, then washed with triply distilled water. The cadmium disk electrodes were polished successively with 600 grit SiC and Microcut sheets and were rinsed with triply distilled water.

**Electrolytes.**—The electrolytes were prepared from triply distilled water, reagent grade KOH, and ZnO (New Jersey Zinc USP-19).

**Electrochemical studies.**—After assembly, the solutions were deaerated by bubbling nitrogen through the solution for 15 min prior to the start of measurements. The nitrogen was purified by passage through molecular sieves. The cyclic voltammetry studies were made in voltage envelopes that were more negative than  $-0.63\text{V}^2$  for copper and  $-1.1\text{V}$  for cadmium. At no time, except for cyclic voltammetry on Au, did the voltage go into a potential region where the substrate could oxidize.

In the case of Cu and Au two types of potential step experiments were carried out. In one case electrodes were held initially at a potential of  $-1.0\text{V}$  and then pulsed to potentials between  $-1.1$  and  $-1.25\text{V}$  for 100 sec. This was followed by an anodic pulse to  $-1.0\text{V}$ . The purpose of this potential profile was to quantify the charge associated with underpotential deposition of zinc. Measurement of the charge on the anodic pulse gives more accurate results because of the smaller contribution of hydrogen evolution to the total current. In the other experiments the electrodes were held initially at  $-1.0\text{V}$  and then pulsed to increasingly negative potentials between  $-1.30$  and  $-1.46\text{V}$  for 100 sec. This was followed by an anodic pulse to  $-1.25\text{V}$  for 100 sec, followed by a second anodic pulse to  $-1.0\text{V}$ . The purpose of the latter po-

tential profile was to quantify the charge associated with bulk zinc deposition and alloy formation. The cathodic potential which first yielded anodic charge on pulsing to  $-1.25\text{V}$  was taken to indicate the onset of zinc deposition. The difference between this potential and the Nernst potential is the nucleation overvoltage. In the case of Cd the potential profile was first to hold the electrode at  $-1.1\text{V}$  then pulse to potentials between  $-1.25$  to  $-1.46\text{V}$  for 100 sec and a final pulse to  $-1.1\text{V}$ . In all the experiments particular care was taken to prevent dissolution of the substrate during the course of the experiments.

### Scanning electron microscopy and x-ray diffraction.

—Sample preparation for the scanning electron microscopy and the x-ray diffraction studies was as follows: The zinc was deposited on the "flag" sheet electrodes until a required number of coulombs was deposited. The electrode was immediately removed from the electrolyte, washed repeatedly in distilled water, rinsed in acetone, air dried, and stored in a desiccator until mounted in either the scanning electron microscope or the x-ray goniometer. The x-ray diffraction pattern was determined using  $\text{Cu-K}\alpha$  radiation. The samples prepared for the morphology and deposit orientation studies were deposited from  $8.4\text{M KOH} + 0.74\text{M ZnO}$ . Four samples on Cu, Au, and Cd substrates were prepared. The deposition conditions were  $0.5 \text{ C/cm}^2$  at  $-1.40\text{V}$ ,  $2 \text{ C/cm}^2$  at  $-1.42\text{V}$ ,  $5 \text{ C/cm}^2$  at  $-1.44\text{V}$ , and  $2 \text{ C/cm}^2$  at  $15 \text{ mA/cm}^2$ . On Zn only  $2 \text{ C/cm}^2$  samples deposited at  $15 \text{ mA/cm}^2$  were examined.

### Results

**Cyclic voltammetry.**—Figure 1 shows cyclic voltammograms on Cu sheet in the voltage envelope  $-0.6$  to  $-1.4\text{V}$  in  $1\text{M KOH} + 10^{-3}\text{M ZnO}$ . There is a well-defined underpotential deposition pattern at  $-1.08\text{V}$ . There are two other dissolution peaks at  $-1.18$  and  $-1.32\text{V}$ . On the anodic sweep there is a small cathodic current peak at  $-1.0\text{V}$ .

The cyclic voltammograms on Au were very dependent on the positive limit of the voltage envelope. When the positive limit was  $-0.45\text{V}$  no clear underpo-

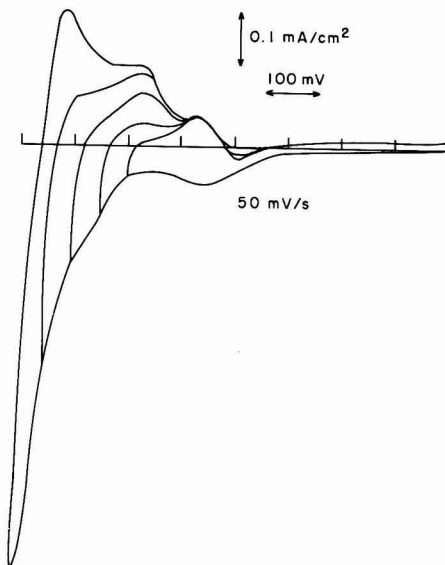


Fig. 1. Cyclic voltammograms on Cu sheet in  $1\text{M KOH} + 10^{-3}\text{M ZnO}$  in the potential envelope  $-0.6$  to  $-1.4\text{V}$ ; sweep rate  $50 \text{ mV/s}$ .

<sup>2</sup> All potentials are with respect to an  $\text{Hg/HgO}$  reference electrode in the same electrolyte.

tential deposition pattern could be observed. However, when the positive limit was extended into the oxide region (Fig. 2) a clear underpotential deposition pattern was found at  $-0.85\text{V}$ . The results are very similar to those found by Despic in sulfate solutions (13).

Figure 3 is a cyclic voltammogram on Cd in  $1\text{M KOH} + 0.08\text{M ZnO}$  in the voltage envelope  $-1.1$  to  $1.42\text{V}$ . There was no evidence of underpotential deposition or alloy formation. The current pattern can be ascribed simply to zinc deposition and dissolution.

Investigations were also carried out in  $6\text{M KOH} + 0.8\text{M ZnO}$  and in  $8.4\text{M KOH} + 0.74\text{M ZnO}$ . The overall features of the cyclic voltammograms were similar to those reported here.

**Potentiostatic pulse studies.**—Figures 4-6 show the current transients for cathodic and anodic pulses on Cu, Au, and Cd substrates in  $8.4\text{M KOH} + 0.74\text{M ZnO}$ . All anodic pulses were at  $-1.25\text{V}$ .

Figure 7 shows a comparison of anodic stripping charges for two potentiostatic pulse profiles on Cu and Au in  $8.4\text{M KOH} + 0.74\text{M ZnO}$ . The results indicate that in both cases at  $-1.25\text{V}$  approximately a monolayer of underpotential deposited zinc is formed prior to bulk deposition. In the case of bulk deposition most of the deposit is stripped at  $-1.25\text{V}$ . When deposition is carried out at more negative potentials, the second anodic pulse to  $-1.0\text{V}$  results in the dissolution of additional zinc (up to 30 monolayers).

Figure 8 shows the results on Cd. The results are consistent with simple deposition of zinc with a high nucleation overvoltage. Complete dissolution of the bulk deposit occurs at  $-1.25\text{V}$  and no additional anodic dissolution was observed at  $-1.1\text{V}$ .

**X-ray diffraction.**—In addition to the diffraction lines for Zn and Cu, the deposit on zinc had diffraction peaks at  $2\theta = 24.8^\circ, 37.7^\circ, 42.1^\circ$ , and  $57.7^\circ$ . The strong diffraction peak at  $42.1^\circ$  could be attributed to the hexagonal Cu-Zn brass phase, and the peak at  $37.7^\circ$  to the  $\gamma$  brass phase. Unfortunately, the other strong reflections for these phases coincide with those of copper. In the case of the deposit on Au there were many reflection peaks that could not be attributed to Au or Zn. These were  $2\theta = 22.7^\circ, 25.5^\circ, 27.9^\circ, 32.3^\circ, 46.2^\circ, 47.7^\circ, 49.2^\circ, 52.0^\circ, 53.4^\circ, 54.8^\circ, 63.7^\circ$ , and  $67.3^\circ$ .

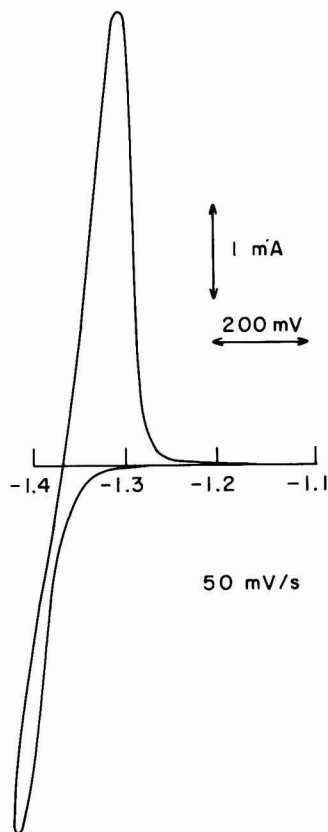


Fig. 3. Cyclic voltammogram on Cd disk ( $0.686\text{ cm}^2$ ) in the  $1\text{M KOH} + 0.08\text{M ZnO}$  in the potential envelope  $-1.1$  to  $-1.42\text{V}$ ; sweep rate  $50\text{ mV/sec}$ .

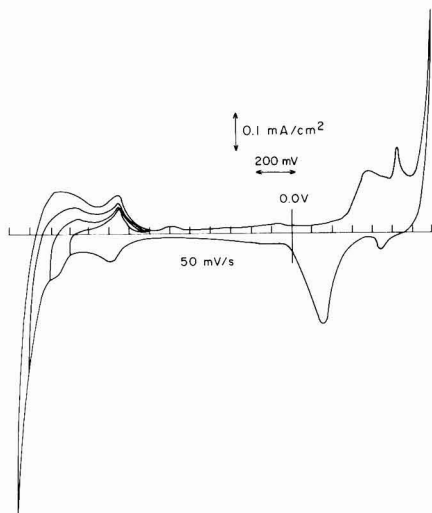


Fig. 2. Cyclic voltammograms on Au sheet in  $1\text{M KOH} + 10^{-3}\text{M ZnO}$  in the potential envelope  $0.7$  to  $-1.35\text{V}$ ; sweep rate  $50\text{ mV/sec}$ .

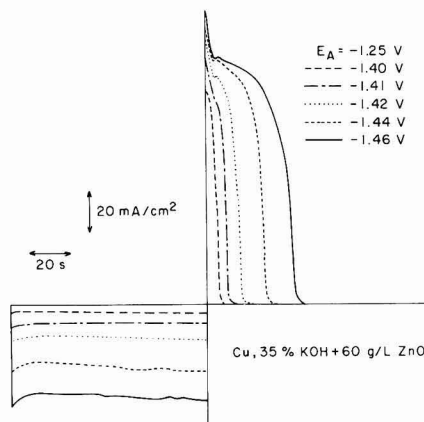


Fig. 4. Current transients for zinc deposition on Cu sheet at various potentials for 100 sec, followed by an anodic stripping pulse at  $-1.25\text{V}$ .

Some of the peaks ( $22.7^\circ, 27.9^\circ, 32.3^\circ, 47.7^\circ$ , and  $49.2^\circ$ ) could be attributed to the cubic  $\gamma_1\text{-AuZn}_3$  phase ( $49.2^\circ, 52.0^\circ, 53.4^\circ, 54.8^\circ$ , and  $67.3^\circ$ ) while others could be attributed to the tetragonal  $\alpha\text{-Au}_3\text{Zn}$  phase. The diffrac-



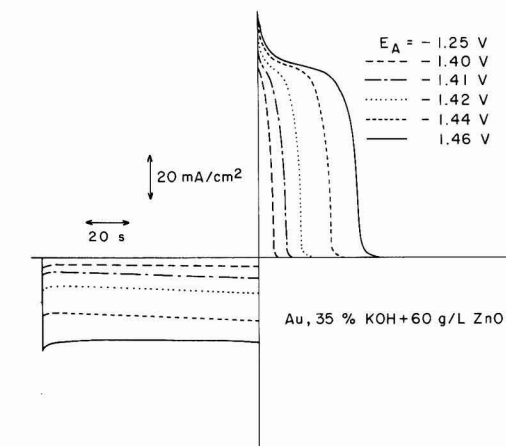


Fig. 5. Current transients for zinc deposition on Au sheet at various potentials for 100 sec, followed by an anodic stripping pulse at  $-1.25$  V.

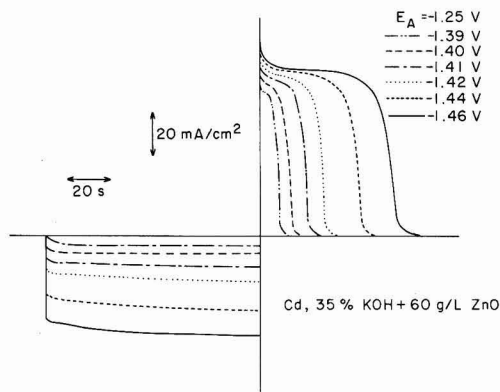


Fig. 6. Current transients for zinc deposition on Cd sheet at various potentials for 100 sec, followed by an anodic stripping pulse at  $-1.25$  V.

tion peak at  $46.2^\circ$  is common to both phases. In the x-ray pattern for the deposit on Cd only reflections that could be attributed to either Cd or Zn were found.

**Deposit orientation and morphology.**—The deposits on all four substrates had an orientation that was preferentially parallel to the basal plane. The morphology of the deposits on Cu, Au, and Cd are shown in Fig. 9–11. On Cu, Au, and Cd the deposit consisted of hexagonal platelets. On Cd the platelets were layered and more compact than those of Cu. On Zn the morphology was identical to that found by Bockris *et al.* (9) and the orientation was parallel to the basal plane. Deposit orientation and morphology did not vary with the deposition conditions investigated.

### Discussion

Quantitative treatment of the cyclic voltammograms and the cathodic current transients is essentially impossible because of the unknown contribution of the hydrogen evolution reaction. Nevertheless the electrochemical results yield valuable information which complements the results of the scanning electron microscopy and x-ray diffraction analysis.

**Underpotential deposition of zinc.**—The results in Fig. 1, 2, and 7 indicate that approximately a mono-

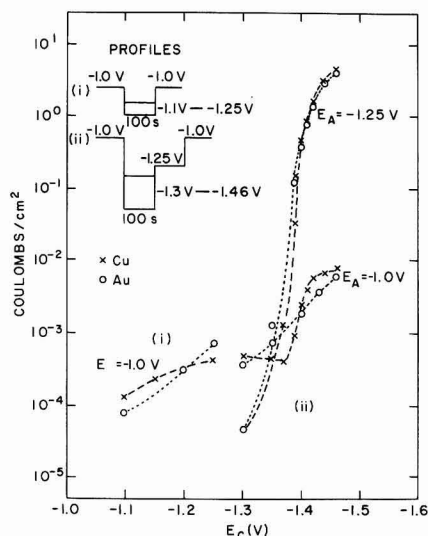


Fig. 7. Anodic stripping charge vs. deposition potential for zinc on Cu and Au sheet in 8.4M KOH + 0.74M ZnO. Potential profiles are given in figure. Deposition time, 100 sec.

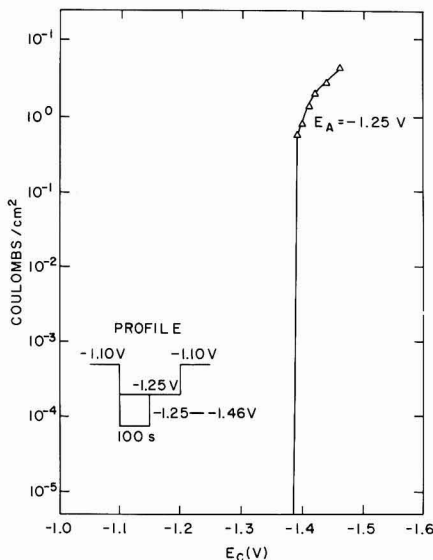


Fig. 8. Anodic stripping charge vs. deposition potential for zinc and Cd sheet in 8.4M KOH + 0.74M ZnO. Potential profile is given in figure. Deposition time, 100 sec.

layer of underpotential deposited zinc is formed on Au and Cu, at  $-1.25$  V, prior to bulk deposition. If one takes the underpotential shift as the difference between the bulk and monolayer stripping peaks (18), then the respective underpotential shifts on Au and Cu are 0.45 and 0.22 V. These are in good agreement with the difference in work function between zinc and the substrate (18). According to Trasatti (21) the work function for Cd is lower than that of Zn and in agreement with the empirical relationship (18); no underpotential was observed on Cd.

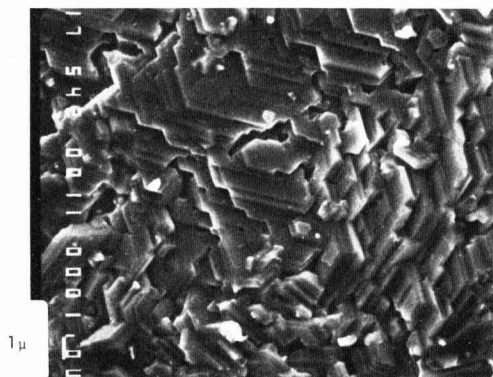


Fig. 9. Scanning electron micrograph of zinc deposit on Cu sheet. Deposit conditions were  $2 \text{ C/cm}^2$  at  $15 \text{ mA/cm}^2$  from  $8.4\text{M KOH} + 0.74\text{M ZnO}$ . Magnification  $5400\times$ .

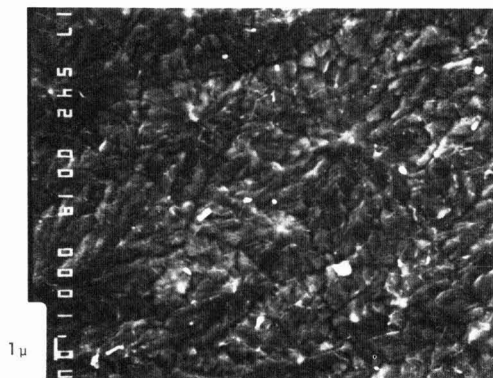


Fig. 10. Scanning electron micrograph of zinc deposit on Au sheet. Deposit conditions were  $2 \text{ C/cm}^2$  at  $15 \text{ mA/cm}^2$  from  $8.4\text{M KOH} + 0.74\text{M ZnO}$ . Magnification  $5400\times$ .

The cyclic voltammogram on Cu (Fig. 1) is fairly complex. Apart from the underpotential deposition pattern with a current peak at  $-1.08\text{V}$ , there is a shoulder on the cathodic current scan between  $-1.2$  and  $-1.35\text{V}$ . On going to more negative potentials, an anodic current peak develops at  $-1.18\text{V}$ . When the cathodic scan goes into the zinc deposition region, a third anodic peak appears at  $-1.32\text{V}$ . This behavior is very similar to that found for cadmium deposition on Au in acetate buffered  $\text{CdSO}_4$  electrolyte (22). The cathodic current shoulder between  $-1.2$  and  $-1.35\text{V}$  and the anodic peak at  $-1.18\text{V}$  can be ascribed to alloy formation in the potential region between the Nernst potential and the underpotential deposition region. The anodic peak at  $-1.32\text{V}$  can be ascribed to dissolution of bulk zinc.

One peculiar feature of the cyclic voltammogram on Cu is the small cathodic current at  $-1.0\text{V}$  on the anodic sweep. This can be explained by the inhibition of hydrogen evolution by the adsorbed zinc layer. Such inhibition by underpotential deposited layers is well known (23, 24). On the anodic sweep, when the layer is stripped, hydrogen evolution occurs and the current makes an excursion into the cathodic region at approximately  $-1.0\text{V}$ .

The behavior of zinc on Au is very similar in some respects to zinc on Cu. In addition to underpotential deposition of zinc, there is evidence for alloy forma-

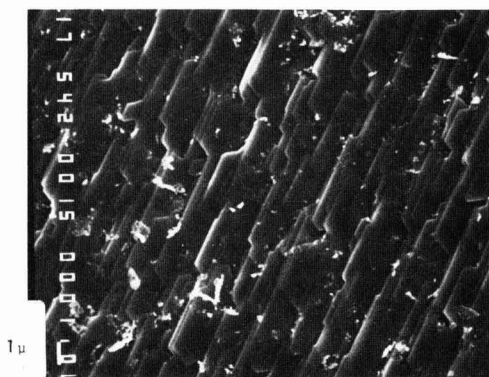


Fig. 11. Scanning electron micrograph of zinc deposit on Cd sheet. Deposit conditions were  $2 \text{ C/cm}^2$  at  $15 \text{ mA/cm}^2$  from  $8.4\text{M KOH} + 0.74\text{M ZnO}$ . Magnification  $5400\times$ .

tion as the cathodic scan is extended to potentials between the underpotential deposition region and the Nernst potential. Underpotential deposition of zinc on Au is enhanced by extending the cyclic voltammograms into the oxide region. This may be due to a re-ordering of the Au surface. Also, it has recently been found that the adsorption behavior of metals can be modified by extended polarization at a preset potential (25). One proposed mechanism is that the adsorption behavior is modified by adsorbed or absorbed oxygen. A similar mechanism may apply here.

**Bulk deposition and alloy formation.**—As in the case of Ag (2), there is no discernible nucleation overvoltage for zinc deposition on Cu and Au substrates (Fig. 7). Similar results were found by Despic (13, 26) for zinc deposition on Cu and Au in sulfate solutions. However, in this present case there is evidence for alloy formation between the underpotential deposition potential and the Nernst potential, and this may account for the apparent absence of a nucleation overvoltage.

The cyclic voltammetry, potential pulse studies, and x-ray diffraction analysis confirm alloy formation in the case of both Cu and Au. In the case of Cu diffraction peaks that could be attributed to either a  $\gamma$ -brass or a hexagonal Cu-Zn brass phase were observed. The overlap of the other strong lines of these phases with those of copper precluded unequivocal determination of the alloy phase. In the case of Au the situation is much clearer since several diffraction peaks could be uniquely attributed to either the  $\text{AuZn}_3$  or the  $\text{Au}_3\text{Zn}$  phase. These two alloys are probably found at different depths in the substrate. The results in Fig. 7 indicate the formation of an alloy to a depth of at least 30 monolayers in both cases.

The cyclic voltammetry, potential pulse, and x-ray analysis measurements on Cd are consistent with simple zinc deposition with a high nucleation overvoltage. The absence of alloy formation is in agreement with the finding that the solubility of Zn in Cd is practically nil at  $100^\circ\text{C}$  (27).

**Deposit morphology and orientation.**—The basal orientation of the deposit on Cu is in agreement with that found on single crystal copper in sulfate solutions and with that found when zinc is condensed on Cu from the vapor phase (28). The hexagonal growth habit is typical for growth of a hexagonal close-packed crystal structure oriented parallel to the basal plane (29). Visual inspection of the scanning electron micrographs of the deposits obtained on Cu, Ag (2), and Cd indicates that the density of the zinc deposit

increases in the order  $\text{Cu} > \text{Ag} > \text{Cd}$ . This is the order of decreasing peak current for the anodic stripping pulse at  $-1.25\text{V}$  (Fig. 7). It is also the order of increasing deposit adherence that was found by Oxley and Fleischman (14, 15). Copper substrates in particular encourage the growth of an active hexagonal deposit with many kink sites and edges. This encourages the growth of a deposit whose surface area increases with thickness. This also results in an increase in the dissolution activity of the deposit with increasing thickness.

### Summary

1. Approximately a monolayer of zinc is formed on polycrystalline Cu and Au prior to bulk deposition. There is excellent agreement between the underpotential shift and the difference in work function between the substrate and zinc.

2. Alloy formation of zinc with the substrate was found in the case of Cu and Au. Copper forms an undetermined brass phase, and Au forms  $\text{Au}_3\text{Zn}$  and  $\text{AuZn}_3$ .

3. Bulk deposition proceeds without any detectable nucleation overvoltage on Cu and Au. On Cd the nucleation overvoltage is high. In all cases the deposits are preferentially oriented parallel to the basal plane.

### Acknowledgments

This work was supported by the U.S. Department of Energy (Contract No. DE-AC02-76CH00016) and the Naval Ship Engineering Center (NAVSEC). The authors acknowledge helpful discussions with A. Himy of NAVSEC, O. C. Wagner of the U.S. Army Electronics Research and Development Command (ERADCOM), Professor B. E. Conway of the University of Ottawa, and W. E. O'Grady, R. R. Adzic, W. Visscher, and S. Srinivasan of Brookhaven National Laboratory (BNL). The authors wish to thank O. Kammerer (BNL) for the x-ray analysis and R. L. Sabatini (BNL) for the scanning electron microscopy. One of the authors (G.A.) had financial support from the Research Fund of Serbia, Yugoslavia, during the course of this work.

Manuscript submitted Dec. 4, 1980; revised manuscript received ca. June 1, 1981.

Any discussion of this paper will appear in a Discussion Section to be published in the June 1982 JOURNAL. All discussions for the June 1982 Discussion Section should be submitted by Feb. 1, 1982.

Publication costs of this article were assisted by the Brookhaven National Laboratory.

### REFERENCES

1. J. McBreen, E. Gannon, and M. G. Chu, Abstract 91, p. 248, The Electrochemical Society Extended Abstracts, Hollywood, Florida, October 5-10, 1980.
2. G. Adzic, J. McBreen, and M. G. Chu, *This Journal*, **128**, 1691 (1981).
3. R. W. Powers, *Electrochem. Technol.*, **5**, 429 (1970).
4. R. D. Naybour, *Electrochim. Acta*, **13**, 763 (1968).
5. R. D. Naybour, *This Journal*, **116**, 520 (1969).
6. F. Mansfield and S. Gilman, *ibid.*, **117**, 588 (1970).
7. F. Mansfield and S. Gilman, *ibid.*, **117**, 1154 (1970).
8. F. Mansfield and S. Gilman, *ibid.*, **117**, 1521 (1970).
9. J. O'M. Bockris, Z. Nagy, and D. Drazic, *ibid.*, **120**, 30 (1973).
10. J. M. Keen and J. P. G. Farr, *ibid.*, **109**, 668 (1962).
11. M. F. Ahmed, B. S. Shuhadri, and F. Pushpanaden, *J. Mater. Sci.*, **12**, 549 (1977).
12. K. I. Popov, D. N. Keca, and M. D. Andjelic, *J. Appl. Electrochem.*, **9**, 19 (1978).
13. A. R. Despic, in "Electrode Processes," S. Bruckenstein, J. D. E. McIntyre, B. Miller, and E. Yeager, Editors, pp. 235-245, The Electrochemical Society Softbound Proceedings Series, Princeton, NJ (1979).
14. J. E. Oxley and C. W. Fleischman, Third Quarterly Report to NASA Contract No. NA85-9591, Leeson Moss Laboratories, Great Neck, NY, March 1966, NASA Assession No. 66-26870.
15. H. G. Oswin and K. F. Blurton, in "Zinc Silver Oxide Batteries," A. Fleischer and J. J. Lander, Editors, John Wiley & Sons, New York (1971).
16. E. L. Littauer, Private communication.
17. M. Knaster, Abstract 92, p. 250, The Electrochemical Society Extended Abstracts, Hollywood, Florida, October 5-10, 1980.
18. D. M. Kolb, in "Advances in Electrochemistry and Electrochemical Engineering," Vol. 11, H. Gerischer and C. W. Tobias, Editors, John Wiley & Sons, New York (1978).
19. J. M. Booe, *This Journal*, **99**, 197C (1952).
20. T. P. Dirkse and E. G. Vrieland, *ibid.*, **106**, 997 (1959).
21. S. Trasatti, *J. Electroanal. Chem. Interfacial Electrochem.*, **33**, 351 (1971).
22. J. W. Schultz, F. D. Koppitz, and M. M. Lohregel, *Ber. Bunsenges. Phys. Chem.*, **78**, 693 (1974).
23. R. R. Adzic, A. V. Tripkovic, and N. M. Markovic, *J. Electroanal. Chem. Interfacial Electrochem.*, In press.
24. F. Furuya and S. Motoo, *ibid.*, **98**, 195 (1979).
25. H. Siegenthaler and E. Schmidt, Extended Abstracts, 31st ISE Meeting, Venice, Italy, September 22-26, 1980, Abstract No. A44.
26. A. R. Despic, Abstract 402, p. 1013, The Electrochemical Society Extended Abstracts, Hollywood, Florida, October 5-10, 1980.
27. W. Boos, *Metallwirtschaft*, **11**, 603 (1932).
28. O. Haase, *Z. Naturforsch.*, **11**, 862 (1956).
29. I. Sunagawa, in "Crystal Growth and Characterization," R. Ueda and J. B. Mallin, Editors, pp. 347-359, North Holland Publishing Co., Amsterdam (1975).

# Substrate Effects on Zinc Deposition from Zincate Solutions

## II. Deposition on Pb, Tl, Sn, and In

J. McBreen,\* M. G. Chu,\* and G. Adzic\*<sup>1</sup>

Brookhaven National Laboratory, Department of Energy and Environment, Upton, New York 11973

### ABSTRACT

The deposition of zinc on Pb, Tl, Sn, and In has been investigated using cyclic voltammetry, potential pulse methods, x-ray diffraction, and scanning electron microscopy. There is no evidence of underpotential deposition on any of the substrates and the nucleation overvoltage is 30–40 mV. Thallium forms a surface alloy with zinc and there is evidence that zinc diffuses into Pb. In the case of Sn and Tl the deposit had an intermediate orientation and on Pb and In the deposit was oriented perpendicular to the basal plane. Deposit orientation has been correlated with the degree of mismatch of zinc with the substrate. The morphology of the zinc was dense on all substrates and there was no evidence for the hexagonal type of deposit that is usually found on Zn and Cu.

The deposition of zinc on Sn and Pb has been investigated by Oxley and Fleischman (1,2). They found that the deposits were more adherent than on Cu, Ag, or Cd, with the best adherence being on Pb.

There is an extensive literature on the effect of Pb and Sn ions on zinc deposits in alkaline electrolyte (3–7). Initial work was carried out by Kudryatzev (3). Since then several investigators have confirmed that Pb (4–6) and Sn (7) ion additions inhibit zinc dendrite growth. It has also been shown that Pb ion additions affect the specific area of the zinc deposit, suppress self-discharge, and improve the mechanical and discharge characteristics of the electrodes (5). The effect of Pb ion additions on zinc deposits in aqueous zinc chloride and zinc sulfate electrolytes has been investigated (8,9). In both cases additions of Pb ions change the deposit and promote zinc growth perpendicular to the basal plane.

In recent years there have been several reports on the effect of PbO, TiO<sub>2</sub>, SnO<sub>2</sub>, SnCl<sub>2</sub>, H<sub>2</sub>O, In<sub>2</sub>O<sub>3</sub>, and In(OH)<sub>3</sub> additions to the pasted battery zinc electrodes (10–13). It has been found that in the case of PbO and TiO<sub>2</sub> additions to zinc electrodes in nickel-zinc cells that the oxides are reduced to the metal prior to zinc deposition on the first charge (13). The mechanism by which these additives modify the electrode has been attributed to a substrate effect.

The present study was part of an investigation of substrate effects on zinc deposition on several metals from zincate solution. The techniques used were cyclic voltammetry, potential pulse methods, scanning electron microscopy, and x-ray diffraction.

### Experimental

**Cell.**—The cell for the electrochemical studies is described elsewhere (15).

**Working electrode.**—Two types of working electrodes were used. One was a simple "flag" type sheet electrode (1 × 1 cm); the other was a machined disk electrode (0.686 cm<sup>2</sup>). The electrodes were polycrystalline and were at least 99.998% pure. The preparation of the Pb, Tl, In, and Sn electrodes is given below; no common electrode preparation method could be used.

**Lead.**—Lead sheet was first immersed in a solution of 20% hydrogen peroxide and 80% glacial acetic acid

for 15 sec, then washed with triply distilled water (14). The lead disk electrodes were first polished with 600 grit SiC paper and then chemically etched in a solution of 80% glacial acetic and 20% hydrogen peroxide for 15 sec. Finally the electrode was rinsed with methanol.

**Thallium.**—The preparation of thallium sheet was the same as that for lead sheet electrode. The thallium disk electrodes were polished with 600 grit SiC and then washed in 6N KOH followed by a rinse in triply distilled water.

**Indium.**—Indium electrodes were first washed in acetone and rinsed with triply distilled water.

**Tin.**—Tin sheet electrode was only washed with triply distilled water. The tin disk electrodes were first polished with 600 grit SiC paper and then washed with triply distilled water.

**Electrolytes.**—The electrolytes were prepared from triply distilled water, reagent grade KOH, and ZnO (New Jersey Zinc USP-19).

**Electrochemical studies.**—After cell assembly, the solutions were deaerated by bubbling nitrogen through the solutions for 15 min prior to the start of measurement. The nitrogen was purified by passage through molecular sieves. The cyclic voltammetry was made in voltage envelopes that were more negative to –0.84V for Pb, –0.9V for Tl, –1.15V for In, and –1.2V for Sn. At no time did the voltage scan go into a potential region where the substrate could oxidize. Double cathodic-anodic pulse measurements were made in an effort to quantify the amount of the deposit, determine the nucleation overvoltage, and obtain further evidence for alloy formation. This procedure consisted of a cathodic pulse for 100 sec at increasingly negative potentials between –1.25 and –1.46V followed by an anodic pulse at –1.25V for 100 sec and a final pulse to a potential slightly negative of the dissolution potential of the substrate. In the case of Pb, Tl, In, and Sn, the respective potentials of the final anodic pulses were –1.0, –1.0, –1.19, and –1.15V. The cathodic deposition potential which first yielded an anodic charge at –1.25V was taken to indicate the onset of zinc deposition. The difference between this potential and the Nernst potential is the nucleation overvoltage. Any additional dissolution that occurred on stepping to potentials more positive to –1.25V was ascribed to zinc that had alloyed or diffused into the substrate.

\* Electrochemical Society Active Member.

<sup>1</sup> Present address: Institute of Chemical Power Sources, ICTM, Beograd, Yugoslavia.

Key words: electrodeposition, alloy, SEM.

**Scanning electron microscopy and x-ray diffraction.**—Sample preparation for the scanning electron microscopy and the x-ray diffraction studies was as follows. The zinc was deposited on the "flag" sheet electrodes at a fixed potential until a required number of coulombs was deposited. The electrode was immediately removed from the electrolyte, washed repeatedly in distilled water, rinsed in acetone, air dried, and stored in a desiccator until mounted in either the scanning electron microscope or the x-ray goniometer. The diffraction pattern was determined using Cu-K $\alpha$  radiation. The sample prepared for the morphology and deposit orientation studies was deposited from 8.4M KOH + 0.74M ZnO. Four samples on each substrate were prepared. The deposited conditions were 0.5 C/cm<sup>2</sup> at -1.40V, 2 C/cm<sup>2</sup> at -1.42V, 5 C/cm<sup>2</sup> at -1.44V, and 2 C/cm<sup>2</sup> at 15 mA/cm<sup>2</sup>.

### Results

**Cyclic voltammetry.**—Figure 1 is a cyclic voltammogram on a Pb disk electrode in 1M KOH + 0.08M ZnO in the potential envelope -0.83 to -1.45V. The cathodic current has a distinct nucleation loop with no zinc deposition occurring on the cathodic sweep till a potential of -1.4V is reached. Cyclic voltammograms with negative limits at -1.43V displayed one anodic current peak at -1.28V. When the negative limit was extended to -1.45V a second anodic peak appeared at -1.35V (Fig. 1); when the limit was -1.55V a third anodic peak appeared at -1.3V. Results in Fig. 2 show the effect of various voltage arrests on the anodic behavior of the cyclic voltammogram. Figure 3 shows cyclic voltammograms for thallium in 1M KOH + 0.08M ZnO in the voltage envelope -0.9 to -1.4 and -1.45V. There is no evidence of underpotential deposition on Tl. At -1.4V there is no zinc deposition. At 1.45V there is deposition and a very distinct nucleation loop. Figure 4 shows cyclic voltammograms for more negative limits down to -1.65V. When the negative limit is -1.65V another anodic peak is observed -0.8V. The main feature of zinc deposition on Tl is that there is no underpotential deposition; there is evidence of a nucleation overvoltage for zinc deposition. The behavior of Sn is shown in Fig. 5. There is no evidence of underpotential deposition or alloy formation. Almost identical results were found on In substrates.

**Potentiostatic pulse studies.**—Figures 6-9 show the current transients for cathodic and anodic pulse on Pb,

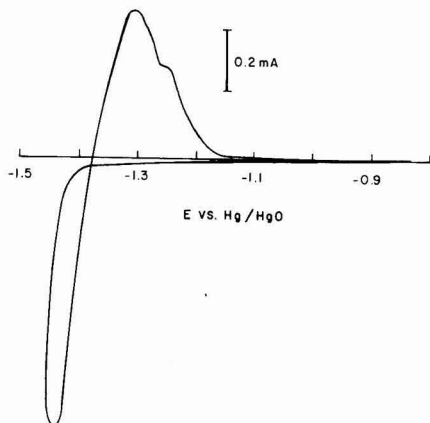


Fig. 1. Cyclic voltammogram on Pb disk (0.686 cm<sup>2</sup>) in 1M KOH + 0.08M ZnO; sweep rate 100 mV/sec. Negative limit -1.45V.

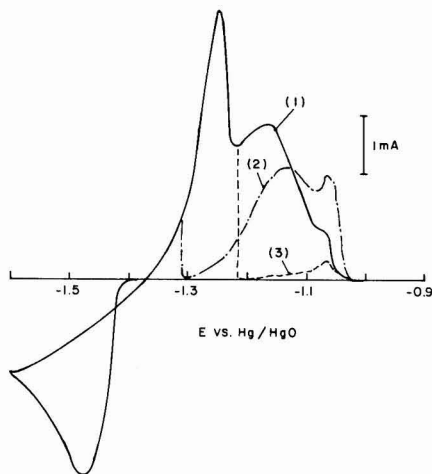


Fig. 2. Cyclic voltammograms on Pb disk (0.686 cm<sup>2</sup>) in 1M KOH + 0.08M ZnO; sweep rate 10 mV/sec. (Curve 1) continuous cyclic voltammograms, (curve 2) with a 5 sec anodic arrest at -1.3V, (curve 3) with a 5 sec anodic arrest at -1.21V.

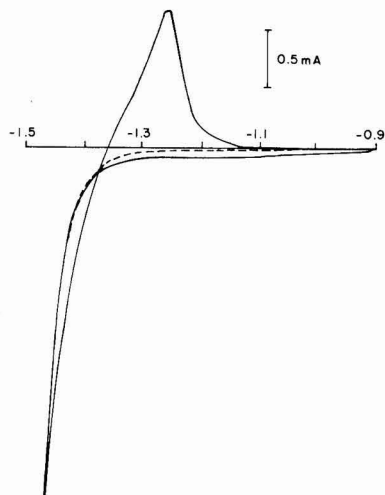


Fig. 3. Cyclic voltammograms for Tl disk (0.686 cm<sup>2</sup>) in 1M KOH + 0.08M ZnO; broken line for a negative limit at -1.4V; solid line for a limit at -1.45V. Sweep rate 100 mV/sec.

Tl, Sn, and In substrates (1 × 1 cm) in 8.4M KOH + 0.74M ZnO. Cathodic pulses vary from -1.40 to -1.46V. All anodic pulses were at -1.25V.

Figures 10 and 11 show the anodic stripping charge for various potentiostatic pulse profiles in 8.4M KOH + 0.74M ZnO for Pb, Tl, In, and Sn, respectively. On Pb and Tl substrates, most of the dissolution of bulk deposit occurs at -1.25V; the remainder of the deposit is stripped at -1.0V. On In and Sn substrates, all of the dissolution of bulk deposit occurs at -1.25V; no dissolution was observed at the higher potential.

**X-ray diffraction result.**—In the case of the Tl sample prepared for morphology and deposit orientation studies strong diffraction peaks at  $2\theta = 23.5^\circ, 26^\circ, 27.2^\circ, 31^\circ, 38.5^\circ$ , and  $48.5^\circ$  were observed. In the case of Pb, In, and Sn, all the diffraction peaks could be attributed to either zinc or the substrate.



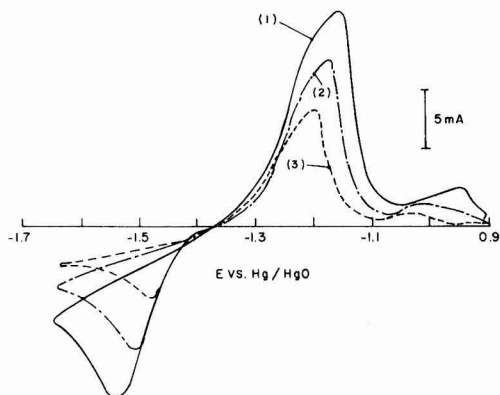


Fig. 4. Sweep rate dependence of cyclic voltammograms on Tl disk ( $0.686 \text{ cm}^2$ ) in  $1\text{M KOH} + 0.08\text{M ZnO}$ . Sweep rates: (curve 1)  $100 \text{ mV/sec}$ , (curve 2)  $50 \text{ mV/sec}$ , (curve 3)  $20 \text{ mV/sec}$ .

**Deposit orientation and morphology.**—The zinc deposits on both Pb and In were oriented perpendicular to the basal plane. On Tl and Sn the deposit had an intermediate orientation. Figures 12 to 15 show scanning electron micrographs of zinc deposits on each substrate. There is no evidence of the hexagonal structures found on Ag (15), Cu and Cd (16). On In and Sn the deposits had a very dense appearance.

#### Discussion

**Zinc deposition.**—No underpotential deposition was observed on any of these substrates. This is to be expected since the work function for Sn is only  $0.05 \text{ eV}$  higher than that of zinc and for the other metals is considerably lower (17). The nucleation overvoltage is high on all metals. Thallium was the only material with which zinc formed an alloy. This was confirmed by the additional anodic peak, at approximately

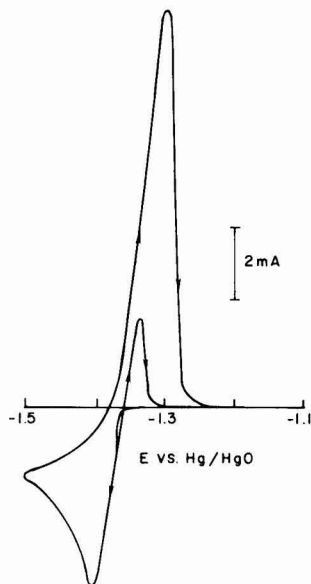


Fig. 5. Cyclic voltammograms on Sn disk ( $0.686 \text{ cm}^2$ ) in  $1\text{M KOH} + 0.08\text{M ZnO}$ ; sweep rate  $50 \text{ mV/sec}$ .

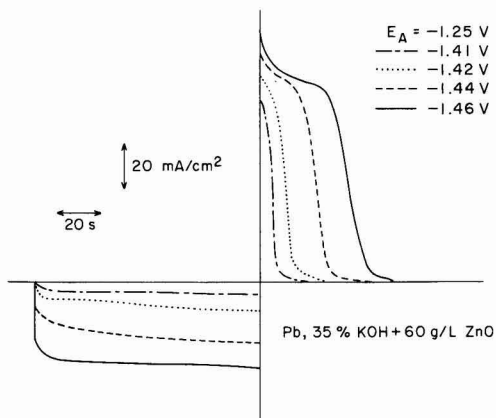


Fig. 6. Current transients for double cathodic/anodic pulse experiments on Pb sheet in  $8.4\text{M KOH} + 0.74\text{M ZnO}$ . Deposition potentials are indicated on the figure. Anodic pulses were to  $-1.25\text{V}$ .

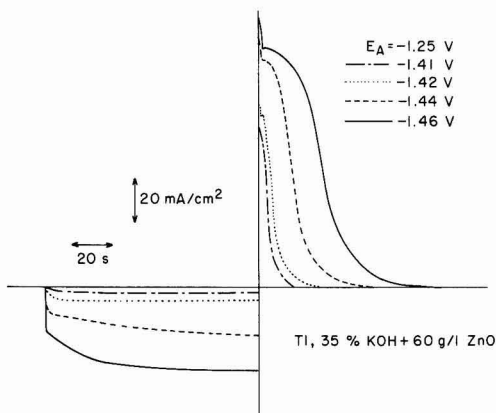


Fig. 7. Current transients for double cathodic/anodic pulse experiments on Tl sheet in  $8.4\text{M KOH} + 0.74\text{M ZnO}$ . Deposition potentials are indicated on the figure. Anodic pulses were to  $-1.25\text{V}$ .

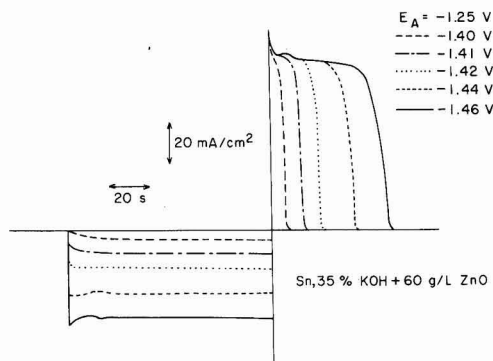


Fig. 8. Current transients for double cathodic/anodic pulse experiments on Sn sheet in  $8.4\text{M KOH} + 0.74\text{M ZnO}$ . Deposition potentials are indicated on the figure. Anodic pulses were to  $-1.25\text{V}$ .

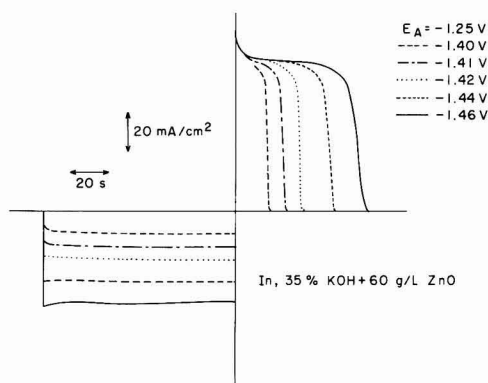


Fig. 9. Current transients for double cathodic/anodic pulse experiments on In sheet in 8.4M KOH + 0.74M ZnO. Deposition potentials are indicated on the figure. Anodic pulses were to  $-1.25\text{V}$ .

$-1.0\text{V}$ , in the cyclic voltammograms (Fig. 5). The double anodic pulse also showed additional dissolution on going to  $-1.0\text{V}$ . This additional dissolution was observed on the cyclic voltammograms at slow sweep rates and in the potential pulse measurements after holding the electrode at  $-1.25\text{V}$  for periods as long as 300 sec. Thus it could not be ascribed to residual passivated zinc. In addition, the x-ray diffraction results showed several diffraction peaks that could not be ascribed to either Zn or Tl. No literature data for x-ray patterns of Zn-Tl alloys could be found.

The cyclic voltammetry results (Fig. 4 and 5) and the double anodic pulse measurements (Fig. 11) indicate that alloy formation of zinc with Tl is quite different than alloy formation with Ag (15), Au or Cu (16). There is no evidence for alloy formation at potentials positive to the Nernst potential. Actually the cyclic voltammogram displays a nucleation loop (Fig. 4) and no zinc is deposited at potentials more positive

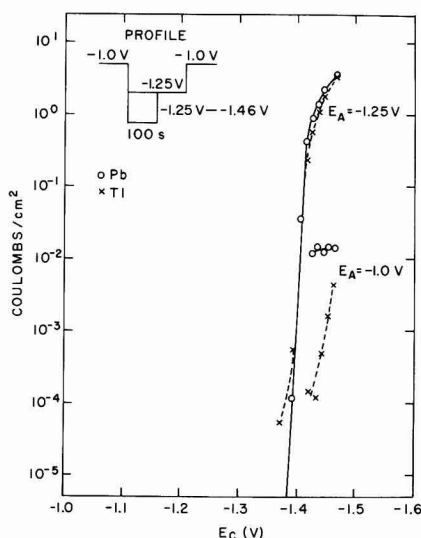


Fig. 10. Anodic stripping charge vs. deposition potential for Pb and Tl sheet in 8.4M KOH + 0.74M ZnO. Deposition time was 100 sec. Potential profiles are indicated on the figure.

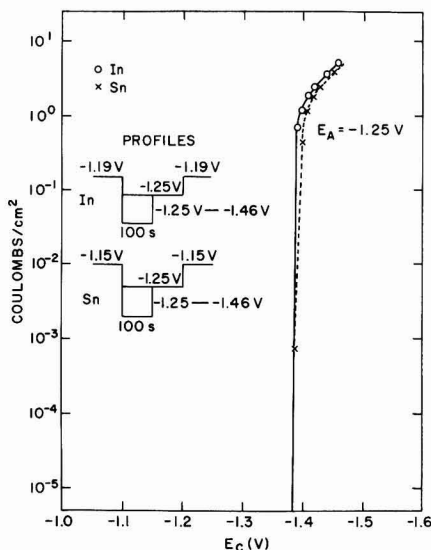


Fig. 11. Anodic stripping charge vs. deposition potential from Sn and In sheet in 8.4M KOH + 0.74M ZnO. Deposition time was 100 sec. Potential profiles are indicated on the figure.

to  $-1.4\text{V}$ . Apparently the presence of bulk zinc is required on the Tl surface before alloy formation. There is a possibility that in the case of Ag, Au, and Cu, the underpotential deposited layer catalyzes alloy formation at potentials positive to the Nernst potential. It is difficult to quantify the amount of alloy formation from the double anodic pulse measurements. On pulsing to  $-1.25\text{V}$ , the current tailed off (slowly) over a long period of time (Fig. 7). This may be due to some alloy dissolution at  $-1.25\text{V}$  after stripping the bulk deposit.

The behavior of zinc on Pb is very complex as indicated by the cyclic voltammetry and potential pulse measurements. The behavior was similar in some respects to that observed with substrates that alloyed with zinc. However, no Pb-Zn alloy is known and the x-ray diffraction data showed only reflections for Pb and Zn. The cyclic voltammograms indicate that there are at least three dissolution processes. This could be rationalized on the basis of dissolution of nonepitaxial

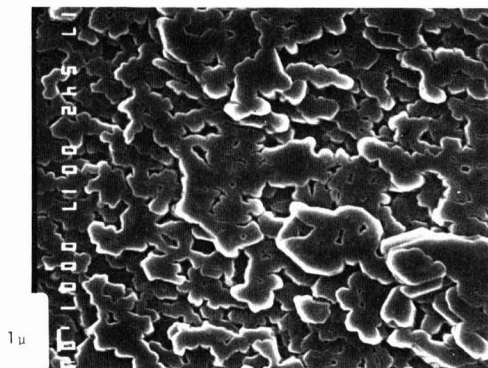


Fig. 12. Scanning electron micrograph of a zinc deposit on Pb sheet. Electrolyte was 8.4M KOH + 0.74M ZnO. Deposition conditions were  $2\text{C}/\text{cm}^2$  at  $15\text{mA}/\text{cm}^2$ . Magnification  $5400\times$ .

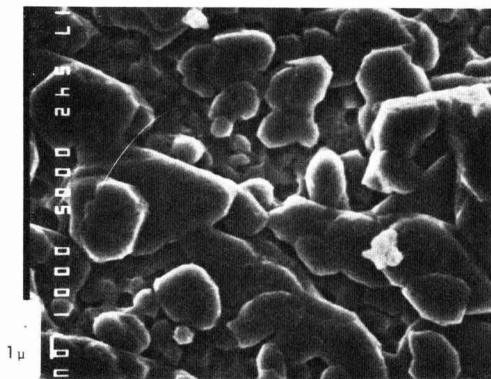


Fig. 13. Scanning electron micrograph of a zinc deposit on Ti sheet. Electrolyte was 8.4M KOH + 0.74M ZnO. Deposition conditions were 2 C/cm<sup>2</sup> at 15 mA/cm<sup>2</sup>. Magnification 5400 $\times$ .

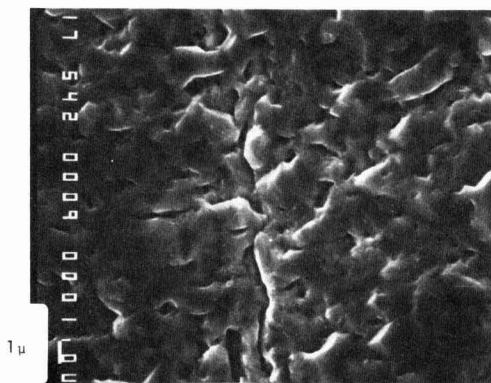


Fig. 14. Scanning electron micrograph of zinc deposit on Sn sheet. Electrolyte was 8.4M KOH + 0.74M ZnO. Deposition conditions were 2 C/cm<sup>2</sup> at 15 mA/cm<sup>2</sup>. Magnification 5400 $\times$ .

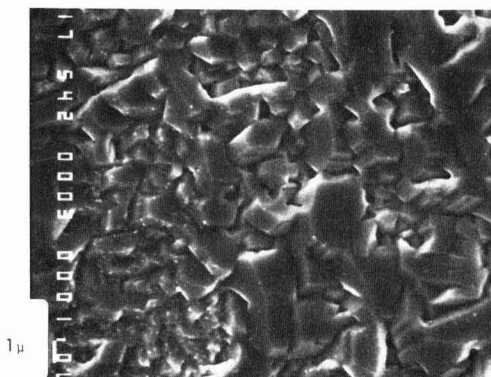


Fig. 15. Scanning electron micrograph of zinc deposit on In sheet. Electrolyte was 8.4M KOH + 0.74M ZnO. Deposition conditions were 2 C/cm<sup>2</sup> at 15 mA/cm<sup>2</sup>. Magnification 5400 $\times$ .

growth, epitaxial growth, and zinc that diffuses into the lead. The concept of the dissolution of epitaxial and nonepitaxial growth has been invoked to explain the dissolution of Cd deposits on Cu (18), and a simi-

lar mechanism may be operative here. It is known that the diffusivity of Zn in Pb is abnormally high (19, 20). It is about six orders of magnitude higher than the self-diffusion of Pb in Pb. Extrapolation of the data of Ross *et al.* (19) indicates a diffusivity of  $8.24 \times 10^{-11}$  cm<sup>2</sup> sec<sup>-1</sup> for Zn in Pb at 25°C. If one assumes that the area under curve 3, Fig. 3 is due to dissolution of zinc that diffuses into Pb, then the amount of Zn in the substrate is  $1.4 \times 10^{-3}$  C. The total zinc that diffuses into the Pb is given by

$$Q = 4FAC_0 \left( \frac{Dt}{\pi} \right)^{1/4}$$

where  $F$  is the Faraday constant,  $A$  the electrode area,  $D$  the diffusivity of Zn in Pb,  $C_0$  the concentration of zinc directly beneath the Pb surface, and  $t$  the time the substrate was covered with Zn (21). The total time  $t$ , including the arrest time, was 78 sec. This yields a value of  $C_0$  of 0.06 atom percent Zn in Pb, a value that is reasonably close to the theoretical solubility of Zn in Pb (22).

The electrochemical behavior of the zinc deposit on In and Sn was unique in that the deposit activity does not increase with deposit thickness (Fig. 9 and 10). The limiting discharge current on stepping to -1.25V does not change with thickness. This would indicate that the surface area of the zinc remains constant as the deposit grows. This may be a feature associated with epitaxial growth perpendicular to the basal plane. The stripping current behavior also differed from that of Pb and Ti in that there was no tailing of the current. This is consistent with no interaction of the zinc with the substrate bulk.

**Deposit morphology and orientation.**—The zinc deposits on Pb, Ti, In, and Sn differed from those found on Ag (15), Cu, Au, Cd, and Zn (16) in that the deposits were not oriented parallel to the basal plane. Consequently the deposits did not display the usual hexagonal platelets that are obtained from growth in a direction parallel to the basal plane.

The only correlation that can be made is that substrates with atomic radii close to that of zinc encourage growth parallel to the basal plane, and substrates with atomic radii much larger than zinc encourage growth perpendicular to the basal plane. The latter deposits tend to be more dense. Table I summarizes data on the interatomic distances in the substrates investigated (23) and give the degree of mismatch with the basal plane spacing of zinc. It is best to compare substrates that do not form alloys with zinc such as Cd, Sn, In, and Pb, since alloy formation certainly must rearrange the atoms of the substrate. In going from Cd to Sn to In and Pb the deposit changes from a basal to an intermediate and then to a perpendicular orientation. According to Finch and his co-workers (24), the critical mismatch is about 15%. This appears to be the case here.

### Summary

1. The nucleation overvoltage for zinc on Pb, Ti, Sn, and In in alkaline zincate solutions is 30-40 mV.

Table I. Substrate interatomic distance in comparison to interatomic distances in the zinc basal plane

Metal	Interatomic distance (Å)	Differences with interatomic distance of Zn in basal plane (%)
Cu	2.556	-4.1
Ag	2.889	8.4
Au	2.883	8.1
Cd	2.979, 3.293	11.78
Sn	3.02, 3.17	13.32
In	3.24, 3.37	21.57
Tl	3.401, 3.456	29.68
Pb	3.500	31.3
Zn	2.665, 2.912	

2. Thallium is the only metal that alloys with Zn during deposition.

3. As opposed to the deposits found on Ag, Cu, Au, Cd, and Zn, the deposits were not oriented parallel to the basal plane. On Sn and Ti the deposit had an intermediate orientation and on In and Pb the deposit was oriented perpendicular to the basal plane. Deposit orientation and morphology has been correlated with the degree of mismatch of Zn with the substrate.

#### Acknowledgments

This work was supported by the U.S. Department of Energy (Contract No. DE-AC02-76CH00016) and the Naval Ship Engineering Center (NAVSEC). The authors acknowledge helpful discussions with A. Himy of NAVSEC, O. C. Wagner of the U.S. Army Electronics Research and Development Command (ERADCOM), Professor B. E. Conway of the University of Ottawa, and W. E. O'Grady, R. R. Adzic, W. Visscher, and S. Srinivasan of Brookhaven National Laboratory (BNL). The authors wish to thank O. Kammerer (BNL) for the x-ray analysis and R. L. Sabatini (BNL) for the scanning electron microscopy. One of the authors (G.A.) had financial support from the Research Fund of Serbia, Yugoslavia, during the course of this work.

Manuscript submitted Dec. 4, 1980; revised manuscript received ca. June 1, 1981.

Any discussion of this paper will appear in a Discussion Section to be published in the June 1982 JOURNAL. All discussions for the June 1982 Discussion Section should be submitted by Feb. 1, 1982.

Publication costs of this article were assisted by the Brookhaven National Laboratory.

#### REFERENCES

1. J. E. Oxley and C. W. Fleischman, Third Quarterly Report to NASA, Contract No. NA85-9591, Leeson Moos Laboratories, Great Neck, NY, March 1986, NASA Assessment No. 66-26870.
2. H. G. Oswin and K. F. Blurton, "Zinc Silver Oxide

- Batteries," A. Fleischer and J. J. Lander, Editors, John Wiley & Sons, New York (1971).
3. N. T. Kudryatzev, *Tr. Konf. Korro. Metal*, **2**, 119 (1943).
4. J. W. Diggle and A. Damjanovic, *This Journal*, **117**, 65 (1970).
5. K. L. Hampartsumian and R. V. Moshtev, in "Power Sources 3," D. H. Collins, Editor, pp. 495-510, Oriol Press, Newcastle upon Tyne (1971).
6. F. Mansfield and S. Gilman, *This Journal*, **117**, 588 (1970).
7. F. Mansfield and S. Gilman, *ibid.*, **117**, 588 (1970).
8. D. J. Mackinnon, J. M. Brannen, and V. I. Lakshmannon, *J. Appl. Electrochem.*, **9**, 603 (1979).
9. D. J. Mackinnon, J. M. Brannen, and R. C. Kerby, *ibid.*, **9**, 55 (1979).
10. O. Wagner and A. Himy, in "Proceedings of 27th Power Sources Conference," p. 135, The Electrochemical Society, Princeton, NJ (1976).
11. A. Himy and O. C. Wagner, U.S. Pat. 4,084,047.
12. S-P Poa, G-M-C Chiang, and T-C Lin, *Science Development Monthly (Taiwan)*, **6**, 1013 (1978).
13. J. McBreen, S. Gannon, and M. G. Chu, Abstract 91, p. 248, The Electrochemical Society Extended Abstracts, Hollywood, Florida, Oct. 5-10, 1980.
14. W. G. McQ. Tegart, "Electrocatalytic and Chemical Polishing of Metals," Pergamon Press, Oxford (1959).
15. G. Adzic, J. McBreen, and M. G. Chu, *This Journal*, **128**, 1691 (1981).
16. M. G. Chu, J. McBreen, and G. Adzic, *This Journal*, **128**, 2281 (1981).
17. S. Trasatti, *J. Electroanal. Chem. Interfacial Electrochem.*, **33**, 351 (1971).
18. J. N. Jovicevic, D. M. Drazic, and A. R. Despic, *Electrochim. Acta*, **22**, 589 (1977).
19. R. A. Ross, H. B. Vanfleet, and D. L. Decker, *Phys. Rev. B*, **9**, 4026 (1974).
20. D. L. Decker, R. A. Ross, W. E. Evenson, and H. B. Vanfleet, *ibid.*, **15**, 507 (1977).
21. W. Seith, "Diffusion in Metallen," p. 8, Springer Verlag, Berlin (1955).
22. G. Lumsden, *Discuss. Faraday Soc.*, **4**, 62 (1948).
23. R. W. G. Wyckoff, "Crystal Structures," Vol. 1, John Wiley & Sons, New York (1963).
24. G. J. Finch, H. Wilman, and L. Yang, *Discuss. Faraday Soc.*, **1**, 144 (1947).

## Electrodeposition of Silicon from Solutions of Silicon Halides in Aprotic Solvents

A. K. Agrawal\* and A. E. Austin\*

Battelle, Columbus Laboratories, Columbus, Ohio 43201

#### ABSTRACT

Amorphous silicon has been electrodeposited from nonaqueous baths using  $\text{SiHCl}_3$  as the silicon source. A typical bath composition was 1.0M  $\text{SiHCl}_3$  in propylene carbonate containing 0.1M tetrabutyl ammonium chloride as the supporting electrolyte. Deposits were made potentiostatically at around  $-2.5\text{V}$  vs. Pt reference at temperatures  $35^\circ\text{--}145^\circ\text{C}$  under an argon atmosphere. A variety of materials including Pt, Ti, Ti-6Al-4V alloy, n-Si, and indium-tin oxide coated fused silica were used for the substrate. The as-deposited silicon contains some hydrogen bonded as  $\text{SiH}_2$  or  $\text{SiH}$ . The quality and hydrogen content of the deposits are controllable by selecting the proper bath composition and operating temperature. The electrodeposition process offers an inexpensive route for producing  $\alpha$ -Si films for possible solar cell applications.

The successful development of low cost solar cells for large-scale terrestrial power generation calls for new technology for attaining required cost reductions of 30-fold from the present. Amorphous silicon films

produced by various vapor phase deposition processes are being actively considered for solar cell applications (1). We investigated electrodeposition as a process for producing silicon directly on low cost metal substrates. As is well known, silicon cannot be electrodeposited from aqueous electrolytes because of hydrolysis of its salts and very large negative potentials

\* Electrochemical Society Active Member.

Key words: amorphous silicon, solar cell, electrodeposition, nonaqueous bath.

required for the cathode. The use of a wide range of nonaqueous organic solvents was investigated. Appropriate media were found to be solutions of silicon halides in dipolar aprotic organic solvents that are essentially anhydrous (2). The process yielded amorphous silicon of 1-5  $\mu\text{m}$  thickness on a variety of substrates. Process details, deposit quality, and composition of the electrodeposited  $\alpha$ -silicon are discussed here.

### System Development

Initially a number of solutes (silicon source—chloro and bromo silanes mainly), nonaqueous solvents, and supporting electrolytes (tetraalkyl ammonium salts) were investigated for the process. The screening was done by cyclic voltammetry experiments and followed by electrodeposition onto a platinum or Ti-6Al-4V substrate [see Ref. (2)]. After extensive trials the most suitable choices for the solute, solvent, and supporting electrolyte were trichlorosilane, propylene carbonate (PC), and tetraalkyl ammonium chlorides, respectively. The main considerations in the selection were stability of various components in the bath at operating cathode potentials in the anticipated temperature range of 35°–150°C, and the product quality.

Although  $\text{SiHCl}_3$  is quite soluble ( $>1\text{M}$ ) in PC, the  $\text{SiHCl}_3$  is barely ionized in the solvent. As a result the solution conductivity is extremely low ( $35\ \mu\text{mho cm}^{-1}$ ) for an efficient operation of the cell. Tetraalkyl ammonium chlorides were therefore added to the cell to increase the conductivity of the bath and thereby reduce the operating cell voltages.

**Cyclic voltammetry.**—Preliminary cyclic voltammetry experiments were done on platinum electrodes in PC with tetrabutyl ammonium chloride (TBAC) as the supporting electrolyte but without any  $\text{SiHCl}_3$  present. This was done to check the inertness of the bath and also to determine the safe working potential range. In the voltammograms no current waves, either cathodic or anodic, were observed in the potential range +0.8 to  $-3.0\text{V vs. Pt}$ . This indicated an absence of reactions and proved the inertness of the bath. However, when the scanning was extended beyond the above potentials, in separate experiments, large current waves resulted at both ends. These waves were due to the breakdown of the bath constituents. The potential range beyond  $-3.0\text{V vs. Pt}$  was therefore considered unsafe for the cell operation but safe between +0.8 and  $-3.0\text{V vs. Pt}$ . Chloride ion oxidation starts beyond  $+0.8\text{V vs. Pt}$ .

A cyclic voltammogram for  $\text{SiHCl}_3$  in PC and TBAC is shown in Fig. 1. Two reduction waves at cathodic potentials near  $-1.2$  and  $-2.3\text{V vs. Pt}$  are evident. During scanning in the positive direction from the most negative potential  $-2.7\text{V vs. Pt}$ , no anodic waves corresponding to either of the cathodic waves were observed. This implies that the cathodic reactions are highly irreversible. The first wave at  $-1.3\text{V vs. Pt}$  is thought to be from the reduction of trace amounts of HCl present in the bath. This HCl results from a re-

action between  $\text{SiHCl}_3$  and  $\text{H}_2\text{O}$ , which finds its way as a trace impurity in PC or TBAC. In the second cycle the first wave completely disappeared, probably because of an exhaustion of HCl from the bath. Formation of HCl by hydrolysis of chlorosilanes, e.g.,  $\text{R}_3\text{SiCl} + \text{H}_2\text{O} \rightarrow \text{R}_3\text{SiOH} + \text{HCl}$ , and the reduction of HCl on electrolysis in nonaqueous solvents have been reported by Corriu *et al.* (3).

The second wave in the voltammogram in Fig. 1 is from the reduction of  $\text{SiHCl}_3$  to  $\alpha$ -Si. The current peak is located at  $-2.3\text{V vs. Pt}$ . Repeated cycling of the potential between +0.8 and  $-2.7\text{V vs. Pt}$  produced a gradual shrinking of the peak and also a slight negative shift of the peak potential in successive cycles. These changes are thought to be from a buildup of  $\alpha$ -Si deposit on the substrate during each cycle and the resulting IR drop therein. The presence of only a strong single peak, after the HCl removal, suggests that the reduction of  $\text{SiHCl}_3$  is essentially a one-step process. Multiple peaks corresponding to stage-wise reduction of  $\text{SiHCl}_3$  were never observed.

### Experimental

All experiments including screening experiments were done inside a dry glove box under an argon atmosphere. Initially a reagent grade PC after careful drying over molecular sieves and purification by vacuum fractional distillation was used for the solvent. The distillate was kept at all times under an argon atmosphere. Gas chromatographic analysis of the distillate gave a maximum of 10 ppm  $\text{H}_2\text{O}$  and 100 ppm propylene glycols. The conductivity of the distillate was  $0.5\text{--}1.0\ \mu\text{mho}$ . Later, high purity, very low water, glass distilled PC from Burdick and Jackson Laboratories was used in all experiments, without any further treatment. Cyclic voltammetry results and the quality of deposits with the latter PC justified its use. Trichlorosilane used as solute was from Silar Corporation. Tetraalkyl ammonium chlorides, i.e., tetraethyl (TEAC), tetrapropyl (TPAC), TBAC, tetrapentyl (TPnAC), and tetrahexyl (THAC) were obtained from the Ventron Corporation and these were purified by recrystallization under argon atmosphere according to the procedures described in Mann (4).

Electrodeposition experiments were carried out potentiostatically in Teflon cells using an internal platinum reference electrode. A Teflon cell of 15 ml capacity used with 2 cm diam substrates is shown in Fig. 2. The counterelectrode was made from vitreous carbon, whereas a variety of substrates were used for the cathode, including Pt, Ti-6Al-4V alloy, commercially pure titanium, n-silicon, and transparent indium-tin oxide on fused silica. All metallic substrates were mechanically polished to a mirror smooth finish for

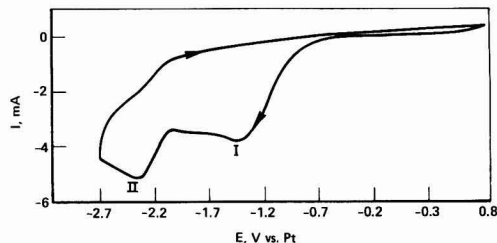


Fig. 1. A cyclic voltammogram of platinum substrate at 35°C in PC containing 0.1M TBAC and 0.2M  $\text{SiHCl}_3$ .

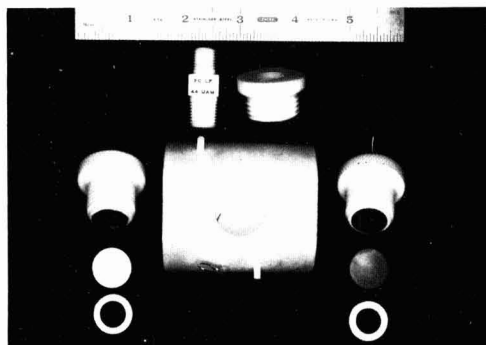


Fig. 2. A Teflon cell used in electrodeposition experiments shown disassembled.



use as a cathode. These were cleaned with deionized water and rinsed off with acetone prior to use. A deposition potential around  $-2.5V$  vs. Pt was used in most of the experiments.

Deposits were made at  $35^{\circ}\text{--}145^{\circ}\text{C}$ . Experiments above  $35^{\circ}\text{C}$  required a heated pressure chamber for the cell because of the high volatility of  $\text{SiHCl}_3$  (bp  $33^{\circ}\text{C}$ ). For runs at high temperatures the Teflon cell after assembling and filling with the solution was sealed in the chamber. The chamber was then pressurized with argon. The pressure was maintained at 20-30 psi (140-210 kPa) above the vapor pressure of  $\text{SiHCl}_3$  at the operating temperature of the cell, e.g., 110 psig (800 kPa) for a  $90^{\circ}\text{C}$  run. This prevented the loss of  $\text{SiHCl}_3$  from the cell.

During deposition the cell current was monitored, and in most cases a digital integrator was also used to show the cumulative charge passed at any time. Deposit thickness was calculated using Faraday's law assuming 4 electron transfer reduction, 100% current efficiency, and a deposit density of  $2.0\text{ g/cm}^3$ . The thickness was checked in a few instances by weight gain of the substrate and a measurement of the tapered section of the deposit with SEM. A good correspondence between the calculated thickness and measured thickness supported the assumptions.

### Results and Discussion

In very early experiments a tank-type 300 ml capacity bath was used as a cell. The bath was reused 3 or 4 times for the deposition without changing the solution but after replenishing the  $\text{SiHCl}_3$ . It was noticed that the starting currents in subsequent runs, under identical operating conditions, were smaller than in the previous runs. It was reasoned that some by-product is generated during the  $\text{SiHCl}_3$  reduction. This by-product adsorbed on the cathode surface in competition with the active  $\text{SiHCl}_3$  species and hindered the reduction process. As a result, the practice was changed to using a fresh bath for each deposit. However, in order to save on expensive chemicals the cell design was changed and the volume was reduced to  $\sim 15\text{ ml}$  solution for a 2 cm diam substrate. All the results described here are for the later practice using the new cell.

A typical deposit made on Ti-6Al-4V substrate at  $35^{\circ}\text{C}$  is shown in Fig. 3. A typical bath contained 0.1M TBAC and 0.25M  $\text{SiHCl}_3$ . The starting currents in general were  $2\text{--}5\text{ mA/cm}^2$ , but decayed rapidly after about 0.5 min at a rate proportional to  $t^{-1/4}$  to  $t^{-1}$

(where  $t$  is time) with thickening of the deposit (see Fig. 4). The drop in current with time was partly due to the  $IR$  drop in the growing film, and for the rest the reasons are not completely understood at this time. A  $1\text{ }\mu\text{m}$  thick deposit required more than 1000 min. The process was subsequently improved to give better yields. The effect of process variables, such as solute concentration, temperature, and the size of cation in the supporting electrolyte are discussed below. The supporting electrolyte used in most of the experiments was TBAC at 0.1M concentration unless mentioned otherwise.

**Temperature.**—Increasing the temperature above  $35^{\circ}\text{C}$  resulted in a higher starting current which remained higher during the course of deposition. The electrodeposition currents for two temperatures of  $35^{\circ}$  and  $70^{\circ}\text{C}$  are shown in Fig. 4 for comparison. It should be noted in the figure that although the current for the  $70^{\circ}\text{C}$  run is higher by at least a factor of two over most of the deposition period, the rate of decay for the two runs is almost identical. The identical nature of two curves suggests that the deposition process in both cases is the same. The activation energy for the process was calculated from the Arrhenius plots of  $i$  vs.  $1/T$  shown in Fig. 5, for the temperature range  $35^{\circ}\text{--}90^{\circ}\text{C}$ . Three time intervals 0.1, 1, and 100 min were chosen for the calculations, but all three gave the same value of activation energy  $2 \pm 0.2\text{ kcal}$ . The low activation energy for the process suggests that the rate-determining step is probably an electrosorption process. Higher temperatures usually resulted in thicker and smoother deposits. Deposit thickness of  $\sim 1\text{ }\mu\text{m}$  could be obtained in about 1000 min by operating the cell at  $70^{\circ}\text{C}$ , as opposed to  $\sim 0.5\text{ }\mu\text{m}$  at  $35^{\circ}\text{C}$ .

**Solute concentration.**—The solute concentration in the bath in the range 0.1-1.0M had a significant effect on the rate of current decay as well as on the quality of deposit. The rate of decay, particularly in the first 10 min, was considerably retarded with increasing  $\text{SiHCl}_3$  concentration. Consequently a deposit of  $1\text{ }\mu\text{m}$  thickness could be produced in about an hour or less with 1.0M  $\text{SiHCl}_3$  in the bath at  $50^{\circ}\text{C}$  or higher. The deposits were also more uniform and smoother in texture than those made with lower concentrations of  $\text{SiHCl}_3$ . Concentrations above 1M  $\text{SiHCl}_3$  offered no further improvements.

Although the rate of current decay was affected by the solute concentration, the starting current changed little with the increasing  $\text{SiHCl}_3$  concentration. The starting current was strictly dependent upon the type of substrate used for the cathode.

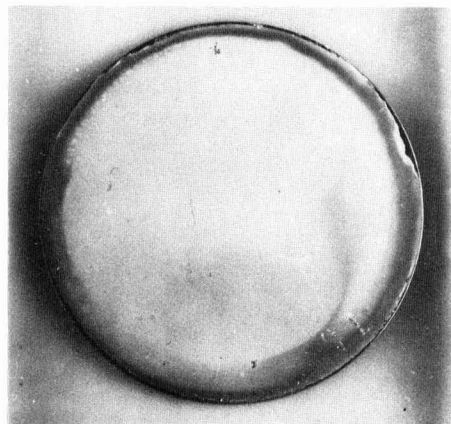


Fig. 3. Photomicrograph of silicon deposit on titanium alloy ( $4\times$ ).

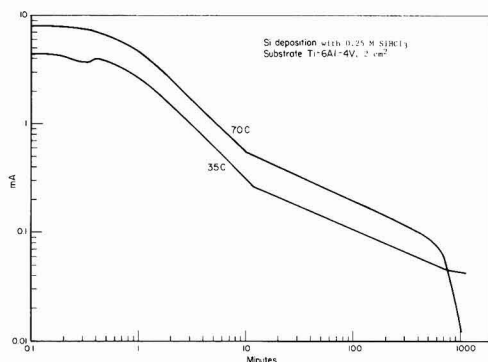


Fig. 4. Comparison of the electrodeposition current for two temperatures,  $35^{\circ}$  and  $70^{\circ}\text{C}$  at  $-2.5V$  vs. Pt with 0.25M  $\text{SiHCl}_3$ . Substrate area:  $2\text{ cm}^2$ .

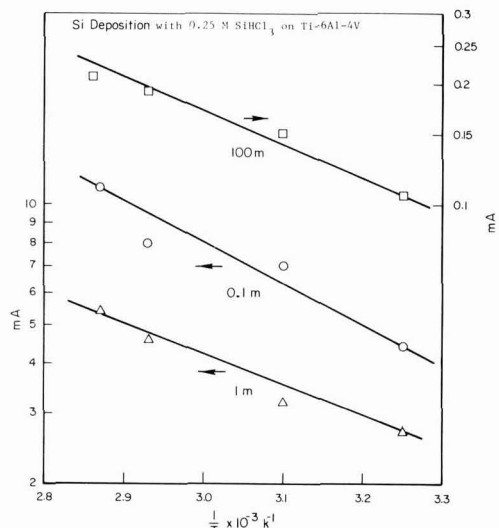


Fig. 5. Arrhenius plots of  $i$  vs.  $1/T$  at 0.1, 1, and 100 m

**Supporting electrolyte.**—From the low activation energy and the current decay behavior during the deposition, it was hypothesized that the process is adsorption controlled. It was, therefore, concluded that by changing the cation size of the supporting electrolyte in the bath, the deposition rate and the quality of the deposit, particularly the morphology, could be controlled. As a result, silicon deposition was experimented using different supporting electrolytes of the tetraalkylammonium chloride series. The tetraalkylammonium chlorides used in the experiments were TEAC, TPAC, TBAC, TPnAC, and THAC. The concentration of the supporting electrolyte in each of the experiments was kept constant at 0.1M. The nominal bath temperature was 35°C and the  $\text{SiHCl}_3$  concentration 0.5M.

The morphology of the Si deposit and the deposition current decay both were strongly affected by the size of the cation in the bath. In general, the deposits were coarser with increasing cation size; with smaller cations TEAC and TPAC the deposits were very smooth, at 2000 magnification with SEM no separate nodules could be detected. With THAC, the deposits were extremely coarse and loosely adherent to the titanium substrate. The adherence appeared to improve with lowering of the cation size in the bath.

The starting current on the Ti substrate in all the cases was  $2.6 \pm 0.2 \text{ mA/cm}^2$ , irrespective of the cation size. However, after a few monolayers of Si deposition the current decay was greatly affected by the cation size. The smaller the cation in the bath, the higher was the rate of current decay. The current decay with TEAC was so rapid that deposit thickness was limited to only  $\sim 0.3 \mu\text{m}$  before the deposition rate reached to nearly zero ( $\sim 0.01 \text{ mA/cm}^2$ ) value. With THAC, on the other hand, the rate of decay was very small, and the current stayed with deposition at about  $1 \text{ mA/cm}^2$ . The starting current of  $2.6 \text{ mA/cm}^2$  appears to be controlled only by the number of active sites available on the Ti substrate for the adsorption of active  $\text{SiHCl}_3$ . It is only after the first few monolayers that the cation size of the supportive electrolyte became important.

In order to improve the morphology of electrodeposited silicon, mixed supporting electrolytes of TBAC and TPAC were tried in the bath. Typical experiments with the mixed TBAC and TPAC electro-

lyte were made at 50°C and cathode potential of  $-2.6\text{V}$  vs. Pt. The total concentration of the mixed electrolyte in the bath was always maintained at 0.1M with 1.0M  $\text{SiHCl}_3$ . The TPAC:TBAC compositions tried were 1:100, 10:100, 50:50, 100:10, and 100:1. The optimum composition for TPAC:TBAC was found to be 100:10. With this TPAC:TBAC ratio good deposits of about  $1 \mu\text{m}$  could be obtained in less than 2 hr. With any other mixture the rates were significantly lower.

The nodule size in the deposits in general decreased with the increasing proportion of TPAC in the mixture. For comparison purposes, four deposits from different bath compositions are shown in Fig. 6. The lower two of the deposits in Fig. 6 are from pure electrolytes TPAC and TBAC, whereas the upper ones are from 10:100 TPAC to TBAC and 10:100 TBAC to TPAC ratios. The deposit from the bath with 10:100 TBAC to TPAC ratio is fine grained and smoother in comparison to the others. Table I gives the deposit thickness and their resistivity, as measured in the solution, from different electrolyte mixtures. The resistivity generally increased with decreasing nodule size and increasing smoothness.

**Composition and properties.**—Silicon deposits were analyzed for composition with EDAX, Auger spectrometer, and SIMS. The EDAX analysis showed no other metallic element besides Si. Transfer of specimens from the deposit dry box to the Auger chamber resulted in surface oxidation of deposits. This produced insulating film on the specimen surface, and subsequently presented problems with Auger analysis because of the electron charging. Auger analysis after argon sputtering showed  $\text{Si}_{1LL}$  peak at 92 eV. Analyses with SIMS indicated Si, oxygen ( $\approx 3\% \text{ SiO}$ ), and less than 0.01% of trace impurities C, Mg, Al, K, and Na in the deposits. Chlorine was not detected with either SIMS or Auger in any of the deposits analyzed.

The deposits contain some hydrogen, which is driven off on annealing with a threshold at 350°C and a peak of evolution at 470°C. The amount of hydrogen in the deposits varied with the deposition tem-

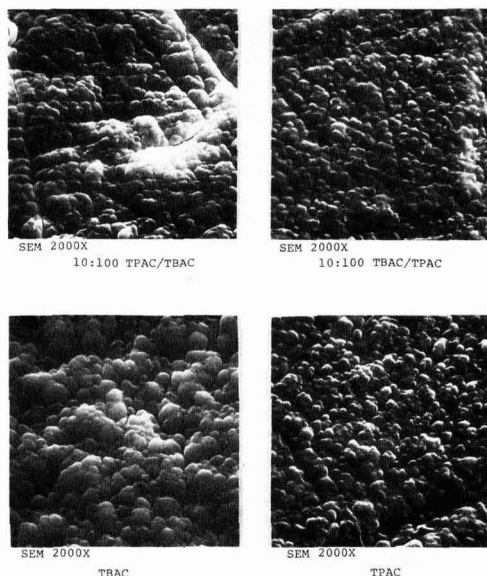


Fig. 6. Micrographs of silicon deposits made with varying supporting electrolyte ratio of TBAC and TPAC on titanium substrate at 50°C.

Table I.  $\alpha$ -Si characteristics from mixed TBAC and TPAC electrolyte baths

Ratio TBAC:TPAC	Thickness ( $\mu\text{m}$ )	Resistivity <sup>a</sup> ( $\Omega\text{-cm} \times 10^7$ )
0:100	0.36	12
1:100	0.68	12
10:100	0.91	1.5
50:50	0.51	7.5
100:10	1.36	3.9
100:1	1.07	2.3

<sup>a</sup> Resistivity as measured in deposition cell using a Wayne-Kerr bridge.

perature. The hydrogen in deposits made at 35°C was determined by thermal evolution in mass spectrometer, whereas other deposits were analyzed by nuclear reaction with  $^{15}\text{N}$  beam (5). The hydrogen content was estimated to be 35% in deposits made at 35°C, 20% at 50°C, and only 16% at 90°C.

There is indication from infrared spectra that the hydrogen in deposited silicon is chemically bonded in the form of  $\text{SiH}$ ,  $\text{SiH}_2$ , and  $\text{SiH}_3$ , mostly as  $\text{SiH}_2$  (6, 7). The nature of bonding changes from  $\text{SiH}_2$  to  $\text{SiH}$  as the temperature of the deposition bath is raised; the change was detected by a shift in the IR absorption spectra at  $2100\text{ cm}^{-1}$  and appearance of absorption band at  $650\text{ cm}^{-1}$ . The IR absorption spectra of electrodeposited silicon was interpreted in the light of work by Lucovsky *et al.* (8) with amorphous silicon produced by other techniques.

The electrodeposited silicon showed photoconduction as well as photovoltaic properties. The nature of hydrogen bonding in the deposits and some of their photoelectric properties are subjects of another paper (9).

Amorphous nature of the deposits was determined with x-ray diffraction and transmission electron diffraction. X-ray diffraction of silicon deposits produced no crystalline pattern but only a broad diffused band, indicative of amorphous material. Transmission electron diffraction at 100 kV of free silicon films that were lifted off from the substrate, gave also diffused rather than a crystalline pattern. At 100 kV any microcrystallinity of the order of 10–20 Å would have been easily revealed. For the present purposes, the deposited material is therefore considered amorphous.

### Conclusions

Amorphous silicon can be deposited from a non-aqueous bath containing PC as solvent,  $\text{SiHCl}_3$  as

solute, and tetraalkyl ammonium chlorides as the supporting electrolytes. The deposit growth is nodular 1–3  $\mu\text{m}$  in size. An increase in bath temperature ( $35^\circ \leq T \leq 145^\circ\text{C}$ ) and solute concentration ( $0.1 \leq C \leq 1.0\text{M}$ ) favors faster deposition rates, more uniform and smoother deposits. Nodule size and therefore smoothness can also be controlled by using a mixed supporting electrolyte from the tetraalkyl ammonium chloride series.

As deposited  $\alpha$ -silicon contains some bonded hydrogen as  $\text{SiH}_2$  or  $\text{SiH}$ . The hydrogen is driven off on annealing at temperatures  $\sim 470^\circ\text{C}$ . The electrodeposition process offers an inexpensive route for producing  $\alpha$ -Si films for possible solar cell applications.

### Acknowledgment

This research was supported by Battelle Memorial Institute, the Northwest Mutual Life Insurance Company, the U.S. Department of Energy under Contracts DE-AC03-78-ET-20521 and SERI Subcontract XS-9-8249-1. The authors wish to thank Dr. W. A. Lanford of State University of New York for supplying hydrogen analyses.

Manuscript submitted Dec. 12, 1980; revised manuscript received June 5, 1981. This was Paper 363 presented at the St. Louis, Missouri, Meeting of the Society, May 11–16, 1980.

Any discussion of this paper will appear in a Discussion Section to be published in the June 1982 JOURNAL. All discussions for the June 1982 Discussion Section should be submitted by Feb. 1, 1982.

Publication costs of this article were assisted by Battelle Memorial Institute.

### REFERENCES

1. J. I. B. Wilson and D. Weaire, *Nature*, **275**, 93 (1978).
2. A. E. Austin, U.S. Pat. 3,990,953 (1976).
3. R. J. P. Corriu, G. Dabosi, and M. Martineau, *J. Chem. Soc. Chem. Commun.*, 457 (1979).
4. C. K. Mann, in "Electroanalytical Chemistry," Vol. 3, A. J. Bard, Editor, Marcel Dekker, Inc., New York (1979).
5. W. A. Lanford, *Solar Cells* **2**, 351 (1980).
6. A. E. Austin, A. K. Agrawal, and G. T. Noel, Final Report, November 8, 1979, DOE/ET/2052C4.
7. A. E. Austin, A. K. Agrawal, and G. T. Noel, "Electrodeposited Amorphous Silicon for Solar Cell Applications," Final Report to DOE/SERI, September 30, 1980.
8. G. Lucovsky, R. J. Nevranich, and J. C. Knights, *Phys. Rev. B*, **19**, 2064 (1979).
9. A. E. Austin, To be published.

# Resistance to Flow of Current to Scratched Electrodes

H. J. Pearson,<sup>1</sup> G. T. Burstein,\* and R. C. Newman

Department of Metallurgy and Materials Science, University of Cambridge, Cambridge CB2 3QZ, England

## ABSTRACT

The electrolyte resistance to flow of current to a scratched electrode is calculated assuming the scratch to be shallow and represented by a rectangular planar strip. The resulting equation agrees with experimentally measured ohmic resistances to long, narrow rectangular strip electrodes. Also presented are corrections to the previously published formula for the ohmic resistance to a disk electrode due to finite dimensions of the counterelectrode and the electrochemical cell for systems with radial symmetry.

Rapid mechanical scratching or abrasion of potentiostatically controlled metal electrodes in aqueous electrolytes provides a method of examining the electrochemical properties of metal surfaces initially free from oxide films (1-10). Under external potential control, initially passive electrodes can react at very high anodic current densities on scratching before reverting to the passive state. Important features of an experimental device for studying scratched electrodes are a rapid rate of bare surface generation, an accurately known bare surface area, and minimal surface heating during abrasion. These criteria are satisfied most closely by a device which creates a single narrow shallow scratch on a rotating disk electrode (6-10). The purpose of the present paper is to consider the effects of electrolyte resistance during electrochemical reactions at scratched electrodes under potentiostatic control, where the current passing on the scratched surface flows to a counterelectrode. The related problem of the open-circuit potential distribution across a scratch in a passive film has been investigated by Doig and Flewitt (11) and Melville (12). However, the use of similar open-circuit results to criticize the soundness of the potentiostatic scratching technique (11) is not valid since the current distribution in the two cases is quite different. Many potentiostatic scratching experiments are performed on specimens whose overall surfaces are not coated: the area of exposed metal carries a slow steady-state reaction. Ohmic potential changes occurring around the scratch due to high current densities from the scratch itself can interfere with measurements of scratch current densities. This has been observed when the electrode as a whole is active or carries a readily reducible oxide film (7,9)).

Newman (13) has presented a calculation of the ohmic potential drop due to current flow between a rotating disk electrode embedded in an insulating surface and a counterelectrode at infinity. He solves the Laplace equation for the potential distribution by transforming to rotational elliptic coordinates (oblate spheroidal coordinates). This exact method of solution is only possible because of the symmetry of the problem and is not available for more general electrode geometries. Here we show that knowledge of the approximate form of the current distribution near the electrode leads to accurate expressions for the ohmic potential drop for various electrode shapes, in particular a thin strip of finite length representing a scratch in a passive film. The technique also allows calculation of the corrections required for counterelectrodes of finite size and distance from a rotating

disk working electrode. Confirmation of the calculations is obtained by measuring the ohmic resistance to segments of narrow strip electrodes using a double galvanostatic pulse technique.

## Mathematical Model

Consider a plane counterelectrode situated at a position  $z = 0$  (where  $z$  is the axis perpendicular to the planes of the counter and working electrodes), and a plane working electrode of given geometry embedded in an insulating plane at  $z = d$ . The Laplace problem for the ohmic component of the potential given by

$$\nabla^2 \phi = 0 \quad [1]$$

may be considered as having the following boundary conditions

$$\phi = 0 \text{ at } z = 0 \quad [2a]$$

$$\frac{\partial \phi}{\partial z} = \frac{1}{\sigma} f(x, y) \text{ at } z = d \quad [2b]$$

where  $x$  and  $y$  are the axes parallel to the counter and working electrode surfaces.  $f(x, y)$  is zero on the insulated portion of the plane  $z = d$  and represents the current distribution at the surface of the working electrode. The exact value of  $f(x, y)$  is such that the value of  $\phi$  is constant on the surface of the electrode. However, calculation will proceed by assuming forms of  $f(x, y)$  close to, but not necessarily identical to, the real expression. The first class of geometries that we consider will use an infinite plane counterelectrode at  $z = 0$ . A further idealized calculation will yield estimates for the corrections due to finite counterelectrode and cell size. The model deals first with the disk electrode as considered by Newman (13) and proceeds to an electrode geometry representing that of a finite, long, narrow, rectangular scratch.

*Disk working electrode with plane counterelectrode of infinite size.*—Here the boundary value problem is solved by Fourier-Bessel transform in the radial direction. Details are given in Appendix A. For comparison with the results of Newman (13) we consider two current distributions on the disk electrode of radius  $a$

$$f(x, y) = ai_0(a^2 - r^2)^{-1/2} \text{ for } r < a \quad [3a]$$

$$f(x, y) = i_0 \text{ for } r < a \quad [3b]$$

where

$$x^2 + y^2 = r^2 \quad [4]$$

The distribution represented by Eq. [3a] is the same as that for the exact problem solved with the counterelectrode and probe at infinity. Equation [3b] is an artificial distribution included to show the relative insensitivity of the ohmic resistance to the precise form of the current distribution on the electrode. For  $d \gg a$  Eq. [3b] gives

\* Electrochemical Society Active Member.

<sup>1</sup> Present address: Department of Applied Mathematics and Theoretical Physics, University of Cambridge, Cambridge, England.

Key words: disk working electrode, plane counterelectrode, rectangular strip working electrode.

$$R = \frac{V}{I} \approx \frac{1}{4a\sigma} \left( 1 - 2\beta \frac{a}{d} \right) \quad [5]$$

where  $\beta = \ln(2/\pi) = 0.2206$ . This gives a small correction to the result of Newman (13)

$$R = \frac{1}{4a\sigma} \quad [6]$$

due to the finite distance of the counterelectrode. For Eq. [3a] the potential varies across the disk. Taking the potential at the center of the disk as representative we find

$$R_0 = \frac{V_0}{I} = \frac{1}{\pi a \sigma} \left( 1 - 2\beta \frac{a}{d} \right) \quad [7]$$

Taking the potential at the edge of the disk as representative we find

$$R_a = \frac{V_a}{I} = \frac{2}{\pi^2 a \sigma} \left( 1 - 2\beta \frac{a}{d} \right) \quad [8]$$

Thus any suitable average of Eq. [7] and [8] gives a similar result to Eq. [5], for example

$$R = \frac{1}{2a\sigma} \left( \frac{1}{\pi} + \frac{1}{\pi^2} \right) = \frac{1}{3.6a\sigma} \quad [9]$$

A constant current distribution also clearly gives a reasonable value for the ohmic resistance.

**Disk working electrode with plane counterelectrode of finite size.**—This uses a disk-shaped counterelectrode of radius  $p$ , coaxial with the working electrode and distance  $d$  from it. For this case we also define the cell as a coaxial cylinder of radius  $c$ . Using cylindrical polar coordinates  $(r, \theta, z)$  the Laplace Eq. [1] is solved subject to the following boundary conditions

$$\frac{\partial \phi}{\partial z} = \frac{1}{\sigma} f(r, \theta) \text{ at } z = 0, d \quad [10a]$$

$$\frac{\partial \phi}{\partial r} = 0 \text{ at } r = c \quad [10b]$$

This now restricts current flow to within the finite cell and specifies the current distribution on the counter and working electrodes. The problem given by Eq. [1] and [8] with distribution of the form [3a] is solved in the manner given in Appendix B using a Fourier-Bessel series expansion. The solution is

$$R = \frac{d}{\pi \sigma c^2} + \frac{1}{\pi \sigma} \sum_{n=1}^{\infty} \frac{1}{\lambda_n^2 J_0^2(\lambda_n)} \left[ \frac{\sin(\lambda_n a/c)}{a} + \frac{\sin(\lambda_n p/c)}{p} \right] \quad [11]$$

where the  $\lambda_n$  are the positive solutions of the equation  $J_1(\lambda_n) = 0$ . The first term on the right-hand side of Eq. [11] is simply the electrolyte resistance within the cylindrically shaped cell. The second and third terms are the end corrections for the finite size of the working and counterelectrodes, respectively. For  $a/c \ll 1$  the second term is the resistance found previously for the disk electrode with  $c$  and  $d$  infinite (section above). The first and third terms, being independent of  $a$ , should represent a good estimate of the correction for finite cell geometry for small scratches as well as disk electrodes and, hence, will be negligible for small scratches. Note that for  $p/c = 0.5$  the third term is half the first term.

**Rectangular strip working electrode and plane counterelectrode.**—We now consider the ohmic resistance to flow of current between a finite length rectangular strip electrode (length  $v = 2b$ , width

$w = 2a$ ,  $b > a$ ) and a planar counterelectrode. This shape of working electrode is selected since it most accurately represents a rectangular scratch of negligible depth in a metal surface. Details of the calculation are given in Appendix C for the following current distributions analogous to those used above

$$f(x, y) = a i_0 (a^2 - x^2)^{-1/2}, \quad -a \leq x \leq a, \quad -b \leq y \leq b \quad [12a]$$

$$f(x, y) = i_0, \quad -a \leq x \leq a, \quad -b \leq y \leq b \quad [12b]$$

For distribution [12a] we have for  $d \gg b > a$

$$R = \frac{1}{2\pi \sigma b} \ln \{ 2[(1 + b^2/a^2)^{1/2} + b/a] \} \quad [13]$$

For the additional inequality that  $b \gg a$ , Eq. [13] simplifies to

$$R = \frac{1}{2\pi \sigma b} \ln(4b/a)$$

For current distribution [12b], and for  $d \gg b \gg a$

$$R = \frac{1}{2\pi \sigma b} [\ln(2b/a) + 1] \quad [14]$$

Equation [13] will be used for comparison with the experimentally determined ohmic resistances (see below).

### Experimental

The apparatus used for scratching potentiostatically controlled rotating disk electrodes has been described previously (6-10). The electrochemical cell used for measurement of the ohmic potential drop was similar in design and dimensions; its internal diameter was 10.5 cm and its capacity 1000 cm<sup>3</sup>.

The working electrodes were designed to simulate rectangular scratches and were made in the following way. Rotating electrodes were prepared in which the edges of copper foils of various thicknesses were exposed to the electrolyte, as shown in Fig. 1. Three foil thicknesses were used: 39, 126, and 936  $\mu\text{m}$ . The foils were set in epoxy resin so that the rectangular edges were exposed, with the insulating resin forming the rotating disk (8 mm diam). Surfaces were abraded to a 1200 grit finish, cleaned ultrasonically, and degreased. Different lengths of the resulting straight, narrow, rectangular strip copper electrodes were exposed by applying a thin mask of lacquer to insulate varying proportions of the electrode length. Rotation at 33 Hz was used for convenience to remove bubbles adhering to the working electrode surface; however, electrode rotation had no effect on the measured ohmic potentials.

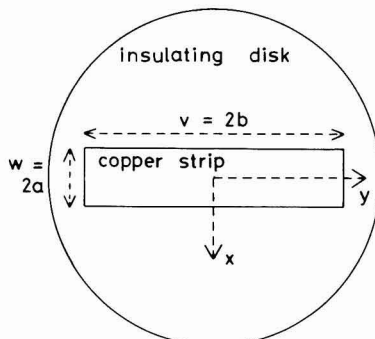


Fig. 1. Schematic diagram of rectangular strip electrode embedded in an insulating rotating disk.



The counterelectrode was a circular platinum disk of 5 cm diam mounted symmetrically below the working electrode surface at a distance of 6 cm. A small hole cut through the center of the counterelectrode allowed a Luggin probe to emerge through it from the bottom of the cell. The probe tip of  $\sim 1$  mm internal diameter was positioned 4 cm vertically below the working electrode surface. This probe distance is effectively infinite within this cell geometry. Potentials were measured with respect to a saturated calomel reference electrode.

Electrolytes were prepared from analytical grade reagents and distilled water. Their conductivities were measured to  $\pm 2\%$  with a conductivity bridge (Wayne-Kerr B642 Auto-Balance Universal Bridge).

The ohmic resistances were measured using a double galvanostatic pulse technique, delivered from a potentiostat (Wenking Type OPA 69, response time 1  $\mu$ sec) programmed to operate as a galvanostat. Square current pulses were generated by feeding the output of a waveform generator (Chemical Electronics Type WG 01) into the potentiostat. Double current pulses, each of 3 msec duration, were used, both in the anodic direction. The initial current density was zero, and the first pulse (A) was adjusted to give an anodic current density of  $\sim 2$  A cm $^{-2}$ . The second pulse (B) was adjusted to increase the anodic current density to  $\sim 4$  A cm $^{-2}$ . Pulse A allowed fast electrode processes such as double layer charging to approach completion; the instantaneous potential change, which occurred as a result of the current pulse B, was used as a measure of the ohmic potential drop in the electrolyte. This was checked by measuring the ohmic potential drop as a function of the current amplitude of pulse B for constant electrode length and width, demonstrating that the relationship was indeed ohmic (see below). Electrode response to the double pulse was stored in a transient recorder (Datalab Type DL 905) and displayed oscillographically. The working electrode was resurfaced between measurements to prevent significant recession of the metal surface into the epoxy resin mount due to anodic dissolution.

All experiments were performed at  $291 \pm 2$  K.

### Results and Discussion

Figure 2 shows the relationship between the measured potential change  $\Delta E$ , due to current pulse B and the pulse amplitude  $\Delta I$ , for constant amplitude of pulse A. The relationship is ohmic and the slope gives

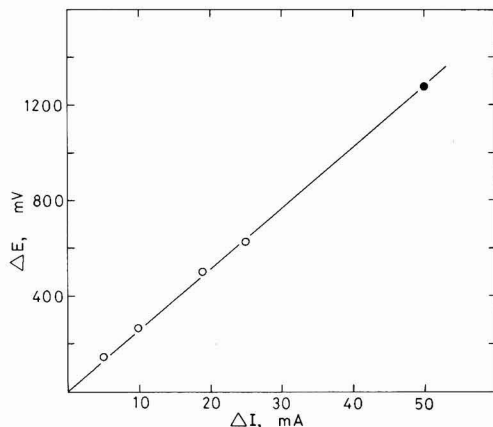


Fig. 2. Measured potential change as a function of applied current pulse (B) amplitude (○). Also shown is one point (●) from pulse A. Electrolyte: 1M KOH,  $\sigma = 15.4 \Omega^{-1} \text{ m}^{-1}$ . Strip electrode,  $w = 39 \mu\text{m}$ ,  $v = 5.48$  mm.

the electrolyte resistance  $R$  ( $25.3 \Omega$  measured from Fig. 2;  $23.9 \Omega$  calculated from Eq. [13]). Figure 2 also shows one measurement for a different amplitude of pulse A, which yields a similar value of  $R$ .

The resistance to flow of current through an acetate buffer solution (0.75M HOAc, 0.75M NaOAc) to rectangular electrodes of three different widths,  $w$  ( $= 2a$ ), is plotted as a function of inverse electrode length  $v^{-1}$  ( $v = 2b$ ) in Fig. 3. The solid lines in Fig. 3 represent the theoretical electrolyte resistance predicted from Eq. [13] using the measured electrolyte conductivity. Deviation from the predicted behavior occurs for the widest electrode ( $w = 936 \mu\text{m}$ ) for  $v^{-1} > 0.4$ . This represents the condition  $v/w = b/a < 2.5$  and is, in fact, expected from Eq. [13], which is not symmetrical in  $a$  and  $b$ . Apart from this the experimental data are in excellent agreement with the theoretical predictions. Similar behavior is shown in Fig. 4 for different electrolytes of several conductivities: again significant deviation from the predicted behavior occurs only for  $v/w < 2.5$ .

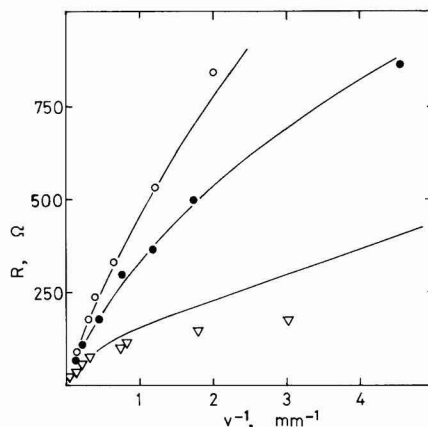


Fig. 3. Electrolyte resistance as a function of electrode length for 0.75M HOAc, 0.75M NaOAc,  $\sigma = 3.3 \Omega^{-1} \text{ m}^{-1}$ . ○,  $w = 39 \mu\text{m}$ ; ●,  $w = 126 \mu\text{m}$ ; ▽,  $w = 936 \mu\text{m}$ . The lines shown are the theoretical lines calculated from Eq. [13].

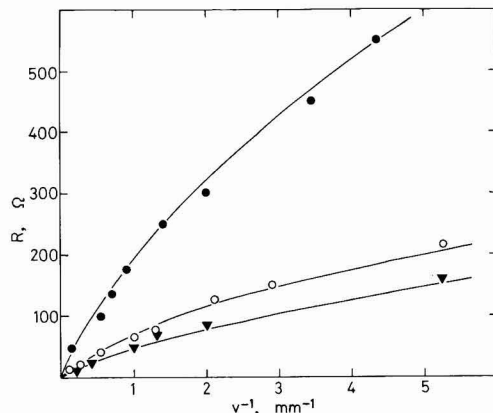


Fig. 4. Electrolyte resistance as a function of electrode length. ●, 0.53M  $(\text{NH}_4)_2\text{SO}_4$ ,  $\sigma = 7.0 \Omega^{-1} \text{ m}^{-1}$ ,  $w = 58 \mu\text{m}$ ; ○, 1M KOH,  $\sigma = 15.4 \Omega^{-1} \text{ m}^{-1}$ ,  $w = 126 \mu\text{m}$ ; ▼, 1M  $\text{H}_2\text{SO}_4$ ,  $\sigma = 32.8 \Omega^{-1} \text{ m}^{-1}$ ,  $w = 39 \mu\text{m}$ . The lines shown are the theoretical lines calculated from Eq. [13].

The predicted dependence on electrode width using Eq. [13] is shown in Fig. 5 for  $b \gg a$  ( $v \gg w$ ), and agreement is obtained with the measured data. Measurements were also made in several different electrolytes as a function of solution conductivity, and these are shown in Fig. 6 together with the theoretical lines from Eq. [13]. The graph shows that the measured resistance is indeed inversely proportional to the electrolyte conductivity, and the data are in accord with Eq. [14]. Figure 6 also shows that the measured ohmic potentials lie across the electrolyte and are not due to any surface film on the electrode.

However, in electrolytes in which a highly resistive film grows on the metal surface during current pulse A, one would expect the measured ohmic resistances to be higher than those predicted from Eq. [13] by

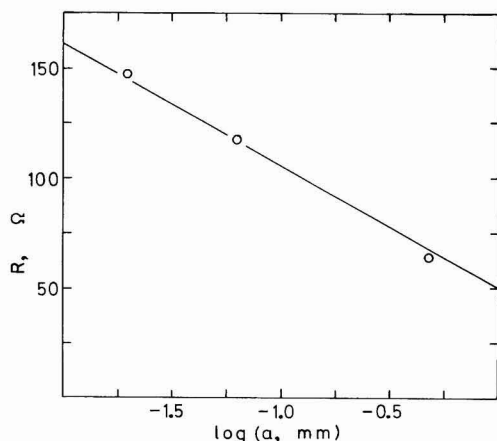


Fig. 5. Dependence of electrolyte resistance on width of strip electrode for constant length (4.0 mm). 0.75M HOAc, 0.75M NaOAc,  $\sigma = 3.3 \Omega^{-1} \text{ m}^{-1}$ . The line shown is that calculated from Eq. [13].

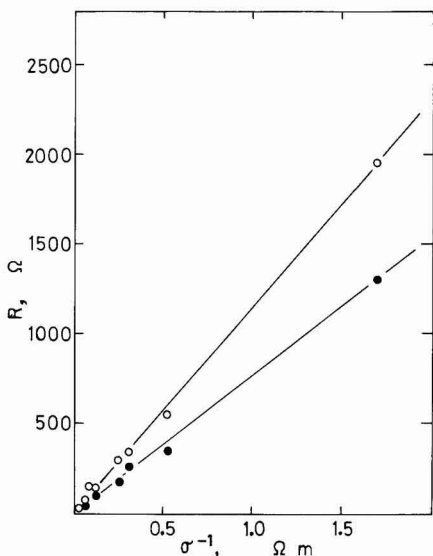


Fig. 6. Electrolyte resistance as a function of conductivity for  $v = 1.6 \text{ mm}$ .  $\circ$ ,  $w = 39 \mu\text{m}$ ;  $\bullet$ ,  $w = 126 \mu\text{m}$ . The lines shown are calculated from Eq. [13].

an amount equal to the ohmic resistance of the film. Two such cases are shown in Fig. 7. In both of these electrolytes (1M  $\text{K}_2\text{CO}_3$ , pH 11.6 and 0.5M  $\text{K}_2\text{CO}_3$ , 0.5M  $\text{KHCO}_3$ , pH 9.8) the copper electrode surface was green after galvanostatic pulsing, owing to formation of a copper carbonate film. In both these cases the measured resistances were considerably higher than those predicted from Eq. [13]. Furthermore, successive galvanostatic double pulses in these electrolytes without resurfacing the electrode between measurements gave ohmic resistances which increased with the number of pulses, showing that film thickening occurred. Whether this increased resistance is due to the film lattice itself or to the electrolyte resistance within pores in the film is not known. Clearly, however, a working electrode which does not produce salt films in carbonate electrolytes, such as Pt or Au, could be used to determine the ohmic resistances of these solutions.

It is clear from Eq. [13] (and Eq. [14]) that for a rectangular scratch in a rotating disk electrode the minimum ohmic potential drop across the electrolyte is achieved when the scratch length and width are both minimum, since the total current  $I (= vwi)$  decreases more rapidly with decrease in scratch area than does  $R$ , and thus the product  $IR$  also decreases. Practical limitations on the scratch area, however, arise from the ability to detect very small current transients arising from very small scratches. The technique which has been employed in recent experiments to scratch rotating disk electrodes (6-10) used a diamond stylus assembly which was allowed to fall under its own inertia onto the disk creating a long ( $\sim 2 \text{ mm}$ ), narrow ( $\sim 40 \mu\text{m}$ ) scratch at a distance of  $\sim 2 \text{ mm}$  from the center of the disk, at a rate determined by the electrode rotation rate. This has simplified the calculation by imposing the inequality  $b \gg a$  (see above). It also ensures that the scratch is of constant width, thereby approximating rectangularity. The ends of the scratch, which are the contact-making and contact-breaking regions, are tapered: Under the above conditions they comprise only  $\sim 5\%$  of the total scratch area. As  $b$  approaches  $a$ , not only must Eq. [13] be used in its full form, but the scratch ceases to be approximately rectangular, and the equation becomes inaccurate. Thus a long narrow scratch, of sufficiently large area to provide a detectable current transient, provides the most quantifiable reaction

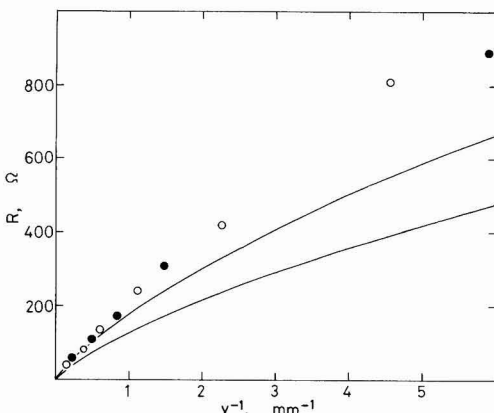


Fig. 7. Measured resistance as a function of electrode length (for  $w = 39 \mu\text{m}$ ) for carbonate electrolytes.  $\circ$ , upper line: 0.5M  $\text{K}_2\text{CO}_3$ , 0.5M  $\text{NaHCO}_3$ ,  $\sigma = 8.2 \Omega^{-1} \text{ m}^{-1}$ .  $\bullet$ , lower line: 1M  $\text{K}_2\text{CO}_3$ ,  $\sigma = 11.4 \Omega^{-1} \text{ m}^{-1}$ . The lines shown are calculated from Eq. [13].

parameters of the freshly generated metal surface. The model described above also assumes that the scratch has no depth. For the experiments described (6-10) the scratch depth of  $\sim 3 \mu\text{m}$  was small compared with the width, and was thus negligible.

Doig and Flewitt (11) have criticized the scratched electrode technique using calculations made for the ohmic potential drop to a scratch in a metal surface under open-circuit conditions. In that case the current from the scratch as anode flows to the unscratched area of the same specimen acting as cathode. It is fallacious to apply that calculation directly to a potentiostatically controlled scratched disk, however, since the current now flows to a counterelectrode and not to other parts of the working electrode. That this is so is demonstrated by the ability to record a current transient: if all the current from the scratch flowed to other parts of the working electrode no transient would be detectable. Doig and Flewitt showed that for a scratch current density of  $0.3 \text{ A cm}^{-2}$  flowing from a scratch  $10 \mu\text{m}$  wide to the surrounding unscratched metal surface in a solution of conductivity  $10 \Omega^{-1} \text{ m}^{-1}$  the ohmic potential drop could be as high as 500 mV. However, under the potentiostatic conditions actually used in these experiments, and with a scratch length of 2 mm, Eq. [13] gives the ohmic potential drop as only 6 mV.

#### Acknowledgment

We are grateful to the British Petroleum Company for the financial support of R.C.N.

Manuscript submitted Aug. 29, 1980; revised manuscript received March 28, 1981.

Any discussion of this paper will appear in a Discussion Section to be published in the June 1982 JOURNAL. All discussions for the June 1982 Discussion Section should be submitted by Feb. 1, 1982.

#### APPENDIX

##### A. Disk Working Electrode with Plane Counterelectrode of Infinite Size

The problem to be solved is

$$\nabla^2 \phi = 0 \quad [\text{A-1}]$$

$$\phi = 0 \quad \text{for } z = 0 \quad [\text{A-2}]$$

$$\left. \frac{\partial \phi}{\partial z} \right|_d = \frac{1}{\sigma} f(r) \quad \text{for } r < a \quad [\text{A-3}]$$

$$= 0 \quad \text{for } r > a$$

In cylindrical polar coordinates  $(r, \theta, z)$  we have axial symmetry and may take

$$\phi = \int_0^\infty A(k) J_0(kr) \sinh(kz) dk \quad [\text{A-4}]$$

where  $J_0$  is the zero order Bessel function of the first kind. This form of  $\phi$  satisfies [A-1] and [A-2]; the transform  $A(k)$  is determined by [A-3] through the relation

$$\left. \frac{\partial \phi}{\partial z} \right|_d = \int_0^\infty k A(k) J_0(kr) \cosh(kd) dk$$

Inverting this expression gives

$$\sigma \cosh(kd) \cdot A(k) = \int_0^a r f(r) J_0(kr) dr$$

which is then substituted in [A-4] to give an expression for  $\phi$ .

(a) For

$$f(r) = a i_0 (a^2 - r^2)^{-1/2}$$

then

$$\sigma A(k) = \frac{a i_0}{\cosh(kd)} \frac{\sin(ak)}{k}$$

thus

$$\sigma \phi(r, d) = i_0 a \int_0^\infty \frac{\sin(ak)}{k} J_0(kr) \tanh(kd) dk$$

In order to find the ohmic drop we evaluate  $V/I$ , where  $V$  is the potential at the disk electrode, given by  $\phi(O, d)$  and  $I$  is the total current flowing. The latter is given by

$$I = \int_0^a 2\pi r f(r) dr = 2\pi a^2 i_0$$

Evaluating  $V$  we have

$$\sigma \phi(O, d) = i_0 a \int_0^\infty \frac{\sin(ak)}{k} \tanh(kd) dk \quad [\text{A-5}]$$

For  $d \gg a$ , that is to say, the counterelectrode many disk radii away from the working electrode,  $\tanh(kd)$  differs from unity, while  $(\sin(ak))/k$  is given to a good approximation by the constant value  $a$ . So we may write [A-5] as

$$\begin{aligned} \sigma \phi(O, d) &= i_0 a \int_0^\infty \frac{\sin(ak)}{k} dk \\ &- i_0 \int_0^\infty a^2 (1 - \tanh(kd)) dk + i_0 a O\left(\frac{a}{d}\right)^3 \\ &= i_0 a \left[ \frac{\pi}{2} - \ln \frac{2a}{d} + O\left(\frac{a}{d}\right)^3 \right] \\ R &= \frac{V}{I} \approx \frac{1}{4a\sigma} \left[ 1 - \frac{2 \ln 2}{\pi} \left(\frac{a}{d}\right) \right] \end{aligned}$$

and the correction for the finite counterelectrode distance to the Newman result (13)

$$R = (4a\sigma)^{-1}$$

is of the order  $a/d$  ( $\ll 1$ ) as might be expected.  $O(a/d)^3$  represents all terms of order  $(a/d)^3$ .

(b) For  $f(r) = i_0$

by similar arguments to above

$$\begin{aligned} \sigma \phi(O, d) &= a i_0 \int_0^\infty \frac{J_1(ak)}{k} \tanh(kd) dk \\ &\approx a i_0 \left( 1 - \ln \frac{2a}{d} \right) \end{aligned}$$

and so

$$R_0 = \frac{1}{\pi a \sigma} \left( 1 - \ln \frac{2a}{d} \right)$$

Also

$$\sigma \phi(a, d) = \frac{2a i_0}{\pi} \left( 1 - \ln \frac{2a}{d} \right)$$

whence

$$R_a = \frac{2}{\pi^2 a \sigma} \left( 1 - \ln \frac{2a}{d} \right)$$

##### B. Disk Working Electrode with Plane Counterelectrode of Finite Size

The problem to be solved is

$$\nabla^2 \phi = 0 \quad [\text{B-1}]$$

$$\left. \frac{\partial \phi}{\partial z} \right|_d = \frac{1}{\sigma} f_1(r) \quad \text{at } z = d \quad [\text{B-2}]$$

$$= \frac{1}{\sigma} f_2(r) \quad \text{at } z = 0$$

$$\left. \frac{\partial \phi}{\partial r} \right|_0 = 0 \quad \text{at } r = c \quad [\text{B-3}]$$

A suitable representation of  $\phi$  satisfying [B-1] and [B-3] is

$$\sigma \phi = A_0 z + \sum_{n=1}^{\infty} \left[ A_n \exp\left(-\frac{\lambda_n z}{c}\right) \right]$$

$$+ B_n \exp\left(\frac{\lambda_n z}{c}\right) \left] J_0\left(\frac{\lambda_n r}{c}\right) \quad [\text{B-4}] \right.$$

where the  $\lambda_n$ 's are the positive roots of  $J_1(\lambda_n) = 0$ . We take

$$\begin{aligned} f_1(r) &= i_0 a (a^2 - r^2)^{-1/2} & \text{for } r < a \\ &= 0 & \text{for } c > r > a \\ f_2(r) &= i_0 a^2 p^{-1} (p^2 - r^2)^{-1/2} & \text{for } r < p \\ &= 0 & \text{for } c > r > p \end{aligned}$$

Then, as in Appendix A

$$\begin{aligned} \sigma A_0 &= \frac{2a^2 i_0}{c^2} \\ \sigma A_n &= \frac{2i_0}{\lambda_n^2 J_0^2(\lambda_n)} \\ &\quad \frac{\frac{a^2}{pc} \sin\left(\frac{\lambda_n p}{c}\right) \exp\left(-\frac{\lambda_n d}{c}\right) - \frac{a}{c} \sin\left(\frac{\lambda_n a}{c}\right)}{1 - \exp\left(-\frac{2\lambda_n d}{c}\right)} \\ \sigma B_n &= \frac{2i_0}{\lambda_n^2 J_0^2(\lambda_n)} \\ &\quad \frac{\frac{a^2}{pc} \sin\left(\frac{\lambda_n p}{c}\right) \exp\left(\frac{\lambda_n d}{c}\right) - \frac{a}{c} \sin\left(\frac{\lambda_n a}{c}\right)}{\exp\left(\frac{2\lambda_n d}{c}\right) - 1} \end{aligned}$$

for  $n = 1, 2, 3, \dots$

If  $d/c > 1$  and  $a/p$  is not too small, then the first term in the expansion for  $A_n$  and the second term in the expansion for  $B_n$  are both small and may be ignored, giving

$$\begin{aligned} R &= \frac{\phi(d, 0) - \phi(0, 0)}{I} = \frac{d}{\pi \sigma c^2} \\ &+ \frac{1}{\pi \sigma} \sum_{n=1}^{\infty} \frac{1}{\lambda_n^2 J_0^2(\lambda_n)} \left[ \frac{\sin\left(\frac{\lambda_n a}{c}\right)}{a} + \frac{\sin\left(\frac{\lambda_n p}{c}\right)}{p} \right] \end{aligned}$$

#### C. Rectangular Strip Working Electrode and Plane Counterelectrode

The problem to be solved is

$$\nabla^2 \phi = 0 \quad [\text{C-1}]$$

$$\phi = 0 \quad \text{at } z = 0 \quad [\text{C-2}]$$

$$\frac{\partial \phi}{\partial z} = \frac{1}{\sigma} f(x, y) \quad \text{at } z = d \quad [\text{C-3}]$$

The rectangular strip is given by  $|x| \leq a$ ,  $|y| \leq b$ ;  $f(x, y) = 0$  outside these limits.

The solution is found in terms of a double Fourier transform in  $x$  and  $y$

$$\begin{aligned} \sigma \phi &= \frac{1}{4\pi} \int_{-\infty}^{\infty} \int_{-\infty}^{\infty} A_1(k_1) A_2(k_2) \exp i(k_1 x + k_2 y) \\ &\quad \sinh(kz) dk_1 dk_2 \end{aligned}$$

where

$$k^2 = k_1^2 + k_2^2$$

This form satisfies [C-1], [C-2], and [C-3] and yields

$$\begin{aligned} f(x, y) &= \frac{1}{4\pi^2} \int_{-\infty}^{\infty} \int_{-\infty}^{\infty} \exp i(k_1 x + k_2 y) \\ &\quad A_1(k_1) A_2(k_2) k \cosh(kd) dk_1 dk_2 \quad [\text{C-4}] \end{aligned}$$

(a) Suppose the current density on the rectangular strip is constant,  $i_0$

$$I = 4abi_0$$

Inverting [C-4] gives

$$A_1(k_1) A_2(k_2) k \cosh(kd)$$

$$= i_0 \int_{-a}^a \int_{-b}^b \exp -i(k_1 x + k_2 y) dx dy$$

$$= 4i_0 \frac{\sin(k_1 a)}{k_1} \frac{\sin(k_2 b)}{k_2}$$

Therefore

$$\sigma \phi(0, 0, d)$$

$$= \frac{i_0}{\pi^2} \int_{-\infty}^{\infty} \int_{-\infty}^{\infty} \frac{\sin(k_1 a)}{k_1} \frac{\sin(k_2 b)}{k_2} \frac{\tanh(kd)}{k} dk_1 dk_2$$

To evaluate this integral we transform to polar coordinates:  $k_1 = k \sin \theta$ ,  $k_2 = k \cos \theta$ ,  $dk_1 dk_2 = k dk d\theta$ , and note that only a very small error is made by putting  $\tanh(kd) = 1$ . Then

$$\sigma \phi(0, 0, d)$$

$$= \frac{4i_0}{\pi^2} \int_0^{\pi/2} \int_0^{\infty} \frac{\sin(ak \sin \theta) \sin(bk \cos \theta)}{k^2 \cos \theta \sin \theta} dk d\theta$$

The  $k$  integration gives

$$\begin{aligned} \frac{\pi b}{2 \sin \theta} & \quad a \sin \theta > b \cos \theta \\ \frac{\pi a}{2 \cos \theta} & \quad a \sin \theta < b \cos \theta \end{aligned}$$

leading to a final answer of

$$\sigma \phi(0, 0, d) \approx \frac{\pi}{2} a i_0 \left[ \ln \left( \frac{2b}{a} \right) + 1 \right]$$

for a long thin strip, where  $b \gg a$ . This gives

$$R = \frac{1}{2\pi \sigma b} \left[ \ln \left( \frac{2b}{a} \right) + 1 \right]$$

(b) For the more realistic current distribution

$$f(x, y) = a i_0 (a^2 - x^2)^{-1/2}, \quad |x| < a, \quad |y| < b$$

the calculation is similar, with  $(\sin(k_1 a))/k_1$  replaced by  $J_0(ak_1)$ . The final result for this case is

$$R = \frac{1}{2\pi \sigma b} \ln \left\{ 2 \left[ \left( 1 + \frac{b^2}{a^2} \right)^{1/2} + \frac{b}{a} \right] \right\}$$

for  $d \gg b > a$ .

#### LIST OF SYMBOLS

$a$	radius of disk-shaped working electrode; half-width of strip working electrode
$A(k)$	transform of potential
$A_n$	coefficient in expansion for potential
$b$	half-length of strip working electrode
$B_n$	coefficient in expansion for potential
$c$	radius of cylindrical cell
$d$	distance between working and counterelectrodes
$E$	electrode potential
$i$	current density
$I$	current
$J_0$	zero order Bessel function
$J_1$	first order Bessel function
$k$	wave number
$O$	terms of order ...
$p$	radius of counterelectrode
$r$	polar coordinate
$R$	resistance
$v$	length of strip working electrode
$V$	potential difference
$w$	width of strip working electrode
$x$	cartesian coordinate
$y$	cartesian coordinate
$z$	polar, cartesian coordinate
$\ln(2/\pi)$	
$\beta$	
$\theta$	polar coordinate
$\lambda_n$	positive roots of equation $J_1(\lambda_n) = 0$
$\sigma$	electrolyte conductivity
$\phi$	potential

## REFERENCES

1. E. Kunze and K. Schwabe, *Corros. Sci.*, **4**, 109 (1964).
2. T. Hagyard and W. B. Earl, *This Journal*, **114**, 694 (1967).
3. N. D. Tomashov and L. P. Vershinina, *Electrochim. Acta*, **15**, 501 (1970).
4. T. R. Beck, *ibid.*, **18**, 807 (1973).
5. T. R. Beck, *ibid.*, **18**, 815 (1973).
6. F. P. Ford, G. T. Burstein, and T. P. Hoar, *This Journal*, **127**, 1325 (1980).
7. G. T. Burstein and R. C. Newman, *Electrochim. Acta*, **25**, 1009 (1980).
8. G. T. Burstein and D. H. Davies, *Corros. Sci.*, **20**, 1143 (1980).
9. R. C. Newman and G. T. Burstein, *ibid.*, **21**, 119 (1981).
10. G. T. Burstein and D. H. Davies, *This Journal*, **128**, 33 (1981).
11. P. Doig and P. E. J. Flewitt, *Philos. Mag.*, **38**, 27 (1978).
12. P. H. Melville, *This Journal*, **126**, 2081 (1979).
13. J. Newman, *ibid.*, **113**, 501 (1966).

## Conductivity of Beta-Alumina Highly Doped with Iron

John H. Kennedy and Susan M. Stuber

Department of Chemistry, University of California, Santa Barbara, California 93106

### ABSTRACT

Complex plane impedance diagrams were used to determine the ionic conductivity of Fe-doped  $\beta$ -alumina over the composition range  $\text{Na}_{1.3}\text{Al}_{3.86}\text{Fe}_{1.14}\text{O}_{17.15}$  (10% Fe by weight) to  $\text{Na}_{1.3}\text{Al}_{7.18}\text{Fe}_{3.82}\text{O}_{17.15}$  (30% Fe by weight). The influence of starting material [ $\text{Fe}_2\text{O}_3$ ,  $\text{Fe}_2(\text{C}_2\text{O}_4)_3 \cdot 6\text{H}_2\text{O}$ ,  $\text{Fe}(\text{C}_2\text{O}_4) \cdot 2\text{H}_2\text{O}$ ,  $\text{Fe}(\text{NO}_3)_3 \cdot 9\text{H}_2\text{O}$ ] upon grain boundary and bulk properties was studied. The ionic conductivity of all doped materials increased over that of undoped  $\beta$ -alumina. The best materials obtained resulted from doping with  $\text{Fe}(\text{C}_2\text{O}_4) \cdot 2\text{H}_2\text{O}$ . At the 10% doping level, bulk conductivity reached a maximum coinciding with a minimum in activation energy. Electronic conductivity was investigated by a "floating" blocking technique. The electronic conductivity was small at the 15% dopant level, representing  $<10^{-3}\%$  of the total conductivity, but increased rapidly and at the 30% dopant level was  $\sim 0.1\%$  of the total conductivity. Preliminary Mössbauer studies showed a steady increase in the Fe(III)/Fe(II) ratio as dopant levels increased.

A previous study of  $\beta$ -alumina doped with small amounts of iron [ca. 2 weight percent (w/o)] investigated the oxidation states and site symmetry of the iron dopant and concluded that both Fe(II) and Fe(III) were present after air sintering (1). Conductivity results for iron-doped  $\beta$ -alumina containing up to 8 w/o Fe showed an increase in bulk conductivity up to 4 w/o Fe while 8 w/o material was of lower density and conductivity when the same sintering conditions were used (2). It becomes apparent that sintering conditions must be adjusted as the dopant level changes in order to achieve the maximum density and conductivity particularly when higher doping levels are attempted.

In the present study iron doping of 10-30 w/o has been carried out, and changes in bulk and grain boundary conductivity are reported. The influence of starting material and sintering conditions on the properties of the sintered pellets has also been studied. It was anticipated that high doping levels of iron in  $\beta$ -alumina could be attained because  $\text{Fe}_2\text{O}_3$  and  $\text{Al}_2\text{O}_3$  form solid solutions across the whole composition range and  $\beta$ -alumina analogs of the type  $\text{MFe}_{11}\text{O}_{17}$  are also known (3, 4).

### Experimental

Sodium  $\beta$ -alumina (Alcoa XB-2 "Superground") was doped with iron using Fe(III) nitrate,  $\text{Fe}_2\text{O}_3$ , Fe(II) oxalate, and Fe(III) oxalate as starting materials. In some of the samples investigated,  $\text{Na}_2\text{CO}_3$  was added as a starting material in order to see the influence on the final  $\text{Na}^+$  concentration. The presence of  $\text{Na}_2\text{CO}_3$  seemed to have no effect on the outcome. However, the important factor for maintaining sample control with regard to  $\text{Na}^+$  concentration in-

volved a fresh packing of coarse  $\beta$ -alumina powder surrounding the pellets. All samples were packed in 300 mesh  $\beta$ -alumina during sintering. Details of the doping and firing procedures have been published previously (1).

Pellets of approximately 1.27 cm diam and 0.2 cm thickness were isostatically pressed and then sintered. Sintering time and temperature necessary to yield highest density material (typically 3.15-3.25 g/cm<sup>3</sup>) were determined for each iron concentration. Material of the highest density invariably also exhibited the highest conductivity. In general, 0-10 w/o Fe material could be sintered at 1600°C for 3 hr while 15-25 w/o Fe was sintered at 1540°C for 3 hr. Recent measurements with more highly doped iron (>25%) indicate that sintering temperature must be decreased to about 1500°C to achieve optimum results. When pellets are fired at too high a temperature they shrink to a small diameter but are porous and are of low density, mechanical strength, and conductivity. All samples were fired in air.

The sintered disks were prepared for electrode deposition by polishing with successively finer grades of silicon carbide paper. Finishing was accomplished by polishing with 9, 6, and 3  $\mu\text{m}$  diamond impregnated lapping wheels. The polishing solvent was ethanol. The polished samples were then ultrasonically cleaned in acetone. The disks were then heated at 300°C for 24 hr before electrodes were applied.

Electrodes were deposited on the disks by a Technics, Incorporated Hummer Sputtering and Deposition instrument using a gold target. The electrodes were nominally 2.5  $\mu\text{m}$  thick.

Complex impedance/admittance diagrams were recorded between 25° and 325°C by placing the sample in a furnace which was inside a helium-filled glove box (Overly P-100). Accurate temperature control

Key words: complex plane analysis, Fe-beta-alumina, solid electrolyte.



was achieved by a digital setting Eurotherm controller. Measurements from  $10^{-4}$  to  $10^{+6}$  Hz were made using a Schlumberger-Solartron 1174 Frequency Response Analyzer interfaced to a Hewlett-Packard 9845-S desktop computer. Most often impedance measurements were taken directly and inversion of the data to the admittance mode, if desired, was part of the 9845 program. The computer was programmed to accept measurements from the frequency response analyzer in the a,b (cartesian coordinates) mode and generally 16 data points per decade of frequency were taken, although this feature was programmable. In addition to tabulating the results, the program output was in the form of a complex plane plot which could then be fit to a series of semicircles and straight lines by curve fitting routines (5). An example is shown in Fig. 1.

A correction program was incorporated to compensate for inductive and capacitive effects observed at high frequency ( $10^5$ - $10^6$  Hz). The signal across the sample was normally 100 mV but other signals may be selected as part of the computer program.

X-ray diffraction patterns were obtained using a diffractometer to determine percentage of  $\beta'$ -alumina present.

Sodium analysis was accomplished by dissolving the samples in boiling, concentrated phosphoric acid and analyzing the solution by atomic absorption. Exchangeable sodium was also determined by ion exchanging the samples with molten  $\text{AgNO}_3$  and measuring the mass change (2).

## Results

An equivalent circuit which approximates polycrystalline  $\beta$ -alumina has been reported (2, 6) which allows the calculation of bulk and grain boundary effects from complex plane diagrams. Values reported here were determined using the techniques reported previously (2) plus computer program curve-fitting routines developed since the previous study (5).

The conductivity in all doped samples increased compared to undoped  $\beta$ -alumina. However, differences were observed depending on the starting material used for doping. Densities, sodium content, conductivities, and activation energies were all sensitive to the starting composition. Because firing resulted in decomposition of all starting materials to the oxide form but the observed final Fe(II/III) ratio was dependent on firing conditions, these differences were attributed to differences in particle size and attainment of homogeneity. In general it was found that doping with Fe(II) oxalate gave pellets with the highest density and conductivity at each doping level investigated. Therefore, results with this particular dopant starting material will be emphasized. Results are shown in Table I for all Fe(II) oxalate compositions. In addition, other materials with data of particular interest discussed in the text are also presented.

A maximum bulk conductivity,  $\sigma_b$ , was observed at ~10 w/o Fe followed by a steady decrease in the conductivity values up to the highest levels investigated to date (30 w/o). At the same time the activation energy for bulk conductivity was a minimum at the 10 w/o doping level. These trends can be seen in Fig. 2 and Fig. 3. At first it was thought that the decrease in conductivity reflected less-than-optimum sintering conditions as was experienced for early work with 8 w/o iron doped  $\beta$ -alumina (2). However, densities near theoretical were obtained for several samples and all attempts to improve the density and conductivity over those shown in Table I have failed.

Table I. Properties of Fe-doped  $\beta$ -alumina

Nominal composition dopant	Nominal formula (iron as +3)	Density (g/cm <sup>3</sup> )	% Na		$\beta$ : $\beta'$ (%)	Fe(III) Fe(II)	$\sigma_b \times 10^{-3}$ ( $\Omega \text{ cm}$ ) <sup>-1</sup>	$\sigma_b \times 10^{-3}$ ( $\Omega \text{ cm}$ ) <sup>-1</sup>	$\sigma_b \times 10^{-3}$ ( $\Omega \text{ cm}$ ) <sup>-1</sup>	$E_a$ (bulk) (kcal/mol)	$E_a(\text{tot})$ (kcal/mol)	$\sigma$ electronic ( $\Omega \text{ cm}$ ) <sup>-1</sup>
			AA	Ag exch.								
20% Fe(II) oxalate	$\text{Na}_{0.2}\text{Al}_{0.8}\text{Fe}_{0.2}\text{O}_{17.15}$	3.05	6.76	4.57	99%:1%	4	$6.71 \times 10^{-3}$	$7.76 \times 10^{-3}$	$3.38 \times 10^{-3}$	3.02	6.44	$1.1 \times 10^{-8}$
20% Fe(III) oxalate	$\text{Na}_{0.2}\text{Al}_{0.8}\text{Fe}_{0.2}\text{O}_{17.15}$	2.92	5.21				$1.78 \times 10^{-3}$	$4.71 \times 10^{-3}$	$1.01 \times 10^{-3}$	4.047	4.77	
25% Fe(II) oxalate	$\text{Na}_{0.2}\text{Al}_{0.75}\text{Fe}_{0.25}\text{O}_{17.15}$	2.96	4.16	5.3	98%:2%	7	$0.85 \times 10^{-3}$	$4.8 \times 10^{-3}$	$2.23 \times 10^{-3}$	3.32	6.65	
25% FeO <sub>3</sub>	$\text{Na}_{0.2}\text{Al}_{0.75}\text{Fe}_{0.25}\text{O}_{17.15}$	2.72	6.17				$0.88 \times 10^{-3}$	$3.7 \times 10^{-3}$	$2.23 \times 10^{-3}$	7.46	9.43	$(1.25 \times 10^{-8} \text{ of total})$
30% Fe(II) oxalate	$\text{Na}_{0.2}\text{Al}_{0.7}\text{Fe}_{0.3}\text{O}_{17.15}$	3.29			80%:20%		$3.3 \times 10^{-6} (?)$	$8.2 \times 10^{-3}$	$8.4 \times 10^{-3}$	3.97	8.34	$3 \times 10^{-8} \text{ of total}$
30% FeO <sub>3</sub>	$\text{Na}_{0.2}\text{Al}_{0.7}\text{Fe}_{0.3}\text{O}_{17.15}$	3.27					$2.17 \times 10^{-3}$	$3.7 \times 10^{-3}$	$2.54 \times 10^{-3}$	5.32	5.64	$1.07 \times 10^{-8} \text{ of total}$ (0.047% of total)

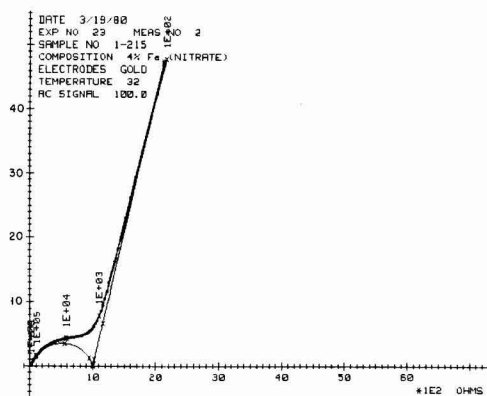


Fig. 1. Impedance diagram showing experimental data and mathematical fitting into semicircle and straight line components.

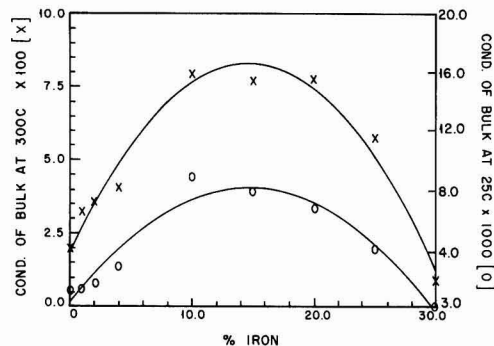


Fig. 2. Bulk conductivity at 25° and 300°C as a function of iron content.

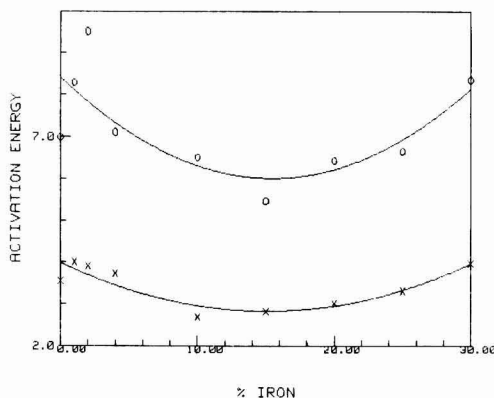


Fig. 3. Activation energy of bulk (X) and grain boundary (O) as a function of iron content.

The grain boundary conductivity also reached a maximum in the same doping region as the bulk conductivity but the actual peak value was observed at 15 w/o Fe as shown in Table I and Fig. 4. The activation energy showed the same small trend toward lower values in the 10-20 w/o doping region as did the activation energy for bulk conductivity.

Grain boundary contribution to the total resistance of a sample at 300°C was so small that measured

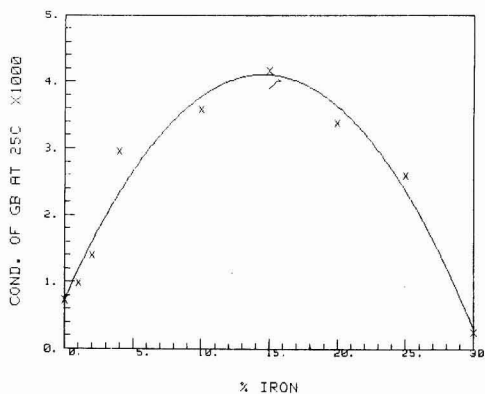


Fig. 4. Grain boundary conductivity at 25°C as a function of iron content.

values are not very meaningful. The cross-over temperature above which bulk resistance was the dominant factor occurred a little above room temperature (<80°C for most materials). Below this temperature grain boundary resistance was greater than the bulk resistance.

Admittance diagrams in the  $10^{-2}$ - $10^{-4}$  Hz frequency range gave no evidence for the existence of any appreciable electronic conductivity, i.e., the lowest frequency semicircle had a real-axis intercept of zero mhos (infinite resistance) within experimental accuracy (Fig. 5). This conclusion was supported by d-c measurements with gold blocking electrodes (Fe-doped  $\beta$ -alumina is not stable in the presence of sodium so that the traditional Wagner blocking technique was not possible). A reasonably stable steady-state current was reached after 1-2 days at each applied voltage, and a plot of current vs. applied voltage is shown in Fig. 6. The slope of the line indicated a resistance of  $2.3 \times 10^6 \Omega$  which translated to a conductivity value of  $1.2 \times 10^{-7} (\Omega\text{-cm})^{-1}$  for 15% Fe-doped  $\beta$ -alumina. Since true equilibrium may not have been reached, this probably represents a maximum value for electronic conductivity in this "floating" system (i.e., no reference potential as in a Wagner blocking technique). The bulk conductivity for this material was  $7.9 \times 10^{-3} (\Omega\text{-cm})^{-1}$  at 25°C so that electronic conductivity contributed <10<sup>-3</sup>% of the total conductivity. As can be seen from Table I the

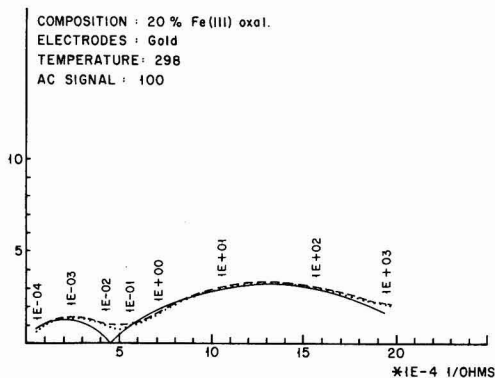


Fig. 5. Admittance diagram for 20% Fe in  $\beta$ -alumina doped from Fe(III) oxalate. Low frequency intercept of zero (within experimental uncertainty) gives no evidence for electron hopping.

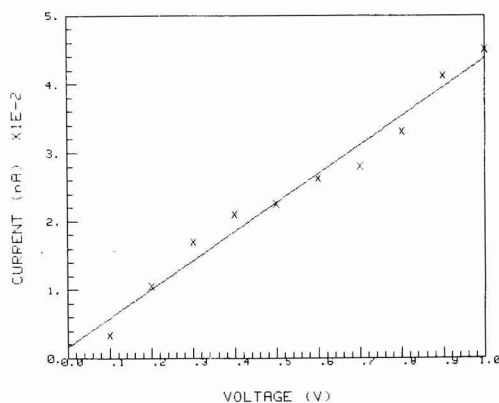


Fig. 6. Plot of current vs. applied voltage for 15% Fe in  $\beta$ -alumina doped from Fe(II) oxalate.

percentage electronic conductivity increased rapidly to nearly 0.1% when the iron content reached 30%. Roland reported (7,8) that electronic conductivity in iron-doped  $\beta$ -alumina was significant at these doping levels and projected that at 53 w/o Fe electronic conductivity would equal ionic conductivity. Results from this study show that the percentage electronic conductivity does increase with increasing Fe content but the point at which  $t_i = t_e$  would not be reached until at least 60 w/o Fe were present assuming the observed trend continued. This point will be discussed further later on.

A critical factor in the electrochemical properties of iron-doped  $\beta$ -alumina is the Fe(III)/Fe(II) ratio. It is well known that metal ions in the plus two oxidation state tend to increase the conductivity of  $\beta$ -alumina, probably by incorporating more conductive  $\text{Na}^+$  and/or by decreasing the concentration of  $\text{O}^{2-}$  interstitials needed for charge compensation. A Mössbauer study of low iron doping showed the existence of both Fe(II) and Fe(III) in nearly equal proportions (1). A more accurate calculation based on peak areas attributable to Fe(II) and Fe(III) shows that the Fe(III)/Fe(II) ratio was about 1.7 at the 2.95 w/o doping level. Higher doping levels also showed the existence of Fe(II), but preliminary results indicated that the Fe(III)/Fe(II) ratio increased to 4 at 20 w/o Fe and to 7 at 25 w/o Fe. Details of the Mössbauer study will be published later. Similar results showing an increase in the Fe(III)/Fe(II) ratio at higher doping levels were also reported by Burzo and Ardelean in their work with iron-doped glasses (9).

Another factor which was considered to play a role in the electrochemical properties of Fe- $\beta$ -alumina was the possible presence of  $\beta''$ -alumina. Low doping levels of Fe reported previously showed only single phase  $\beta$ -alumina (1,2). However,  $\text{Mg}^{2+}$  stabilizes the  $\beta''$ -form and perhaps other  $\text{M}^{2+}$  ions could play the stabilizing role to produce compositions of the type  $\text{Na}_{2-x}\text{M}_{1-x}\text{Al}_{10+x}\text{O}_{17}$ . X-ray diffraction patterns of  $\beta$ -alumina doped with at least 10 w/o Fe generally indicated the presence of the  $\beta''$ -phase. The amount of  $\beta''$ -phase remained small even at high doping levels which may be a result of the small amount of Fe(II) in highly doped Fe- $\beta$ -alumina. Amounts of  $\beta''$ -phase estimated from diffraction line intensities are given in Table I. The technique for estimating  $\beta/\beta''$  involved comparing diffractometer peak heights for the following  $d$ -spacings:  $d = 2.039$  and  $d = 1.939$  for  $\beta$  compared to  $d = 1.978$  for  $\beta''$ ;  $d = 2.687$  and  $d = 2.514$  for  $\beta$  compared to  $d = 2.605$  for  $\beta''$ . The peak heights were normalized to the peak heights reported for pure  $\beta$

and  $\beta''$ -alumina. It should be noted that the material showing the highest bulk conductivity [10 w/o from iron(II) oxalate] also contained the highest concentration of  $\beta''$ -alumina.

### Discussion

Previous work involving M(II) doping showed that conductivity increases correlated well with M(II) content and also with sodium content (2). One possible charge compensation mechanism involves replacement of an Al(III) by an M(II) in the spinel block with incorporation of an additional sodium ion in the conduction plane. When  $\beta$ -alumina is doped with iron, some of the iron is present as Fe(II) and, therefore, this mechanism would be possible. However, unlike other plus two metal dopants such as Mn, Co, and Ni, the sodium content did not continue to increase as the dopant level increased (2). In Table I it can be seen that with higher doping levels the sodium content did not correlate well with doping level and, if anything, was no higher than undoped  $\beta$ -alumina.

These results are not unexpected when one considers the Mössbauer results. As the dopant level increased the percentage Fe(II) decreased so rapidly that the concentration of Fe(II) in 25 w/o Fe was less than in 20 w/o Fe (3 vs. 4%). The maximum concentration of Fe(II) probably occurred in the 10-20 w/o region which correlates well with conductivity.

Another charge compensation mechanism involves a decrease in blocking oxide interstitials as the M(II) concentration increases. One would predict a decrease in activation energy for this mechanism and no necessary change in sodium content. As can be seen in Fig. 3, the lowest activation energies were observed with 10-20 w/o Fe, but, if anything, a slight increase at low doping levels compared to undoped  $\beta$ -alumina [data taken from Ref. (2)]. Thus, it appears that at low doping levels (<5 w/o Fe) a significant amount of Fe(II) is present which incorporates additional sodium ions resulting in an increase in bulk conductivity. At higher doping levels the amount of Fe(II) reaches a maximum in the 10-20 w/o region and this doping is at least partially charge compensated by a decrease in oxide interstitials leading to a lower activation energy. At doping levels >20 w/o Fe the amount of Fe(II) drops, and the conductivity begins to fall as the activation energy begins to increase.

This simple picture is clouded by the presence of  $\beta''$ -phase. One would expect a higher conductivity for  $\beta''$ -form compared to  $\beta$ , and this may account for some of the increased conductivity in the 10-20 w/o region. However,  $\beta''$ -phase was also found in the 30 w/o material so that the previous argument involving Fe(II) concentrations probably predominates.

The increasing electronic conductivity at high doping levels most likely reflects the shorter average distance between iron atoms. If an electron hopping mechanism exists it would be necessary to maintain a significant amount of Fe(II) in the structure at high doping levels. It was shown in a previous study (1) that Fe(III) may be reduced to Fe(II) in  $\beta$ -alumina by treatment with 90%  $\text{N}_2$ /10%  $\text{H}_2$  at 1200°C. An increase in the Fe(II) content at high doping levels may result in a substantial increase in electronic conductivity making these materials potentially valuable mixed conductors. The Fe(II)/Fe(II) ratio is most probably a sensitive function of sintering temperature and sintering atmosphere and this fact could explain the higher electronic conductivity values reported by Roland (7,8). However, no information on the Fe(III)/Fe(II) ratio is available for his materials. At present we are continuing these studies of  $\beta$ -alumina highly doped with iron to investigate the possibility of increasing the electronic conductivity (and possibly the ionic conductivity as well) by increasing the amount of Fe(II).

## Acknowledgment

The authors acknowledge financial support of this project by the National Science Foundation, Grants DMR 77-24562 and DMR 8002676. The authors also thank Professor Paul Barrett of the Physics Department for the use of his Mössbauer equipment and helpful discussions.

Manuscript submitted Aug. 4, 1980; revised manuscript received ca. April 3, 1981.

Any discussion of this paper will appear in a Discussion Section to be published in the June 1982 JOURNAL. All discussions for the June 1982 Discussion Section should be submitted by Feb. 1, 1982.

Publication costs of this article were assisted by the University of California.

## REFERENCES

1. J. R. Akridge, B. Srouf, C. Meyer, Y. Gros, and J. H. Kennedy, *J. Solid State Chem.*, **25**, 169 (1978).
2. J. H. Kennedy, J. R. Akridge, and M. Kleitz, *Electrochim. Acta*, **24**, 781 (1979).
3. A. T. Howe and G. J. Dudley, *J. Solid State Chem.*, **30**, 157 (1979).
4. T. Takahashi and K. Kuwabara, *ibid.*, **29**, 27 (1979).
5. M. Kleitz and J. H. Kennedy, "Proceedings of Fast Ion Transport in Solids, P. Vashishta, J. N. Mundy, and G. K. Shenoy, Editors, pp. 185-188, Elsevier-North Holland, Inc., New York (1979).
6. A. Hooper, *J. Phys. D. Appl. Phys.*, **10**, 1487 (1977).
7. J. P. Roland, Ph.D. Thesis, Purdue University (1978).
8. J. P. Roland, T. Y. Tseng, and R. W. Vest, *J. Am. Ceram. Soc.*, **62**, 567 (1979).
9. E. Burzo and I. Ardelean, *Mater. Res. Bull.*, **14**, 1425 (1979).

## Effects of Cadmium Impurities on the Electrowinning of Zinc

F. R. Foulkes,\* J. W. Smith, R. Kalia, and D. W. Kirk\*

Department of Chemical Engineering and Applied Chemistry,  
University of Toronto, Toronto, Ontario, Canada M5S 1A4

## ABSTRACT

A study was carried out on the effect of cadmium, a major impurity in commercial zinc electrolytes, on the zinc plating current efficiency in acid sulfate baths. The synthetic electrolyte ( $200 \text{ g} \cdot \text{dm}^{-3} \text{ Zn}^{++}$  and  $0\text{--}100 \text{ mg} \cdot \text{dm}^{-3} \text{ Cd}^{++}$ ) was continuously circulated through the electrolysis cell. The electrolysis was carried out with a current density of  $480\text{--}490 \text{ A} \cdot \text{m}^{-2}$  at  $37^\circ\text{C}$ . Hydrogen overpotential, potential sweep, atomic absorption, x-ray diffraction, and electron microscopy were used to determine the effect of cadmium on the behavior of the zinc plate. The results indicate that cadmium may either increase or decrease the zinc plating current efficiency. For  $\text{Cd}^{++}$  less than  $20 \text{ mg} \cdot \text{dm}^{-3}$ , increasing cadmium concentrations in the electrolyte reduce the hydrogen overpotential and the zinc plating current efficiency. For  $\text{Cd}^{++}$  greater than  $20 \text{ mg} \cdot \text{dm}^{-3}$ , increasing cadmium concentrations cause a refinement in the structure of the zinc plate with subsequent increase in the hydrogen overpotential and in the zinc plating current efficiency. The incorporation of cadmium into the zinc plate neither significantly alters the crystal orientation of the deposit nor alters the hydrogen evolution mechanism.

The effects of metallic ion impurities on the electro-winning of zinc from acidic sulfate solutions have been the subject of a large number of investigations (1-3). Metallic impurities are known to affect the current efficiency, deposit morphology, and product purity. In general, metal impurities more noble than zinc and having less negative hydrogen overvoltages tend to reduce the current efficiency (4) and accelerate the rate of dissolution of the electrodeposited zinc in both acidic and alkaline media (5, 6). Although lead is a more noble metal, lead ions are recognized to either increase or not affect the zinc plating current efficiency (1, 7). This effect is attributed to a more negative hydrogen overvoltage on lead [ $-1.09\text{V}$  for Pb,  $-0.75\text{V}$  for Zn in  $\text{H}_2\text{SO}_4$  at  $16^\circ\text{C}$  and  $1 \text{ A} \cdot \text{m}^{-2}$  (8)]. Similarly, magnesium also is known to retard the corrosion of zinc (9).

Cadmium also has a large hydrogen overvoltage, but there is disagreement in the literature concerning its effects on zinc electrodeposition. It has been reported that cadmium increases (10), does not affect (11), and decreases (1, 7) the current efficiency. It

also has been reported that cadmium retards zinc corrosion (12-14) as well as accelerates it (15). The present work was undertaken to clarify the effects of cadmium impurities on the electrowinning of zinc.

## Experimental

**Cell.**—The experimental cell (Fig. 1) was constructed of Lucite. The grooves in the side walls permitted the maintenance of a uniform and reproducible electrode gap of 3.7 cm. The electrical connections were sealed at the gastight lid, so that the rate of hydrogen evolution during deposit dissolution could be measured using a soap-bubble flowmeter at outlet G when the spent electrolyte outlet (F) was closed.

The cathodes were cut from  $0.35 \text{ mm}$  thick aluminum foil. Before use, they were treated for 2 min with  $2.0\text{M}$  NaOH solution, washed with distilled water, treated with  $0.05\text{M}$   $\text{H}_2\text{SO}_4$  solution, washed again with distilled water, and dried in an oven at  $100^\circ\text{C}$ . This cathode pretreatment procedure was found to be essential in order to obtain reproducible results. The backs, edges, and upper faces of the cathodes were masked with "invisible sellotape." By so decreasing the effective area of the cathode compared with that of the anode, a uniform deposit was obtained. The anode,

\* Electrochemical Society Active Member.

Key words: electrodeposition, cathode, impurity, current efficiency.

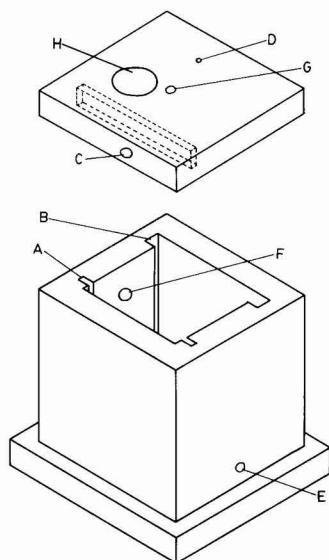


Fig. 1. Electrolytic cell. A, slot for cathode; B, slot for lead anode; C, electrical connection to cathode; D, electrical connection to anode; E, inlet; F, outlet; G, hydrogen outlet to flowmeter; H, opening for reference electrode.

made from lead containing 2% silver, was anodized in 2M  $\text{H}_2\text{SO}_4$  for 1 hr at  $360 \text{ A} \cdot \text{m}^{-2}$  before use.

**Reagents.**—The electrolyte was prepared by dissolving Fisher certified  $\text{ZnSO}_4$ <sup>1</sup> and  $\text{H}_2\text{SO}_4$  in double distilled water to yield a solution containing  $62 \text{ g} \cdot \text{dm}^{-3}$  Zn and  $200 \text{ g} \cdot \text{dm}^{-3}$  free acid. Cadmium sulfate (Analar, B.D.H.) was used for making a stock solution containing  $2.0 \text{ g} \cdot \text{dm}^{-3}$   $\text{Cd}^{++}$  which was further diluted as required to be added as  $5 \text{ cm}^3$  aliquots to  $500 \text{ cm}^3$  of zinc electrolyte.

**Measurements.**—A cathodic current density of  $480\text{--}490 \text{ A} \cdot \text{m}^{-2}$  was maintained during all the electro-deposition experiments. Cathodic voltages were measured against a saturated calomel electrode (SCE)<sup>2</sup> using a Corning pH meter, Model 7. Fresh electrolyte was pumped to the cell at a constant rate of  $2.0 \text{ cm}^3 \cdot \text{min}^{-1}$  using a Teflon-lined solution metering pump. The temperature of both the cell and electrolyte was maintained at  $37^\circ \pm 1^\circ \text{C}$  in a constant temperature bath.

Unless otherwise specified, the electrolysis was carried out for 90 min. For current efficiency determinations the cathode was removed from the cell immediately after a run, washed with distilled water, dried at  $60^\circ \text{C}$ , and weighed to constant weight. For cathode dissolution experiments the pump was shut off immediately after the electrolysis, the cell outlet closed, and the rate of hydrogen evolution measured with a soap-bubble gas flowmeter.

The current efficiency determinations were reproducible to  $\pm 0.3\%$ , while the time required to dissolve the deposit in a sulfuric acid solution varied by  $\pm 10 \text{ min}$  for apparently identical plates.

### Results and Discussion

The effect of cadmium on the zinc plating current efficiency is shown in Fig. 2. The electrolyte contained  $200 \text{ g} \cdot \text{dm}^{-3}$   $\text{H}_2\text{SO}_4$  and  $62 \text{ g} \cdot \text{dm}^{-3}$   $\text{Zn}^{++}$  with varying cadmium concentrations. It can be seen from

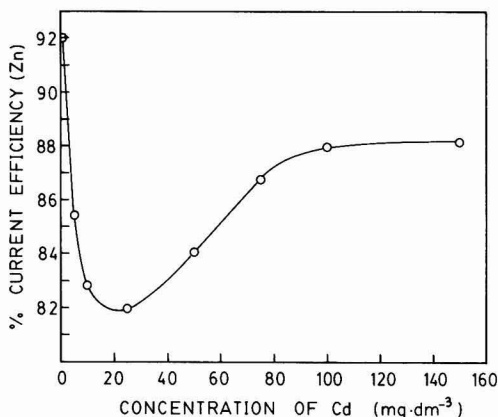


Fig. 2. Effect of cadmium concentration on zinc plating current efficiency. Electrolyte:  $\text{H}_2\text{SO}_4$   $200 \text{ g} \cdot \text{dm}^{-3}$ , Zn  $62 \text{ g} \cdot \text{dm}^{-3}$ . Temperature  $37^\circ \text{C}$ .

the figure that the current efficiency has a minimum at about  $20\text{--}25 \text{ mg} \cdot \text{dm}^{-3}$   $\text{Cd}^{++}$ . Increasing cadmium concentrations to this level causes a decrease in the zinc plating current efficiency, while increasing cadmium concentration above this level causes an increase in the zinc plating current efficiency. This behavior is undoubtedly the cause of some of the confusion concerning cadmium effects on current efficiency. In the range  $0\text{--}20 \text{ mg} \cdot \text{dm}^{-3}$   $\text{Cd}^{++}$ , Kerby and Ingraham (1) reported a decrease in the zinc plating current efficiency from 92% to 80% with increasing cadmium concentration. Similarly Nikiforov (16) has reported increasing current efficiency with decreasing cadmium concentration for concentrations less than  $6 \text{ mg} \cdot \text{dm}^{-3}$ . These observations are in agreement with our work.

For a greater concentration range Turomshina and Stender (9) reported no change in the zinc plating current efficiency with  $10 \text{ mg} \cdot \text{dm}^{-3}$   $\text{Cd}^{++}$ . As can be seen from Fig. 2, the current efficiency is very sensitive to small concentrations of  $\text{Cd}^{++}$  and a small concentration of  $\text{Cd}^{++}$  impurity would result in there being no apparent difference in the current efficiency with the  $100 \text{ mg} \cdot \text{dm}^{-3}$   $\text{Cd}^{++}$  solution. Figure 2 also shows that at concentrations greater than  $\sim 100 \text{ mg} \cdot \text{dm}^{-3}$  cadmium does not seem to greatly alter the current efficiency and it is possible to speculate that the reduction in zinc plating current efficiency reported by Turomshina and Stender (9) for a  $1000 \text{ mg} \cdot \text{dm}^{-3}$   $\text{Cd}^{++}$  was the result of increased cadmium plating.

Since the major competing reaction with zinc deposition at low impurity levels is hydrogen evolution, the effect of cadmium on the hydrogen overpotential was studied. Zinc deposits from the electrolytes containing various cadmium concentrations were immersed in a sulfuric acid bath ( $200 \text{ g} \cdot \text{dm}^{-3}$  without  $\text{Zn}^{++}$  or  $\text{Cd}^{++}$  present) at  $37^\circ \text{C}$ . The cathodic potentials required to yield a current density of  $480 \text{ A} \cdot \text{m}^{-2}$  were recorded. Using the calculated value for the reversible hydrogen potential for this solution at  $37^\circ \text{C}$  ( $-0.2576 \text{ V}$  vs. SCE; see Appendix A), the hydrogen overpotentials were calculated and the results plotted in Fig. 3. The results show that the magnitude of the hydrogen overpotential  $\eta_h$  displays a maximum for the zinc deposit obtained from an electrolyte containing  $20 \text{ mg} \cdot \text{dm}^{-3}$   $\text{Cd}^{++}$ . It is clear that the minimum for the zinc plating current efficiency observed in Fig. 2 is related to the maximum in the hydrogen overpotential observed in

<sup>1</sup> Impurities:  $\leq \text{Fe } 0.0003\%$ ,  $\text{Pb } 0.0008\%$ ,  $\text{As } 0.2 \text{ ppm}$ ,  $\text{Mn } 1 \text{ ppm}$ .

<sup>2</sup> All voltages are reported vs. SHE unless otherwise noted.



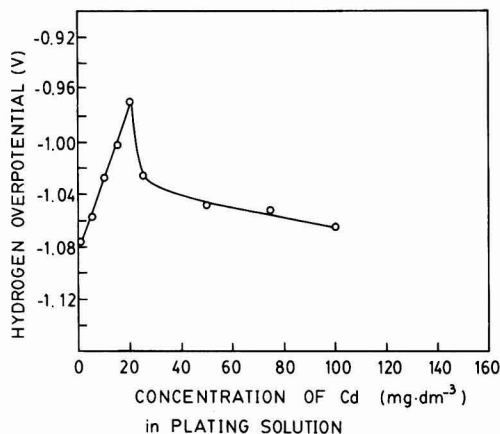


Fig. 3. Hydrogen overpotential for zinc plated from solutions containing various cadmium concentrations. Electrolyte: 2M  $\text{H}_2\text{SO}_4$ . Temperature = 37°C.  $E_{\text{rev}} = -0.2576\text{V}$ . Current = 480  $\text{A} \cdot \text{m}^{-2}$ .

Fig. 3. At low cadmium concentrations ( $\leq 20 \text{ mg} \cdot \text{dm}^{-3}$ ) increasing cadmium concentrations cause a decrease in the magnitude of the hydrogen overpotential and hence cause an increase in the rate of hydrogen evolution. This results in a lower zinc plating current efficiency. Conversely, increasing cadmium concentrations greater than  $20 \text{ mg} \cdot \text{dm}^{-3}$  cause an increase in the magnitude of the hydrogen overpotential which improves the zinc plating current efficiency as observed in Fig. 2.

In order to elucidate the effect of cadmium on the hydrogen overpotential of the zinc deposits, polarization profiles were measured for pure zinc and pure cadmium plates electrodeposited from solutions without added impurities and tested in a sulfuric acid electrolyte without  $\text{Zn}^{++}$  or  $\text{Cd}^{++}$  present. The results are shown in Fig. 4. For current densities less than  $10 \text{ A} \cdot \text{m}^{-2}$  the profile for zinc remains horizontal at the potential  $-0.75\text{V}$ . This portion of the curve reflects the equilibrium potential of  $0.76\text{V}$  for the reaction  $\text{Zn}^{++} + 2e^- \rightarrow \text{Zn}$  at 35°C. At greater current densities the evolution of hydrogen begins. From 30–800  $\text{A} \cdot \text{m}^{-2}$  a second linear region is found. The Tafel slope of  $-0.105$  results from the kinetics of the hydrogen evolution reaction on zinc. The transfer co-

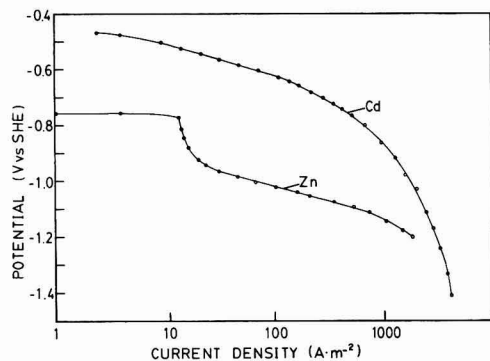


Fig. 4. Polarization plot of pure zinc plate and pure cadmium plate from solutions containing only zinc or cadmium ions, respectively. Electrolyte:  $200 \text{ g} \cdot \text{dm}^{-3} \text{H}_2\text{SO}_4$ . Temperature = 37°C.

efficient,  $\alpha$ , calculated from the Tafel slope is 0.58 and indicates that  $\text{H}_3\text{O}^+ + e^- \rightarrow \text{H}_{\text{ads}} + \text{H}_2\text{O}$  is the rate-determining step (17). This finding is in agreement with that of other workers (6, 18–20). Measurement of the hydrogen evolution transfer coefficient in pure sulfuric acid solutions for zinc plates obtained from solutions with cadmium concentrations from 0 to  $100 \text{ mg} \cdot \text{dm}^{-3}$  produced an average transfer coefficient of 0.498 with a deviation of  $\pm 0.078$ . These measurements show that the transfer coefficient does not change significantly with the addition of cadmium to the plating bath. Thus the rate-determining step for the hydrogen evolution reaction does not change with the addition of cadmium to the plating bath and cannot be the cause of the maxima observed in Fig. 2 and 3.

The polarization plot in Fig. 4 reveals that higher current densities can be sustained on pure cadmium plate than on pure zinc plate for the same potential. There is some variance in the literature concerning this point. Values of hydrogen overpotential on zinc and cadmium in 2N  $\text{H}_2\text{SO}_4$  at 25°C are reported to be 0.926 and 1.211V at  $500 \text{ A} \cdot \text{m}^{-2}$ , respectively (21). Mantell (22) gives values of 1.06 and 1.22V at  $100 \text{ A} \cdot \text{m}^{-2}$  for zinc and cadmium in 2N  $\text{H}_2\text{SO}_4$  at 25°C. These indicate that cadmium has the greater overpotential in contrast to that shown in Fig. 4. However, hydrogen bubble overvoltages reported by Glasstone (23) for Zn and Cd are 0.70 and 0.48V in 1N sulfuric acid at room temperature. More recent data by Pickett (24) at 25°C give values of 0.94 and 0.90V at  $100 \text{ A} \cdot \text{m}^{-2}$  for Zn and Cd, respectively. These differences may reflect the effect of different impurity levels in the zinc and cadmium plates. From the experimental results of Fig. 4 it is clear that, for the zinc and cadmium plates obtained from the synthetic electrolytes, zinc has a higher hydrogen overpotential than cadmium. The approximate exchange current densities estimated from Fig. 4 (by extrapolation of the linear portion of the  $V$  vs.  $\log i$  plot) are 0.4 and  $1.5 \text{ A} \cdot \text{m}^{-2}$  for zinc and cadmium, respectively, again indicating that the hydrogen is more easily evolved on cadmium than on zinc. While these values are quite different from theoretical exchange current densities, they are in good agreement with those reported ( $0.2 \text{ A} \cdot \text{m}^{-2}$ ) by Lowenheim (8). The results indicate that for plating baths in the absence of other deliberate impurity additions, the incorporation of cadmium into the zinc plate should cause an increase in the hydrogen evolution rate. Thus the zinc plating current efficiency should decrease with increasing cadmium content in the zinc plate. This would explain the initial decrease in the current efficiency observed in Fig. 2. To confirm that cadmium was being incorporated into the zinc plate, the zinc deposits were analyzed for their cadmium content.

The results of the atomic absorption analysis are shown in Fig. 5. In order to ensure complete ionization of the sample, ionization was carried out using either a flame or a graphite furnace. Comparable results were obtained in either case. It is clear from Fig. 5 that the percent of cadmium in the deposit increases monotonically with cadmium concentration in the electrolyte. The increase is linear for cadmium concentrations less than  $\approx 50 \text{ mg} \cdot \text{dm}^{-3}$ . This behavior simply demonstrates that at these concentrations cadmium is under limiting diffusion current control. Calculations (see Appendix B) show that the limiting diffusion currents are:  $i_{\text{H}^+} \approx 17,000 \text{ A} \cdot \text{m}^{-2}$ ;  $i_{\text{Cd}^{++}} \approx 0.6 \text{ A} \cdot \text{m}^{-2}$  (maximum at a concentration of  $100 \text{ mg} \cdot \text{dm}^{-3}$ );  $i_{\text{Zn}^{++}} \approx 670 \text{ A} \cdot \text{m}^{-2}$ . Thus under these conditions, the partial current for cadmium plating ( $i_{\text{Cd}^{++}}$ ) is proportional to the cadmium concentration in the bulk of the electrolyte (25).

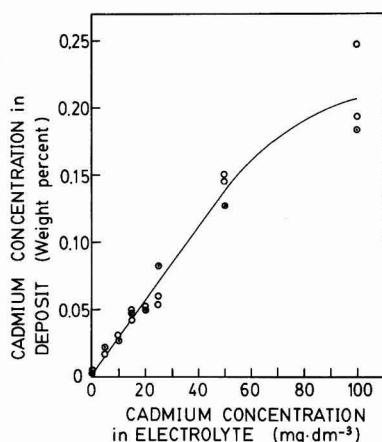


Fig. 5. Cadmium content of zinc plate from electrolytes with various cadmium concentrations, by atomic absorption analysis. Deposits from electrolyte:  $200 \text{ g} \cdot \text{dm}^{-3} \text{ H}_2\text{SO}_4$ ,  $62 \text{ g} \cdot \text{dm}^{-3} \text{ Zn}$ . Current density  $480 \text{ A} \cdot \text{m}^{-2}$ . Temperature  $37^\circ\text{C}$ . Sample ionization, by flame  $\circ$ ; by graphite furnace  $\square$ .

An increase in cadmium concentration in the electrolyte results in a zinc plate with a greater cadmium content, which promotes the hydrogen evolution reaction and decreases the zinc plating current efficiency. While this explains the current efficiency and overpotential behavior at low cadmium concentrations ( $\leq 20 \text{ mg} \cdot \text{dm}^{-3}$ ) seen in Fig. 2 and 3, the behavior at greater cadmium concentrations ( $> 20 \text{ mg} \cdot \text{dm}^{-3}$ ) is not explained by this model.

In order to study other possible changes in the reaction, cyclic potential sweep measurements were conducted for the zinc plates in a sulfuric acid bath ( $200 \text{ g} \cdot \text{dm}^{-3}$ ). Some typical potential scans are shown in Fig. 6. A relatively high sweep rate ( $100 \text{ mV} \cdot \text{sec}^{-1}$ ) was used to reduce the effect of changing surface area during the measurement. The samples were masked so that the same geometrical area was represented. From the potential scans it is clear that there are no hydrogen adsorption peaks. This is consistent with the fact that hydrogen does not strongly adsorb on zinc (6). The composition of the plate does, however, affect the rate of hydrogen evolution at any potential. In Fig. 7 the variation of the cathodic current density with plate composition is shown at various potentials. These measurements were conducted at room temperature ( $23^\circ\text{C}$ ) and again show that a maximum cathodic current density (hydrogen evolution rate) is found for the zinc plates obtained from solutions with  $20 \text{ mg} \cdot \text{dm}^{-3} \text{ Cd}^{++}$ . No obvious changes in the hydrogen evolution reaction mechanism are apparent from these measurements. To determine whether any macroscopic change in the zinc deposit was caused by changes in the cadmium content, scanning electron micrographs were taken. The results are shown in Fig. 8. It is clear from the photographs that a certain amount of grain refinement does take place with increasing cadmium content. This grain refinement of the zinc plate has also been reported by Mackinnon, Brannen, and Kerby (26) for increasing cadmium content in industrial acid sulfate baths. Other changes in zinc plate morphology from the presence of impurities have also been reported. The concentration of lead in the plating solution has been shown to alter both morphology and orientation (27). Antimony and glue additions will likewise alter the surface plate characteristics (4). In addition to impurities, overpotential

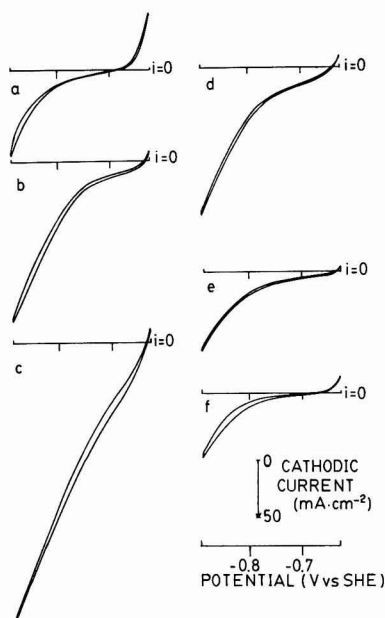


Fig. 6. Potential sweep profiles of zinc plates. Electrolyte:  $\text{H}_2\text{SO}_4$   $200 \text{ g} \cdot \text{dm}^{-3}$ . Temperature =  $22.5^\circ\text{C}$ . Sweep rate =  $100 \text{ mV} \cdot \text{sec}^{-1}$ . Zinc plates obtained from synthetic industrial electrolyte containing  $200 \text{ g} \cdot \text{dm}^{-3} \text{ H}_2\text{SO}_4$ ,  $62 \text{ g} \cdot \text{dm}^{-3} \text{ Zn}$ , and (a)  $0 \text{ mg} \cdot \text{dm}^{-3} \text{ Cd}$ ; (b)  $15 \text{ mg} \cdot \text{dm}^{-3} \text{ Cd}$ ; (c)  $20 \text{ mg} \cdot \text{dm}^{-3} \text{ Cd}$ ; (d)  $25 \text{ mg} \cdot \text{dm}^{-3} \text{ Cd}$ ; (e)  $50 \text{ mg} \cdot \text{dm}^{-3} \text{ Cd}$ ; (f)  $100 \text{ mg} \cdot \text{dm}^{-3} \text{ Cd}$ .

can have an important role in the type of crystal growth (28). The work of Vagramyan, Leach, and Moon indicated that at low overpotentials metal deposition causes crystal growth to take place along close-packed crystal directions while at higher overpotentials more random growth occurs. X-ray diffraction patterns of the zinc plates were measured to determine whether there were any changes resulting from the differences in cadmium content. The analysis of the patterns showed no change in the orientations with the exception of the weakening of the (102) with greater cadmium concentrations. The preferred

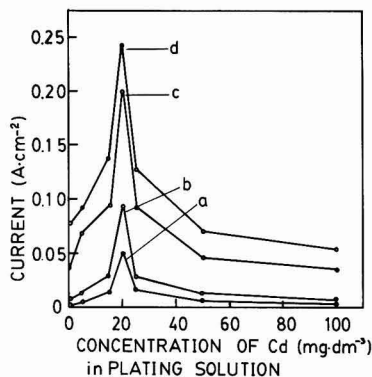


Fig. 7. Cathodic current density for zinc plated from solutions containing various cadmium concentrations. Electrolyte  $200 \text{ g} \cdot \text{dm}^{-3} \text{ H}_2\text{SO}_4$ . Temperature =  $22.5^\circ\text{C}$ . Potential: (a)  $0.7\text{V}$ ; (b)  $0.758\text{V}$ ; (c)  $0.858\text{V}$ ; (d)  $0.888\text{V}$ .

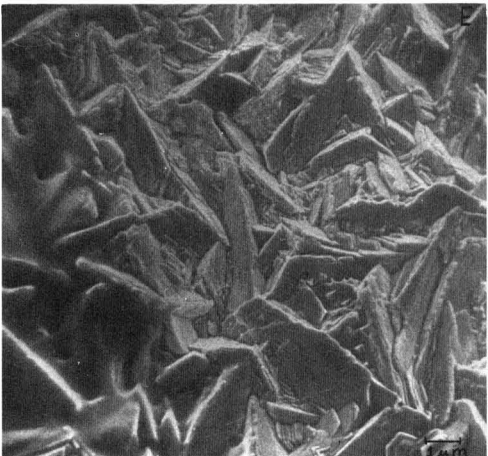
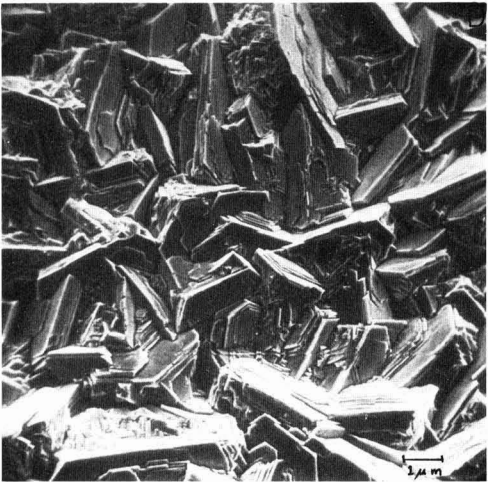
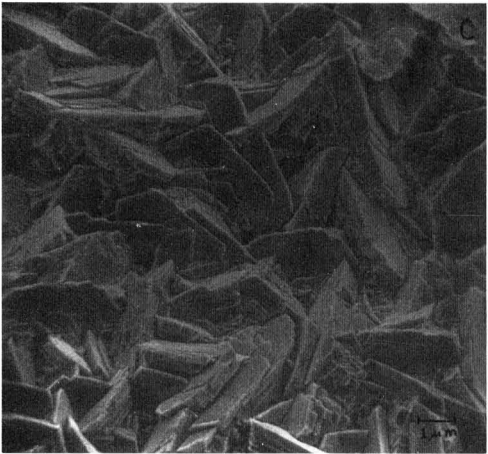
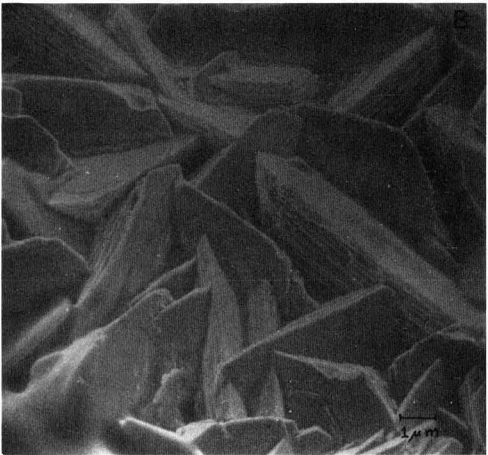
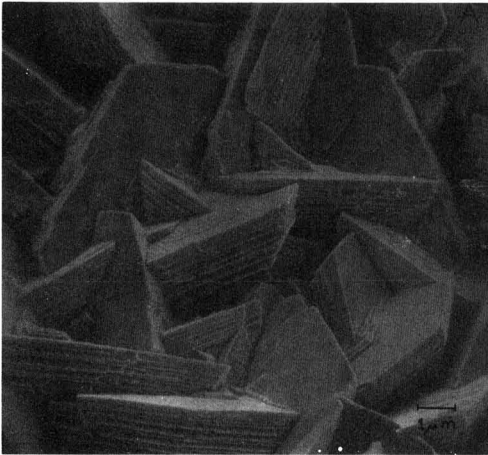


Figure 8 continued on next page

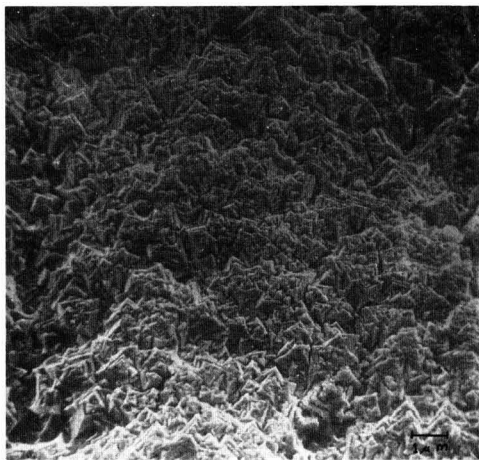


Fig. 8. Scanning electron micrographs of deposit morphology. Zinc deposit from solution containing  $200 \text{ g} \cdot \text{dm}^{-3} \text{H}_2\text{SO}_4$  + various cadmium concentrations. Temperature =  $37^\circ\text{C}$ . Current density  $480 \text{ A} \cdot \text{m}^{-2}$ . A,  $0 \text{ Cd}^{++}$ ; B,  $10 \text{ mg} \cdot \text{dm}^{-3} \text{Cd}^{++}$ ; C,  $15 \text{ mg} \cdot \text{dm}^{-3} \text{Cd}^{++}$ ; D,  $20 \text{ mg} \cdot \text{dm}^{-3} \text{Cd}^{++}$ ; E,  $25 \text{ mg} \cdot \text{dm}^{-3} \text{Cd}^{++}$ ; F,  $50 \text{ mg} \cdot \text{dm}^{-3} \text{Cd}^{++}$ ; G,  $100 \text{ mg} \cdot \text{dm}^{-3} \text{Cd}^{++}$ .

orientations (112), (002), and (103) were not affected, but the patterns from the zinc plates with greater cadmium concentrations were more continuous with less spread in the diffraction bands. This change resulted from the fine grain size at higher cadmium concentrations. Changes in crystal structure orientation can be ruled out as the cause of the increase of hydrogen overpotential with cadmium concentration.

One change that is apparent (from Fig. 8) with increasing cadmium concentrations is the increase in the number of crystallites and finer grain size in the zinc plates. The change in crystallite size causes a change in the surface area of the sample. Based on a fixed geometrical area, a decrease in the surface area would result in an increase in the current density and hence a greater apparent overpotential. It is partially due to this effect that shiny platinum has a greater hydrogen overpotential than platinized platinum. From the scanning electron micrographs in Fig. 8 it is clear that increasing cadmium concentrations cause smoother deposits and hence the surface roughness factor should decrease. The variation of overpotential with surface morphology has been studied by Bockris and Raxumney (29). They found that the transition in surface morphology from large pyramidal crystal structures to finer polycrystalline structures was accompanied by an increase in overpotential. During zinc deposition, increasing overpotential has been found to cause smaller crystallites (28). For the deposition of copper, the magnitude of the increase of the overpotential was reported to be  $\approx 120 \text{ mV}$  (29). From Fig. 2, the increase in the magnitude of the hydrogen overpotential is about  $92 \text{ mV}$  and therefore it is not unreasonable to assign the cause of the increase to the change in morphology of the zinc plates. Although the change in morphology does not affect the reaction mechanism (since the transfer coefficient did not change with zinc plate composition), the exchange current density could be affected. The hydrogen exchange current density depends on surface activity as well as on the effective surface area. If surface area change is ignored for the moment, a decrease in the exchange current density would increase the overpotential. The decrease

in the exchange current density could be caused by the transition to fine grain deposits (29). Thus three factors must be considered to explain the overpotential behavior. The first is the co-deposition of cadmium with zinc. This initially results in a surface with a greater hydrogen exchange current density. The second factor is the increased number of nucleation sites resulting from the cadmium co-deposition. This results in a finer grained deposit. The third factor is the decrease in the hydrogen exchange current density resulting from the change in surface morphology. Thus a maximum would be expected in the hydrogen exchange current density for the zinc deposit with increasing cadmium content. Support for this behavior is given in Fig. 9. The hydrogen exchange current density determined from potential sweep data in sulfuric acid ( $200 \text{ g} \cdot \text{dm}^{-3}$  without  $\text{Zn}^{++}$  or  $\text{Cd}^{++}$  present) at  $22.5^\circ\text{C}$  is plotted against cadmium concentration in the plating bath. An average of 10 runs was used for each point. A distinct maximum is formed at  $20 \text{ mg} \cdot \text{dm}^{-3} \text{Cd}^{++}$ . Although data from potential sweeps at  $100 \text{ mV} \cdot \text{sec}^{-1}$  must be viewed with some caution, the relative behavior of the zinc deposits is clear. An advantage of the data from the potential sweeps is that there is little area change during the course of the measurement. From Fig. 9 the exchange current density does increase initially with increasing cadmium content up to about  $20 \text{ mg} \cdot \text{dm}^{-3} \text{Cd}^{++}$ . At greater cadmium concentrations the exchange current density decreases as a result of the change in morphology (finer deposits) and the decrease of the effective area. The magnitude of the change in the exchange current density is much larger than would be predicted by a surface area changes and must be primarily due to the increase of activity of the fine grained deposits.

### Conclusions

The effect of cadmium on the zinc plating current efficiency in acid sulfate baths is dependent on cadmium concentration. At less than about  $20 \text{ mg} \cdot \text{dm}^{-3} \text{Cd}^{++}$ , increasing cadmium concentrations lower the zinc plating current efficiency by decreasing the hydrogen overpotential on the zinc plate. This effect is superseded at greater cadmium concentrations by the refinement of the zinc plate and subsequent in-

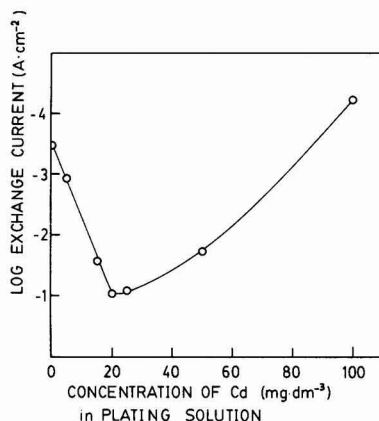


Fig. 9. Hydrogen exchange current density for zinc plated from electrolytes containing various cadmium concentrations. Data from potential sweep measurements. Electrolyte  $\text{H}_2\text{SO}_4$   $200 \text{ g} \cdot \text{dm}^{-3}$ . Temperature =  $22.5^\circ\text{C}$ . Sweep rate =  $100 \text{ mV} \cdot \text{sec}^{-1}$ . (Average of 10 runs per determination.)

crease of the hydrogen overpotential as a result of the morphology change and surface area decrease. The incorporation of cadmium into the zinc plate does not cause any significant change in the crystal orientations of the zinc plate nor does it alter the mechanism of hydrogen evolution.

### Acknowledgments

We would like to express our appreciation for the assistance given by Powesland Engineering Limited, Texasgulf Canada Limited, and Canadian Electrolytic Zinc and also for the financial assistance provided by the Natural Sciences and Engineering Research Council of Canada. Our thanks also go to Dr. A. Iribarne for the atomic absorption analysis and to J. W. Dowkes for the photographs of the zinc plate micrographs.

Manuscript submitted Feb. 13, 1981; revised manuscript received May 24, 1981.

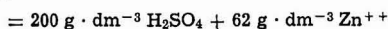
Any discussion of this paper will appear in a Discussion Section to be published in the June 1982 JOURNAL. All discussions for the June 1982 Discussion Section should be submitted by Feb. 1, 1982.

Publication costs of this article were assisted by the University of Toronto.

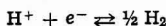
## APPENDIX

### A. Theoretical Hydrogen Voltage

#### Electrolyte



$$\text{pH} = 0.35$$



$$\epsilon_{\text{H}} = \epsilon_{\text{H}}^{\circ} - \frac{RT}{F} \ln \frac{(P_{\text{H}_2})^{1/2}}{a_{\text{H}^+}}$$

$$= -\frac{RT}{F} \ln (P_{\text{H}_2})^{1/2} + \frac{2.303 RT}{F} \log a_{\text{H}^+}$$

at  $P_{\text{H}_2} = 1 \text{ atm}$ ,  $\epsilon_{\text{H}} = -0.0215 \text{ V}$  vs. SHE at  $37^\circ\text{C}$  and at  $37^\circ\text{C}$  SCE =  $0.2361 \text{ V}$  vs. SHE (30) and  $(\epsilon_{\text{H}})_{37^\circ\text{C}} = -0.2576 \text{ V}$  vs. SCE.

The contribution of the liquid junction potential for the SCE in this solution is estimated as follows. The Planck-Henderson theory (31) gives

$$E_j \approx \left( \frac{2.303 RT}{F} \right) \left[ \frac{\sum_i \lambda_i (M_{\text{is}} - M_{\text{ir}})}{\sum_i \lambda_i |Z_i| (M_{\text{is}} - M_{\text{ir}})} \right] \log \left[ \frac{\sum_i \lambda_i |Z_i| M_{\text{ir}}}{\sum_i \lambda_i |Z_i| M_{\text{is}}} \right]$$

where  $E_j$  = liquid junction potential,  $\lambda_i$  = equivalent conductivity for ion  $i$ ,  $M_{\text{ir}}$  = concentration of ion  $i$  in reference electrolyte,  $M_{\text{is}}$  = concentration of ion  $i$  in solution, and  $Z_i$  = charge on ion.

The concentrations of the  $[\text{H}^+]$ ,  $[\text{HSO}_4^-]$ ,  $[\text{SO}_4^{2-}]$ , and  $[\text{Zn}^{++}]$  are calculated in Appendix B.  $[\text{K}^+]$  and  $[\text{Cl}^-]$  are assumed to be completely dissociated at saturation at  $37^\circ\text{C}$ .

Equivalent ion conductivities ( $\lambda_i$ ) at infinite dilution +  $37^\circ\text{C}$  were obtained by graphical interpolation of data given by Quist and Marshall (32).

Walden's Rule was used to extend the data to the concentrated solutions. From this the above equation yields the value  $E_j \approx 0.0183 \text{ V}$  indicating that the overpotentials may be in error by this amount.

### B. Limiting Current Density Calculations

Electrolyte  $2.04 \text{ M H}_2\text{SO}_4 + 0.948 \text{ M ZnSO}_4$  at  $37^\circ\text{C}$   $\text{pH} = 0.35$ . The limiting current densities may be estimated from the equation (17)

$$i_{\text{lim}} = \frac{ZFDC^{\circ}}{(1-t)S}$$

where  $Z$  is the charge on the ion,  $F$  is Faraday's constant,  $D$  is the diffusion coefficient,  $C^{\circ}$  is the concentra-

tion of the ion in the bulk of the solution,  $t$  is the transport number, and  $S$  is the diffusion layer thickness.

The concentrations of  $[\text{SO}_4^{2-}] + [\text{HSO}_4^-]$  were calculated knowing the dissociation constant for  $\text{H}_2\text{SO}_4$ .

For  $2 \text{ M H}_2\text{SO}_4$ ,  $[\text{SO}_4^{2-}] = 0.7$ ,  $[\text{HSO}_4^-] = 1.3$ ,  $K_2 = 7.24 \times 10^{-3}$  at  $37^\circ\text{C}$  (33, 34)

$$K_2 = \frac{\gamma_{\text{H}^+} \cdot \gamma_{\text{SO}_4^{2-}}}{\text{HSO}_4^-} \cdot \frac{(\text{H}^+) \cdot (\text{SO}_4^{2-})}{(\text{HSO}_4^-)} \approx 0.01 \frac{(\text{H}^+) \cdot (\text{SO}_4^{2-})}{(\text{HSO}_4^-)}$$

$$[\text{H}^+] = 1.92, [\text{HSO}_4^-] = 2.17, [\text{SO}_4^{2-}] = 0.821,$$

$$[\text{Cd}^{++}] \approx 0, [\text{Zn}^{++}] = 0.948$$

The transport number

$$t_i = \frac{i_i}{i_T} = \frac{Z_i C_i \lambda_i}{\sum Z_i C_i \lambda_i}$$

using  $\lambda_{i37^\circ\text{C}}$  [equivalent conductivity ( $\Omega^{-1} \cdot \text{m}^2 \text{equiv}^{-1}$ )]  $t_{\text{H}^+} = 0.60$ ,  $t_{\text{Zn}^{++}} = 0.10$ ,  $t_{\text{Cd}^{++}} \approx 0$ ,  $t_{\text{HSO}_4^-} = 0.17$ ,  $t_{\text{SO}_4^{2-}} = 0.13$  and using  $\delta \approx 0.03 \text{ cm}$ , i.e., boundary layer thickness with some stirring from gas evolution

$$i_{\text{H}^+} \approx 17,000 \text{ A} \cdot \text{m}^{-2}, i_{\text{Zn}^{++}} \approx 670 \text{ A} \cdot \text{m}^{-2}$$

for

$$[\text{Cd}^{++}] = 5 \text{ mg} \cdot \text{dm}^{-3} \quad i_{\text{Cd}^{++}} \approx 3 \times 10^{-2} \text{ A} \cdot \text{m}^{-2}$$

$$[\text{Cd}^{++}] = 100 \text{ mg} \cdot \text{dm}^{-3} \quad i_{\text{Cd}^{++}} \approx 0.6 \text{ A} \cdot \text{m}^{-2}$$

Despite the assumptions in using  $\lambda_i^{\circ}$  for  $\lambda_i$  and a diffusion layer thickness  $0.03 \text{ cm}$  it is clear that  $\text{Cd}^{++}$  will be diffusion controlled.

## REFERENCES

1. R. C. Kerby and T. R. Ingraham, Mines Branch Rep. R243, Dept. of Energy, Mines and Resources, Ottawa (1971).
2. D. R. Fasnacht, Ph.D. Thesis, University of Missouri-Rolla (1978).
3. H. Fukubayashi, Ph.D. Thesis, University of Missouri-Rolla (1972).
4. B. A. Lamping and T. S. O'Keefe, *Metall. Trans. (B)* **7**, 551 (1976).
5. A. G. Pecherskaya and V. V. Stender, *Zh. Prikl. Khim.*, **23**, 920 (1950).
6. R. J. Brodd and V. E. Leger, "Encyclopedia of Electrochemistry of the Elements," Vol. V, Marcel Dekker Inc., New York (1976).
7. V. F. Turomshina and V. V. Stender, *Zh. Prikl. Khim.*, **28**, 372 (1955).
8. F. A. Lowenheim, "Modern Electroplating," p. 15, John Wiley & Sons, Inc., New York (1963).
9. M. Saloma and H. Holtan, Sr., *Acta Chem. Scand. Ser. A*, **28**, 86 (1974).
10. G. C. Bratt, *Electrochem. Technol.*, **2**, 323 (1964).
11. B. Peyer, M. Micho, S. Vasil, and S. Georgi, *Rubsdoliv Mat. (Sofia)*, **Met.**, **21**, 28 (1966).
12. R. Pietelli, *Chim. Ind. (Milan)*, **22**, 109 (1940).
13. Z. Wada and K. Makamura, *Rep. Inst. Sci. Tech. Univ. Tokyo*, **8**, 63 (1954).
14. J. E. Oxley and J. R. Humphrey, NASA Contract Rep. 1968, NASA-CR-100814.
15. S. Stanislav, *Rudodoliv Met. (Sofia)*, **21**, 25 (1966).
16. A. F. Nikiforov, *Tsvetn. Met.*, **4**, 28 (1975).
17. J. O'M. Bockris and A. K. N. Reddy, "Modern Electrochemistry," Plenum Press, New York (1970).
18. A. L. Rotenyan, N. P. Fedotieff, and L. U. Sok, *Zh. Fiz. Khim.*, **31**, 1295 (1957).
19. G. M. Westrip, *J. Chem. Soc.*, **125**, 112 (1924).
20. A. N. Frumkin, V. S. Bagotskii, Z. A. Iofa, and B. N. Kabanov, "Kinetics of Electrode Processes," *Izd. Moskov Gos. Univ.* (1952).
21. M. Knobel, "International Critical Tables," Vol. 6, p. 329.
22. C. L. Mantell, "Industrial Electrochemistry," p. 1969, McGraw Hill Book Co., New York (1950).
23. S. Glasstone, "Introduction to Electrochemistry," p. 443, Van Nostrand Co. Inc., New York (1942).
24. D. S. Pickett, "Electrochemical Reactor Design," p. 71, Elsevier Publishing Co., Amsterdam (1977).
25. A. Brenner, "Electrodeposition of Alloys: Principles and Practice," Vol. 3, pp. 94-96, Academic Press, New York (1963).



26. D. J. Mackinnon, J. M. Brannen, and R. C. Kerby, *J. Appl. Electrochem.*, **9**, 71 (1979).
27. D. J. Mackinnon, J. M. Brannen, and R. C. Kerby, *ibid.*, **9**, 55 (1979).
28. T. Vagramyan, J. S. Leach, and J. R. Moon, *J. Mater. Sci.*, **14**, 1170 (1979).
29. J. O'M. Bockris and G. A. Razumney, "Fundamental Aspects of Electrocrystallization," Plenum Press, New York (1967).
30. M. Lavallee, O. F. Schanne, and N. C. Herbert, Editors, "Glass Microelectrodes," John Wiley & Sons, Inc., New York (1969).
31. J. S. Newmann, "Electrochemical Systems," p. 126, Prentice-Hall, Englewood Cliffs, NJ (1973).
32. A. S. Quist and W. L. Marshall, *J. Phys. Chem.*, **69**, 2984 (1965).
33. T. F. Young, *Rec. Chem. Prog.*, **12**, 81 (1951).
34. R. A. Robinson and R. H. Stokes, "Electrolyte Solutions," 2nd ed., p. 382, Butterworths, London (1970).

## Effects of the Brine Impurities on the Cell Performance of the Diaphragm-Type Chlor-Alkali Cell

F. Hine,\* M. Yasuda,\* and K. Fujita<sup>1</sup>

Nagoya Institute of Technology, Nagoya 466, Japan

### ABSTRACT

A laboratory cell equipped with the deposited asbestos diaphragm was operated with impure brine to investigate the effects of the hardness on the cell performance. The concentration distribution of NaOH in the diaphragm was established by three factors: diffusion, migration, and the hydraulic flow. It is pointed out that the migration flux was larger than the diffusion flux under the operating conditions of the diaphragm cell.

The amalgam process is best for producing chlorine and pure caustic. However, no new constructions using amalgam cells are being announced at present, and many amalgam cell plants are being converted to diaphragm cells, especially in Japan, due to environmental concerns with mercury pollution (1). It is estimated that now about 70% of the world production of chlorine and caustic comes from diaphragm cells.

Although the diaphragm cell process has a long history, innovations were delayed by a poor market for the impure caustic and the relatively high consumption of energy, both electricity and steam.

Recently, the invention of dimensionally stable anodes (DSA) by Beer (2), and the development of the modified asbestos diaphragms (3, 4), for example, the HAPP of Hooker and the TAB of Diamond Shamrock, have brought a new phase in diaphragm-type chlor-alkali technology.

The d-c electric power for cell operation and steam for evaporating the weak caustic liquor are major energy requirements, thus the overall consumption of energy by these factors must be minimized.

Consumption of electric power could be optimized by the reduction of several factors: the anode overvoltage (2, 5); the cathode overvoltage, (6-11); the solution IR drop, especially the bubble effects of chlorine and hydrogen gases (12-24); and the IR drop through the diaphragm (16). This paper deals with this last factor.

The brine is fed to the electrolytic cells after purification and under pH control, if necessary. Even so, the hardness ( $Mg^{2+}$  and  $Ca^{2+}$ ) in the anolyte may plug the porous diaphragm, resulting in a gradual increase in the cell voltage for long-time operation. This also decreases the brine flow rate because the hydraulic resistance of the porous diaphragm increases.

The transport of  $OH^-$  through the diaphragm is by diffusion, migration, and hydraulic flow. All these

factors are affected significantly by plugging of the diaphragm with precipitates. This causes changes in the operating conditions affecting cell performance (17).

In this paper the limitations on hardness of the feed brine based on experimental results of an accelerated test are discussed. The transport phenomena of NaOH through the diaphragm was also studied.

### Experimental

A small "Lucite" cell as shown in Fig. 1 was used. A titanium sheet, 2 cm long, 2 cm wide, and 0.5 mm thick, coated with a thermally deposited mixture of  $RuO_2$  and  $TiO_2$  was used as the anode. The cathode was made of Ni sheet ( $2 \times 2$  cm). A modified asbestos mat was used as the diaphragm. Chrysotile fiber [5g of Hooker, Grade H-1, 0.4g of E-CTFE powder (Allied Chemical, "Halar 5004"), and a small amount of surfactant in 2M NaOH] was vacuum-deposited on a steel mesh, dried at 120°C for 1 hr, peeled off from the mesh, then heated at 270°C for 3 hr for setting. The thickness was about 4 mm, and the effective area was 19.6 cm<sup>2</sup> (5 cm diam).

Two Luggin-Haber probes were located about 0.5 mm from the diaphragm to measure the IR drop. A

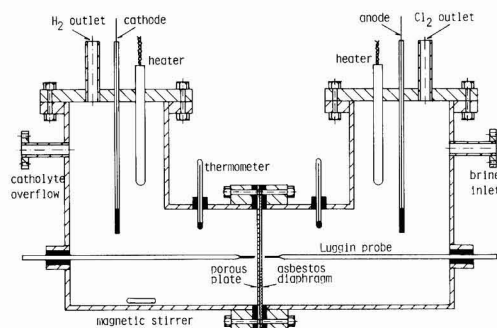


Fig. 1. An experimental electrolytic cell

\* Electrochemical Society Active Member.

<sup>1</sup> Present address: Nihama Works, Sumitomo Chemical Industry Company, Nihama, Japan.

Key words: current efficiency, flow rate, diffusion, electrical resistance, migration.

saturated calomel electrode,  $\text{Hg}/\text{Hg}_2\text{Cl}_2/\text{satd. KCl}$  (at  $30^\circ\text{C}$ ), was used as a reference electrode for the anode Luggin, and a mercuric oxide electrode,  $\text{Hg}/\text{HgO}/3.5\text{M NaOH}$  (at  $30^\circ\text{C}$ ), was employed for the cathode Luggin.

Electric heaters were located in both the anode and the cathode compartments to maintain the solution temperature. A magnetic stirrer was located under the cathode compartment.

A saturated NaCl solution, 5.1M NaCl prepared with pure salt and distilled water, in the brine reservoir (ca. 50 liters) was pumped up to the level tank (ca. 10 liters) located about 3m above the cell. The brine was fed to the anode compartment at a given rate. The electrolytic solution passed through the diaphragm and flowed out of the cathode compartment to the catholyte reservoir by gravity.

Chlorine liberated at the anode was collected in a gas holder (ca. 5 liters) located about 3.5m above the cell and was sent to an absorption column containing caustic soda solution. Hydrogen generated at the cathode was purged to the air after a water wash.

The required amounts of  $\text{MgCl}_2$  or  $\text{CaCl}_2$  were added to the brine reservoir to investigate the effects of these brine impurities.

The rate of feed brine was adjusted to yield a 50% decomposition with respect to pure brine. The flow rate decreased and the NaOH concentration in the catholyte increased when an impure brine was fed to the cell.

The current density was kept constant during each experiment.

The amperage and the IR drop were recorded continuously whereas the flow rate of the electrolyte was measured at certain intervals, say every 30 min. The catholyte effluent was titrated every 24 hr. Thus the current efficiency for production of caustic soda (C.E. in percent) was calculated by Eq. [1]

$$\text{C.E.(\%)} = \frac{\text{Practical amount of NaOH produced}}{\text{Theoretical amount of NaOH to be produced}} \times 100 \quad [1]$$

A three-compartment cell illustrated in Fig. 2 was employed to determine the diffusion and migration of  $\text{OH}^-$ . The cell was equipped with a cation exchange membrane ("Nafion 390") between the anode compartment and the center compartment to eliminate transport of  $\text{OH}^-$  and  $\text{Cl}^-$  as well as hydraulic flow of the electrolytic solution. Each compartment has a volume of about 300 cm. The alkali strength in the cathode compartment was kept constant at 2.2M NaOH during the experiment, whereas 5M NaCl ( $\text{pH} \approx 2$ ) was fed to the center compartment at the start-up time. The NaOH concentration in this room increased with time due to diffusion of  $\text{OH}^-$ . Thus the "superficial" diffusion coefficient of  $\text{OH}^-$  through the diaphragm can be evaluated.

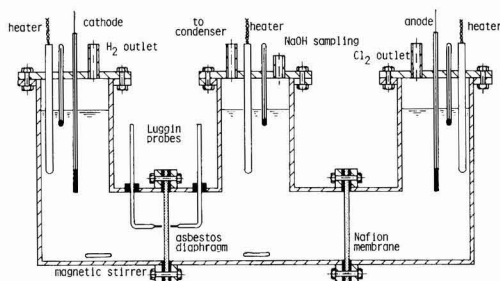


Fig. 2. A three-compartment electrolytic cell

The electrolyte level was equalized to avoid a hydraulic pressure between adjacent compartments. A reflux condenser was located on the top of each compartment to minimize the change of the solution composition by evaporation.

The anode, cathode, and reference electrodes were the same as for the cell shown in Fig. 1.

The potential drops between the Luggin probes were recorded continuously. The electrolytic solutions in the three compartments were titrated at intervals to obtain the transport of  $\text{OH}^-$ . The pH of the anolyte was unchanged during the experiments.

The diaphragm thickness was varied: 1.2, 2.4, and 4.8 mm. The material was the same as in the cell in Fig. 1. The current density ( $0 \sim 25 \text{ A/dm}^2$ ) and the solution temperature ( $30^\circ \sim 90^\circ\text{C}$ ) were varied.

## Results and Discussion

**Effects of the brine hardness.**—It was confirmed that the flow rate of brine, the IR drop, the NaOH concentration, and the current efficiency were unchanged for 10 days or more when the purified brine was fed to the electrolytic cell.

Figure 3 shows the results obtained during electrolysis of brine containing 100 mg/liter  $\text{Mg}^{2+}$  at  $10 \text{ A/dm}^2$  current density. For three days, all the data were unchanged during the electrolysis of a pure brine. When an impure brine was fed to the anode compartment of the cell, the flow rate decreased with time due to plugging of the diaphragm, which results in a rise in the caustic strength in the catholyte. Also the IR drop increased gradually. The current efficiency decreased, presumably due to the enhancement of diffusion. Similar results would be obtained with impure brines containing different amount of the hardness, either Mg or Ca.

On the other hand, the IR drop decreased, as shown in Fig. 4, when the brines containing hardness of a high concentration were electrolyzed at relatively high current densities. The caustic strength of the catholyte increased considerably. A significant reduc-

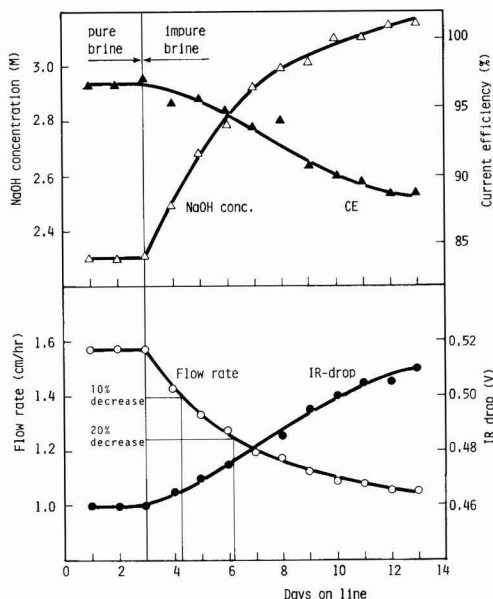


Fig. 3. Flow rate, IR drop, NaOH concentration, and current efficiency. Conditions: current density =  $10 \text{ A/dm}^2$ ;  $\text{Mg}^{2+}$  concentration = 100 mg/liter.

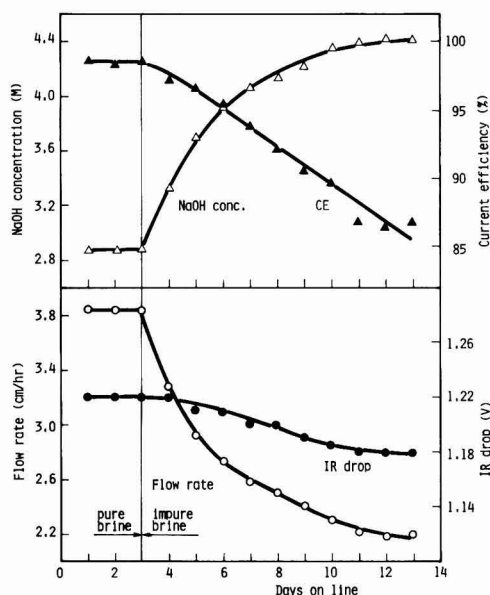


Fig. 4. Flow rate, IR drop, NaOH concentration, and current efficiency. Conditions: current density = 30 A/dm<sup>2</sup>; Mg<sup>2+</sup> concentration = 80 mg/liter.

tion in the electrical resistivity of the diaphragm is due to a rise in the caustic strength (see Table I). The brine flow, the NaOH concentration, and the current efficiency are affected by the brine hardness, but the IR drop depends on the solution composition in the diaphragm and the operating temperature rather than on the clogging of the diaphragm.

Since the flow rate of electrolyte decreases gradually with time due to plugging, and influences the cell performance, it can be used as a parameter for evaluating the effects of hardness in feed brine. In Fig. 3, for example, the flow rate decreased by 10% for 1.3 days and by 20% for 3.2 days after switching the feed brine.

The diaphragm of the laboratory cell was plugged more quickly compared to commercial cell operation since the feed brine contained Mg<sup>2+</sup> at a relatively high concentration (100 mg/liter) in this experiment. The operable period is, of course, extended when the brine hardness is decreased. Figure 5 illustrates the operable period vs. Mg content based on the accelerated test with relatively high contents of Mg in the feed brine (10 ~ 100 mg/liter). Experiments were conducted, using the galvanostatic method, at 10, 20, and 30 A/dm<sup>2</sup>. The dotted line shows the 10% decrease of the flow rate and the solid line the 20% decrease. It is clear that the operable period is reciprocally proportional to the Mg content. Plugging occurs quickly at high current densities since the flow

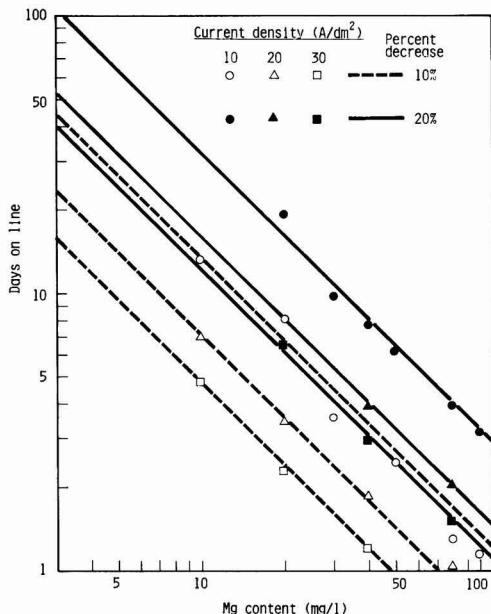


Fig. 5. Days on line vs. Mg content as functions of the percent reduction of the brine flow and the current density.

rate of the brine is large to yield a given decomposition (50%); but the product of period (d) and current (i) was almost constant (Table II). Magnesium in the feed brine precipitates as hydroxide and is collected or filtrated on the asbestos mat. Magnesium hydroxide is a typical compressible precipitate (18, 19), and hence the rate of brine flow may decrease appreciably within a short time if the pressure drop is high. Since the pressure differential through the diaphragm is small, say one tenth of the brine filter, the effect of the compressibility of precipitate on the flow rate seems to be small.

Figure 6 illustrates similar results for Ca in the feed brine, which are essentially the same as for Mg. However, it is important that the  $i \times d$  increases with an increase in the current density (see Table II), probably due to a different mechanism of plugging of the diaphragm by Ca precipitate than by Mg precipitate. Although these results were obtained by the accelerated test by electrolysis of brines containing a very high hardness concentration, they agreed

Table I. Resistivity of mixed solutions of NaCl and NaOH at 50°C

Composition (M)		Resistivity (Ω-cm)
NaCl	NaOH	
Satd. (ca. 5.1M)		3.06
2.5		3.79
2.5	2.5	2.05
5	1	2.21
4	2	2.04
3	3	1.91
2	4	1.76

Table II. Operable periods with impure brine at various current densities. Hardness: 10 mg/liter Mg<sup>2+</sup> or Ca<sup>2+</sup>

Brine impurity	Percent reduction of brine flow	Current density, $i$ (A/dm <sup>2</sup> )	Days (d)	$i \times d$
Mg	10	10	13.5	135
		20	7.0	140
		30	4.7	141
		(avg)		138.7
	20	10	32.3	323
		20	16.1	322
		30	12.0	360
		(avg)		335.0
	10	10	20.5	205
		20	15.2	304
		30	11.7	551
		(avg)		335.0
Ca	20	10	53.0	530
		20	36.0	720
		30	27.0	810

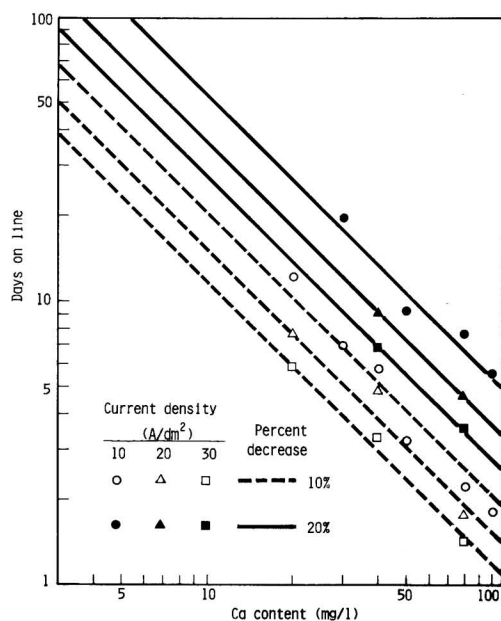


Fig. 6. Days on line vs. Ca content as functions of the percent reduction of the brine flow and the current density.

well with our plant experiences. In practical operation, the brine level is varied in accordance with the permeability of the diaphragm so as to keep the flow rate and, hence, the percent decomposition constant.

The flow rate of the brine containing 2.5 mg/liter Ca through a commercial diaphragm cell operated at 31  $A/dm^2$  would decrease by about 20% when the brine level is unchanged for 100 days of operation, which agrees with Fig. 6.

In conclusion, we believe that Fig. 5 and 6 are applicable as a guide to commercial cell operation.

The concentration distributions of Mg and Ca in the diaphragm were determined since their behavior seems to differ. A diaphragm mat after electrolysis was sliced into four equal sections (1 mm thick each). Each segment was immersed in dilute HCl (1 ~ 3N HCl depending on the amount of precipitate), and the Mg content in the filtrate was measured by atomic absorption spectrochemical analysis. Because a small amount of Mg from the chrysotile fiber is dissolved by the acid solution, this effect was calibrated for. A large amount of magnesium hydroxide is deposited in the first and the second segments on the anode side as shown in Fig. 7 since the asbestos mat became completely alkaline due to back-migration of  $OH^-$ . On the contrary, Ca was precipitated more uniformly throughout the porous mat.

Since the Mg content in the brine was high, an amount of  $Mg(OH)_2$  was deposited on the surface of diaphragm, whereas Ca did not do so. This is clearly a filtration mechanism associated with chemical reaction. According to chemical analysis, the catholyte contained 0.2 ~ 0.5 mg/liter Mg or 1.5 ~ 2.5 mg/liter Ca, due to leakage since the brine hardness was significantly higher.

MacMullin states in a private letter that "magnesium deposits on the diaphragm surface facing the anodes and penetrates to a lesser extent in the calcium. Calcium is deposited throughout the diaphragm and Hine's work indicates that at low value of calcium might be expected that calcium washed through. Mag-

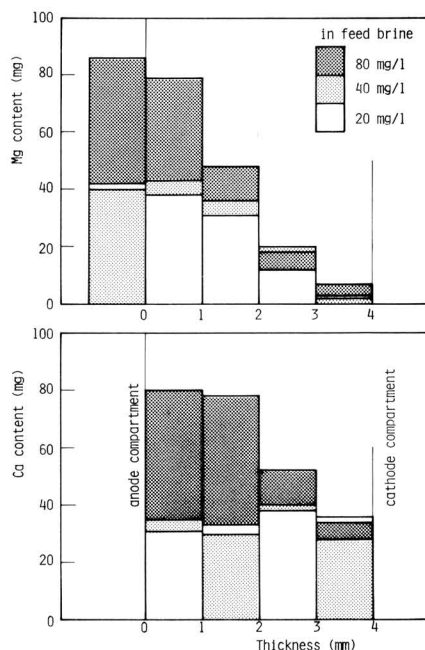


Fig. 7. Distribution of magnesium and calcium precipitates in the diaphragm (5 cm diam and 0.4 cm thick) after electrolysis.

nesium hydroxide is considerably less soluble than calcium hydroxide."

**Permeation of the brine without electrolysis.**—Experiments without electrolysis were conducted so as to separate diffusion from migration of alkali. The catholyte consisting of NaCl and NaOH was circulated between the reservoir (ca. 60 liters) and the cathode compartment to keep the solution composition constant. The hydraulic head between the anolyte and the catholyte was kept constant at 60 cm, which corresponded to the flow rate required for electrolysis of pure brine at 50% decomposition and 15  $A/dm^2$ . A small current (1  $A/dm^2$ ) was switched on briefly at certain intervals to determine the IR drop through the diaphragm.

As is shown in Fig. 8, the flow rate decreased gradually, and the electric resistance of the diaphragm became larger due to plugging, whereas the anolyte pH was unchanged during experiment. The phenomena were the same for electrolysis, but blocking was rapid because of a different distribution of precipitates in the mat as shown in Fig. 9. Both Mg and Ca deposited closely to the cathode side.

Since  $Mg^{2+}$  deposits as  $Mg(OH)_2$ , the concentration distribution of Mg indicates the  $OH^-$  distribution in the porous mat. Consequently, the experimental results would show that the contribution of migration for an overall permeation of alkali during electrolysis is significant compared with diffusion.

**Experiments with a three-compartment cell.**—An example of the results obtained with the three-compartment cell (Fig. 2) is shown in Fig. 10. The NaOH concentration in the cathode compartment and in the center compartment increased almost proportionally to the time of electrolysis.

It is well known that the diffusion flux under steady-state conditions is represented by the equation

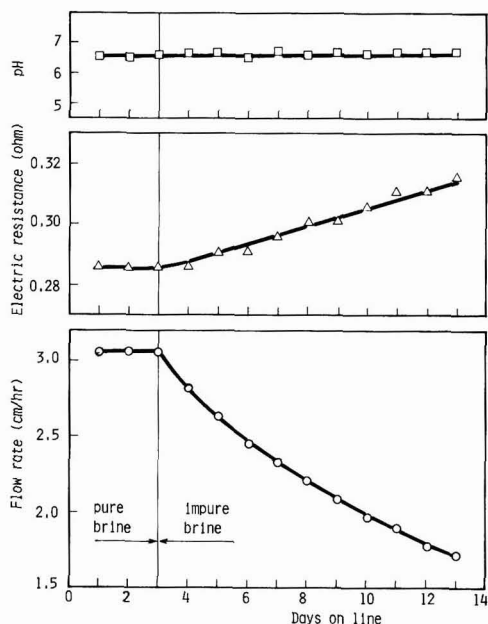


Fig. 8. Flow rate, electric resistance of the diaphragm, and the pH of anolyte at zero current.  $Mg^{2+}$  concentration = 50 mg/liter.

$$j = -DA \frac{dC}{dx} \quad [2]$$

Assume that  $dC/dx$  is equal to  $\Delta C/L$ , where  $\Delta C$  is the difference of the  $OH^-$  concentration between two sides. Thus the diffusion coefficient  $D$  can be obtained by Eq. [2].

Figure 11 shows the Arrhenius plots for diffusion. The activation energy is evaluated to be about 3 ~ 4 kcal/mol.

It is well known that the diffusion coefficient for electrolytes at room temperature is in the order of  $10^{-5}$  cm<sup>2</sup>/sec (20) whereas the experimental results in Fig. 11 show it to be in the order of  $10^{-6}$  cm<sup>2</sup>/sec because of limitations of mass transport through the diaphragm. The diffusion flux through the porous medium depends on the formation factor,  $F_c$ , of the medium

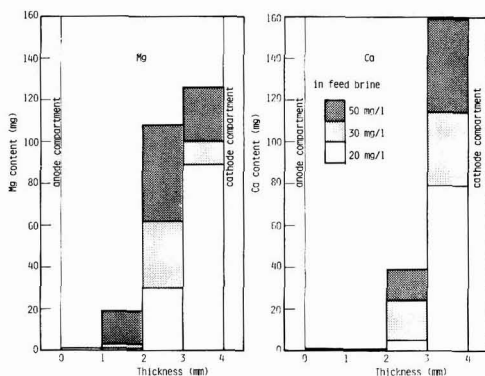


Fig. 9. Distribution of magnesium and calcium precipitates in the diaphragm (5 cm diam and 0.4 cm thick) without electrolysis.

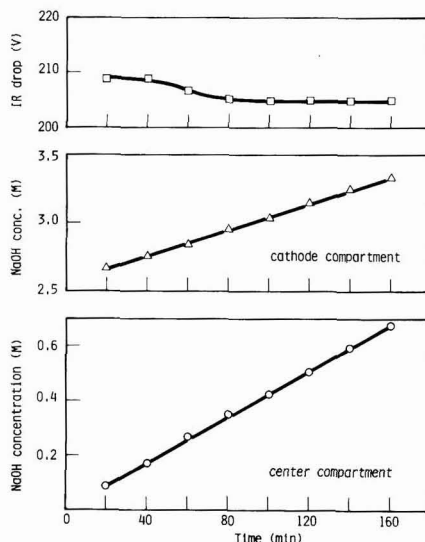


Fig. 10. NaOH concentration and IR drop as functions of the time of electrolysis. Conditions: diaphragm thickness = 2.4 mm. Temperature = 70°C. Current density = 20 A/dm<sup>2</sup>.

$$F_c = \frac{D^0}{D} = \frac{x^2}{\epsilon} \quad [3]$$

An equation for  $D^0$  vs.  $t(^{\circ}C)$  was established by the method of least squares. The data listed in the International Critical Tables (20) were employed. Thus  $D^0$  at 30°C was calculated to be  $1.88 \times 10^{-5}$  cm<sup>2</sup>/sec, compared to  $0.55 \times 10^{-5}$  cm<sup>2</sup>/sec for  $D$  (see Fig. 11).

Substituting these data into Eq. [3]

$$F_c = \frac{1.88}{0.55} \approx 3.42$$

On the other hand,  $F_c$  can also be obtained by the ratio of the specific resistances as follows (17)

$$F_c = \frac{\rho}{\rho_0} \quad [4]$$

where  $\rho$  is the superficial resistivity of the porous medium in  $\Omega \cdot \text{cm}$  and  $\rho_0$  is the resistivity, also in  $\Omega \cdot \text{cm}$ , of the electrolyte. From Fig. 10, the electric resistance of a porous diaphragm of 19.6 cm<sup>2</sup> in area and 0.4 cm

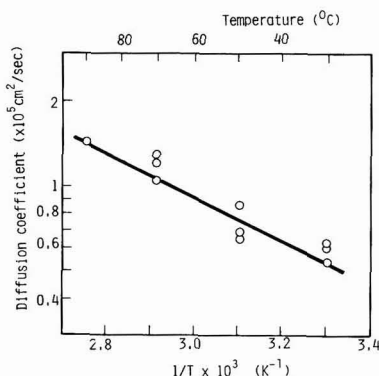


Fig. 11. Diffusion coefficient as a function of the temperature



thick filled with 2.5m NaCl is estimated to be 0.28 $\Omega$ . Therefore

$$\rho = \frac{0.28 \times 19.6}{0.4} \approx 13.72 \Omega \cdot \text{cm}$$

The specific resistance of 2.5m NaCl is 3.79  $\Omega \cdot \text{cm}$  (see Table I). Thus, we have  $F_c$  as follows

$$F_c = \frac{13.72}{3.79} \approx 3.62$$

It is clear that both calculations agree well with each other.

**Mass transport through the diaphragm.**—The mass transport problems through the diaphragm in chlor-alkali cells have been investigated by many authors [see Ref. (17)].

Stender *et al.* have calculated the mass transport of  $\text{OH}^-$ ,  $j_{\text{OH}}$  (24)

$$j_{\text{OH}} = -D \frac{dC}{dx} + UC \quad [5]$$

$$U = \frac{F}{RT} \frac{D}{\kappa} i - v \quad [6]$$

Integrating Eq. [5] with the boundary conditions

$$C = C^0 \quad \text{at} \quad x = 0 \quad (\text{at cathode side})$$

$$\text{and} \quad C = 0 \quad \text{at} \quad x = \delta \quad (\text{at anode side})$$

Equations [7] and [8] are obtained

$$j_{\text{OH}} = \frac{C^0 U}{1 - \exp\left(-\frac{U\delta}{D}\right)} \quad [7]$$

and

$$\frac{C}{C^0} = \frac{1 - \exp\left(-\frac{U}{D}(\delta - x)\right)}{1 - \exp\left(-\frac{U}{D}\delta\right)} \quad [8]$$

where the thickness of the alkaline zone  $\delta$  is assumed to be equal to the thickness of diaphragm  $L$ . Also the current efficiency for  $\text{OH}^-$  is

$$\text{C.E.}(\%) = \frac{1}{1 + \frac{U}{v} \left(1 - \exp\left(-\frac{U\delta}{D}\right)\right)^{-1}} \times 100 \quad [9]$$

When a thin diaphragm is employed,  $U\delta \ll D$ . Therefore

$$\text{C.E.}(\%) = \frac{1}{1 + \frac{D}{v\delta}} \times 100 \quad [10]$$

When  $U > 0$ , the  $C$  vs.  $x$  curves become convex as shown in Fig. 12 (see Eq. [8]). When  $U < 0$ , on the other hand, the curves are concave. Assume that  $D = 10^{-5} \text{ cm}^2/\text{sec}$ ,  $\delta = 0.5 \text{ cm}$ ,  $v = 10^{-3} \text{ cm/sec}$ ,  $\kappa = 0.5 \text{ mho/cm}$ ,  $T = 373 \text{ K}$ , and  $i = 0.2 \text{ A/dm}^2$ , therefore for practical operation, we have

$$\frac{U\delta}{D} \approx -7$$

Consequently, the  $C$  vs.  $x$  curves are clearly concave, and the reduction of current efficiency is controlled by migration and diffusion of  $\text{OH}^-$ .

The flux of alkali through a unit area of the diaphragm ( $A = 1$  in Eq. [2]) in a three-compartment cell,  $j_{\text{OH}}$ , can be represented by the sum of the diffusion flux,  $j_{\text{OH}}(d)$ , and the migration flux,  $j_{\text{OH}}(m)$ , since there is no flow of brine

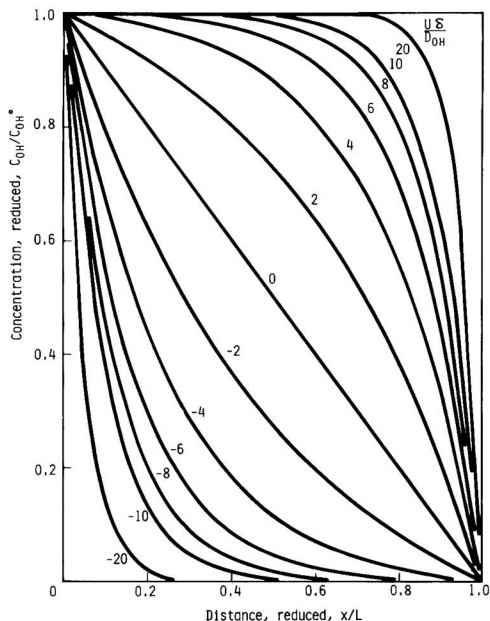


Fig. 12. Distribution of the NaOH concentration in the diaphragm

$$j_{\text{OH}} = j_{\text{OH}}(d) + j_{\text{OH}}(m) \quad [11]$$

$$j_{\text{OH}}(d) = -D \frac{dC}{dx} \quad [12]$$

$$j_{\text{OH}}(m) = \frac{F}{RT} \frac{D}{\kappa} C i = -\frac{F}{RT} D C \frac{d\phi}{dx} \quad [13]$$

Assuming that

$$\frac{dC}{dx} = \frac{C}{\delta} \quad \text{and} \quad \frac{d\phi}{dx} = \frac{\Delta\phi}{\delta}$$

we have

$$K = \frac{j_{\text{OH}}(m)}{j_{\text{OH}}(d)} \approx \frac{F}{RT} \Delta\phi \quad [14]$$

where  $K$  is the ratio of  $j_{\text{OH}}(m)$  to  $j_{\text{OH}}(d)$ . The diffusion flux  $j_{\text{OH}}(d)$  can be obtained by experiment without electrolysis, whereas the  $\text{OH}^-$  flux during electrolysis is the sum of  $j_{\text{OH}}(d)$  and  $j_{\text{OH}}(m)$ . Thus  $j_{\text{OH}}(m)$  can be evaluated. Factor  $K$ , calculated by Eq. [14], is listed in Table III and is in good agreement with experiment. The  $K$  is proportional to the  $IR$  drop, but the line in Fig. 13 is independent of other factors.

Since the  $IR$  drop through the diaphragm in practical cells is 0.3 ~ 0.4V,  $j_{\text{OH}}(m)$  is one order of magnitude greater than  $j_{\text{OH}}(d)$ . Therefore,  $j_{\text{OH}}(m)$  must be minimized to improve the current efficiency. Operation at high temperatures is feasible for this purpose because  $D$  and  $\kappa$  increase. Use of a thin diaphragm decreases  $K$  since  $j_{\text{OH}}(d)$  increases, whereas  $j_{\text{OH}}(m)$  remains constant because  $\Delta\phi/\delta$  is unchanged.

At high current densities, both  $\Delta\phi$  and  $K$  become large. On the other hand, the flow rate of the brine is increased proportionally to the current density to keep the brine decomposition constant. Since the effect of the flow rate on the current efficiency is larger than that of other factors under operating conditions, operation at high current densities, say 25 ~ 35 A/dm<sup>2</sup>, is desirable to improve the current efficiency.

Table III. Mass transfer of OH<sup>-</sup> through the diaphragm.  
Diaphragm thickness = 2.4 mm (an example).

Temp (°C)	Current density (A/dm <sup>2</sup> )	IR drop (mV)	OH <sup>-</sup> flux $j_{OH}(m) + j_{OH}(d)$ (g-ions/liter hr)	$j_{OH}(m)/j_{OH}(d)$	
				Experi- mental	Calcu- lated
30	0		0.015		
	1	26	0.025	0.67	1.0
	5	95	0.065	3.3	3.6
50	0		0.020		
	1	18	0.030	0.50	0.65
	10	80	0.080	3.0	2.9
70	0		0.120	5.0	5.4
	1	14	0.030		
	5	60	0.090	0.17	0.47
90	10	110	0.135	2.0	2.0
	15	158	0.180	3.5	3.7
	20	205	0.255	5.0	5.4
90	0		0.035	7.7	6.9
	1	11	0.040		
	5	50	0.085	0.14	0.35
10	10	100	0.135	1.4	1.6
	15	138	0.190	2.9	3.2
	20	190	0.260	4.4	4.4
25	20	190	0.260	6.4	6.1
	25	235	0.290	7.3	7.5

### Conclusion

The performance of diaphragm-type chlor-alkali cells is related closely to the transport phenomena of OH<sup>-</sup> and the physicochemical properties of the diaphragm. The overall mass-transfer through the diaphragm is composed of the diffusion flux, the migration flux, and the hydraulic flow. Of these, diffusion and migration have been discussed in this paper.

The concentration distribution of alkali in the diaphragm without electrolysis differs greatly from that with electrolysis because the migration flux is significantly large. Also the OH<sup>-</sup> concentration distribution varies with the current density for the same reason.

Hardness in the feed brine deposits in the porous diaphragm and affects the electrical conduction and mass transport through the diaphragm. Cell performance as measured by the current efficiency and the cell voltage becomes less favorable as the diaphragm is plugged. The limits of hardness in the feed brine have been discussed with the results obtained by an accelerated test involving electrolysis of brines containing high hardness concentrations.

### Acknowledgments

The authors wish to express many thanks for useful discussions with Dr. W. C. Gardiner and Mr. R. B. MacMullin. Also thanks are due to M. Nozaki, Y. Takahashi, M. Inosaka, and K. Nakamoto for their efforts on experimental work and discussion.

Manuscript submitted March 20, 1981; revised manuscript received June 9, 1981. This was Paper 411 presented at the Minneapolis, Minnesota, Meeting of the Society, May 10-15, 1981.

Any discussion of this paper will appear in a Discussion Section to be published in the June 1982 JOURNAL. All discussions for the June 1982 Discussion Section should be submitted by Feb. 1, 1982.

Publication costs of this article were assisted by F. Hine.

### LIST OF SYMBOLS

A	area (cm <sup>2</sup> )
C	concentration (mols/cm <sup>3</sup> )
C°	concentration of OH <sup>-</sup> in catholyte (mols/cm <sup>3</sup> )
C.E.	current efficiency with respect to OH <sup>-</sup> (%)
D	diffusion coefficient in diaphragm (cm <sup>2</sup> /sec)
D°	diffusion coefficient in solution (cm <sup>2</sup> /sec)
d	days on line (days)
F	Faraday's constant (23,060 kcal/g-equiv. · V)
F <sub>c</sub>	formation factor
i	current density (A/cm <sup>2</sup> )
j	flux (mols/cm <sup>2</sup> · sec)
j <sub>OH</sub>	overall flux of OH <sup>-</sup> (mols/cm <sup>2</sup> · sec)
j <sub>OH</sub> (d)	diffusion flux of OH <sup>-</sup> (mols/cm <sup>2</sup> · sec)
j <sub>OH</sub> (m)	migration flux of OH <sup>-</sup> (mols/cm <sup>2</sup> · sec)
K	ratio j <sub>OH</sub> (m)/j <sub>OH</sub> (d)
L	thickness of diaphragm (cm)
R	gas constant (1.987 cal/mol · K)
T	temperature (K)
U	see Eq. [6] (cm/sec)
v	flow rate (cm/sec)
x	distance (cm)
δ	thickness of alkaline zone (cm)
ε	void fraction
κ	electrical conductivity (mho/cm)
ρ	electric resistivity of diaphragm (Ω · cm)
ρ <sub>0</sub>	electric resistivity of electrolyte (Ω · cm)
φ	potential (V)
Δφ	potential difference (V)
χ	tortuosity

### REFERENCES

1. F. Hine, N. Yokota, and T. Takasaki, *Int. Chem. Eng.*, **17** (1), 1 (1977).
2. Belgian Pat. 710,551; British Pat. 6490/67.
3. R. W. Fenn and A. D. Babinsky, Paper 340 presented at The Electrochemical Society Meeting, Toronto, Ontario, Canada, May 11-16, 1975.
4. D. J. Harvey and J. R. Fowler, *Chem. Eng. Progr.*, **72** (4), 47 (1976).
5. M. P. Grotheer and C. J. Harke, in "Chlorine Bicentennial Symposium," T. C. Jeffery, P. A. Dana, and H. S. Holden, Editors, p. 209, The Electrochemical Society Softbound Proceedings Series, Princeton, NJ (1974).
6. C. A. Melendres, Paper 345 presented at The Electrochemical Society Meeting, Toronto, Ontario, Canada, May 11-16, 1975.
7. D. W. Carnell and C. R. S. Needes, Paper 260 presented at The Electrochemical Society Meeting, Boston, Massachusetts, May 11-16, 1979.
8. W. W. Carlin and W. B. Darlington, Paper 261 presented at The Electrochemical Society Meeting, Boston, Massachusetts, May 11-16, 1979.
9. I. Malkin and J. R. Brannan, Paper 262 presented at The Electrochemical Society Meeting, Boston, Massachusetts, May 11-16, 1979.
10. M. C. M. Man and A. C. C. Tseung, Paper 263 presented at The Electrochemical Society Meeting, Boston, Massachusetts, May 11-16, 1979.
11. S. Matsura, Y. Ozaki, K. Motani, Y. Ohhashi, and Y. Onoue, Paper 417 presented at The Electrochemical Society Meeting, St. Louis, Missouri, May 11-16, 1980.
12. F. Hine, M. Yasuda, R. Nakamura, and T. Noda,

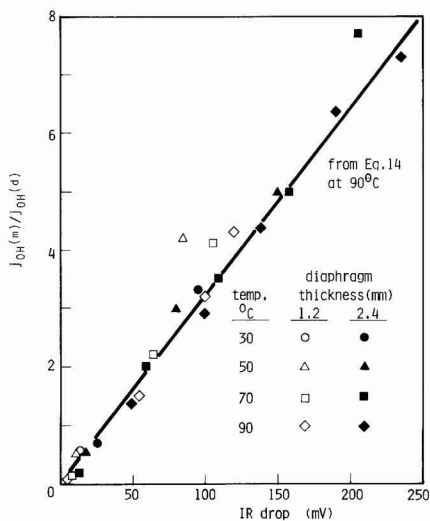


Fig. 13. The ratio of the migration flux to the diffusion flux vs. IR-drop curve under various conditions of the diaphragm thickness and the solution temperature.

- This Journal* 122, 1185 (1975).
13. F. Hine and T. Sugimoto, Paper 459 presented at The Electrochemical Society Meeting, Seattle, Washington, May 21-26, 1978.
  14. F. Hine and K. Murakami, *This Journal*, 127, 292 (1980).
  15. F. Hine and K. Murakami, *This Journal*, 128, 64 (1981).
  16. F. Hine, M. Yasuda, and T. Tanaka, *Electrochim. Acta*, 22, 429 (1977).
  17. F. Hine, *Soda and Chlorine (Japanese)*, 31, 219 (1980).
  18. F. Hine, S. Yoshizawa, and S. Okada, *Kogyo Kagaku Zasshi (J. Chem. Soc. Jpn., Ind. Chem. Section)*, 62, 769, 773 (1959).
  19. F. Hine, T. Sugimori, S. Yoshizawa, and S. Okada, *ibid.*, 62, 955 (1959).
  20. "International Critical Tables," Vol. 5, p. 67 (1929).
  21. R. B. MacMullin and G. A. Muccini, *AIChE J.*, 2, 393 (1956).
  22. K. S. Spiegler, *This Journal*, 113, 161 (1966).
  23. F. A. L. Dullien, *AIChE J.*, 21, 820 (1975).
  24. V. V. Stender, O. S. Ksenzhek, and V. N. Lazarev, *Zh. Prikl. Khim.*, 40, 1293 (1967). English translation was supplied by R. B. MacMullin.

## Growth of Thick Anodic Oxide Films on Nickel in Borate Buffer Solution

B. MacDougall\* and M. J. Graham

*Division of Chemistry, National Research Council of Canada, Ottawa, Ontario, Canada K1A 0R9*

### ABSTRACT

Anodic galvanostatic charging of nickel in pH 7.65 borate buffer solution produces a finely porous oxide film which is distinctly different from the passive film of NiO. The porous film which is probably NiOOH can grow to thicknesses in excess of 1000 Å. It is reduced to a lower oxidation state during galvanostatic reduction, giving a distinct cathodic potential arrest. The oxide, however, remains on the surface during the cathodic treatment and reapplication of the anodic charging current results in an anodic arrest that is almost the mirror image of the cathodic arrest. The reversible conversion charge increases with increasing time of polarization in the O<sub>2</sub> evolution region, in conjunction with an increase in porous film thickness as determined by x-ray emission and Auger electron spectroscopies. In fact, the conversion charge is a close monitor of porous film thickness over a wide range of thicknesses and has been used to study film growth kinetics as a function of temperature, charging rate, and prior electrode treatment. The kinetics of porous oxide growth are interpreted in terms of an outer porous film growing on top of an inner compact film, the latter probably being the passive film. It is suggested that breakdown and repair events in the compact inner film generate the Ni<sup>2+</sup> which is incorporated into the porous film, and that the stability of the passive film thus determines the growth rate of the porous film. This model explains the influences of temperature and electrode surface condition on oxide growth rate as well as the existence of breakaway-type kinetics and its dependence on charging rate.

The anodic oxidation of nickel in the passive potential region has been extensively studied in a variety of electrolytes, e.g., borate buffer solution (1-3) and neutral and acid sulfate solutions (1, 4-22). The composition of the passive oxide film formed in neutral and acid solutions is generally thought to be NiO with a maximum thickness reported anywhere from 12 Å (4, 13, 23, 24) to 18 Å (1, 9). In borate electrolyte, considerably thicker oxide films can be grown at potentials in the oxygen evolution region (1-3, 25, 26). The oxide formed in this potential region is a higher oxide of nickel, probably NiOOH (26). Unlike the passive film of NiO, this oxide gives a distinct galvanostatic reduction arrest which is believed to be associated with its conversion to a lower oxide of nickel, e.g., Ni(OH)<sub>2</sub> (or NiO). Subsequent anodic charging of the lower oxide also gives a distinct potential arrest as the lower oxide converts back again to the higher oxide (1, 27). This electrochemical conversion reaction is similar to that proposed for charging and discharging the nickel electrode in the nickel alkaline battery (27, 28), and while extensive research has been published in this area [cf., for example, (29)], little work has appeared concerning the kinetics and

mechanism of anodic growth of thick conversion oxide films on nickel surfaces by direct oxidation of the metal. The present investigation considers the factors influencing the growth kinetics of thick anodic oxide films on nickel in pH 7.65 borate buffer solution, and a model will be suggested for the mechanism of film growth.

### Experimental

Polycrystalline specimens, 1 × 2.5 × 0.02 cm thick, were prepared from Materials Research Corporation zone-refined nickel sheet of 99.996% purity (4). They were degreased with benzene, chemically polished, electropolished for 2 min at 23°C in a 57 volume percent sulfuric acid solution at 0.5 A cm<sup>-2</sup>, and then annealed at 800°C in a vacuum of 10<sup>-8</sup> Torr. The specimens were again electropolished immediately before use in an experiment. Potentials quoted in this paper are referred to the saturated calomel electrode which is 0.245V with respect to the standard reversible hydrogen electrode. Electropolished nickel electrodes were galvanostatically anodized without cathodic reduction of the prior oxide film. Solutions were de-aerated pH 7.65 borate buffer, and were analyzed for Ni<sup>2+</sup> by carbon rod atomic absorption spectroscopy, the lower limit of detection by this method being 0.2 μg cm<sup>-2</sup> (sample area = 5 cm<sup>2</sup>; cell volume = 50

\* Electrochemical Society Active Member.

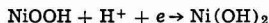
Key words: electrode, passivity, oxidation, conversion, defects.

ml). X-ray emission (30, 31) and Auger electron spectroscopies (Physical Electronics Incorporated Model 590) were used to determine oxide film thicknesses.

### Results

#### Cathodic and anodic galvanostatic charging profiles.—

Figure 1 shows the cathodic and anodic charging profiles for electropolished nickel electrodes anodized for various times at  $80 \mu\text{A cm}^{-2}$  in the oxygen evolution region [potentials  $>0.95\text{V}$  (25, 26)]. Anodic charging generates a species which, when the charging polarity is switched from anodic to cathodic, undergoes reduction and gives a distinct potential arrest at  $\sim 0.75\text{V}$ . When reduction of this species is complete, the potential rapidly shifts into the hydrogen evolution region. Upon immediate reapplication of the anodic charging current, an anodic arrest occurs at about the same potential as the cathodic arrest; the cathodic and anodic arrest charges are equivalent. Oxides formed at potentials in the passive region do not give rise to this reversible arrest since the  $\sim 12\text{\AA}$  thick passive film of NiO (4, 13, 23, 24) is inert to both conversion to a higher oxide of nickel and to cathodic reduction. During anodic charging in the oxygen evolution region, a very finely porous (26) higher oxide of nickel is generated, perhaps NiOOH as has been previously suggested by a number of workers (1, 3, 27). The charge-consuming reaction would thus be associated with interconversion of the nickel ion in the oxide between the  $3+$  and  $2+$  oxidation states e.g., by a reaction such as



The term "conversion charge" will denote the cathodic arrest charge associated with this reaction.

To investigate the kinetics of the conversion reaction, a constant quantity of higher oxide was formed (e.g., by anodizing at  $80 \mu\text{A cm}^{-2}$  for 24 hr at  $25^\circ\text{C}$ ) and this was reduced and reoxidized at charging rates of 4, 80, and  $200 \mu\text{A cm}^{-2}$ . The conversion charge was constant ( $6.6 \pm 0.3 \text{ mC cm}^{-2}$ ) at all three charging rates indicating that the conversion reaction is a rapid, reversible process under activation rather than diffusion control. A fixed quantity of porous oxide gives the same conversion charge at all electrolyte temperatures from  $5^\circ$  to  $45^\circ\text{C}$  so that the kinetic results obtained for growth of the conversion oxide at different temperatures may be directly compared.

**Oxide film examination.**—The degree of hydration of oxides in the above conversion reaction is still open to question. Electrodes removed from solution in the oxidized state were blue-black in color, but this color-

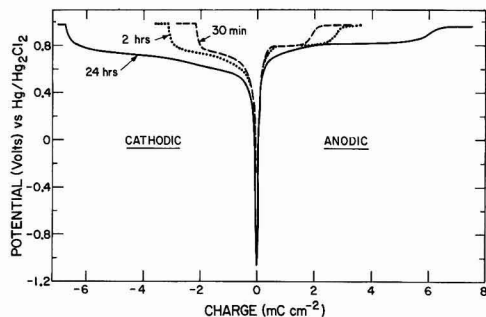


Fig. 1. Cathodic and anodic galvanostatic charging profiles, at  $80 \mu\text{A cm}^{-2}$ , for nickel electrodes anodized at  $80 \mu\text{A cm}^{-2}$  for various times in the  $\text{O}_2$  evolution region: (---) 30 min; (···) 2 hr; (—) 24 hr. The charging current was switched from cathodic to anodic as soon as the potential shifted into the  $\text{H}_2$  evolution region (i.e.,  $-1.06\text{V}$ ); for comparison, the profiles are centered at the point of transition from cathodic to anodic charging.

ation slowly disappeared and the oxide film eventually became transparent. (This is exactly what happens when an oxidized electrode is cathodically reduced in solution, i.e., the dark color becomes less distinct during the cathodic conversion arrest and at the end of the arrest the film is transparent.) Because the films change with time, difficulties are presented in attempting phase identification of the oxide in the oxidized state; reflection electron diffraction of a thick oxide film did confirm, however, the presence of  $\beta\text{-NiOOH}$  in addition to NiO. Oxide films in the reduced state examined by electron diffraction and Auger spectroscopy appeared to be NiO rather than  $\text{Ni(OH)}_2$ . It may be, though, that the porous film in the reduced state is  $\text{Ni(OH)}_2$ , but that this species dehydrates in the vacuum system, i.e.,  $\text{Ni(OH)}_2 \rightarrow \text{NiO} + \text{H}_2\text{O}$ . In any event, the conversion reaction of  $\text{Ni}^{3+} \rightarrow \text{Ni}^{2+}$  involves a 1-electron transfer, and assuming a current efficiency of 100%, the amount of oxide can be estimated from the conversion charge. The conversion charge increases with increasing time in the oxygen evolution region (Fig. 1), and thus the measured conversion charge can be used to determine the kinetics of porous oxide growth, provided that the relationship between conversion charge and quantity of porous oxide is constant over a wide range of film thicknesses. To check this, electrodes anodized at  $80 \mu\text{A cm}^{-2}$  for 30 min and 24 hr (at  $25^\circ\text{C}$ ) were removed from the solution and analyzed for oxygen content. The conversion charges for the 30 min and 24 hr treatments were  $2.2 \text{ mC cm}^{-2}$  and  $6.6 \text{ mC cm}^{-2}$ , respectively, compared with an increase in oxygen content (as determined by x-ray and Auger techniques) from  $0.54 (\pm 0.05)$  to  $1.27 (\pm 0.13) \mu\text{g oxygen cm}^{-2}$  (25). This increase in oxygen thus correlates reasonably well with the conversion charge increase. The relationship holds even for very thick films ( $\approx 10 \mu\text{g oxygen cm}^{-2}$ ), indicating that the oxide growth kinetics can be determined from galvanostatic charging experiments.

**Kinetics of porous oxide growth.**—Figures 2 and 3 show the increase in conversion charge with time of anodic charging at 4, 80, and  $200 \mu\text{A cm}^{-2}$  for electrolyte temperatures of  $5^\circ$ ,  $25^\circ$ , and  $45^\circ\text{C}$ . It is immediately evident that the temperature at which the oxide is grown plays a much more important role than

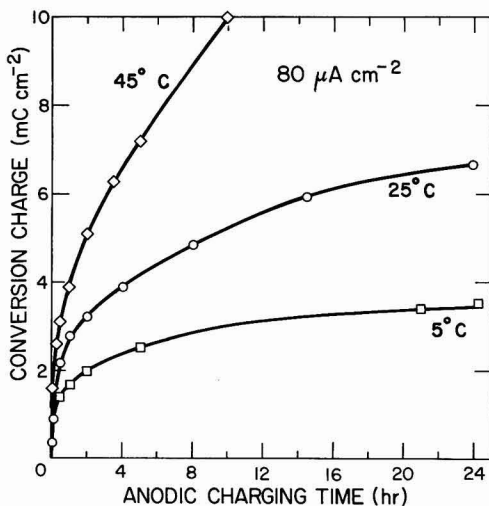


Fig. 2. Increase in conversion charge with time of anodic charging at  $80 \mu\text{A cm}^{-2}$  at various temperatures: (—□—)  $5^\circ\text{C}$ ; (—○—)  $25^\circ\text{C}$ ; (—◇—)  $45^\circ\text{C}$ .

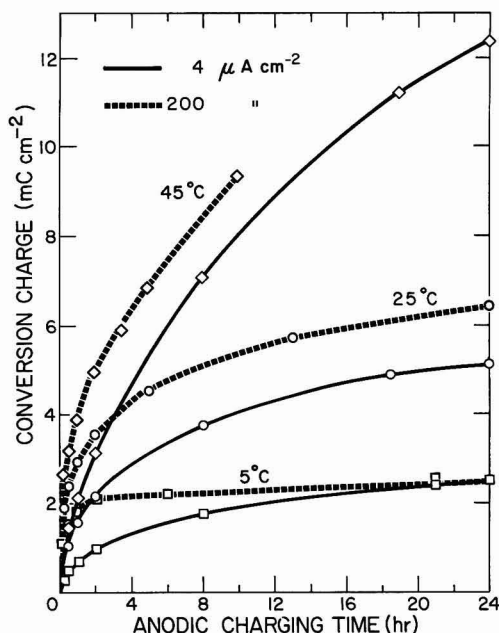


Fig. 3. Increase in conversion charge with time of anodic charging at 4 (—) and 200 (---)  $\mu\text{A cm}^{-2}$  at various temperatures. (—□—) 5°C; (—○—) 25°C; (—◇—) 45°C. The conversion charge was determined by cathodic charging at 80  $\mu\text{A cm}^{-2}$ .

the anodizing current. Obviously, the current efficiency for oxide growth is higher at the lower charging rate, but the values are  $\leq 1\%$  at all charging rates and temperatures with most of the charge being consumed by oxygen evolution (25). When the film is sufficiently thick, breakaway-type kinetics are observed with the oxide growth rate increasing rapidly (Fig. 4 and 5). It is also seen in Fig. 5 that oxide growth is much faster on etched nickel (electropolished and then etched for 60 sec in 5%  $\text{HNO}_3$ ) than on electropolished nickel.

### Discussion

Previous electrochemical and Auger results suggest that the conversion oxide has a porous structure, and that the porosity is on too fine a scale to be detected by electron microscopy (25). It is difficult to explain the conversion charge kinetic curves (Fig. 2-5), where the rate slows and then increases dramatically, on the basis of growth processes of the porous oxide alone. A more reasonable model of the oxidation

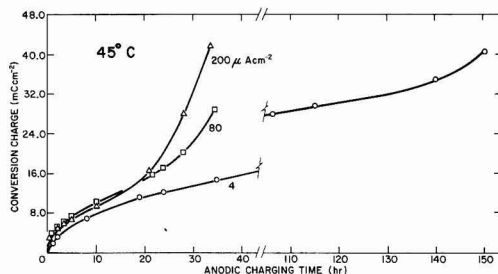


Fig. 4. Increase in conversion charge with time of anodic charging at 45°C using different charging rates: (—○—) 4  $\mu\text{A cm}^{-2}$ ; (—□—) 80  $\mu\text{A cm}^{-2}$ ; (—△—) 200  $\mu\text{A cm}^{-2}$ .

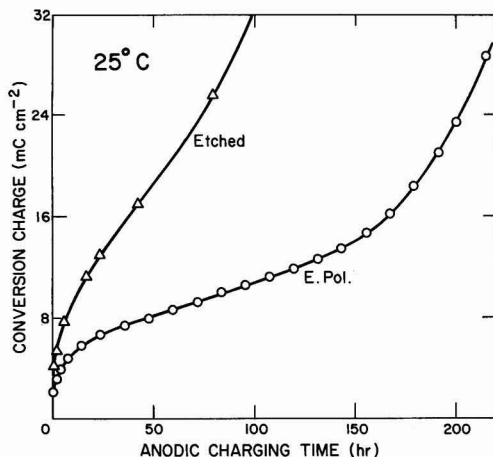
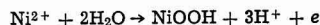


Fig. 5. Increase in conversion charge with time of anodic charging at 80  $\mu\text{A cm}^{-2}$  at 25°C for electropolished nickel (—○—) and etched nickel (—△—). Etching was in 5%  $\text{HNO}_3$  for 60 sec.

mechanism would involve the presence of a compact oxide film beneath the outer porous film. It is suggested that the compact film is the 9-12 Å passive film of  $\text{NiO}$  as illustrated schematically in Fig. 6. It is known from previous work that the passive oxide has a defect character and the local breakdown of the film, in the passive potential region, generates  $\text{Ni}^{2+}$  in solution. In the oxygen evolution potential region, the  $\text{Ni}^{2+}$  arising from passive film breakdown could be oxidized to a higher oxide of nickel and this would give rise to the porous film, perhaps by the reaction



An alternative reaction would be



which has a reversible potential of 0.2V (vs.  $\text{Hg}_2\text{Cl}_2$ ). In the proposed model for porous film formation, growth would be controlled solely by the frequency of breakdown events in the passive film which would depend on the stability of the passive film as well as

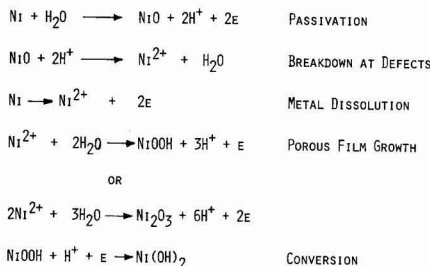
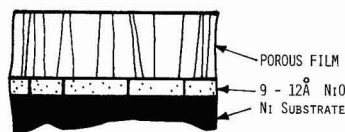


Fig. 6. Schematic illustration of the growth of the thick porous film on top of the compact passive film of  $\text{NiO}$ . The reaction sequence indicates the possible mechanisms for growth and conversion of the porous film.



the electrolyte environment. It is known that the state of perfection of the passive film increases and the anodic corrosion current (due mainly to  $\text{Ni} \rightarrow \text{Ni}^{2+} + 2\text{e}$ ) decreases with time of anodization after a potential step into the passive region, the decrease being rapid at first and then quite slow (24). It may be that the initial rapid decrease of anodic current with time correlates with the initial slowing down of the oxide growth kinetics in the oxygen plateau region (Fig. 2-4). That is, as the passive film becomes more perfect, less  $\text{Ni}^{2+}$  is generated so less porous film can form. The linear-type kinetics (cf. Fig. 5, E. Pol.) could be associated with the passive film reaching a virtual steady state of perfection and therefore having a constant breakdown frequency, after some time of anodization in the oxygen region. This would correlate with the almost constant corrosion current in the passive potential region after long times of potentiostatic holding. The results then suggest that the changes in the corrosion current with time of potentiostatic holding in the passive potential region are similar to the changes in the nickel dissolution current in the oxygen plateau region during galvanostatic oxidation.

The breakaway kinetics (Fig. 4 and 5), observed after the porous film has reached a significant thickness, can be explained by a localized pH decrease at the base of the porous film, i.e., in the vicinity of the passive film. This arises because the oxidation reaction generates protons which must diffuse out from the body of the porous film for pH equilibration. When the porous film is too thick, the protons are not able to diffuse out rapidly enough for pH equilibration, so that a local decrease in pH occurs [cf. (32)-(35)]. The frequency of breakdown events at the passive film is highly dependent on the solution pH with the result that a decrease in pH causes this frequency to increase. This results in more rapid generation of  $\text{Ni}^{2+}$  and consequently a more rapid growth of the porous film. Growth kinetics at 4, 80, and  $200 \mu\text{A cm}^{-2}$  support this interpretation (Fig. 4), breakdown occurring at a lower porous film thickness at  $200 \mu\text{A cm}^{-2}$  since the higher charging current is generating a more rapid, local pH change. At  $4 \mu\text{A cm}^{-2}$ , a much thicker oxide film is required before breakaway-type kinetics are observed.

This model of porous oxide film growth readily explains the previously noted thickness anisotropy<sup>1</sup> from grain to grain on polycrystalline nickel electrodes (25). It has been established in a number of earlier papers that the defect character of the passive oxide film is highly dependent on the crystal orientation of the substrate (23), the passive film on some grains being more defective than on others. Thus, with a polycrystalline sample, those grains with the most defective passive film will have the highest growth rates for the porous film. The rate of the porous film growth on a particular metal grain is therefore a monitor of the stability of the passive film on that grain.

The proposed model also explains the observations regarding temperature, anodic charging rate, and the influence of surface pretreatment on porous oxide growth kinetics. With increasing temperature, the porous film growth rate increases dramatically (Fig. 2 and 3). To quantify this increase with increasing electrolyte temperature, the extensive linear-type growth region can be used (cf. for example, Fig. 5). Growth kinetics for the porous film in this region are (charging rate  $80 \mu\text{A cm}^{-2}$ ):  $0.6\text{A hr}^{-1}$  at  $25^\circ\text{C}$  and  $5.5\text{A hr}^{-1}$  at  $45^\circ\text{C}$ . This compares with an increase of the corrosion current in the passive potential region from  $0.01 \mu\text{A cm}^{-2}$  at  $25^\circ\text{C}$  to  $0.1 \mu\text{A cm}^{-2}$  at

$45^\circ\text{C}$ . Thus, the increase in the porous film growth rate with temperature follows the increase in current measured in the passive potential region, a result to be expected if the dual oxide model is correct. The observation that the anodic charging rate has little influence on the growth kinetics of the porous film is also to be expected since the anodic charging current should have little or no influence on the defect character of the underlying passive film. With increased anodic current, the oxygen plateau potential shifts in the anodic direction and the extra charge is consumed by oxygen evolution. The influence of surface pretreatment on the growth rate of porous films (Fig. 5) is understandable in terms of the much less stable prior oxide film on etched nickel (36). Since the prior oxide is less stable, the anodic corrosion current is higher with more  $\text{Ni}^{2+}$  available for incorporation into (and therefore growth of) the porous film. In the proposed model where the passive film persists beneath the porous oxide, any factor which increases the corrosion rate of the passive film also increases the growth rate of the porous film.

### Summary

Anodic galvanostatic charging of nickel in pH 7.65 borate buffer solution produces a finely porous oxide film whose thickness is dependent on the time of charging and the electrolyte temperature. The anodically formed porous film is probably  $\beta\text{-NiOOH}$  which undergoes a facile cathodic reduction to a lower oxidation state, likely  $\text{Ni}(\text{OH})_2$ . The conversion from the higher to lower oxide, and vice versa, gives a distinct galvanostatic arrest structure; the arrest charge is related to the quantity of porous oxide and can thus be used to study the kinetics of porous film growth. The kinetics are explained by a model which suggests that the compact passive film persists beneath the porous film and controls the latter's growth. Factors which increase the corrosion rate of the passive film (e.g., increasing temperature and different surface pretreatment) also increase the growth rate of the porous film, suggesting that breakdown and repair events in the underlying passive film provide  $\text{Ni}^{2+}$  which is anodically incorporated into the porous film. In fact, the measured corrosion current of the passive film appears to directly determine the growth rate of the porous film.

Manuscript submitted Feb. 23, 1981; revised manuscript received ca. June 5, 1981.

Any discussion of this paper will appear in a Discussion Section to be published in the June 1982 JOURNAL. All discussions for the June 1982 Discussion Section should be submitted by Feb. 1, 1982.

Publication costs of this article were assisted by the National Research Council of Canada.

### REFERENCES

1. J. L. Ord, J. C. Clayton, and D. J. DeSmet, *This Journal*, **124**, 1714 (1977); also J. Ord in "Proceedings of the Fourth International Symposium on Passivity," R. P. Frankenthal and J. Kruger, Editors, p. 273, Airlie, Virginia, Published by The Electrochem. Society, Princeton, NJ (1978).
2. M. Okuyama and S. Haruyama, *Corros. Sci.*, **14**, 1 (1974).
3. N. Sato and K. Kudo, *Electrochim. Acta*, **19**, 461 (1974).
4. B. MacDougall and M. Cohen, *This Journal*, **121**, 1152 (1974).
5. N. Sato and G. Okamoto, *ibid.*, **110**, 605 (1963).
6. N. Y. Bune, *Zasch. Met.*, **3**, 50 (1967).
7. A. Jouanneau, M. Keddam, and M. C. Petit, *Electrochim. Acta*, **21**, 287 (1976).

<sup>1</sup> This thickness anisotropy is also evident during cathodic charging of a thick, dark porous film; the oxide on some grains becomes transparent long before that on other grains.

8. R. M. Latanision and H. Opperhauser, *Corrosion*, **27**, 509 (1971).
9. T. Dickinson, A. F. Povey, and P. M. A. Sherwood, *J. Chem. Soc. Faraday Trans. I*, **73**, 327 (1977).
10. P. Marcus, J. Oudar, and I. Olefiard, *J. Microsc. Spectrosc. Electron.*, **4**, 63 (1979).
11. T. Ohtsuka and K. E. Heusler, *J. Electroanal. Chem. Interfacial Electrochem.*, **100**, 319 (1979).
12. J. Siejka, C. Cherki, and J. Yahalom, *This Journal*, **119**, 991 (1972); also *Electrochim. Acta*, **17**, 161 (1972).
13. B. MacDougall and M. Cohen, *This Journal*, **123**, 191 (1976); also **124**, 1185 (1977).
14. M. Zamin and M. B. Ives, *ibid.*, **126**, 470 (1979).
15. U. Ebersbach, K. Schwabe, and K. Ritter, *Electrochim. Acta*, **12**, 927 (1967).
16. M. Turner, G. E. Thompson, and P. A. Brook, *Corros. Sci.*, **13**, 985 (1973).
17. J. Mieluch, *Rocz. Chem. Ann. Soc. Chim. Polonorum*, **49**, 365 (1975).
18. W. Paatsch, *Corros. Sci.*, **37**, 59 (1973).
19. L. N. Yagupol'skaya and A. A. Gordonnaya, *Zashch. Met.*, **4**, 712 (1968).
20. R. D. Armstrong, *J. Electroanal. Chem. Interfacial Electrochem.*, **28**, 221 (1970).
21. J. R. Vilche and A. J. Arvia, in "Proceedings of the Fourth International Symposium on Passivity," R. P. Frankenthal and J. Kruger, Editors, p. 861, Airlie, Virginia. Published by The Electrochemical Society (1978).
22. B. Droste and H. G. Feller, *ibid.*, p. 802.
23. B. MacDougall and M. Cohen, *ibid.*, p. 827.
24. B. MacDougall, D. F. Mitchell, and M. J. Graham, *Isr. J. Chem.*, **18**, 125 (1979).
25. B. MacDougall, D. F. Mitchell, and M. J. Graham, *This Journal*, **127**, 1248 (1980).
26. B. MacDougall, D. F. Mitchell, and M. J. Graham, *Corrosion* **81**, Toronto, Canada, April 1981, Pub. by NACE, in press.
27. M. A. Hopper and J. L. Ord, *This Journal*, **120**, 183 (1973).
28. J. L. Ord, *Surf. Sci.*, **56**, 413 (1976).
29. G. W. D. Briggs, in "Electrochemistry—Special Periodical Reports," Vol. 4, p. 33, published by the Chemical Society (1974).
30. D. F. Mitchell and P. B. Sewell, *Thin Solid Films*, **23**, 109 (1974).
31. P. B. Sewell, D. F. Mitchell, and M. Cohen, "Developments in Applied Spectroscopy," Vol. 7A, pp. 61-79, Plenum Press, New York (1969).
32. S. Gottesfeld and S. Srinivasan, *J. Electroanal. Chem. Interfacial Electrochem.*, **86**, 89 (1978).
33. S. Gottesfeld and J. D. E. McIntyre, *This Journal*, **126**, 742 (1979).
34. S. Gottesfeld, J. D. E. McIntyre, G. Beni, and J. L. Shay, *Appl. Phys. Lett.*, **33**, 208 (1978).
35. S. Gottesfeld, M. Yaniv, D. Laser, and S. Srinivasan, *J. Phys.*, **38**, C5-145 (1977).
36. B. MacDougall and M. J. Graham, *Electrochim. Acta*, **26**, 705 (1981).

## Effect of Surface Etching and Morphology on the Stability of $\text{CdSe/S}_x$ <sup>±</sup> Photoelectrochemical Cells

Gary Hodes\* and Joost Manassen

*Department of Plastics Research, The Weizmann Institute of Science, Rehovot, Israel*

and David Cahen\*

*Department of Structural Chemistry, The Weizmann Institute of Science, Rehovot, Israel*

### ABSTRACT

The stability of single crystal CdSe photoelectrodes in polysulfide electrolyte is shown to be a function of the etching treatment used. This is explained by changes in real electrode surface area caused by different etchants, leading to a variation in real photocurrent density. The effect of photocurrent density on stability is measured, and used to semiquantitatively explain the observed variation in stability with etching. The effect is shown to be consistent for three different crystal faces, and is extended to polycrystalline electrodes.

Since the earliest reports showing that polychalcogenide electrolytes can stabilize n-Cd-chalcogenides as photoanodes in a photoelectrochemical cell, PEC, (1-3), it has become apparent that this stability is very ill defined. For example, the stability of the CdSe/polysulfide system has been reported to vary between minutes (4) to months (5). The variables which have been shown to affect the degree of stability are: electrode crystal structure and exposed crystal face, electrolyte composition, stirring, and photocurrent density (5-8).

In the CdSe/S<sub>x</sub><sup>±</sup> system it has been shown that stabilization of the photoanodes is connected with the exchange of Se from the CdSe by S from the electrolyte leading to a polycrystalline CdS layer on top of the CdSe (1,4-6, 9-11). Under favorable circumstances

cell output is stable because the CdS layer stops growing after reaching a certain thickness (probably less than ~100Å), at which point Se/S exchange is replaced by S/S exchange. If, however, Se/S exchange continues, even at a much reduced rate, the CdS layer continues to grow. This thicker layer will start to impede the transfer of minority carriers from the bulk solid to the solution phase, leading to increased deactivation. The resistance to the transfer of the minority carriers can be due to blocking by the higher bandgap CdS layer and/or reduced electrical conductivity of this layer. However, the similar stability behavior of CdS, where such a blocking layer is not expected, suggests that the degradation in output is due primarily to the increased polycrystallinity of the surface CdS layer, leading either to trapping and recombination of holes at the grain boundaries (8,10,11) or if the surface layer is porous and inactive, impeding the dissolution of

\* Electrochemical Society Active Member.

Key words: CdSe photoelectrodes, photoelectrode surface area, photoetching.

photogenerated S [which is the rate-determining step (12)] away from the active surface through the porous CdS layer (8,9).

Therefore photocorrosion is related to the competition between several possible reactions by the photo-generated holes: oxidation of polysulfide from the solution (the desired reaction); oxidation of the freshly formed CdS layer, which renews the solid/solution interface; or oxidation of the CdSe itself, which is the photocorrosion reaction and leads to increased S/Se substitution, and eventually, degradation of the output. Any change in conditions which facilitates the overall electrochemical oxidation of polysulfide and removal of the reaction photoproducts from the surface, should change the balance of the competitive reactions in favor of decreasing exchange, and thus increasing stability. We have shown that polycrystalline electrodes are more stable than single crystal ones, and explain this by the higher real surface area of the less smooth polycrystalline electrodes, leading to a lower real photocurrent density (5) which has previously been shown to cause increased stability (6). This follows from the competitive nature of the possible reactions (13); if the photocurrent density is not too high, the oxidation of polysulfide (actually the dissolution of S from the surface) can occur as fast as (or faster than) the hole flux to the surface. At higher photocurrent densities (i.e., greater hole fluxes), if the overall polysulfide oxidation step cannot keep up with the arrival of holes at the surface, we expect degradation according to the principles previously discussed.

This picture is, however, too simple, and the purpose of the work reported here is to investigate more fully than previously the effect of real surface area of CdSe photoelectrodes, together with the influence of several etching treatments, on the output stability of these electrodes in polysulfide electrolyte. By trying to achieve a picture, that is as complete as possible, of the various factors influencing the output stability of such PEC's, it may become feasible to manipulate the variables influencing these factors in such a way so as to achieve stable PEC's with output stability under normal day/night conditions, that is constant for years.

### Experimental

All the CdSe crystals were cut from the same boule, which was "as-grown" (from Dr. W. Girit, IVIC, Caracas), with an approximate resistivity of 15  $\Omega\text{cm}$ . Crystals were cut along the (0001), (10 $\bar{1}$ 0), and (11 $\bar{2}$ 0) faces. All orientations were checked by x-ray diffraction. Using the anomalous dispersion factors the (0001) face was shown to be the Cd-one (14). Polycrystalline CdSe electrodes were prepared by painting an aqueous slurry of CdSe (Alfa 99.999%) mixed with a  $\text{ZnCl}_2$  flux onto a Ti substrate, and annealing 10 min at 630°C in argon (15). Single crystal electrodes were all polished to a mirror finish using alumina polishing suspension down to 0.3  $\mu\text{m}$ . The different etching treatments on these polished electrodes were, all at room temperature:

1. Dip in 4%  $\text{Br}_2$  in MeOH for 5 sec; rinse with polysulfide ( $\text{S}_x^{2-}$ ) and then with water. Repeat.  $\text{Br}_2/\text{MeOH}$ .
2. Dip in  $\text{CrO}_3:\text{HCl}:\text{H}_2\text{O}$  in 6:10:4 w/w ratio, for 5 sec; rinse with  $\text{S}_x^{2-}$  and then with water. Repeat. " $\text{CrO}_3$ ."
3. Dip in fresh aqua regia, 15 sec; rinse with  $\text{S}_x^{2-}$ , then with water. Repeat. AR.
4. AR followed by " $\text{CrO}_3$ " i.e., as 3, followed by 2.
5. AR followed by photoetch, i.e., as 3, followed by illumination in  $\text{HNO}_3:\text{HCl}:\text{H}_2\text{O}$  (0.3:9.7:90) electrolyte, short circuited to a carbon counter-electrode in the same electrolyte, under AMI illumination for 4-5 sec; then rinsing in  $\text{S}_x^{2-}$  and  $\text{H}_2\text{O}$  (16). The polycrystalline electrode was etched for 4-5 sec in 3%  $\text{HNO}_3$  in HCl (aqua regia was too vigorous an etchant for these thin

layers), rinsed in  $\text{S}_x^{2-}$  and water, and photoetched as above.

The electrolyte in all cases was 1M each KOH,  $\text{Na}_2\text{S}$ , and S in deionized water. The experiments were all carried out using the same bulk solution stored under argon. Each stability run was obtained using a fresh quantity of this solution. The stability runs were carried out potentiostatically under essentially short-circuit conditions using Pt counter and reference electrodes. The cell was thermostated in a water bath at 35°C, and no stirring was employed. Illumination was by a stabilized quartz-iodine lamp, and illumination was controlled to give the required photocurrent density in all cases. In some cases, where the photocurrent density initially increased with time for constant illumination, which often happens in this system, the illumination intensity was reduced slightly to maintain the initial current, (otherwise a meaningful comparison could not be made).

### Results and Discussion

It has been shown previously (6) that the (0001) face of a CdSe crystal is less stable as a photoanode in  $\text{S}_x^{2-}$  than the (11 $\bar{2}$ 0) face. Since we wished to compare the effect of change in surface roughness by use of different etchants, which could preferentially expose planes other than that initially chosen, we had to verify that the various etchants did not expose any crystal face(s) preferentially. Therefore, we investigated three different faces, namely (0001), (10 $\bar{1}$ 0), and (11 $\bar{2}$ 0), assuming that, if preferential exposure of a more stable face did occur upon etching, the dependence on etchant of these three faces would be different. Figures 1 and 2 show the photocurrent densities of these faces after the various etching treatments, as a function of time, plotted on a logarithmic scale. The (0001) and (10 $\bar{1}$ 0) faces behaved identically (within experimental error). The interesting result is that, in spite of entirely different stabilities of the (11 $\bar{2}$ 0) face on the one hand and the (0001) and (10 $\bar{1}$ 0) faces on the other hand, they respond very similarly to the various etching treatments. Stabilization by a factor of  $\sim 50$  is obtained when going from the entirely smooth surface to one that has been photoetched. This behavior indicates that we are not dealing with preferential exposure of more or less stable faces by the different etchants used.

To correlate these results with the effects of the various etchants on the real surface area, we show in

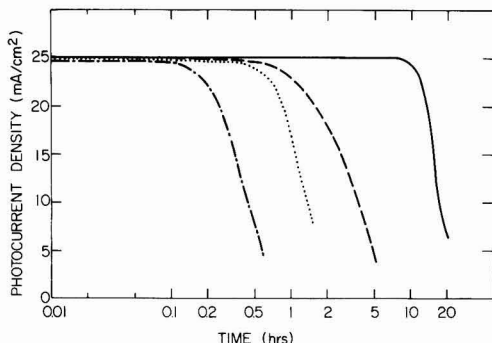


Fig. 1. Output stability of the (10 $\bar{1}$ 0) face of a CdSe crystal in a polysulfide electrolyte (1M each KOH,  $\text{Na}_2\text{S}$ , and S) at 35°C. — Polished and  $\text{Br}_2/\text{MeOH}$  (for (0001) face) or " $\text{CrO}_3$ " (for (10 $\bar{1}$ 0) face) etched; . . . . . aqua regia (AR) etch followed by " $\text{CrO}_3$ " etch; - - - - - AR etch; — AR etch followed by photoetch. An essentially identical picture was obtained for the (0001) (Cd) face.

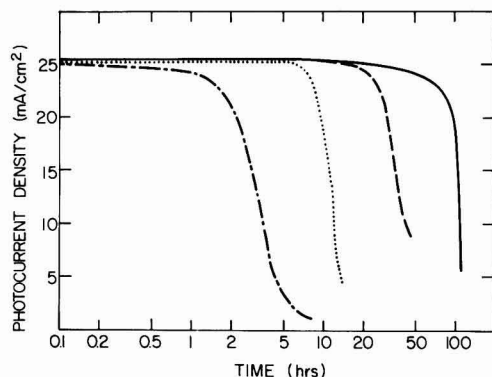


Fig. 2. As Fig. 1, but for the  $(11\bar{2}0)$  face

Fig. 3-11 SEM pictures of the surfaces of the 3 faces, each after 3 different etching treatments. (SEM pictures of the  $\text{Br}_2/\text{MeOH}$  or " $\text{CrO}_3$ " only, etches are not shown, since these surfaces were all mirror-smooth, and featureless under the SEM.)

Figures 3, 4, and 5 show AR +  $\text{Br}_2/\text{MeOH}$ , AR, and AR + photoetch for the  $(0001)$  face of CdSe. We can see an increase in surface roughness going from Fig. 3 to 5. Figures 6, 7, and 8 [for the  $(10\bar{1}0)$  face] and 9, 10,

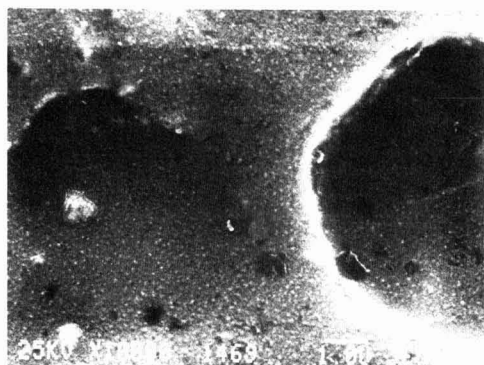


Fig. 3. SEM micrograph (10,000 times magnification) of the  $(0001)$  face after AR followed by  $\text{Br}_2/\text{MeOH}$  etch.

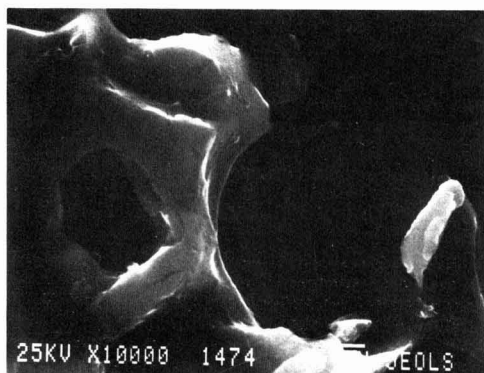


Fig. 4. SEM micrograph of  $(0001)$  face after AR etch

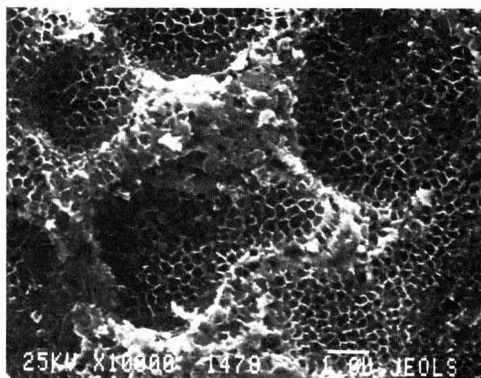


Fig. 5. SEM micrograph of  $(0001)$  face after AR + photoetch

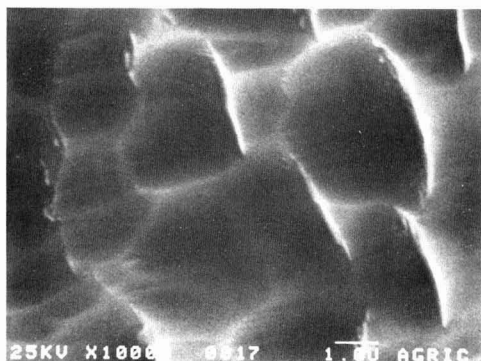


Fig. 6. SEM micrograph of  $(10\bar{1}0)$  face after AR + " $\text{CrO}_3$ " etch

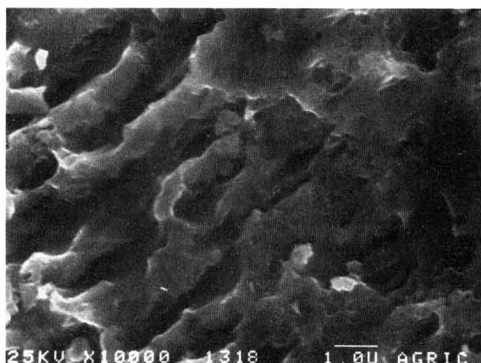


Fig. 7. SEM micrograph of  $(10\bar{1}0)$  face after AR etch

and 11 [for the  $(11\bar{2}0)$  face] show precisely the same trend, although the etch patterns vary from one face to another. Figure 12 shows a photograph of the  $(11\bar{2}0)$  crystal face with 3 differently etched regions. Even such a visual observation of the surface shows the strikingly different effects of different etchants.

Thus, the increase in stability in going from left to right in Fig. 1 and 2 correlates with an increase in surface area, in agreement with our reasoning given previ-



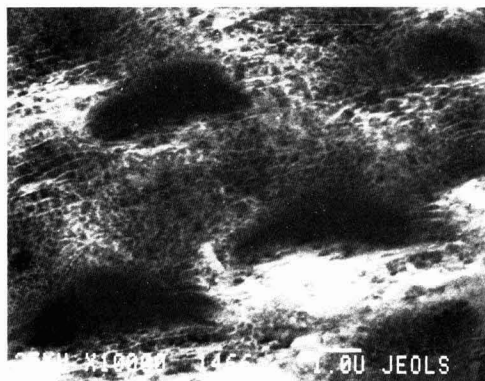


Fig. 8. SEM micrograph of (1010) face after AR + photoetch

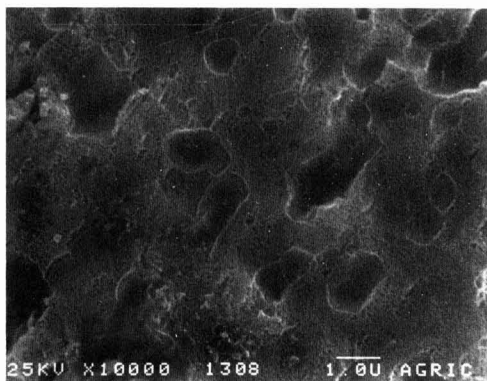


Fig. 11. SEM micrograph of (1120) face after AR + photoetch

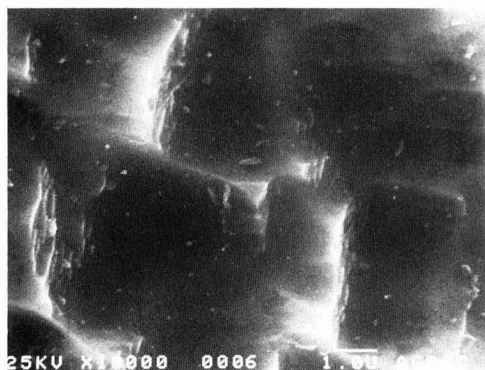
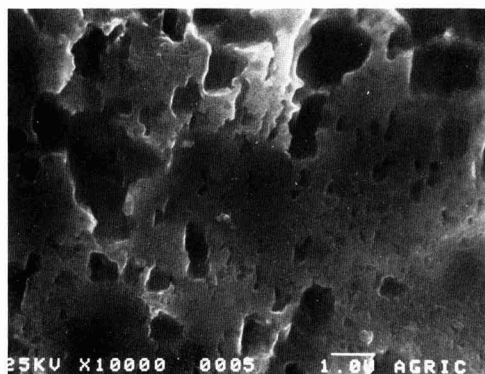
Fig. 9. SEM micrograph of (1120) face after AR + "CrO<sub>3</sub>" etch

Fig. 10. SEM micrograph of (1120) face after AR etch

ously on the basis of the difference between single crystal and polycrystalline CdSe.

Although we have not yet developed a method, reliable enough to measure these variations in surface area quantitatively (but diffuse reflectance together with photoacoustic measurements do show some promise in this respect), and in any case, such measurements would be of limited value, since an increase in real surface area by a certain factor need not reflect an in-

crease in the active surface area by the same factor, it is of interest to see if such variation is sufficient to explain the effect of stability. Figure 13A shows the effect of photocurrent density on stability for the smooth, Br<sub>2</sub>/MeOH etched, (0001) face (we have given the x-axis in time, and not coulombs, in order to facilitate comparison with other figures). In Fig. 13B these and similar data are used to show directly the dependence of the amount of photocharge that can be passed, as a function of initial photocurrent density.

Because of the long measuring times at lower current densities, the curve could not be extended in this direction. But based on general experience we expect the curve to straighten out and to give a practically infinite lifetime at some finite lower (<10 mA/cm<sup>2</sup>) current density. The strong dependence of stability on the initial photocurrent density, also described in Ref. (6),

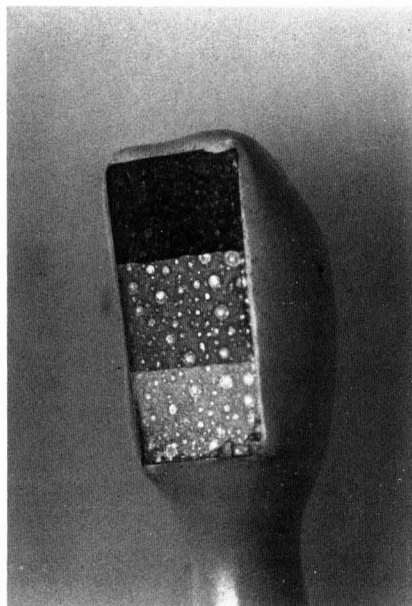


Fig. 12. Photograph (10× magnification) of a (1120) face of a CdSe crystal. The three different regions are obtained after: AR followed by "CrO<sub>3</sub>" etch (lightest region); AR etch alone (middle region); and AR followed by photoetch (darker region).



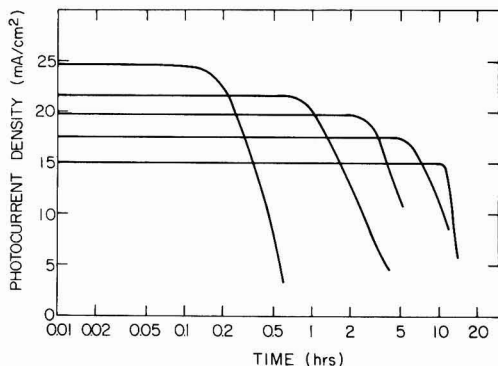


Fig. 13A. Effect of photocurrent density variation (by varying illumination intensity) on stability of polished, and subsequently  $\text{Br}_2/\text{MeOH}$  etched, (0001) CdSe crystal at  $35^\circ\text{C}$ .

can be seen clearly. Using Fig. 13A we can understand the results shown in Fig. 1 and 2. Those were obtained at an initial current density of  $25 \text{ mA/cm}^2$ . We see from Fig. 13A that a roughness factor of  $\sim 1.6$  ( $24.5 \text{ mA}/15 \text{ mA}$ ), which would decrease real current density to  $\sim 15 \text{ mA/cm}^2$ , would increase the lifetime by a factor of about fifty. The SEM pictures in Fig. 3-11 show that the range of roughness factors resulting from the different treatments are probably much higher and the most logical explanation for the increased stability is therefore this increase in surface area with concurrent decrease in real current density.

As mentioned earlier, the increase in active surface area need not be the same as the increase in real surface area, and will probably be smaller, since the presence of small pores of other surface irregularities may lead to transport problems which could partially offset

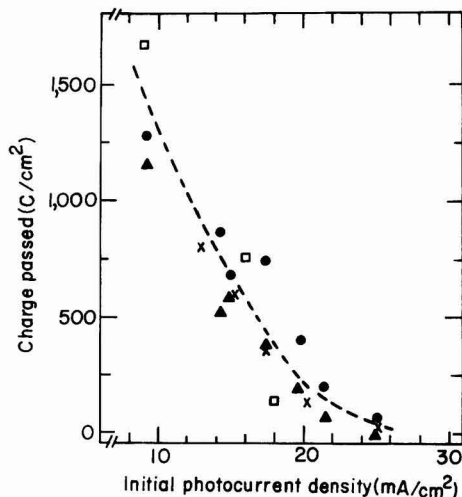


Fig. 13B. Dependence of the amount of photocharge, that can be passed through a CdSe electrode (as in 13A) until destabilization, on the initial photocurrent density. The data are from Fig. 13A ( $\bullet$ ,  $\blacktriangle$ ) and similar ones obtained with crystals cut from the same boule ( $\times$ ,  $\circ$ ).  $\bullet$ ,  $\times$ ,  $\square$ : Only photocharge passed until the current density decreases to  $5 \text{ mA/cm}^2$  is taken into account, because of varying behavior and long measuring times at lower current densities.  $\blacktriangle$ : As  $\bullet$ , but for the photocharge passed at constant current density ( $=$  initial current density), i.e., while the electrode is 100% stable.

the gain due to increased surface area. This makes it very difficult to treat the above effect in any more quantitative detail.

Since our original reasoning for the effect of surface area on stability came from the comparison between single crystal and thin layer polycrystalline CdSe (5), it is of interest to see how the most stable form of a single crystal photoetched (11 $\bar{2}$ 0) face compares in stability with photoetched thin layer electrodes. This is shown in Fig. 14. Note the high photocurrent densities used here ( $50 \text{ mA/cm}^2$ ) in order to measure a degradation in a reasonably short period of time. While there is a definite difference in stability between the two electrodes, the difference is considerably less than that noted earlier in comparing polycrystalline CdSe with the AR-etched (0001) face of CdSe, for what are now obvious reasons. The main difference is in the slow and diminishing rate of deactivation of the polycrystalline electrode, compared with the single crystal. This slow rate of deactivation is characteristic of our polycrystalline electrodes. It may be due to the very large degree of surface irregularity of these electrodes (see Fig. 15). Some areas will be photoelectrochemically more active than others. Thus, the more active ones may deactivate first, since the local current density at them will be relatively high. As the photocurrent falls,

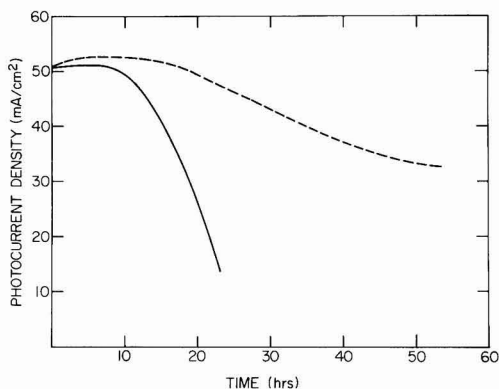


Fig. 14. Comparison of stability of thin layer polycrystalline painted CdSe (3%  $\text{HNO}_3$  in HCl etch followed by photoetch) (broken line), and (11 $\bar{2}$ 0) face of single crystal CdSe (AR followed by photoetch) (solid line).

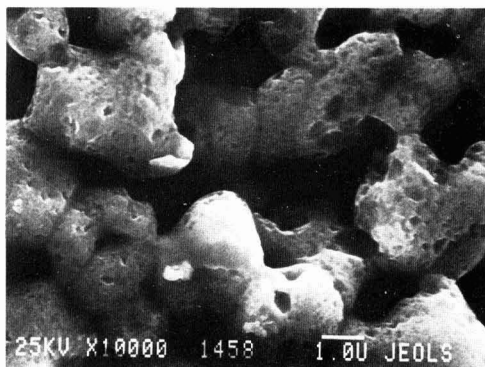


Fig. 15. SEM micrograph (10,000 $\times$  magnification) of a painted polycrystalline CdSe electrode after 3%  $\text{HNO}_3$  in HCl etch and use in  $\text{S}_x$ - solution.

the previously less active areas now become (relatively speaking) the most active, but at a lower current density, hence a slower rate of deactivation. While this explanation is admittedly rather simplistic, it can serve as a basis for explaining the slow and decreasing rate of deactivation of polycrystalline electrodes.

It should be noted that the electrolyte used here (1M each  $\text{OH}^-$ ,  $\text{S}^{2-}$ , S) is far from being the most stabilizing electrolyte for this system. Therefore, the stability results shown here should not be interpreted as reflecting the maximum attainable stability of this system. In a more stabilizing electrolyte, the stability will in fact be much greater (8).

Although not the main point of this study, it is of interest to attempt to understand the difference in stability of the various faces. A possible reason may be found by considering the number of bonds that have to be broken to free a  $\text{Cd}^{2+}$  ion from the surface. In the (1120) plane there are two in-plane bonds and one into the bulk phase. The (1010) plane has only one in-plane bond and one or two into the bulk phase, while the (0001) plane has no in-plane bonds but one or three into the bulk phase. Thus, one could argue that the (1120) plane is more stable since always three bonds need to be broken in order to free a Cd ion. If this is so, then the decomposition potential of a semiconductor photoelectrode must be dependent on the crystal face exposed. The different bonding at the surface may also influence the electrochemical reaction through different surface-solute interaction, and thus change the relative energetics of the two competing processes. In this case, the decomposition potential need not necessarily change. Finally, if photocorrosion is connected with the diffusion of  $\text{Cd}^{2+}$  through the bulk to the surface, such as has been reported to occur for CdTe photoanodes (17), then the varying stability of different faces may be due to varying rates of diffusion (or migration in the space charge layer) of the  $\text{Cd}^{2+}$  in the different crystal directions.

According to the strong dependence of lifetime on current density, we might expect the electrode at constant illumination to be less stable at short circuit than at maximum power, because of the higher current density passed. But according to our experience this is not true and we find that at constant illumination, most of our electrodes are more stable at short circuit than at maximum power. We shall deal with this interesting phenomenon in a subsequent publication. Suffice here to note that apparently, current density is not the only parameter influencing stability, but the electrode potential under the actual working conditions plays a

role as well. In view of the rate-determining dissolution of sulfur, it is likely that changes in electrode potential influence the stability through variations in surface potential (or changes in the Helmholtz layer), rather than simply by a change in band bending.

#### Acknowledgments

This work was supported by the U.S.-Israel Binational Science Foundation, Jerusalem, Israel, and by Ormat Turbines, Yavne, Israel. We thank L. Leiserowitz for help with the x-ray diffraction measurements, and W. Gariat for supplying the crystals.

Manuscript submitted Feb. 26, 1981; revised manuscript received May 28, 1981.

Any discussion of this paper will appear in a Discussion Section to be published in the June 1982 JOURNAL. All discussions for the June 1982 Discussion Section should be submitted by Feb. 1, 1982.

Publication costs of this article were assisted by the Weizmann Institute of Science.

#### REFERENCES

1. G. Hodes, J. Manassen, and D. Cahen, *Nature*, **261**, 403 (1976).
2. A. B. Ellis, S. W. Kaiser, and M. S. Wrighton, *J. Am. Chem. Soc.*, **98**, 1635 (1976).
3. B. Miller and A. Heller, *Nature*, **262**, 680 (1976).
4. R. N. Noufi, P. A. Kohl, J. W. Rogers, Jr., J. M. Whitte, and A. J. Bard, *This Journal*, **126**, 949 (1979).
5. D. Cahen, G. Hodes, and J. Manassen, *ibid.*, **125**, 1623 (1978).
6. A. Heller, G. P. Schwartz, R. G. Vadimsky, S. Menezes, and B. Miller, *ibid.*, **125**, 1156 (1978).
7. M. A. Russak, J. Reichman, H. Witzke, S. K. Deb, and S. N. Chen, *ibid.*, **127**, 725 (1980).
8. G. Hodes, J. Manassen, and D. Cahen, *Solar Energy Mater.*, In press.
9. K. T. L. DeSilva and D. Haneman, *This Journal*, **127**, 1554 (1980).
10. H. Gerischer and J. Gobrecht, *Ber. Bunsenges. Phys. Chem.*, **82**, 520 (1978).
11. D. Cahen, B. Vainas, and J. Vandenberg, *This Journal*, **128**, 1484 (1981).
12. D. Lando, J. Manassen, G. Hodes, and D. Cahen, *J. Am. Chem. Soc.*, **101**, 3969 (1978).
13. D. Cahen, J. Manassen, and G. Hodes, *Solar Energy Mater.*, **1**, 343 (1979).
14. E. P. Warekois, M. C. Lavine, A. N. Mariano, and H. C. Gatos, *J. Appl. Phys.*, **33**, 690 (1962).
15. G. Hodes, J. Manassen, D. Cahen, and M. David, *This Journal*, **127**, 2252 (1980).
16. R. Tenne and G. Hodes, *Appl. Phys. Lett.*, **37**, 428 (1980).
17. C. Vazquez-Lopez et al., *J. Appl. Phys.*, **50**, 5391 (1979).

# The Relationship of Transport Properties and $^1\text{H}$ NMR Spectra to the Structure of Molten Methylpyridinium Halides

David S. Newman,\* Rick R. Rhinebarger,\* David Siconolfi,\* and Olumuyiwa A. Banjoko\*

Department of Chemistry, Bowling Green State University, Bowling Green, Ohio 43403

## ABSTRACT

The equivalent conductance, viscosity, and  $^1\text{H}$ NMR spectra of several molten symmetric and asymmetric methylpyridinium halides were measured as a function of temperature. From these measurements, correlations between structure, spectra, and transport properties were made. From these correlations conclusions about the dynamics of motion in these and in other organic melts were drawn.

Molten pyridinium salts alone or in combination with molten aluminum halides are of considerable importance as the electrolyte in batteries and as the solvent for synthetic and mechanistic studies of organic and inorganic compounds. In recent years they have also become important as a possible heat storing media in solar heating and air conditioning systems as well as solvents for coal solubilization and decomposition reactions (1). In addition to these practical considerations, molten pyridinium salts offer a convenient vehicle for understanding the nature of the molten state because their relatively low melting points make them accessible to NMR techniques as well as to conventional transport measurements. This, combined with the myriad different pyridinium salts that are easily synthesized, makes it possible to observe the effects of small structural changes, such as moving a methyl group from the 4 to the 3 position on the pyridine ring, on both transport and spectral properties. From these effects a qualitative understanding of molecular motion in these and probably other molten organic liquids can be obtained.

In an earlier study (2) we reported the equivalent conductance,  $\Lambda$ , of 4-methylpyridinium bromide to be about 8% lower than the conductance of N-methylpyridinium bromide over approximately the same temperature range. We attributed this surprising result to complex formation in the 4-methyl salt which reduces the number of charge carriers per unit volume relative to the N-methyl salt. The complex probably forms by means of hydrogen bonding between the nitrogen proton and the bromide ion and this, of course, cannot occur in the N-methyl salt (3-5). The  $^1\text{H}$ NMR spectrum of 4-methylpyridinium bromide showed no line width broadening greater than 0.02 ppm, over a nearly 50° temperature range, indicating the barrier to complex formation is less than about 40 kJ/mol (1). There is, however, a change in proton chemical shift, as the anion changed from  $\text{Br}^-$  to  $\text{Cl}^-$ , that correlates well with the conductance data and this is discussed later. Herein we extend our investigation to include other symmetrical methylpyridinium salts as well as the asymmetrical methylpyridinium halides. We also assess the nature of the complex species in 4-methylpyridinium chloride and in 4-methylpyridinium bromide and estimate the magnitude of their association constants. In addition, we comment on the mechanism of molecular motion in methylpyridinium melts.

## Experimental Details

All transfer operations were carried out in a dry box in which  $\text{N}_2$  gas was circulated over molecular

sieves to remove water. A fiber optic light pipe was used to conduct light into the Dow Corning 710 oil which served as the heat bath. The flexible light pipe greatly facilitated the density and viscosity measurements. The bath was held constant to  $\pm 0.1^\circ\text{C}$ . A Varian CFT-20 NMR machine with variable temperature capability was used to obtain the  $^1\text{H}$ NMR spectra.

The preparation of the salts, conductivity measurements, density measurements, viscosity measurements, and  $^1\text{H}$ NMR techniques are all described in detail elsewhere (6-9).

## Results

The density,  $\rho$ , the specific conductance,  $\kappa$ , the viscosity,  $\eta$ , and the  $^1\text{H}$ NMR spectra of molten 2-methylpyridinium chloride (2-mepyr/ $\text{HCl}$ ), 2-methylpyridinium bromide (2-mepyr/ $\text{HBr}$ ), 3-methylpyridinium chloride (3-mepyr/ $\text{HCl}$ ), and 3-methylpyridinium bromide (3-mepyr/ $\text{HBr}$ ) were measured as a function of temperature over an approximately 50°C temperature range. These salts, together with their melting points, are shown in Fig. 1. The  $\eta$ 's of 4-methylpyridinium bromide and chloride as well as the  $\eta$  of N-methylpyridinium chloride (N-mepyr/ $\text{Cl}$ ) were measured as a function of temperature. The  $\kappa$  of molten 4-mepyr/ $\text{HCl}$  was also measured as a function of temperature. The values of  $\rho$  used to compute  $\eta$  and  $\Lambda$  for the symmetric salts were taken from an earlier study (7). The  $^1\text{H}$ NMR spectra of the three molten 4-methylpyridinium halides were obtained relative to an external standard of either  $(\text{CH}_3)_2\text{SO}$  or  $(\text{CH}_3)_2\text{SO}_2$ . Figure 2 shows the spectrum of 4-mepyr/ $\text{HI}$  at  $172^\circ\text{C}$  relative to  $(\text{CH}_3)_2\text{SO}_2$ . Figures 3 and 4 show the spec-

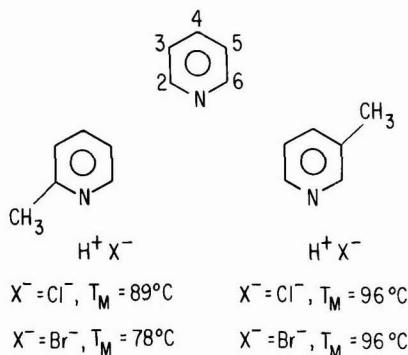


Fig. 1. The asymmetric methylpyridinium halides, their melting points, and the numbering system used in this study.

\* Electrochemical Society Active Member.  
Key words: molten pyridinium salts, transport properties, NMR spectra.

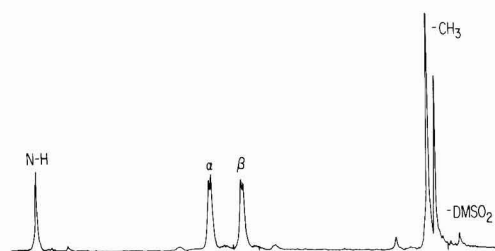


Fig. 2. The HNMR spectrum of 4-mepyr/HI relative to  $(\text{CH}_3)_2\text{SO}_2$  at  $172^\circ\text{C}$ .

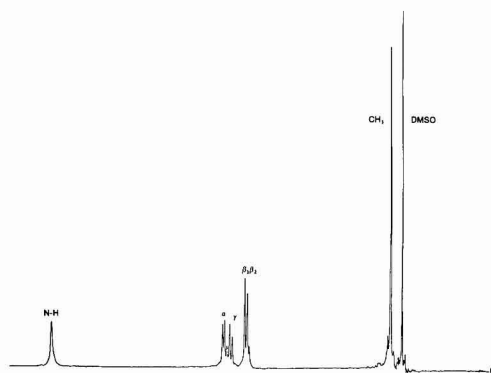


Fig. 3. The HNMR spectrum of 2-mepyr/HCl relative to DMSO at  $100^\circ\text{C}$ .

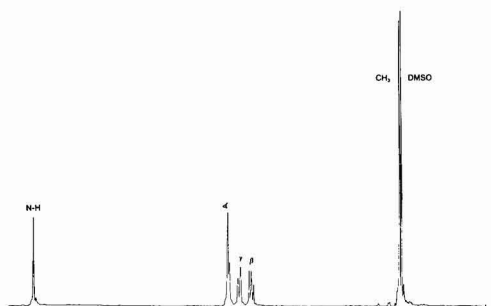


Fig. 4. The HNMR spectrum of 3-mepyr/HCl relative to DMSO at  $100^\circ\text{C}$ .

tra of 2-mepyr/HCl and 3-mepyr/HCl, respectively, at  $100^\circ\text{C}$  relative to DMSO. There was no discernable peak narrowing or chemical shift change as a function of temperature greater than 0.02 ppm in any of the melts so only one spectrum of each cation need be shown.

Table I lists the chemical shifts,  $\delta$ , for the several asymmetric methylpyridinium salts studied, relative to a standard of DMSO. Table II lists the  $\delta$ 's for the symmetric methylpyridinium salts relative to an external standard of  $(\text{CH}_3)_2\text{SO}_2$ . The  $(\text{CH}_3)_2\text{SO}_2$  peak is 0.45 ppm downfield from DMSO. Table III lists the densities of the asymmetrical melts.

Figure 5 is a graph of  $\ln \eta$  vs.  $T^{-1}$  for the four asymmetric salt melts and it should be noted that there is a slight, but distinct, curvature in the plots. Figure 6 shows the  $\ln \eta$  vs  $T^{-1}$  behavior of the symmetric melts and here the graphs are linear over the temperature

Table I. The proton chemical shifts of the asymmetric pyridinium halides relative to DMSO

Salt	$-\text{CH}_3$	$\alpha$	$\gamma$	$\beta$	N-H
2-mepyr/HCl	0.42	6.43	5.58	6.21	13.62
2-mepyr/HBr	0.63	6.51	5.76	6.43	13.28
3-mepyr/HCl	0.09	6.54	5.68	6.15	13.87
3-mepyr/HBr	0.28	6.71	5.90	6.34	13.30

Table II. Proton chemical shifts,  $\delta$ , of 4-methylpyridinium halides in ppm relative to an external standard of  $\text{CH}_3\text{SO}_2\text{CH}_3$

Melt	$\alpha$	$\beta$	$\text{CH}_3$	N-H	$\Delta(\text{H} - \alpha)$	$\Delta(\alpha - \beta)$
4-mepyr Cl	6.25	5.28	-0.18	13.68	7.43	0.97
4-mepyr Br	6.42	5.44	0.03	12.66	6.24	0.98
4-mepyr I	6.62	5.67	0.19	11.66	5.04	0.95

Table III. Density of asymmetric pyridinium salts as a function of temperature  $\rho$  ( $\text{g}/\text{cm}^3$ ) =  $a + b/T(\text{K})$

Salt	$a$	$-(b \times 10^3)$	Temperature range (K)
2-mepyr/HCl	1.334	0.5657	363-408
2-mepyr/HBr	1.711	0.7279	350-395
3-mepyr/HCl	1.329	0.5525	374-419
3-mepyr/HBr	1.690	0.6890	370-415

range studied. Figure 7 shows  $\ln \Lambda$  vs.  $T^{-1}$  for the four methylchlorides while Fig. 8 is a plot of  $\ln \Lambda$  vs.  $T^{-1}$  for the four methyl bromide isomers. It is obvious from Fig. 7 that N-mepyr/Cl is a much better conductor than the 4-methyl salt and that this unexpected phenomenon first observed in the bromide melts is even more pronounced in the chloride melts.

## Discussion

To validly compare properties of one melt with those of another, the melts must be in the same state. In order to ensure they are in the same state, a reference state must be agreed upon. Historically, most authors, including us, have used the salt's normal melting point,  $T_M$ , as the reference state and compared properties at a convenient multiple of  $T_M$ . This is tantamount to saying that each salt is in the same state if it is the same relative distance into its liquid range on a  $p$  vs.  $T$  plane. This, of course, assumes that the start of the liquid range is  $T_M$ , but recent evidence has called this assumption into question, especially for complicated salts like the methylpyridinium halides (10).

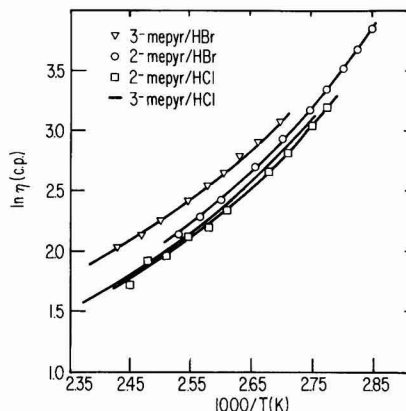


Fig. 5. Log of the viscosity (in cp) vs.  $1000/T$  for each of the asymmetric methylpyridinium halides.

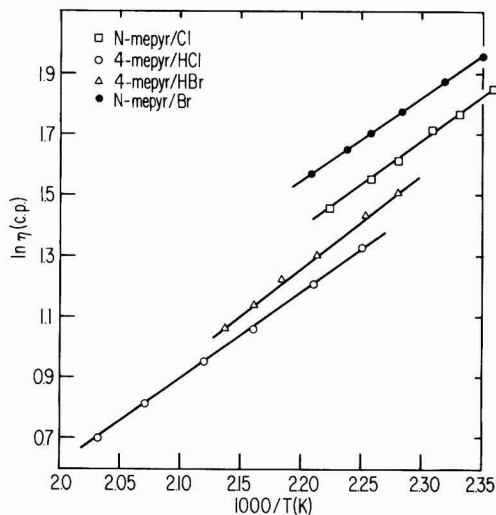


Fig. 6. Log of the viscosity (in cp) vs.  $1000/T$  for each of the symmetric methylpyridinium halides.

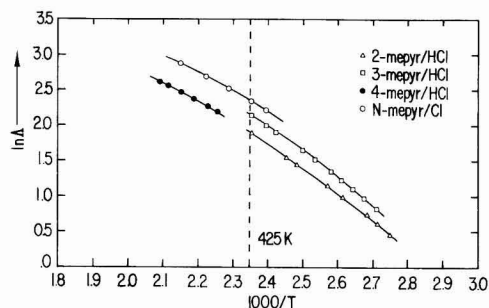


Fig. 7. Log of the equivalent conductance vs.  $1000/T$  for the four methylpyridinium chlorides.

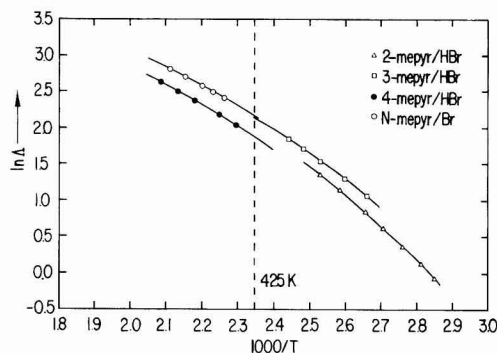


Fig. 8. Log of the equivalent conductance vs.  $1000/T$  for the four methylpyridinium bromides.

For these systems, a more appropriate standard state is either the boiling point,  $T_b$ , or the glass transition temperature,  $T_g$ . Since we do not know the  $T_g$ 's for our salts and many of them dissociate before they boil, we have selected a "common temperature" of 425 K as the reference state.

Table IV lists viscosities, densities, equivalent conductances, and Walden products of the eight salts at 425 K. This choice of reference implies that all of the compounds have the same liquid range and, *mutatis mutandis*, that  $T_g$  is a more reliable approximation to the start of the liquid state than is  $T_M$ .

Enough evidence from measurements of the liquid ranges of disubstituted benzenes exists to support our choice of reference state. To cite one example, the o-, m-, and p-fluorotoluenes boil at 388, 387, and 385 K, respectively, have  $T_g$ 's of 120, 122, and 123 K, respectively, but have  $T_M$ 's of 211, 185, and 216 K, respectively (10).

#### Evidence for the existence of complex species.—

Comparing the equivalent conductance of an N-methyl salt with the equivalent conductance of the corresponding 4-methyl salt, over the entire temperature range, indicates that the N-methyl salt is the better conductor. Because isomers are being compared, and the N-methyl melts are slightly more dense than the 4-methyl melts, suggesting motion is relatively more restricted, the most plausible explanation for this difference in  $\Lambda$  is that there are fewer charge carriers per unit volume in the 4-methyl salts than in the corresponding N-methyl salts because complex species are present. The alternative explanation, that there are the same number of charge carriers per unit volume, but they move slower, is still possible, but based on the spectroscopic data and observed viscosities is far less likely. The formation of a complex almost certainly involves hydrogen bonding between the nitrogenic proton and the halide ion, which means we should obtain further evidence for the existence of a complex from the  $^1\text{H}$ NMR spectra of the three 4-methylpyridinium ions (Fig. 2 and Table II). In these melts the ring and methyl protons are deshielded more by the  $\text{I}^-$  than by  $\text{Br}^-$ , and more by  $\text{Br}^-$  than by  $\text{Cl}^-$ , so that there is actually a sign reversal of  $\delta$  for  $\text{CH}_3$  relative to the dimethylsulfone external standard. On the contrary, the nitrogenic proton is deshielded more by the  $\text{Cl}^-$  than by the  $\text{Br}^-$  and more by the  $\text{Br}^-$  than the  $\text{I}^-$ . This dramatic change in chemical shift order correlates very well with the conductivity data and is compelling evidence for believing that the  $\text{N-H}^+$  forms a stronger hydrogen bond with  $\text{Cl}^-$  than it does with  $\text{Br}^-$ . It probably does not hydrogen bond to  $\text{I}^-$  at all (5). In an isolated methylpyridinium ion, the proton is well shielded by the nitrogen's lone pair of electrons, presumably located in an  $\text{sp}^2$  orbital. The halide ion strongly attracts this proton, partially dislodging it from the protection of its shielding electrons, and causes it to resonate at a lower frequency. This phenomenon is more pronounced in the  $\text{Cl}^-$  melts than in the  $\text{Br}^-$  melts due to the larger charge to volume ratio in  $\text{Cl}^-$  than in  $\text{Br}^-$ . This same trend is present in the asymmetric chlorides and bromides as well. The reasons why the ring protons respond to the halide differently are still not perfectly clear, but it is very likely that hydrogen bonding is not the major factor. Probably exigencies of packing are responsible for the observed chemical

Table IV. Transport properties, densities, and Walden products of the four isomers of methylpyridinium chloride and the four isomers of methylpyridinium bromide at 425 K

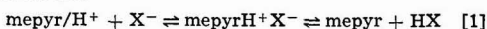
Isomer	$\Lambda$ ( $\text{cm}^2/\Omega$ equiv. $^{-1}$ )	$\eta$ (cp)	$\rho$ ( $\text{g}/\text{cm}^3$ )	$\Lambda\eta$
2-mepyr/HCl	6.68	3.90	1.093	26.1
3-mepyr/HCl	8.58	3.87	1.094	33.2
4-mepyr/HCl	6.61	5.06	1.094	33.5
N-mepyr/Cl	10.5	6.24	1.137	65.5
2-mepyr/HBr	7.76	4.78	1.401	37.1
3-mepyr/HBr	8.41	6.65	1.397	55.9
4-mepyr/HBr	6.53	5.41	1.405	35.4
N-mepyr/Br	9.00	7.27	1.445	65.4



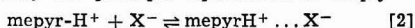
shifts. The crystal structure of pyridinium iodide indicates the  $I^-$  is sandwiched between the  $\pi$  clouds of two pyridinium rings (11) and it is not unlikely that this sort of structure would tend to persist in molten 4-mepyr/HI. On the other hand, the  $Cl^-$  ion, by virtue of its strong tendency to form hydrogen bonds with the nitrogenic proton, will reside much of the time at the  $N-H^+$  end of the molecule, as it does in solid pyridinium/HCl (12). The  $Br^-$  will occupy an intermediate position, on the average. This means the  $I^-$  ion perturbs the pyridine ring current more than the  $Br^-$  and the  $Br^-$  perturbs it more than the  $Cl^-$ . The ring current, which diamagnetically shields protons, will be least effective in the iodide, next least effective in the  $Br^-$  melts, and most effective in the  $Cl^-$  melts at shielding protons on neighboring molecules; hence the observed order of deshielding of the ring protons and  $CH_3$  groups (13). These phenomena taken together, account for the observed chemical shifts in a qualitative way and when correlated with the conductivity data yield fairly decent evidence for the existence of some sort of complex species in these melts.

**The  $N-H^+$  contribution to the conductivity.**—Before discussing the nature of the complex, we comment on the protonic contribution to the conductivity. It is obvious that the 2- and 3-methylpyridinium chlorides have about the same viscosities, but the 3-methyl salt's equivalent conductance is 22% greater. The most likely reason for this, since the molecular dimensions, densities, and molecular geometry are so similar, is that there is a greater protonic contribution to the conductivity of the 3-methyl salt, than to the conductivity of the 2-methyl salt (3, 4, 14). The 3-methylpyridine is less basic than the 2-methylpyridine (15), so its proton is held less tightly and can make a greater contribution to the conductivity. The  $-CH_3$  group at the 2 position of the ring would also interfere with facile proton transfer (or complex formation for that matter) thus further reducing the proton's contribution to the 2-methyl salt's conductivity. A similar protonic contribution is probably occurring in the bromide melts, as well, though here it seems less pronounced. At this point it is unclear if an actual Grotthuss mechanism occurs (Fig. 9b), in which there is a transfer of charge or virtual movement without an actual proton diffusion, or a hopping mechanism occurs, in which a given proton hops from site to site, and during one of its excursions reaches an electrode. Nevertheless, there is almost certainly some protonic contribution to the conductance and this contribution seems to be greater in the chloride melts than in the bromide melts.

**The nature of the complex species and equilibria in the melts.**—The spectroscopic and conductivity data suggest that in melts containing  $N-H^+$ , an equilibrium of the sort



is present with the proton oscillating within its double minimum potential well. This sort of equilibrium has been suggested by Shuppert and Angell to exist in pyridinium HCl melts (4). Since neither spectral measurements nor chemical analysis has turned up any evidence of free methylpyridine or  $HX$ , we think these species are present in very low concentration and consequently the principal equilibrium is simply



A rough estimate of the association constant,  $K_A$ , for  $4\text{-mepyr}H^+ \dots X^-$  can be made using the following line of reasoning. If there were no complex formation in the 4-methyl melts, their conductivities would be similar to those of the corresponding N-methyl melts because the respective molecular sizes, densities, and

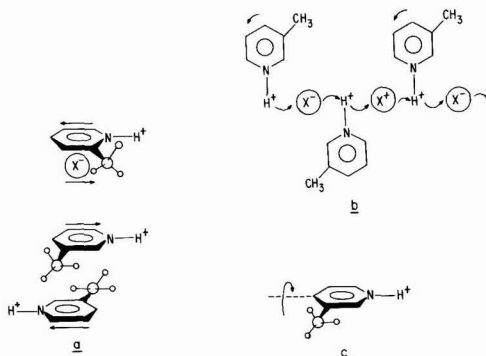


Fig. 9. Contributions to molecular motion in methylpyridinium melts. a, Methyl groups interfering with each other as ions pass each other (in plane); b, possible Grotthuss mechanism; c, out of plane rotation about the C...N axis.

symmetries are similar. We therefore assume that to a first approximation the measured  $\Lambda$ 's for the N-methyl salts are the  $\Lambda$ 's the corresponding 4-methyl salts would have if they were completely dissociated. We next attribute the lower conductance of the 4-methyl salts to formation of the complex species described by Eq. [2]. The degree of dissociation can be approximated, as it is in the case of weak electrolyte solutions, by the Arrhenius notion.

$$\alpha \approx (\Lambda_{4\text{-meth}}/\Lambda_{N\text{-meth}})_{425\text{ K}} \quad [3]$$

$K_A$  is then given by the expression

$$K_A = \frac{[4\text{-mepyr}H^+ \dots X^-]}{[4\text{-mepyr}-H^+][X^-]} = \frac{1 - \alpha}{\alpha^2} \quad [4]$$

where  $c$  is the average concentration in moles per liter at 425 K. It is possible to further correct the  $\Lambda_{4\text{-meth}}$  for protonic contribution by assuming this protonic contribution is roughly the same as it is in the 3-methyl melt. The protonic contribution to the 3-methyl melt's conductance is estimated in the following manner. If the difference in conductivity between the 3-mepyr melts and the corresponding 2-mepyr salts is mostly due to the protonic contribution, and if this contribution is negligible in the 2-methyl salts for the reasons mentioned earlier, then at  $T_c$  the protons contribute  $1.90 (\Omega \text{ equiv.})^{-1} \text{ cm}^2$  to the 3-mepyr/HCl conductance and  $0.65 (\Omega \text{ equiv.})^{-1} \text{ cm}^2$  to the 3-mepyr/HBr conductance. Subtracting these values from the appropriate  $\Lambda_{4\text{-meth}}$ 's gives a corrected conductance  $\Lambda'_{4\text{-meth}}$  which contains only contributions from the methylpyridinium ion and the halide ion. The value of  $\Lambda'$  for the chloride is  $4.71 \text{ cm}^2 (\Omega \text{ equiv.})^{-1}$  and for the bromide it is  $5.90 \text{ cm}^2 (\Omega \text{ equiv.})^{-1}$ . Values for  $K_A$ ,  $\alpha$ , and  $\Delta G$ , the free energy of complex formation, are listed in Table V.

Although the method for estimating the  $K_A$ 's is somewhat convoluted, the values obtained give at least correct order of magnitude association constants. The greater basicity of the 4-methylpyridine than the 3-methylpyridine almost certainly reduces the protonic contribution to the 4-methyl melt's conductivity, but this is compensated for because if there

Table V. Association constants for 4-mepyr/HCl and 4-mepyr/HBr

Salt	$\alpha$	$K_A$	$\Delta G$ (kJ/mol)
4-mepyr/HCl	0.448	$3.81 \times 10^{-2}$	3.4
4-mepyr/HBr	0.655	$9.9 \times 10^{-3}$	8.2

were no labile protons and no hydrogen bonding the conductance of the 4-methyl salt should be a bit higher than that of the N-methyl salt (which serves as the  $\Lambda_0$  in the Arrhenius equation) because of lower density. Moreover, the  $K_A$  of the Br<sup>-</sup> melt is smaller than that of the Cl<sup>-</sup> melt, as is expected based on the differences in charge density of the halide. These  $K_A$ 's represent a significant complex ion contribution to the structure of the 4-methyl chloride and bromide melts and certainly will influence transport properties.

**Comparison between asymmetric and symmetric salts.**—The most obvious difference between the symmetric and asymmetric isomers of a given salt is the melting point; the symmetric salts melting considerably higher than the corresponding asymmetric salts (this difference also persists in the iodide melts) (16). A second difference is that the  $\ln \eta$  vs.  $T^{-1}$  graphs for the asymmetric salts exhibit some curvature while the  $\ln \eta$  vs.  $T^{-1}$  graphs for the symmetric melts are linear.

In contrast to these differences, both symmetric and asymmetric salts of a particular halide ion have similar viscosities at a common temperature. For example, at the standard temperature, 425 K, which is just above the high temperature end of the asymmetrical salt's liquid range, and just below the symmetrical salts' melting point, 4-mepyr/HCl has an extrapolated  $\eta$  of about 4.5 cp whereas the 2- and 3-mepyr/HCl have  $\eta$ 's equal to about 4.6 cp. The conductivities of the salts are also relatively unaffected by symmetry *per se*. For instance, the conductances of 2- and 4-methylpyridinium chloride lie on essentially the same curve. Taking these data in the aggregate, we conclude that symmetry, *per se*, has relatively little effect on transport properties or spectral properties, but manifests itself mainly through differences in observed melting points and protonic contributions to the melt's conductivity. Far and away, a more significant factor in determining relative values of transport properties is the presence or absence of hydrogen bonding. This conclusion is in sharp contrast to one reached earlier (8,9) where we suggested symmetry, rather than H-bonding, was the most important factor in determining transport properties in pyridinium melts. Our earlier conclusion was arrived at using a melting point reference state, and the difference between the two conclusions dramatically illustrates the importance of the particular reference state used.

**The role of hydrogen bonding.**—We can now assemble the diverse results of our experiments into a fairly coherent pattern and assess the contribution of hydrogen bonding to structure and to ionic motion.

The equivalent conductance of the symmetrical chloride and bromide melts decreases 37% and 27%, respectively, when the methyl group is moved from the nitrogen to the 4 position of the ring. At the same time  $\eta$  decreases 19% and 25%, respectively. The only plausible explanation for these results is the one we suggested earlier and that is that complex formation reduces the number of charge carriers per unit volume thereby lowering the conductivity. These same complexes reduce the melt's viscosity by, in effect, lowering interionic friction and shortening the length of the hydrogen-bonded species along the  $C_4-N-H^+-X^-$  axis relative to the separated ions (17, 18). Therefore, the H-bonded salts are poorer conductors, but less viscous than the N-methyl melts.

Undoubtedly, additional factors are also contributing to the differences in transport properties between the two types of melt. For example, within the time frame of diffusional motion, the N-methyl melt may still have vestiges of its crystal structure in which the halide ion is above and to one side of the ring (as it is

in the N-mepyr/I crystal (19). This fluctuating asymmetry will increase the interionic friction due to one melt layer interfering with another and consequently increase the viscosity relative to the hydrogen bonded melts. However, these factors are difficult to isolate and seem much less important than hydrogen bonding itself.

We think the fact that the corresponding N-H<sup>+</sup> containing chlorides and bromides have such similar  $\Lambda$ 's is one more indication of the importance of hydrogen bonding. The Cl<sup>-</sup> ion forms stronger hydrogen bonds than the Br<sup>-</sup> ion, and consequently has its mobility considerably reduced. What might be considered "normal" behavior is exhibited by the N-methyl salts, in which there is a 14% decrease in  $\Lambda$  between the Cl<sup>-</sup> and the Br<sup>-</sup> melts and a 13% decrease between the Br<sup>-</sup> and I<sup>-</sup> melts (2, 16).

**Details of ionic motion and melt structure.**—The principal charge carrier in all of the pyridinium melts studied is the halide ion. This is consistent with our earlier results and those of King and co-workers (20, 14, 2). Attractive forces and steric factors dominate, hence the relatively low ratio of about 1.1 for  $E_\eta$  to  $E_\Lambda$  and the likely, very little if any, expansion upon melting. Bloom and Reinsborough (21) found Pyr/HCl expands only 2% on melting and preliminary results in our laboratory indicate 3-methylpyridinium chloride actually contracts when it melts. This should be contrasted with typical inorganic salts which expand 15–25% on melting and have  $E_\eta/E_\Lambda$  ratios of between 2 and 5 (22, 23).

It is difficult to identify particular modes of motion that are favored over others because there is no special difference between symmetrical and asymmetrical salts with regard to their transport properties and relatively little difference between viscosity and conductivity with regard to energies of activation. The best one can say is it looks as if inplane rotation, or rocking back and forth about an axis perpendicular to the plane of the molecule, may be favored over out of plane rotation (Fig. 9c). In other words, the cations translate as rotating or rocking weighted disks rather than rotating weighted cylinders. The reason for arriving at this conclusion is that all of the cations sweep out about the same area, but the asymmetric cations sweep out considerably larger cylindrical volumes, rotating out of plane (9c), than do the symmetric cations. Since the asymmetric ions require greater volumes, and space is at a premium, they should have higher viscosities and higher energies of activation. This is contrary to our experimental results. Because the planar area of the disklike cation is considerably greater than half the area of an edge, and because only one end is charged, the ion is prevented from freely rotating. Consequently it is unlikely that the cations are translating as rotating spheres as are the halide ions.

The  $E_\eta/E_\Lambda$  ratio of  $\sim 1.1$  further implies that viscosity and conductivity meet with the same sort of barriers. (24). Ions are moving past each other, Fig. 9a, and it matters little whether two cations pass each other or a cation and anion pass each other, the energies required are quite similar.

**Errors and comparison with other workers.**—Comparing our proton chemical shifts in the 2-mepyr/HCl melt with the chemical shifts in the same melt reported by Angell and Shuppert (25) we agree within experimental error on the location of the  $\alpha$ ,  $\beta$ ,  $\gamma$ , and methyl peaks, but differ by  $-0.85$  ppm on the N-H<sup>+</sup> chemical shift, ours being 16.2 ppm and theirs being 17.05 corrected to TMS. One possible reason for this discrepancy is that a trace of water may still be present in our melts, but not in theirs. This water molecule would tend to lie on, or near, the N-H<sup>+</sup> and shield it

from the magnetic field. On the other hand, they used an internal standard of  $(\text{CH}_3)_4\text{NCl}$  which exchanges with  $\text{H}^+$  and with other  $\text{CH}_3^+$  groups (25), but also increases the  $\text{Cl}^-$  concentration which would deshield the  $\text{N-H}^+$  proton and cause it to resonate at lower frequencies. There does not seem to be any other melt spectra in the literature to compare our data with. Our melting point of  $89^\circ\text{C}$  for 2-methylpyridinium chloride is identical to the one reported by Angell, Hodge, and Cheeseman for the same compound and our specific conductances are within  $\pm 2\%$  of theirs (3). Our conductivity data for the  $\text{N-mepyr/Cl}$  is within  $\pm 2\%$  of the values reported by King and co-workers (20). Overall, we estimate our equivalent conductance data to be correct to  $\pm 2\%$  and our viscosity data to be accurate to  $\pm 3\%$ . Our analyses of the pyridinium salts were in all cases  $99\pm\%$ .

Perhaps the largest error in this study is the assumption that all the melts have the same liquid range, but since no conclusion depends on an exact knowledge of  $T_g$  or  $T_b$ , this error should not seriously affect our conclusions.

### Conclusion

By systematically varying the structure of the methylpyridinium cation and changing the anion, correlations between structure, spectra, and transport properties in molten pyridinium salts can be made in a relatively simple and straightforward manner. From these correlations, several conclusions can be reached about the structure of the melt and its relation to transport properties. The conclusions drawn are the following:

1. Hydrogen bonding exerts a strong influence on transport properties, species present, and melt structure.
2. Symmetry of the cation, *per se*, has little influence on either melt structure or transport properties.
3. The anion is the principal charge carrier in the methylpyridinium melts.
4. There are complex species in the 2-, 3-, and 4-methylpyridinium chloride and bromides.
5. There is probably a protonic contribution to the conductivity of those melts in which the  $\text{N-H}^+$  is present. The protons move either through a Grotthuss mechanism or through a hopping mechanism.
6. In the molten pyridinium halides, and probably in molten organic salts generally, attractive forces dominate over repulsive forces, and there is very little free space, hence the  $E_\eta/E_A$  ratio of 1.1.

### Acknowledgment

The authors wish to thank C. Austen Angell for his helpful discussions.

Manuscript submitted Aug. 25, 1980; revised manuscript received ca. May 12, 1981. This was Papers 331 and 332 presented at the Pittsburgh, Pennsylvania, Meeting of the Society, Oct. 15-20, 1978.

Any discussion of this paper will appear in a Discussion Section to be published in the June 1982 JOURNAL.

All discussions for the June 1982 Discussion Section should be submitted by Feb. 1, 1982.

Publication costs of this article were assisted by Bowling Green State University.

### REFERENCES

1. D. S. Newman, R. Winans, and R. L. McBeth, Paper 660 presented at The Electrochemical Society Meeting, Hollywood, Florida, Oct. 5-10, 1980.
2. D. S. Newman, R. T. Tillack, D. P. Morgan, and W. C. Wan, *This Journal*, **124**, 856 (1977).
3. C. A. Angell, I. M. Hodge, and P. A. Cheeseman, in "International Symposium on Molten Salts," J. P. Pemsler, J. Braunstein, K. Nobe, D. R. Morris, and N. E. Richards, Editors, p. 139, The Electrochemical Society Softbound Proceedings Series, Princeton, NJ (1976).
4. J. W. Shuppert and C. A. Angell, *J. Chem. Phys.*, **67**, 3050 (1977).
5. N. Goldstein and J. L. Ragle, *ibid.*, **70**, 5072 (1979).
6. M. S. Rozhdestvenskii and L. M. Brode, *J. Appl. Chem. USSR*, **10**, 722 (1937).
7. D. S. Newman, D. P. Morgan, and R. T. Tillack, *J. Chem. Eng. Data*, **21**, 279 (1976).
8. D. S. Newman and O. A. Banjoko, Paper 332 presented at The Electrochemical Society Meeting, Pittsburgh, Pennsylvania, Oct. 15-20, 1978.
9. D. S. Newman, R. R. Rhinebarger, and D. Siconolfi, Paper 331 presented at The Electrochemical Society Meeting, Pittsburgh, Pennsylvania, Oct. 15-20, 1978.
10. J. Wong and C. A. Angell, "Glass-Structure by Spectroscopy," Chap. 1, Marcel Dekker, Inc., New York (1976).
11. H. Hart, *Acta Crystallogr.*, **31**, 178 (1975).
12. C. Rerat, *ibid.*, **15**, 427 (1962).
13. J. Robinson, R. C. Dugle, H. L. Chum, D. Koran, and R. A. Osteryoung, *J. Am. Chem. Soc.*, **101**, 3776 (1979).
14. D. S. Newman, W. Rohr, D. Kirklin, and H. D. Frame, *This Journal*, **119**, 797 (1972).
15. A. Albert and E. P. Serjeant, "Ionization Constants of Acids and Bases," p. 145, Methuen and Co., Ltd., London (1962).
16. D. S. Newman and R. M. Stevens, in "Third International Symposium on Molten Salts," G. Mamantov, Editor, The Electrochemical Society Softbound Proceedings Series, Princeton, NJ (1981).
17. J. Gordon, "The Organic Chemistry of Electrolyte Solutions," p. 400, John Wiley & Sons, Inc., New York (1975).
18. K. Bauge and J. W. Smith, *J. Chem. Soc. (A)*, 616 (1966).
19. R. A. Lalancette, W. Furey, J. N. Costanza, P. R. Hemmes, and F. Jordan, *Acta Crystallogr., Sect. B*, **34**, 2950 (1978).
20. R. A. Carpio, L. A. King, R. E. Linstrom, J. C. Nardi, and C. H. Hussey, *This Journal*, **126**, 1644 (1979).
21. H. Bloom and V. C. Reinsborough, *Aust. J. Chem.*, **21**, 1525 (1968).
22. J. O'M. Bockris and A. K. N. Reddy, "Modern Electrochemistry," Vol. 1, p. 525, Plenum/Rosetta Editions, New York (1973).
23. H. Bloom and E. Heymann, *Proc. R. Soc. London, Ser. A*, **188**, 392 (1947).
24. G. J. Janz, R. D. Reeves, and A. T. Ward, *Nature (London)*, **204**, 1188 (1964).
25. C. A. Angell and J. W. Shuppert, *J. Phys. Chem.*, **84**, 538 (1980).

# The Kinetics and Mechanism of the Electroreduction of Sulfur Dioxide in Nonaqueous Media

## I. Reduction in Solutions of Tetraethylammonium Perchlorate in N,N-Dimethylformamide

C. L. Gardner\* and D. T. Fouchard\*

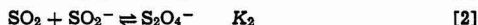
Defence Research Establishment Ottawa, Ottawa, Ontario, Canada K1A 0Z4

and W. R. Fawcett\*

The Guelph-Waterloo Centre for Graduate Work in Chemistry (Guelph Campus),  
Department of Chemistry, University of Guelph, Guelph, Ontario, Canada N1G 2W1

### ABSTRACT

Polarographic studies of the electroreduction of sulfur dioxide in dimethylformamide containing 0.1M tetraethylammonium perchlorate have shown that at 20°C, the mechanism of electroreduction is given by the reactions

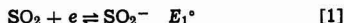


The standard rate constant for the electron transfer reaction [1] has been found to be  $1.0 \pm 0.2$  cm/sec. This rate of electron transfer is very fast, being of the same order of magnitude as that observed for reduction of aromatic hydrocarbons (21). The association constant,  $K_2$ , for reaction [2] has been found to be  $8400 \pm 2000$  dm<sup>3</sup> mol<sup>-1</sup>. This is an order of magnitude larger than the association constant measured in bulk solution using ESR spectroscopy (20). In addition to formation of the complex,  $\text{S}_2\text{O}_4^-$ , the results show that a second follow-on reaction is also important. Evidence is presented that this follow-on reaction is the disproportionation of  $\text{SO}_2^-$  to form SO and  $\text{SO}_3^{2-}$ . The equilibrium constant for this reaction has been found to be  $0.6 \pm 0.4$ . The dimerization of  $\text{SO}_2^-$  to form dithionite is not important during the initial stages of reduction at room temperature and over the range of  $\text{SO}_2$  concentration ( $1 \times 10^{-4}$ – $5 \times 10^{-3}$ ) used in these experiments. However, at low temperatures, the formation of dithionite is favored.

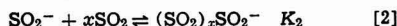
In recent years considerable effort has gone into the development and commercialization of the lithium-sulfur dioxide battery. While these efforts have resulted in successful exploitation of this battery system, there remain a number of environmental (1) and safety (2) problems to be solved.

By contrast, work reported on the basic chemistry and electrochemistry of the reduction of sulfur dioxide has been limited. While it is generally agreed that the major product formed during the discharge of the lithium-sulfur dioxide battery is lithium dithionite, previous work has indicated that the reduction mechanism is influenced by the choice of solvent and electrolyte.

It is generally agreed that the initial one-electron transfer step



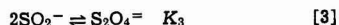
is followed by one or more follow-on reactions. In N,N-dimethylformamide (DMF), a stable, blue paramagnetic product is formed (3-7) which has been ascribed to a complex of the form



The number,  $x$ , of neutral  $\text{SO}_2$  molecules in the complex has been the subject of some controversy. Thus,

Dinse and Mobius (5) concluded that  $x = 2$  by measuring the ratio of the concentrations of  $(\text{SO}_2)_x\text{SO}_2^-$  and  $\text{SO}_2^-$  using ESR spectroscopy. On the other hand, Rinker and Lynn (4) concluded that  $x = 1$ . The recent work of Kastening and Gostisa-Mihelcic (6) which was based on ESR measurement of the  $[(\text{SO}_2)_x\text{SO}_2^-]/[\text{SO}_2^-]$  ratio coupled with direct electrochemical measurement of the  $\text{SO}_2$  concentration has shown that the complex has the stoichiometry  $\text{S}_2\text{O}_4^-$  (i.e.,  $x = 1$ ). This is also in agreement with kinetic measurements made by the same authors (8).  $K_2$  was determined to be  $230$  dm<sup>3</sup> mol<sup>-1</sup> at 25°C. The larger value of  $x = 2$  obtained by Dinse and Mobius appears to be the result of their failing to correct for the change in the bulk  $\text{SO}_2$  concentrations after electrolysis. However, since details of the experiments are not given in their paper this cannot be confirmed.

In addition to the formation of the complex species,  $\text{S}_2\text{O}_4^-$ , dimerization of the  $\text{SO}_2^-$  to form dithionite has also been shown to be important (9)



Reaction [3] is the major follow-on reaction in dimethylsulfoxide solution, the value of  $K_3$  being  $10^5$  dm<sup>3</sup> mol<sup>-1</sup> at 55°C.

In view of the potential importance of studies of the basic electrochemistry and chemistry of the reduction process in helping to resolve some of the remaining

\* Electrochemical Society Active Member.  
Key words: high energy density batteries.

problems of the primary lithium-sulfur dioxide battery and in indicating directions for further improvement of the system (e.g., the development of a rechargeable Li/SO<sub>2</sub> battery), we have recently undertaken a systematic study of the effect of solution composition on the kinetics and mechanism of the electroreduction of sulfur dioxide in nonaqueous media. In this paper, we describe results that we have obtained for the electroreduction of SO<sub>2</sub> in solutions of 0.1M tetraethylammonium perchlorate (TEAP) in DMF. Additional work on the effect of solvent and electrolyte on the kinetics and mechanism of the electroreduction of SO<sub>2</sub> will be described in another paper as will results of simultaneous electrochemical-electron spin resonance measurements.

### Experimental

Current-potential data were obtained using a PAR Model 170 Electrochemistry System. All measurements were made in a jacketed 3-electrode glass cell. The working electrode was normally a dropping mercury electrode except in the cyclic voltammetric experiments where a hanging mercury drop electrode was used. The counterelectrode was a platinum cylinder and the reference electrode a silver wire in a solution of 0.05M AgNO<sub>3</sub> and 0.05M TEAP in DMF. This solution was changed daily because of photoreduction of the Ag<sup>+</sup>. The solution in the reference electrode compartment was isolated from the working solution by fritted glass disks.

Kinetic data for the electron transfer process were obtained using the phase sensitive a-c admittance method described previously (10). Admittance data were obtained as a function of d-c potential in the vicinity of the d-c half-wave potential over the frequency range from 160 to 1050 Hz using a 10 mV (peak-to-peak) a-c signal. Pulse polarographic measurements were also made for many of the systems. In these experiments, a potential pulse is applied for 45 msec at the end of the drop life, the average current being measured during the final 5 msec.

The procedures followed for purifying and drying the DMF (Aldrich Spectrophotometric grade) and TEAP (Eastman) have been described previously (10-12). Anhydrous SO<sub>2</sub> was used as received from Matheson. A stock SO<sub>2</sub> solution was prepared by bubbling SO<sub>2</sub> in DMF. The concentration of the stock SO<sub>2</sub> solution (~0.5M) was determined by titration. All solvents, salts, and stock solutions were stored in a controlled atmosphere glove box (Vacuum Atmospheres Limited) where the argon atmosphere was continually purged of oxygen and water. Further dilution of the stock SO<sub>2</sub> solution to prepare the working solutions (0.1-5 mM) was carried out in the glove box and all solutions were bubbled with argon to remove traces of oxygen. The experiments were conducted in the same glove box. The temperature of the cell was maintained constant by passing methanol, controlled at the desired temperature, through an outer jacket surrounding the working compartment of the cell.

### Results

**Cyclic voltammetry.**—Reduction of sulfur dioxide in a 0.1M TEAP/DMF solution gives a well-defined cyclic voltammogram as shown in Fig. 1. The presence of a follow-on reaction is indicated by the appearance of more than one oxidation peak on the reverse sweep and the ratio of the peak anodic to the peak cathodic currents for the reduction reaction which is less than one (13). These results are in qualitative agreement with those reported earlier by Martin and Sawyer (3).

**D-C polarography.**—In order to study the reduction process in more detail, d-c polarographic measurements were made as a function of both SO<sub>2</sub> concentration and temperature. These polarograms are broader than is expected for a simple one-electron transfer

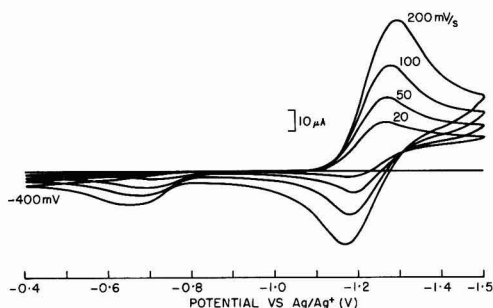


Fig. 1. Cyclic voltammogram for the reduction (forward sweep) of 10<sup>-2</sup>M SO<sub>2</sub> at a hanging mercury drop electrode in N,N-dimethylformamide containing 0.1M tetraethylammonium perchlorate with varying sweep rates as indicated.

reaction, plots of log ( $i/i_d - i$ ) having nonlinear slopes greater than 59 mV per decade. In addition, the half-wave potential is dependent both on SO<sub>2</sub> concentration and temperature.

The effect of concentration on the half-wave potential is shown in Fig. 2 and on the plots of log ( $i/i_d - i$ ) vs.  $E$  in Fig. 3. It is seen that, as the concentration is increased, there is a positive shift of the half-wave potential and a marked increase in the curvature of the log ( $i/i_d - i$ ) plots. There is also a linear variation of the limiting current,  $i_d$ , with concentration. The half-wave potential and shape of the polarograms were found to be independent of drop time in the range from 1 to 5 sec.

Figure 2 also shows that decreasing the temperature causes a positive shift of the half-wave potential. As one might expect, there is also a marked decrease in the limiting current. The plots of log ( $i/i_d - i$ ) vs.  $E$  (Fig. 4) show that the polarograms are sharpened as the temperature is decreased.

**A-C polarography.**—A-C admittance measurements were made on each of the SO<sub>2</sub> solutions in order to measure the rate of electron transfer (10). Above 0°C, the a-c admittance data give good Randle's plots (Fig. 5). At lower temperatures deviation from linearity is observed. Analysis of the a-c data allows (10) both the standard rate constant for the electron transfer reaction and the diffusion coefficient to be determined (see Table I). In calculating these parameters, allowance has been made for the fact that, at the standard electrode potential,  $E_1^\circ$ , the SO<sub>2</sub> concentration is less than half the bulk SO<sub>2</sub> concentration as a result of the follow-on reaction. The actual concentration was determined from the d-c polarograms.

The a-c peak potential (as measured from the peak of the out-of-phase component of the a-c admittance) was found to be 20-50 mV negative with respect to the half-wave potentials from d-c polarography and independent of concentration and temperature, having a constant value of -1.30V against the Ag/Ag<sup>+</sup> reference electrode.

**Pulse polarography.**—Pulse polarography was used to study the reduction process for times intermediate between those used for the d-c and a-c measurements.

Table I. A-C polarography analysis

Temp (°C)	$k_s$ (cm sec <sup>-1</sup> )	$D$ (cm <sup>2</sup> sec <sup>-1</sup> ) × 10 <sup>6</sup>
30	1.2	8.68
25	1.0	6.76
20	0.9	5.23
10	0.7	3.03
0	0.5	1.69
-10	0.4	0.90



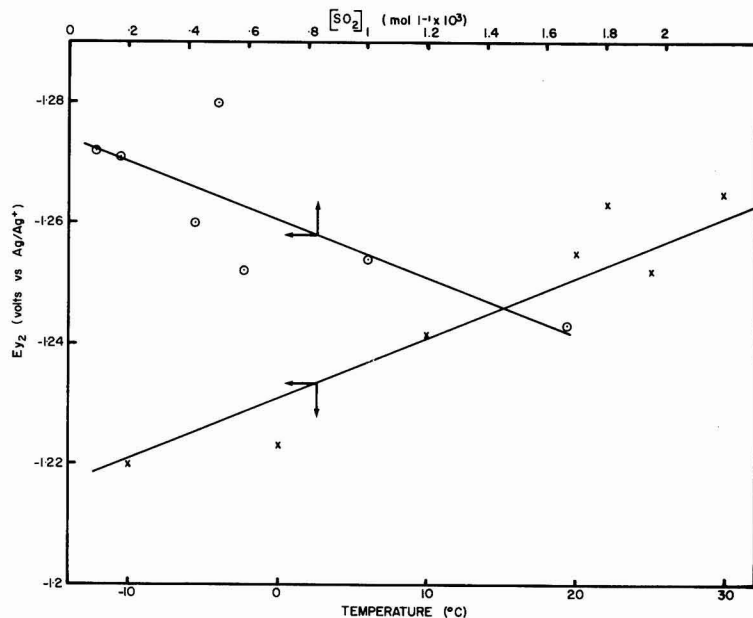


Fig. 2. Effect of reactant concentration and temperature on the half-wave potential for the electroreduction of  $\text{SO}_2$  in the same solution as Fig. 1.

More specifically, the current was sampled at the end of a 45 msec pulse. This can be compared with times in the 1-6 msec range used in the a-c measurements and the 2 sec drop time used for most of the d-c measurements. Pulse polarography measurements were made using both cathodic and anodic sweeps.

Pulse polarograms obtained for solutions of  $\text{SO}_2$  in 0.1M TEAP/DMF using a negative sweep give half-wave potentials which are negative with respect to the d-c half-wave potentials. In addition, the plots of

$\log (i/i_d - i)$  vs.  $E$  (Fig. 6) are more linear and have slopes closer to 59 mV per decade.

When the potential is swept positively from a point on the reduction wave, the pulse polarogram has two distinct waves (Fig. 7): one at  $-1.3\text{V}$  and one at  $-0.7\text{V}$ . The relative heights of the two waves depend both on concentration and initial potential. Table II gives the heights of the two waves as a function of initial potential for several different concentrations of  $\text{SO}_2$ . At the higher concentrations ( $\geq 10^{-3}\text{M}$ ) a slight

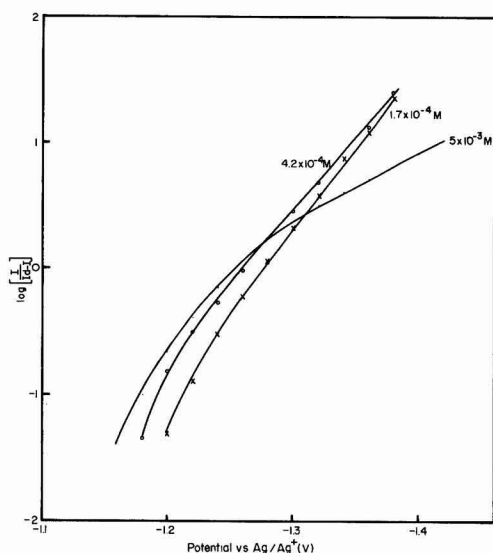


Fig. 3. Plots of  $\log [i/(i_d - i)]$  against electrode potential on the basis of d-c polarographic data for the electroreduction of  $\text{SO}_2$  with varying concentration of  $\text{SO}_2$  as indicated. Electrolyte as in Fig. 1.

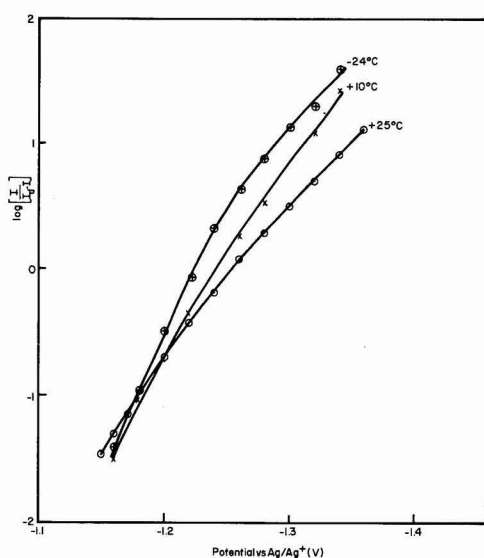


Fig. 4. Plots of  $\log [i/(i_d - i)]$  against electrode potential on the basis of d-c polarographic data for the electroreduction of  $\text{SO}_2$  with varying temperature of the electrochemical cell as indicated. Electrolyte as in Fig. 1.

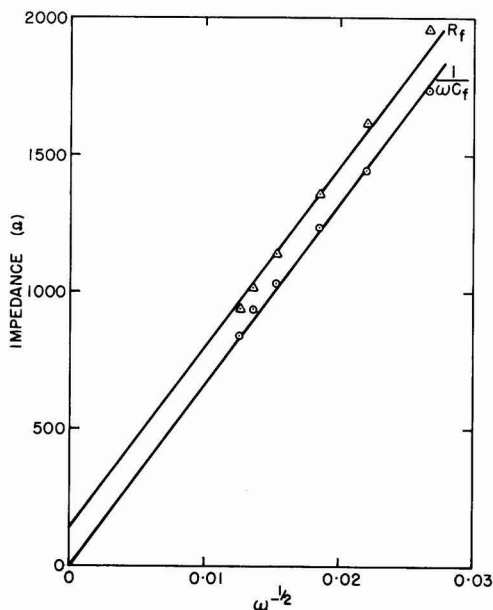


Fig. 5. Randle's plot of a-c admittance data for the electroreduction of  $10^{-3}\text{M}$   $\text{SO}_2$  in the same system as Fig. 1.

maximum is observed in the wave at  $-0.7\text{V}$  suggesting that weak adsorption is taking place (14).

### Discussion

As discussed earlier, previous work has shown that the  $\text{SO}_2^-$  produced in the primary electron transfer step can undergo the two follow-on reactions [2] and [3]. In the discussion that follows, the experimental results are discussed initially in terms of reactions [1] to [3] assuming  $\alpha = 1$  (i.e., the complex is assumed to have the stoichiometry  $\text{S}_2\text{O}_4^{2-}$ ).

Information regarding the mechanism of the electroreduction of  $\text{SO}_2$  in TEAP/DMF solutions can be obtained by comparing the experimental polarograms with theoretical predictions based on the proposed mechanism. In our description of the shape of the d-c polarograms, we assume that reactions [2] and [3] are

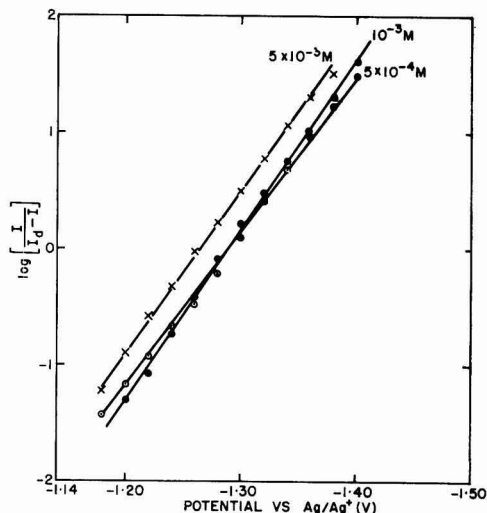


Fig. 6. Plots of  $\log [(i/i_d) - i]$  against potential for pulse polarographic data obtained with varying  $\text{SO}_2$  concentrations as indicated. Other conditions as in Fig. 1.

at equilibrium.<sup>1</sup> This assumption is supported by the observation that the measured half-wave potentials are independent of drop time. The present approach differs from that of Bonnetterre and Cauquis (9) who have described their cyclic voltammetric and rotating disk studies of the reduction of  $\text{SO}_2$  in dimethylsulfoxide in terms of dimerization of  $\text{SO}_2^-$  using a reaction layer approximation. If it is assumed that the Nernst and Ilkovic equations hold, then the following general expression can be derived (see Appendix) which describes the shape of the d-c polarogram

$$E - E_1^\circ = \frac{RT}{F} \ln \left\{ \frac{1}{2} \left( \frac{i_d - i}{i} \right) \right. \\ \left. \left\{ \left( 1 + K_2 \left( \frac{i_d - i}{i} \right) \right) + \left[ \left( 1 + K_2 \left( \frac{i_d - i}{i} \right) \right)^2 + \frac{4K_3 i}{g} \right]^{1/2} \right\} \right\} \quad [4]$$

<sup>1</sup> This assumption is not valid on the time scale used for the a-c, pulse polarographic, and cyclic voltammetric measurements.

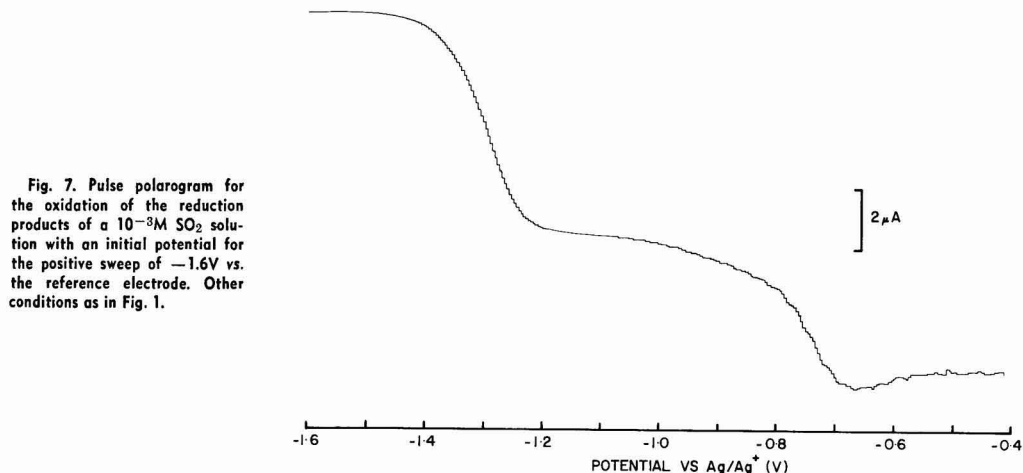


Fig. 7. Pulse polarogram for the oxidation of the reduction products of a  $10^{-3}\text{M}$   $\text{SO}_2$  solution with an initial potential for the positive sweep of  $-1.6\text{V}$  vs. the reference electrode. Other conditions as in Fig. 1.

where  $i_d$  is the limiting current and  $g$  the Ilković constant.

It is of interest to consider the simpler situations where either reaction [2] or [3] predominates.

When  $K_3 = 0$  (i.e., complex formation is the dominant follow-on reaction), Eq. [4] can be simplified to give

$$E - E_1^\circ = \frac{RT}{F} \ln \left\{ \left( \frac{i_d - i}{i} \right) \left[ 1 + K_2 \left( \frac{i_d - i}{g} \right) \right] \right\} \quad [5]$$

In this case it can be shown that the follow-on reaction [2] causes a shift of the polarogram to positive potentials and broadens the wave so that plots of  $\log(i/i_d - i)$  vs.  $E$  have slopes greater than 59 mV per decade.

If, on the other hand, it is assumed that dimerization of  $\text{SO}_2^-$  according to [3] is the major follow-on reaction (i.e.,  $K_2 = 0$ ), then Eq. [4] can be simplified to give

$$E - E_1^\circ = \frac{RT}{F} \ln \left\{ \frac{1}{2} \left( \frac{i_d - i}{i} \right) \left( 1 + \sqrt{\frac{4K_3 i}{g}} \right) \right\} \quad [6]$$

In this case, a positive shift of the polarograms is also predicted, but the polarographic waves are sharpened so that slopes of less than 59 mV per decade are obtained from plots of  $\log(i/i_d - i)$  vs.  $E$ .

It follows that the qualitative behavior of the d-c polarograms (Fig. 3) obtained for the reduction of  $\text{SO}_2$  in 0.1M TEAP/DMF solutions at room temperature corresponds to the predictions based on Eq. [5].

The experimental shift of the half-wave potential with respect to the standard potential for the  $\text{SO}_2/\text{SO}_2^-$  couple can be compared with theoretical predictions. Thus substituting the relationships that, at the half-wave potential

$$i = \frac{i_d}{2} = \frac{g[\text{SO}_2]^\circ}{2} \quad [7]$$

then, from Eq. [5], the dependence of the half-wave potential on  $\text{SO}_2$  concentration can be written

$$E_{1/2} - E_1^\circ = \frac{RT}{F} \ln \left( 1 + \frac{K_2[\text{SO}_2]^\circ}{2} \right) \quad [8]$$

Thus, a plot of  $\exp((E_{1/2} - E_1^\circ)F/RT)$  against  $[\text{SO}_2]^\circ$  should be linear with a slope of  $K_2/2$  and unit intercept. A value of  $E_1^\circ = -1.30\text{V}$  is obtained<sup>2,3</sup> from the peak potential of the out-of-phase component of the a-c admittance. Figure 8 shows values of  $\exp((E_{1/2} - E_1^\circ)F/RT)$  plotted against  $[\text{SO}_2]^\circ$ . From the slope, a value of  $K_2 = 8400 \pm 2000 \text{ dm}^3 \text{ mol}^{-1}$  is obtained for the association constant for reaction [2]. On the other hand, the intercept is found to be  $2.5 \pm 0.8$ , that is, not unity as predicted by Eq. [8]. The large value of the intercept suggests that some other reaction is contributing to the shift of the half-wave potential.

Some support for this conclusion is obtained from the pulse polarographic experiments. Regarding the two distinct waves observed on the positive sweep, the first at  $-1.3\text{V}$  is ascribed to the oxidation of  $\text{SO}_2^-$ . The second wave at  $-0.7\text{V}$  has been ascribed previously by Martin and Sawyer (3) and ourselves (15) to oxidation of the complex species  $\text{S}_2\text{O}_4^{2-}$ . As mentioned previously, the relative heights of these two waves are dependent on both  $\text{SO}_2$  concentration and initial potential (Table II). From these results it is seen that

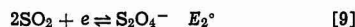
<sup>2</sup> The assumption is made that the diffusion coefficients for  $\text{SO}_2$  and  $\text{SO}_2^-$  are equal.

<sup>3</sup> As discussed later in the paper, on the time scale used for the a-c measurements, the follow-on reaction is sufficiently slow that the reaction can be considered as a simple one-electron transfer reaction. In this case, the peak of the out-of-phase component of the a-c admittance will occur when the surface concentrations of  $[\text{SO}_2]$  and  $[\text{SO}_2^-]$  are equal. The situation in this case is similar to that described by Fawcett and Lasia (10).

Table II. Pulse polarography—anoctic sweeps

$[\text{SO}_2]$ mol dm <sup>-3</sup> $\times 10^{-3}$	Initial potential volts vs. Ag/Ag <sup>+</sup>	wave 2 wave 1
5.0	-1.4	0.31
1.67	-1.6	0.54
1.0	-1.6	0.61
0.70	-1.6	0.77
0.58	-1.6	0.56
0.5	-1.6	0.50
	-1.36	0.58
	-1.24	1.0
	-1.20	1.83
0.20	-1.6	0.93
0.187	-1.6	0.79
0.10	-1.4	1.18

the relative intensity of wave 2 with respect to wave 1 decreases with increasing  $\text{SO}_2$  concentration instead of increasing linearly with increasing  $\text{SO}_2$  concentration as one would anticipate on the basis of  $\text{S}_2\text{O}_4^{2-}$  being formed by reaction [2]. In addition, an estimate of the standard potential  $E_2^\circ$  for  $\text{S}_2\text{O}_4^{2-}$  oxidation can be obtained from the association constant  $K_2$ . On the basis of fundamental thermodynamics, the standard potential for the reaction



is given by

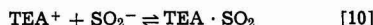
$$E_2^\circ - E_1^\circ = \frac{RT}{F} \ln K_2$$

Assuming  $K_2 = 8400 \text{ dm}^3 \text{ mol}^{-1}$ , it is found that standard potential for the  $2\text{SO}_2/\text{S}_2\text{O}_4^{2-}$  couple is 226 mV more positive than that for the  $\text{SO}_2/\text{SO}_2^-$  couple whereas a 600 mV difference is observed between the two oxidation waves in the pulse polarogram.

For these reasons it is concluded that the assignment of the wave at  $-0.7\text{V}$  to oxidation of  $\text{S}_2\text{O}_4^{2-}$  is incorrect. The failure to observe an oxidation wave for  $\text{S}_2\text{O}_4^{2-}$  can be explained by reaction [2] being sufficiently labile that the  $\text{S}_2\text{O}_4^{2-}$  is completely removed during the 45 msec pulse due to oxidation of the  $\text{SO}_2^-$  (reaction [2]).

The wave at  $-0.7\text{V}$  must therefore be ascribed to the oxidation of another product produced during the reduction of sulfur dioxide. Since this reaction causes a potential shift that is independent of  $\text{SO}_2$  concentration, it is concluded that the reaction is first or pseudo-first order. The following suggestions can be made:

- (a) Formation of a cation complex



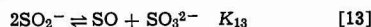
- (b) Formation of an anion complex



- (c) Formation of a solvent complex

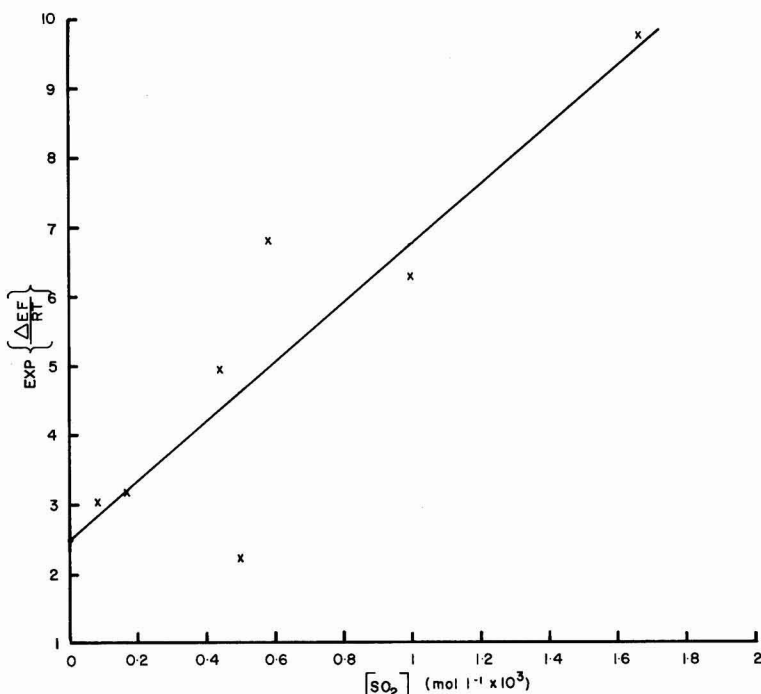


- (d) Disproportionation



The formation of a complex between  $\text{SO}_2^-$  and either the cation or the anion of the supporting electrolyte (reactions [10] and [11]) can be eliminated since the ratio of the two waves in the anodic pulse polarogram has been found to be independent of the concentration of the supporting electrolyte. The two waves were also observed at the same potential in hexamethylphosphoramide indicating that the reaction does not involve formation of a complex with the solvent. However, the results are consistent with a disproportionation of the  $\text{SO}_2^-$  according to reaction [13]. In this scheme the wave at  $-0.7\text{V}$  can be attributed to the oxidation of  $\text{SO}_3^{2-}$ . If it is assumed that the equilibrium for this reaction is established slowly compared to the 45 msec

Fig. 8. Graphical determination of the association constant  $K_2$  and the disproportionation constant  $K_{13}$  according to Eq. [15] from plots of the exponent of the shift in half-wave potential from the standard potential against the bulk  $\text{SO}_2$  concentration.



pulse then it is clear that two oxidation waves corresponding to oxidation of  $\text{SO}_2^-$  and  $\text{SO}_3^{2-}$  will be observed. In addition, at low  $\text{SO}_2$  concentrations where the formation of the  $\text{S}_2\text{O}_4^{2-}$  complex is negligible, the ratio of the  $\text{SO}_3^{2-}$  wave to the  $\text{SO}_2^-$  wave should be constant.

As the  $\text{SO}_2$  concentration is increased, the ratio of the  $\text{SO}_3^{2-}$  wave to the  $\text{SO}_2^-$  wave should decrease because the contribution that the complex makes to the  $\text{SO}_2^-$  wave will increase. This is observed experimentally where the ratio of the two waves goes from 1.2 in a  $10^{-4}\text{M}$   $\text{SO}_2$  solution to 0.3 in a  $5 \times 10^{-3}\text{M}$   $\text{SO}_2$  solution. Using data for the free energy of formation of  $\text{Li}_2\text{SO}_3$  and  $\text{SO}_3$ , it has been estimated (16) that  $E^\circ$  for the system  $2\text{Li} + \text{SO}_3 \rightarrow \text{Li}_2\text{SO}_3$  is  $\sim 3.7\text{V}$ . The corresponding value for  $2\text{Li} + 2\text{SO}_2 \rightarrow \text{Li}_2\text{S}_2\text{O}_4$  is about 3.0V. This indicates that the oxidation wave for  $\text{SO}_3^{2-}$  should occur approximately 700 mV more positive than the oxidation wave for  $\text{SO}_2^-$ . This is in reasonable agreement with the experimentally observed potential shift (600 mV).

The SO formed in reaction [13] is expected to further disproportionate (17) to form elemental sulfur and  $\text{SO}_2$ . This mechanism is supported by the work of Rinker and Lynn (18) who have shown that both sulfite and elemental sulfur are formed during the reduction of  $\text{SO}_2$  in DMF at sodium amalgam. Similar reactions have been postulated for the decomposition of dithionite in aqueous media (19). Experiments to measure the oxidation potential of  $\text{SO}_3^{2-}$  directly were unsuccessful because of the low solubility of the available sulfite salts.

It is easily shown that, when the disproportionation reaction is included in the reaction scheme, the shape of the d-c polarogram is given by the expression

$$E - E_1^\circ = \frac{RT}{F} \ln \left[ \left( \frac{i_d - i}{i} \right) \left( 1 + 2K_{13}^{1/2} + K_2 \left( \frac{i_d - i}{g} \right) \right) \right] \quad [14]$$

and the corresponding shift in half-wave potential by the relationship

$$E_{1/2} - E_1^\circ = \frac{RT}{F} \ln \left( 1 + 2K_{13}^{1/2} + K_2 \frac{[\text{SO}_2]^\circ}{2} \right) \quad [15]$$

Equation [15] is of the same general form as Eq. [8]; however, in this case a plot of  $\exp(E_{1/2} - E_1^\circ)F/RT$  against  $[\text{SO}_2]^\circ$  should give a linear plot with intercept  $1 + 2K_{13}^{1/2}$  and a slope equal to  $K_2/2$  as before. From the experimental intercept (Fig. 8) of  $2.5 \pm 0.8$ , a value of  $K_{13} = 0.6 \pm 0.4$  is obtained. At low concentration the ratio of the two waves in the anodic pulse polarogram should be approximately  $1/K_{13}^{1/2}$ . Using the value of  $K_{13} = 0.6$  obtained above, it is seen that the ratio of the two waves should be about 1.3 at low  $\text{SO}_2$  concentrations. Experimentally, a ratio of 1.2 is observed for a  $10^{-4}\text{M}$  solution, the lowest concentration measured.

An estimate of  $K_2$  can also be obtained by measuring the surface concentration of  $\text{SO}_2$  at the equilibrium potential. As a result of the follow-on reactions, the surface concentrations of  $\text{SO}_2$  and  $\text{SO}_2^-$  are less than half of the bulk concentration at the standard potential. It can be shown (Appendix) that the following relationship holds

$$K_2 = \frac{[\text{SO}_2]^\circ - 2(1 + K_{13}^{1/2})[\text{SO}_2]_{E=E_1^\circ}}{[\text{SO}_2]_{E=E_1^\circ}^2} \quad [16]$$

It follows that a plot of  $[\text{SO}_2]^\circ/[\text{SO}_2]_{E=E_0}$  against  $[\text{SO}_2]_{E=E_0}$  should give a straight line with slope equal to  $K_2$  and intercept  $2(1 + K_{13}^{1/2})$ . A plot of these data are shown in Fig. 9 from which the estimates  $K_2 = 2400 \pm 2000$  and  $K_{13} = 0.4 \pm 0.1$  are obtained. The value for  $K_{13}$  is in agreement with the potential shift analysis, but the  $K_2$  value does not agree with the previous estimate. On the whole, however, we feel the potential shift analysis is more reliable as it is less affected by distortions which occur on the upper part

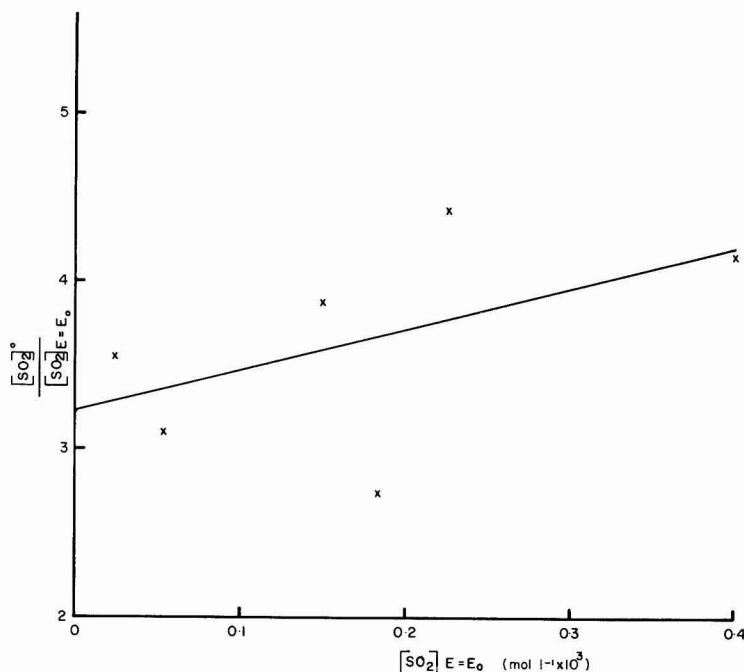


Fig. 9. Graphical determination of the association constant  $K_2$  and the disproportionation constant  $K_{13}$  from a plot of the ratio of the bulk  $SO_2$  concentration  $[SO_2]^\circ$  to the  $SO_2$  concentration at the electrode surface at the standard potential  $[SO_2]_{E=E_0}$  against  $[SO_2]_{E=E_0}$  according to Eq. [16].

of the wave and which become more significant as the  $SO_2$  concentration is increased. This distortion is probably due to a second reduction process.

The values of  $K_2$  obtained from these measurements are at least an order of magnitude higher than the value of  $600 \text{ dm}^3 \text{ mol}^{-1}$  determined by Laman *et al.* (20) in TEAP solutions and of  $230 \text{ dm}^3 \text{ mol}^{-1}$  determined by Kastening *et al.* (6) in tetraethylammonium bromide solution using ESR spectroscopy.

The reason for the large difference in the value of  $K_2$  obtained by the two methods is not clear. It is interesting to note, however, that ESR transients measured using a constant current pulse (20) can only be simulated if the larger (i.e., electrochemical) value of  $K_2$  is used. This suggests that the ESR measurement underestimates the value of  $K_2$  for some reason.

As the temperature is decreased, considerable changes occur in the reaction mechanism. Positive shifts in the half-wave potential along with a sharpening of the d-c polarogram all point to an increasing contribution of the dimerization reaction (reaction [3]) to the reduction mechanism as the temperature is lowered. This suggestion is confirmed by the observation that the intense ESR signal due to the paramagnetic complex  $S_2O_4^{\cdot -}$  in a partially reduced  $0.05M$   $SO_2$  solution completely disappears when the sample is cooled to  $77 \text{ K}$ . At room temperature, our own results as well as those of Kastening and Gostisa-Michelcic (6) indicate that the contribution of the dimerization reaction is not significant. From Ref. (6) it can be shown from the ratio of the two paramagnetic species and the  $SO_2$  concentration measured after electrolysis that very little if any of the  $SO_2^{\cdot -}$  formed during the initial stages of the electroreduction of  $SO_2$  dimerizes to form  $S_2O_4^{\cdot -}$  at room temperature.

Dithionite is, of course, the major product when the electroreduction is carried to completion (i.e., one electron per  $SO_2$  molecule). In addition, other complex species such as  $S_3O_6^{2-}$  have been observed by Martin and Sawyer (3) during the later stages of the electroreduction.

Analysis of the d-c polarographic limiting current data yields a diffusion coefficient of  $1.52 \times 10^{-5} \text{ cm}^2 \text{ sec}^{-1}$  at  $20^\circ\text{C}$ . A least squares fit of the limiting current data as a function of temperature yields an activation energy of  $8.5 \pm 0.3 \text{ kJ mol}^{-1}$  for the diffusion process.

Analysis of the pulse polarograms recorded using a cathodic sweep (Fig. 6) show clearly that the follow-on reactions have much less influence on the shape of the pulse polarogram than on the d-c polarogram. Thus, the half-wave potentials are closer to the standard electrode potential and plots of  $\log(i/i_d - i)$  against  $E$  are much more linear and have slopes closer to  $59 \text{ mV}$ . Systematic deviations remain, however, indicating that one or more of the follow-on reactions are fast enough to influence the shape of the pulse polarograms.

In order to obtain information on the kinetics of the electron transfer reaction, phase sensitive a-c admittance measurements were made. For temperatures above  $0^\circ\text{C}$ , the a-c admittance data give linear Randle's plots as shown in Fig. 5. These results indicate that, under these conditions, the follow-on reaction is sufficiently slow that the reaction can be considered as a simple one-electron transfer reaction on the time scale used for these measurements. In addition, the half-wave potentials are considerably more negative than those determined from d-c polarography and are independent of concentration. These results indicate that, by using a-c polarography, the primary electron transfer step can be studied without interference from follow-on reactions. The observation that deviations from linearity are observed in the Randle's plots for frequencies less than about  $160 \text{ Hz}$  in the  $10^{-3}M$  solution provides a crude estimate of the half-life of the  $SO_2^{\cdot -}$  radical which must be about  $10 \text{ msec}$  under these conditions. The influence of the  $SO_2$  concentration on the rate of conversion of  $SO_2^{\cdot -}$  into  $S_2O_4^{\cdot -}$  can be seen by the fact that deviations from linearity are observed at higher frequencies as the concentration of the  $SO_2$  is increased.

The results indicate that the electron transfer rate is very fast. At  $25^\circ\text{C}$ ,  $k_s = 1.0 \pm 0.2 \text{ cm/sec}$ . The uncer-

tainty in determining  $k_0$  is high as rates of this order of magnitude are at the limit of the a-c admittance technique. Analysis of the effect of temperature on the rate of electron transfer allows an activation energy of 20.4 kJ/mol to be determined. Electron transfer rates for the electroreduction of aromatic hydrocarbons are of the same order of magnitude (21) as those measured for the reduction of  $\text{SO}_2$ .

### Acknowledgment

The authors wish to thank Dr. A. S. Baranski for his helpful discussions and suggestions.

Manuscript submitted Sept. 24, 1980; revised manuscript received April 10, 1981. This was Paper 43 presented at the Los Angeles, California, Meeting of the Society, Oct. 14-19, 1979.

Any discussion of this paper will appear in a Discussion Section to be published in the June 1982 JOURNAL. All discussions for the June 1982 Discussion Section should be submitted by Feb. 1, 1982.

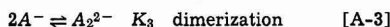
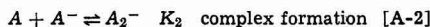
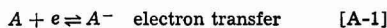
Publication costs of this article were assisted by the Defence Research Establishment Ottawa. This article was issued as DREO Report No. 848.

### APPENDIX

#### Shape of the d-c Polarogram

In describing the shape of the d-c polarogram it is assumed initially that:

(a) The mechanism of reaction is as follows



(b) That reactions [A-2] and [A-3] are in equilibrium; therefore

$$K_2 = \frac{[A_2^-]}{[A][A^-]} \quad [\text{A-4}]$$

and

$$K_3 = \frac{[A_2^{2-}]}{[A^-]^2} \quad [\text{A-5}]$$

(c) That the  $A/A^-$  couple determines the electrode potential and that the Nernst equation holds

$$\frac{[A]}{[A^-]} = P = \exp \left\{ \frac{(E - E_0)F}{RT} \right\} \quad [\text{A-6}]$$

(d) That the Ilković equation holds; it follows that

$$i = g([A]^\circ - [A]_0) \quad [\text{A-7}]$$

and

$$i_d = g[A]^\circ \quad [\text{A-8}]$$

where  $[A]^\circ$  is the bulk  $\text{SO}_2$  concentration and  $[A]_0$  the concentration at the surface.

(e) That the system is at steady state (i.e., flux in = flux out); thus

$$g_A \{ [A]^\circ - [A]_0 \} = g_A [A^-]_0 + 2g_{A_2^-} [A_2^-]_0 + 2g_{A_2^{2-}} [A_2^{2-}]_0 \quad [\text{A-9}]$$

and assuming

$$g_A = g_{A^-} = 2g_{A_2^-} = 2g_{A_2^{2-}} = g \quad [\text{A-10}]$$

we then find that

$$\frac{i_d}{g} = [A]^\circ = [A]_0 + [A^-]_0 + [A_2^-] + [A_2^{2-}] \quad [\text{A-11}]$$

Substituting [A-4] to [A-10] into [A-11] we find that

$$\frac{i_d}{g} = \frac{(i_d - i)}{g} + \frac{(i_d - i)}{gP} + K_2 \frac{(i_d - i)^2}{g^2 P} + K_3 \frac{(i_d - i)^2}{g^2 P^2} \quad [\text{A-12}]$$

The equation for  $P$  is

$$P = \frac{1}{2} \left\{ \frac{i_d - i}{i} \right\} \left\{ \left( 1 + K_2 \frac{(i_d - i)}{g} \right) + \left[ \left( 1 + K_2 \frac{(i_d - i)}{g} \right)^2 + \frac{4K_3 i}{g} \right]^{1/2} \right\} \quad [\text{A-13}]$$

From [A-6]

$$E - E_0 = \frac{RT}{F} \ln P \quad [\text{A-14}]$$

The above expression describes the shape of the polarogram in the general case where both reactions [A-2] and [A-3] are important. It is also of interest to consider the special cases where:

(a)  $K_3 = 0$  (i.e., complex formation is the dominant follow-on reaction). In this case, Eq. [A-4] can be simplified to give

$$E - E_0 = \frac{RT}{F} \ln \left[ \left( \frac{i_d - i}{i} \right) \left( 1 + K_2 \frac{(i_d - i)}{g} \right) \right] \quad [\text{A-15}]$$

At the half-wave potential  $i = i_d/2$ . Substitution of this relationship into [A-15] allows the following relationship to be obtained for the shift of the half-wave potential with respect to the standard potential

$$E_{1/2} - E_0 = \frac{RT}{F} \ln \left( 1 + \frac{K_2 [A]^\circ}{2} \right) \quad [\text{A-16}]$$

Measurement of the shift of the half-wave potential thus allows  $K_2$  to be determined.

An estimate of  $K_2$  can also be obtained from the concentration of  $A$  at  $E_0$  which can be obtained from the d-c polarogram using the Ilković equation at  $E = E_0$ ,  $P = 1$  and  $[A]_{E_0} = [A^-]_{E_0}$ . Substitution into [A-11] thus yields

$$[A_2^-]_{E_0} = [A]^\circ - 2[A]_{E_0} \quad [\text{A-17}]$$

therefore

$$K_2 = \frac{[A_2^-]}{[A][A^-]} = \frac{[A]^\circ - 2[A]_{E_0}}{[A]^2_{E_0}} \quad [\text{A-18}]$$

(b)  $K_3 = 0$  (i.e., dimerization is the major follow-on reaction). In this case Eq. [14] can be simplified to give

$$E - E_0 = \frac{RT}{F} \ln \left\{ \frac{1}{2} \left( \frac{i_d - i}{i} \right) [1 + (1 + \sqrt{4K_2 i/g})] \right\} \quad [\text{A-19}]$$

### REFERENCES

1. K. Crumrine, E. Juergens, and C. Colburn, "Investigation of the Environmental Consequences of the Disposal of the Lithium/Organic Electrolyte/ $\text{SO}_2$  Battery," Versar Inc. (1978) AD A059512.
2. A. N. Dey, "Safety Studies of Lithium-Sulphur Dioxide Cells," P. R. Mallory and Co. Inc. (1978) AD A062708.
3. R. P. Martin and D. T. Sawyer, *Inorg. Chem.*, **11**, 2644 (1972).
4. R. G. Rinker and S. Lynn, *J. Phys. Chem.*, **72**, 4706 (1968).
5. K. P. Dinse and K. Mobius, *Z. Naturforsch., Teil A*, **23**, 695 (1968).
6. B. Kastening and B. Gostisa-Mihelcic, *J. Electroanal. Chem. Interfacial Electrochem.*, **100**, 801 (1979).
7. F. Magno, G. A. Mazzocchin, and B. Bontompelli, *ibid.*, **57**, 89 (1974).
8. B. Kastening, B. Gostisa-Mihelcic, and J. Divisek, *Faraday Disc.*, **56**, 341 (1973).
9. R. Bonnatere and C. Cauquis, *Electroanal. Chem.*, **32**, 215 (1971).
10. W. R. Fawcett and A. Lasia, *J. Phys. Chem.*, **82**, 1114 (1978).
11. W. R. Fawcett, P. A. Forte, R. O. Loutfy, and J. Prokipeak, *Can. J. Chem.*, **50**, 263 (1972).
12. A. S. Baranski and W. R. Fawcett, *J. Chem. Soc. Faraday Trans. 1*, **76**, 1962 (1980).
13. R. S. Nicholson and I. Shain, *Anal. Chem.*, **36**, 706 (1964).



14. J. B. Flanagan, K. Takahashi, and F. C. Anson, *J. Electroanal. Chem. Interfacial Electrochem.*, **85**, 257 (1977).
15. C. L. Gardner, D. T. Fouchard, F. C. Laman, and W. R. Fawcett, in "Power Sources for Biomedical Implantable Applications and Ambient Temperature Lithium Batteries," B. B. Owens and N. Margalit, Editors, p. 545, The Electrochemical Society Softbound Proceedings Series, Princeton, NJ (1979).
16. G. E. Blomgren, V. Z. Leger, T. Kalnoki-Kis, M. L. Kronenberg, and R. J. Brodd, *Proc. 11th Internat. Power Sources Symposium*, 1978.
17. A. N. Dey and P. Bro, *This Journal*, **125**, 1574 (1978).
18. R. G. Rinker and S. Lynn, *Ind. Eng. Chem. Prod. Res. Dev.*, **8**, 338 (1969).
19. R. Pointeau, in "Nouveau traité général de minéralogie," Vol. 13, P. Pascal, Editor, Part II, pp. 1184-1196, Masson, Paris, (1956-1963).
20. F. C. Laman, C. L. Gardner, and D. T. Fouchard, in preparation.
21. A. C. Aten, C. Buthker, and G. J. Hoijtink, *Trans. Faraday Soc.*, **55**, 324 (1959).

# The Kinetics and Mechanism of the Electroreduction of Sulfur Dioxide in Nonaqueous Media

## II. Effects of Electrolyte and Solvent on the Mechanism of Reduction

C. L. Gardner\* and D. T. Fouchard\*

*Defence Research Establishment Ottawa, Energy Conversion Division, Ottawa, Ontario, Canada K1A 0Z4*

and W. R. Fawcett\*

*Guelph-Waterloo Centre for Graduate Work in Chemistry,  
Department of Chemistry, University of Guelph, Guelph, Ontario, Canada N1G 2W1*

### ABSTRACT

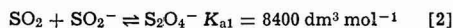
The effect of solvent and supporting electrolyte on the mechanism of the electroreduction of  $\text{SO}_2$  has been studied using polarography. It has been found that both the solvent and the electrolyte have a strong influence on the course of the reduction process. The reduction proceeds via the free radical intermediate  $\text{S}_2\text{O}_4^{\cdot -}$  in systems containing large cations but leads directly to  $\text{S}_2\text{O}_4^{2-}$  when the system contains small cations. In addition, it has been shown that the stability of the  $\text{S}_2\text{O}_4^{\cdot -}$  decreases with increasing basicity of the solvent. These effects have been interpreted in terms of ion pairing in the system.

The reduction of sulfur dioxide is industrially important for both the operation of the newly developed (1) high energy density lithium/sulfur dioxide battery and for the manufacture of dithionite salts (2) which are used in large quantities as an industrial reducing agent. In a previous paper (3), polarographic studies of the electroreduction of  $\text{SO}_2$  in 0.1 mol  $\text{dm}^{-3}$  solutions of tetraethylammonium perchlorate (TEAP) in *N,N*-dimethylformamide (DMF) have been described. In agreement with earlier work (4-8) it was found that, in this medium, the reduction process proceeds via a stable, blue paramagnetic complex of  $\text{SO}_2$  and  $\text{SO}_2^{\cdot -}$  having a 1:1 stoichiometry. Both ESR (9) and Raman (10) spectroscopic studies indicate that this species is a loosely bonded charge transfer complex. The polarographic studies have shown that the initial stages of the electroreduction process in 0.1 mol  $\text{dm}^{-3}$  TEAP/DMF can be explained in terms of the following reactions

#### (a) Electron transfer

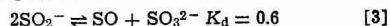


#### (b) Complex formation



and

#### (c) Disproportionation



At later stages of the reduction process a red complex that has been ascribed (4) to the complex species  $\text{SO}_2 \cdot \text{S}_2\text{O}_4^{2-}$  and finally dithionite are formed (10).

There are indications, however, that the choice of solvent and electrolyte has an important effect on the reduction mechanism. For example, Bonnetterre and Cauquis (11) concluded that the major follow-on reaction in dimethylsulfoxide solution is the dimerization of  $\text{SO}_2^{\cdot -}$  to form dithionite according to the reaction



In the present paper, we report results of studies that we have carried out to examine the effects that both the solvent and the electrolyte have on the mechanism of the electroreduction of sulfur dioxide in nonaqueous media.

### Experimental

The electroreduction of dilute solutions ( $\sim 10^{-3}$  mol  $\text{dm}^{-3}$ ) of sulfur dioxide has been studied using three different solvents and six different supporting electrolytes. The solvents, which were chosen for their different solvating abilities, included *N,N*-dimethylformamide (DMF) (Aldrich Spectrophotometric grade), acetonitrile (AN) (Aldrich Spectrophotometric grade), and hexamethylphosphoramide, HMPA, (Sigma). The

\* Electrochemical Society Active Member.

Key words: sulfur dioxide, high energy density batteries.

supporting electrolytes, which were chosen for variation of cation size, included tetraethylammonium perchlorate (TEAP) (Eastman), tetrabutylammonium perchlorate (TBAP) (Eastman), potassium perchlorate (Fisher), sodium perchlorate (Analar), and lithium perchlorate (Research Inorganic Chemical Company). The procedures followed for purifying and drying the solvents and salts have been described previously (12-14).

All potential measurements given in this paper were measured against a reference electrode that consisted of a silver wire in a solution of  $0.05 \text{ mol dm}^{-3} \text{ AgNO}_3$  and  $0.05 \text{ mol dm}^{-3} \text{ TEAP}$  in the solvent being used for the experiment. The reference electrode solution was changed daily due to photodecomposition of  $\text{Ag}^+$  in DMF. Other details of the electrochemical methods used to make the electrochemical measurements have been described in the first part of this study (3). Electron spin resonance measurements were made using a Varian E-Line spectrometer. The electrochemical ESR cell used for these measurements was similar to that designed by Goldberg and Bard (15). This cell was filled and sealed in the glove box to exclude moisture and air and ESR measurements were then made after partial electrolysis of the solution.

### Results and Discussion

**Effects of cation on the mechanism of reduction in DMF.**—The results to be described in this section show that the mechanism of reduction of  $\text{SO}_2$  becomes more complex when supporting electrolytes other than TEAP or TBAP are used in DMF solvent.

A comparison of the cyclic voltammograms in different electrolytes shows a transition from a quasi-reversible reduction in TBAP and TEAP to an irreversible reduction when a small cation such as  $\text{Li}^+$  is used. The cyclic voltammograms of  $\text{SO}_2$  in TBAP are almost identical to those presented earlier for TEAP (3). These voltammograms show a quasi-reversible peak at  $-1.3 \text{ V}$  and a minor oxidation peak at about  $-0.7 \text{ V}$ , the latter being ascribed (3) to the oxidation of  $\text{SO}_3^{2-}$  produced from reaction [3]. When  $\text{LiClO}_4$  is used as electrolyte (Fig. 1), the reduction reaction is essentially irreversible, the  $\text{SO}_2$  being removed rapidly by a follow-on reaction. In this case, there is evidence for the formation of an additional major product which is oxidized at more positive potentials ( $-1.0 \text{ V}$ ). Only a small oxidation peak is observed at  $-0.7 \text{ V}$ . In TEAP and  $\text{LiClO}_4$  solutions, a linear relationship is observed between  $i_p$ , the peak current of the reduction wave, and  $\nu^{1/2}$  where  $\nu$  is the sweep rate.

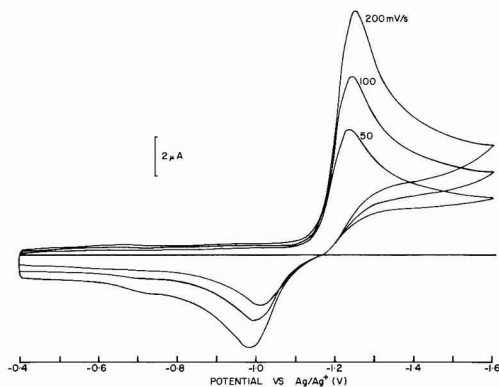


Fig. 1. Cyclic voltammograms for the reduction (forward sweep) of  $10^{-3} \text{ mol dm}^{-3} \text{ SO}_2$  at a hanging mercury drop electrode (HMDE) in  $N,N$ -dimethyl formamide (DMF) containing  $0.1 \text{ mol dm}^{-3} \text{ LiClO}_4$  with varying sweep speeds as indicated.

The cyclic voltammograms of  $\text{SO}_2$  in  $0.1 \text{ mol dm}^{-3} \text{ KClO}_4$  and  $\text{NaClO}_4$  (Fig. 2 and 3) are more complex. The distinct prewave and large oxidation wave on the reverse sweep seen in  $\text{KClO}_4$  solution is characteristic (16) of product adsorption.

For both  $\text{NaClO}_4$  and  $\text{KClO}_4$ ,  $i_p/\nu^{1/2}$  decreases with increasing  $\nu$ . This behavior is ascribed to product adsorption in both electrolytes. This suggestion is confirmed by d-c and pulse polarographic measurements as discussed later. Because of product adsorption, interpretation of the number and position of the oxidation peaks observed in  $\text{KClO}_4$  and  $\text{NaClO}_4$  is difficult. Qualitatively, however, it appears that the cyclic voltammogram of  $\text{SO}_2$  in  $\text{KClO}_4$  most closely resembles that in TEAP while the voltammogram in  $\text{NaClO}_4$  more closely resembles that in  $\text{LiClO}_4$ .

In order to study the reduction process in more detail, d-c polarographic measurements were also made on all of the solutions. Both the shape and the half-wave potential were dependent on the nature of the base electrolyte. This is illustrated in Fig. 4 where plots of  $\log(i/i_d - i)$  vs.  $E$  are presented. The half-wave potentials and limiting current constants, based on maximum currents, are given in Table I.

The d-c polarogram of  $\text{SO}_2$  in TBAP is virtually identical with that in TEAP which has been described in detail previously (3). The d-c polarographic data are consistent (3) with the reduction proceeding via reactions [1]–[3] in both electrolytes.

The shape of the d-c polarogram for  $\text{SO}_2$  in  $\text{LiClO}_4$  or  $\text{LiBr}$  is quite different (Fig. 4) from that described above for  $\text{SO}_2$  in TEAP. In this case, the follow-on reaction causes the polarogram to be sharpened so that plots of  $\log(i/i_d - i)$  vs.  $E$  have a slope of about  $45 \text{ mV}$  per decade, the half-wave potential

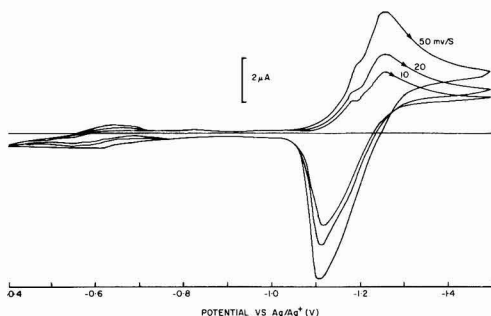


Fig. 2. Cyclic voltammograms for the reduction of  $10^{-3} \text{ mol dm}^{-3} \text{ SO}_2$  at an HMDE in DMF containing  $0.1 \text{ mol dm}^{-3} \text{ KClO}_4$  with varying sweep speeds as indicated.

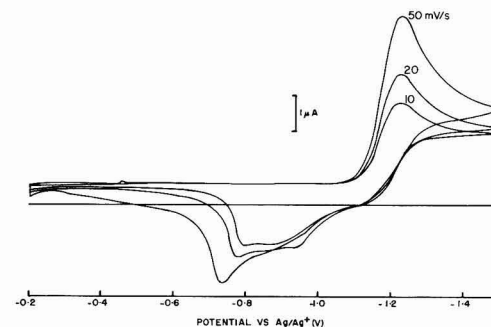


Fig. 3. Cyclic voltammogram for the reduction of  $10^{-3} \text{ mol dm}^{-3} \text{ SO}_2$  at an HMDE in DMF containing  $0.1 \text{ mol dm}^{-3} \text{ NaClO}_4$  with varying sweep speeds as indicated.

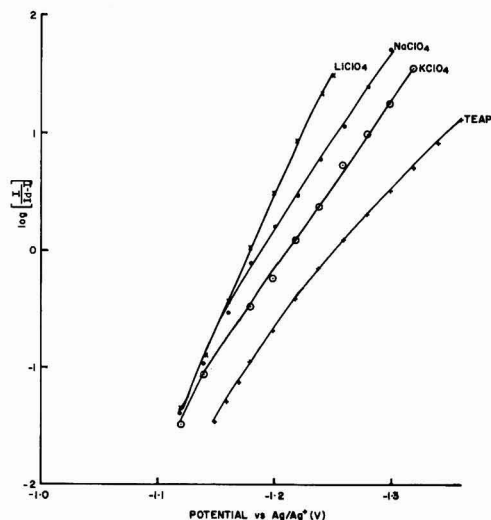


Fig. 4. Plots  $\log(i/i_d - i)$  against electrode potential on the basis of d-c polarographic data for the electroreduction of  $\text{SO}_2$  in DMF containing different electrolytes as indicated.

being  $-1.18\text{V}$ . The effects of temperature on the half-wave potential and limiting current constant are shown in Table II.

This behavior is consistent (3) with a change of mechanism so that dimerization of the  $\text{SO}_2^-$  to form dithionite (reaction [4]) becomes the major follow-on reaction, i.e.



Dithionite is known (17) to be the major product in the discharge of the lithium/sulfur dioxide battery.

If it is assumed that reaction [4] is at equilibrium on the time scale used to make the d-c polarographic measurements and that the Nernst and Ilkovic equations hold then the shape of the d-c polarogram is described (3) by the equation

$$E - E^\circ = \frac{RT}{F} \ln \left\{ \frac{1}{2} \left( \frac{i_d - i}{i} \right) \left( 1 + \sqrt{\frac{4K_{a2}}{g}} \right) \right\} \quad [5]$$

where  $E^\circ$  is the standard electrode potential for the  $\text{SO}_2/\text{SO}_2^-$  couple,  $i_d$  is the limiting current, and  $g$  is the Ilkovic coefficient. At the half-wave potential, Eq. [5] reduces to

Table I. D-C polarographic data. Reduction of  $\text{SO}_2$  in DMF using various supporting electrolytes

	TEAP	$\text{KClO}_4$	$\text{NaClO}_4$	$\text{LiClO}_4$
Half-wave potential (volts vs. $\text{Ag}/\text{Ag}^+$ )	-1.263	-1.212	-1.187	-1.183
Limiting current constant ( $i_d/\text{cm}^{2/3}t^{1/6}$ )	2.532	2.576	2.509	2.873

Table II. D-C polarographic data. Reduction of  $\text{SO}_2$  in  $0.1\text{M}$   $\text{LiClO}_4/\text{DMF}$  at various temperatures

Temp ( $^\circ\text{C}$ )	Half-wave potential (volts vs. $\text{Ag}/\text{Ag}^+$ )	Limiting current constant ( $i_d/\text{cm}^{2/3}t^{1/6}$ )
-10	-1.22	2.135
0	-1.21	2.322
20	-1.195	2.873

$$E^{1/2} - E^\circ = \frac{RT}{F} \ln \left\{ \frac{1}{2} (1 + \sqrt{2K_{a2} [\text{SO}_2]^\circ}) \right\} \quad [6]$$

Taking the value of  $E^\circ = -1.30\text{V}$  estimated from a-c polarographic measurements as described later, then from the half-wave potential of  $-1.18\text{V}$  at  $24^\circ\text{C}$  a value of  $23.3 \times 10^6 \text{ dm}^3 \text{ mol}^{-1}$  is obtained for  $K_{a2}$ .

ESR measurements support this change in reduction mechanism in changing from TEAP to  $\text{LiClO}_4$  solutions. In  $\text{LiClO}_4$  solutions no paramagnetic intermediates are detected even at relatively high  $\text{SO}_2$  concentrations ( $\sim 10^{-2}\text{M}$ ). Under similar conditions an intense ESR signal is detected (6, 7, 9) for the polarographic complex  $\text{S}_2\text{O}_4^{2-}$  in TEAP solutions. The measurement of diffusion-limited currents for the reduction of  $\text{SO}_2$  in TEAP and  $\text{LiClO}_4$  also reflects the difference in reduction mechanism. In TEAP the limiting currents (and hence the apparent diffusion coefficient of  $\text{SO}_2$ ) are significantly lower (Fig. 5) than the  $\text{LiClO}_4$  solutions. This is undoubtedly caused by the scavenging of  $\text{SO}_2$  by  $\text{SO}_2^-$  to form  $\text{S}_2\text{O}_4^{2-}$ .

Interpretation of the d-c polarograms for  $\text{SO}_2$  in  $\text{KClO}_4$  and  $\text{NaClO}_4$  solutions is more difficult. In both systems distinct adsorption prewaves are observed. This is in agreement with the cyclic voltammogram for  $\text{SO}_2$  in  $\text{KClO}_4$  solutions which also showed effects due to product adsorption (Fig. 1). At  $53^\circ\text{C}$ , the polarogram for the reduction in  $\text{NaClO}_4$  solution shows a distinct kinetic maximum. From the cyclic voltammetric and d-c polarographic data, it appears that the situation in  $\text{KClO}_4$  and  $\text{NaClO}_4$  solutions is intermediate between that in TEAP and  $\text{LiClO}_4$ . It is thus probable that both  $\text{S}_2\text{O}_4^{2-}$  and  $\text{S}_2\text{O}_4^{\cdot-}$  are formed by reactions [2] and [4] in these solutions. Pulse polaro-

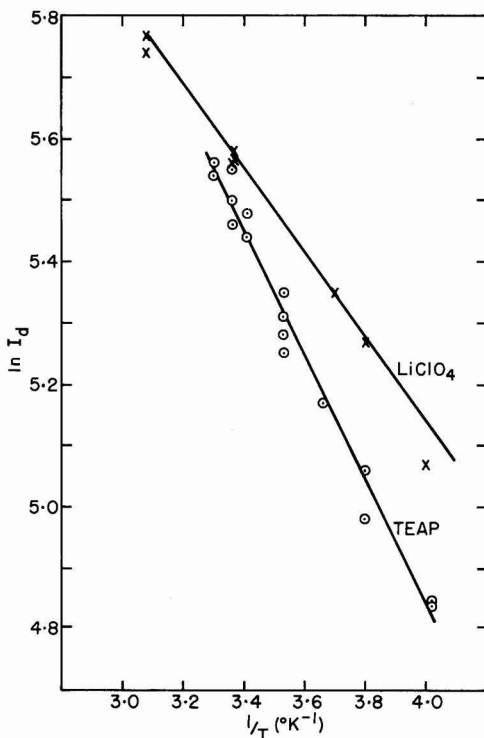


Fig. 5. Effect of temperature on the limiting current constant for the reduction of  $\text{SO}_2$  in DMF containing TEAP and  $\text{LiClO}_4$  as indicated.

graphic measurements support this conclusion. Using a negative potential sweep, the pulse polarogram for  $\text{SO}_2$  in all of the electrolytes consists of a single wave that gives a linear plot of  $\log(i/i_d - i)$  vs.  $E$  (Fig. 6). It is seen that there is a regular increase in slope of these curves from 68 to 46 mV per decade in going from TEAP to  $\text{LiClO}_4$ . This change of slope can be attributed to the shift in mechanism from formation of the free radical complex  $\text{S}_2\text{O}_4^{\cdot-}$  in TEAP to the formation of dithionite in  $\text{LiClO}_4$ . The theoretical description of the shape of the d-c polarogram when both reactions [2] and [4] contribute has been given previously (3). It can be shown that this gradual change of slope is consistent with the transition from one product to the other (i.e.,  $\text{S}_2\text{O}_4^{\cdot-}$  to  $\text{S}_2\text{O}_4^{2-}$ ).

The pulse polarographic data obtained using a positive potential sweep from various points on the reduction wave provide some information regarding the reaction mechanism. As has been discussed in detail previously (3), the pulse polarogram of  $\text{SO}_2$  in TEAP solutions obtained using a positive potential sweep shows two distinct waves, one wave at  $-1.3\text{V}$  that is attributed to the oxidation of  $\text{SO}_2^-$ , and a second wave at  $-0.7\text{V}$  that is attributed to oxidation of  $\text{SO}_3^{2-}$ . The failure to detect a wave due to oxidation of  $\text{S}_2\text{O}_4^{\cdot-}$  was attributed to the labile equilibrium that exists between  $\text{SO}_2^-$  and  $\text{S}_2\text{O}_4^{\cdot-}$ . It is believed that this equilibrium is sufficiently rapid that all of the  $\text{S}_2\text{O}_4^{\cdot-}$  is depleted through oxidation of  $\text{SO}_2^-$  before the current is sampled at the end of the 45 msec pulse.

The anodic pulse polarograms of  $\text{SO}_2$  in  $\text{KClO}_4$  (Fig. 7) and  $\text{NaClO}_4$  are more complex, the polarograms exhibiting large maxima. This behavior has been described by Flanagan and co-workers (18) who have shown that this effect is caused by product adsorption. This is in agreement with the d-c polarographic and cyclic voltammetric results which have also indicated that product adsorption is taking place as discussed previously. It is interesting to note that, when the initial potential is set just at the foot of the d-c polarogram, a small wave at  $-0.7\text{V}$  is observed. This indicates that the disproportionation of  $\text{SO}_2^-$  to form  $\text{SO}_3^{2-}$  takes place in these solutions as well.

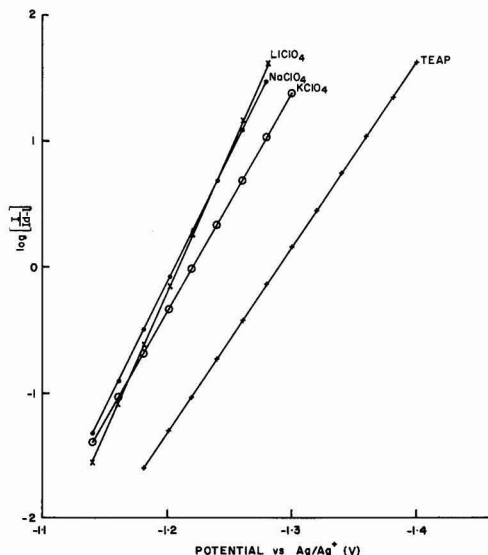


Fig. 6. Plots of  $\log(i/i_d - i)$  against electrode potential on the basis of pulse polarographic data for the electroreduction of  $\text{SO}_2$  in DMF containing different electrolytes as indicated.

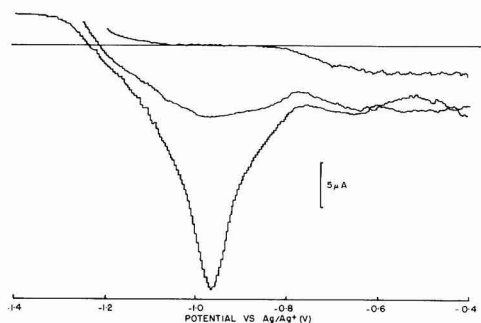


Fig. 7. Pulse polarogram for the oxidation of the reduction products of a  $10^{-3} \text{ mol dm}^{-3} \text{ SO}_2$  in DMF containing  $0.1 \text{ mol dm}^{-3} \text{ KClO}_4$  with initial potential as indicated.

In  $\text{LiClO}_4$  solutions (Fig. 8), the anodic pulse polarogram shows three distinct waves at  $-1.3$ ,  $-1.0$ , and  $-0.7\text{V}$ . At  $-1.3\text{V}$  the net current flowing is cathodic indicating that the  $\text{SO}_2^-$  produced in the primary reduction is completely removed during the 45 msec pulse. The major oxidation wave occurs at  $-1.0\text{V}$  and probably results from oxidation of dithionite which is thought to be the major product from the follow-on reactions. A small wave is also observed at  $-0.7\text{V}$  indicating that some  $\text{SO}_3^{2-}$  is also produced.

The experiments described above indicate that the electrolyte cation has a strong influence on the course of the electroreduction process. Thus, in TEAP solutions, the reduction process proceeds via the free radical complex  $\text{S}_2\text{O}_4^{\cdot-}$  as well as a red complex that has been ascribed to  $\text{SO}_2 \cdot \text{S}_2\text{O}_4^{2-}$  on route to dithionite on complete electrolysis. In  $\text{LiClO}_4$  solutions, on the other hand, dithionite is formed directly by dimerization of  $\text{SO}_2^-$ . The influence of electrolyte cation on the mechanism of reduction can be explained in terms of the effect of ion pairing on the position of the various equilibria (19). It appears that the formation of dithionite is favored when strong ion pairing occurs in solutions containing a small cation such as lithium. On the other hand when a large cation such as  $\text{TEA}^+$  is used and ion pairing is expected to be weak, the formation of the complex species is favored. With  $\text{Na}^+$  and  $\text{K}^+$  in solution, the degree of ion pairing is expected to be intermediate between these two extremes.

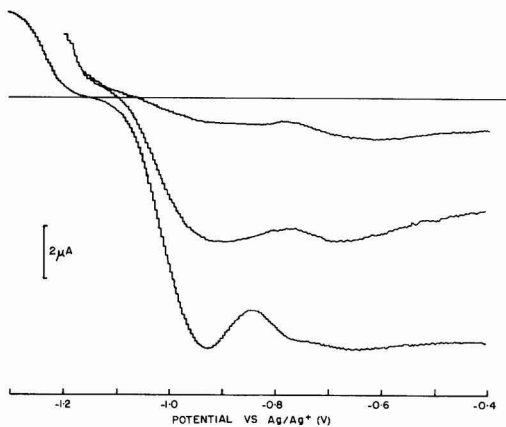


Fig. 8. Pulse polarogram for the oxidation of the reduction products of  $10^{-3} \text{ mol dm}^{-3} \text{ SO}_2$  in DMF containing  $0.1 \text{ mol dm}^{-3} \text{ LiClO}_4$  with initial potential as indicated.

**Effects of solvent on the mechanism of reduction.**—As mentioned previously, the electroreduction of sulfur dioxide has been studied in three different solvents (DMF, HMPA, and AN) of varying solvating ability to examine the effect of solvent on the mechanism of reaction. Measurements have been made in each of these solvents using TEAP, NaClO<sub>4</sub>, and LiClO<sub>4</sub> as electrolyte.

The d-c polarographic data for the reduction of SO<sub>2</sub> in 0.1 mol dm<sup>-3</sup> solutions of TEAP in each of the three solvents are shown in Fig. 9. The shapes of the log (*i*/*i*<sub>d</sub> - *i*) plots are very similar in HMPA and DMF. On the other hand, in AN a marked broadening of the curve occurs at negative potentials similar to that seen at high SO<sub>2</sub> concentrations in DMF (3). It is possible that this broadening is due to a second reduction process such as the direct reduction of S<sub>2</sub>O<sub>4</sub><sup>2-</sup>. It was also noted that there is a fairly large variation in limiting current which can be related to the variation in diffusion coefficient due to a corresponding variation in solvent viscosity.

The general features of the polarograms in all solvents with TEAP as electrolyte suggest that the reduction of SO<sub>2</sub> in these systems proceeds via reactions [1]–[3]. In this case the shift in the half-wave potential can be related (3) to the equilibrium constants *K*<sub>a1</sub> and *K*<sub>d</sub> by the relationship

$$E^{1/2} - E^{\circ} = \frac{RT}{F} \ln \left\{ 1 + 2K_d^{1/2} + \frac{K_{a1}}{2} [\text{SO}_2]^{\circ} \right\} \quad [7]$$

where [SO<sub>2</sub>]<sup>°</sup> is the bulk SO<sub>2</sub> concentration.

Using the method described earlier (3), the disproportionation constant *K*<sub>d</sub> was determined to be 1.5 in HMPA. The pulse polarogram for SO<sub>2</sub> in AN (Fig. 10) obtained using a positive potential sweep is quite different than that obtained in DMF or HMPA. In AN, a fairly weak broad wave is observed at about -0.85V which is absent when the initial potential is held at the foot of the reduction wave. This indicates that SO<sub>3</sub><sup>2-</sup> is not produced in this reaction and that *K*<sub>d</sub> = 0.0 in AN. The broad wave at -0.85V is tentatively assigned to the oxidation of S<sub>2</sub>O<sub>4</sub><sup>2-</sup>.

An estimate of the standard potential for the process SO<sub>2</sub> + *e* ⇌ SO<sub>2</sub><sup>-</sup> was obtained from the peak

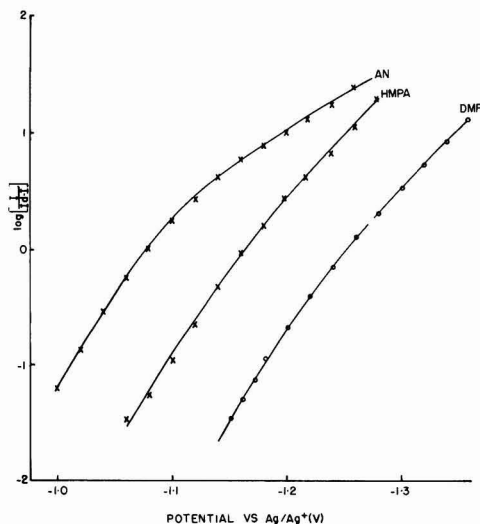


Fig. 9. Plots of log (*i*/*i*<sub>d</sub> - *i*) against electrode potential on the basis of d-c polarographic data for the electroreduction of SO<sub>2</sub> in various solvents as indicated containing 0.1 mol dm<sup>-3</sup> TEAP.

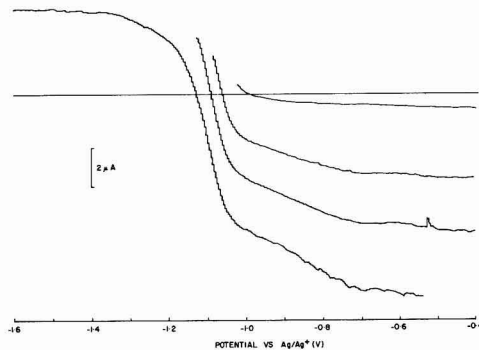


Fig. 10. Pulse polarogram for the oxidation of the reduction products of 10<sup>-3</sup> mol dm<sup>-3</sup> SO<sub>2</sub> in AN containing 0.1 mol dm<sup>-3</sup> TEAP with initial potential as indicated.

potential of the out-of-phase component of the a-c admittance. Using the measured d-c polarographic half-wave potentials and Eq. [7], values of *K*<sub>a1</sub> = 0, 8400, and 17,000 dm<sup>3</sup> mol<sup>-1</sup> are obtained in HMPA, DMF, and AN, respectively. From these results, it is seen that the solvent has an important effect on the stability of the complex and thus the reaction mechanism. These results provide further evidence of the importance of ion pairing in determining the position of equilibrium among the various components of the reacting system. As the basicity of the solvent decreases (20) (HMPA > DMF > AN) the ability of the cation in the system to interact with negatively charged components of the reaction system increases; thus, it appears that the negatively charged complex S<sub>2</sub>O<sub>4</sub><sup>2-</sup> is most stable in AN where it can most strongly interact with the cation, in this case, TEA<sup>+</sup>.

The electroreduction of SO<sub>2</sub> was also studied in 0.1 mol dm<sup>-3</sup> solutions of LiClO<sub>4</sub> and NaClO<sub>4</sub> using each of the three solvents. In these electrolytes, the experimental results are complicated by the apparent kinetically limited reduction in HMPA and extremely strong adsorption of product in AN. Because of these complications, very few conclusions regarding the effect of solvent on the reaction mechanism could be reached. Perhaps the most revealing results are the data obtained by pulse polarography recorded using a negative sweep with 0.1 mol dm<sup>-3</sup> LiClO<sub>4</sub> electrolyte (Fig. 11). From these curves it is concluded that the formation of dithionite is the major follow-on reaction in AN and DMF. In HMPA (Fig. 11) the slope of the log (*i*/*i*<sub>d</sub> - *i*) plot is much larger (~91 mV per decade) and the half-wave potential is considerably more positive than that measured using d-c polarography. It is suggested that this behavior is the result of a kinetic limitation of the reduction of SO<sub>2</sub> in this system.

The very strong product adsorption that occurs in AN leads to some curious results. In LiClO<sub>4</sub> or NaClO<sub>4</sub> solutions, it is not possible to record a d-c polarogram because the electrode becomes blocked by the adsorbed product. As shown in Fig. 12, the normal pulse polarogram recorded in 0.1 mol dm<sup>-3</sup> solution of LiClO<sub>4</sub> in AN using an anodic sweep also shows dramatically the effects of adsorption. In this case a large adsorption peak is observed at very positive potentials rather than the normal oxidation waves seen when HMPA or DMF are used as the solvent (Fig. 12). This gives the normal pulse polarogram a very unusual appearance.

### Conclusions

These studies have indicated that the choice of solvent and electrolyte has a major effect on the

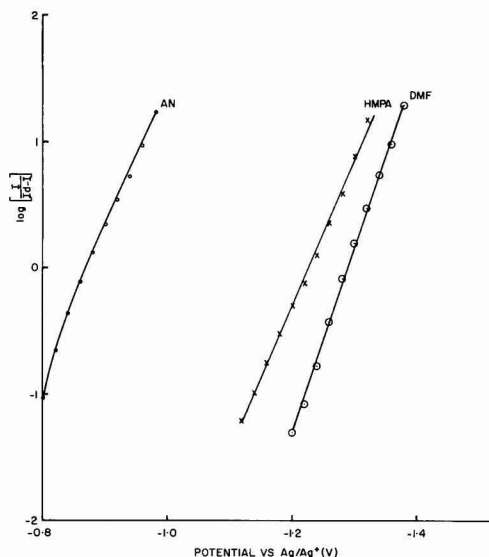


Fig. 11. Plots of  $\log (i/i_d - i)$  against electrode potential on the basis of pulse polarographic data for the electroreduction of  $\text{SO}_2$  in various solvents as indicated containing  $0.1 \text{ mol dm}^{-3} \text{ LiClO}_4$ .

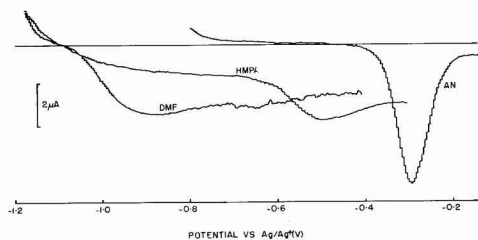


Fig. 12. Pulse polarogram for the oxidation of the reduction products of  $10^{-3} \text{ mol dm}^{-3} \text{ SO}_2$  in various solvents as indicated containing  $0.1 \text{ mol dm}^{-3} \text{ LiClO}_4$ .

mechanism of reduction of sulfur dioxide in nonaqueous media. The influence of solvent and electrolyte on the reaction mechanism can be interpreted in terms of ion pairing in the system.

In DMF solution, it has been shown that, in solutions containing a large cation such as  $\text{TEA}^+$  which leads to relatively weak ion-pairing, the reduction

process proceeds via the free radical complex  $\text{S}_2\text{O}_4^{\cdot -}$  during the initial stages of electrolysis. When a small cation such as  $\text{Li}^+$  is used, on the other hand, dithionite is formed directly by dimerization of the primary reduction product  $\text{SO}_2^{\cdot -}$ . In addition, it has been shown that the stability of  $\text{S}_2\text{O}_4^{\cdot -}$  decreases with increasing basicity of the solvent.

Manuscript submitted Feb. 9, 1981; revised manuscript received May 29, 1981.

Any discussion of this paper will appear in a Discussion Section to be published in the June 1982 JOURNAL. All discussions for the June 1982 Discussion Section should be submitted by Feb. 1, 1982.

Publication costs of this article were assisted by the Defence Research Establishment Ottawa. This article was issued as DREO Report No. 849.

#### REFERENCES

- W. P. Kilroy, in "28th Power Sources Symposium," p. 198, June 12-15, 1978, The Electrochemical Society, Princeton, NJ (1978).
- R. G. Rinker and S. Lynn, *Ind. Eng. Chem. Prod. Res. Dev.*, **8**, 338 (1969).
- C. L. Gardner, D. T. Fouchard, and W. R. Fawcett, *This Journal*, **128**, 2337 (1981).
- R. P. Martin and D. T. Sawyer, *Inorg. Chem.*, **11**, 2644 (1972).
- R. G. Rinker and S. Lynn, *J. Phys. Chem.*, **72**, 4706 (1968).
- K. P. Dinse and K. Mobius, *Z. Naturforsch. Teil A*, **23**, 695 (1968).
- B. Kastening and B. Gostisa-Mihelcic, *J. Electroanal. Chem. Interfacial Electrochem.*, **100**, 801 (1969).
- F. Magno, G. A. Manochin, and G. Bontempelli, *ibid.*, **57**, 89 (1974).
- F. C. Laman, C. L. Gardner, and D. T. Fouchard, *J. Phys. Chem.*, Submitted for publication.
- W. A. Adams, C. L. Gardner, and D. T. Fouchard, *Proc. 7th International Raman Conf.*, Ottawa, 1980, North/Holland Publishing Co., Amsterdam, p. 202.
- R. Bonnetterre and G. Cauquis, *J. Electroanal. Chem. Interfacial Electrochem.*, **32**, 215 (1971).
- W. R. Fawcett and A. Lasia, *J. Phys. Chem.*, **82**, 1114 (1978).
- W. R. Fawcett, P. A. Forte, R. O. Loutfy, and J. Prockipcak, *Can. J. Chem.*, **50**, 263 (1972).
- A. S. Baranski and W. R. Fawcett, *J. Chem. Soc. Faraday Trans. I*, **76**, 1962 (1980).
- I. B. Goldberg and A. J. Bard, *J. Phys. Chem.*, **75**, 3281 (1971).
- R. H. Wopschall and I. Shain, *Anal. Chem.*, **39**, 1514 (1967).
- P. Bro, H. Y. Yang, C. Schlaikjer, and H. Taylor, Tenth IECEC Conference, p. 423 (1975).
- J. B. Flanagan, K. Takahashi, and F. C. Anson, *J. Electroanal. Chem. Interfacial Electrochem.*, **63**, 257 (1977).
- "Ions and Ion Pairs in Organic Reactions," M. Swarc, Editor, Wiley, New York (1972).
- W. R. Fawcett and T. M. Krygowski, *Can. J. Chem.*, **54**, 3282 (1976).



# Electrocatalysis for Chlorine Electrode Reaction on RuO<sub>2</sub> Electrode in NaAlCl<sub>4</sub> Melt

I. Uchida,\* H. Urushibata, and S. Toshima

Department of Applied Chemistry, Faculty of Engineering, Tohoku University, Aramaki-Aoba, Sendai 980, Japan

## ABSTRACT

In molten AlCl<sub>3</sub>-NaCl with near equimolar compositions, electrocatalysis of the chlorine electrode reaction ( $2\text{Cl}^- = \text{Cl}_2 + 2e^-$ ) on RuO<sub>2</sub> electrodes has been investigated at 175°C. Melt-stable RuO<sub>2</sub> electrodes were prepared by a thermal decomposition method on semiconductive SnO<sub>2</sub> films deposited on Pyrex substrates. Tafel relationships for chlorine evolution and reduction were studied as functions of  $p\text{Cl} (= -\log a_{\text{Cl}^-})$  and partial pressure of Cl<sub>2</sub>, and several kinetic parameters including reaction orders with respect to Cl<sup>-</sup> and Cl<sub>2</sub> were determined. The mechanistic analysis based on the theoretical kinetic derivatives revealed that the chlorine electrode reaction on RuO<sub>2</sub> obeys a Volmer-Tafel type mechanism under the activated Temkin condition:  $\text{Cl}^- = \text{Cl}_{\text{ad}} + e^-$  (fast),  $\text{Cl}_{\text{ad}} + \text{Cl}_{\text{ad}} \rightleftharpoons \text{Cl}_2$  (slow). The exchange current density at the standard condition ( $p\text{Cl} = 1.1$ ,  $P_{\text{Cl}_2} = 1$  atm) was  $132 \pm 22 \mu\text{A}/\text{cm}^2$ , and this figure was found to be 15–20 times larger than that on glassy carbon electrodes. The difference of this electrocatalytic activity was ascribed to the mechanistic difference between the two electrode materials and not to the difference of electrode roughness. Capacity data to check this viewpoint were also presented.

Electrocatalysis of the chlorine electrode reaction in molten salt systems is of special interest from the viewpoint of developing molten salt batteries and electrolytic metal winning processes. The only anode material available so far is carbon, which is not sufficiently stable in chloroaluminate melts, showing considerable swelling and disintegration (1, 2). In previous works (3, 4), we have shown that Sb-doped tin oxide acts as stable working electrodes for chlorine evolution. Highly doped SnO<sub>2</sub> having carrier densities of the order of  $10^{20} \text{ cm}^{-3}$  behaves as an electron-tunneling electrode which allows the electron to pass through the space charge layer formed at the semiconductor/melt interface (5). The comparative study carried out on SnO<sub>2</sub> and glassy carbon (GC) electrodes showed that the polarization behavior for chlorine evolution on SnO<sub>2</sub> increasingly approached that on GC with increasing carrier density (4). In this case, however, electrocatalytic activity would not be expected for SnO<sub>2</sub> electrodes because the electron tunneling process governs the chlorine evolution. Considering that SnO<sub>2</sub> can be utilized as a catalyst support and a current collector, we have proposed the possibility of developing DSA-type, SnO<sub>2</sub>-based electrocatalysts usable in melts by applying the oxide-coating techniques employed in the production of DSA.

DSA-type electrodes used for the electrolysis of brine have a multilayer structure consisting of the upper layer of electrocatalyzers such as RuO<sub>2</sub> and the intermediate layer of titanium dioxide acting as the catalyst support which is formed on the underlying titanium substrate (6), and their physicochemical properties and electrochemical behavior have been studied extensively (7–12). Specially for chlorine evolution, a number of studies have been carried out with various electrochemical techniques (13–17). Iwakura *et al.* studied the reaction mechanism and catalytic activity for chlorine evolution on several kinds of metal oxides (RuO<sub>2</sub>, IrO<sub>2</sub>, MnO<sub>2</sub>, etc.) on the basis of crystal field theory (18, 19). Kazarinov *et al.* reported the double layer structure on Ru-Ti oxide anodes in various electrolyte solutions (20), and Rolison *et al.* investigated the electrochemical behavior of

RuO<sub>x</sub> electrodes in organic solvents (21). Although there are so many works concerning ruthenium oxide anodes, no workers have reported the electrocatalytic effect of ruthenium oxide on chlorine evolution in molten salt systems.

One of the problems for the use of so-called DSA-type anodes in chloride melts is the instability of Ti substrates. If the oxide anode has a pinhole or a crack and Ti metal comes into contact with melt, anodic dissolution of Ti will take place vigorously. To avoid this problem, ruthenium oxide used in this work was prepared on SnO<sub>2</sub> films on Pyrex substrates. With the electrodes thus prepared, we examined the electrocatalytic effect for chlorine evolution and the reduction in this melt system at 175°C and carried out the mechanistic study using kinetic parameters collected under various conditions. In comparison with the kinetic behavior of the chlorine electrode reaction on glassy carbon electrodes in the same melt system (22), the salient feature of ruthenium oxide as the electrocatalyzer has been demonstrated.

## Experimental

**Melt preparation.**—The AR grade NaCl and AlCl<sub>3</sub> which was rendered iron free by sublimation were mixed under a dry nitrogen atmosphere. After melting the mixture, a sequence of purification procedures (HCl gas treatment, Al displacement, and preelectrolysis) was performed as described previously (23, 24).

**Electrodes.**—Ruthenium oxide was prepared on Sb-doped tin oxide films with thermal decomposition of RuCl<sub>3</sub>. The SnO<sub>2</sub> films were prepared on rectangular Pyrex glass plates by a spray method using tin(IV) chloride solution containing 5 mol percent (m/o) SbCl<sub>3</sub> (23). A dilute n-propanol solution of RuCl<sub>3</sub> · 3H<sub>2</sub>O (0.02M) was applied to the thin SnO<sub>2</sub> film by the dip coating method, and then the liquid film of RuCl<sub>3</sub> on the SnO<sub>2</sub> substrate was dried in an oven at 120°C for 30 min and heated in air at 500°C for 20 min. This procedure was repeated 20 times to attain uniform coating of the oxide film, and finally the electrode thus prepared was annealed for 10 hr at 500°C in air.

Visual inspection showed that the SnO<sub>2</sub> film was covered with a blue-black, compact layer with satis-

\* Electrochemical Society Active Member.

Key words: fused salts, Tafel slope, electrocatalysis, anode.

factory uniformity. SEM observation revealed a pore-free structure, and x-ray analysis showed the presence of all the principal  $\text{RuO}_2$  peaks in comparison with those of ASTM cards (File No. 21-1171). The underlying  $\text{SnO}_2$  film acts as a catalyst support as well as a current collector. The adhesion of  $\text{RuO}_2$  to  $\text{SnO}_2$  was proved quite satisfactory. No damage was observed when the electrode was subjected to gentle scraping or thermal shocks.

The electrical contact with the electrode was made through a gold layer which was printed on the  $\text{SnO}_2$  film by using a gold paint (C-5040, Sumitomo Mining Company). The unnecessary part of the oxide surface and the gold contact were insulated with a thick layer of Teflon coating (30-J, Mitsui Fluorochemical Company). These techniques were described in previous paper (23). Details of the electrode construction are shown in Fig. 1. Hereafter this type of electrode is called the  $\text{SnO}_2$ -based  $\text{RuO}_2$  electrode.

Prior to experiments, the electrode surface was slightly polished with fine alumina powder ( $0.3\ \mu\text{m}$ , Buehler Limited) and degreased with a methanol solution of  $\text{NaOH}$ . Then, it was soaked in a mixed acid of concentrated  $\text{HNO}_3$  and  $\text{H}_2\text{SO}_4$  for 1 hr and washed thoroughly with distilled water. After the above surface conditioning, the electrode was dried in an oven ( $120^\circ\text{C}$ ) for 12 hr.

Glassy carbon electrodes (GC) were sealed into Pyrex tubes as described previously (25). Their surface conditioning was similar to that of the  $\text{RuO}_2$  electrode. The counterelectrode was a W sheet with a large area.

Two types of reference electrodes, whose constructions were described previously (22), were used: the Al reference electrode confined in a Pyrex bulb (membrane type) and the chlorine electrode on a large area GC rod under an atmospheric pressure of chlorine (gas electrode type). The melt composition of the reference room was a  $\text{NaCl}$ -saturated  $\text{NaAlCl}_4$  melt. All the potentials quoted without description are given with respect to the gas electrode.

**Apparatus and procedures.**—Experiments were performed in a Pyrex vessel at  $175^\circ\text{C}$ . The electrochemical cell assembly equipped with gas delivering systems ( $\text{N}_2$  and  $\text{Cl}_2$ ) and a temperature control system were essentially the same as that in previous works (22,

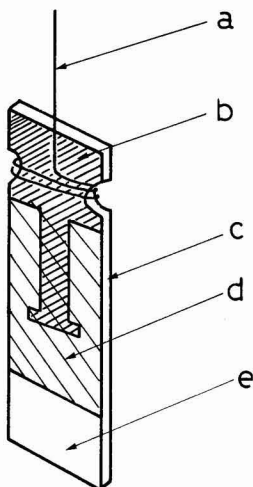


Fig. 1. Electrode construction of the  $\text{SnO}_2$ -based  $\text{RuO}_2$  electrode. a, Au lead; b, printed Au layer; c, Pyrex; d,  $\text{SnO}_2$ -based  $\text{RuO}_2$  covered with Teflon; e,  $\text{SnO}_2$ -based  $\text{RuO}_2$  electrode surface.

23). Nitrogen gas was rendered oxygen free by passing it through heated copper fibers and drying it with anhydrous  $\text{Mg}(\text{ClO}_4)_2$  and  $\text{P}_2\text{O}_5$ . Chlorine gas was dried by passing it through concentrated  $\text{H}_2\text{SO}_4$  and anhydrous  $\text{Mg}(\text{ClO}_4)_2$ . The gas delivering system had a gas mixing chamber where  $\text{N}_2$  and  $\text{Cl}_2$  were mixed at a desired ratio. The gas mixture was blown into the melt for 1 hr and allowed to flow over the melt during the experiments. The gases sampled from the mixing chamber were subjected to iodometry for determination of the partial pressure of chlorine (22).

The concentration of chloride ion depends on the melt composition ( $\text{NaCl} + \text{AlCl}_3$ ). At the equimolar composition, chloride ion activity determined by the acid-base equilibrium of Eq. [3] is  $10^{-2.54}$  ( $-\log a_{\text{Cl}^-} = 2.54 = p\text{Cl}$ ) (29). The highest activity of  $\text{Cl}^-$  ( $p\text{Cl} = 1.1$ ) is attained in the melt saturated with  $\text{NaCl}$  (49.75 m/o  $\text{AlCl}_3$ ) which is used as the standard state in this melt (29). All the measurements carried out in this work were, therefore, started with this standard condition, and then  $p\text{Cl}$  was changed by partial electrolysis. Part of chloride ion in the cell compartment which was separated from a counter-electrode with a fritted disk was removed coulometrically by chlorine evolution, and the exact  $p\text{Cl}$  value was determined from the shift of chlorine electrode potential. The use of the off-gas reaction to change  $p\text{Cl}$  and of the gas electrode as a  $p\text{Cl}$  indicator electrode were described previously (22).

Measurements of voltammograms and differential capacities were carried out as described previously (22-24). For measurements of Tafel relationships, a logarithmic amplifier (Philbrick Nexas, 4350) was used for curve tracing. Tafel plots were always started from the rest potentials with a scan rate of 1 mV/sec and were recorded on an X-Y recorder (Watanabe Denki, WX 4401).

## Results and Discussion

**Electrode roughness.**—Many workers observed large background current levels of the order of several  $\text{mA}/\text{cm}^2$  in aqueous systems with their  $\text{RuO}_2$  electrodes prepared on Ti substrate (8-12), ascribing the anomaly to electrode roughness. The surface roughness is an important factor in calculation of the exchange current density, which is a measure of the electrocatalytic activity to be examined in this study. In order to check the roughness of our  $\text{RuO}_2$  electrodes prepared on  $\text{SnO}_2$ , the differential capacity and background cyclic voltammograms were measured and compared with those of metal electrodes as shown in Fig. 2 and 3. The anodic limit of the melt is chlorine evolution taking place at potentials positive to ca. 2.1V vs. Al, and we have the double layer region at less noble potentials. The capacity value of the  $\text{SnO}_2$ -based  $\text{RuO}_2$  electrode in the double layer region was  $25\text{--}30\ \mu\text{F}/\text{cm}^2$  on the basis of geometric area, which is comparable to those of Pt and W electrodes, while the GC showed large discrepancy. Fellner *et al.* reported that the double layer capacity on Hg electrodes in the melt at  $160^\circ\text{C}$  is  $14\text{--}20\ \mu\text{F}/\text{cm}^2$  at a potential range from 0.1 to 0.7V vs. Al (26). Adopting Fellners' value as a true capacity of the double layer, we may conclude that the roughness factor of our  $\text{RuO}_2$  electrode is 1.5-2.0, while that of GC is 6-8. This feature was confirmed by the background voltammograms shown in Fig. 3.

The background current levels for GC observed in the double layer region were several times as large as those for the  $\text{RuO}_2$  electrode, whereas the anodic current due to chlorine evolution increased more rapidly on the  $\text{RuO}_2$  electrode than on GC despite its lower roughness, indicating the marked catalytic activity of the  $\text{RuO}_2$  electrode. It is widely accepted that the roughness of Ti-supported  $\text{RuO}_2$  electrodes largely

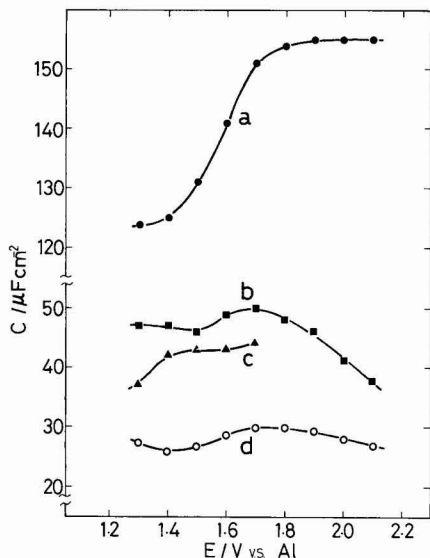


Fig. 2. Capacity vs. potential curves for different electrode materials in the melt of  $p\text{Cl} = 1.1$  at  $f = 1$  kHz. a, GC; b, W; c, Pt; d,  $\text{SnO}_2$ -based  $\text{RuO}_2$ .

depends on coating methods and annealing conditions (7-12). The estimated values of their roughness factor show large scattering; below 10 (21) and 8-20 (10) for compact  $\text{RuO}_2$  electrodes and 60-200 (10) and above 200 (9) for porous  $\text{RuO}_2$  electrodes. Rolison *et al.* prepared Ti-supported  $\text{RuO}_2$  electrodes with low roughness factors below 10 and observed low background current levels less than  $100 \mu\text{A}/\text{cm}^2$  (21), which are comparable to the background current levels obtained in this work. Similarly low current levels were also observed in aqueous solutions with  $\text{SnO}_2$ -based  $\text{RuO}_2$  electrodes (27). All the evidence collected with SEM observation, capacity measurements, and background voltammograms, therefore, indicates

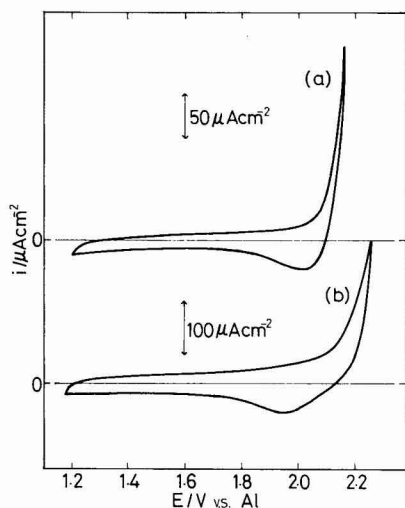
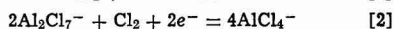


Fig. 3. Background cyclic traces in the melt of  $p\text{Cl} = 1.1$  at  $v = 50$   $\text{mV sec}^{-1}$ . (a)  $\text{SnO}_2$ -based  $\text{RuO}_2$  electrode, (b) GC electrode.

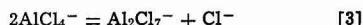
that the real surface area of our  $\text{RuO}_2$  electrode is not considerably different from the geometric area, the ratio of the real to the geometric area being estimated to be two at most. The causes of the low roughness can be attributed partly to the optically flat surface of the Pyrex substrate, the use of dilute coating solutions ( $0.02\text{M RuCl}_3$ ), and the relatively long annealing time (10 hr at  $500^\circ\text{C}$ ).

**Comparison of Tafel plots between  $\text{SnO}_2$ -based  $\text{RuO}_2$  and GC electrodes.**—Figure 4 shows the Tafel plots for chlorine evolution and reduction in the melt of  $p\text{Cl} = 1.1$  on (a) GC and (b)  $\text{RuO}_2$  electrodes. At low overpotentials chlorine evolves from free chloride ions whose activity is specified by the  $p\text{Cl}$  value, and the current plateau is ascribed to the diffusion process of  $\text{Cl}^-$  (28), because the limiting value depends on  $p\text{Cl}$ , irrespective of electrode materials. The cathodic limiting current is due to the diffusion of  $\text{Cl}_2$  (22), depending on the partial pressure of  $\text{Cl}_2$ .

There are two overall reactions concerning chlorine evolution



The standard potential of reaction [2] is located at  $0.62\text{V}$  positive to the potential of reaction [1] ( $p\text{Cl} = 1.1$ ,  $p\text{Cl}_2 = 1$  atm) according to the thermodynamic calculation using the equilibrium constant ( $K = 1.06 \times 10^{-7}$ ) of the following acid-base reaction (29)



In the present study, we are concerned with reaction [1], which is the primary reaction taking place at low  $p\text{Cl}$  and low overpotentials.

The polarization behavior obtained during reverse scanning is not shown in Fig. 4 for simplicity. Deep scanning ( $\eta \sim 500$  mV) resulted in so-called hysteresis curves and subsequent scanning showed different results. However, those changes in the polarization easily recovered to the original one by agitating the bulk melt, and irreversible changes indicating surface degradation were not observed. The hysteresis effect is ascribed to the change in  $p\text{Cl}$  at the electrode surface.

The chlorine evolution on semiconductive  $\text{SnO}_2$  electrodes is less reversible than that on GC as reported previously (4). Hence, the reversible be-

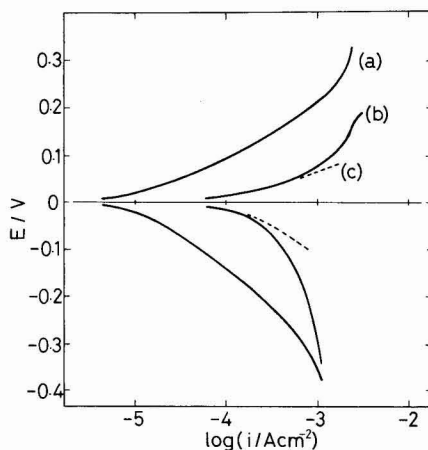
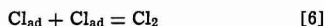
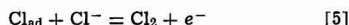


Fig. 4. Comparison of Tafel plots between  $\text{SnO}_2$ -based  $\text{RuO}_2$  and GC electrodes in the melt of  $p\text{Cl} = 1.1$  under an atmospheric pressure of  $\text{Cl}_2$ . (a) GC electrode, (b)  $\text{SnO}_2$ -based  $\text{RuO}_2$  electrode, (c) curve (b) corrected for concentration overvoltages.

havior of curve (b) is obviously ascribed to the activity of the electrocatalyzer prepared on  $\text{SnO}_2$ . Because of the improved reversibility, the Tafel region of the  $\text{RuO}_2$  electrode is narrow and largely curved, showing a great participation of the diffusion process. In order to obtain kinetic parameters, the concentration overvoltage was corrected with the conventional method described by Vetter (30). The dotted line in Fig. 4 shows the corrected Tafel plots. The anodic ( $b_+$ ) and cathodic ( $b_-$ ) Tafel slopes were  $72 \pm 8$  and  $-105 \pm 8$  mV/decade, respectively, and the exchange current density ( $i_0$ ) based on the geometric area was  $132 \pm 22 \mu\text{A}/\text{cm}^2$  for several experiments. The  $i_0$  value on GC was  $8.9 \mu\text{A}/\text{cm}^2$  based on the geometric area, being in good agreement with the previous result,  $8.6 \pm 0.8 \mu\text{A}/\text{cm}^2$  (22). Comparing the two  $i_0$ 's it is seen that the former value is 15 times larger than the latter value, or more if taking into account the higher roughness of GC electrodes. The electrocatalytic activity of the  $\text{RuO}_2$  electrode is therefore quite noticeable.

**The reaction mechanism on  $\text{RuO}_2$  electrode.**—For the overall reaction [1], the following elementary reactions have been proposed (1, 22, 31–33)

overall



Using the stoichiometric number ( $\nu$ ) defined by reaction [7], one can specify possible combinations of the above elementary reactions

$$\nu = \frac{nF i_0}{RT} \left( \frac{\partial E}{\partial i} \right)_{E \rightarrow 0} \quad [7]$$

Near-equilibrium polarization behavior ( $i$  vs.  $E$ ) obtained in the melt of  $p\text{Cl} = 1.1$  is shown in Fig. 5, the so-called polarization resistance,  $(\partial E / \partial i)_{E \rightarrow 0}$ , being easily determined. The  $\nu$  value calculated from the  $i_0$  and the  $n$  ( $= 2$ ) values was 0.94, being close to unity. Therefore, the reaction mechanisms corresponding to the fact that  $\nu = 1$  are three combinations of them

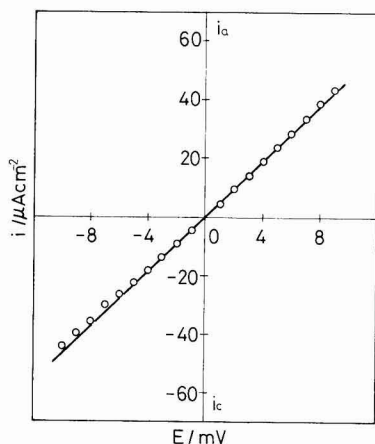


Fig. 5. Micropolarization behavior of  $\text{SnO}_2$ -based  $\text{RuO}_2$  electrode in the melt of  $p\text{Cl} = 1.1$  under  $P_{\text{Cl}_2} = 1$  atm.

(A) fast, reaction [4] + slow, reaction [5]

(B) fast, reaction [4] + slow, reaction [6]

(C) fast, reaction [5] + slow, reaction [4]

The rate equations for the above reaction schemes have to involve some adsorption isotherm which the adsorbed intermediate obeys. Langmuir, nonactivated Temkin, and activated Temkin isotherms are applied in formulating the rate equations, and then the theoretical kinetic parameters are subjected to comparison with the experimental values to determine which reaction scheme is the most probable. Mechanistic analysis based only on Tafel slopes, however, would fail in the determination because some of the isotherms yield the same Tafel slope for the different schemes. In connection with this, kinetic analyses based on reaction orders are quite informative. In a previous study (22), the reaction orders with respect to  $\text{Cl}^-$  and  $\text{Cl}_2$  played decisive roles in determining the reaction mechanism of chlorine electrode reaction on GC electrode in the melt.

Figures 6 and 7 show the dependence of Tafel plots on  $p\text{Cl}$  and  $P_{\text{Cl}_2}$  (partial pressure of  $\text{Cl}_2$ ), where the concentration overvoltages are corrected for each plot. Cathodic Tafel plots showed slightly curved features which were presumably due to experimental uncertainty of the cathodic diffusion current ( $i_{\text{dc}}$ ). The correction term  $(1 - i/i_{\text{dc}})$  is very sensitive to the  $i_{\text{dc}}$  value because available  $i$  values are limited only to one order range below the  $i_{\text{dc}}$ . Using those data, we can obtain six kinetic parameters; three reaction orders of  $i_0$ ,  $i_a$ , and  $i_c$  with respect to  $\text{Cl}^-$ , and also similar three parameters with respect to  $\text{Cl}_2$ . The former three parameters were calculated from Fig. 8, where anodic current values ( $i_a$ ) at  $E = 0.105\text{V}$ , cathodic current values ( $i_c$ ) at  $E = -0.030\text{V}$ , and  $i_0$  values are plotted against  $-p\text{Cl}$  ( $= \log a_{\text{Cl}^-}$ ) at a constant  $P_{\text{Cl}_2}$  ( $= 1$  atm). The latter ones were obtained from Fig. 9 where  $i_a$  and  $i_c$  at  $E = \pm 0.080\text{V}$  and  $i_0$  were plotted against partial pressures of  $\text{Cl}_2$  at a constant  $p\text{Cl}$  ( $= 1.1$ ). The reaction orders thus collected are summarized in Table I.

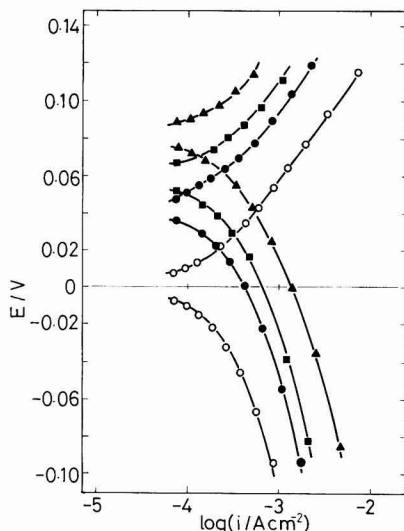


Fig. 6.  $p\text{Cl}$  dependence of Tafel plot for chlorine electrode on  $\text{SnO}_2$ -based  $\text{RuO}_2$  in  $\text{NaAlCl}_4$  melts under an atmospheric pressure of  $\text{Cl}_2$  at  $175^\circ\text{C}$ . ( $\circ$ )  $p\text{Cl} = 1.1$ , ( $\bullet$ )  $p\text{Cl} = 1.58$ , ( $\blacksquare$ )  $p\text{Cl} = 1.78$ , ( $\blacktriangle$ )  $p\text{Cl} = 2.02$ .

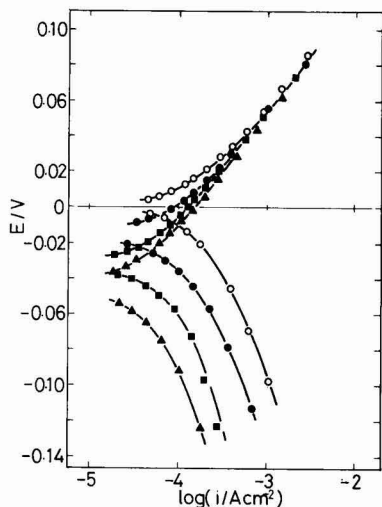


Fig. 7.  $P_{Cl_2}$  dependence of Tafel plot for chlorine electrode on  $SnO_2$ -based  $RuO_2$  in a  $NaAlCl_4$  melt of  $pCl = 1.1$  at  $175^\circ C$ . ( $\circ$ )  $P_{Cl_2} = 1$  atm, ( $\bullet$ )  $P_{Cl_2} = 0.52$  atm, ( $\blacksquare$ )  $P_{Cl_2} = 0.22$  atm, ( $\blacktriangle$ )  $P_{Cl_2} = 0.11$  atm.

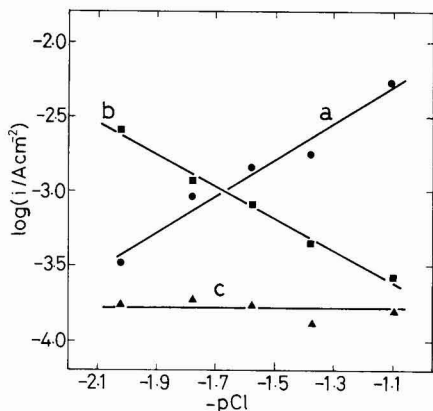


Fig. 8.  $pCl$  dependence of current ( $i$ ) under a constant  $P_{Cl_2} (= 1$  atm). a, Anodic current densities at  $E = 105$  mV; b, cathodic current densities at  $E = -30$  mV; c, exchange current densities.

The data shown in Table I were inspected first from the viewpoint of the  $i_0$  derivatives, which must be the most reliable parameters because their definition does not involve any arbitrary choice of electrode potential. The theoretical  $i_0$  derivatives with respect to  $pCl$  and  $P_{Cl_2}$  are tabulated in Table II for the mechanism (A), (B), and (C) with the three adsorption

Table I. Experimental reaction orders with respect to  $Cl^-$  and  $Cl_2$  on a  $RuO_2$  electrode in  $NaAlCl_4$  melt at  $175^\circ C$

$(\partial \log i_0 / \partial \log a_{Cl^-})_{P_{Cl_2}}$	0
$(\partial \log i_0 / \partial \log P_{Cl_2})_{pCl}$	0.6
$(\partial \log i_a / \partial \log a_{Cl^-})_E, P_{Cl_2}$	1.2
$(\partial \log i_c / \partial \log a_{Cl^-})_E, P_{Cl_2}$	-1.1
$(\partial \log i_a / \partial \log P_{Cl_2})_E, pCl$	0
$(\partial \log i_c / \partial \log P_{Cl_2})_E, pCl$	1.0

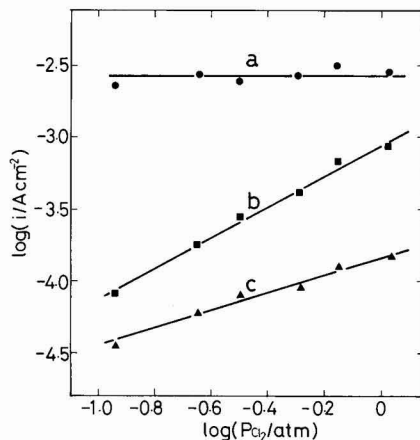
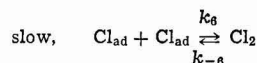
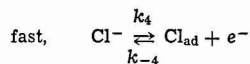


Fig. 9.  $P_{Cl_2}$  dependence of current ( $i$ ) at a constant  $pCl (= 1.1)$ . a, Anodic current densities at  $E = 80$  mV; b, cathodic current densities at  $E = -80$  mV; c, exchange current densities.

isotherms. The table was constructed on the bases of our calculations described previously (22) and literature (34). Since the experimental  $i_0$  derivatives are 0 with respect to  $Cl^-$  and 0.6 with respect to  $Cl_2$ , it is seen at first glance that mechanism (B) under the activated Temkin isotherm is the most probable scheme.

The validity of the Temkin condition can be seen in the anodic and cathodic reaction orders with respect to  $Cl^-$ . Table III shows both theoretical reaction orders for mechanism (B) with the different isotherms (22, 35). Apparently, only the activated Temkin isotherm gives a tendency consistent with the results shown in Table I. This mechanistic conclusion was also confirmed by comparison between the theoretical and experimental reaction orders with respect to  $Cl_2$ . As shown in Table IV, the former values for the anodic and cathodic processes are 0 and 1, being in excellent agreement with the experimental values.

For mechanism (B) under activated Temkin condition, the following rate equation is derived (22, 36), assuming a quasi-equilibrium state for the fast process, reaction [4]



$$i = 2Fk_6(K_4)^{2(1-\beta)}a_{Cl^-}^{-2(1-\beta)} \exp[2(1-\beta)fE] - 2Fk_{-6}(K_4)^{-2\beta}a_{Cl^-}^{-2\beta}P_{Cl_2} \exp(-2\beta fE) \quad [8]$$

where  $K_4 = k_4/k_{-4}$ ,  $f = F/RT$ ,  $\beta$  is the symmetric factor of the adsorption process, and  $E$  is the potential difference from the reference electrode. Neglecting the backward reaction, we obtain Tafel relationships for the anodic and cathodic processes

$$\ln i_a = \ln(2Fk_6) + 2(1-\beta) \ln(K_4) + 2(1-\beta) \ln(a_{Cl^-}) + 2(1-\beta)fE \quad [9]$$

$$\ln i_c = \ln(2Fk_{-6}) - 2\beta \ln(K_4) - 2\beta \ln(a_{Cl^-}) + \ln(P_{Cl_2}) - 2\beta fE \quad [10]$$

The kinetic derivatives shown in Table IV are easily obtained from reactions [9] and [10]. Some of the reaction orders involve the parameter  $\beta$ , which is usu-

Table II. The theoretical reaction orders ( $i_0$  derivatives) with respect to  $\text{Cl}^-$  and  $\text{Cl}_2$  in the chlorine electrode reaction

Mechanism	Langmuir				Nonactivated Temkin		Activated Temkin	
	$\theta \approx 0$		$\theta \approx 1$		$x$	$y$	$x$	$y$
	$x$	$y$	$x$	$y$				
(A)	0.5	0.75	0.5	0.25	0.5	0.75	0.5	0.5
(B)	0	1	0	0	0	1	0	0.5
(C)	0.5	0.25	0.5	-0.25	0.5	0.25	0.5	0

In calculations, symmetry factor of electron transfer step ( $\alpha$ ) and adsorption step ( $\beta$ ) were assumed as 0.5.  $x = (\partial \log i_0 / \partial \log a_{\text{Cl}^-})_{P_{\text{Cl}_2}}$ ,  $y = (\partial \log i_0 / \partial \log P_{\text{Cl}_2})_{P_{\text{Cl}^-}}$ .

Table III. The theoretical reaction orders with respect to  $\text{Cl}^-$  for mechanism (B) under different adsorption isotherms

Reaction order	Langmuir		Nonactivated Temkin	Activated Temkin*
	$\theta \approx 0$	$\theta \approx 1$		
$(\partial \log i_0 / \partial \log a_{\text{Cl}^-})_{P_{\text{Cl}_2}}$	2	0	2	1
$(\partial \log i_0 / \partial \log P_{\text{Cl}_2})_{P_{\text{Cl}^-}}$	0	-2	0	-1

\*  $\beta = 0.5$ .

Table IV. Theoretical Tafel slopes and reaction orders for mechanism (B) under activated Temkin condition

$(\partial \log i_0 / \partial \log a_{\text{Cl}^-})_{P_{\text{Cl}_2}}$	0
$(\partial \log i_0 / \partial \log P_{\text{Cl}_2})_{P_{\text{Cl}^-}}$	$1 - \beta$
$(\partial \log i_0 / \partial \log a_{\text{Cl}^-})_{P_{\text{Cl}_2}}$	$2(1 - \beta)$
$(\partial \log i_0 / \partial \log P_{\text{Cl}_2})_{P_{\text{Cl}^-}}$	$-2\beta$
$(\partial \log i_0 / \partial \log P_{\text{Cl}_2})_{P_{\text{Cl}^-}}$	0
$(\partial \log i_0 / \partial \log P_{\text{Cl}_2})_{P_{\text{Cl}^-}}$	1
$(\partial E / \partial \log i_0)$	$1/2(1 - \beta)f^*$
$(\partial E / \partial \log i_0)$	$-1/2\beta f^*$

\*  $f^* = F/2.3RT$ .

ally regarded as 0.5 as assumed in the foregoing sections. Thus the  $\beta$  value, which can be calculated with the data shown in Table I, may be used to evaluate the consistency of our conclusion. The calculated  $\beta$  was 0.4 from the  $i_0$  derivative, and 0.4 and 0.55 from the reaction orders with respect to  $\text{Cl}^-$ . Using the average value of  $\beta$  ( $= 0.45$ ), we can also calculate the theoretical Tafel slopes;  $b_+ = 80.9$  mV and  $b_- = -98.9$  mV, being in good agreement with the experimental results ( $b_+ = 72 \pm 8$  mV and  $b_- = -105 \pm 8$  mV). Thus there is no inconsistency in our mechanistic analysis.

The polarization behavior of the  $\text{RuO}_2$  electrode shown in Fig. 4 is again represented in a different manner, taking into account the presented reaction mechanism. The rate equation [8] can be rewritten as follows

$$i/[1 - \exp(-2f\eta)] = i_0 \exp[2(1 - \beta)f\eta] \quad [11]$$

where  $\eta$  is the overvoltage. In this case the reference electrode is the reversible chlorine electrode ( $p_{\text{Cl}} = 1.1$ ,  $P_{\text{Cl}_2} = 1$  atm), hence  $\eta = E$  for the condition of Fig. 4. Since the backward reaction is not omitted in reaction [11], the plot of  $\log \{i/[1 - \exp(-2f\eta)]\}$  vs.  $\eta$  describes the polarization behavior corrected for the backward reaction rate over a broad range of current density (37) and gives a straight line with the slope of  $2(1 - \beta)F/2.3RT$ . Figure 10 shows this relationship in a potential range where the concentration overvoltage can be negligible. The  $\beta$  value

( $= 0.45$ ) obtained from the slope and the  $i_0$  value at  $\eta = 0$  again coincided with the above values.

Consequently, the chlorine electrode reaction on  $\text{RuO}_2$  in  $\text{NaAlCl}_4$  melt with near equimolar compositions occurs according to a Volmer-Tafel mechanism, where the Tafel reaction (atom-atom recombination) is a rate-determining step for both anodic and cathodic reactions. This mechanism is in contrast with that on GC, which obeys a Volmer-Heyrovsky type mechanism involving the Heyrovsky reaction (atom-ion recombination) as a rate-determining step, i.e., mechanism (A) as revealed previously (22). Mechanisms (A), (B), and (C) are analogous to the mechanism of hydrogen electrode in aqueous systems. It is widely accepted that in acidic solutions the hydrogen evolution on highly catalytic substrates such as Pt obeys the Volmer-Tafel mechanism, while the Volmer-Heyrovsky mechanism prevails on other metals such as Au and Ni, giving smaller exchange current densities (38). Similar kinetic correlation seems to be applied to chlorine evolution in aqueous systems. Several authors suggested that the rate-determining step of the chlorine evolution is the Tafel reaction on  $\text{RuO}_2$  electrodes (6, 16, 39) and the Heyrovsky reaction on vitreous (39) and graphite electrodes (40). The electrocatalytic activity of  $\text{RuO}_2$  electrodes in the melt, which is associated with the Tafel reaction, may be understandable from this phenomenological aspect.

## Conclusions

Ruthenium oxide electrodes have a noticeable electrocatalytic effect on the chlorine electrode reaction in molten  $\text{NaAlCl}_4$ . The exchange current density at the standard conditions ( $p_{\text{Cl}} = 1.1$ ,  $P_{\text{Cl}_2} = 1$  atm, at  $175^\circ\text{C}$ ) is  $132 \pm 22 \mu\text{A}/\text{cm}^2$ , while the corresponding  $i_0$  on GC is  $8.9 \mu\text{A}/\text{cm}^2$ . The chlorine evolution obeys a Volmer-Tafel type mechanism under the activated Temkin condition

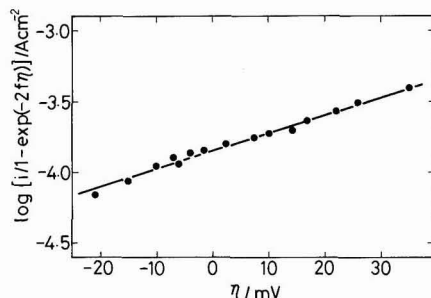
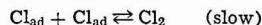
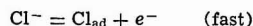


Fig. 10. Polarization behavior of  $\text{SnO}_2$ -based  $\text{RuO}_2$  electrode corresponding to the data of Fig. 4. The data were plotted according to Eq. [11].



The rate-determining step is the combination (Tafel) reaction. The chlorine reduction also obeys the same mechanism in the reverse direction.

### Acknowledgment

Part of the experimental data has been obtained by Mr. Isao Sato during his undergraduate research training.

Manuscript submitted June 24, 1980; revised manuscript received May 22, 1981.

Any discussion of this paper will appear in a Discussion Section to be published in the June 1982 JOURNAL. All discussions for the June 1982 Discussion Section should be submitted by Feb. 1, 1982.

Publication costs of this article were assisted by Tohoku University.

### REFERENCES

1. G. L. Holleck, *This Journal*, **119**, 1158 (1972).
2. U. Anders and J. A. Plambeck, *Can. J. Chem.*, **47**, 3055 (1969).
3. I. Uchida and S. Toshima, *J. App. Electrochem.*, **9**, 647 (1979).
4. I. Uchida, H. Urushibata, and S. Toshima, *This Journal*, **127**, 757 (1980).
5. I. Uchida, K. Niki, and H. A. Laitinen, *ibid.*, **125**, 1759 (1978).
6. G. Bianchi, *J. App. Electrochem.*, **1**, 231 (1971).
7. Ya. M. Kolotyrkin, *Denki Kagaku*, **47**, 390 (1979).
8. D. Galizzioli, F. Tontardini, and S. Trasatti, *J. App. Electrochem.*, **4**, 57 (1974); **5**, 203 (1975).
9. L. D. Burke, O. J. Murphy, J. F. O'Neill, and S. Venkatesan, *J. Chem. Soc., Faraday Trans. 1*, **73**, 1659 (1977).
10. G. Lodi, E. Sivieri, A. De Battisti, and S. Trasatti, *J. App. Electrochem.*, **8**, 135 (1978).
11. L. Burke and O. J. Murphy, *J. Electroanal. Chem. Interfacial Electrochem.*, **96**, 19 (1979).
12. D. V. Kokoulina, T. V. Ivanova, Yu. I. Krasovitskaya, Z. I. Kudryavtseva, and L. I. Krishtalik, *Elektrokhimiya*, **13**, 1511 (1977).
13. R. G. Erenburg, L. I. Krishtalik, and V. I. Bystrov, *ibid.*, **8**, (1972).
14. R. G. Erenburg, L. I. Krishtalik, and I. P. Yaroshkevskaya, *ibid.*, **11**, 1072 (1975).
15. L. J. Janssen, L. M. C. Starman, J. G. Visser, and E. Barendrecht, *Electrochim. Acta*, **22**, 1093 (1977).
16. I. R. Burrows, D. A. Denton, and J. A. Harrison, *ibid.*, **23**, 493 (1978).
17. D. A. Denton, J. A. Harrison, and R. I. Knowles, *ibid.*, **24**, 521 (1979).
18. T. Arikado, C. Iwakura, and H. Tamura, *ibid.*, **23**, 9 (1978).
19. M. Inai, C. Iwakura, and H. Tamura, *ibid.*, **24**, 993 (1979).
20. V. E. Kazarinov and V. V. Andreev, *Elektrokhimiya*, **14**, 577 (1978).
21. D. R. Rolison, K. Kuo, M. Umana, D. Brundage, and R. W. Murray, *This Journal*, **126**, 407 (1979).
22. H. Urushibata, I. Uchida, and S. Toshima, *J. Electroanal. Interfacial Electrochem.*, **117**, 43 (1981).
23. I. Uchida, H. Urushibata, and S. Toshima, *ibid.*, **96**, 45 (1979).
24. I. Uchida, H. Urushibata, and S. Toshima, *This Journal*, **127**, 995 (1980).
25. H. A. Laitinen, Y. Yamamura, and I. Uchida, *ibid.*, **125**, 1450 (1978).
26. P. Fellner, M. Chrenková-Paučířová, A. Silný, and K. Mantiasovský, *Electrochim. Acta*, **25**, 189 (1980).
27. H. Urushibata and I. Uchida, Unpublished data.
28. G. Letisse and B. Tremillon, *J. Electroanal. Chem. Interfacial Electrochem.*, **17**, 371 (1968).
29. L. G. Boxall, H. L. Jones, and R. A. Osteryoung, *This Journal*, **120**, 223 (1973).
30. K. J. Vetter, "Electrochemical Kinetics," p. 163, Academic Press, New York (1967).
31. S. Sernger, I. Galasiu, and D. Geana, *Electrochim. Acta*, **24**, 115 (1979).
32. R. Tunold, H. M. Bø, K. A. Paulsen, and J. O. Ytredal, *ibid.*, **16**, 2101 (1971).
33. W. E. Triaca, C. Solomons, and J. O'M. Bockris, *ibid.*, **13**, 1949 (1968).
34. B. E. Conway, "Theory and Principles of Electrode Processes," p. 174, Ronald Press, New York (1965).
35. G. Faite, G. Fiori, and J. W. Augustynski, *This Journal*, **116**, 928 (1969).
36. T. Yokoyama and M. Enyo, *Electrochim. Acta*, **24**, 997 (1979).
37. P. Delahay, "Double Layer and Electrode Kinetics," p. 163, Interscience, New York (1965).
38. J. O'M. Bockris and A. K. N. Reddy, "Modern Electrochemistry," Vol. 2, p. 1250, Plenum Press, New York (1970).
39. B. V. Tilak, *This Journal*, **126**, 1343 (1979).
40. L. J. Janssen and J. G. Hoogland, *Electrochim. Acta*, **15**, 941 (1970).

## Electrochemical Photovoltaic Cells Based on n-GaAs in Propylene Carbonate

M. E. Langmuir,\* P. Hoenig, and R. D. Rauh\*

EIC Laboratories, Incorporated, Newton, Massachusetts 02158

### ABSTRACT

Electrochemical photovoltaic cells (EPC's) have been characterized based on n-GaAs and propylene carbonate electrolytes. Photovoltages are limited to ~0.7V due to electrode corrosion and lack of specific adsorption by the redox systems studied. Polarization of photo and counterelectrodes, resulting from low redox solubilities and electrolyte conductivities, are responsible for lower fill factors and short-circuit photocurrents for nonaqueous compared to aqueous EPC's. Potentially, these losses can be offset by higher voltages and long-term stabilities, particularly if specifically adsorbing redox couples can be found.

Nonaqueous electrolytes hold the promise of enhancing long-term stability in electrochemical photovoltaic cells (EPC's). In this paper we characterize

n-GaAs, propylene carbonate (PC) based EPC's with regard to limitations on photovoltage and photocurrent.

Propylene carbonate has been chosen as a representative solvent for its wide anodic and cathodic stability range, and because we have established procedures for

\* Electrochemical Society Active Member.

Key words: photoelectrochemistry, propylene carbonate, gallium arsenide.

its effective drying and purification (1). In addition, PC supports a stable  $\text{Li}^+/\text{Li}$  reference electrode (2) which is simple to use and which can be employed without danger of solution contamination. We note, however, that the low conductivity of PC electrolytes (relative to  $\text{H}_2\text{O}$ ) probably prevents its use in practical devices as currently conceptualized. Nevertheless, the aspects of photoelectrochemical operation discovered in PC can be generalized to other nonaqueous systems.

We will first ask: What are the limits to the photovoltage in such a cell? In the ideal two-electrode EPC, the counterelectrode senses the rest potential of the solution and is thus equivalent to  $V_{\text{redox}}$ . The photoelectrode has a maximum onset voltage corresponding to its flatband potential,  $V_{\text{FB}}$ , leading to the relation

$$V_{\text{oc}} = V_{\text{FB}} - V_{\text{redox}} \quad [1]$$

This simple relation is fundamental to EPC operation. The relation is meaningless, however, if the redox couple in the cell is not oxidized or reduced by the photoelectrode so as to stabilize it against photocorrosion. Thus, we further specify the limiting photovoltage in a stable cell by

$$V_{\text{oc}}(\text{max}) = V_{\text{FB}} - V_{\text{c}} \quad [2]$$

where  $V_{\text{c}}$  is the anodic or cathodic corrosion potential of the photoanode or photocathode, respectively. One of the potential advantages of nonaqueous solvents is to allow the maximization of Eq. [1] through the maximization of Eq. [2] assuming that corrosion reactions are rendered more difficult than in  $\text{H}_2\text{O}$ .

Two factors appear to complicate the use of Eq. [1] as a simple predictor for cell design. The first is that  $V_{\text{FB}}$  is influenced by the redox couple when specific adsorption occurs. For example, in the aqueous-based  $\text{CdX}/\text{X}_n^{-2}$ ,  $\text{X}^{-2}$  cells ( $\text{X} = \text{S}, \text{Se}, \text{or Te}$ ),  $V_{\text{FB}}$  is shifted negative by such adsorption (3). Most documented cases of this kind of influence on  $V_{\text{FB}}$  occur in protic media due to acid-base equilibria involving surface OH or XH groups (4). Thus, we might be able to test Eq. [1] in aprotic media like PC without this additional variable.

The other complicating factor involves the observation that half-cell photovoltages equivalent to  $V_{\text{FB}}$  are often unattainable. In solid-state Schottky barrier devices, this is often ascribed to the intermediacy of "surface states" (5). The latter may be viewed as surface-bound redox centers which act as very efficient captors of electrons or holes. As a result, such centers "pin" the Fermi level, thus restricting the photovoltage. It may be possible to modify, chemically, such states. Improvements in cell operation due to certain semiconductor etching treatment, oxidation, hydrogenation, or treatment with  $\text{Ru}^{+3}$  have been ascribed to such surface-state modification (6-9). Recent observations by Wrighton, Bard and co-workers suggest Fermi level pinning at some semiconductor liquid junctions (10).

The other major question regarding cell operation concerns the factors which influence the photocurrent. The effects on photocurrent yields of redox potential, interaction of the electrolyte with the electrode surface states, and the doping, orientation, and crystalline quality of the photoelectrode are little understood. Surface states can, for example, influence the voltage onset and sharpness of the rise of photocurrent-voltage curves. Recombination via the surface has been used to explain the so-called "foot problem" in EPC  $i$ - $V$  curves, characteristic of inefficient electrodes with low fill factor (3, 11).

### Experimental

**Materials preparation and handling.**—Several different redox couples were employed in this study. Acetyl ferrocene (acFc), ferrocene (Fc), and NN'-tetramethyl-*p*-phenylenediamine (TMPD) were sublimed before use.  $\text{I}_2$  was also sublimed *in vacuo* before use. Both KI and tetrabutylammonium bromide (Eastman)

were dried *in vacuo* over  $\text{P}_2\text{O}_5$ . Bromine (Ventron, ultrapure) was used as received. The propylene carbonate (PC),  $\text{LiAsF}_6$  electrolyte preparation and purification were described previously (1).

All manipulations were carried out in an Ar-filled glove box containing  $<10$  ppm  $\text{H}_2\text{O}$ . The  $\text{acFc}^+$ ,  $\text{Fc}^+$ , and  $\text{TMPD}^+$  were produced by electrolysis of acFc, Fc, and TMPD solutions at constant current. Concentrations were verified spectrophotometrically.

**Electrochemical cell and reference electrode.**—Most experiments were carried out in a demountable thin layer photoelectrochemical research cell shown in Fig. 1. The cell has a liquid path length of  $\sim 0.4$  mm. Irradiation occurs through an optically transparent electrode of tin oxide (NESA) or indium-tin oxide (NESATRON).

The electrodes are mounted in a Macor machinable glass block. Filling was carried out in the glove box ( $<10$  ppm  $\text{H}_2\text{O}$ , Ar atmosphere) through the holes containing the demountable Pt electrodes. The photoelectrode is provided with an ohmic contact and a Ni lead wire and is sealed into the block using an epoxy cement previously tested for solvent compatibility. All the desired electrochemical and photoelectrochemical measurements can be made in this cell. Typically, one of the Pt electrodes served as a reference electrode, placing  $V_{\text{redox}}$  at 0 volts in each cell.

As the supporting electrolyte in the cells was  $\text{LiAsF}_6$ , we were able to calibrate the internal reference electrode vs.  $\text{Li}^+/\text{Li}$  (in a separate measurement), since PC is compatible with Li metal. The  $\text{Li}^+/\text{Li}$  potential is known vs. aqueous SCE in a variety of nonaqueous solvents. The liquid-junction corrected value of  $E^\circ(\text{Li}^+/\text{Li})$  is  $-2.94\text{V}$  vs. (SCE)<sub>aq</sub> in PC (12). The potentials of some of the specific redox solutions in PC which we have employed are listed in Table I.

**Electrode materials.**—All investigations were carried out on the  $<100$  face of an n-GaAs crystal ( $0.11\ \Omega\text{-cm}$ , partially Zn compensated) of  $0.07\text{ cm}^2$  area. Usually the n-GaAs surface was etched prior to each experiment according to the procedures of Kohl and Bard (13), which produced a shiny surface with a nonuniform distribution of etch pits (etch A). In several experiments on the effects of surface preparation on n-GaAs photoelectrodes, the matte etching procedure of Parkinson, Heller, and Miller was employed, which produced a high area, nonreflective surface (etch B). Etch B followed by treatment for 30 sec in a  $0.01\text{M}$   $\text{RuCl}_3$ ,  $0.1\text{M}$   $\text{HNO}_3$  solution is denoted as etch C.

**Photoelectrochemical measurements.**—Illumination of the working electrode was achieved with a 150W xenon lamp, the output of which was passed through a water filter with Pyrex windows. Light intensity was measured using an EG&G Model 450 Radiometer/

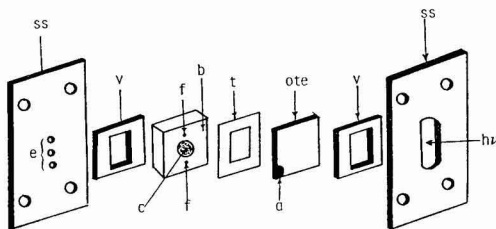


Fig. 1. Demountable thin layer photoelectrochemical research cell. The crystal (c) is mounted in a Macor block (b), which also contains holes (f) for filling and auxiliary wire electrodes. The optically transparent counterelectrode (OTE) is separated by a Teflon spacer (t), and has an Ag epoxy reinforced electrode contact (a). The package is confined using Viton rubber spacers (v) and stainless steel front and back plates (ss) with holes for electrodes (e). The plates are secured with bolts and wing nuts through the four corner holes.

Table I. Measured redox potentials for couples in propylene carbonate

Couple*	$V_{\text{redox}}$ (vs. SCE <sub>aq</sub> )**
Br <sub>2</sub> /Br <sup>-</sup> (0.01M/0.05M)	+0.96
acFc <sup>+</sup> /acFc (0.007M/0.03M)	+0.59
Fc <sup>+</sup> /Fc (0.007M/0.063M)	+0.34
I <sub>2</sub> /I <sup>-</sup> (0.01M/0.05M)	+0.16
TMPD <sup>+</sup> /TMPD (0.01M/0.09M)	-0.01
Li <sup>+</sup> /Li	-2.94

\* acFc: acetyl ferrocene, Fc: ferrocene, TMPD: tetramethylphenylenediamine.

\*\* Liquid junction corrected values.

Photometer at a constant distance from the source. The cell was then always placed at that distance. The intensity was adjusted using various neutral density filters. Although the Xe source yields an imperfect representation of the solar spectrum, it is a convenient white light source and is used here to compare results under typical broad band radiation.

Current-voltage curves were obtained with a Wenking LT73 potentiostat. A function generator specially designed for voltammetry provided a linear voltage scan with a preset starting voltage and adjustable scan rate. The current-voltage curves were measured on an X-Y recorder.

Half-cell measurements were made with respect to one of the Pt internal reference electrodes, using the window OTE as the counterelectrode. For solar cell measurements, the OTE was either shorted to the Pt reference electrode, or was used as both the counter and reference electrode. Both configurations gave equivalent results.

Linear sweep voltammograms of the redox couple on n-GaAs were obtained for different light intensities using a Pyrex filter to eliminate the u.v. component below 320 nm of the 150W Xe arc spectrum. The scan rate was 20 mV/sec for all cases. The reported data are not corrected for reflection or light absorption by the OTE or the solution and therefore give a true picture of the efficiency of the cell operated as a solar cell. Measurements of output stability of the solar cells were made at the potential yielding the maximum power on the cell's figure of merit *i*-*V* curve.

## Results and Discussion

**Factors influencing the photovoltage.**—A typical series of current-voltage curves are shown in Fig. 2 for the cell

n-GaAs | PC, 0.01M LiAsF<sub>6</sub> | optically transparent electrode  
Fc<sup>+</sup>/Fc (0.007/0.063M)

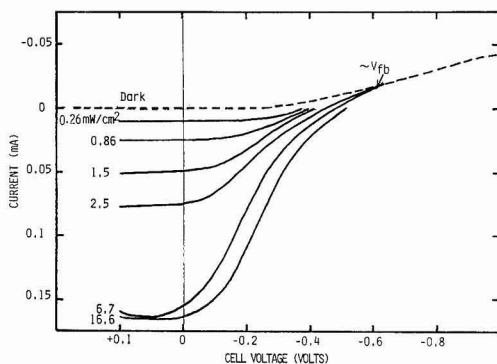


Fig. 2. Current vs. voltage at various light intensities for the photoelectrochemical cell n-GaAs (0.07 cm<sup>2</sup>) | Fc<sup>+</sup> (0.007M), Fc (0.063M), LiAsF<sub>6</sub> (0.01M), PC/NESATRON OTE. Light source is an Xe arc, Pyrex filter.

In this cell, which contains a rather dilute redox electrolyte, the mechanisms of current and voltage control are evident. In the dark, no anodic current flows. However, a dark cathodic current is observed with an onset of around -0.2V<sup>1</sup> vs. Pt/redox. The magnitude of this current is proportional to the concentration of oxidized species. Its onset is considerably positive of the flatband potential of n-GaAs (see below).

The positive onset of dark current with respect to  $V_{\text{FB}}$  is indicative of a process involving the tunneling of electrons from the conduction band through the space charge region. We have measured this onset as a function of  $V_{\text{redox}}$ . In Fig. 3, the voltage onset of dark current ( $V_{\text{dark}}$ ) is plotted vs.  $V_{\text{redox}}$ , both on the aqueous SCE scale. In the region from 0 to +1V vs. SCE,  $V_{\text{dark}}$  is directly proportional to  $V_{\text{redox}}$ . This result would be consistent with a surface-state controlled barrier potential, which would render  $V_{\text{FB}} - V_{\text{redox}}$  independent of  $V_{\text{redox}}$ . It is also possible that the dark reaction occurs via a few metal-like areas on the crystal surface.

Returning to Fig. 2, we see next that, on irradiation, an anodic photocurrent is produced. The onset of photocurrent at each intensity corresponds to the open-circuit voltage,  $V_{\text{oc}}$ . It occurs at the voltage where dark and photocurrents are exactly equal. Thus, the dark current-voltage behavior of the photoelectrode is important in determining the open-circuit voltage of the cell. If  $V_{\text{dark}}$  always occurred at the same potential, we might hope to adjust  $V_{\text{redox}}$  to minimize the dark current effect. This is, however, not the case, as seen in Fig. 3.

Even though a dark current always opposes the photocurrent, regardless of  $V_{\text{redox}}$ , cells studied here with large separations between  $V_{\text{redox}}$  and the apparent flatband voltage (see below) still have larger open-circuit voltages. In Fig. 4, the open-circuit photovoltages of these cells are plotted vs.  $V_{\text{redox}}$ . Note that these are photovoltages of two-electrode cells in which the counterelectrode is the OTE. The measurements were made at a high light intensity, where the photovoltage exhibits saturation. For the couples studied, the variation of  $V_{\text{oc}}$  at saturation is quite linear with  $V_{\text{redox}}$  for any given crystal and surface preparation. For crystals cut from the same slice, but for different runs of the same polishing/etching regime, photovoltages are reproducible to about  $\pm 10\%$ .

<sup>1</sup> Electrochemical measurements were made in both two- and three-electrode configurations. For the cell featured in Fig. 2, the counterelectrode has been shown to be more polarizable than the n-GaAs, and due to its larger area has a negligible contribution to the total cell polarization at the current levels employed. In other systems where the redox reactions have kinetic limitations, such as in I<sub>2</sub>/I<sup>-</sup> cells, this is not always the case.

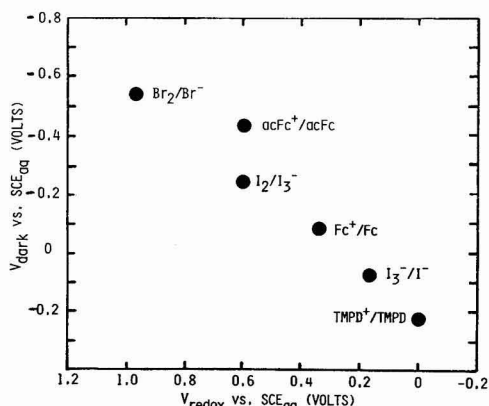


Fig. 3. Variation of voltage onset of cathodic dark current ( $V_{\text{dark}}$ ) with redox potential ( $V_{\text{redox}}$ ) for the half-cell n-GaAs/redox couple, 0.01M LiAsF<sub>6</sub>, PC.

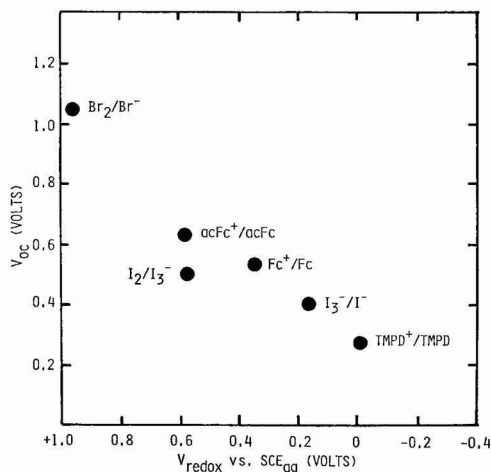
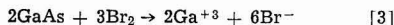


Fig. 4. Variation of open-circuit voltage ( $V_{oc}$ ) with redox potential ( $V_{redox}$ ) for the photoelectrochemical cell n-GaAs/redox couple, 0.1M LiAsF<sub>6</sub>, PC/NESA OTE. Illumination is 150W Xe source, 55 mW/cm<sup>2</sup>.

An important point concerning photovoltages in photoelectrochemical cells is illustrated by the case of the Br<sub>2</sub>/Br<sup>-</sup> couple, which is an exception to the above discussion. With Br<sub>2</sub> present, GaAs corrodes even in the dark according to the reaction



Hence, the redox couple is ineffective in stabilizing the semiconductor. In these cases, the cell exhibits a voltage in the dark, approximately given by the difference  $V_{redox} - V_c$ . This bucking voltage acts in series with the photovoltage, which is now  $V_{FB} - V_c$ . The difference  $V_{FB} - V_{redox}$  can be made large by choosing any redox couple, but the resulting photovoltages cannot be related to the band bending in the photoelectrode unless it is established that the redox couple is indeed photoelectrochemically oxidized or reduced.

In Fig. 5,  $V_{oc}$  and  $V_{dark}$  of the semiconductor are summarized along with  $V_{redox}$ , but with all potentials presented on the aqueous SCE scale. It is seen that  $V_{oc}$  under high light intensities is about -0.2V for the n-GaAs half-cell regardless of the redox couple in solution. This either represents the flatband potential of n-GaAs, or is the effective potential of a surface level which, when reduced at more negative potentials, is totally effective in quenching the photocurrent.

Also shown in Fig. 5 are the values of  $V_{oc}$  for each cell at the lowest light intensity used, 0.26 mW/cm<sup>2</sup>.

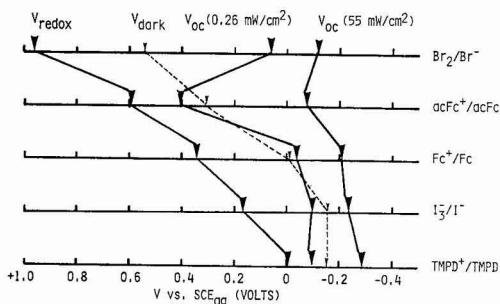


Fig. 5. Diagram showing variations of  $V_{dark}$  and  $V_{oc}$  at low and high light intensity, with redox couple potential for n-GaAs photoelectrochemical cells in PC.

Except for the case of Br<sub>2</sub>/Br<sup>-</sup>, these are close to the voltage onsets of cathodic dark current. The trend is toward a larger difference between high and low intensity  $V_{oc}$ 's with increasingly positive  $V_{redox}$  (discounting, again, Br<sub>2</sub>/Br<sup>-</sup>). The slopes  $dV/d(\log I)$  in the linear region of these plots are revealed in Table II. In a classical photodiode, this slope is 59 mV, but in these cells it is usually somewhat larger. This phenomenon has been noted recently by Sakata *et al.* (14) for some other photoelectrochemical cells. They assign a value of  $\delta$  to the ratio 59 mV/( $dV/d(\log I)$ ). A small value of  $\delta$  means that the photocurrent is effective in overcoming the dark current, as is certainly expected under conditions of large band bending. In general, the onset of dark current is more likely to determine the onset of photocurrent at low intensity. However, the onset of photocurrent tends toward  $V_{FB}$  at saturation. Hence, measurements made at low intensity are more likely to show "Fermi level pinning," since  $V_{dark}$  is proportional to  $V_{redox}$  (Fig. 3).

One major issue to be resolved in these and other n-GaAs cells is the true position of the flatband potential. Capacitance-voltage analysis obtained in the dark indicates a flatband potential for n-GaAs in PC of  $-1.1 \pm 0.2$  V vs. SCE, in agreement with Kohl and Bard in acetonitrile (13), although considerable frequency dependence characterizes the slope of the Mott-Schottky plots. However, other estimates of  $V_{FB}$  can be made by observing the intersection of dark and light  $i$ - $V$  curves (cf. Fig. 2) or by measuring the bias voltage at which the instantaneous photovoltage, obtained using a pulsed dye laser, is zero (Fig. 6). Both methods give a  $V_{FB}$  of about -0.2V vs. SCE. In addition, the plot of  $V_{oc}$  vs.  $V_{redox}$  shown in Fig. 4 extrapolates to the same value of  $V_{FB}$ . Comparison with Table II indicates that, if the more positive values of  $V_{FB}$  are accepted, then the redox couples employed all have potentials lying within the n-GaAs gap. If the value of -1V is accepted, then several of the couples lie beneath the valence bandedge, and it would be surprising if they could react with photogenerated holes.

We have tested the stability of the n-GaAs cell with all the couples and found over several hours operation at 1 mA/cm<sup>2</sup> that only the Br<sub>2</sub>/Br<sup>-</sup> cell shows significant degradation of photocurrent or change in electrode surface morphology as determined by microscopic examination. Furthermore, in all cases except Br<sub>2</sub>/Br<sup>-</sup>, the photoelectrochemical oxidation of the redox species can be observed visually at the n-GaAs surface. Although this does not prove total stabilization, it does indicate that hole transfer to the reduced redox species is by far the dominant process except with Br<sup>-</sup>. Experiments with just Br<sup>-</sup> in the electrolyte show no visual evidence of Br<sub>2</sub> production at the irradiated n-GaAs surface.

Therefore, the accumulated results cast doubt on the validity of C-V measurements for predicting  $V_{FB}$  in this case. It is possible that surface states accessible only at potentials  $< -0.2$  V vs. SCE influence the capacitance at cathodic voltages, leading to anomalously negative values for  $V_{FB}$  determined in this manner.

**Photocurrents, fill factors, and cell efficiencies.**—The other important features of Fig. 2 are related to the photocurrents. For light intensities of up to 2.5 mW/

Table II. Variations of photovoltage with light intensity for the cell n-GaAs | PC, redox, 0.1M LiAsF<sub>6</sub> | NESA OTE

Solution	$V_{redox}$ (meas)	$dV/d(\log I)$ (mV)	$\delta = \frac{59 \text{ mV}}{dV/d(\log I)}$
Br <sub>2</sub> /Br-	(0.01/0.05M)	0.96	1.3
acFc+/acFc	(0.007/0.03M)	0.59	0.35
Fc+/Fc	(0.007/0.063M)	0.34	0.47
I <sub>2</sub> /I-	(0.01/0.05M)	0.16	0.67
TMPD+/TMPD	(0.01/0.09M)	-0.01	1.1

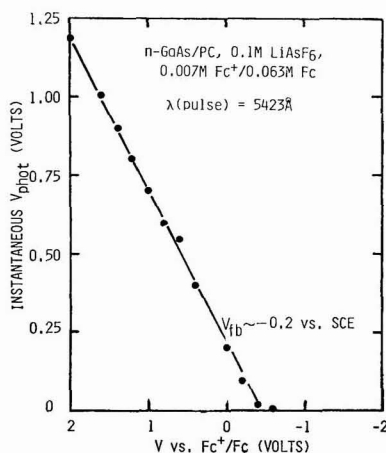


Fig. 6. Instantaneous photovoltage as a function of electrode bias on internal reference scale.

$\text{cm}^2$ , the photocurrents are limited by the number of photons absorbed by the n-GaAs and thus by the number of holes produced. At the higher intensities, the photocurrents become limited by the supply of ferrocene to the electrode surface. An approximation of the steady-state diffusional current is given by Eq. [4] (16)

$$i(\text{mA}/\text{cm}^2) = \frac{1000nFCD}{d} \quad [4]$$

where  $d$  is the electrode separation ( $\sim 0.04$  cm),  $C$  is the concentration (in  $\text{mols}/\text{cm}^3$ ), and  $D$  the diffusion coefficient. In the present case,  $C = 6.3 \times 10^{-5}$   $\text{mols}/\text{cm}^3$  and  $10^{-5}$  is a reasonable value for  $D$  (15). The resulting limiting current is  $\sim 1.5$   $\text{mA}/\text{cm}^2$ . Experimental results of the limiting photocurrents observed for oxidation of  $0.05\text{M}$   $\text{I}^-$  and  $0.032\text{M}$  acFc at n-GaAs are plotted as a function of light intensity in Fig. 7.

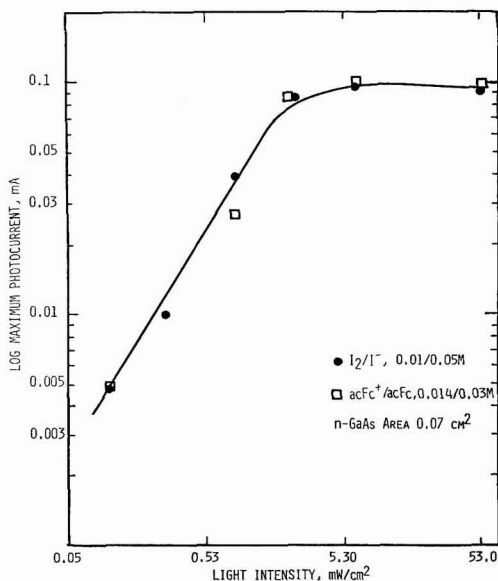


Fig. 7. Limiting photocurrent as a function of light intensity for n-GaAs in PC,  $0.1\text{M}$   $\text{LiAsF}_6$ , redox couple, NESATRON counterelectrode.

The diffusion-limited current density in both cases is  $\sim 1.4$   $\text{mA}/\text{cm}^2$ , attained at light intensities  $> 5$   $\text{mW}/\text{cm}^2$  for these concentrations, close to that predicted by Eq. [4].

The fill factor or "squareness" of the current-voltage curves in the region between 0 volts and  $V_{oc}$  is an important variable in determining cell efficiencies. As shown in Fig. 8, contributions to the final curve arise from polarizations at the photoelectrode and counterelectrode, as well as from solution resistance. The production of photocurrent is also sensitive to the efficiency of light absorption and to lifetime of minority carriers. Cells based on n-GaAs/propylene carbonate,  $\text{Fc}^+/\text{Fc}$  ( $0.007/0.063\text{M}$ ) have been tested in which we have varied the counterelectrode, the concentration of supporting electrolyte, and the surface treatment of the n-GaAs. Some of the results are summarized in Table III, and indicate some of the limitations of the present system.

All cells listed in Table III exhibited diffusionally limited currents at high light intensities. Efficiencies in the range where currents were limited only by the hole flux, i.e.,  $0-2$   $\text{mW}/\text{cm}^2$  white light, were 4-8% while efficiencies at solar intensities were  $< 1\%$ . Kohl and Bard (13) have reported the same type of decrease in efficiency with increasing intensity for n-GaAs/acetonitrile-based systems. Short-circuit photocurrents were enhanced by 25-30% by employing a black matte etched GaAs surface rather than a reflective shiny surface. Another increase in photocurrents was observed by decreasing the sheet resistance of the optically transparent counterelectrode. NESATRON glass ( $\text{SnO}_x$ ,  $150$   $\Omega\text{-cm}$ ) gave short-circuit currents which were about 50% less than the more conductive, though  $\sim 20\%$  less transmissive, NESATRON ( $\text{SnO}_x \cdot \text{In}_2\text{O}_3$ ,  $5$   $\Omega\text{-cm}$ ). Fill factors and efficiencies were also enhanced in the NESATRON cells, despite a reduction in voltage which may relate to NESATRON's higher optical absorption. An attempt to decrease the surface recombination velocity by adsorbing  $\text{Ru}^{+3}$  on the n-GaAs surface proved unsuccessful (surface treatment C, in the table). In the original work by Heller and co-workers, a pretreatment in  $\text{Se}^{-2}/\text{Se}_n^{-2}$  aqueous electrolyte was employed (6, 7). We have demonstrated in other work that such pretreatment is also necessary for observation of the  $\text{Ru}^{+3}$  effect in nonaqueous electrolytes (17).

At high light intensity, concentration polarization develops for all these cells over the first minute of cell operation. This effect is demonstrated in Fig. 9 for a cell based on  $0.007\text{M}$   $\text{Fc}^+$ ,  $0.063\text{M}$   $\text{Fc}$ , and is due, at least in part, to the limiting concentration of  $\text{Fc}$  achievable in PC. The wavelength of the incoming light has a significant effect on the cell efficiency. This is due to the wavelength dependence on solution and semiconductor absorbances, as well as that of photocurrent production due to differences in light penetration depth into the semiconductor. For the GaAs cell, sev-

Table III. Effects of n-GaAs surface treatments on performance of the EPC n-GaAs/ $\text{Fc}^+$  ( $0.007\text{M}$ ),  $\text{Fc}$  ( $0.053\text{M}$ ),  $\text{LiAsF}_6$  ( $0.1\text{M}$ ), PC/NESATRON OTE. Figures in parentheses are for NESATRON OTE.

	Source intensity ( $\text{mW}/\text{cm}^2$ ) (150W Xe arc, 300-1200 nm)		
	0.9	6.7	53
<b>Etch A</b>			
$V_{oc}$ (V)	0.53	0.55	0.59
$i_{sc}$ ( $\text{mA}/\text{cm}^2$ )	0.17	1.7	1.7
$P_{max}$ ( $\text{mW}/\text{cm}^2$ )	0.04	0.23	0.28
$\eta$ (%)	4.4	3.4	0.5
<b>Etch B</b>			
$V_{oc}$ (V)	0.55 (0.46)	0.58	0.59 (0.54)
$i_{sc}$ ( $\text{mA}/\text{cm}^2$ )	0.23 (0.40)	1.7	2.1 (2.91)
$P_{max}$ ( $\text{mW}/\text{cm}^2$ )	0.06 (0.07)	0.26	0.44 (0.7)
$\eta$ (%)	6.9 (7.8)	3.9	0.8 (1.32)
<b>Etch C</b>			
$V_{oc}$ (V)	0.52	—	0.54
$i_{sc}$ ( $\text{mA}/\text{cm}^2$ )	0.14	—	1.65
$P_{max}$ ( $\text{mW}/\text{cm}^2$ )	0.04	—	0.24
$\eta$ (%)	4.4	—	0.45



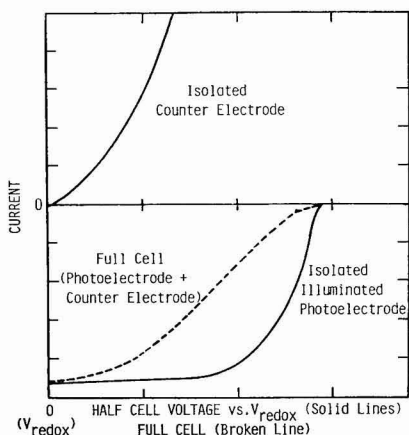


Fig. 8. Hypothetical steady-state current-voltage curves illustrated for half-cell components of an electrochemical photovoltaic cell (solid line) and for the resulting full cell (broken line).

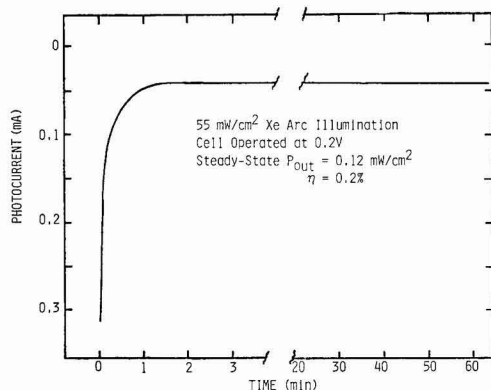


Fig. 9. Output and stability of photoelectrochemical cell n-GaAs (0.07 cm²) | Fc⁺ (0.007M), Fc (0.063M), LiAsF₆ (0.5M) PC | NESATRON OTE under high intensity white light illumination.

eral experiments were done with monochromatic light using a 765 nm interference filter and a power of 0.9 mW/cm². At this wavelength, absorbance by Fc⁺ is small, and the cell action spectrum is nearly maximized. As shown in Fig. 10, instantaneous conversion efficiencies of 14% were obtained, followed by relaxation to a somewhat lower steady-state value of 9% due to electrode polarization. These values are comparable with those reported by Kohl and Bard for GaAs in acetonitrile using red light. White light from the Xe source of the same intensity gave ~6.6% conversion efficiency.

### Conclusions

Measurements of n-GaAs photoelectrodes with a variety of redox couples in PC electrolytes have indicated several limiting factors in EPC devices. Photovoltages were sensitive to the position of  $V_{\text{redox}}$ , but were limited to  $<0.7\text{V}$  by decomposition of the semiconductor. Redox couples which lie too positive of  $V_{\text{FB}}$ , are likely to act as etchants; indeed,  $\text{Br}_2$  is a common etchant for GaAs. Furthermore, the redox couples explored in this work appear not to have adsorptive effects on the onset of photocurrent, which occurred at a common potential of  $\sim -0.2\text{V}$  vs. SCE in all the PC-based systems. In aqueous solutions, negative shifts of  $V_{\text{FB}}$  due to adsorption of redox species can provide an

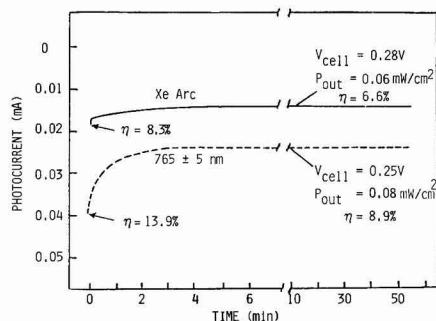


Fig. 10. Output and stability of photoelectrochemical cell n-GaAs (0.07 cm²) | Fc⁺ (0.007M), Fc (0.063M), LiAsF₆ (0.5M) PC | NESATRON OTE under white light (—) and monochromatic (---) illumination of 0.9 mW/cm². Cells operated at voltages ( $V_{\text{cell}}$ ) yielding maximum power.

increased range of photovoltages, e.g., n-GaAs/aqueous  $\text{Se}_2^{2-}$ ,  $\text{Se}^{2-}$  devices. Although more positive-lying redox couples can stabilize GaAs in PC than in water (e.g., ferrocene,  $\text{I}_3^-$ ), photovoltages are no greater in the nonaqueous systems due to the lack of such adsorptive effects. Nevertheless, nonaqueous systems do have the advantage of allowing a wider variety of stabilizing redox couples than aqueous solutions. We anticipate that less noxious electrolytes than alkaline  $\text{Se}_2^{2-}/\text{Se}^{2-}$  can be developed in nonaqueous systems.

We have shown that efficiencies degrade seriously with increasing light intensity in PC-based electrolytes. We assume these losses to be related to limited redox electrolyte solubility and low electrolyte conductivity. Such losses are accumulated at both cell electrodes and are manifested as reductions in short-circuit currents and fill factors. We note that even the most conductive nonaqueous electrolytes, such as those based on acetonitrile, are still at least ten times more resistive than their aqueous counterparts. Nevertheless, if high photovoltages can be achieved in nonaqueous systems because of their increased stabilizing range, then high efficiencies can be achieved even with reduced currents, i.e.,  $P_{\text{max}} = 10 \text{ mA/cm}^2 \times 1\text{V}$ , rather than  $P_{\text{max}} = 20 \text{ mA/cm}^2 \times 0.5\text{V}$ . However, surface adsorbed redox couples in nonaqueous electrolytes or other semiconductor surface modifications may be necessary to achieve such high voltages.

### Acknowledgment

This work was supported by the Solar Energy Research Institute under contract to the Department of Energy, Subcontract No. XP-9-8002-7.

Manuscript submitted March 11, 1981; revised manuscript received ca. May 11, 1981.

Any discussion of this paper will appear in a Discussion Section to be published in the June 1982 JOURNAL. All discussions for the June 1982 Discussion Section should be submitted by Feb. 1, 1982.

### REFERENCES

1. R. D. Rauh, T. F. Reise, and S. B. Brummer, *This Journal*, **125**, 186 (1978).
2. J. N. Butler, in "Advancement in Electrochemical and Electrochemical Engineering," Vol. 7, P. Delahay, Editor, pp. 106-114, Interscience, New York (1970).
3. A. B. Ellis, S. W. Kaiser, J. M. Bolts, and M. S. Wrighton, *J. Am. Chem. Soc.*, **99**, 2839 (1977).
4. M. A. Butler and D. S. Ginley, *This Journal*, **125**, 228 (1978).
5. S. M. Sze, "Physics of Semiconductor Devices," pp. 363 ff., Wiley-Interscience, New York (1969).
6. B. Parkinson, A. Heller, and B. Miller, *Appl. Phys. Lett.*, **33**, 521 (1978).



7. W. D. Johnson, H. I. Leamy, B. A. Parkinson, A. Heller, and B. Miller, *This Journal*, **127**, 90 (1980).
8. H. Hovel, in "Solar Cells: Semiconductors and Semimetals," Vol. 11, R. K. Willardson and A. C. Beer, Editors, Academic Press, New York (1975).
9. C. H. Seager and D. S. Ginley, *Appl. Phys. Lett.*, **34**, 337 (1979).
10. A. J. Bard, A. B. Bocarsly, F. F. Fan, E. G. Walton, and M. S. Wrighton, *J. Am. Chem. Soc.*, **102**, 3671 (1980).
11. R. H. Wilson, *J. Appl. Phys.*, **48**, 4292 (1977).
12. N. Matsuura, K. Uimoto, and Z. Takeuchi, *Bull. Chem. Soc. Jpn.*, **47**, 813 (1974).
13. P. A. Kohl and A. J. Bard, *This Journal*, **126**, 603 (1979).
14. T. Sakata, T. Kawai, and K. Tanimura, *Ber. Bunsenges. Phys. Chem.*, **83**, 486 (1979).
15. D. Sawyer, "Experimental Electrochemistry for Chemists," John Wiley & Sons, Inc., New York (1975).
16. R. Parsons, "Handbook of Electrochemical Constants," Butterworths, London (1959).
17. M. E. Langmuir, R. H. Micheels, and R. D. Rauh, Paper IX-18, Third International Conference on Photochemical Conversion and Storage of Solar Energy, Boulder, Colorado, Aug. 3-8, 1980.

## Photoelectrochemical Evaluation of the n-CdSe/Methanol/Ferro-Ferricyanide System

Rommel Noufi,\*<sup>1</sup> Dennis Tench,\* and Leslie F. Warren\*

*Rockwell International, Microelectronics Research and Development Center, Thousand Oaks, California 91360*

### ABSTRACT

Factors limiting the short-circuit photocurrent for the n-CdSe/methanol/ferro-ferricyanide system to 17.5 mA/cm<sup>2</sup> have been identified. The principal limiting factor is apparently specific adsorption of hexacyanoferrate species on the electrode surface, which occurs at higher redox couple concentrations and slows the overall charge transfer process. Ion pairing also occurs, resulting in a low mass transport rate (smaller diffusion coefficients and increased solution viscosity), and probably enhances the degree of specific adsorption.

In a previous publication (1), the systematic development of a nonaqueous ferro-ferricyanide electrolyte for stabilization of n-CdSe photoanodes was described. Selection of the solvent was discussed in terms of inherent stability provided, the rate of the redox reaction, the tendency toward specific adsorption of the redox species, and the equilibrium potential of the redox couple with respect to the flatband potential (attainable open-circuit voltage). Results were presented for cells of the type n-CdSe/methanol, Fe(CN)<sub>6</sub><sup>3-/4-</sup>/Pt which had been operated for up to 700 hr at 6 mA/cm<sup>2</sup> with no detectable degradation in either the electrode surface or the photoresponse.

Although the Fe(CN)<sub>6</sub><sup>3-/4-</sup>/methanol system itself was subsequently found to be photolytically unstable (substitution for cyanide slowly occurs), additional work was warranted since this system serves as a prototype for stabilizing nonaqueous redox electrolytes. In the present paper, the factors limiting the attainable photocurrent for n-CdSe in this system are discussed.

### Electrolyte Preparation

Tetraethylammonium ferricyanide was prepared by the metathesis of Ag<sub>3</sub>Fe(CN)<sub>6</sub> with Et<sub>4</sub>NBr (where Et = ethyl) in methanol (2), recrystallized twice from an acetonitrile-acetone mixture, and then subjected to high vacuum to remove traces of solvent. Tetraethylammonium ferrocyanide was prepared as an off-white crystalline powder by anaerobic neutralization of H<sub>2</sub>Fe(CN)<sub>6</sub> (3) with excess Et<sub>4</sub>NOH (Southwestern Analytical Chemicals) in water, treated *in vacuo* to remove the solvent, and recrystallized from an i-propanol/acetone mixture in an inert atmosphere. This chemical procedure for preparing the air-sensitive

(Et<sub>4</sub>N)<sub>4</sub>Fe(CN)<sub>6</sub> is faster and less tedious than the electrochemical synthesis used previously (1). Tetraethylammonium fluoroborate was precipitated from a solution of Et<sub>4</sub>NBr and 48% fluoroboric acid in ethanol by addition of i-propanol, and was then recrystallized twice from ethanol. The methanol solvent (Baker Analyzed) was refluxed over Mg, and then fractionally distilled under an inert atmosphere.

### Electrodes

Reference electrodes were isolated in a separate compartment which was connected to the main cell through a medium glass frit. Both Ag/AgCl and saturated calomel reference electrodes were used with comparable results.

The Pt disk electrode (0.13 cm<sup>2</sup>) used to study the kinetics of the Fe(CN)<sub>6</sub><sup>3-/4-</sup>/Pt reaction was mounted concentric and flush with the end of a 12 mm diam Kel-F cylinder by hot pressing. After mounting, the electrode was polished on successively finer aqueous alumina powder slurries to 1 μm particle size, and was then cleaned ultrasonically in water. Before each use, the electrode was further cleaned by immersion in boiling concentrated nitric acid.

The n-CdSe electrodes (0.18 cm<sup>2</sup> × 1 mm thick) were cut from rods supplied by Cleveland Crystals, Incorporated (Cleveland, Ohio) and had from 10<sup>16</sup> to 10<sup>18</sup> carriers/cm<sup>3</sup>. Ohmic contacts were made with an In-Ga alloy. Before use, n-CdSe electrodes were polished to 0.05 μm particle size, then etched in 3M nitric acid or a 1:25 mixture of concentrated nitric and hydrochloric acids (with comparable results). For long-term studies, n-CdSe electrodes were mounted in Kel-F by hot pressing. Results for electrodes mounted in silicone adhesive/sealant (Dow Corning Corporation, Midland, Michigan) were comparable.

\* Electrochemical Society Active Member.

<sup>1</sup> Present address: Solar Energy Research Institute, Golden, Colorado 80401.

Key words: semiconductor photoanodes, nonaqueous solvents, performance characteristics.

### Electrochemical Measurements

All electrochemical measurements were made in Pyrex glass cells inside an inert atmosphere dry box using a PAR Model 173 Potentiostat/Galvanostat in conjunction with a PAR Model 175 Universal Programmer. The effects of solution resistance were always eliminated by electronic  $iR$  compensation. Electrodes were illuminated by a tungsten-halogen lamp through a quartz window. The illumination intensity was measured with a Pyroelectric Radiometer (Molelectron, Sunnyvale, California).

### Results and Discussion

Performance characteristics were measured for n-CdSe photoanodes in methanol solutions as a function of the ferro-ferricyanide redox couple concentration. The best output parameters (5.5% conversion efficiency,  $FF \approx 0.47$ ) were obtained for electrodes with  $5 \times 10^{16}$  carriers/cm<sup>3</sup> in solutions containing 0.25M each of chemically prepared  $Fe(CN)_6^{3-/4-}$  species. A typical power curve is shown in Fig. 1. The measured open-circuit voltage is very close to the maximum value expected for this system (0.7V). Photocurrent measurements as a function of light intensity indicated that the maximum stable short-circuit current is 17.5 mA/cm<sup>2</sup> in stirred solutions and 7.5 mA/cm<sup>2</sup> in unstirred solutions (at 95 mW/cm<sup>2</sup>). Transient photocurrents were larger at higher light intensities but rapidly decayed to the steady values. Currents of 17.5 mA/cm<sup>2</sup> were passed for as long as 2 hr.

Possible causes for such photocurrent limitations include decreased redox reaction rate and/or inadequate mass transport of the redox species in the electrolyte caused by ion pairing and/or specific adsorption of one or both of the electroactive species. The inherent electrode kinetics for the ferro-ferricyanide couple in methanol were studied by cyclic voltammetry at a rotating Pt disk electrode (4). Kinematic viscosity measurements were made as a function of the redox couple concentration so that the relative effects of changes in the fluid flow characteristics, reactant diffusion coefficients, and electron transfer rate could be ascertained. The dependence of the

photocurrent for n-CdSe photoanodes on light intensity was determined in both the methanol/ferro-ferricyanide and the established aqueous polysulfide systems as a means of detecting solid-state limitations.

Figure 2 shows plots of the diffusion-limited currents ( $i_L$ ) for the ferro-ferricyanide reaction at a rotating Pt disk electrode as a function of the redox couple concentration. For both the anodic and cathodic branches,  $i_L$  goes through a maximum at about 0.15M  $Fe(CN)_6^{3-/4-}$ . Also, at concentrations above 0.05M, specific adsorption becomes significant, as indicated by higher Tafel slopes (180-250 mV/decade) than obtained at lower concentrations ( $\sim 120$  mV/decade). The decrease in  $i_L$  at higher concentrations could result from a decrease in the diffusion coefficient of the hexacyanoferrate species, stemming from increased ion pairing, and/or an increase in the electrolyte viscosity. That  $i_L$  is practically diffusion limited at all redox couple concentrations is shown by the Levich plots (4) in Fig. 3.

Figure 4 shows plots of the diffusion coefficients for the  $Fe(CN)_6^{3-/4-}$  species (calculated from the Levich equation) and the electrolyte kinematic viscosity (measured with a Cannon-Fenske viscometer) vs. the redox couple concentration. The viscosity is practically constant at low  $Fe(CN)_6^{3-/4-}$  concentrations but increases sharply at about 0.2M, which corresponds approximately to the maximum in the diffusion-limited current for the redox reaction (0.15M). However, the diffusion coefficient decreases by almost an order of magnitude (from  $28 \times 10^{-6}$  to  $3 \times 10^{-6}$  cm<sup>2</sup>/sec) from 0.01 to 0.1M  $Fe(CN)_6^{3-/4-}$ , indicating that considerable ion pairing occurs even at relatively low redox couple concentrations. Ion pairing of hexacyanoferrate species with tetraalkylammonium cations in solvents with low acceptor numbers has also been detected polarographically (2).

The relative effects of the electrolyte kinematic viscosity ( $\nu$ ) and the diffusion coefficients ( $D$ ) in reducing the diffusion-limited currents can best be seen by plotting  $D^{2/3}$  and  $\nu^{-1/6}$ , which are the terms appearing in the Levich equation (4)

$$i_L = 1.94 \times 10^7 C_R D_R^{2/3} \nu^{-1/6} \omega^{1/2}$$

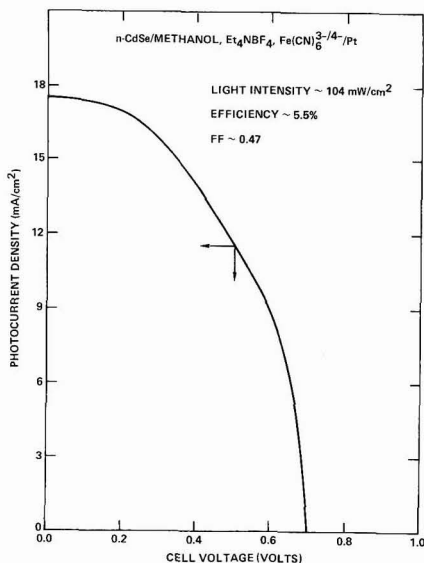


Fig. 1. Photocurrent density vs. voltage for the cell n-CdSe/methanol, 0.25M  $Fe(CN)_6^{3-/4-}$ , 0.1M  $Et_4NBF_4$ /Pt under illumination at 104 mW/cm<sup>2</sup>.

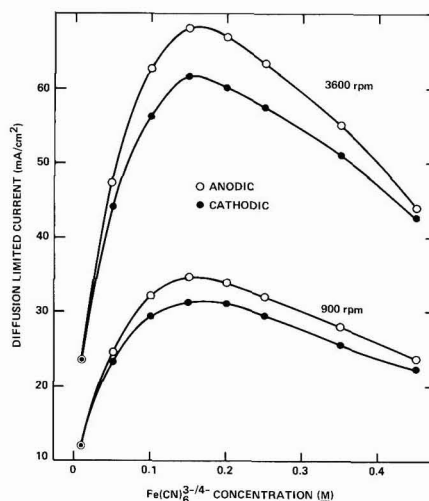


Fig. 2. Diffusion-limited currents vs. the  $Fe(CN)_6^{3-/4-}$  concentration for a rotating 0.13 cm<sup>2</sup> Pt disk electrode in methanol/0.1M  $Et_4NBF_4$  electrolyte containing equal concentrations of the oxidized and reduced species. The scan rate was 20 mV/sec and  $i_L$  was determined at an overvoltage of 1.00V in each case.

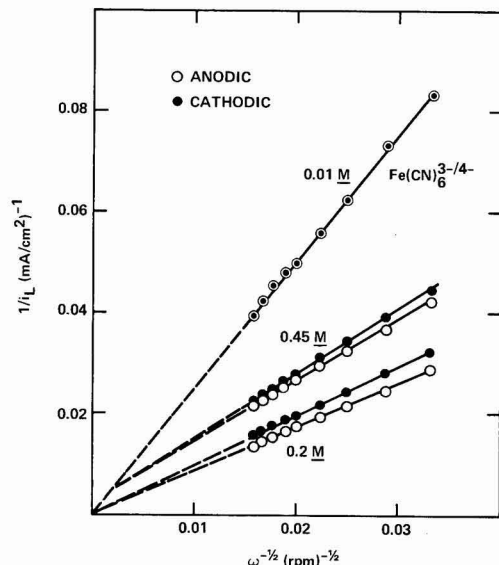


Fig. 3. Levich plots (4) for the  $\text{Fe}(\text{CN})_6^{3-/4-}$  reaction at a rotating Pt disk electrode in methanol/0.1M  $\text{Et}_4\text{NBF}_4$  (conditions same as for Fig. 2).

where  $i_L$  is in  $\text{mA}/\text{cm}^2$ ,  $C_R$  is the concentration of reactant in  $\text{mol}/\text{ml}$ ,  $D_R$  is the reactant diffusion coefficient in  $\text{cm}^2/\text{sec}$ ,  $\nu$  is the electrolyte kinematic viscosity in  $\text{cm}^2/\text{sec}$ , and  $\omega$  is the disk electrode rotation rate in  $\text{rpm}$ . Such plots are shown in Fig. 5, where  $\nu^{-1/6}$  is seen to decrease linearly and relatively slowly (note scale difference) with  $\text{Fe}(\text{CN})_6^{3-/4-}$  concentration,

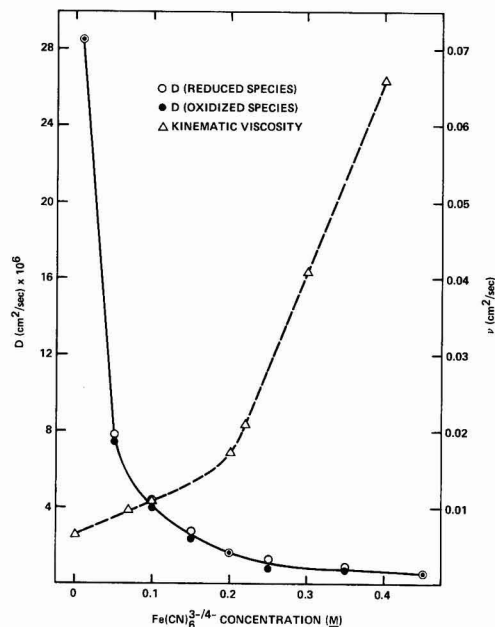


Fig. 4. Plots of the diffusion coefficients ( $D$ ) of  $\text{Fe}(\text{CN})_6^{3-/4-}$  species and the kinematic viscosity of 0.1M  $\text{Et}_4\text{NBF}_4$ /methanol solutions as functions of the  $\text{Fe}(\text{CN})_6^{3-/4-}$  concentration.

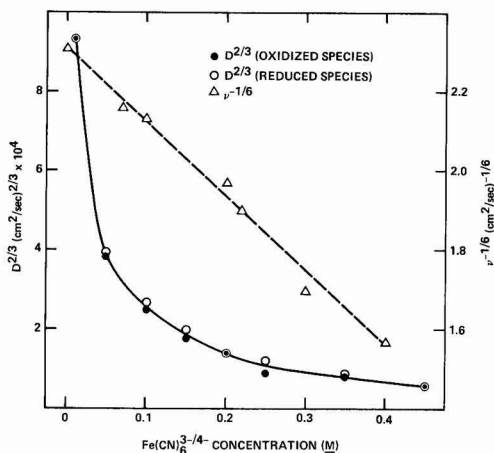


Fig. 5. Plots of  $D^{2/3}$  and  $\nu^{-1/6}$  for the data in Fig. 4

whereas  $D^{2/3}$  decreases sharply to about 0.1M and then more gradually. Thus, the decrease in  $i_L$  at concentrations above 0.15M results from a combination of the effects of  $\nu^{-1/6}$  and  $D^{2/3}$ .

Plots of the short-circuit photocurrent at single crystal n-CdSe photoanodes in 0.25M  $\text{Fe}(\text{CN})_6^{3-/4-}$ /methanol and in aqueous polysulfide electrolyte vs. light intensity are shown in Fig. 6. The linear plot (passing through the origin) for the aqueous system indicates that solid-state limitations are not predominant. Therefore, the nonlinearity in the methanol/ $\text{Fe}(\text{CN})_6^{3-/4-}$  plot and the upper limit of 17.5  $\text{mA}/\text{cm}^2$  for the steady-state photocurrent are apparently associated with electrolyte effects. The data can be adequately explained by assuming the occurrence of strong specific adsorption of a ferricyanide species, which is the product of the photoelectrochemical redox reac-

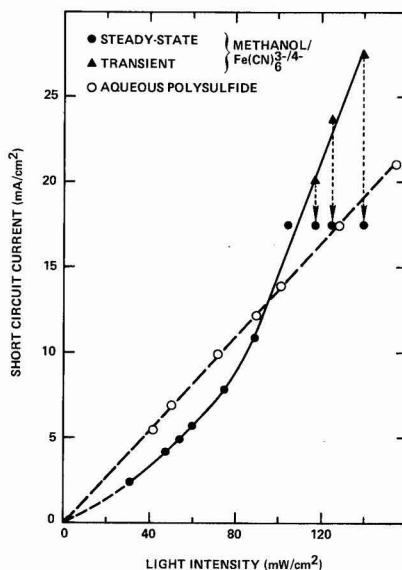


Fig. 6. Short-circuit currents vs. light intensity (tungsten-halogen lamp) for n-CdSe electrodes in 0.25M tetraethylammonium  $\text{Fe}(\text{CN})_6^{3-/4-}$ /0.1M  $\text{Et}_4\text{NBF}_4$ /methanol and in aqueous 2.2M  $\text{Na}_2\text{S}$ /0.1M S/0.1M NaOH electrolytes.

tion. Thus, at the lower light intensities, for which the currents are lower, the reaction rate is under mixed electron transfer/product desorption control, i.e., the rates of electron transfer (which is determined by the availability of photoholes in the semiconductor) and product desorption are comparable. As the light intensity (and consequently the current) is increased, the electron transfer rate increases and product desorption becomes the slow reaction step. In this case, higher currents can be passed for a short time but product accumulation on the electrode surface ultimately limits the current to a constant value determined by the rate of desorption. This model is consistent with the transient photocurrents (at the higher light intensities) decaying to the steady-state value (Fig. 6), and with the higher Tafel slopes (on Pt) for higher redox couple concentrations. The adsorbed species may be either the ferricyanide species normally present in solution or some reaction intermediate, and it may be ion paired since the viscosity data indicate that ion pairing is prevalent at  $\text{Fe}(\text{CN})_6^{3-4-}$  concentrations above 0.1M. Note that specific adsorption is known to also occur for the aqueous polysulfide system but would not affect the linearity of the corresponding plot in Fig. 6 if adsorption/desorption is fast compared to the electron transfer step, which involves two electrons.

### Summary and Conclusions

The photocurrent for n-CdSe photoanodes in the methanol/ferro-ferricyanide system is limited to 17.5 mA/cm<sup>2</sup>, apparently by specific adsorption of ferri-

cyanide redox species. Ion pairing in this system also has a pronounced effect on the redox couple diffusion coefficients and the electrolyte viscosity at higher redox couple concentrations. Such factors would be expected to be of general importance in photoelectrochemical cells employing nonaqueous electrolytes.

### Acknowledgment

The authors gratefully acknowledge support of this work by the Solar Energy Research Institute under Subcontract No. XG-0-9276.

Manuscript submitted March 23, 1981; revised manuscript received ca. June 8, 1981.

Any discussion of this paper will appear in a Discussion Section to be published in the June 1982 JOURNAL. All discussions for the June 1982 Discussion Section should be submitted by Feb. 1, 1982.

Publication costs of this article were assisted by Rockwell International.

### REFERENCES

1. R. Noufi, D. Tench, and L. F. Warren, *This Journal*, **127**, 2709 (1980).
2. E. Gritzner, K. Danksagmuller, and V. Gutmann, *J. Electroanal. Chem. Interfacial Electrochem.*, **72**, 177 (1976).
3. G. Bauer, "Handbook der Präparativen Anorganischen Chemie," F. Enke, Verlag, Stuttgart (1960).
4. V. G. Levich, "Physicochemical Hydrodynamics," Prentice-Hall, Englewood Cliffs, NJ (1962).

## Technical Notes



### Kinetics of Electroless Copper Plating

#### V. Mass Transport at Cylindrical Surfaces

Francis M. Donahue\*

Department of Chemical Engineering, The University of Michigan, Ann Arbor, Michigan 48109

In a previous communication, properties of mass transport in electroless copper plating baths were presented for the common case of linear transport (1). Since some studies have been performed on cylindrical samples (2-4), it is worthwhile to determine the effects of this geometry on mass transfer phenomena.

The steady-state mass balance for a transporting species, "j," for cylindrical geometry in the absence of a homogeneous reaction and with concentration variation only in the radial direction is

$$\frac{d^2c_j}{dR^2} + \frac{1}{R} \frac{dc_j}{dR} = 0 \quad [1]$$

The boundary conditions for the case considered here are

$$c_j = c_{sj} \quad \text{at} \quad R = R_o \quad [2a]$$

and

$$c_j = c_{bj} \quad \text{at} \quad R = R_o + \delta \quad [2b]$$

The solution of Eq. [1] for these boundary conditions is

$$c_j = c_{bj} + (c_{sj} - c_{bj}) \frac{\ln\left(\frac{R_o + \delta}{R}\right)}{\ln\left(\frac{R_o + \delta}{R_o}\right)} \quad [3]$$

The flux of the transporting species at the sample-solution interface is

$$N_j = -10^{-3} D_{jm} (dc_j/dR)_{R=R_o} \quad [4]$$

Differentiating Eq. [3] and setting  $R = R_o$ , the flux becomes

$$N_j = (10^{-3} D_{jm}/\delta) (c_{sj} - c_{bj}) \frac{\delta/R_o}{\ln(1 + \delta/R_o)} \quad [5]$$

Comparing Eq. [5] with Eq. [1a] of Ref. (1) shows that the flux at a cylindrical sample reduces to that for linear transport when the ratio of the boundary layer thickness to the sample radius is less than 0.1.

\* Electrochemical Society Active Member.  
Key words: mass transport, baths, plating.

The boundary layer thickness for rotating cylinders can be computed from the macroconvection mass transfer coefficient (1) and the diffusivity. The boundary layer thickness for the cylinders used by Dumesic and co-workers (3) at the lowest rotation speed (150 rpm) was computed using Donahue's corrected value of the macroconvection mass transfer coefficient (1) and their diffusivity for cupric ion. Since the ratio,  $\delta/R_o$ , was less than 0.01, the flux of cupric ion was correctly described by the authors in terms of the linear transport equation.

When microconvection controls the transport process (e.g., in the absence of forced convection, but the presence of gas evolution), the boundary layer thickness is a function of the plating rate (1), i.e.

$$\delta = 0.026 \tau_p^{-0.53} \quad [6]$$

Insertion of Eq. [6] in Eq. [5] provides some insight into the roles of plating rate and sample radius under these conditions. However, it is more convenient to define an "effective" mass transfer coefficient,  $k_{cj}'$ , by

$$k_{cj}' = \frac{10^3 N_j}{c_{sj} - c_{bj}} \quad [7]$$

or, from Eq. [5]

$$k_{cj}' = \frac{D_{jm}/R_o}{\ln(1 + \delta/R_o)} \quad [8]$$

which can be rearranged to

$$\frac{k_{cj}'}{D_{jm}} = \frac{1/R_o}{\ln(1 + \delta/R_o)} \quad [9]$$

where the right-hand side of the equation is a function of the plating rate and sample radius and independent of the transporting species. Figure 1 shows the behavior of the left-hand side of this equation as functions of sample radius and plating rate. From this figure one concludes that the stationary cylinders of Dumesic and co-workers (3) exhibited linear transport even at the lowest plating rates. On the other hand, the wire samples of Donahue and co-workers (2, 4), i.e.,  $R_o = 0.016$  cm, exhibit substantial deviation from the linear transport line even at the highest plating rates. Therefore, when computing interfacial concentrations, they cannot use the linear transport equations given previously (1), but must use Eq. [5].

#### Acknowledgment

This material is based upon work supported by the National Science Foundation under Grant No. ENG-7511869.

Manuscript submitted Nov. 7, 1980; revised manuscript received March 16, 1981.

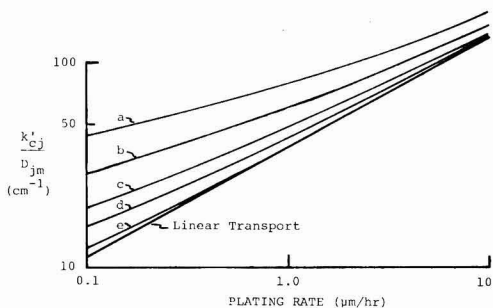


Fig. 1. Relationship between  $k_{cj}'/D_{jm}$  and electroless copper plating rate for microconvection conditions.

Symbol	$R_o$ (cm)
a	0.01
b	0.02
c	0.05
d	0.10
e	0.50

Any discussion of this paper will appear in a Discussion Section to be published in the June 1982 JOURNAL. All discussions for the June 1982 Discussion Section should be submitted by Feb. 1, 1982.

Publication costs of this article were assisted by the National Science Foundation.

#### LIST OF SYMBOLS

$c_j$	concentration of species "j" (M)
$c_{bj}$	bulk concentration of species "j" (M)
$c_{sj}$	interfacial concentration of species "j" (M)
$D_{jm}$	diffusivity of species "j" in the solution (cm <sup>2</sup> /sec)
$k_{cj}'$	"effective" mass transfer coefficient of species "j" (cm/sec)
$N_j$	flux of species "j" (mol/cm <sup>2</sup> -sec)
$R$	radial distance (cm)
$R_o$	cylinder radius (cm)
$\tau_p$	plating rate (μm/hr)
$\delta$	mass transfer boundary layer thickness (cm)

#### REFERENCES

1. F. M. Donahue, *This Journal*, **127**, 51 (1980).
2. F. L. Shippey and F. M. Donahue, *Plating*, **60**, 43 (1973).
3. J. Dumesic, J. A. Koutsky, and T. W. Chapman, *This Journal*, **121**, 1405 (1974).
4. F. M. Donahue, K. L. M. Wong, and R. V. Bhalla, *ibid.*, **127**, 2340 (1980).

## Electrodeposition of Palladium on Iron and Steel for Electrochemical Hydrogen Permeation Studies

R. Driver\*

CSIRO Division of Applied Physics, Sydney, Australia 2070

In the highly sensitive electrochemical technique for studying hydrogen permeation in metals (1, 2), a thin test membrane acts as a bipolar electrode in a two-compartment cell. A fraction of the hydrogen produced at the cathodically polarized (inlet) side diffuses through the membrane and is oxidized as it reaches the

anodically polarized (exit) side. To obtain meaningful permeation rate data, it is necessary to ensure that ionization of hydrogen at the exit surface occurs much faster than the competing, nonelectrochemical, hydrogen atom recombination reaction, and that the measured ionization current is free of any spurious components associated with anodic dissolution or passivation of the exit surface.

\* Electrochemical Society Active Member.  
Key words: membrane, permeation, metals.

In principal, these objectives may be achieved by coating the exit surface with a very thin layer of palladium, an inert and highly permeable material which has virtually no effect on the overall rate of hydrogen transport. Electrolytic deposits have usually been employed, but descriptions of the plating methods are both meager and conflicting and very little attention has apparently been directed at monitoring the thickness or integrity of the coatings. As pointed out by Heidersbach *et al.* (3), there is wide variation in existing hydrogen permeation data and this could be due partly to poor control of the palladium deposits applied to membrane exit surfaces.

The present work was undertaken to establish a simple and reliable laboratory method for obtaining good quality palladium electrodeposits on iron and steel, the materials most commonly used in hydrogen diffusion studies. A simple porosity test was used to determine the minimum deposit thickness for complete coverage. The chemical factors underlying the operation of the plating bath are discussed briefly.

### Experimental

**Sample preparation.**—Plating experiments were performed on coupon specimens of surface area 4–10 cm<sup>2</sup>, cut from Johnson Matthey "Specpure" iron sheet, 1.0 mm thick, and from bright mild steel sheet, 0.78 mm thick. After degreasing in hot petroleum (bp 100°–120°C), any rust or oxide bloom was removed by treatment with a commercial acid-based rust remover, or alternatively, by appropriate pickling in 0.5M H<sub>2</sub>SO<sub>4</sub>. The former procedure had the advantage of leaving a brilliantly clean surface, almost free of etching. The samples were then rinsed in distilled water, dried with alcohol, and finally polished with steel wool.

**Plating solution.**—The alkaline plating electrolyte was prepared from palladium diammine dinitrite, Pd(NH<sub>3</sub>)<sub>2</sub>(NO<sub>2</sub>)<sub>2</sub> ("Palladium P Salt"), using the composition recommended by Hedrich and Raub (4), i.e., 0.1M Pd(NH<sub>3</sub>)<sub>2</sub>(NO<sub>2</sub>)<sub>2</sub>, 100 g/l NH<sub>4</sub>NO<sub>3</sub>, and 10 g/l NaNO<sub>2</sub>, with addition of sufficient ammonia to adjust the pH between 8 and 10. It is convenient to dissolve the palladium complex in ammonia solution before adding the other constituents. The solution is then diluted approximately to volume and pH adjusted (using graduated indicator paper) either by further addition of ammonia or by warming the solution to expel the excess. The question of the optimum bath pH is discussed later. The same bath may be prepared just as conveniently by substituting 0.1M palladium nitrate, Pd(NO<sub>3</sub>)<sub>2</sub>, for the nitrite complex, in which case the required sodium nitrite concentration is 24 g/liter.

**Electroplating procedure.**—Experiments to establish a satisfactory plating procedure were performed in a simple beaker cell. The current source was a Wenking Model POS73 scanning potentiostat operated in galvanostatic mode with an external control resistor. The anode was a sheet of bright platinum foil, the area of which was comparable with that of the cathode specimen. The cell was first filled with 0.5M H<sub>2</sub>SO<sub>4</sub> and the specimen was activated by anodic polarization at 5 mA/cm<sup>2</sup> for 30 sec. The cell and electrodes were then rinsed quickly with dilute ammonia to ensure complete removal of hydrogen ions, the plating solution introduced, and deposition commenced immediately, without stirring, at a current density of 20 mA/cm<sup>2</sup>. The current was maintained at this value for 30 sec, and then reduced uniformly at 0.5 mA/cm<sup>2</sup> sec to a constant value of 5 mA/cm<sup>2</sup> and deposition continued for a further 18 min. Plated specimens were dried with alcohol, and the coating thickness was determined from the gain in mass. All experiments were conducted at 22°C.

**Porosity test.**—Porosity was assessed using a method based on the FerroxyI test for detecting pinholes in

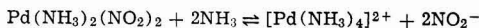
tinplate (5). Specimens were just submerged in a solution containing 0.2M K<sub>3</sub>[Fe(CN)<sub>6</sub>] and 0.0025M KCl. Exposed iron is rapidly attacked, and within a few minutes, the presence of pores is revealed by telltale spots of "blue rust" formed by reaction between ferrous and ferricyanide ions.

### Results and Discussion

Although various plating solutions have been mentioned for palladium (6), the above formulation is better suited to laboratory applications and under appropriate conditions is capable of yielding smooth deposits with a high gloss, even from an unstirred bath. The given procedure yielded pore-free coatings 1.5–1.6 μm in thickness for a total plating time of about 19 min, corresponding to a current efficiency of 55–60% (at 100% current efficiency, the Pd deposition rate at 5 mA/cm<sup>2</sup> is 0.138 μm/min). Deposits generally displayed some porosity at thickness < 1.3 μm, although this could be as little as 1–2 pores/cm<sup>2</sup> at about 1 μm. Sample cleanliness is essential for the attainment of pore-free deposits. Except in the case of extremely thin foil specimens, a palladium coating of about 2 μm will not materially affect the hydrogen permeation kinetics.

The relatively high initial current density was designed to obtain more or less complete coverage as soon as possible. This procedure was prompted by the gradual formation of an unidentified precipitate containing iron during deposition attempts at current densities < 1 mA/cm<sup>2</sup>. Initial plating densities exceeding 20 mA/cm<sup>2</sup> are not recommended, as the deposit structure may suffer due to increasing hydrogen content (7). The follow-up plating density of 5 mA/cm<sup>2</sup> was chosen to maximize current efficiency and to minimize the degree of hydrogen ion buildup at the anode, the effects of which are discussed later.

With this bath, discharge of palladium takes place from the tetrammine palladium (II) ion, formed according to the equilibrium

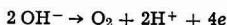


and hence the performance is very dependent on the pH. As the pH is lowered, the tetrammine gradually reverts to the insoluble diammine complex and palladium deposits (7) obtained at pH 7–8 reportedly contain occluded Pd(NH<sub>3</sub>)<sub>2</sub>(NO<sub>2</sub>)<sub>2</sub>. This can eventually lead to blistering coatings at pH < 7. As the pH increases, reduction of the [Pd(NH<sub>3</sub>)<sub>4</sub>]<sup>2+</sup> ion occurs at more negative potentials which favor discharge of hydrogen. These effects determine the recommended operating range of pH 8–9. Since the bath loses ammonia continuously on exposure to the atmosphere, regular pH checks are essential.

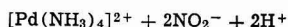
The low current efficiency of this bath, even under optimum conditions of pH and current density, is apparently due to reduction of nitrite and/or nitrate ions (4), rather than hydrogen discharge, which only becomes important at high pH or at current densities > 30 mA/cm<sup>2</sup>. The efficiency of the unstirred bath also depends on the palladium concentration, which should be maintained fairly close to the recommended value of 0.1M. When the palladium content had been depleted by 20–30%, the observed current efficiency dropped below 50%, and more importantly, deposits of given thickness were significantly more porous than those from a relatively fresh solution. Efficiency and performance were fully restored by appropriate evaporation. Alternatively, the bath may be replenished by addition of the palladium complex dissolved in dilute ammonia. In the absence of proper pH control, the bath can be depleted very rapidly by crystallization of Pd(NH<sub>3</sub>)<sub>2</sub>(NO<sub>2</sub>)<sub>2</sub> on the anode, where the dis-



charge of hydroxyl ions causes a substantial drop in local pH, i.e.



followed by



At 5 mA/cm<sup>2</sup>, crystallization was only observed at pH ≤ 8, but higher current densities might be expected to exacerbate this problem.

### Conclusion

Good quality palladium electrodeposits on iron and steel may be readily obtained from an unstirred bath at room temperature. Complete coverage and passivation of these substrates requires an electroplated coating >1 μm and preferably 1.5–2 μm thick. A palladium layer of these dimensions will not affect the rate of hydrogen transport through ferrous specimens. The coatings should be individually checked for porosity as this could vary with different substrates.

## Dependence of Flatband Potentials of n-TiO<sub>2</sub> on Electrolytes and Electrolyte Concentrations

James R. Wilson and Su-Moon Park\*

Department of Chemistry, University of New Mexico, Albuquerque, New Mexico 87131

The flatband potential of a semiconductor electrode is an important parameter in designing a photoelectrochemical cell. The importance of the flatband potential of a given semiconductor material in locating energy levels of the conduction and valence bands (1–3), and for predicting its stabilities has been discussed elsewhere (4–6). Flatband potentials have been reported to be dependent on the pH of the medium (1, 3). The pH dependency of flatband potentials has been characterized by a straight line with a slope of 59 mV/pH according to the equation

$$E_{\text{FB}} = E_{\text{FB}}^0 - 0.059 \text{ pH}$$

where  $E_{\text{FB}}^0$  is the value at pH = 0. The pH dependency is ascribed to the adsorption of the hydroxyl ion at the electrode surface (1), which in turn is dependent on the pH of the medium.

In the present note, we report the effect of electrolytes and electrolyte concentrations on the flatband potential of an n-TiO<sub>2</sub> electrode. This study was carried out on the assumption that electrolyte species other than the hydronium or hydroxyl ion could also be the potential determining species at the semiconductor-electrolyte interface.

Reagents used were of reagent or analytical reagent grade and obtained from Baker, Eastman Organic, Mallinckrodt, or Merck. Most reagents were used as received, but a few salts were recrystallized from double distilled water. A Princeton Applied Research (PAR) 175 Universal Programmer, a PAR 173 potentiostat-galvanostat, and a PAR 176 I/E converter have been used to control the potential at the working electrode and to record the photocurrent. A Tectronics Model 5115 storage oscilloscope was used to record faster measurements such as the capacitance current produced by applying a small triangular a-c signal (± 10 mV) superimposed on a d-c bias potential. An Oriel

Manuscript received March 24, 1981.

Any discussion of this paper will appear in a Discussion Section to be published in the June 1982 JOURNAL. All discussions for the June 1982 Discussion Section should be submitted by Feb. 1, 1982.

Publication costs of this article were assisted by CSIRO.

### REFERENCES

1. J. O'M. Bockris and M. A. V. Devanathan, Tech. Report 4, Office of Naval Research, NR 036-028 (1961).
2. M. A. V. Devanathan and Z. Stachurski, *Proc. Roy. Soc. London, Ser. A*, **270**, 90 (1962).
3. R. Heidersbach, J. Jones, and M. Surkein, 2nd Intern. Congr. on Hydrogen in Metals, p. 1, Paris (1977).
4. H. D. Hedrich and C. J. Raub, *Metalloberflaeche*, **31**, 512 (1977).
5. P. Hersch, J. B. Hare, A. Robertson, and S. M. Sutherland, *J. Appl. Chem.*, **11**, 246 (1961).
6. J. Fischer and D. E. Weimer, "Precious Metal Plating," p. 213, Robert Draper Ltd., Teddington (1964).
7. H. D. Hedrich and C. J. Raub, *Surf. Technol.*, **8**, 347 (1979).

450W Xe arc lamp powered by an Oriel 8540 Universal power supply was used as a light source. Monochromatic light was produced by an Oriel 7240 monochromator (bandpass = 20 nm). The illumination intensity was measured with the International Light Model 700 Radiometer. The pH was monitored by a Cambridge 5-700 combination electrode with a Sargent-Welch Model NX Digital pH meter. The photocurrent was recorded on a Houston Model 2000 X-Y recorder.

The electrolyte concentration was controlled by dispensing small volumes of a concentrated electrolyte solution from a buret. This has the advantage of maintaining the same electrode position in the solution throughout the experiment.

An n-TiO<sub>2</sub> electrode, furnished by Dr. Mike A. Butler, Sandia Laboratories, was cut from a large single crystal perpendicular to the c-axis. The TiO<sub>2</sub> electrode was doped in a quartz tube furnace under the hydrogen atmosphere at 450°C for 2 hr, whenever necessary. The electrode thus doped had a donor density of  $\sim 1.0 \times 10^{19}/\text{cm}^3$ , as measured from the slope of a Mott-Schottky plot (1, 2).

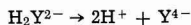
Due to the irreproducibilities encountered in flatband potential measurements by the Mott-Schottky method (7, 8), a photoresponse method (9) was used. This method is based on a measurement of the photocurrent ( $I$ ) as a function of the applied potential ( $E$ ). From the  $I$ - $E$  measurements, a plot of  $I^2$  vs.  $E$  was obtained. The flatband potential was then obtained from the intercept of the  $E$ -axis. Since the results obtained from this method were found to be affected by experimental parameters such as the voltage scan rate and the wavelengths of light illuminated (10), we employed a scan rate of 1 mV/sec and a wavelength of 360 nm for electrode illumination. The illumination intensity was about 0.71 mW/cm<sup>2</sup>. In order to check the reproducibility of this method, the pH dependency of the flatband potential was obtained; an extremely well-correlated straight line with a slope of  $-53 \text{ mV/pH}$  was observed.

\* Electrochemical Society Active Member.

Key words: flatband potential, complexation effect, n-TiO<sub>2</sub>.

Of eight inorganic salts studied, only one showed a slight concentration effect on the flatband potential. Compounds such as NaCl, KCl, NaI, KNO<sub>3</sub>, Na<sub>2</sub>SO<sub>4</sub>, K<sub>2</sub>SO<sub>4</sub>, and NaClO<sub>4</sub> did not show any effects. The values of flatband potentials of TiO<sub>2</sub> were the same in solutions of these salts and independent of their concentrations. Addition of NaH<sub>2</sub>PO<sub>4</sub> to water moved the flatband potential to a more positive value, which would be expected from the resultant change in pH. While the flatband potential varied slightly with NaH<sub>2</sub>PO<sub>4</sub> concentration,  $E_{FB}$  values corrected against the corresponding change in pH were constant.

The fact that most inorganic salts did not exert any effects on flatband potentials indicates that both cations and anions of the salts studied did not show significant specific adsorption toward the electrode material. A small change in the flatband potential when NaH<sub>2</sub>PO<sub>4</sub> was added has been ascribed to the change in pH due to the hydrolysis of the salt. Thus, we decided to perform the same study for complexing agents. Complexing agents used were NaCN, sodium citrate, ethylenediaminetetraacetic acid (EDTA), and 8-hydroxyquinoline. Of these, neither NaCN nor sodium citrate showed any significant effects, while EDTA and 8-hydroxyquinoline did. The effect of the concentration of EDTA on the flatband potential of n-TiO<sub>2</sub> is shown in Fig. 1. Note that the measurements were made in solutions of pH's 11 and 12. The intercept of the two curves shown in Fig. 1 was identical with the  $E_{FB}$  values that were obtained at pH = 11 and 12 without EDTA present for its pH-dependence studies. The effects shown in Fig. 1 were not observed at lower pH's. This indicates that the dissociated form (Y<sup>4-</sup>) of EDTA (H<sub>2</sub>Y<sup>2-</sup>) according to the equilibrium reaction



is important as a potential determining species at the electrode surface. Indeed, when the shift in the flatband potential is normalized by dividing it by the molar concentration of the dissociated form of EDTA ([Y<sup>4-</sup>]), it was approximately constant with about 9% average deviation. The normalized shift thus calculated was  $\sim 0.36$  V/M Y<sup>4-</sup>. The fact that Y<sup>4-</sup> is a potential determining species also implies that the complexation of Y<sup>4-</sup> with surface ions may be responsible for the observed results.

For 8-hydroxyquinoline, the results were similar. No effects were observed at low pH, whereas the flatband

potential shifted to a more positive direction at high pH, where hydroxide on the 8-hydroxyquinoline (8-HQ) molecule would be dissociated. The shift in the flatband potential was to the extent of 0.14V at a 8-hydroxyquinoline concentration of 27 mM. At a higher 8-HQ concentration, no photocurrent was observed.

We attribute the observed behavior to the complexation of donor ions such as Ti<sup>3+</sup> at the semiconductor surface. When EDTA or 8-hydroxyquinoline is present in the solution, the dopants at the surface may be complexed, shifting the energy levels of the electron donor ions. We believe that the surface complexation affects the energy level of the semiconductor more than of the solution side. This will shift the flatband potential in a more positive direction. The complexation effect was more dramatic for 8-HQ, probably because it forms the insoluble complex (precipitate), possibly blocking the electrode surface.

The reason that the addition of cyanide and citrate did not affect the flatband potential may be that these ions are not strong enough complexing agents toward Ti<sup>3+</sup>. It is readily predicted that both EDTA and 8-hydroxyquinoline would be stronger complexing agents than citrate and cyanide for Ti<sup>3+</sup>, although no quantitative data except for EDTA are available in the literature (11). Further work is in progress in our laboratory along the lines described.

### Acknowledgments

Financial support of this research by Sandia Corporation through the Sandia-University Research Program (SURP), New Mexico Energy and Mineral Department, and the Research Allocations Committee is gratefully acknowledged. We also express our gratitude to Dr. Michael A. Butler of Sandia Laboratories for providing us a TiO<sub>2</sub> single crystal.

Manuscript submitted March 16, 1981; revised manuscript received May 11, 1981.

Any discussion of this paper will appear in a Discussion Section to be published in the June 1982 JOURNAL. All discussions for the June 1982 Discussion Section should be submitted by Feb. 1, 1982.

Publication costs of this article were assisted by the University of New Mexico.

### REFERENCES

1. H. Gerischer in "Physical Chemistry—An Advance Treatise," Vol. IXA, H. Eyring, D. Handerson, and W. Yost, Editors, Academic Press, New York (1970).
2. V. Myamlin and R. V. Pleskov, "Electrochemistry of Semiconductors," Plenum Press, New York (1967).
3. J. M. Bolts and M. S. Wrighton, *J. Phys. Chem.*, **80**, 2641 (1976).
4. H. Gerischer, *J. Electroanal. Chem. Interfacial Electrochem.*, **82**, 133 (1977).
5. A. J. Bard and M. S. Wrighton, *This Journal*, **124**, 1706 (1977).
6. S.-M. Park and M. E. Barber, *J. Electroanal. Chem. Interfacial Electrochem.*, **99**, 67 (1979).
7. E. C. Dutoit, F. Cardon, and W. P. Gomes, *Ber. Bunsenges. Phys. Chem.*, **80**, 475 (1976).
8. R. DeGryse, W. P. Gomes, F. Cardon, and J. Vennick, *This Journal*, **122**, 711 (1975).
9. M. A. Butler, *J. Appl. Phys.*, **48**, 1914 (1977).
10. J. R. Wilson, Ph.D. Dissertation, The University of New Mexico (1980).
11. L. G. Sillen and A. E. Martell, "Stability Constants of Metal-Ion Complexes," The Chemical Society, London, 1964 and volumes thereafter.

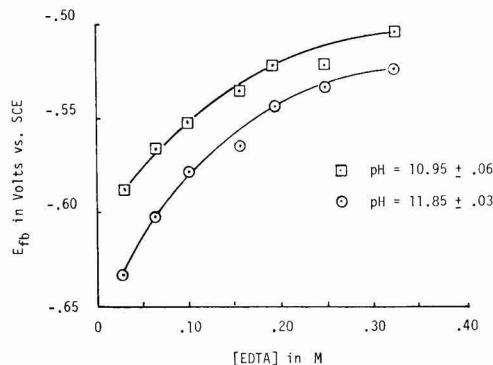


Fig. 1. The flatband potential of an n-TiO<sub>2</sub> electrode as a function of the EDTA concentration. Wavelength of light illuminated was 360 nm.

# Photoactivity of Polycrystalline $\alpha$ -Fe<sub>2</sub>O<sub>3</sub> Electrodes Doped with Group IVA Elements

John H. Kennedy,\* Menahem Anderman, and Ruth Shinar

Department of Chemistry, University of California, Santa Barbara, California 93106

Success in obtaining significant photocurrents with polycrystalline, SiO<sub>2</sub>-doped  $\alpha$ -Fe<sub>2</sub>O<sub>3</sub> photoanodes (1) gave rise to a study of the photoelectrochemical properties of other group IVA elements as dopants. Recently, photochemical properties of SnO<sub>2</sub>- and CaO-doped  $\alpha$ -Fe<sub>2</sub>O<sub>3</sub> electrodes were investigated elsewhere (2) but only 1 and 5% doping levels were studied.

In the present work  $\alpha$ -Fe<sub>2</sub>O<sub>3</sub> material was mixed with 0.002-5 atomic percent (a/o) GeO<sub>2</sub> and SnO<sub>2</sub> and with 0.01-5 a/o (initial composition) PbO<sub>2</sub>. Emission spectroscopy and x-ray diffraction were used to check the initial and final doping levels and for the possible presence of two-phase materials. Photoelectrochemical results were compared to those obtained at Si(IV)- and Ti(IV)-doped  $\alpha$ -Fe<sub>2</sub>O<sub>3</sub> electrodes.

## Experimental

Electrodes were prepared from high purity, 99.999%  $\alpha$ -Fe<sub>2</sub>O<sub>3</sub> (Alfa Products) by mixing with the dopant powder, pressing, and sintering as described elsewhere (1). The dopants were Alfa Products 99.9% GeO<sub>2</sub>, B and A 99% SnO<sub>2</sub> or Alfa Products 99.9% SnO<sub>2</sub>, and Research Organic/Inorganic Chemical Corporation 95% PbO<sub>2</sub> or Apache 99.9% PbO<sub>2</sub>.

Pressed pellets were sintered at 1250°-1370°C for 3-40 hr. Table I summarizes the dopant concentrations, sintering temperatures, and sintering times needed to prepare the best electrodes. The electrodes were 1.29 cm diam when initially pressed but some shrinking occurred during sintering so that final electrodes were ~1 cm<sup>2</sup>.

Electrical connections were made using silver epoxy as previously described (3). Densities were 75-90% of the theoretical value, and resistances measured at 1 kHz with a conductivity bridge were usually 50-2500  $\Omega$ .

Samples containing Ca<sup>2+</sup> (starting material: Matheson, Coleman & Bell CaCO<sub>3</sub>) and Pb<sup>2+</sup> (starting material: Mallinckrodt, Analytical Reagent PbO) were also prepared. 0.5 a/o Ca<sup>2+</sup>-doped  $\alpha$ -Fe<sub>2</sub>O<sub>3</sub> pellets were sintered at 1370°C for about 15 hr and at 1330°C for 70 hr. In both cases the resistances were very high (>200 k $\Omega$ ). 0.5 a/o Pb<sup>2+</sup>-doped electrodes were sintered at 1370°C for 5 hr. Resistances were ~2 k $\Omega$ .

Pellet weight was checked before and after sintering. Differences between starting and final dopant concentration were also determined by emission spectroscopy. Both powders and ground sintered pellets of pure and doped  $\alpha$ -Fe<sub>2</sub>O<sub>3</sub> were analyzed by a Norelco x-ray diffractometer.

The cell arrangement, and optical and electrochemical measurement procedures were described previously (1). Lamp intensity was measured with a Yellow Springs Instrument Company Kettering Model 65A radiometer, and the photocurrent spectra were normalized to the lamp output spectrum. When using a monochromator light intensities in the range 350-560 nm were 4-18% mW/cm<sup>2</sup>. The lamp intensity at the electrode surface was about 300 mW/cm<sup>2</sup> when no monochromator was employed. This was reduced to about 180 mW/cm<sup>2</sup> when a filter was used (pass light <540 nm).

## Results

No loss of weight during sintering was observed in the case of pure  $\alpha$ -Fe<sub>2</sub>O<sub>3</sub>, Si<sup>4+</sup>-, Sn<sup>4+</sup>-, and Ge<sup>4+</sup>-

(sintered at 1300°C) doped electrodes, but some loss of weight was observed in Ge<sup>4+</sup>-doped pellets sintered at ~1350°C, probably due to some evaporation of GeO<sub>2</sub> at high sintering temperatures (4).

A significant weight loss was observed in the Pb<sup>4+</sup>-doped pellets as expected, since PbO<sub>2</sub> decomposes at 290°C and PbO, the final decomposition product, melts at 888°C and evaporates appreciably (4).

Emission spectroscopy confirmed the above results. Si<sup>4+</sup>-, Ge<sup>4+</sup>-, and Sn<sup>4+</sup>-concentrations in the ground pellets (after sintering) were the same, within experimental error, as in the mixed powders (before sintering). In the case of Ge<sup>4+</sup>-doped pellets a reduction in the final concentration of the dopant was observed when sintered at relatively high temperatures. For example, the final doping level of the 0.5 a/o Ge(IV) sample sintered at 1350°C for 13 hr was ~0.1 a/o. It should be kept in mind that emission spectroscopy is not a highly accurate analytical technique but significant differences between initial and final composition could be readily observed. For the lead-doped electrodes only low levels of lead (~200 ppm) were observed in the final sintered pellets independent of initial concentration, sintering temperature, or sintering time.

X-ray patterns of ground sintered pellets indicated the existence of single phase  $\alpha$ -Fe<sub>2</sub>O<sub>3</sub> even at doping levels of 5 a/o GeO<sub>2</sub> and SnO<sub>2</sub>. On the other hand, x-ray diffraction of the starting mixtures containing as little as 0.5 a/o GeO<sub>2</sub> and SnO<sub>2</sub> clearly showed the presence of dopant phases along with  $\alpha$ -Fe<sub>2</sub>O<sub>3</sub>. Also, no evidence for the presence of other phases was found for electrodes containing up to 2 a/o SiO<sub>2</sub>.

Most of the photoactivity experiments were carried out on low doping level electrodes. High doping levels were used mainly to check for possible weight loss during sintering and for the presence of two-phase materials.

To ensure homogeneity in the electrodes some pellets were sintered at elevated temperatures for very long periods (>3 days) compared to the time required to obtain pellets of relatively low resistance. No noticeable change in the photoactivity could be observed by the long sintering cycle. In addition, some sintered samples were ground and resintered. Occasionally densities were slightly improved but no significant changes in the photoactivity were observed.

Photocurrent density vs. applied potential at 400 nm for  $\alpha$ -Fe<sub>2</sub>O<sub>3</sub> electrodes doped with group IVA elements is shown in Fig. 1. The indicated doping levels are those of the final electrodes. Initial concentration for the lead-doped electrode is given in parentheses.

The photocurrent was measured in 1F NaOH. Results for 0.05 a/o Ti<sup>4+</sup>-doped electrodes are also shown for comparison. Dark currents in the range shown were always lower than 8  $\mu$ A/cm<sup>2</sup>. As can be seen the elec-

Table I. Composition and sintering conditions for group IVA-doped  $\alpha$ -Fe<sub>2</sub>O<sub>3</sub> electrodes

Dopant	Doping level (a/o)	Sintering temperature, °C	Sintering time, hr
SiO <sub>2</sub>	0.25-2	1350	20-30
GeO <sub>2</sub>	0.002-0.01	1300	5-20
SnO <sub>2</sub>	0.002-0.01	1300-1370	8-15
PbO <sub>2</sub>	0.05-0.2 (initial)	1330-1370	7-30

\* Electrochemical Society Active Member.

Key words: semiconductor electrode, polycrystalline, doped  $\alpha$ -Fe<sub>2</sub>O<sub>3</sub>, photoactivity.

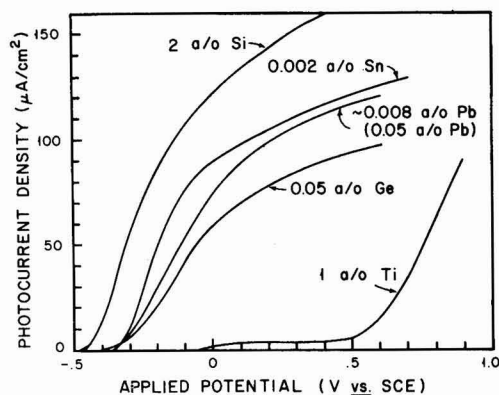


Fig. 1. Photocurrent density as a function of applied potential at 400 nm for  $\alpha$ -Fe<sub>2</sub>O<sub>3</sub> electrodes doped with group IVA elements and with TiO<sub>2</sub>. Solution: 1F NaOH.

trodes doped with group IVA elements exhibited significant photocurrents even at 0V vs. SCE in a basic solution. The highest photocurrents at relatively low potentials (<0.5V vs. SCE) were observed at 2 a/o Si<sup>4+</sup>-doped electrode. Although there were differences in photocurrents at low applied potentials among the different electrodes the photocurrent plateau values reached at higher potentials (~1V vs. SCE) were about the same for nearly all electrodes.

Figure 2 shows the spectral response for the photocurrent (quantum) efficiency in 1F NaOH for several electrodes. In general there was no significant difference between the effect of GeO<sub>2</sub> and SnO<sub>2</sub> as dopants. Both of the lower doping levels 0.002-0.01 a/o showed higher photocurrent densities at 0V vs. SCE than those obtained at higher (>0.05 a/o) doping levels. At doping levels >1 a/o the photocurrents at 0V vs. SCE were negligible for both dopant types. This doping level effect is demonstrated in Fig. 3 for Sn(IV)-doped electrodes. It should be noted that this effect was not observed for SiO<sub>2</sub>-doped electrodes and we did not succeed in preparing TiO<sub>2</sub>-doped electrodes at a level lower than 0.05 a/o. Photoelectrochemical performance of all electrodes reported was stable for long periods (>3 days at 0.4-1.8 mA) of irradiation. The onset of photocurrent spectral response (~bandgap) of all group IVA-doped electrodes was the same within experimental error. A value of ~2.2 eV was obtained by plotting  $(\eta h\nu)^{1/2}$  vs.  $h\nu$ , where  $\eta$  is the photocurrent

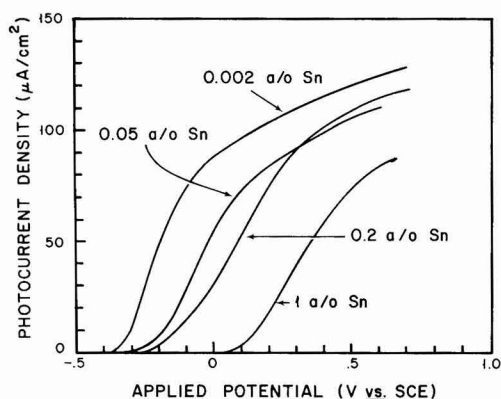


Fig. 3. Photocurrent density as a function of applied potential at 400 nm for  $\alpha$ -Fe<sub>2</sub>O<sub>3</sub> electrodes doped with various amounts of Sn(IV). Solution: 1F NaOH.

(quantum) efficiency. An example for SiO<sub>2</sub>- and GeO<sub>2</sub>-doped electrodes is shown in Fig. 4.

The turn-on voltage for several SiO<sub>2</sub>-, GeO<sub>2</sub>-, and SnO<sub>2</sub>-doped electrodes was measured as a function of pH as shown in Fig. 5 for the SiO<sub>2</sub>- and GeO<sub>2</sub>-doped electrodes. Straight lines were obtained for each electrode with slopes in the range of -(60-68) mV/pH. These results were within experimental error of -59 mV/pH, the value expected for the pH dependence of the flatband potential. Although the turn-on voltage does not correspond exactly to the flatband potential (3) the pH dependence is usually identical. The turn-on voltage shifted to negative potentials as the dopant level decreased, as can be seen in Fig. 3 for Sn(IV)-doped electrodes.

It had been observed previously (1, 5) that dipping Si(IV)- and Ti(IV)-doped electrodes in 1F KI at pH 9 improved photocurrents observed in strong base solution. However, dipping Ge(IV)- and Sn(IV)-doped electrodes did not significantly improve the photocurrent. Soaking in KI solution appears to be effective only for electrodes showing less than optimum photoactivity perhaps by removing surface recombination sites. It should be noted that undoped high purity  $\alpha$ -Fe<sub>2</sub>O<sub>3</sub> was highly resistive and exhibited no photocurrent during the tenure of our experiments.

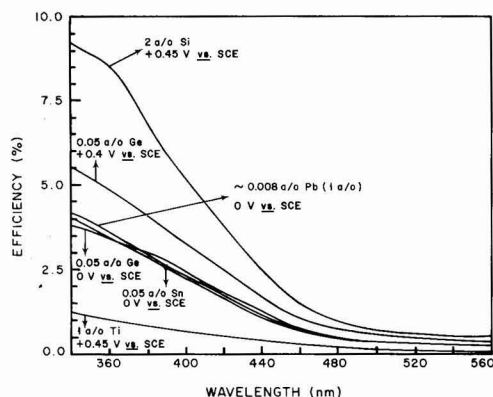


Fig. 2. Spectral response for photocurrent efficiency (uncorrected for reflection losses at the cell window and the electrode surface) of doped  $\alpha$ -Fe<sub>2</sub>O<sub>3</sub> electrodes in 1F NaOH.

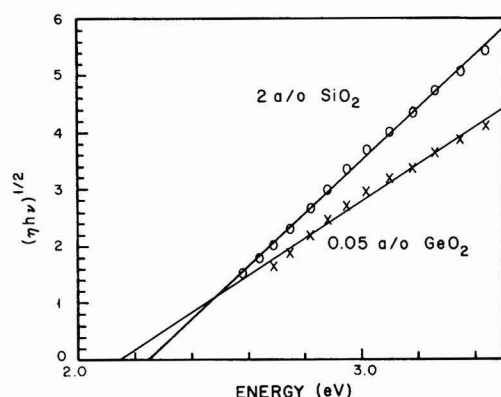


Fig. 4.  $(\eta h\nu)^{1/2}$  vs.  $h\nu$ . (o): 2 a/o Si(IV); (x) 0.05 a/o Ge(IV)-doped  $\alpha$ -Fe<sub>2</sub>O<sub>3</sub> electrodes.  $E_g$ : 2 a/o Si(IV) = 2.25 eV; 0.05 a/o Ge(IV) = 2.15 eV.

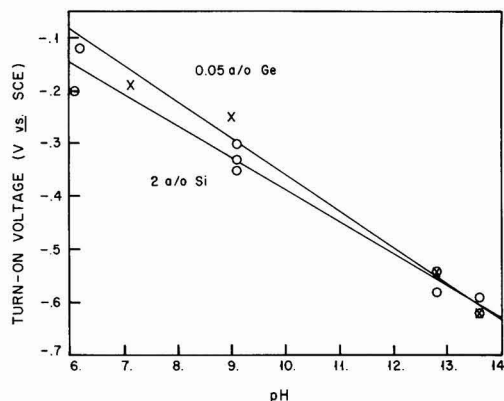


Fig. 5. Turn-on voltage vs. pH. (o): 2 a/o Si(IV); (x): 0.05 a/o Ge(IV)-doped  $\alpha$ -Fe<sub>2</sub>O<sub>3</sub> electrodes. Slopes: 2 a/o Si(IV) =  $-60 \pm 3$  mV/pH; 0.05 a/o Ge(IV) =  $-68 \pm 5$  mV/pH.

### Discussion

It appears that all IVA elements are effective dopants for  $\alpha$ -Fe<sub>2</sub>O<sub>3</sub> photoanodes. This is consistent with the general aliovalent doping concept that the +4 ion introduces an electron into the conduction band



One could argue that group IVB elements should be equally effective whereas the experimental evidence indicates that titanium is not as effective as silicon. The difference may lie in the additional energy levels introduced by the aliovalent metal ion centers present. A Ti<sub>Fe</sub><sup>3+</sup> center may trap an electron to form Ti<sub>Fe</sub><sup>2+</sup>, i.e., a Ti(III) ion. Such centers may also act as electron hole recombination sites thereby decreasing photocurrent efficiency. Lower members in group IVB may not display this behavior, and recently Horowitz (6) showed that single crystal Fe<sub>2</sub>O<sub>3</sub> doped with ZrO<sub>2</sub> was more effective than titanium doping.

A second conclusion is that photocurrent decreases at a given applied potential as the doping level increases as shown in Fig. 3 for SnO<sub>2</sub>-doped electrodes. This is expected when one considers the effect of donor density on space charge layer thickness. As the donor density increases the space charge layer becomes thinner and fewer photons are absorbed in the space charge region. Photons may still be absorbed at a greater depth in the Fe<sub>2</sub>O<sub>3</sub> electrode but hole mobility is so low that few reach the space charge region to be driven to the surface. The apparent shift in turn-on voltage to more anodic values with increasing doping level is not expected although this point was observed and discussed in a previous paper (3).

However, it must be kept in mind that the dopant may play other roles besides introducing electronic

defects especially at high doping levels. For example, they may act as traps and recombination centers leading to lower photocurrent efficiency at high doping levels.

The results with lead-doped electrodes are more difficult to explain because the final oxidation state is not +4 as with the other dopants. In fact, doping with PbO gave electrodes with photoelectrochemical properties similar to PbO<sub>2</sub>-doped electrodes. Doping with a +2 ion could lead to p-type material although doping with Ca(II) produced only highly resistive electrodes. However, the behavior of lead-doped  $\alpha$ -Fe<sub>2</sub>O<sub>3</sub> electrodes indicates that it is n-type like other members of group IV. Because doping levels need not be high, and in fact, better performance is observed with lower doping levels (Fig. 3) it may be that traces of Pb(IV) account for the photoelectrochemical behavior. Fredlein and Bard (7) also observed n-type behavior for single crystal  $\alpha$ -Fe<sub>2</sub>O<sub>3</sub> grown from a PbO melt. The Pb content was 1-10 a/o, but photocurrents were small unless heat-treated. These authors assumed that lead was present as Pb(IV) because the electrodes were n-type. All electrodes were stable for long periods of illumination with many electrodes being studied over periods of several weeks with no significant change in photoelectrochemical properties.

### Acknowledgment

This work is supported by the Division of Chemical Sciences, Office of Basic Energy Sciences, v.s. Department of Energy.

Manuscript submitted Feb. 26, 1981; revised manuscript received May 5, 1981.

Any discussion of this paper will appear in a Discussion Section to be published in the June 1982 JOURNAL. All discussions for the June 1982 Discussion Section should be submitted by Feb. 1, 1982.

Publication costs of this article were assisted by the University of California.

### REFERENCES

1. J. H. Kennedy, R. Shinar, and J. P. Ziegler, *This Journal*, **127**, 2307 (1980).
2. M. Gori, H. R. Grüniger, and G. Calzaferri, *J. Appl. Electrochem.*, **10**, 345 (1980).
3. J. H. Kennedy and K. W. Frese, Jr., *This Journal*, **125**, 723 (1978).
4. G. V. Samsonov, Editor, "The Oxide Handbook," IFI/Plenum Data Corporation, New York (1973).
5. J. H. Kennedy, R. Shinar, and J. P. Ziegler, Paper X-3 presented at the Third International Conference on Photochemical Conversion and Storage of Solar Energy, University of Colorado, Boulder, Colorado, August, 1980.
6. G. Horowitz, Paper IX-6 presented at the Third International Conference on Photochemical Conversion and Storage of Solar Energy, University of Colorado, Boulder, Colorado, August, 1980.
7. R. A. Fredlein and A. J. Bard, *This Journal*, **126**, 1892 (1979).





# Environmental Stability and Failure Mechanisms of Chromated Lead/Tin Alloy Joints Bonded with an Ethylene-Acrylic Acid Copolymer

## I. Acidic Conditions

Fumio Yamamoto, Shinzo Yamakawa, and Makoto Wagatsuma

*Nippon Telegraph and Telephone Public Corporation,  
Ibaraki Electrical Communication Laboratory, Tokai, Ibaraki 319-11, Japan*

### ABSTRACT

The environmental stability and the failure mechanisms of a cathodically chromated lead/tin (38/62) alloy joint bonded with an ethylene-acrylic acid (EAA) copolymer have been investigated in acidic solutions. Immersion of the joint in acidic solutions causes rapid decrease in peel strength and finally interfacial separation. ESCA analysis of the peeled surfaces shows that this decrease in peel strength is due to an interfacial degradation between the chromate film and the underlying alloy (consisting both of lead and tin phases). The retention time, during which a joint retains the initial peel strength, decreases with increasing anode current density of the alloy in acidic solutions or with decreasing polarization resistance. This result suggests that the interfacial failure at the chromate-alloy interface results from anodic dissolution of the underlying alloy. A failure mechanism of the chromated alloy joint in acidic solutions has been proposed: The degradation at the chromate-alloy interface occurs through rapid anodic dissolution of the lead phase and slow anodic dissolution of the tin phase.

The long-term exposure of metal joints bonded with ethylene-acrylic acid (EAA) copolymers to humid environments causes the loss in joint strength (1-4). We have reported that cathodic chromate treatments of lead/tin alloys greatly enhances the environmental stability of the alloy joints bonded with an EAA copolymer and that the joint strength is kept unchanged in distilled water for more than 2 years (5, 6). However, these joints seem to have poor environmental stability in acidic solutions since both lead and tin metals are rapidly corroded in acidic solutions (7). This paper is concerned with the environmental stability in acidic solutions and the failure mechanisms of a cathodically chromated lead/tin alloy joint bonded with an EAA copolymer.

### Experimental

The preparation of T-peel specimens consisting of adherend (0.5 mm)-adhesive (0.2 mm)-adherend (0.5 mm) and the T-peel testing were described elsewhere (5). The adherend used was a cathodically chromated lead/tin (38/62) alloy. The adhesive used was an EAA copolymer (1) supplied by Union Carbide Company (melt index 50 g/10 min, acrylic acid content 20 weight percent, density 0.96 g/cm<sup>3</sup>, glass transition temperature 31°C). To evaluate the environmental stability of the joints, the peel specimens were immersed in acidic solutions, and the T-peel strength was mea-

sured at 25°C immediately after immersion. The pH range of the solutions was 0.8-5.6, and the temperature range was 20°-70°C. The acidic solutions were 2-HOCOC<sub>6</sub>H<sub>4</sub>COOK-HCl (pH 0.8, 2.5, and 3.2), CH<sub>3</sub>COONa-HCl (pH 4.5), 2-HOCOC<sub>6</sub>H<sub>4</sub>COOK-NaOH (pH 5.0), and CH<sub>3</sub>COOH-CH<sub>3</sub>COONa (pH 5.6) buffers.

The corrosion resistance of untreated and chromated alloy sheets in acidic solutions were evaluated from anode current density ( $I_p$ ) by a potentiostatic method or from polarization resistance ( $R_p$ ) (8-10) by a coulometric method (11-15). The potentiostatic measurements were made using a Hokuto potentiometer, and the anode current density was measured at an overpotential of 50 mV under nitrogen gas. The surface area of untreated and chromated alloy sheets used as the working electrodes was ca. 2 cm<sup>2</sup>. A platinum sheet of ca. 2 cm<sup>2</sup> and a saturated calomel electrode were used as the counter and reference electrodes, respectively. The anode current density decreased with time of applying overpotential and leveled off after 30-60 sec. The leveled-off anode current density was recorded as an  $I_p$  value. The coulometric measurements were made using a Hokuto galvanostat connected with a pulse generator (pulse width 10  $\mu$ sec) without removing dissolved oxygen. The overpotential-time curves were displayed on a storage oscilloscope. The amount of charge density applied was 0.1-0.3  $\mu$ C/cm<sup>2</sup>, and the induced initial overpotentials were in the range 2-10 mV. The polarization resistance calculated from the overpotential-time curves decreased with

Key words: ESCA, anodic dissolution, interfacial degradation, metal-polymer joint.



water immersion of alloy sheets and leveled off after ca. 20 min immersion. The leveled-off polarization resistance was recorded as an  $R_p$  value. To check the validity of the  $R_p$  values measured by the coulometric method,  $R_p$  values of alloy sheets in various acidic solutions were also measured from polarization curves. In this case,  $R_p$  values were calculated using  $R_p = \beta_a \beta_c / I_o (\beta_a + \beta_c)$ , where  $\beta_a$  and  $\beta_c$  are anodic and cathodic Tafel slopes, respectively, and  $I_o$  is corrosion current density. The  $R_p$  values measured from the coulometric measurements were in agreement with those from the polarization curves within an error of 20%. The amount of oxides on the alloy surfaces was measured by electrolytic reduction in an aqueous solution of 0.1 mol/liter  $\text{NH}_4\text{Cl}$  at a constant current density of  $90 \mu\text{A}/\text{cm}^2$  under nitrogen gas, in the same way as in the previous work (5).

The original chromated alloy and EAA surfaces before bonding and the fractured surfaces of the joints were analyzed by x-ray photoelectron spectroscopy (ESCA). ESCA spectra were recorded on an A.E.I. ES 200 spectrometer using  $\text{Al } K\alpha_{1,2}$  radiation. Typical operating conditions were: x-ray gun, 10 kV, 20 mA; pressure in the sample chamber,  $1 \times 10^{-7}$  Torr. The binding energies were calibrated with respect to the carbon 1s electron peak at 284.9 eV due to residual pump oil on the sample surface. Electron probe x-ray microanalysis (XMA) was also used for the surface analysis of chromated alloy sheets. XMA was carried out using a Shimadzu EMX-SM7. XMA data were taken at a probe operating voltage of 15 kV and a sample current of 1 nA.

### Results and Discussion

**Chromate films on a lead/tin alloy surface.**—Figure 1 shows an SEM micrograph and lead and tin images of a lead/tin (38/62) alloy surface cathodically chromated for 5 sec. The presence of a chromate film on the alloy surface was not detected by XMA analysis because its film thickness was much thinner (ca. 100 Å) (5) than the XMA sampling depth (several micrometers), whereas it was detected by ESCA and IMA (ion microanalyzer) (5). From the lead and tin images (Fig. 1), it is apparent that the alloy surface consists both of lead and tin phases. The XMA analysis showed that the tin content in the lead phase and the lead content in the tin phase were less than a few percent.

It is well known that most chromate films deposited on metals have considerable cracks (16). Figure 2 shows the changes in oxygen 1s ESCA spectrum of the chromated alloy surface with heating. The chromated alloy sheet was heated in ESCA chamber for 20 min at each temperature, and ESCA spectra from its alloy surface were measured immediately at the same temperature. The intensity of oxygen 1s decreases with increasing heating temperatures and after heating at 180°C reaches ca. 70% of that heated at 60°C. The disappeared oxygen 1s peak at 532.3 eV has been assigned to adsorbed oxygen or water by Ansell *et al.* (17). Figure 3 shows the changes in the amount of alloy oxides of the chromated alloy surface with heating for 20 min at each temperature. The amount of oxides on the chromated alloy surfaces corresponds to that of the underlying alloy oxides at cracks of the chromate film. The amount of oxides increases gradually with heating at temperatures of more than 100°C and then increases rapidly with the rupture of chromate film due to the melt of the underlying alloy at ca. 183°C. These results indicate that many cracks, which are probably formed by contraction in volume due to escaped water, are present in the chromate film on the alloy surface heated at temperatures of more than 100°C. Since chromated alloy joints were prepared by heating for 5 min with a hot press at 120°C (5), the chromate film in the joints should have many cracks.

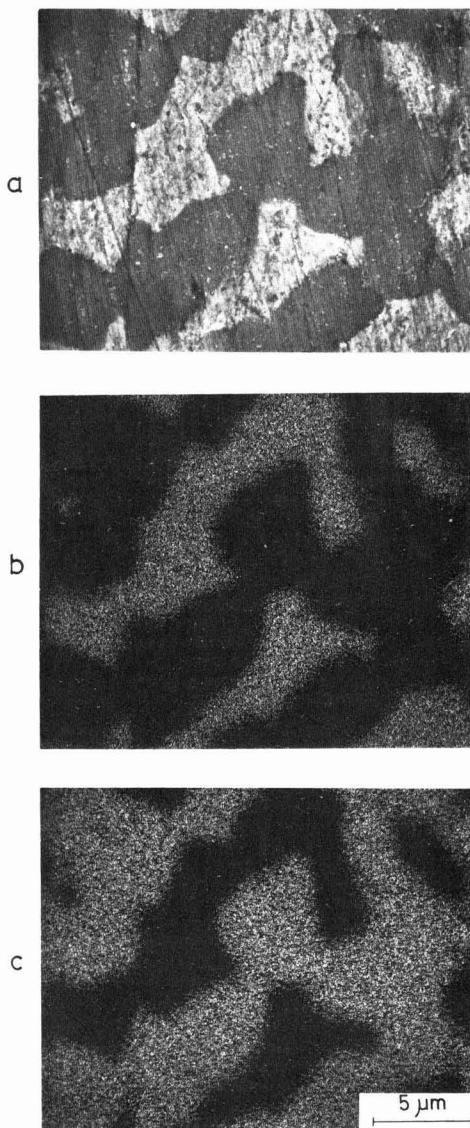


Fig. 1. An SEM micrograph (a) and lead (b) and tin (c) images of a chromated lead/tin (38/62) alloy surface.

**Bond durability.**—Figure 4 shows the changes in peel strength with immersion in a  $\text{CH}_3\text{COONa-HCl}$  buffer (pH 4.5) for a chromated alloy joint. Figure 5 shows the change in peel strength retention time (during which the initial peel strength is kept unchanged) with immersion temperature. The peel strength retention time decreases with increasing immersion temperature and was only 5 days at 70°C. On the other hand, the peel strength retention time of the chromated alloy joint immersed in distilled water at 50°C was more than 2 years (6). Apparently, the joint deteriorates more rapidly in the acidic solution than in distilled water. SEM observations of fractured surfaces showed that the small areas or spots of peel strength  $\approx 0 \text{ kg}/\text{cm}$ , different in peel strength from the surrounding area of peel strength which was 6.0–6.5  $\text{kg}/$

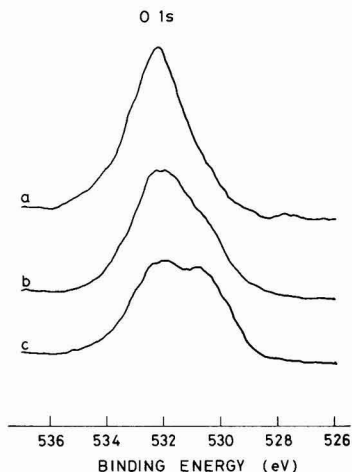


Fig. 2. Changes in oxygen 1s ESCA spectrum with heating for a chromated alloy surface. The alloy was heated in ESCA sample chamber for 20 min at each temperature. Heating temperatures were: (a) 60°C, (b) 120°C, (c) 180°C.

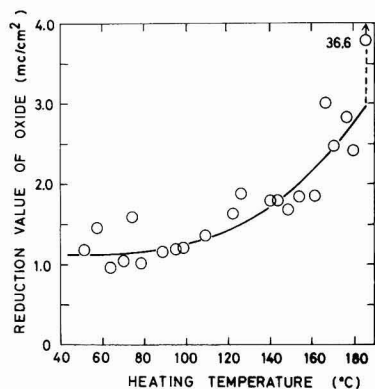


Fig. 3. Changes in amount of oxides with 20 min heating for a chromated alloy surface measured by electrolytic reduction in an aqueous solution of 0.1 mol/liter  $\text{NH}_4\text{Cl}$  at a constant current density of 90  $\mu\text{A}/\text{cm}^2$ .

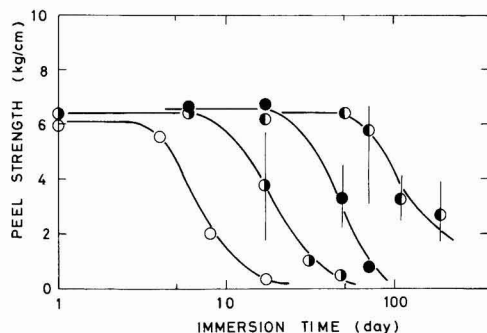


Fig. 4. Changes in peel strength with immersion in a  $\text{CH}_3\text{COONa}$ -HCl buffer (pH 4.5) for a chromated lead/tin (38/62) alloy joint bonded with an EAA copolymer. Immersion temperatures were: (●) 40°C, (●) 50°C, (○) 60°C, (○) 70°C.

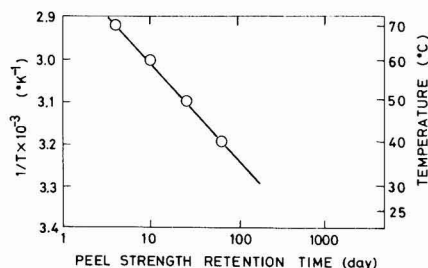


Fig. 5. Arrhenius plot for peel strength retention time of a chromated alloy joint in a  $\text{CH}_3\text{COONa}$ -HCl buffer (pH 4.5).

cm, appeared over the whole part of the interface, the area and number of the spots increased gradually with immersion, and then finally an interfacial separation occurred.

Table I summarizes the peel strength retention times of the chromated alloy joint in various acidic solutions. In most cases, the peel strength retention time decreases with decreasing pH of acidic solutions. However, there are some exceptions: the peel strength retention time in a  $\text{CH}_3\text{COONa}$ -HCl buffer (pH 4.5) at 50°C and that in a 2-HOCOC<sub>6</sub>H<sub>4</sub>COOK-HCl buffer (pH 3.2) at 50°C.

**Locus of failure.**—Figure 6 shows ESCA spectra of fractured chromated alloy and EAA surfaces of chromated alloy joints peeled with low peel strength after immersion in a  $\text{CH}_3\text{COONa}$ -HCl buffer (pH 4.5), together with those of original chromated alloy and EAA surfaces. Each fractured surface peeled with low peel strength after immersion in the other buffers showed ESCA spectra similar to those in Fig. 6. The fractured alloy surface shows the increase in tin intensities (metal peak, 484.3 eV; oxide peak, 486.5 eV), the decrease in oxygen intensity (532.3 eV), and the disappearance of chromium oxide (577.0 eV). On the other hand, the fractured EAA surface shows the decrease in carbon intensity (285.0 eV), the remarkable increase in oxygen intensity, and the appearance of tin and chromium oxides. Apparently, the exposure of tin and chromium oxides on the fractured EAA surface is due to the transfer from the chromated alloy surface. Further, the remarkable increase in oxygen intensity on the fractured EAA surface is due to the transfer of the chromate film from the alloy surface. On the other hand, the increase in tin intensities on the fractured alloy surface is probably due to exposure of the underlying lead/tin alloy by the transfer of the chromate film to the EAA surface. These results indicate that the failure occurs between the chromate film and the underlying alloy, although it is not clear whether the failure occurs at the chromate-underlying alloy oxide layer interface, in the alloy oxide layer, or at the alloy oxide layer-alloy metal interface. On the other hand, the water absorption of the EAA copolymer was as low as ca. 0.44 w/o in the pH 4.5 buffer at 50°C. This value

Table I. Peel strength retention time in various acidic solutions

Acidic solution	pH	Temperature (°C)	Peel strength retention time (days)
2-HOCOC <sub>6</sub> H <sub>4</sub> COOK-HCl buffer	0.8	50	30
2-HOCOC <sub>6</sub> H <sub>4</sub> COOK-HCl buffer	2.5	50	40
2-HOCOC <sub>6</sub> H <sub>4</sub> COOK-HCl buffer	3.2	50	40
$\text{CH}_3\text{COONa}$ -HCl buffer	4.5	70	4
$\text{CH}_3\text{COONa}$ -HCl buffer	4.5	60	10
$\text{CH}_3\text{COONa}$ -HCl buffer	4.5	50	26
$\text{CH}_3\text{COONa}$ -HCl buffer	4.5	40	64
2-HOCOC <sub>6</sub> H <sub>4</sub> COOK-NaOH buffer	5.0	50	>900
$\text{CH}_3\text{COOH}$ - $\text{CH}_3\text{COONa}$ buffer	5.6	70	75
$\text{CH}_3\text{COOH}$ - $\text{CH}_3\text{COONa}$ buffer	5.6	40	600

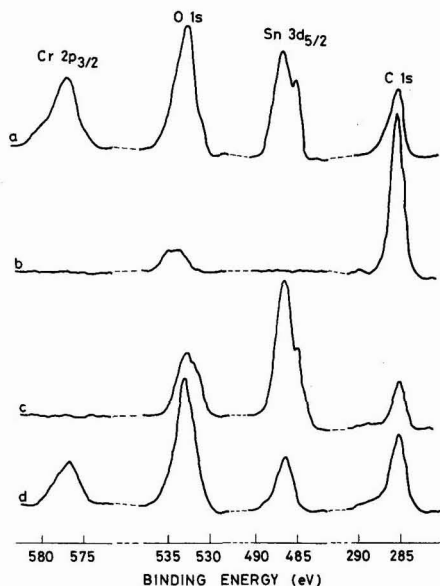


Fig. 6. ESCA spectra of original chromated alloy (a) and EAA (b) surfaces and fractured chromated alloy (c) and EAA (d) surfaces of a chromated alloy joint peeled with low peel strength after immersion in a  $\text{CH}_3\text{COONa-HCl}$  buffer (pH 4.5).

was nearly equal to that (0.36 w/o) in distilled water. Therefore, the mechanical properties of EAA copolymer such as stress-strain and failure behavior were not affected by immersion in acidic solutions. As a result, as long as the failure occurred cohesively in the EAA copolymer, the initial peel strength was kept unchanged (6). Thus, the decrease in peel strength occurs in acidic solutions with the change in locus of failure from the EAA copolymer to the chromate-underlying alloy interface.

**Relationship between bond durability and alloy corrosion.**—It seems likely that the interfacial failure between the chromate film and the underlying alloy in acidic solutions is due to anodic dissolution of the underlying alloy. To clarify the relation between the decrease in peel strength and the chromated alloy corrosion, the anode current density ( $I_p$ ) from the potentiostatic method and the polarization resistance ( $R_p$ ) from the coulometric method were measured for untreated and chromated alloys in acidic solutions, in which immersion tests of chromated alloy joints were carried out. Figure 7 shows the changes in  $I_p$  value

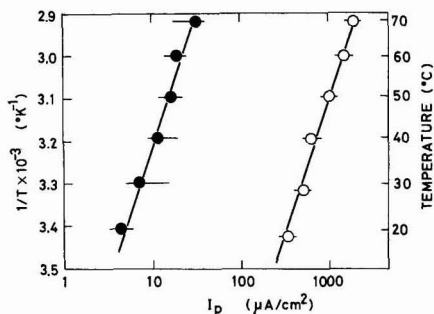


Fig. 7. Arrhenius plots for  $I_p$  values of untreated (O) and chromated (●) alloy sheets in a  $\text{CH}_3\text{COONa-HCl}$  buffer (pH 4.5).

with immersion temperature for untreated and chromated alloy sheets in a  $\text{CH}_3\text{COONa-HCl}$  buffer (pH 4.5). On both the surfaces, the  $I_p$  value increases with increasing immersion temperature. The  $I_p$  values on chromated alloy are ca. 1/500 times those on untreated alloy. Since the chromate film itself is corrosion-resistant, the  $I_p$  values measured on chromated alloy surfaces mean those on regions uncovered with the chromate film [e.g., grain boundaries (5) and cracks in the chromate film]. The  $I_p$  values on untreated and chromated alloy surfaces show the same temperature dependence (Fig. 7). This fact also supports the view that the  $I_p$  value on chromated alloy surfaces measures a leak current density from the underlying alloy. Therefore, the corrosion properties of chromated alloys depend on both the area uncovered with the chromate film and the corrosion of the underlying alloy itself. In this paper, since the chromate treatment was carried out under the same conditions, the area uncovered with the chromate film is thought to be the same for all chromated samples. Accordingly, since the corrosion resistance of the chromated alloy can be related to that of untreated alloy, the  $I_p$  and  $R_p$  values of untreated alloy in acidic solutions were compared with the peel strength retention time of chromated alloy joints in acidic solutions.

Figures 8 and 9 show log-log plots of  $I_p$  and  $R_p$  of untreated alloy vs. peel strength retention time for chromated alloy joints at various immersion temperatures in various acidic solutions. In spite of the use of different acidic solutions and different immersion temperatures, the peel strength retention time is inversely proportional to the  $I_p$  value and proportional to the  $R_p$ ,

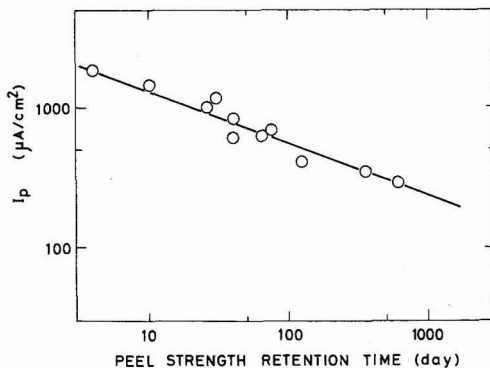


Fig. 8. Log-log plot of  $I_p$  vs. peel strength retention time of chromated alloy joints at various immersion temperatures in various acidic solutions.

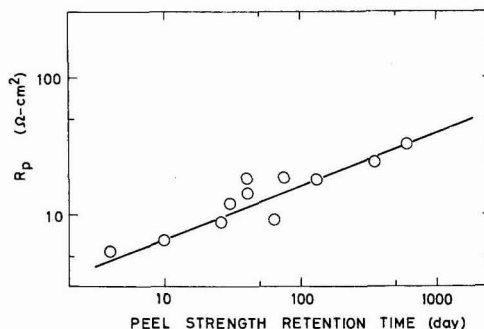
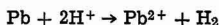


Fig. 9. Log-log plot of  $R_p$  vs. peel strength retention time of chromated alloy joints at various temperatures in various acidic solutions.

value. In other words, the peel strength retention time increases with decreasing anodic dissolution of the underlying alloy, i.e., decreasing  $I_p$  value or increasing  $R_p$  value. Thus, it is concluded that the decrease in peel strength is due to the anodic dissolution of the underlying alloy.

**Failure mechanism in acidic solutions.**—Figure 10 shows a schematic diagram of chromated lead/tin alloy-EAA interfaces degraded in acidic solutions. The alloy surface consists both of lead and tin phases (Fig. 1). Since the lead phase was corroded more rapidly than the tin phase when untreated alloy sheets were immersed in acidic solutions, the lead phase-EAA interface of chromated alloy joints are assumed to degrade rapidly in acidic solutions by anodic dissolution of lead according to the reaction.



Therefore, the joint strength of chromated alloy joints is due mainly to interfacial forces at the tin phase-EAA interfaces. In chromated alloy joints immersed in acidic solutions, hydrogen ions diffuse into the adhesive joints along the lead phase-chromate film interfaces. At the same time, hydrogen ions may diffuse through the EAA copolymer, pass through the cracks (Fig. 2) of chromate film, and then reach the tin phase-chromate film interfaces. Subsequently, at the tin phases in contact with the chromate film, the growth of tin oxide layer and the anodic dissolution occur gradually according to the reaction



The decrease in peel strength occurs simultaneously

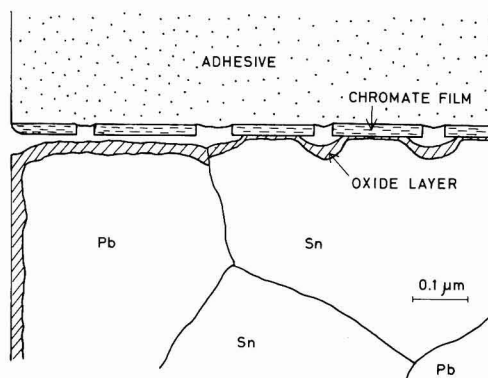


Fig. 10. Schematic diagram of chromated lead/tin alloy-EAA interfaces degraded in acidic solutions.

with anodic dissolution of the tin phases. After complete anodic dissolution of all the tin phases in contact with the chromate film, interfacial separation occurs between the chromate film and the underlying alloy. In conclusion, the environmental stability of chromated lead/tin alloy joints in acidic solutions depends on the corrosion properties of the tin phase in acidic solutions, and the failure of chromated alloy joints proceeds with anodic dissolution of the tin phases.

The  $I_p$  and  $R_p$  values of untreated alloy were 1.0  $\mu\text{A}/\text{cm}^2$  and 3.2  $\text{k}\Omega\cdot\text{cm}^2$  in distilled water, respectively. It is estimated from Fig. 8 and 9 that the peel strength retention time of chromated alloy joints is more than 10 years in distilled water. This estimation is in fair agreement with an experimental result (6) that the decrease in peel strength of chromated alloy joints does not occur even after immersion in distilled water for 2 years.

#### Acknowledgment

The authors wish to thank Dr. K. Kudo and Mr. S. Tsuru for many helpful discussions.

Manuscript submitted March 4, 1980; revised manuscript received June 25, 1981.

Any discussion of this paper will appear in a Discussion Section to be published in the June 1982 JOURNAL. All discussions for the June 1982 Discussion Section should be submitted by Feb. 1, 1982.

Publication costs of this article were assisted by Nippon Telegraph and Telephone Public Corporation.

#### REFERENCES

1. H. G. Frank, M. C. McGugh, and W. E. Ropp, 17th Int. Wire and Cable Symposium, Atlantic City, NJ (1968).
2. B. Wargotz, *J. Appl. Polym. Sci.*, **13**, 1965 (1969).
3. W. H. Smarook and S. Bonotto, *Polym. Eng. Sci.*, **8**, 41 (1968).
4. B. Wargotz, *J. Appl. Polym. Sci.*, **12**, 1873 (1968).
5. F. Yamamoto and S. Yamakawa, *ibid.*, **25**, 2479 (1980).
6. F. Yamamoto, S. Yamakawa, and M. Wagatsuma, *ibid.*, **25**, 2731 (1980).
7. H. H. Uhlig, "Corrosion Handbook," John Wiley & Sons, Inc., New York (1948).
8. K. Kanno, M. Suzuki, and Y. Sato, *Boshoku Gijutsu*, **26**, 697 (1977).
9. E. J. Simmons, *Corrosion*, **11**, 255t (1955).
10. W. J. Schwerdtfeger and O. N. McDorman, *This Journal*, **99**, 407 (1952).
11. P. Delahay, *J. Phys. Chem.*, **66**, 2204 (1962).
12. P. Delahay, *Anal. Chem.*, **34**, 1161 (1962).
13. P. Delahay, *Anal. Chim. Acta*, **27**, 90 (1962).
14. W. H. Reinmuth and C. E. Wilson, *Anal. Chem.*, **34**, 1159 (1962).
15. W. H. Reinmuth, *ibid.*, **34**, 1272 (1962).
16. F. W. Eppenstein and M. R. Jenkins, *Metal Finishing*, No. 9, 29 (1975).
17. R. O. Ansell, T. Dickinson, A. F. Povey, and P. M. A. Sherwood, *This Journal*, **124**, 1360 (1977).

# Environmental Stability and Failure Mechanisms of Chromated Lead/Tin Alloy Joints Bonded with an Ethylene-Acrylic Acid Copolymer

## II. Alkaline Conditions

Fumio Yamamoto, Shinzo Yamakawa, and Shinji Tsuru

Nippon Telegraph and Telephone Public Corporation,  
Ibaraki Electrical Communication Laboratory, Tokai, Ibaraki 319-11, Japan

### ABSTRACT

The environmental stability and the failure mechanisms of a cathodically chromated lead/tin (38/62) alloy joint bonded with an ethylene-acrylic acid (EAA) copolymer (20 weight percent acrylic acid) have been investigated in alkaline solutions. The environmental stability has been compared with that of the alloy joint bonded with an ethylene-ethyl acrylate copolymer grafted with acrylic acid (EEA-g-AA). The peel strength of the EAA joint decreases rapidly with immersion in alkaline solutions. This decrease in peel strength results from stepwise swelling of the EAA adhesive layer from the edges of the joint to the inside, which swelling occurs by alkaline ions diffusing into the joint inside. On the other hand, the decrease in peel strength of the EEA-g-AA joints occurs from stepwise interfacial degradation from the joint edges, with no swelling of the EEA-g-AA adhesive layer. The interfacial failure mechanism is discussed in comparison with that of the EAA joint.

Cathodically chromated lead/tin alloy joints bonded with an ethylene-acrylic acid (EAA) copolymer have high peel strength in dry conditions (1) and show high environmental stability in distilled water (2). However, immersion of the joints in acidic aqueous solutions causes a rapid decrease in peel strength and finally an interfacial separation (3). This decrease in peel strength is due to an interfacial degradation or failure between the chromate film and the underlying alloy. This interfacial failure is due to anodic dissolution of the underlying alloy. In alkaline solutions, on the other hand, lead/tin alloys are corroded since both lead and tin are amphoteric metals (4). Therefore, it is interesting to see whether the interfacial failure of lead/tin alloy joints occurs in alkaline solutions via the same mechanism as that in acidic solutions or via the other failure mechanism. This paper is concerned with the environmental stability in alkaline solutions and the failure mechanism of a cathodically chromated lead/tin (38/62) alloy joint bonded with an EAA copolymer used in previous papers (1-3). The failure mechanism in alkaline solutions is compared with that of the alloy joint bonded with an ethylene-ethylacrylate copolymer grafted with acrylic acid (EEA-g-AA).

### Experimental

The preparation of T-peel specimens consisting of adherend (0.5 mm)-adhesive (0.2 mm)-adherend (0.5 mm) and the T-peel testing were described elsewhere (1). A cathodically chromated lead/tin (38/62) alloy sheet was used as the adherend. An EAA copolymer sheet (EAA-1), used in previous works (1-3), was used as the adhesive in this work, together with an ethylene-ethyl acrylate copolymer grafted with acrylic acid (EEA-g-AA). The EEA copolymer, supplied by Nippon Unicar Company, was homogeneously grafted with acrylic acid in benzoyl peroxide-containing xylene solutions at 120°C under nitrogen gas (5). The properties of ethylene copolymers investigated in this work are given in Table I. To evaluate the environmental stability of the joints, the peel specimens were

immersed in alkaline solutions at temperatures of 40°-70°C, and the T-peel strength was measured at 25°C immediately after immersion. The alkaline solutions used were:  $H_2BO_3$  + KCl-NaOH (pH 8.0 and 8.5),  $NaHCO_3$ -NaOH (pH 10.0),  $Na_2HPO_4$ -NaOH (pH 11.0), and KCl-NaOH (pH 12.0 and 13.0) buffers, and 0.1N NaOH solution (pH 14.0). The locus of failure of these joints was determined from analysis of the fractured surfaces by x-ray photoelectron spectroscopy (ESCA) and scanning electron microscopy (SEM).

### Results and Discussion

**Water immersion test.**—Figure 1 shows the changes in peel strength with immersion at various temperatures in a  $NaHCO_3$ -NaOH buffer (pH 10.0) for an EAA-1 joint. Figure 2 shows the changes in peel strength with immersion in various alkaline solutions at 50°C for the same EAA-1 joint. The peel strength decreases rapidly at relatively high pH values and temperatures as in acidic solutions (3). The peel strength retention time (during which the initial peel strength is kept unchanged) decreases with increasing immersion temperature or pH of alkaline solutions. Figure 3 shows the changes in peel strength in various alkaline solutions at 50°C for an EEA-g-AA joint. The peel strength retention time also decreases with increasing pH of alkaline solutions. However, the peel strength retention times of the EEA-g-AA joint is

Table I. Properties of acrylic acid-containing copolymers

Sample	Melt index (ASTM D1238) (g/10 min)	Acrylic acid content (w/o)	Ethyl acrylate content (w/o)	Density (g/cm <sup>3</sup> )	Glass transition temperature (°C)
EAA-1*	50	20	—	0.96	31
EAA-2*	9.0	8	—	0.932	12
EAA-3*	11.0	3.5	—	0.925	-5
EEA-g-AA†	6.4	4.7	18	0.931	-27

\* Ethylene-acrylic acid copolymer.

† Ethylene-ethyl acrylate copolymer grafted with acrylic acid.

Key words: ESCA, interfacial degradation, metal-polymer interface, adhesive joint.

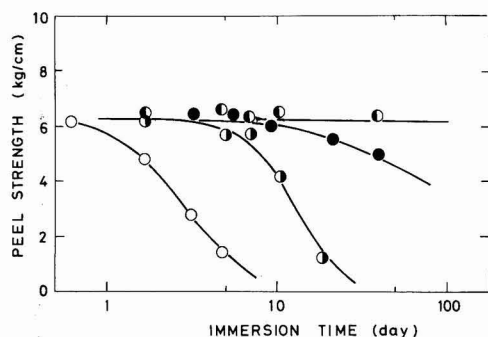


Fig. 1. Changes in peel strength with immersion in an  $\text{NaHCO}_3\text{-NaOH}$  buffer (pH 10.0) for an EEA-1 joint. Immersion temperatures were: (●) 40°C; (◐) 50°C; (○) 60°C; (○) 70°C.

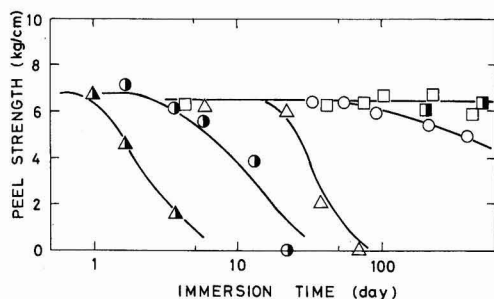


Fig. 2. Changes in peel strength with immersion in various alkaline solutions at 50°C for an EEA-1 joint. Alkaline solutions were: (▲) 0.1N NaOH solution, pH 14.0; (◐) KCl-NaOH buffer, pH 12.0; (△)  $\text{Na}_2\text{HPO}_4\text{-NaOH}$  buffer, pH 11.0; (○)  $\text{NaHCO}_3\text{-NaOH}$  buffer, pH 10.0; (□)  $\text{H}_3\text{BO}_4 + \text{KCl-NaOH}$  buffer, pH 8.5; (■)  $\text{H}_3\text{BO}_4 + \text{KCl-NaOH}$  buffer, pH 8.0.

longer than those of the EEA-1 joint when both the joints are immersed in the same alkaline solution; the EEA-g-AA joint is more stable in alkaline solutions than the EEA-1 joint.

**Locus of failure.**—The peel strength of the EEA-1 joint decreases as rapidly in alkaline solutions as in acidic solutions. However, the progress of the interfacial failure in alkaline solutions has been found to be significantly different from that in acidic solutions. Immersion of the joint in acidic solutions causes first the small areas or the spots of peel strength  $\approx 0$  kg/cm over the whole part of the interface, next the increases in the area and the number of the spots, and finally an interfacial separation (3). In alkaline solutions, on the other hand, the failure initiates from the edges of the joint in contact with the alkaline solutions and proceeds into the joint inside with water immersion. Figure 4 shows SEM micrographs of fractured chromated alloy and EAA surfaces of the EEA-1 joint peeled after immersion in an  $\text{NaHCO}_3\text{-NaOH}$  buffer (pH 10.0). The SEM micrographs show a distinct front of failure on both the peeled surfaces. On the peeled alloy surface, the part of smooth surface corresponds to the undegraded region of the joint inside, which was peeled with a high peel strength similar to the initial peel strength. The part of rough surface corresponds to the degraded region of the joint edges, which was peeled with a low peel strength of ca. 0 kg/cm. The rough surface topography results from the residual adhesive, which had been transferred from the adhesive side to the alloy side through the cohesive

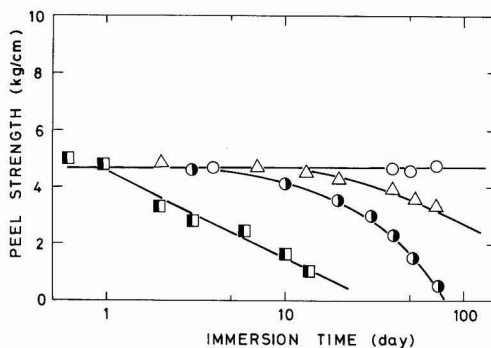


Fig. 3. Changes in peel strength with immersion in various alkaline solutions at 50°C for an EEA-g-AA joint. Alkaline solutions were: (■) KCl-NaOH buffer, pH 13.0; (◐) KCl-NaOH buffer, pH 12.0; (○)  $\text{NaHCO}_3\text{-NaOH}$  buffer, pH 10.0.

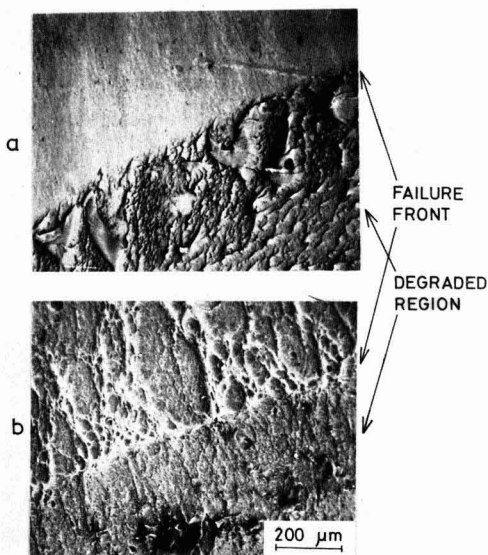


Fig. 4. SEM micrographs of fractured chromated alloy (a) and EAA (b) surfaces of an EEA-1 joint peeled after immersion in an  $\text{NaHCO}_3\text{-NaOH}$  buffer (pH 10.0).

failure of the adhesive layer. On the other hand, on the peeled EAA side, remarkable swelling of the EAA adhesive was observed on the degraded region. The front of swelling coincided approximately with the front of the interfacial degradation. The undegraded EAA surface, peeled with high peel strength, shows a rough surface topography similar to that peeled in dry conditions (1). This rough topography results from plastic deformation of the adhesive.

Figure 5 shows ESCA spectra of the fractured chromated alloy and EAA surfaces corresponding to those of Fig. 4, together with those of original chromated alloy and EAA surfaces. The degraded parts of both the peeled surfaces show an overall ESCA spectrum similar to that of the original adhesive surface, although there is a slight ESCA peak of tin. This ESCA result and the presence of the residual adhesive on the degraded alloy surface (Fig. 4a) indicate that the failure of the degraded region of the joint occurs within the adhesive when the joint is peeled. On the



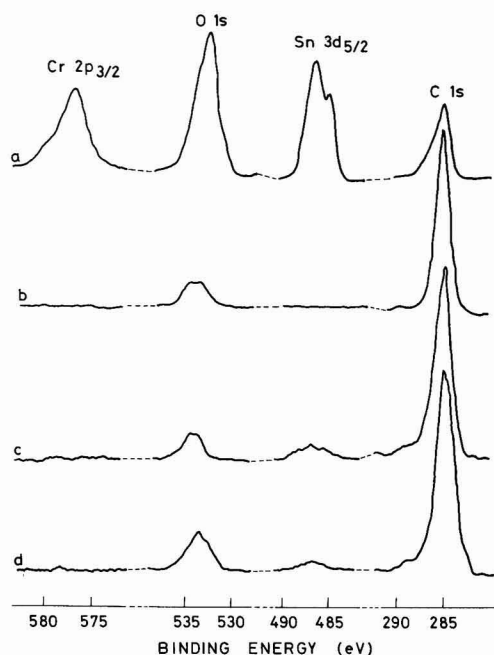


Fig. 5. ESCA spectra of original chromated alloy (a) and EAA (b) surfaces and fractured chromated alloy (c) and EAA (d) surfaces of an EAA-1 joint peeled with low peel strength after immersion in an  $\text{NaHCO}_3\text{-NaOH}$  buffer (pH 10.0).

other hand, peeled alloy and EAA surfaces of the dry joint (1) and the undegraded region of immersed joints showed ESCA spectra similar to those (c, d) of Fig. 5. This result indicates that the locus of failure in the dry joint or in the undegraded region of the joint inside, in which the initial peel strength is kept unchanged, also is the cohesive failure of the adhesive itself. In other words, both the undegraded and degraded regions of the EAA-1 joint result in cohesive failure within the adhesive in spite of the significant difference in peel strength. This fact suggests that the decrease in peel strength of EAA-1 joints results from the decrease in mechanical or cohesive strength of the EAA adhesive, but not from anodic dissolution of the underlying alloy (3, 6-8) and from displacement of the adhesive by water (9).

**Failure mechanism of EAA-1 joints in alkaline solutions.**—The anode current density ( $I_p$ ) (3) at an overpotential of 50 mV and the polarization resistance ( $R_p$ ) (3) of a lead/tin (38/62) alloy in the alkaline solutions used were of the order of 100  $\mu\text{A}/\text{cm}^2$  and 500  $\Omega\text{-cm}^2$ , respectively. The estimated peel strength retention time in alkaline solutions, which was obtained from the above  $I_p$  and  $R_p$  values using the relation between peel strength retention time and  $I_p$  or  $R_p$  in Fig. 8 or 9 of the previous paper (3), is more than 10 years. In fact, however, the joint degrades rapidly in alkaline solutions; the measured peel strength retention time is of the order of 10-100 days (Fig. 1 and 2). This disagreement indicates that anodic dissolution of the underlying alloy is not the prime cause for the joint deterioration in alkaline solutions, although it is the prime cause for the joint failure in acidic solutions.

Table II shows water absorption test results of EAA-1 and EEA-g-AA copolymer sheets (used as adhesives in this paper) immersed in an  $\text{NaHCO}_3\text{-NaOH}$

Table II. Water absorption test of acrylic acid-containing copolymer sheets (0.5 mm thick) immersed in an  $\text{NaHCO}_3\text{-NaOH}$  buffer (pH 10.0) in the range 40°-70°C

Sample	Acrylic acid content (w/o)	Water absorption (w/o)			
		40°C	50°C	60°C	70°C
EAA-1*	20	26.2	61.0	128.2	190.4
EAA-2*	8	<0.01	~0.08	0.1	0.3
EAA-3*	3.5	<0.01	~0.03	~0.06	0.2
EEA-g-AA†	4.7	5.2	6.2	8.2	11.2

\* Ethylene-acrylic acid copolymer.

† Ethylene-ethyl acrylate copolymer grafted with acrylic acid.

buffer (pH 10.0) in the temperature range 40°-70°C until there was not further increase in weight. Table III shows those immersed in three buffers of pH 8.5-12.0 at 50°C. Tables II and III also include those of two other EAA copolymers (EAA-2 and EAA-3) containing lower acrylic acid contents. EAA-1 sheets show much higher water absorption values than those of EAA-2, EAA-3, and EEA-g-AA sheets, corresponding to its high acrylic acid content [20 weight percent (w/o)]. Furthermore, the water absorption of the EAA-1 copolymer increases with increasing immersion temperature and pH of alkaline solutions. Also, it was observed that EAA-1 sheets were significantly swollen and became mechanically weak at relatively high water absorption, whereas EAA-2, EAA-3, and EEA-g-AA sheets were not swollen. The significant swelling of EAA-1, which is probably due to ionization or dissociation of carboxyl groups in the copolymer, also indicates that the deterioration of EAA-1 joint in alkaline solutions occurs with decreasing mechanical strength of the bulk EAA due to its remarkable swelling.

Figures 6 and 7 show the degraded depth from the edges of T-peel specimen vs. the square root of immersion time in an  $\text{NaHCO}_3\text{-NaOH}$  buffer (pH 10.0) at various temperatures and in various alkaline solutions at 50°C, corresponding to Fig. 1 and 2, respectively. The degraded depth corresponds to the region peeled with low peel strength of ca. 0 kg/cm and to the swollen region of the EAA-1 adhesive layer. In other words, the degradation or failure front of the interface coincides with the swelling front of the EAA-1 adhesive layer. In an  $\text{NaHCO}_3\text{-NaOH}$  buffer (pH 10.0) at 40° and 50°C (Fig. 6 and 7) and in an  $\text{H}_3\text{BO}_3 + \text{KCl-NaOH}$  buffer (pH 8.5) at 50°C (Fig. 7), the degraded depth is proportional to the square root of immersion time. This result indicates that failure of the EAA-1 joint occurs with swelling of the EAA adhesive layer by alkaline ions diffusing into the joint inside through the adhesive layer.

On the other hand, in an  $\text{NaHCO}_3\text{-NaOH}$  buffer (pH 10.0) at 60° and 70°C (Fig. 6), in a 0.1N NaOH solution (pH 14.0) at 50°C, in a KCl-NaOH buffer (pH

Table III. Water absorption test of acrylic acid-containing copolymer sheets (0.5 mm thick) in three buffers of pH 8.5-12.0 at 50°C

Sample	Acrylic acid content (w/o)	Water adsorption (w/o)		
		pH 8.5*	pH 10.0**	pH 12.0†
EAA-1‡	20	43.0	61.0	174.2
EAA-2‡	8	<0.01	~0.08	0.2
EAA-3‡	3.5	<0.01	~0.03	~0.03
EEA-g-AA§	4.7	6.0	6.2	5.2

\*  $\text{H}_3\text{BO}_3 + \text{KCl-NaOH}$  buffer.

\*\*  $\text{NaHCO}_3\text{-NaOH}$  buffer.

† KCl-NaOH buffer.

‡ Ethylene-acrylic acid copolymer.

§ Ethylene-ethyl acrylate copolymer grafted with acrylic acid.

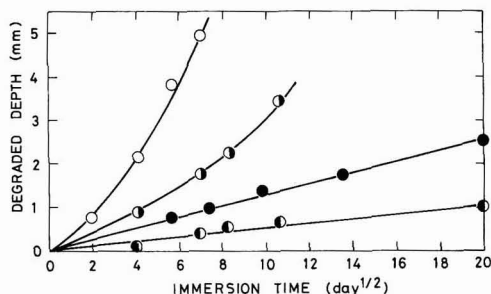


Fig. 6. Degraded depth from the edges of T-peel specimen vs. the square root of immersion time. An EAA-1 joint was immersed in a  $\text{NaHCO}_3\text{-NaOH}$  buffer (pH 10.0) at various temperatures: (●) 40°C; (●) 50°C; (●) 60°C; (○) 70°C.

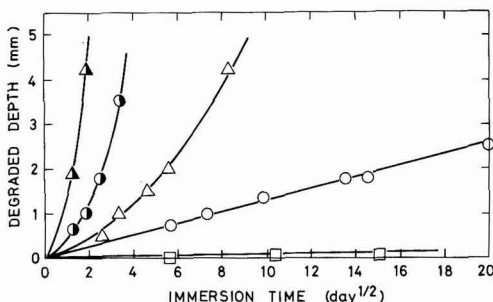


Fig. 7. Degraded depth from the edges of T-peel specimen vs. the square root of immersion time. An EAA-1 joint was immersed at 50°C in various alkaline solutions: (Δ) 0.1N NaOH solution, pH 14.0; (●) KCl-NaOH buffer, pH 12.0; (Δ)  $\text{Na}_2\text{HPO}_4\text{-NaOH}$  buffer, pH 11.0; (○)  $\text{NaHCO}_3\text{-NaOH}$  buffer, pH 10.0; (□)  $\text{H}_3\text{BO}_4 + \text{KCl-NaOH}$  buffer, pH 8.5.

12.0) at 50°C, and in a  $\text{Na}_2\text{HPO}_4\text{-NaOH}$  buffer (pH 11.0) at 50°C (Fig. 7), the degraded depth deviates from the linear relation with the square root of immersion time and accelerates with immersion time. In these cases, the two adherends were bent outside from each other by a remarkable swelling of the EAA copolymer adhesive (see Tables II and III) sandwiched by the two adherends. This waved swelling caused gaps between the adherend and the adhesive. Although the degraded depth values in Fig. 7 deviate from the linear relationship with the square root of immersion time, they give linear lines when replotted against immersion time (Fig. 8). This linear relationship indicates that alkaline solutions easily reach the failure front of EAA joints (or the swelling front of EAA adhesive layer) through above-mentioned gaps between the adherend and the adhesive.

**Failure mechanism of EEA-g-AA joint in alkaline solutions.**—The water absorption of EEA-g-AA sheets having a low acrylic acid content is low in alkaline solutions (Table II) and does not increase appreciably with increasing pH of alkaline solutions (Table III), whereas that of EAA-1 sheets is high and increases appreciably with increasing pH. The EEA-g-AA sheets are not swollen in alkaline solutions, whereas the EAA-1 sheets are appreciably swollen. These results indicate that alkaline ions diffuse into the bulk EAA-1, but do not diffuse into the bulk EEA-g-AA copolymer. However, it has been observed that the failure of the EEA-g-AA joint also initiates from the edges of the joint and proceeds gradually into the joint inside in a manner similar to that of EAA-1 joint. Figure 9 shows

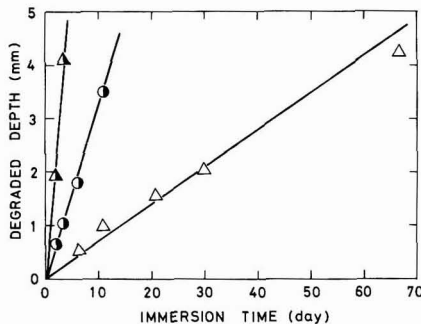


Fig. 8. Degraded depth from the edges of T-peel specimen vs. immersion time. An EAA-1 joint was immersed at 50°C in various alkaline solutions: (Δ) 0.1N NaOH solution, pH 14.0; (●) KCl-NaOH buffer, pH 12.0; (Δ)  $\text{Na}_2\text{HPO}_4\text{-NaOH}$  buffer, pH 11.0.

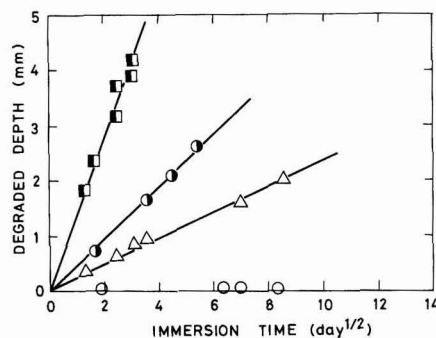


Fig. 9. Degraded depth from the edges of T-peel specimen vs. the square root of immersion time. An EEA-g-AA joint was immersed at 50°C in various alkaline solutions: (■) KCl-NaOH buffer, pH 13.0; (●) KCl-NaOH buffer, pH 12.0; (Δ)  $\text{Na}_2\text{HPO}_4\text{-NaOH}$  buffer, pH 11.0; (○)  $\text{NaHCO}_3\text{-NaOH}$  buffer, pH 10.0.

the relation between the degraded depth from the edges of T-peel specimen and the square root of immersion time in various alkaline solutions at 50°C. The degraded depth is proportional to the square root of immersion time. The bulk EEA-g-AA copolymer sheet has low water absorption values in these alkaline solutions, and its use as an adhesive results in no gap between the adherend and the adhesive. All the results suggest that the rate of the joint failure also is controlled by diffusion of alkaline ions along the alloy-adhesive interface.

Based on the well-documented phase structures of multiphase polymers such as block and graft copolymers, polymer blends, and interpenetrating networks (10), it is reasonable to assume that the grafted poly(acrylic acid) within EEA-g-AA undergoes phase separation. The presence of the grafted poly(acrylic acid) phase domains at the alloy-adhesive interface is responsible for the high peel strength ( $\approx 4 \text{ kg/cm}$ ) of the chromated alloy-EEA-g-AA joint (Fig. 3), because the base EEA copolymer before grafting gives only low peel strength (ca. 0.5 kg/cm). In analogy with the above-mentioned failure mechanism of EAA-1 joints, it is tempting to assume that the decrease in peel strength of alloy-EEA-g-AA joints in alkaline solutions occurs with swelling of the poly(acrylic acid) domains at the interface by alkaline ions diffusing into the joint inside along the interface. We discuss in more details the failure mechanism of EEA-g-AA joints in a later paper.

### Acknowledgment

The authors wish to thank Dr. K. Kudo and Mr. M. Wagatsuma for many helpful discussions.

Manuscript submitted March 4, 1980; revised manuscript received June 25, 1981.

Any discussion of this paper will appear in a Discussion Section to be published in the June 1982 JOURNAL. All discussions for the June 1982 Discussion Section should be submitted by Feb. 1, 1982.

Publication costs of this article were assisted by Nippon Telegraph and Telephone Public Corporation.

### REFERENCES

1. F. Yamamoto and S. Yamakawa, *J. Appl. Polym. Sci.*, **25**, 2479 (1980).
2. F. Yamamoto, S. Yamakawa, and M. Wagatsuma, *ibid.*, **25**, 2731 (1980).
3. F. Yamamoto, S. Yamakawa, and M. Wagatsuma, *This Journal*, **128**, 2374 (1981).
4. H. H. Uhlig, "Corrosion Handbook," John Wiley & Sons, Inc., New York (1948).
5. S. Tsuru, S. Yamakawa, and F. Yamamoto, *Kobunshi Ronbunshu*, **36**, 759 (1979).
6. B. Wargotz, *J. Appl. Polym. Sci.*, **12**, 1873 (1968).
7. B. Wargotz, *ibid.*, **13**, 1965 (1969).
8. R. F. Wegman, *Appl. Polym. Sci.*, **19**, 385 (1972).
9. R. A. Gledhill and A. J. Kinloch, *J. Adhesion*, **6**, 315 (1974).
10. J. A. Maunson and L. H. Sperling, "Polymer Blends and Composites," Plenum Press, New York (1976).

## Kinetics for the Reaction of Hydrogen with a Plutonium-1 Weight Percent Gallium Alloy Powder

Jerry L. Stakebake

Rockwell International, Golden, Colorado 80401

### ABSTRACT

Kinetics for the reaction of hydrogen with plutonium-1 w/o gallium were measured using powder prepared "in situ." The rates obeyed a first-order rate law and were independent of temperature from  $-29^{\circ}$  to  $355^{\circ}\text{C}$ . A pressure dependence proportional to  $P^{1/2}$  was observed at pressures less than 1 kPa. From 1 to 70 kPa the pressure dependence rapidly decreased. Total pressure dependence could be accurately described by a Langmuir equation. Results indicate an adsorption-controlled reaction at low pressures and a reaction-controlled process at high pressures.

Plutonium hydride is frequently employed as an intermediate for preparing the metal or nitride powder and as such plays an important role in the nuclear industry. Even though a number of experimental studies have been carried out to describe the physicochemical properties of the plutonium-hydrogen system, several areas are still poorly defined. Earlier studies (1-7) have described in detail the equilibrium behavior and thermodynamic properties of plutonium hydride. Much less information, however, is available on the kinetics of the reaction of hydrogen with plutonium. Some kinetic data for the reaction of hydrogen with plutonium coupons have been reported by Bowersox (8,9) and Colmenares *et al.* (10). A recent report (11) has also described the decomposition kinetics of plutonium hydride in both the two-phase region below  $\text{PuH}_{0.95}$  and in the nonstoichiometric region between  $\text{PuH}_{1.95}$  and  $\text{PuH}_3$ . Much of the early experimental kinetic data were influenced by oxide films on the metal coupons which increased the importance of hydride nucleation in the reaction. Hydrogen diffusion also plays a role in coupon hydriding and this process is likewise not understood. Therefore, additional work is required in order to fully understand the kinetics of plutonium hydriding as well as the factors which influence the kinetics.

Hydrogen reacts rapidly and exothermally with plutonium metal. The reaction is, however, strongly influenced by impurities in the gas phase hydrogen or on the plutonium metal surface. When impurities are present the reaction is characterized by a period of inhibition followed by a nucleation process on the plutonium surface. Elimination of the effect of impure

hydrogen can be accomplished through gas purification techniques. Oxide films on the surface are more difficult to eliminate. To accomplish this successfully the sample must be prepared *in situ* without exposure to air. The problem of a surface film contaminant was dealt with in another way by Bowersox (8,9). Plutonium coupons were heated under vacuum to about  $300^{\circ}\text{C}$ . During such a treatment the  $\text{PuO}_2$  surface film is converted to  $\text{PuO}$  or more likely a  $\text{Pu}(\text{C},\text{O})$  phase (12). This material is catalytic and enhances the dissociation of hydrogen thus promoting the hydriding reaction. When plutonium coupons were treated in this manner, hydride nucleation sites were rapidly generated and inhibition caused by the oxide film was nearly zero. The problem with this type of approach was that the true plutonium-hydrogen reaction was not being studied. The approach used in the present investigation was to purify the hydrogen gas and then prepare a plutonium powder *in situ*. This procedure results in a relatively clean sample with a high surface area.

A second problem in measuring plutonium hydriding kinetics arises from the exothermal nature of the reaction. The heat of formation of plutonium hydride varies from  $-38$  to  $-50$  kcal/mol depending on the composition of the hydride (3). Self-heating of the sample during reaction makes it difficult to obtain isothermal kinetic data. Use of a heat sink bonded to the plutonium coupon can alleviate the problem to a degree (8,9). However, this was not practical in the present investigation. The significance of not maintaining strictly isothermal conditions will be discussed later.

This paper describes the results from an investigation of the hydriding kinetics of a plutonium-1 weight

Key words: adsorption, corrosion, metals.

percent (w/o) gallium alloy powder. The metal powder was used because it could be prepared with a clean surface and any bulk hydrogen diffusion effects would be minimal. Measurements were carried out over a temperature range of  $-29^{\circ}$ – $355^{\circ}\text{C}$  and at hydrogen pressures of 20 Pa to 67.96 kPa. Kinetic data were evaluated with the reaction model used for uranium powder (13).

### Experimental

**Materials.**—Plutonium metal used in this investigation was a plutonium-gallium alloy which was stabilized in the delta phase. The gallium concentration was 1.03 w/o. There was a total of 1335 ppm of metallic impurities including 855 ppm of americium. Americium is present as a radiolytic decay product of plutonium-241. Coupons for this study were machined to a thickness of 3 mm from cast rods. Individual samples weighed about 1.5g. They were cleaned by mechanically polishing the surface and immediately loaded on the vacuum microbalance.

Ultrapure hydrogen (99.999%) and argon (99.999%) were used in this investigation. These gases were introduced into the system through a bed of uranium hydride to further minimize oxygen contamination. However, surface reactions between hydrogen and the stainless steel walls of the vacuum system still produced some water vapor contamination.

**Apparatus.**—The experimental apparatus used for this investigation has been described in detail elsewhere (13). A Cahn Model 100 microbalance was incorporated into a stainless steel vacuum system. Minimum pressures attainable were in the  $10^{-6}$  Pa ( $10^{-8}$  Torr) range. Hydrogen pressures during reaction were controlled with a Granville-Phillips pressure controller and could be varied from  $10^{-4}$  Pa to  $10^5$  Pa. Pressures were measured with an ionization gauge or a capacitance manometer. Sample temperatures were varied with a resistance heater controlled with a power proportioning programmer. The thermocouple for measuring the sample temperature was located beside the sample and inside the vacuum system. Output from the microbalance, thermocouples, and pressure meters were collected with a data acquisition system and processed using a computer.

**Procedure.**—Plutonium powder was prepared by hydriding and then dehydriding a 1.5g plutonium coupon. Hydride sites were nucleated on the coupon by exposure to 6.65 kPa of hydrogen at  $20^{\circ}\text{C}$  for 2 min. Bulk hydriding was then performed slowly in 67 Pa of hydrogen at  $20^{\circ}\text{C}$ . Although slow, this process produced the highest surface area for the powder. Dehydriding was accomplished by heating the sample at  $450^{\circ}\text{C}$  under vacuum. The objective during dehydriding was to attain a reasonable rate and still minimize any sintering of the powder. Surface areas for the powders were calculated from the argon adsorption isotherm, obtained at  $-196^{\circ}\text{C}$ , using the BET (14) method. Powder hydriding rates were then measured over a range of temperatures ( $-29^{\circ}$ – $355^{\circ}\text{C}$ ) and pressures (0.020–67.96 kPa). Following each run the sample was dehydrided at  $450^{\circ}\text{C}$  and reused for the next hydriding run. A total of fifteen different plutonium samples were used throughout the course of this investigation.

### Reaction Kinetics

The reaction model used to describe the reaction of hydrogen with plutonium metal powder is called the "Progressive Conversion" model (15). This model assumes that once hydrogen is adsorbed on the surface diffusion into the bulk is very rapid and not rate determining. Thus, the reaction takes place uniformly throughout the particle and not strictly at the metal/hydride interface. The general reaction equation is

$$W_t = W_m[1 - [1 + k(n-1)M_0^{(n-1)}t]^{1/(1-n)}] \quad [1]$$

where  $W_t$  = hydrogen reacted in time,  $t$ ;  $W_m$  = total hydrogen reacted;  $k$  = rate constant;  $n$  = order of the reaction; and  $M_0$  = milligram atoms of metal initially available. In the special case where the reaction is first-order ( $n = 1$ ), Eq. [1] becomes

$$W_t = W_m(1 - e^{-kt}) \quad [2]$$

This equation was used throughout this study to evaluate rates of reaction.

### Results and Discussion

**Plutonium powder characterization.**—Gallium metal present in this plutonium alloy powder is nonreactive with respect to hydrogen. The role of gallium is to stabilize the plutonium in the delta phase. This metal phase is more reactive with respect to hydrogen than the room temperature alpha phase found in pure plutonium. The most logical reason for the increased reactivity is the greater metal-metal atomic spacing in the delta alloy. In this structure the  $f$ -electrons are more localized and are not involved in metallic bonding (16). Thus, it has been proposed that they are available for the rapid chemisorption of hydrogen during the hydriding reaction (17). One initial concern was that gallium would become segregated during the hydriding/dehydriding cycles. This would result in a mixture of alpha and delta phase material. X-ray diffraction analysis of the metal powder showed that the metal was in the delta phase and there was only a trace of alpha plutonium. Apparently the gallium remains uniformly distributed throughout the powder.

When the initial hydriding of a plutonium coupon was carried out in 26.6 kPa of hydrogen at  $200^{\circ}\text{C}$  the reaction was very rapid. Powder formed in this manner contained large particles (Fig. 1). Additional hydriding and dehydriding did not reduce the particle size because of the high temperature ( $450^{\circ}\text{C}$ ) required for dehydriding. For this investigation the initial coupon was nucleated in 6.65 kPa of hydrogen at  $20^{\circ}\text{C}$  for about 2 min. During this stage about 1% of the total reaction took place. The remainder of the coupon hydriding was carried out at  $20^{\circ}\text{C}$  in 67 Pa of hydrogen over a period of about 5 hr. Powder formed by this method was finer and more uniform than that prepared by rapid, high temperature hydriding (Fig. 2).

Particle sizes of the powder used were measured with a Quantimet 720 particle analyzer. The particle size distribution is shown by a log-normal plot in Fig. 3. The count mean diameter (CMD) was 5.0  $\mu\text{m}$ , while the standard deviation,  $\sigma_g$ , was 13.4. Total surface areas

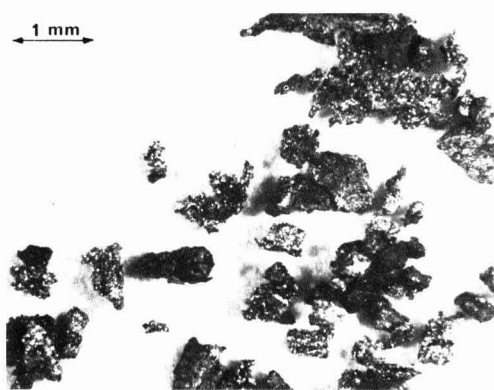


Fig. 1. Plutonium-1 w/o gallium powder prepared at  $200^{\circ}\text{C}$  in 26.6 kPa of hydrogen.

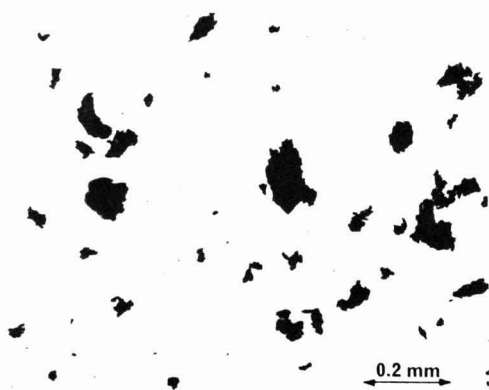


Fig. 2. Plutonium-1 w/o gallium powder prepared at 20°C in 0.067 kPa of hydrogen.

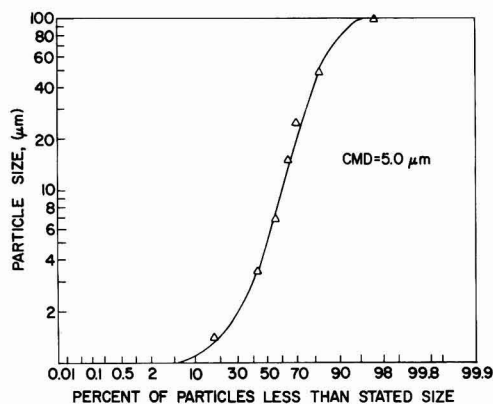


Fig. 3. Log-normal size distribution of plutonium alloy powder. The count median diameter for the particles was 5.0  $\mu\text{m}$  and the geometric standard deviation  $\sigma_g$  was 13.4.

of the samples were measured with the BET (14) technique using argon adsorption at  $-196^\circ\text{C}$ . The surface area of this powder was calculated to be  $0.16\text{ m}^2/\text{g}$ . All of the powders used in this study had surface areas on the order of  $0.1\text{--}0.2\text{ m}^2/\text{g}$ . This range was too small to establish any surface area dependence for the reaction.

**Kinetic evaluation of powder hydriding.**—The applicability of the "Progressive Conversion" model discussed earlier was evaluated under all of the conditions of this investigation. A typical evaluation is illustrated in Fig. 4. This particular hydriding run was made at an initial temperature of  $30^\circ\text{C}$  in  $1.06\text{ kPa}$  of hydrogen. Because of the heat of reaction the average temperature of this run was  $130^\circ\text{C}$ . It is evident that both Eq. [1] and [2] fit the data quite well. Using Eq. [1] the rate constant,  $k$ , was  $1.60\text{ min}^{-1}$  and the calculated order was 0.91. Equation [2] for a first-order reaction produced a rate constant of  $1.46\text{ min}^{-1}$ . For the purpose of this investigation all data were evaluated using Eq. [2].

**Effects of temperature on powder hydriding.**—Hydriding of plutonium metal released significant amounts of heat. With the experimental set-up being used, this heat could not be dissipated and the net result was an increase in sample temperature. This effect is shown in Fig. 5. Because of the rapid heat release thermal

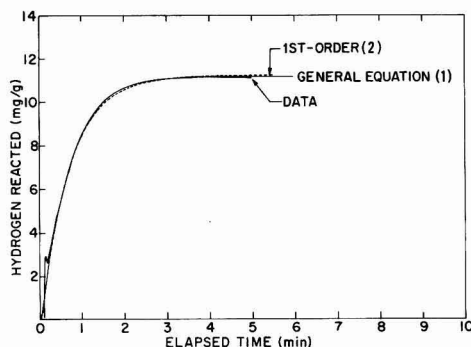


Fig. 4. Evaluation of plutonium powder hydriding rates at  $30^\circ\text{C}$  and  $1.06\text{ kPa}$  using Eq. [1] and [2].

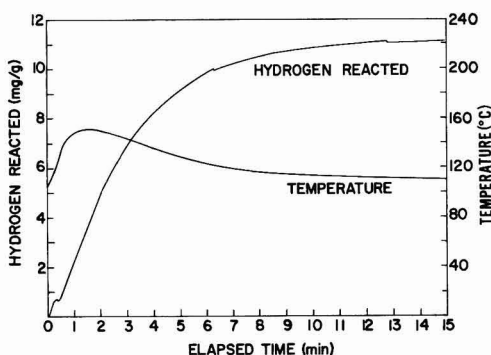


Fig. 5. Exothermic behavior of plutonium powder hydriding at  $100^\circ\text{C}$  in  $0.067\text{ kPa}$  of hydrogen.

gradients were established between the sample and the wall of the chamber. These gradients, which were most pronounced at low pressures and temperatures, are believed to cause the discontinuities observed in Fig. 4 and 5 through their effect on the microbalance. Discontinuities have been observed at about  $0.1\text{--}0.2\text{ min}$  after the start of a run for all experiments at temperatures less than  $140^\circ\text{C}$  and pressures less than  $1.33\text{ kPa}$ .

When the main purpose of an investigation is the measurement of reaction rates, the inability to maintain isothermal conditions could present a problem. Table I summarizes data obtained over a range of temperatures for two pressure levels,  $0.067$  and  $26.6\text{ kPa}$  ( $0.5$  and  $200\text{ Torr}$ ). Temperatures being reported

Table I. Effect of temperature on the hydriding rate of plutonium-1 w/o gallium alloy powder

Run	Pressure (kPa)	$T_0$ ( $^\circ\text{C}$ )	$T_{\text{max}}$ ( $^\circ\text{C}$ )	$T_{\text{avg}}$ ( $^\circ\text{C}$ )	$k$ ( $\text{min}^{-1}$ )
827	0.067	68	140	$126 \pm 9$	0.45
830	0.067	55	127	$119 \pm 13$	0.40
831	0.067	77	162	$156 \pm 8$	0.40
832	0.067	218	266	$261 \pm 8$	0.47
833	0.067	-33	27	$5 \pm 13$	0.42
834	0.067	6	62	$35 \pm 16$	0.48
835	0.067	233	323	$315 \pm 14$	0.41
838	0.067	30	80	$73 \pm 8$	0.40
839	0.067	30	83	$76 \pm 8$	0.40
864	26.60	30	142	$103 \pm 28$	1.78
865	26.60	244	372	$355 \pm 9$	1.69
866	26.60	120	226	$193 \pm 17$	2.10
867	26.60	-96	47	$-29 \pm 43$	2.68
869	26.60	24	148	$106 \pm 27$	2.02
870	26.60	-31	109	$50 \pm 35$	2.38
871	26.60	175	315	$277 \pm 22$	2.25
872	26.60	48	184	$129 \pm 30$	2.42



were gas-phase temperatures measured next to the sample. Because of the significant self-heating during reaction, an average temperature was calculated for each run. In the first set of experiments at 0.067 kPa, an attempt was made to hold the temperature near its maximum. With the exception of the low temperature runs 833 and 834, heat was supplied to the sample with a furnace and temperature programmer. The effectiveness of this approach is shown by the standard deviations of the temperature. This technique was not used for the higher pressure experiments. The lack of temperature programming coupled with reaction rates which were nearly five times larger resulted in significantly higher standard deviations for the average temperatures.

Since actual powder temperatures were unknown, no attempt was made to evaluate the temperature dependence for powder hydriding using the Arrhenius equation. Examination of the gas-phase temperatures shown in Table I indicate that temperature apparently has little effect on the hydriding rate. This is indicative of a very small activation energy. Additional work is required, however, to measure actual powder temperatures and to evaluate the nonisothermal kinetics.

Studies made with plutonium coupons have shown some temperature dependence. Activation energies have been reported to range from 2 to 6 kcal/mol (8-10, 18). Since in the case of bulk coupons such processes as nucleation and diffusion play a significant role, activation energies may be associated with these processes and not the direct reaction between plutonium and hydrogen.

**Effects of hydrogen pressure on powder hydriding rates.**—Experimental runs were conducted at pressures of 20 Pa (0.15 Torr) up to 67.96 kPa (510 Torr). Temperatures were nonisothermal and the variation during the investigation ranged from an average of  $-29^\circ$  to  $355^\circ\text{C}$ . Earlier in this discussion it was shown that hydriding rates were essentially independent of temperature. Only a slight inverse temperature dependence was noted at higher pressures, e.g., 26.6 kPa. This type of behavior was attributed to the role of adsorption at low temperatures and hydride decomposition at high temperatures. The decomposition reaction becomes significant at about  $350^\circ\text{C}$  (11). Because of this temperature influence at the temperature extremes, runs at temperatures less than  $0^\circ\text{C}$  or greater than  $350^\circ\text{C}$  were not used in evaluating pressure effects on hydriding rates.

Data from all runs at various pressures are listed in Table II. These data were analyzed using the equation

$$k_{\text{hyd}} = k_0 P^n \quad [3]$$

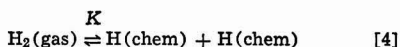
where  $k_{\text{hyd}}$  is the first-order rate constant,  $P$  the hydrogen pressure in kPa,  $k_0$  is a constant, and  $n$  is the order of the hydrogen pressure dependence. A plot of the data using this equation is shown in Fig. 6. A discontinuity is noted at about 1 kPa (8 Torr) indicating the pressure dependence might be evaluated for two pressure ranges. For the pressure range 0-1 kPa (0-8 Torr)  $n$  is equal to 0.45 while for pressures greater than 1 kPa  $n$  is 0.11.

In the low pressure region the rate is proportional to  $P^{1/2}$ . This relationship is typical for dissociative adsorption of hydrogen. For pressures greater than 1 kPa the pressure dependence of the reaction is proportional to 0.11 or very nearly equal to zero. This type of behavior is similar to the Langmuir adsorption isotherm and suggests that hydrogen adsorption may play a major role in the overall hydriding kinetics.

Using Langmuir's kinetic derivation (19) for the adsorption isotherm,  $\theta$  is the fraction of the surface covered with hydrogen and  $1 - \theta$  is the fraction bare. If hydrogen is adsorbed dissociatively

Table II. The effect of pressure on the rate of hydriding of plutonium-1 w/o alloy powder

Run	Pressure (kPa)	$k$ ( $\text{min}^{-1}$ )	$T_{\text{AVE}}$ ( $^\circ\text{C}$ )
862	0.020	0.25	$76 \pm 8$
827	0.067	0.45	$126 \pm 9$
830	0.067	0.40	$119 \pm 13$
831	0.067	0.40	$156 \pm 8$
832	0.067	0.47	$261 \pm 8$
833	0.067	0.42	$5 \pm 13$
834	0.067	0.48	$35 \pm 16$
835	0.067	0.41	$315 \pm 14$
838	0.067	0.40	$73 \pm 8$
839	0.067	0.40	$76 \pm 8$
853	0.075	0.41	$94 \pm 16$
844	0.120	0.64	$61 \pm 6$
849	0.250	0.86	$105 \pm 15$
854	0.332	0.84	$103 \pm 15$
840	0.665	1.23	$164 \pm 7$
841	0.665	1.23	$84 \pm 12$
842	0.665	1.22	$100 \pm 11$
843	1.064	1.46	$130 \pm 9$
848	2.128	1.88	$145 \pm 14$
850	2.128	1.50	$105 \pm 19$
847	3.19	1.90	$106 \pm 20$
855	3.42	1.52	$107 \pm 19$
859	5.32	1.70	$96 \pm 16$
809	6.65	1.68	$238 \pm 17$
810	6.65	1.69	$144 \pm 24$
812	6.65	1.86	$63 \pm 24$
860	13.30	2.06	$107 \pm 18$
864	26.60	1.78	$103 \pm 28$
866	26.60	2.10	$193 \pm 17$
869	26.60	2.02	$106 \pm 27$
870	26.60	2.38	$50 \pm 35$
871	26.60	2.25	$277 \pm 22$
872	26.60	2.42	$129 \pm 30$
861	67.96	2.21	$108 \pm 20$



The rate of adsorption may then be written as

$$v_1 = k_1 P (1 - \theta)^2 \quad [5]$$

and the rate of desorption is

$$v_{-1} = k_{-1} \theta^2 \quad [6]$$

At equilibrium the rates are equal and

$$\frac{\theta}{1 - \theta} = \left( \frac{k_1 P}{k_{-1}} \right)^{1/2} = (KP)^{1/2} \quad [7]$$

Upon rearranging Eq. [7] becomes

$$\theta = \frac{(KP)^{1/2}}{1 + (KP)^{1/2}} \quad [8]$$

The pressure dependence of the surface coverage is shown in Fig. 7. At high pressures  $\theta$  is independent of pressure while at low pressures  $\theta \approx (KP)^{1/2}$ .

In considering the hydriding of plutonium powder

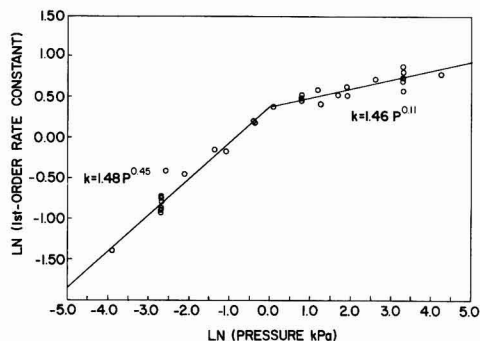
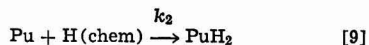


Fig. 6. Effect of hydrogen pressure on plutonium powder hydriding rates with temperatures varying between  $5^\circ$  and  $315^\circ\text{C}$ .



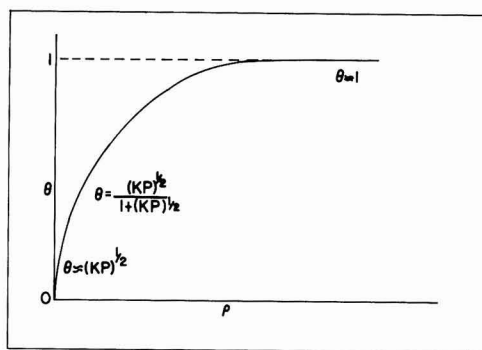


Fig. 7. Variation in surface coverage as a function of pressure for Langmuir-type adsorption.

the temperatures were kept sufficiently low so that the reverse decomposition reaction was negligible. The rate of hydriding has been found to follow a first-order process. If the rate of hydriding is proportional to the hydrogen surface coverage the first-order rate is

$$k_{\text{hyd}} = k_2 \theta \quad [10]$$

or

$$k_{\text{hyd}} = \frac{k_2 (KP)^{1/2}}{1 + (KP)^{1/2}} \quad [11]$$

The relationship given in Eq. [11] has exactly the same form as seen in Fig. 7. At pressures less than 0.02 kPa  $(KP)^{1/2} < 1$ , Eq. [11] becomes

$$k_{\text{hyd}} = k_2 (KP)^{1/2} \quad [12]$$

where the rate of hydriding is proportional to  $P^{1/2}$  and adsorption is rate determining. At high pressures ( $>1000$  kPa) where  $(KP)^{1/2} > 1$  Eq. [11] becomes

$$k_{\text{hyd}} = k_2 \quad [13]$$

Under these conditions the hydriding rate is equal to  $k_2$  and is independent of hydrogen pressure. This behavior has been observed for the hydriding of plutonium-1 w/o gallium powder as illustrated in Fig. 6.

Equation [11] can be tested for the hydriding of plutonium powder by rearranging to the form

$$\frac{P^{1/2}}{k_{\text{hyd}}} = \frac{1}{k_2 K^{1/2}} + \frac{P^{1/2}}{k_2} \quad [14]$$

Plotting  $P^{1/2}/k_{\text{hyd}}$  against  $P^{1/2}$  gives a straight line with the slope  $1/k_2$ . Such a plot is shown in Fig. 8. From an evaluation of the data  $k_2$  was found to be 2.69

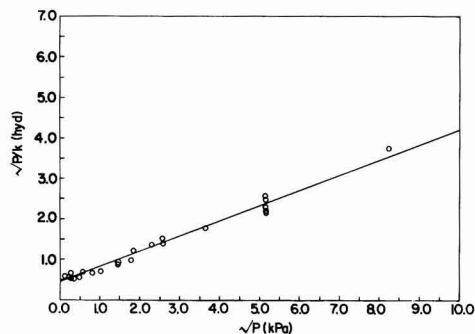


Fig. 8. Modified Langmuir plot for the pressure dependence of plutonium-1 w/o gallium hydriding rates on the hydrogen pressure.

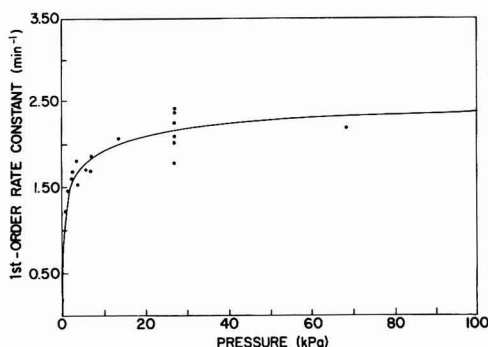


Fig. 9. Variation of experimental and predicted plutonium-1 w/o gallium powder hydriding rates with pressure.

$\text{min}^{-1}$  and  $K$  was equal to  $0.66 \text{ kPa}^{-1}$ . Using these constants hydriding rates have been predicted over the pressure range 0–100 kPa. Results are shown by the solid line in Fig. 9. Predicted rates obtained from Eq. [11] are in good agreement with the experimental values from 0 to 70 kPa.

### Conclusions

The reaction kinetics for the hydriding of plutonium-1 w/o gallium were measured using a metal powder prepared "in situ." This technique successfully minimized oxide formation which introduces a predominant hydride nucleation and growth step in the reaction sequence. Powder hydriding was found to be independent of temperature from  $-29^\circ$  to  $355^\circ\text{C}$ . Hydriding rates exhibited a hydrogen pressure dependence which could be described by a modified Langmuir equation. At pressures less than 1 kPa rates were proportional to  $P^{1/2}$  indicating dissociative adsorption of hydrogen was rate controlling. Above 1 kPa the pressure dependency decreased with complete independence being predicted at about 1000 kPa. In the high pressure region the rates are reaction controlled.

### Acknowledgment

This work was performed under the auspices of U.S. Department of Energy Contract DE-AC04-76DP03533.

Manuscript submitted Jan. 13, 1981; revised manuscript received May 22, 1981.

Any discussion of this paper will appear in a Discussion Section to be published in the June 1982 JOURNAL. All discussions for the June 1982 Discussion Section should be submitted by Feb. 1, 1982.

Publication costs of this article were assisted by Rockwell International.

### REFERENCES

1. R. N. R. Mulford and G. E. Sturdy, *J. Am. Chem. Soc.*, **77**, 3449 (1955).
2. R. N. R. Mulford and G. E. Sturdy, *ibid.*, **78**, 3897 (1956).
3. J. M. Haschke, A. E. Hodges III, C. M. Smith, and F. L. Oetting, *J. Less-Common Metals*, **73**, 41 (1980).
4. S. Takeuchi and K. Suzuki, *Trans. Jpn. Inst. Metals*, **3**, 41 (1962).
5. C. Colmenares and C. Alexander, "Heat of Formation of Plutonium Hydrides," U.S. AEC Report UCID-16799, Lawrence Livermore Laboratory, Livermore, CA (1975).
6. I. B. Johns, "Plutonium Hydride and Deuteride," U.S. AEC Report MDCC-717, Argonne National Laboratory, Argonne, IL (1944).
7. M. I. Ivanov and N. S. Podolskaya, *Russ. J. Phys. Chem.*, **45**, 1682 (1971).
8. D. F. Bowersox, "The Reaction between Plutonium and Deuterium Part I. Rate Measurements by

- Pressure Changes," U.S. AEC Report LA-5515-MS, Los Alamos Scientific Laboratory (1974).
9. D. F. Bowersox, "The Reaction between Plutonium and Deuterium Part II. Rate Measurements by Weight Changes," U.S. AEC Report LA-6681-MS, Los Alamos Scientific Laboratory (1977).
  10. C. A. Colmenares, Lawrence Livermore National Laboratory, Unpublished data (1980).
  11. J. M. Haschke and J. L. Stakebake, in "The Rare Earths in Science and Technology," Vol. 2, G. J. McCarthy, J. J. Rhyne, and H. B. Silber, Editors, p. 577, Plenum Publishing Co., New York (1980).
  12. D. T. Larson and J. M. Haschke, *J. Inorg. Chem.*, in press.
  13. J. L. Stakebake, *This Journal*, **126**, 1596 (1979).
  14. S. Brunauer, P. H. Emmett, and E. Teller, *J. Am. Chem. Soc.*, **60**, 309 (1938).
  15. J. L. Stakebake and G. E. Bixby, "Evaluation of Reaction Kinetics for Gas-Powder System," U.S. DOE Report RFP-2849, Rockwell International, Golden, CO (1979).
  16. C. Bonnelle and G. Lachere, in "Plutonium 1975 and Other Actinides," H. Blank and R. Linder, Editors, North-Holland Publishing Co., Amsterdam (1976).
  17. J. W. Ward, Personal communication (1980).
  18. J. M. Haschke, Personal communication (1980).
  19. M. Langmuir, *J. Am. Chem. Soc.*, **40**, 1361 (1918).

## Effects of Heat-Treatment on Indium-Tin Oxide Films

F. T. J. Smith\* and S. L. Lyu

*Eastman Kodak Company, Research Laboratories, Rochester, New York 14650*

### ABSTRACT

Highly conductive and transparent films of indium-tin oxide have been sputter-deposited from an oxide target. The effects of annealing in oxidizing or reducing atmospheres on the electrical and optical properties of these films have been determined. The electron concentration and related optical properties are reversible functions of the oxygen partial pressure in the annealing atmosphere. The form of this relationship is consistent with a defect model in which most of the Sn dopant is present in neutral complexes with interstitial oxygen. The Hall mobility and refractive index are changed irreversibly by annealing as a result of subtle changes in film structure.

Highly transparent and electrically conducting thin films are useful in a wide variety of applications, for example, transparent Joule heating elements, infrared-reflecting coatings transparent in the visible, and transparent electrodes allowing optical and electrical access to solid-state devices. The oxides of Cd, In, Sn, and Sb have usually been found to have the best combination of properties (1). In particular, films of indium oxide containing some tin oxide are widely used where sheet resistances of less than 10  $\Omega/\text{sq}$  are required.

Films of indium-tin oxide (ITO) can be prepared by spray hydrolysis, but for most electronic applications, sputtering, evaporation, or chemical vapor deposition methods are necessary to achieve the required uniformity. Sputtered films have been prepared by using either conventional sputtering from hot-pressed oxide targets (2) or reactive sputtering from metal targets (3). With oxide targets the optimum composition has been reported to be 5-20 mol percent (m/o)  $\text{SnO}_2$  in  $\text{In}_2\text{O}_3$  (4).

The properties of these films are sensitive to the preparation conditions, in particular the oxygen partial pressure in the sputtering atmosphere (5). Film properties can also be modified by annealing in either oxidizing or reducing atmospheres. It would therefore be desirable to develop an understanding of the effects of film structure and stoichiometry on electrical conductivity and optical transmission. This has been achieved to some extent for pure  $\text{In}_2\text{O}_3$  films (6, 7). In the presence of Sn, however, the situation is much more complex. Precipitation of metallic clusters (8) or possibly an  $\text{Sn}_3\text{O}_4$ -like phase (9) has been reported in some situations. Although the presence of tin leads to a higher conductivity, it is not clear what its role is or

what the mechanism is for the changes in conductivity observed when these films are annealed.

We will present results obtained for films deposited by rf sputtering from a hot-pressed oxide target. Deposition parameters have been optimized to yield films having high electrical conductivity and transparency. We will not describe the dependence of film properties on sputtering parameters in detail, since our results are similar to those reported previously (10). Instead, the results of annealing ITO films at various partial pressures of oxygen will be discussed. We will show that, if the films are not reduced to the point of producing a metallic phase, the effect of annealing on conductivity is a reversible function of oxygen partial pressure. These changes in conductivity can be interpreted in terms of the formation of neutral clusters of tin with interstitial oxygen. Annealing also affects the optical properties of these films, in some cases reversibly, as a result of their relationship to the free-carrier concentration.

### Experimental Methods

An rf diode sputtering system was used (Fig. 1). It has two notable features. First, the target is placed below the substrate so that material sputtered upward is collected. Second, the substrates were loaded through an evacuable load lock, thus avoiding exposure of the target to the atmosphere and preventing adsorption of moisture by the target material, which is somewhat hygroscopic. As a result the run-to-run reproducibility was very high after initial outgassing and presputtering of new targets. The sputtering chamber is a stainless steel cylinder pumped by an oil diffusion pump with a cold trap. System pressures of  $1 \times 10^{-7}$  to  $5 \times 10^{-8}$  Torr were typically obtained between runs. During sputtering, a throttle valve of fixed diameter was used to limit pumping speed, and both argon and

\* Electrochemical Society Active Member.

Key words: conductance, transmittance, sputtering.

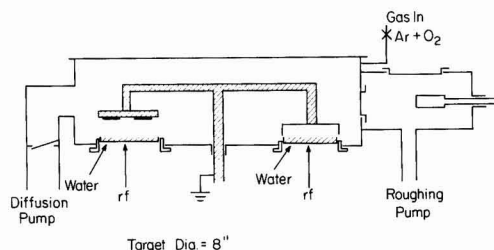


Fig. 1. RF diode sputtering system

oxygen of high purity were introduced to the chamber through metering valves.

A 20 cm diam hot-pressed disk of  $\text{In}_2\text{O}_3$  containing 9 m/o of  $\text{SnO}_2$  was used as a target. This was bonded to a water-cooled copper plate. The substrates were clamped into recesses in a 3 mm thick aluminum disk which in turn was bolted to a 12 mm thick copper plate. This plate acted as a heat sink. Either the substrates or a stainless steel shield could be rotated into position over the target. The target-to-substrate distance was 3.5 cm. To stabilize the system, presputtering onto the stainless steel shield was always done for 30 min before deposition onto the substrates. With a new target, presputtering for 8-12 hr was necessary before film properties became reproducible from run to run. An increased outgassing rate was observed during the first few hours of this procedure.

Polished fused quartz disks 5 cm in diameter and 0.05 cm thick were used as substrates. These were cleaned using ammonia-hydrogen peroxide and hydrochloric acid-hydrogen peroxide mixtures (11).

Optical measurements were made at near-normal incidence using a Cary 14 two-beam spectrophotometer in the visible and near-infrared region and a Beckman AR10 spectrophotometer in the 2-10  $\mu\text{m}$  range. Sheet resistances were measured using a four-point tungsten probe, and both sheet resistance and Hall coefficients were measured by the van der Pauw method. Good agreement ( $\pm 5\%$ ) was found between the two methods for sheet resistance. For the van der Pauw measurements the films were etched into a cloverleaf pattern by using conventional photolithography with hot hydriodic acid as an etchant (12). Silver paste contacts were used.

The measurements were made using a-c current and a d-c magnetic field of 4.3 koe. In some cases electrical measurements were made at high temperatures at various oxygen partial pressures, also by the van der Pauw method. To do this the samples were enclosed in a quartz tube in a furnace placed between the poles of an electromagnet. Mixtures of argon with traces of oxygen were passed through the tube, and the oxygen concentration in the exit gas was measured with a commercial solid-state oxygen meter. For these high temperature measurements, pressure contacts were made by spring-loaded nickel wires. Film thickness was measured by using a profilometer to determine the average height of an etched film edge. Annealing was done in a horizontal tube furnace. The annealing ambient was established by placing the samples in a quartz tube and flowing the appropriate gas over them at  $\sim 0.5$  cm/sec.

### Results and Discussion

A series of films 5000-10,000 Å thick were deposited while sputtering parameters such as gas composition and pressure, power, and substrate-target spacing were varied so as to optimize film properties. That is, these parameters were varied to obtain the highest ratio of visible-wavelength transmission to sheet resistance for films in this thickness range.

Films sputtered in an atmosphere containing a few percent of oxygen had a high resistivity. For example, films  $\sim 7000$  Å thick deposited at a power of 500W in an argon plus 5% oxygen atmosphere at a total pressure of  $2 \times 10^{-2}$  Torr had a sheet resistance of  $2.5 \times 10^3 \Omega/\text{sq}$ . In contrast, films of this thickness deposited in pure argon under the same conditions had a sheet resistance of  $\sim 5 \Omega/\text{sq}$ . Sheet resistance decreased with increase in sputtering power, as reported previously (10). Thus the sheet resistance of films  $\sim 7000$  Å thick deposited from pure argon at  $2 \times 10^{-2}$  Torr decreased from  $\sim 9 \Omega/\text{sq}$  at 200W to  $\sim 4 \Omega/\text{sq}$  at 600W.

Repeated presputtering and deposition in pure argon gradually reduced part of the target surface, as evidenced by the development of a very dark metallic appearance. Films deposited from such a target had sheet resistances a factor of two or more higher than those from a fresh target surface obtained by abrading away the darkened surface layers. Similar observations have been reported elsewhere (2). Presputtering at a reduced power of 300W in a 50%  $\text{O}_2$  plus 50% Ar atmosphere prevented this darkening, apparently by reoxidation of the target surface. Presputtering was therefore always carried out under these conditions for 30 min before each deposition run. Changing the presputtering atmosphere to pure argon for 1-10 min before film deposition had no effect on film properties. Several hours of deposition in pure argon were required before significant reduction of the target occurred, so that only minor changes in target condition would be expected during a single deposition run.

On the basis of these results, all subsequent films were deposited at 500W in a pure argon atmosphere, pressure  $2 \times 10^{-2}$  Torr, after presputtering in an argon-oxygen mixture as described. The oxygen flow was stopped  $\sim 3$  min before deposition was begun. With this procedure, sheet resistances were reproducible to within  $\pm 5\%$  from run to run. Figure 2 shows the sheet resistance of deposited films and the optical transmission at 500 nm, after averaging interference fringes, both as functions of the total deposition time. Under these conditions the deposition rate was 8.5 Å/sec, so that the film thickness increased from 5100 Å after 10 min to 30,600 Å after 60 min. The sheet resistance correspondingly decreased, reaching a value of less than  $1 \Omega/\text{sq}$  after 60 min. The transmission, on the other hand, increased for the first 25 min of deposition and at this point was limited only by the reflectivity of the film. The decrease in transmission of thicker films is presumably due to bulk absorption adding to reflection losses. The decrease at short times is not understood.

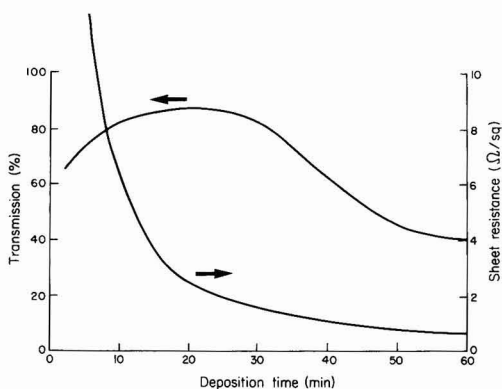


Fig. 2. Dependence of sheet resistance and transmission at 500 nm on total deposition time in  $2.0 \times 10^{-2}$  Torr Ar at 500W power.

If the higher resistivity of films deposited in Ar-O<sub>2</sub> mixtures were due only to differences in carrier concentration resulting from differences in oxygen content, it should be possible to bring all films to the same resistivity by equilibrating them with the same oxidizing or reducing atmosphere. This should take place at a temperature sufficient to allow rapid oxygen diffusion within the bulk of the film. In fact, when films were annealed at 200°C, the resistivity did change and equilibrium was reached within ~30 min. Figure 3 shows the sheet resistance of a relatively resistive film as a function of time at 200°C in nitrogen containing ~20 ppm of oxygen. This film was deposited in an Ar + 5% O<sub>2</sub> mixture. The equilibrium sheet resistance for several films is shown in Fig. 4 as a function of anneal conditions. These data were obtained using films ~8000 Å thick deposited in pure argon, giving an as-deposited sheet resistance of 3.5 Ω/sq (curves a), and at oxygen levels of 5% (curves b) and 10% (curves c), resulting in as-deposited sheet resistances of ~2200 and 7000 Ω/sq, respectively. The coated disks were cleaved into halves, and the halves were annealed in either N<sub>2</sub> + 200 ppm O<sub>2</sub> (broken lines in Fig. 4) or N<sub>2</sub> + 10% H<sub>2</sub> + 50 ppm H<sub>2</sub>O (solid lines). Anneals were carried out for 30 min at 100°C and repeated at 100°C intervals above this. The sheet resistances decreased with increasing anneal temperature, approaching each other and reaching a minimum at 300°-500°C. At higher temperatures the sheet resistance increased rapidly and the films acquired a dark metallic appearance, indicating reduction of the oxides to a metallic phase. The fact that all samples did not reach the same resistivity indicates that simple differences in initial oxygen stoichiometry do not entirely explain the increase in resistivity for films deposited at the higher oxygen levels. Differences in structure were therefore looked for which could explain these differences in resistivity.

Figure 5 is an SEM picture of the surface of a film ~8000 Å thick. This particular film was deposited in

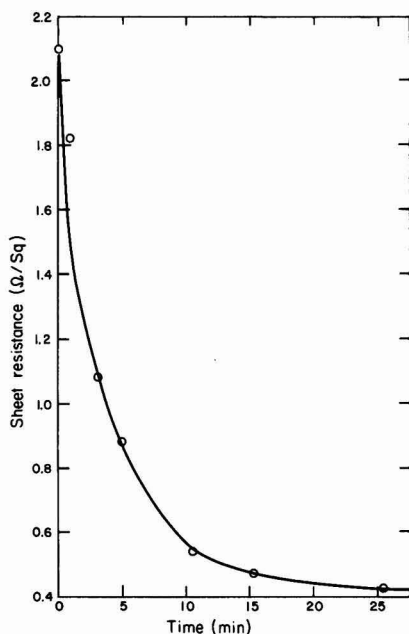


Fig. 3. Dependence of sheet resistance on anneal time at 200°C in nitrogen.

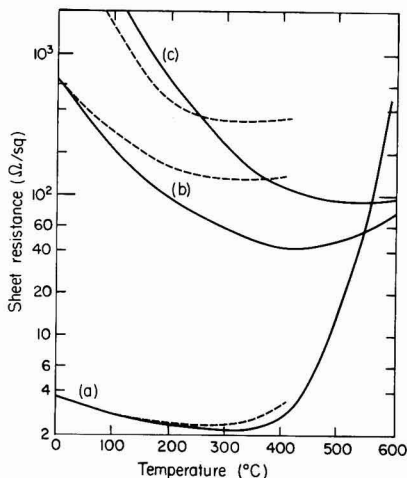


Fig. 4. The equilibrium sheet resistance as a function of temperature for films annealed in N<sub>2</sub> (broken lines) or N<sub>2</sub> + 10% H<sub>2</sub> (solid lines).

pure Ar, but an apparently identical surface morphology is seen for films sputtered in Ar-O<sub>2</sub> mixtures. The films consist of crystallites 1000-2000 Å in diameter which form the rounded hillocks seen in Fig. 5. This structure is very similar to that reported by Fraser and Cook (2) for d-c-sputtered films. Cleaved cross sections of similar films were also examined by SEM. Although this instrument was operating near the limit of resolution, a columnar grain structure could be seen with grain boundaries extending perpendicularly from the film surface to the substrate. X-ray diffraction spectra show the films to have the bcc In<sub>2</sub>O<sub>3</sub> structure. All films had a predominantly [100] texture with a lesser tendency to a [111] orientation. The O<sub>2</sub> level in the sputtering atmosphere had no effect on this surface appearance or orientation. Both [111] (2) and [100] (4) orientations have been reported. The lattice parameter was 10.17 Å for all ITO films, as compared with 10.12 Å for In<sub>2</sub>O<sub>3</sub> deposited from a pure In<sub>2</sub>O<sub>3</sub> target in the same system. Fan *et al.* (5) found the lattice parameter  $a = 10.23$  Å for highly transparent films and an apparently different phase with  $a = 10.15$  Å in dark films deposited at low oxygen level. These authors used a target containing 15 m/o SnO<sub>2</sub> compared with 9 m/o in the present work. The present films presumably correspond with their transparent films, the re-

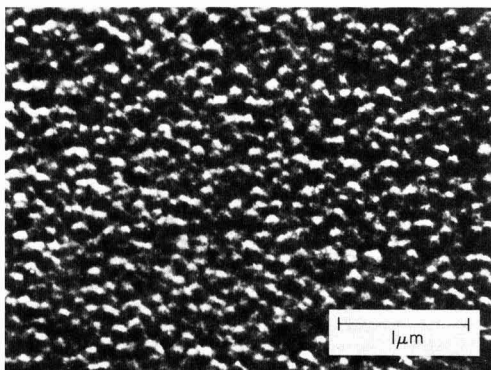


Fig. 5. SEM micrograph of film surface

duction in  $a$  from 10.23 to 10.17 Å resulting from the reduced Sn concentration. Anneals at 400°C in either  $N_2$  or  $O_2$  for 30 min had no effect on either the surface appearance or the x-ray diffraction patterns of any of the films. Thus the differences in resistivity (Fig. 4) for films deposited at various oxygen levels and then all annealed at 400°C in the same atmosphere apparently result from differences in structure which are beyond the resolution of the methods we have used.

Hall coefficient measurements were made to characterize further the effects of annealing on low resistivity films. All films were n-type. The carrier concentration  $n$  was obtained from the Hall coefficient  $R$ , using the expression  $R = r/ne$ . The Hall factor  $r$  has been approximated by unity in view of the high electron concentrations. In any case, the absolute value of  $n$  is not critical to interpretation of the results. In early experiments it was observed that for a given film, if it was not reduced to a metallic phase, e.g., by heating in hydrogen at temperatures above 400°C,  $n$  is a reproducible function of the annealing atmosphere. For example, a series of anneals were carried out at 400°C on a single film ~12,000 Å thick under reducing, then oxidizing, and then again reducing conditions. The results are given in Table I. Annealing in reducing conditions increased  $n$  as compared with the as-deposited film. Annealing in oxygen reduced  $n$  to below its initial value. Subsequent anneals in mildly oxidizing, neutral, and reducing conditions increased  $n$  until it reached essentially the same value it had after the first anneal in reducing conditions. These changes in  $n$  could not be attributed to changes in the film or grain boundary structure, since such changes would not be reversible. On the other hand, the mobility decreased in most instances after annealing in either oxidizing or reducing atmospheres; this could be attributed to structural changes.

To determine whether surface effects are important to the annealing behavior, as has been suggested (13), measurements were made on films of various thicknesses. If the observed changes in  $n$  were due to a surface phenomenon, they would decrease in magnitude linearly with increases in film thickness. Figure 6 shows  $n$  for films ranging in thickness from ~3000 to ~18,000 Å. Results for both as-deposited films and films annealed at 400°C for 30 min in  $N_2 + 5\% H_2$  are shown. Before annealing, the results are quite strongly dependent on the film thickness. This is probably due to relatively small changes in the actual oxygen partial pressure during sputtering. An initial adsorption of oxygen from the sputtering atmosphere followed by a gradual release has been reported (5) in a similar system. At some point an optimum oxygen level was apparently reached, giving rise to the maximum in  $n$  observed. This variation is almost totally removed by the anneal, indicating the result of such anneals to be a bulk effect for these films. However, note that, although the dependence of  $n$  on deposited-film thickness can be removed by annealing, variations in doping level from substrate to surface could exist. It has been reported that the surface of as-deposited ITO films may be tin-rich (9). This could be true for our annealed films but only if the tin-rich layer increased in

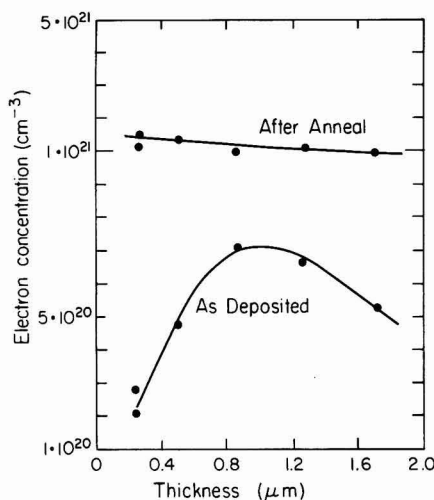


Fig. 6. Electron concentration vs. film thickness for both as-deposited films and films annealed for 30 min at 400°C in  $N_2 + 5\% H_2$ .

thickness linearly with increases in total film thickness so that the average value of  $n$  remained constant, the result shown in Fig. 6.

To summarize these observations,  $n$  is uniquely determined by the temperature and composition of the annealing ambient for a particular film, if it is not reduced enough to cause a phase change, for example, by annealing under strongly reducing conditions above 450°C. Furthermore, the changes in  $n$  caused by annealing result from a bulk effect. To determine  $n$  as a function of the oxygen partial pressure  $p_{O_2}$ , conductivity and Hall coefficient were measured by the van der Pauw method at high temperatures while samples were held in a flowing argon-oxygen mixture. The range of temperatures over which measurements could be made was small, because below 250°C changes occurred too slowly and above 450°C the films were easily reduced and darkened or developed cracks after a few hours at high temperature. Figure 7 shows equilibrium values of  $n$  as a function of  $p_{O_2}$  at 320° and 400°C for a film 8300 Å thick. The mobilities at these temperatures were 15.3 and 14.3  $cm^2/Vsec$ , respectively, and were independent of  $n$ . Over a wide range of  $p_{O_2}$ ,  $n$  is proportional to  $p_{O_2}^{-m}$ . Measurements at intermediate temperatures overlap these but are of the same form with  $m = 0.14 \pm 0.01$ . The same type of relationship but with  $m = 0.166$  has been reported for pure sintered  $In_2O_3$  powder above 600°C (13). The values of  $n$  reported for pure  $In_2O_3$  are, however, several orders of magnitude below those shown in Fig. 7 for a tin-doped film.

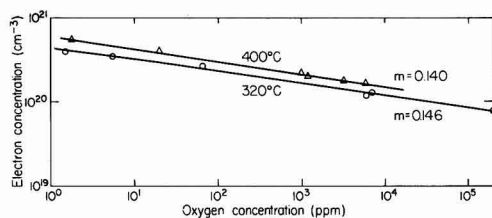


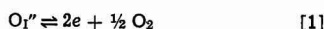
Fig. 7. Equilibrium carrier concentration as a function of oxygen partial pressure for a film 8300 Å thick. Lines show fit to  $n \sim p_{O_2}^{-m}$  with values of  $m$  given.

Table I. Results of a series of anneals at 400°C on an ITO film 12,000 Å thick

Atmosphere	Time (min)	Electron concentration ( $cm^{-3}$ )	Mobility ( $cm^2/Vsec$ )
As deposited		$5.69 \times 10^{20}$	27.9
$N_2 + 5\% H_2$	30	$1.18 \times 10^{21}$	18.8
$O_2$	150	$1.96 \times 10^{20}$	4.81
$N_2 + 1\% O_2$	60	$2.37 \times 10^{20}$	5.24
$N_2$	120	$3.75 \times 10^{20}$	4.97
$N_2 + 5\% H_2$	120	$1.21 \times 10^{21}$	2.16



In undoped  $\text{In}_2\text{O}_3$  this behavior was attributed to the presence of oxygen vacancies which act as doubly ionized donors and are the dominant contributors to  $n$  (13). In the present case this is obviously not the situation since the presence of Sn in the lattice has increased  $n$  substantially. On the other hand, if all of the Sn simply substituted for In and donated one electron, then  $n$  would be equal to the total tin concentration, i.e.,  $n = [\text{Sn}_{\text{In}}] = [\text{Sn}]_{\text{T}} \approx 1.4 \times 10^{21}/\text{cm}^3$ , and independent of  $p_{\text{O}_2}$ . In fact, the measured values of  $n$  are much less than the total tin concentration, as noted previously for tin concentrations above a few percent (14). In the  $\text{In}_2\text{O}_3$  structure,  $\text{O}^{2-}$  ions occupy only  $3/4$  of the tetrahedral interstices formed by the  $\text{In}^{3+}$  ion lattice. It might be expected, therefore, that additional oxygen ions could be accommodated easily into the remaining interstices and act as double acceptors to compensate any  $\text{Sn}^{4+}$  ions introduced onto  $\text{In}^{3+}$  sites. The oxygen partial pressure would then influence  $n$  through the reaction

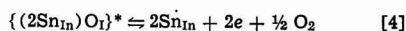


$$K_1 = \frac{n^2 p_{\text{O}_2}^{1/4}}{[\text{O}_i']} \quad [2]$$

Since  $n \ll [\text{Sn}]_{\text{T}}$ , i.e.,  $n \ll 1.4 \times 10^{21}/\text{cm}^3$  over the range of our measurements, most of the  $\text{Sn}_{\text{In}}$  is compensated, therefore,  $2[\text{O}_i'] \approx [\text{Sn}]_{\text{T}}$ . Substituting this into Eq. [2] gives

$$n \approx \left( \frac{K_1 [\text{Sn}]_{\text{T}}}{2} \right)^{1/2} p_{\text{O}_2}^{-1/4} \quad [3]$$

Obviously the value of  $m = 1/4$  predicted by this model does not agree with our results. Making the assumption that interstitial oxygen can accept only one electron leads to  $n \sim p_{\text{O}_2}^{-1/2}$ , in even worse agreement with experiment. On the other hand, if the  $\text{Sn}^{4+}$  ions form pairs in association with the extra oxygen ion to form a neutral complex of local stoichiometry  $\text{Sn}_2\text{O}_4$ , this could be reduced at low oxygen levels to give pairs of  $\text{Sn}_{\text{In}}$  donors



$$K_2 = \frac{[\text{Sn}_{\text{In}}]^2 n^2 p_{\text{O}_2}^{1/4}}{[\{(2\text{Sn}_{\text{In}})\text{O}_i\}]} \quad [5]$$

Since most of the Sn is not electrically active,  $[\{(2\text{Sn}_{\text{In}})\text{O}_i\}] \approx [\text{Sn}]_{\text{T}}/2$ , and since on the other hand  $\text{Sn}_{\text{In}}$  is the dominant donor,  $n \approx [\text{Sn}_{\text{In}}]$ . Substituting these approximations into Eq. [5] gives

$$n \approx \left( \frac{K^2 [\text{Sn}]_{\text{T}}}{2} \right)^{1/4} p_{\text{O}_2}^{-1/4} \quad [6]$$

i.e.,  $m = 0.125$ , in reasonable agreement with the value  $0.14 \pm 0.01$  obtained from our high temperature measurements. Clusters of more than two  $\text{Sn}^{4+}$  ions may be expected at higher Sn levels until a distinct separate  $\text{SnO}_2$  phase is formed. The fact that the conductivity of films deposited at a high oxygen level can never be increased by annealing to as high a value as for films deposited in pure argon could be attributed to a much greater degree of formation of large  $\text{SnO}_2$ -like complexes of this type during deposition as a result of the greater oxygen ion availability. Fan *et al.* (5) have shown in detail the effect on  $n$  of oxygen level in the sputtering atmosphere. They report  $n$  to decrease very steeply with increases in oxygen partial pressure in the region where highly transparent single phase deposits were obtained, also indicating the formation of neutral complexes under oxidizing conditions.

All films were highly transparent in the visible region. The transmission spectrum for a film  $\sim 8000\text{\AA}$

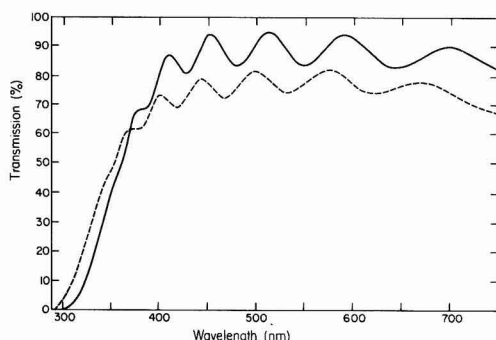


Fig. 8. Transmission spectrum for film  $\sim 8000\text{\AA}$  thick, as-deposited (solid line) and after 30 min anneal at  $400^\circ\text{C}$  in  $\text{N}_2 + 10\% \text{H}_2$  (broken line).

thick (Fig. 8) shows an absorption edge at 300–350 nm and interference fringes at longer wavelengths. Figure 8 also shows the spectrum after this film was annealed in  $\text{N}_2 + 10\% \text{H}_2$  at  $400^\circ\text{C}$  for 30 min. This anneal increased  $n$  from  $5.76$  to  $11.2 \times 10^{20}/\text{cm}^3$ . It also reduced the optical transmission, shifted the absorption edges, and shifted the interference fringes. Transmission was reduced as a result of any anneal in either oxidizing or reducing atmospheres. The refractive index, calculated from the spacing between interference fringes, was also reduced by any annealing procedure. Figure 9 shows the refractive index for both the as-deposited and annealed films of Fig. 8. The reduction in index resulting from annealing is surprisingly large.

The shift in the short-wavelength absorption edge depended on the nature of the annealing atmosphere in the same way that  $n$  does, i.e., anneals in reducing and oxidizing atmospheres gave shifts in opposite directions. Figure 10 shows the shifts in the absorption edge of a single film resulting from a series of anneals and the electron concentrations resulting from each anneal. At values of  $\alpha$  above  $10^3 \text{ cm}^{-1}$ , the square of the absorption coefficient is linearly proportional to the photon energy. A relationship of this sort is expected for direct allowed transitions and has been reported for pure  $\text{In}_2\text{O}_3$  films (15). By extrapolating the linear regions to zero absorption coefficient, values of the apparent direct gap were obtained. Figure 11 shows these results as a function of electron concentration. A linear relationship is observed between  $n^{2/3}$  and the apparent gap, as would be expected if this shift can be attributed to the Moss-Burstein effect (16). In the

case of parabolic bands the shift  $\Delta E = \frac{h^2}{8m} \left( \frac{3n}{\pi} \right)^{2/3}$ .

If the effective electron mass  $m_e$  is much smaller than the effective hole mass, then  $m \approx m_e$ . With this assumption, the data of Fig. 11 give  $m_e = 0.64 m_0$ . This

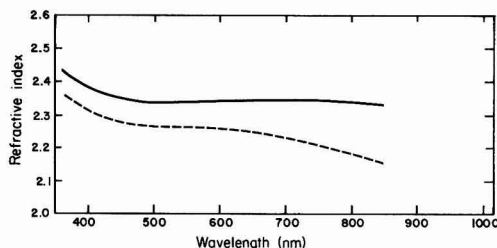


Fig. 9. Refractive index of film  $\sim 8000\text{\AA}$  thick, as deposited (solid line) and after 30 min anneal at  $400^\circ\text{C}$  in  $\text{N}_2 + 10\% \text{H}_2$  (broken line).



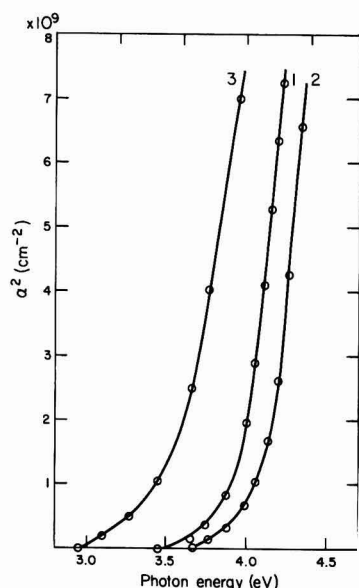


Fig. 10. Energy dependence of square of absorption coefficient for film  $\sim 8000 \text{ \AA}$  thick. Curve 1: as deposited,  $n = 5.76 \times 10^{20} / \text{cm}^3$ ; curve 2: after 30 min  $400^\circ\text{C}$  anneal in  $\text{N}_2 + 10\% \text{ H}_2$ ,  $n = 11.2 \times 10^{20} / \text{cm}^3$ ; curve 3: after 150 min  $400^\circ\text{C}$  anneal in  $\text{O}_2$ ,  $n = 1.96 \times 10^{20} / \text{cm}^3$ .

can be compared with somewhat lower reported values of  $0.54 m_0$  (14) and  $0.5 m_0$  (17) obtained by varying the Sn concentration to vary  $n$ . Since Sn doping at the high levels used would be expected to shift the absorption edge to shorter wavelengths (as a result of the alloying effect), by an amount proportional to the Sn concentration (Vegard's law) this method would be expected to underestimate  $m_0$ . Recently a value of  $0.55 m_0$  was reported by others also using the annealing method to vary  $n$  (18).

The optical properties in the infrared depend strongly on  $n$ . Figure 12 shows the transmission and reflection spectra of an as-deposited film  $\sim 4000 \text{ \AA}$  thick having  $n = 3.8 \times 10^{20} / \text{cm}^3$ . As discussed in detail

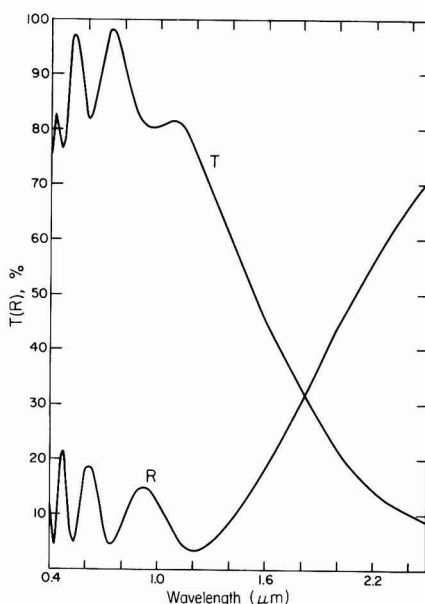


Fig. 12. Transmission  $T$  and reflectivity  $R$  in the infrared for a film  $\sim 4000 \text{ \AA}$  thick with  $n = 3.8 \times 10^{20} / \text{cm}^3$ .

previously (10, 14), free-carrier absorption dominates the optical properties at wavelengths longer than the plasma wavelength, which is  $\sim 1.8 \mu\text{m}$  for this particular film.

From the reflectivity and transmission data for both as-deposited and  $\text{N}_2 + \text{H}_2$  annealed films, the value of the optical absorption coefficient  $\alpha$  was calculated over a range of photon energies of  $0.5\text{--}4.5 \text{ eV}$  (Fig. 13). Both the Moss-Burstein shift at higher energies and

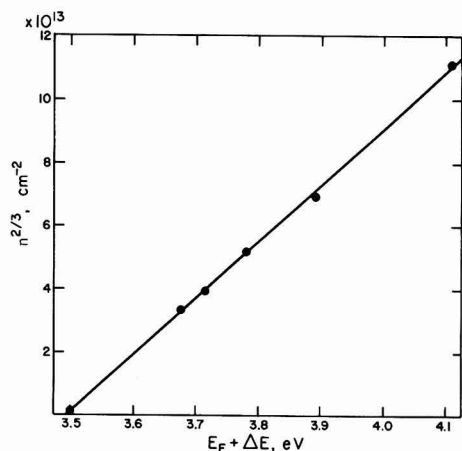


Fig. 11. Dependence of absorption edge on  $n^{2/3}$

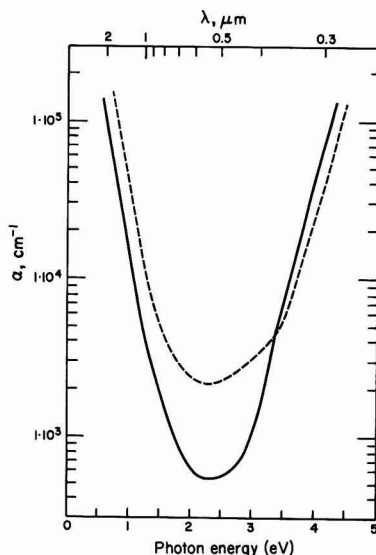


Fig. 13. Absorption coefficient  $\alpha$  as a function of photon energy for as-deposited films (solid line) and after 30 min  $400^\circ\text{C}$  anneal in  $\text{N}_2 + 10\% \text{ H}_2$  (broken line).

the opposite shift at low energies due to the change in plasma frequency are illustrated.

### Conclusions

Highly conductive and transparent films of ITO can be deposited from an oxide target by maintaining the target surface in an oxidized condition but depositing films from a pure argon ambient. The electron concentration in these films and properties which depend on it, such as the absorption edges, are affected reversibly when the films are annealed in mildly reducing or oxidizing conditions. This behavior can be rationalized in terms of the formation of neutral complexes of Sn with oxygen interstitials. Other properties, such as the electron Hall mobility and the refractive index, change nonreversibly, apparently because of permanent structural changes.

### Acknowledgments

We are grateful to L. R. Spaulding for the x-ray diffraction results and to L. E. Brady for application of the SEM.

Manuscript submitted June 3, 1980; revised manuscript received June 4, 1981.

Any discussion of this paper will appear in a Discussion Section to be published in the June 1982 JOURNAL. All discussions for the June 1982 Discussion Section should be submitted by Feb. 1, 1982.

Publication costs of this article were assisted by Eastman Kodak Company.

### REFERENCES

1. J. L. Vossen, in "Physics of Thin Films," Vol. 9, G. Hass, M. F. Francombe, and R. W. Hoffman, Editors, Academic Press, New York (1977).
2. D. B. Fraser and H. D. Cook, *This Journal*, **119**, 1368 (1972).
3. W. W. Molzen, *J. Vac. Sci. Technol.*, **12**, 99 (1975).
4. J. L. Vossen, *RCA Rev.*, **32**, 289 (1971).
5. J. C. C. Fan, F. J. Bachner, and G. H. Foley, *Appl. Phys. Lett.*, **31**, 773 (1977).
6. R. Groth, *Phys. Status Solidi*, **14**, 69 (1966).
7. H. K. Müller, *ibid.*, **27**, 723 (1968).
8. W. G. Haines and R. H. Bube, *J. Appl. Phys.*, **49**, 304 (1978).
9. J. C. C. Fan and J. B. Goodenough, *ibid.*, **48**, 3524 (1977).
10. J. C. C. Fan and F. J. Bachner, *This Journal*, **122**, 1719 (1975).
11. W. Kern and D. A. Puotinen, *RCA Rev.*, **31**, 187 (1970).
12. G. Bradshaw and A. J. Hughes, *Thin Solid Films*, **33**, L5 (1976).
13. J. H. W. deWit, G. van Unen, and M. Lahey, *J. Phys. Chem. Solids*, **38**, 819 (1977).
14. H. Kostlin, R. Jost, and W. Lems, *Phys. Status Solidi*, **29**, 87 (1975).
15. R. L. Weiher and R. P. Ley, *J. Appl. Phys.*, **37**, 299 (1966).
16. T. S. Moss, "Optical Properties of Semiconductors," p. 46, Butterworths, London (1959).
17. V. M. Vainshtein and V. I. Fistul, *Sov. Phys. Semicond.*, **1**, 104 (1967).
18. Y. Ohhata, F. Shinoki, and S. Yoshida, *Thin Solid Films*, **59**, 255 (1979).

# On the Limits of the Filter Concept for Color TV Screens

K. Carl

*Philips GmbH Forschungslaboratorium Aachen, 5100 Aachen, Germany*

J. A. M. Dikhoff

*N. V. Philips' Gloeilampenfabrieken, Eindhoven, The Netherlands*

W. Eckenbach

*Philips GmbH Forschungslaboratorium Aachen, 5100 Aachen, Germany*

and H. G. Junginger

*N. V. Philips' Gloeilampenfabrieken, Heerlen, The Netherlands*

## ABSTRACT

The image contrast of color television tubes is reduced by the diffuse reflection of ambient light at the tube face. A recent method used to compensate this effect makes use of color filters, which are transparent to the phosphor light and absorb the rest of the visible spectrum. The subject of this paper is an investigation of the fundamental optical capability of the color filter concept. The main emphasis is placed on the sandwich system, involving a filter layer between the phosphor layer and the screen glass. Experiments were performed on  $5 \times 5$  cm<sup>2</sup> test samples, using a spectrophotometer for the reflection measurements and a scanning electron microscope for measuring the phosphor light output. They yield a gain in brightness contrast performance (BCP) of 15-28% for combinations of red or blue phosphors with commercially available inorganic filter pigments. The corresponding increase of brightness can be twice as high if the contrast is held constant. Model calculations, assuming isotropic light scattering within the powder layers and linear superposition of multiple reflections between adjacent layers, show good agreement with the experimental results. Ideal square filters yield a BCP gain of 100-120%, whereas a shift of real phosphor spectra or filter spectra along the wavelength axis only yields a gain of a few percent. The conclusion drawn is that the inorganic filter pigments used set a practical limit to the gain in BCP that can be achieved with the color filter concept. Some results on mixtures of phosphors and filters are included. The experimentally found BCP gain amounts to about 7-10%, i.e., only about one-half of the sandwich gain. A simplified model leads to approximately the same values. The different optical behavior of a color pigment in sandwich and mixture arrangements is apparently due to differences in the effective optical path length for ambient light and phosphor light.

Brightness and contrast are important parameters determining image quality in color television. Both can be improved by an enhanced light output. A further improvement of contrast, i.e., the ratio of useful (image) light to disturbing (reflected ambient) light becomes possible by lowering the tube reflection. This can be achieved, for example, by blackening the screen glass or by filling the empty space between phosphor areas with a black powder. A third method, which has recently come into use (1-3), involves spectral filtering. Each of the three phosphors (red, green, and blue) is combined with a suitable filter material, which is transparent in the spectral region of phosphor emission and absorbent in the rest of the visible spectrum. In this way the phosphor light is hardly if at all attenuated, while the ambient light is strongly reduced after being reflected at the tube face.

The color filter concept is explained in more detail in Fig. 1. In a normal, nonfilter tube (on the left) high-energy electrons out of the vacuum penetrate into the phosphor layer, where they are absorbed and generate visible light, which reaches the observer through the glass of the screen. The thin aluminum backing functions as a definite electrode and serves as a mirror for

the visible light. In the sandwich-type filter tube an additional filter layer is placed between each phosphor layer and the screen glass, which must be traversed by the phosphor light as well as by the light from the surrounding. These filter layers, usually inorganic color pigments, have to be applied with exactly the same geometry as the three-color phosphor dots or lines.

A filter effect similar to the sandwich arrangement can be achieved by mixing each phosphor with its corresponding color pigment. The mixture-type filter tube is preferred in practice because of its technological simplicity. Besides contrast improvement, the color filter concept offers the advantage of enlarging the selection of phosphors, because unsuitable chromaticity coordinates can to some extent be corrected by the filter. The quality gain as a result of color filtering is usually (1) expressed in terms of the brightness contrast performance (BCP), which is defined for the red, green, and blue color components, respectively, as follows

$$BCP = \left( \frac{B}{\sqrt{R}} \right)_{\text{with filter}} \bigg/ \left( \frac{B}{\sqrt{R}} \right)_{\text{without filter}} \quad [1]$$

Here  $B$  stands for the tube brightness per color and  $R$

Key words: cathodoluminescence, inorganic, reflectance, solids.

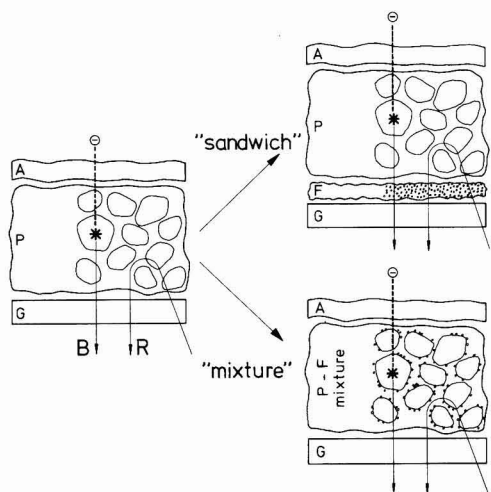


Fig. 1. Filter concept. Light-generating system of a normal, i.e., nonfilter tube (left) and of filter tubes with sandwich or mixture arrangement (right). A = aluminum, P = phosphor, F = filter, G = glass.

denotes the diffuse reflection of the tube for white ambient light, with the specular reflection at the first glass surface excluded. Both B and R are measured with a photopic detector.

The subject of this paper is an investigation of the fundamental optical capability of the color filter concept in color television. The main emphasis is on the sandwich system, results of which have not yet been published. Though somewhat less advantageous for fabrication than the mixture, the sandwich can be regarded as a model system with a more easily understandable mode of operation.

The measurements of the complete color filter systems are assisted by optical model calculations, based on spectrometer measurements on simplified systems, i.e., pigment layers on glass in the case of a sandwich and thick powder layers of pigmented phosphor in the case of a mixture. In the case of the mixture, satisfactory agreement between theory and experiment has not yet been achieved, probably because of greater complexity and additional interaction between phosphor and pigment particles. In the sandwich case, which generally shows greater BCP gains, reasonable agreement between theory and experiment is obtained. This agreement supports further predictions of the theory, i.e., selection of suitable color pigments and their appropriate concentration ranges and an estimate of the theoretical limits of the color filter concept.

### Experimental

**Sample preparation.**—All experiments were made with small test samples of  $5 \times 5 \text{ cm}^2$  with clear glass slides as substrates. Layers of phosphor or pigment were prepared by several techniques, the simplest one being sedimentation of a particle suspension in an organic liquid. Electrophoretic deposition is used especially for pigment suspensions, applying charging additives and an upward electrical field. In the lacquer technique some polymer, e.g., nitrocellulose, is incorporated in the suspension, so that a lacquer film can be prepared by centrifuging. Polyvinylalcohol plus ammonium dichromate (pva, adc) is another example of a lacquer material, which can be photohardened in the usual way (4), thereby facilitating the preparation of sandwiches.

Mixtures are prepared by coating the surface of the phosphor particles with pigment. The adherence of the pigment particles (typical diameter  $0.1 \mu\text{m}$ ) on the phosphor particles (diameter about  $5\text{--}10 \mu\text{m}$ ) is usually improved by the addition of latex. On top of the phosphor layer an aluminum film about  $0.2 \mu\text{m}$  thick is evaporated, supported by an auxiliary nitrocellulose film. Finally all volatile, organic components are removed by baking out at  $430^\circ\text{C}$ .

Investigated pigments are commercially available types of cobalt blue, ultramarine blue, cobalt green, green chromium oxide, cadmium red, and red iron oxide. Standard blue/green/red phosphors are used:  $\text{ZnS:Ag/(Zn,Cd)S:Cu}$  or  $\text{Y}_2\text{SiO}_5\text{:Tb/Y}_2\text{O}_3\text{:Eu}$ .

**Optical measurements.**—The light paths shown in Fig. 1 are only schematic. In reality pigment as well as phosphor particles strongly scatter light. Reliable measurements of their optical properties can therefore only be performed with goniophotometers or with spatially integrating detectors. We used the Zeiss DMR 21 automatic spectrophotometer including a  $150 \text{ mm}$  diam integrating sphere.

The measurements consisted of reflection of complete color filter systems of sandwich or mixture type (compare Fig. 1), reflection and transmission of pigment layers on glass slides, and reflection of pigmented phosphor in  $5 \text{ mm}$  glass cuvettes (so-called  $R_p$ ). Reflection values are related to the reflectivity of the  $\text{BaSO}_4$  standard. If necessary the influence of the cover glass is eliminated, according to the theory in the section on Theory Sandwich.

Measurements usually extend from  $380$  to  $800 \text{ nm}$  wavelength. With respect to phosphor emission and eye sensitivity the range from  $700$  to  $800 \text{ nm}$  is of less importance, but it serves as an additional control, providing nearly absorption-free regions. The continuous measurement values are digitized every  $10 \text{ nm}$  and fed into a computer.

**Brightness measurements.**—The brightness of the "glass-filter/phosphor-Al film" samples under cathode-ray excitation was measured in a scanning electron microscope (type: Philips PSEM 500). The excitation conditions were chosen in such a way as to simulate a "TV-like" phosphor load see (Table I). The light output, i.e., the brightness, was measured with a photopic detector (type: Osram-Si- $V_\lambda$  cell), the spectral sensitivity of which is well matched to the "eye sensitivity." This detector was incorporated into the PSEM and mounted close to the sample.

### Theory Sandwich

The optical action of a sandwich-type color filter tube takes place in the four-layer sandwich glass-filter-phosphor-aluminum (GFPA); compare Fig. 1. The main experimental variations concern the F-part. Because of the difficult preparation of a GFPA sandwich, an FG sandwich is a much more favorable test sample. In the following a model is presented, which

Table I. Conditions of electron beam excitation

	PSEM 500	30 AX tube
High voltage*	25 kV	25 kV
Beam current	$0.1 \mu\text{A}$	$300 \mu\text{A}$
Spot diameter	$30 \mu\text{m}$	$1.5 \text{ mm}$
Scanned area	$4.8 \times 3.6 \text{ mm}^2$	$50 \times 40 \text{ cm}^2$
Number of lines	62.5	625
Line frequency	15 kHz	15 kHz
Current density* in the spot	$\sim 1.4 \times 10^{-2} \text{ A/cm}^2$	$\sim 1.7 \times 10^{-2} \text{ A/cm}^2$
Excitation time* $\dagger$	$0.42 \mu\text{sec}$	$0.2 \mu\text{sec}$

\* Parameters relevant for comparison of PSEM 500 with 30 AX tube.

$\dagger$  Excitation time per phosphor element and frame scan, calculated from spot diameter divided by line frequency and length of scanned area.

allows the evaluation of the BCP of a GFPA sandwich from reflection and transmission measurements of an FG sandwich.

The model involves (i) the interrelation between the optical properties of single layers and sandwiches; (ii) averaging according to the eye sensitivity  $V_\lambda$ , the phosphor emission spectrum  $E_\lambda$ , and the ambient illumination  $N_\lambda$ ; and (iii) normalizing of "tube with filter" relative to "tube without filter." Assumptions are (a) one-dimensional calculation, i.e., no lateral or angular effects; (b) addition of light intensities, i.e., no interference effects, which should be allowed for diffusely scattering phosphor and pigment layers; and (c) no optical contact between glass and powder layer, in other words a small gap between them.

Let  $\rho_1$ ,  $\rho_2$ ,  $\tau_1$ , and  $\tau_2$  be the reflection and transmission of two homogeneous layers. If the two layers are combined to form a sandwich, a geometric series of multiple reflections between adjacent surfaces occurs (see Fig. 2a). The overall transmission  $\tau_{12}$  and reflection  $\rho_{12}$  therefore follow

$$\tau_{12} = \tau_1 \tau_2 (1 + \rho_1 \rho_2 + \rho_1^2 \rho_2^2 + \dots) \\ = \tau_1 \tau_2 / (1 - \rho_1 \rho_2) \quad [2]$$

$$\rho_{12} = \rho_1 + \rho_2 \tau_1^2 (1 + \rho_1 \rho_2 + \rho_1^2 \rho_2^2 + \dots) \\ = \rho_1 + \rho_2 \tau_1^2 / (1 - \rho_1 \rho_2) \quad [3]$$

From Eq. [2] and [3] it is evident that the overall transmission is commutative, but not the overall reflection, i.e.

$$\tau_{12} \equiv \tau_{21}, \quad \rho_{12} \neq \rho_{21} \quad [4]$$

If the single layers are not homogeneous, but have a reflection which depends on the direction of light incidence, Eq. [3] has to be replaced by

$$\rho_{12} = \rho_1' + \rho_2 \tau_1^2 / (1 - \rho_1 \rho_2) \quad [3a]$$

$\rho_1$  and  $\rho_1'$  being the reflection of layer No. 1 from the right and the left side, respectively.

The properties of a single layer can be determined from the sandwich properties by resolving Eq. [2] and [3], e.g.

$$\rho_1 = (\tau_2^2 \rho_{12} - \rho_2 \tau_{12}^2) / (\tau_2^2 - \rho_2^2 \tau_{12}^2) \quad [5]$$

$$\tau_1 = \tau_2 \tau_{12} (1 - \rho_2 \rho_{12}) / (\tau_2^2 - \rho_2^2 \tau_{12}^2) \quad [6]$$

A different problem arises if layer No. 1 is a planar light source. The transmission of light emitted by this light source through a filter layer (No. 2) in front of it follows similarly (see Fig. 2b) as

$$\tau_{(1)2} = \tau_2 (1 + \rho_1 \rho_2 + \rho_1^2 \rho_2^2 + \dots) \\ = \tau_2 / (1 - \rho_1 \rho_2) \quad [7]$$

Equation [2], [3], and [7] can be extended for more than two layers by splitting, e.g.

$$\tau_{123} = \tau_{12/3} = \tau_{12} \tau_3 / (1 - \rho_{21} \rho_3) \quad [8]$$

with  $\tau_{12}$ ,  $\rho_{21}$  according to Eq. [2] and [3]. The kind of splitting has no influence, i.e.,  $\tau_{12/3} \equiv \tau_{123}$ .

The reflection of the TV-sandwich GFPA is obtained by splitting into GF and PA

$$\rho_{GFPA} = \rho_{GF} + \rho_{PA} \tau_{GF}^2 / (1 - \rho_{FG} \rho_{PA}) \quad [9]$$

based on Eq. [3a].  $\rho_{GF}$  is calculated from  $\rho_{FG}$  and  $\tau_{FG}$  using Eq. [5] and [6]. By the same kind of splitting, for the transmission of the planar light source AP through the sandwich FG (in front of it) it follows from Eq. [7] that

$$\tau_{(AP)FG} = \tau_{FG} / (1 - \rho_{FG} \rho_{PA}) \quad [10]$$

Tube reflection  $R$  and relative brightness  $T$  are obtained by spectral averaging

$$R = \int \rho_{GFPA} V_\lambda N_\lambda d\lambda / \int V_\lambda N_\lambda d\lambda - r \quad [11]$$

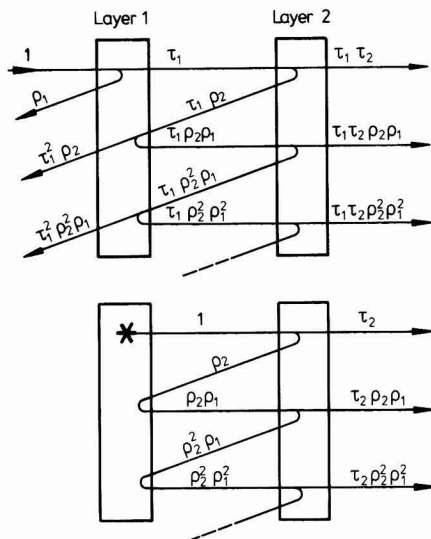


Fig. 2. Light intensities induced by multiple reflections in a sandwich. (a, top)  $\tau_{12}$  and  $\rho_{12}$ ; (b, bottom)  $\tau_{(1)2}$ .

$$T = \int \tau_{(AP)FG} V_\lambda E_\lambda d\lambda / \int V_\lambda E_\lambda d\lambda \quad [12]$$

The specular reflection  $r$  at the first glass surface usually amounts to 0.04.  $T$  is proportional to brightness  $B$ , so that on the grounds of definition [1] BCP becomes

$$\text{BCP} = \left( \frac{T}{\sqrt{R}} \right)_{\text{filter}} \bigg/ \left( \frac{T}{\sqrt{R}} \right)_{\text{filter}} \quad [13]$$

The screen "without filter" forms a three-layer sandwich GPA, which can be evaluated similarly to GFPA. Its characteristic values  $R$  and  $T$  are determined by  $\rho_{PA}$  and by the glass properties  $\rho_G$  and  $\tau_G$ , which are connected with internal glass transmission  $\phi$  and first surface reflection  $r$

$$\rho_G = r + \phi^2 (1 - r) 2r / (1 - r^2 \phi^2) \quad [14]$$

$$\tau_G = (1 - r) 2\phi / (1 - r^2 \phi^2) \quad [15]$$

The computer model described permits the introduction of artificial filter-phosphor combinations as well. Several cases are of interest: (i) Real spectra of filter or phosphor may be shifted along the wavelength axis in order to obtain better coincidence. (ii) Square filters represent the ideal case. With suitable cut-on and cut-off wavelengths they form the theoretical limit of the color filter concept. (iii) A further idealization results from narrow-band or even monochromatic phosphors.

The chromaticity coordinates,  $X$ ,  $Y$  of the three television phosphors must obey international standards. Since the chromaticity may be influenced by color filters, a control is necessary. For this purpose  $X$  and  $Y$  of each phosphor-filter combination are calculated in the known way by forming three integrals of  $E_\lambda \cdot \tau_{(AP)FG}$  multiplied by the three color-matching functions, followed by normalization (5). Small color variations can quantitatively be expressed in multiples of "just noticeable difference," represented by the so-called MacAdam ellipse (6) in the  $X,Y$  plane.

## Results

Results are given for the measured optical properties of the subsystem "filter glass" (FG), the calculated optical properties of the complete system "glass-

filter-phosphor-aluminum" (GFPA) including the model BCP, and the experimentally determined BCP. Figures 3 and 4 show two typical examples of red pigments Cd(S,Se) and  $\alpha$ -Fe<sub>2</sub>O<sub>3</sub>. In Fig. 3a transmission  $\tau_{FG}$  and reflection  $\rho_{FG}$  spectra of thin pigment layers on glass are to be seen. Because of the scattering nature of the pigment particles the curves of transmission and reflection closely resemble each other, i.e., in regions with low absorption both transmission and reflection are high, and vice versa.

Figure 3b shows the reflection  $\rho_{GFPA}$  of the complete sandwich GFPA and the transmission  $\tau_{(AP)FG}$  of the light source AP through the filter FG in front of it. They are calculated from Fig. 3a assuming a constant

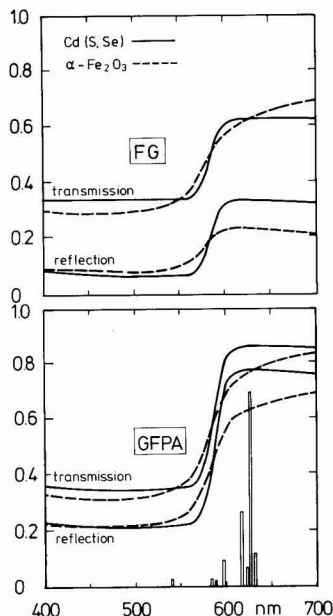


Fig. 3 (a, top)  $\tau_{FG}$  and  $\rho_{FG}$  of two red pigment layers on glass, measured in a spectrometer; (b, bottom)  $\tau_{(AP)FG}$  and  $\rho_{GFPA}$  calculated from (a), together with  $E_A$  of red phosphor Y<sub>2</sub>O<sub>2</sub>S:Eu.

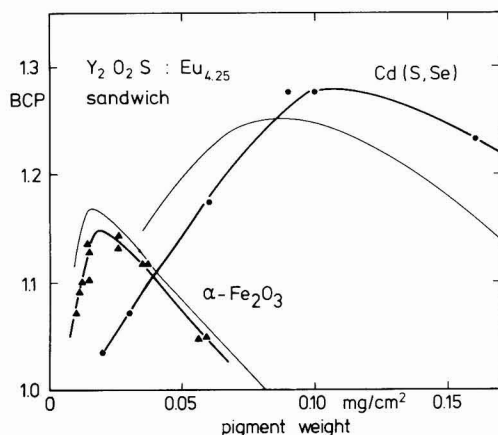


Fig. 4. BCP as a function of pigment weight in a sandwich filter system. The two red pigments are cadmium red and iron oxide. Thin lines refer to model calculations.

Table II. Theoretical  $R$ ,  $T$ , and BCP values of color filter sandwiches with two typical red pigments\*

Filter	mg/cm <sup>2</sup>	$R$	$T$	BCP
Cd(S,Se)	0.099	0.323	0.800	1.25
$\alpha$ -Fe <sub>2</sub> O <sub>3</sub>	0.016	0.306	0.727	1.17
No filter	—	0.763	0.984	1

\* Calculated on the basis of spectrometer measurements of pigment layers on glass substrate.

$\rho_{PA} = 0.80$  and no glass blackening. The main feature is a steepening of the absorption edges due to the mirror action of the PA-double layer. Averaging with the emission  $E_A$  of Y<sub>2</sub>O<sub>2</sub>S:Eu<sub>4.25</sub> phosphor and a "white" ambient light  $N_A$  delivers theoretical values for the tube reflection  $R$ , relative brightness  $T$ , and BCP, listed in Table II.

The superior behavior of Cd(S,Se) pigment compared to  $\alpha$ -Fe<sub>2</sub>O<sub>3</sub> pigment, evidently caused by the steeper absorption edge, appears correspondingly in the thickness dependence of BCP (Fig. 4, thin lines). Experimental BCP values of complete color filter sandwich systems, determined by reflection and brightness measurements, are included in Fig. 4. They exhibit good agreement with the theoretical values for both maximum BCP and optimum filter thickness.

An example for a blue pigment is shown in Fig. 5 and 6, arranged as for Fig. 3 and 4. A cobalt blue layer of 0.22 mg/cm<sup>2</sup> thickness in combination with  $E_A$  of ZnS:Ag phosphor yields model values  $R = 0.350$ ,  $T = 0.869$ , and BCP = 1.30. Figure 5b contains additionally the measured reflection curve of a complete sandwich with a comparable thickness of 0.21 mg/cm<sup>2</sup>. The agreement with the calculated  $\rho_{GFPA}$  is satisfactory; larger deviations below 420 nm originate in the assumption of a constant  $\rho_{PA}$ . Still better agreements can be achieved by taking into account a slight glass absorption and the angular dependence of glass reflection.

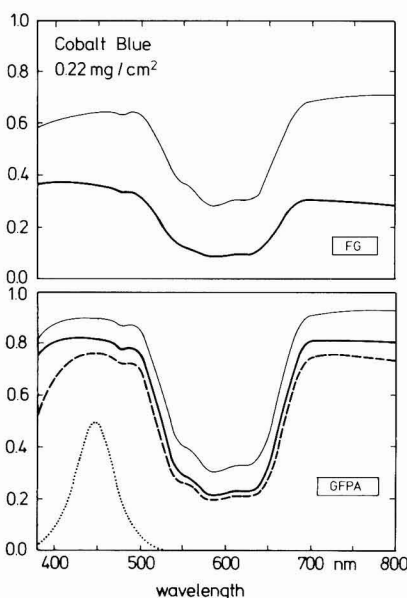


Fig. 5. (a, top)  $\tau_{FG}$  (thin line) and  $\rho_{FG}$  of a cobalt blue layer on glass, (b, bottom)  $\tau_{(AP)FG}$  (thin line) and  $\rho_{GFPA}$  calculated from (a), together with  $E_A$  (dotted line) of blue phosphor ZnS:Ag. The thick dashed line is the measured reflection  $\rho_{GFPA}$ .



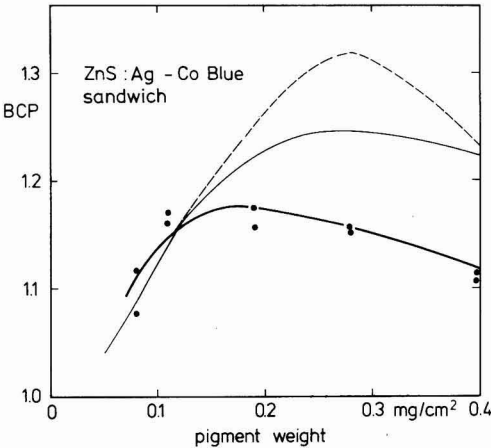


Fig. 6. BCP as a function of cobalt blue pigment weight in a sandwich filter system. The two thin, dashed and full lines refer to model calculations, based on differently deposited pigment layers.

The thickness dependence of BCP is plotted in Fig. 6, for both model calculations and experimental values. The agreement is not so good as with the two red pigments, which may be an effect of pigment processing. The strong influence of preparation technique can be seen by comparing the two thin lines: the dashed and the full ones correspond to different methods of depositing the pigment.

Figure 7 presents results of a green pigment. In this example a layer of 0.06 mg/cm² cobalt green in combination with the green phosphor (Zn,Cd)S:Cu yields  $R = 0.520$ ,  $T = 0.764$ , and  $BCP = 0.94$ , i.e., only a loss. There is little hope of finding a filter-phosphor combination with a clear BCP gain, either with line-emitting or broad-band phosphors, simply because of the high eye sensitivity in the green spectral region.

The results obtained so far with color filter sandwiches are summarized in Table III, the BCP maxima of real filter-phosphor combinations ranging from 1.15 to 1.45. Among the blue pigments cobalt blue is exceeded by ultramarine blue. Unfortunately, however, the latter has poor temperature stability. As expected, idealized square filters offer much higher BCP gains, as illustrated in Fig. 8. While the usual green phosphor (Zn,Cd)S:Cu even with an ideal square filter exhibits only 1.09, the line-emitting green phosphor  $Y_2SiO_5:Tb$  with a 20 nm square filter yields a surprisingly high BCP of 1.65. Narrow-band phosphors with the ability to transmit their whole light output through 10 nm square filters would offer BCP values of 3.39, 2.74, and 4.02 for the red, green, and blue regions, respectively.

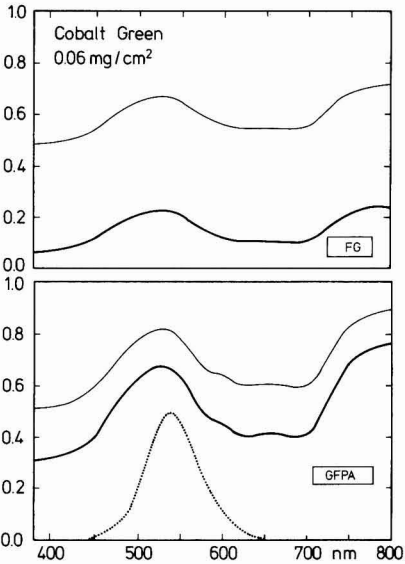


Fig. 7. (a, top)  $\tau_{FG}$  (thin line) and  $\rho_{FG}$  of a cobalt green layer on glass; (b, bottom)  $\tau_{(AP)FG}$  (thin line) and  $\rho_{GFPA}$  calculated from (a) together with  $E_\lambda$  of green phosphor (Zn,Cd)S:Cu (dotted line).

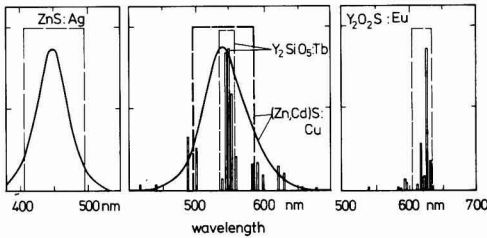


Fig. 8. Emission spectra  $E_\lambda$  of blue, green, and red phosphors, together with transmission  $\tau_F$  of ideal square filters.

The influence of the pigment on the phosphor chromaticity is expressed in the changes  $\Delta X$ ,  $\Delta Y$  of the chromaticity coordinates (see Table III). Up to optimum pigment thicknesses there is only a small shift, providing a slight expansion of the accessible color triangle toward the purple line [about 1 or 2 steps of "just noticeable difference" (6) for the two blue pigments and about 3 or 4 steps for the two red pigments, respectively, exceeding the standardized E.B.U. toler-

Table III. Summary of color filter sandwiches. Maximum BCP obtained by experiment and by model calculation of real and idealized filter phosphor combinations, respectively

Phosphor	Filter	BCP <sub>max</sub> <sup>model</sup>	BCP <sub>max</sub> <sup>exp</sup>	$\Delta X^*$	$\Delta Y^*$
Y <sub>2</sub> O <sub>2</sub> S:Eu <sub>0.25</sub>	Cd(S,Se)	0.13 mg/cm <sup>2</sup>	1.27		
Y <sub>2</sub> O <sub>2</sub> S:Eu <sub>0.25</sub>	$\alpha$ -Fe <sub>2</sub> O <sub>3</sub>	0.02 mg/cm <sup>2</sup>	1.16	1.28	-0.0096
Y <sub>2</sub> O <sub>2</sub> S:Eu <sub>0.25</sub>	"Ideal"	605-635 nm	1.99	1.15	-0.0068
Monochrom. 620 nm	"Ideal"	10 nm width	3.39		
ZnS:Ag	Co-Blue	0.28 mg/cm <sup>2</sup>	1.32		
ZnS:Ag	Ultramarine	0.25 mg/cm <sup>2</sup>	1.45		
ZnS:Ag	"Ideal"	405-495 nm	2.18	1.17	-0.0017
Monochrom. 450 nm	"Ideal"	10 nm width	4.02	0.0002	-0.0068
(Zn,Cd)S:Cu	Co-Green		<1		
(Zn,Cd)S:Cu	"Ideal"	495-585 nm	1.09		
Y <sub>2</sub> SiO <sub>5</sub> :Tb	Co-Green		<1		
Y <sub>2</sub> SiO <sub>5</sub> :Tb	"Ideal"	535-555 nm	1.65		
Monochrom. 540 nm	"Ideal"	10 nm width	2.74		

\* Filter-induced chromaticity displacements  $\Delta X$  and  $\Delta Y$  according to CIE 1931 (5).

ances (7) by no more than a factor of 2]. On the other hand, this shift can be used to compensate the green shift of certain high efficiency red or blue phosphors. For example,  $\text{Y}_2\text{O}_3\text{S}$  phosphor with 3 instead of 4.25% Eu exhibits a chromaticity displacement ( $\Delta X = -0.0093$ ,  $\Delta Y = 0.0086$ ), which is largely canceled by  $0.13 \text{ mg/cm}^2 \text{ Cd(S,Se)}$ .

Pigment as well as phosphor materials frequently exist in the form of mixed crystals, and compositional variations can be simulated by shifting real spectra along the wavelength axis. Our model calculations reveal, however, that no essential BCP improvements can be obtained in this way. In the case of filter variation, BCP increases by only about 1% at the most. Shifting of phosphor spectra yields up to 5% additional BCP gain, but at the cost of an intolerable chromaticity change ( $\Delta X = 0.015$ ,  $\Delta Y = -0.033$  for  $\text{ZnS:Ag}$ ).

### Discussion

The experimentally determined BCP of sandwich-type filter tubes ranges from about 1.15 to 1.25 for commercially available red or blue pigments. Up to now no gain has been found for the green color. The filter-induced chromaticity changes exceed the perception threshold only slightly. They can be used either for a slight increase of color gamut or for the green shift compensation of certain high efficiency phosphors.

Reasonable agreement is obtained between experiments and sandwich model calculations, regarding both maximum BCP value and optimum pigment layer thickness. From this fact the other model predictions acquire a higher probability, too. The model thus helps one in making a selection from among numerous commercial pigments. Those presented belong to the best ones according to model calculations.

Another important model prediction concerns the wavelength shifts of real spectra. Only about 1% additional BCP gain appears to be possible, unless excessive chromaticity displacements take place. Therefore, essential improvements cannot result from variations of mixed crystals. The most important point is the slope of absorption edges. In this respect commercial pigments are probably optimized, because in accordance with color theory (8) the most saturated colors are those with rectangular spectral characteristics, the so-called optimal colors. The conclusion is therefore drawn that the present filter pigments form a practical limit and essentially higher BCP gains are not to be expected.

Ideal square filters yield BCP values of 2-2.2 for the red and the blue, i.e., a gain of 100-120%, while the portion achieved by real filters amounts to about 1/4 to 1/3. This is another indication of the limiting character of the present pigments, since square responses are, of course, quite unrealistic. A further, even more utopian BCP improvement results from narrow-band phosphors with 10 nm square filters.

For all three stages, i.e., real filters, square filters, and narrow-band phosphors with 10 nm square filters, the same sequence green, red, and blue of increasing BCP is observed. This is evidently due to the increasing wavelength distance (about 15, 70, 105 nm) from the maximum of eye sensitivity, which facilitates the discrimination between passband and rejection band. At the third stage, however, differences between green, red, and blue would disappear if the bandwidth approaches zero. In this case, with  $T = 0.984$  and  $R = 0.037$ , BCP arrives at its absolute limit 4.55, as long as antireflection coatings are excluded.

As already stated, blackening of screen glass is frequently used for contrast improvement. From Eq. [7] one can see that brightness or relative brightness  $T$  is approximately proportional to glass transmission  $\tau_g$ . From Eq. [3] it follows that tube reflection  $R$  varies approximately as a function of  $\tau_g^2$ . So indeed contrast,

which is proportional to  $B/R$ , increases approximately as  $1/\tau_g$ , but at the cost of a loss in  $B$ . On the other hand, BCP, forming a kind of geometric means of contrast and brightness, to a first approximation does not depend on  $\tau_g$ , since  $\tau_g$  and square root of  $\tau_g^2$  cancel out.

A given BCP gain can lead to different results, depending on the choice of  $\tau_g$ . If, for example,  $\tau_g$  of the filter tube is increased so that  $R$  (with filter) equals  $R$  (without filter) then  $B$  (with filter) becomes  $B$  (without filter) times BCP. Alternatively,  $\tau_g$  of the filter tube can be chosen so that contrast remains constant, whereby the brightness ratio becomes approximately BCP squared. As the BCP criterion cannot decide which of these alternatives is to be preferred, we propose a new criterion, as demonstrated in Fig. 9. Relative brightness  $T$  is plotted as a function of tube reflection  $R$ . The curve is obtained by variation of internal glass transmission  $\theta$  from 1 (i.e., no glass blackening) to 0 (total glass blackening). The absolutely best combination of  $T$  and  $R$  is no doubt  $T = 1$  and  $R = 0$ .

We now put forward the hypothesis that a real combination ( $T, R$ ) is the better the shorter its distance from the "ideal point" ( $T = 1, R = 0$ ). From this the optimum  $\theta$  for the tube without filter turns out to be  $\theta_{op} = 0.66$ , corresponding to  $\tau_g = 0.61$ , which agrees surprisingly well with the quality maximum known from practice. For sandwich filter tubes with 0.03 and  $0.1 \text{ mg/cm}^2 \text{ Cd(S,Se)}$ ,  $\theta_{op}$  equals 0.79 and 0.89, respectively, agreeing with the experience that the more filter elements (color pigments or also black matrix between phosphor areas) are already present, the lower the optimum glass blackening. Of course, this is not an absolute criterion, which would require detailed physiological knowledge, but it can help one to find a reasonable compromise between brightness and contrast, especially if supplemented by empirical calibration points.

### Outlook for Mixture Systems

Typical results of mixture-type color filter systems are shown in Fig. 10. BCP of the combination  $\alpha\text{-Fe}_2\text{O}_3$

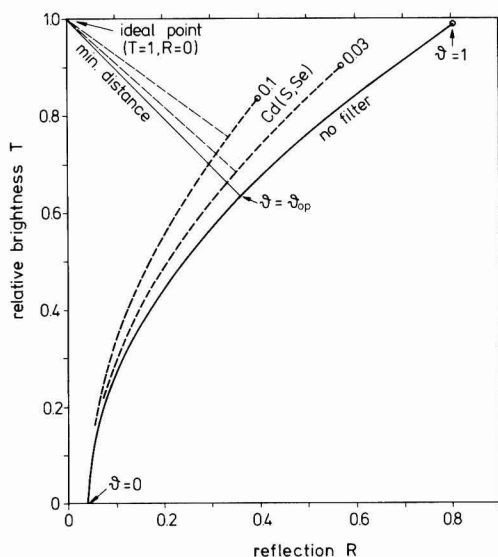


Fig. 9. Relative brightness  $T$  vs. reflection  $R$  (inclusive specular component) for a nonfilter tube and two sandwich filter tubes with 0.03 and  $0.1 \text{ mg/cm}^2 \text{ Cd(S,Se)}$ , calculated from  $\tau_{FG}$  and  $\rho_{FG}$  measurements by variation of the internal glass transmission  $\theta$ . At  $\theta = \theta_{op}$  the distance from the ideal point passes through a minimum.

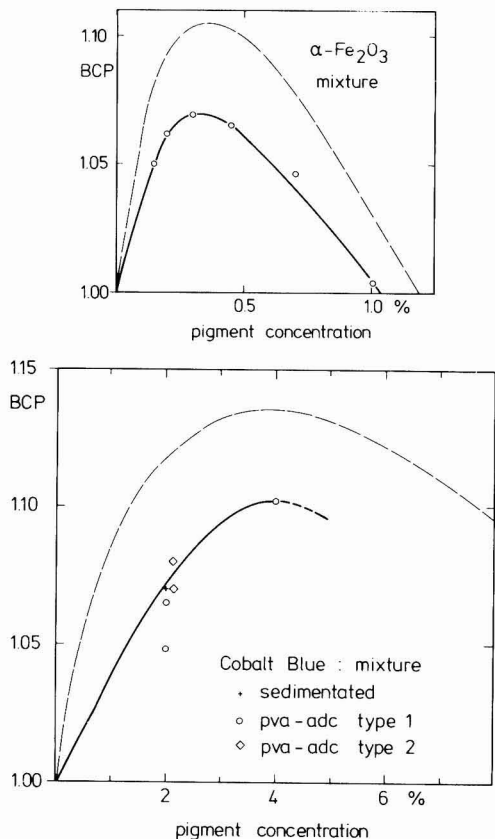


Fig. 10. BCP as a function of pigment concentration in a mixture filter system. The dashed lines refer to model calculations. (a, top) Red pigment  $\alpha\text{-Fe}_2\text{O}_3$ ; (b, bottom) cobalt blue.

with  $\text{Y}_2\text{O}_3\text{:Eu}$  phosphor reaches 1.07 at about 0.3% pigment concentration. For cobalt blue with  $\text{ZnS:Ag}$  phosphor a maximum BCP value of about 1.1 is achieved at about 4% pigment concentration. In both examples the mixture yields only about half the BCP gain of the sandwich (see Fig. 4 and 6, and Table III).

Converted to the phosphor layer thicknesses of about  $3.5 \text{ mg/cm}^2$  for the red and  $3 \text{ mg/cm}^2$  for the blue, the optimum pigment concentration corresponds to layer thicknesses of about  $0.12 \text{ mg/cm}^2$  for cobalt blue and  $0.01$  for  $\alpha\text{-Fe}_2\text{O}_3$ , which are again only about half of the optimum thickness values of the sandwiches. This implies that at low pigment quantities the BCP of sandwiches and of mixtures rises in approximately the same way, but that the BCP of sandwiches continues to rise up to about twice as high a pigment quantity as with mixtures.

A qualitative explanation for this behavior can be derived from electron absorption by the filter pigment instead of the phosphor, which occurs in mixtures only. But in view of the low actual pigment concentration it is clear that this mechanism is not sufficient. The main cause is probably the simple fact that the filter layer in a sandwich system has to be crossed twice by the ambient light, but only once by the phosphor light, whereas in a mixture system the paths for both kinds of light are approximately equal. For a final understanding the different mechanisms of light scattering in sandwiches and mixtures have to be taken into account. In mixtures with a small pigment concentration

the optical interaction between phosphor and pigment proceeds mainly by scattering at the phosphor particles, which are large compared to the light wavelength. In sandwiches the filter-relevant light scattering happens among subwavelength pigment particles within the pigment layer.

The essential experimental findings can be reproduced by a simplified empirical model, the results of which are included as dashed lines in Fig. 10. It is assumed that light generation takes place only in a thin surface region of the phosphor layer adjacent to the aluminum film. By formally regarding the layer with the phosphor-filter mixture as a filter layer and combining a virtual light-emitting layer with the aluminum film, it is possible to treat a mixture-type color filter system with the same computer program as the sandwich.

Transmission and reflection of this type of "filter" layer are determined on the basis of the Kubelka-Munk theory (9), which enables a weakly absorbing, scattering material to be described with the aid of an absorption coefficient  $K$  and a scattering coefficient  $S$ . Measurements of  $R_\infty$ , the reflection of an "infinitely" thick powder layer, yield the ratio  $K/S$ .  $S$  can be evaluated, for example, from reflection measurements of layers with different finite thicknesses.  $S$  depends, as stated above, mainly on the phosphor. This is confirmed by our measurements, which give values of about  $500 \text{ cm}^2/\text{g}$  for the blue phosphor and  $400 \text{ cm}^2/\text{g}$  for the red one, nearly independent of pigment addition and wavelength. So a relatively simple measurement of  $R_\infty$  is generally sufficient to obtain a reasonable prediction of the BCP of a complete mixture system.

### Conclusion

The action of color filters in color television tubes can be understood with the help of relatively simple models, especially in the case of sandwiches. BCP gains up to about 25% have been obtained in sandwiches with commercial filter pigments. This appears to be a practical limit, which could not be essentially exceeded. Mixture-type color filters, though more favorable for production, exhibit only about one-half of the sandwich BCP gain.

### Acknowledgment

The authors wish to thank W. Czarnojan, E. Klein, and H. Lade who conducted most of the experimental work.

Manuscript submitted May 15, 1981. This was Paper 226 presented at the St. Louis, Missouri, Meeting of the Society, May 11-16, 1980.

Any discussion of this paper will appear in a Discussion Section to be published in the June 1982 JOURNAL. All discussions for the June 1982 Discussion Section should be submitted by Feb. 1, 1982.

Publication costs of this article were assisted by Philips GmbH Forschungslaboratorium Aachen.

### REFERENCES

1. S. S. Trond, Abstract 329, p. 817, The Electrochemical Society Extended Abstracts, Seattle, WA, May 21-26, 1978.
2. T. Takahara, T. Wakatsuki, and T. Nishimura, Abstract 219, p. 564, The Electrochemical Society Extended Abstracts, St. Louis, MO, May 11-16, 1980.
3. W. Möller, W. de Rave, and H. Widmann, Abstract 225, p. 576, The Electrochemical Society Extended Abstracts, St. Louis, MO, May 11-16, 1980.
4. S. Larach and A. E. Hardy, *Proc. IEEE*, **61**, 915 (1973).
5. G. Wyszecski and W. S. Stiles, "Color Science," John Wiley & Sons, Inc., New York (1967).
6. D. L. MacAdam, *J. Opt. Soc. Am.*, **32**, 247 (1942).
7. "E.B.U. standard for chromaticity tolerances for studio monitors," E.B.U. Tech. 3213-E, August 1975.
8. E. Schrödinger, *Ann. Phys.*, **62**, 603 (1920).
9. P. Kubelka and F. Munk, *Z. Tech. Phys.*, **12**, 593 (1931).

# Phosphorus-Doped Molybdenum Silicide Films for LSI Applications

S. Inoue,\* N. Toyokura, T. Nakamura, and H. Ishikawa\*

Fujitsu Laboratories Limited, 1015 Kamikodanaka, Nakahara-ku, Kawasaki, Japan

## ABSTRACT

The properties of phosphorus-doped molybdenum silicide as a gate electrode, interconnecting material, and impurity diffusion source for LSI's have been studied. The phosphorus-doped molybdenum silicide films were deposited by co-sputtering using specially designed Mo and Si targets in a  $\text{PH}_3/\text{Ar}$  atmosphere.  $\text{PH}_3$  decomposed to P and  $\text{H}_2$  during sputtering and the phosphorus combined with Mo and Si. Typically, a phosphorus concentration of  $1.5 \times 10^{21} \text{ cm}^{-3}$  in the films was used. As-deposited films ( $\text{Mo/Si} \leq 0.5$ ) had amorphous structure and high resistivity. After the films were annealed at temperatures above  $800^\circ\text{C}$ , they became polycrystalline and resistivity was decreased. The resistivity of the film with a Mo/Si ratio of 2 to 1 was  $7.5 \times 10^{-5} \Omega\text{-cm}$  with annealing at  $1000^\circ\text{C}$  in  $\text{N}_2$ . Phosphorus was able to diffuse from the doped molybdenum silicide films to the Si substrate during annealing in  $\text{O}_2$ . After high temperature annealing up to  $1100^\circ\text{C}$ , the contact resistance between the molybdenum silicide and the silicon substrate was below  $2 \times 10^{-6} \Omega\text{-cm}^2$ . The reliability of doped molybdenum silicide gate MOSFET's is as good as polysilicon gates and the threshold voltage shift is within  $\pm 20 \text{ mV}$  under stress conditions of  $2.5 \text{ MV/cm}$  for 1000 hr at  $150^\circ\text{C}$ .

As LSI device dimensions continue to decrease, the conductivity of the polysilicon used for interconnections and gates is beginning to limit the circuit performance.

Previous investigators have explored the use of refractory metals such as Mo and W for gate electrodes and interconnections in MOSFET circuits (1-6). These metals have significantly higher conductivity than polysilicon, but do not have the ability to withstand the chemical reagents and oxidizing ambient used in LSI fabrication.

In order to overcome these disadvantages, the refractory metal silicides, such as  $\text{MoSi}_2$  and  $\text{WSi}_2$ , have been proposed because of their resistance to oxidizing ambient and chemical reagents (7-11). It has been reported that the contact resistance between the molybdenum silicide and the silicon substrate was increased by high temperature annealing, but this problem has never been solved completely (12, 13). Moreover, as the contact region cannot be doped through the silicide, it must be doped prior to gate electrode deposition. Sometimes, a slight shift of threshold voltage appears due to the mobile ions in the oxide films when silicide is used as the gate electrode (7).

We have developed phosphorus-doped molybdenum silicide films in order to overcome just these problems. This film has several advantages for LSI fabrication.

In this paper we discuss the properties of these phosphorus-doped molybdenum silicide films, the composition of films, the behavior of the phosphorus in the films, the electrical properties of the contact between the silicide and the silicon substrate, and MOS device characteristics.

## Deposition of Phosphorus-Doped Molybdenum Silicide Film

The phosphorus-doped molybdenum silicide film was deposited by a d-c magnetron co-sputtering technique. A conceptual diagram is given as Fig. 1. The deposition was performed from specially designed Si and Mo targets as shown in Fig. 2. A larger proportion of the Mo target (99.95%, 150 mm diam) was covered with fan-shaped high-purity Si.

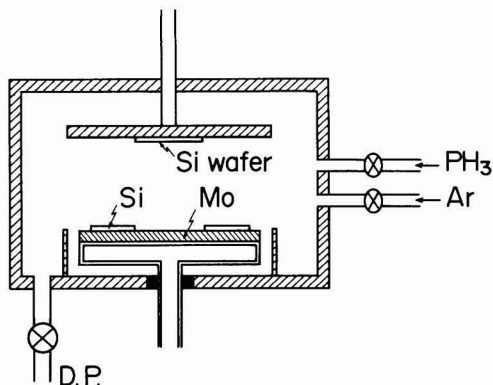


Fig. 1. Conceptual diagram of the phosphorus-doped co-sputtering apparatus.

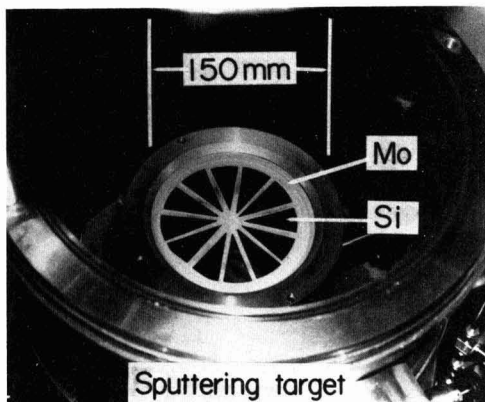


Fig. 2. Photograph of the specially designed Si and Mo targets

\* Electrochemical Society Active Member.

Key words: molybdenum silicide, contact resistance, diffusion, MOSFET.

The chamber was pumped down to  $4 \times 10^{-7}$  Torr ( $5.3 \times 10^{-5}$  Pa) and backfilled to sputtering pressure,  $6 \times 10^{-3}$  Torr (0.8 Pa), by introducing Ar and  $\text{PH}_3$ . Typically,  $\text{PH}_3$  partial pressure of  $1.1 \times 10^{-3}$  Torr (0.15 Pa) was used. The ratio of Mo to Si in the deposited films could be varied by changing the positions of the Si and the sputtering pressure. The phosphorus concentration is varied by controlling the ratio of  $\text{PH}_3$  and Ar in the sputtering gas. The deposition rate was 10–15 Å/sec and d-c power was 160–220W.

### Crystal Structure

Silicide films of various Mo/Si ratios were deposited on the thermally grown  $\text{SiO}_2$ . The Mo/Si ratio in the film was measured by Rutherford backscattering using  $^4\text{He}^+$  ions at 330 keV and  $^3\text{He}^{++}$  ions at 300 keV. Structure information was obtained using x-ray diffraction techniques. When the Mo/Si ratio was lower than 0.5 as-deposited films were an amorphous structure. The amorphous film became a polycrystalline structure after high temperature annealing. The relation between annealing temperature and x-ray diffraction traces is shown in Fig. 3. The Mo/Si ratio in this film was 0.45 (Mo:Si = 1:2.2). This figure shows that the silicide film is crystallized at annealing temperatures above 800°C and exhibits a tetragonal  $\text{MoSi}_2$  structure (JCPDS cards 6-0681).

On the other hand, as-deposited films with Mo/Si ratios higher than 0.5 were crystallized a little as shown in Fig. 4. Figure 4(a) shows the  $\text{Mo}_3\text{Si}$  phase for an Mo/Si ratio of 2.7, and Fig. 4(b) shows  $\text{MoSi}_2$  (hexagonal structure) for an Mo/Si ratio of 0.9. After annealing above 800°C, the  $\text{MoSi}_2$  structure changes from hexagonal to tetragonal.

X-ray diffraction traces for various Mo/Si ratios are shown in Fig. 5. The silicide films on  $\text{SiO}_2$  were annealed at 1000°C for 20 min in  $\text{N}_2$ . Figure 5(a) shows the simple phase  $\text{Mo}_3\text{Si}$  for an Mo/Si ratio of 2.7 (Mo:Si = 1:0.37). When the Si ratio in the film is increased, the film produces  $\text{Mo}_3\text{Si}_2$  and  $\text{MoSi}_2$ , as shown in Fig. 5(b) for an Mo/Si ratio of 0.9 (Mo:Si = 1:1.1). The  $\text{MoSi}_2$  phase is for an Mo/Si ratio of 0.5 (Mo:Si = 1:2) only, as shown in Fig. 5(c). When the Mo/Si ratio falls 0.35 (Mo:Si = 1:2.9), as in Fig. 5(d), the film has the  $\text{MoSi}_2$  phase only.

### Composition of the Films

The depth concentration profile of the samples before and after annealing was obtained by Rutherford

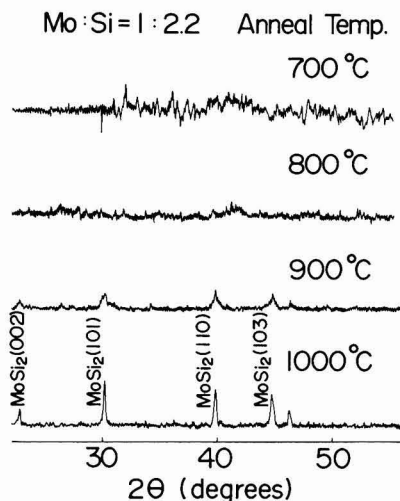


Fig. 3. X-ray diffraction traces as a function of the annealing temperatures. The Mo/Si ratio is 0.45.

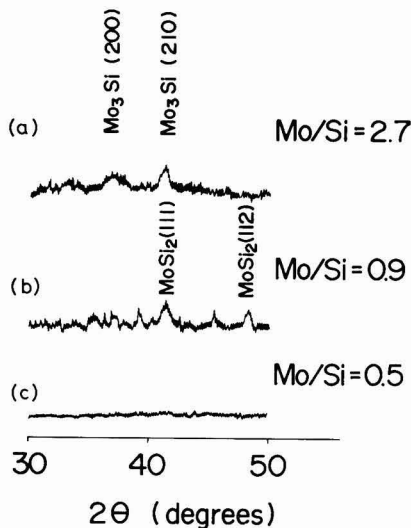
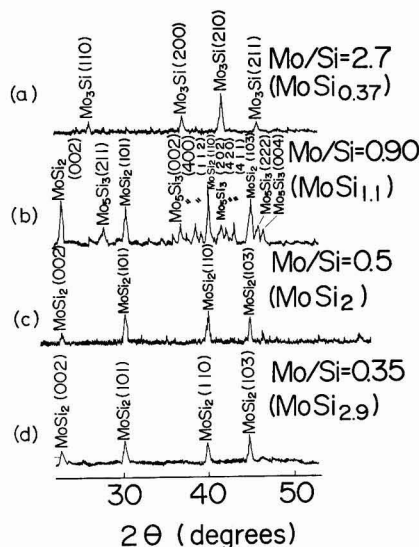


Fig. 4. X-ray diffraction traces of as-deposited films for various Mo/Si ratios: (a) 2.7, (b) 0.9, and (c) 0.5.



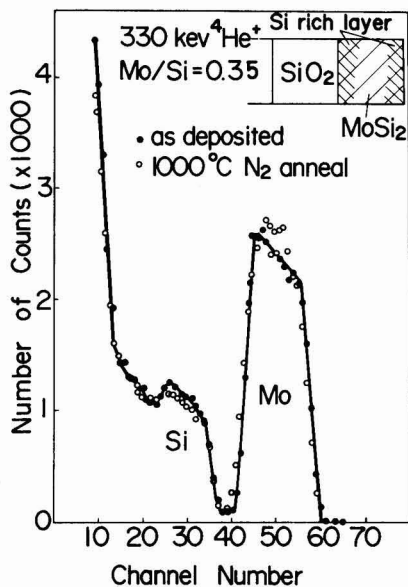


Fig. 6. Backscattering spectra of the thin film on  $\text{SiO}_2$  before and after annealing at  $1000^\circ\text{C}$  for 20 min in  $\text{N}_2$ . The Mo/Si ratio is 0.35.

Figure 7 shows the backscattering spectra of the Si-rich silicide on Si before and after annealing. After annealing, the presence of the phase is confirmed by the height of the respective "step" in the backscattering spectra, indicating a region with a 1:2 Mo/Si ratio. The width of the Mo spectra is decreased and the interface between the silicide and Si moves toward the surface after annealing. This indicates that excess Si in the film is precipitated at the silicide/Si interface and

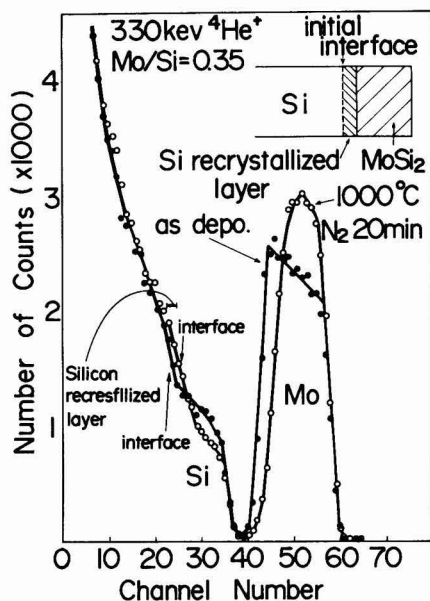


Fig. 7. Backscattering spectra of the film on Si before and after annealing at  $1000^\circ\text{C}$  for 20 min in  $\text{N}_2$ . The Mo/Si ratio is 0.35.

the film is recrystallized as a double layer of  $\text{MoSi}_2$  and Si, as shown in the upper righthand corner of Fig. 7.

The spectrum of the Mo-rich silicide film on  $\text{SiO}_2$  is shown in Fig. 8. This spectrum shows that the ratio of Mo increases at the surface and at the silicide/Si interface, and the Mo/Si ratio at the middle of the film approaches  $\text{MoSi}_2$  after high temperature annealing. A model of this is shown at the top of Fig. 8.

The spectra of the Mo-rich film on Si are shown in Fig. 9. The spectrum of the annealed film indicates that Si diffuses into silicide from the Si substrate and forms a 1:2 Mo/Si ratio. The film thickness increases until the composition changes to  $\text{MoSi}_2$  as shown in Fig. 9.

These backscattering spectra indicate the following results. The composition profile of the as-deposited sample is uniform from the silicide surface to the silicide/ $\text{SiO}_2$  or Si interface. The composition profiles of the films on Si change to 1:2 Mo/Si ratio after annealing. On the other hand, the composition profiles of the films on  $\text{SiO}_2$  vary from the middle of the film to the surface or the silicide/ $\text{SiO}_2$  interface. The middle of the films approaches 1:2 Mo/Si ratio.

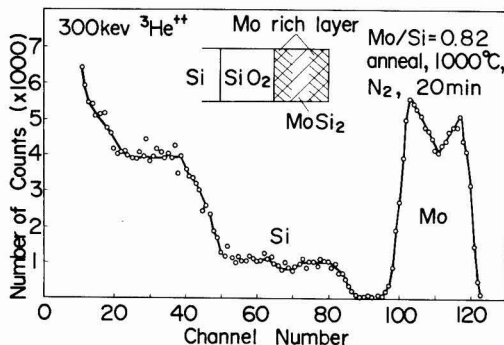


Fig. 8. Backscattering spectrum of the film on  $\text{SiO}_2$  after annealing at  $1000^\circ\text{C}$  for 20 min in  $\text{N}_2$ . The Mo/Si ratio is 0.82.

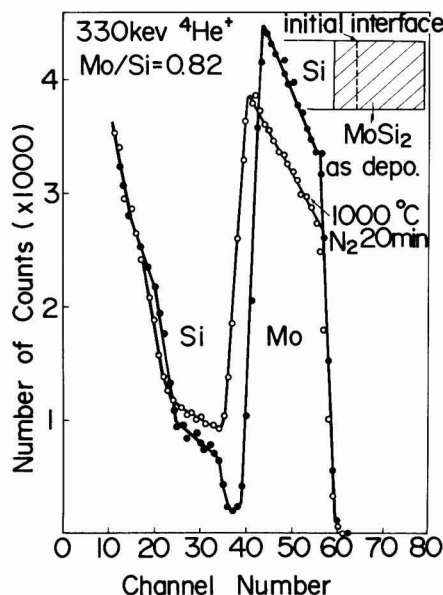


Fig. 9. Backscattering spectra of the film on Si before and after annealing at  $1000^\circ\text{C}$  for 20 min in  $\text{N}_2$ . The Mo/Si ratio is 0.82.



### Behavior of Phosphorus in Molybdenum Silicide Films

The sputtering gas was analyzed by a mass analyzer. The mass spectra of the sputtering gas are shown in Fig. 10. Before sputtering,  $H_2O$ , P,  $PH_1$ ,  $PH_2$ ,  $PH_3$ , and Ar signals were observed in the atmosphere. During sputtering, P,  $PH_1$ ,  $PH_2$ , and  $PH_3$  signals disappeared, and the  $H_2$  signal increased. Thus, it is clear that  $PH_3$  gas decomposes into P and  $H_2$ , and the phosphorus is combined with Mo and Si during the deposit.

Phosphorus-doped molybdenum silicide films with various Mo/Si ratios were deposited on thermally grown  $SiO_2$ . The film thickness was about 3000Å. The phosphorus concentration was measured by neutron activation analysis (14). The doped silicide films on  $SiO_2$  were irradiated for 6 hr in the center of a nuclear reactor at a flux of  $3.7 \times 10^{12}$  n/cm<sup>2</sup> · sec. Subsequently the phosphorus was chemically separated and then precipitated. The precipitate was  $\beta$ -counted several times during the next 30 days to determine the amount of radioactive P-32. The weight of phosphorus in the film was measured through this radioactive tracing process.

Figure 11 shows the relation between the phosphorus concentration in the as-deposited films and the Mo/Si ratio when the film was deposited by sputtering under  $PH_3$  at  $1.1 \times 10^{-3}$  Torr. When the Mo/Si ratio is less than 0.5, the phosphorus concentration in the film is about  $1.5 \times 10^{21}$  cm<sup>-3</sup>. When the Mo/Si ratio is greater than 0.5, the phosphorus concentration decreases. These films were slightly crystallized as described in the previous section. The phosphorus concentration may be related to the crystallization of as-deposited films. When the total pressure was  $6 \times 10^{-3}$  Torr and the  $PH_3$  partial pressure was below  $1.1 \times 10^{-3}$  Torr, the phosphorus concentration appeared to be proportional to the exponent of the  $PH_3$  partial pressure as shown in Fig. 12.

The doped silicide films were annealed in  $O_2$  and  $N_2$  from 800° to 1000°C for 20 min. The phosphorus concentration in the film was measured by neutron activation analysis. Figure 13 shows the relation between the phosphorus concentration and the annealing temperature. When annealing above 900°C in  $N_2$ , the phos-

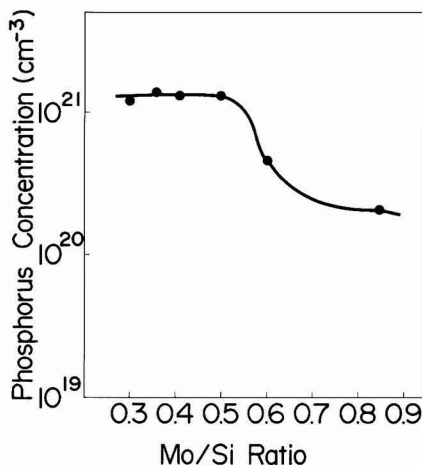


Fig. 11. Phosphorus concentration in the as-deposited films for various Mo/Si ratios.

phorus concentration decreases to a level of  $2.5 \times 10^{18}$  cm<sup>-3</sup> at 1000°C for 20 min. On the other hand, in  $O_2$  annealing, the phosphorus concentration remained almost the same as before annealing. Moreover, when the doped silicide film covered with CVD  $SiO_2$  of 2000Å was annealed in  $N_2$ , the phosphorus concentration was almost the same as before annealing. Therefore, thermal oxide film formed by  $O_2$  annealing on the silicide prevents the out-diffusion of phosphorus from the doped film.

The chemical state of phosphorus was investigated by x-ray photoelectron spectroscopy (XPS).

Typical XPS spectra of phosphorus 2p core level in the doped silicide film is shown in Fig. 14. For comparison, XPS spectra of phosphorus in the doped molybdenum film, doped polysilicon film, and phosphorus evaporated film are also shown in Fig. 14. All spectra were calibrated by the carbon  $C_{1s}$  as a line at 285.0 eV. The doped molybdenum film was deposited on  $SiO_2$  by sputtering with red phosphorus on the Mo targets. The

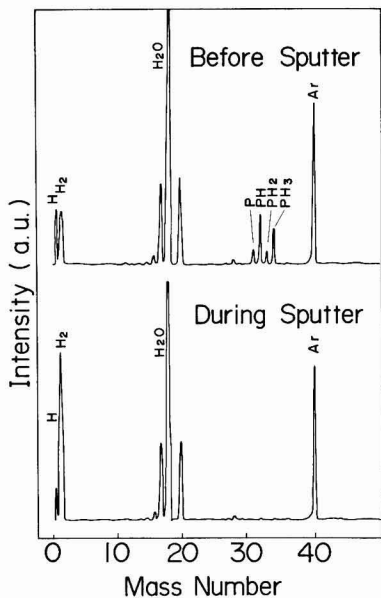


Fig. 10. Mass spectra in the sputtering gas before and during sputtering.

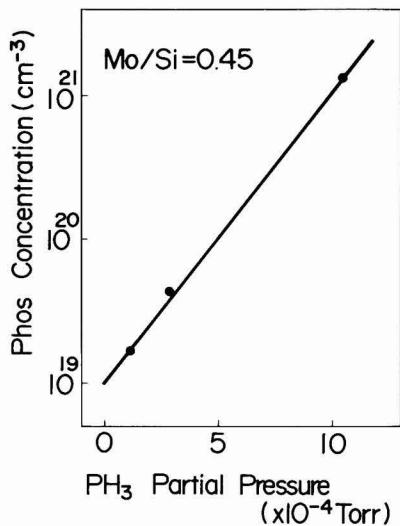


Fig. 12. Phosphorus concentration in the films as a function of the  $PH_3$  partial pressure. The Mo/Si ratio is 0.45.

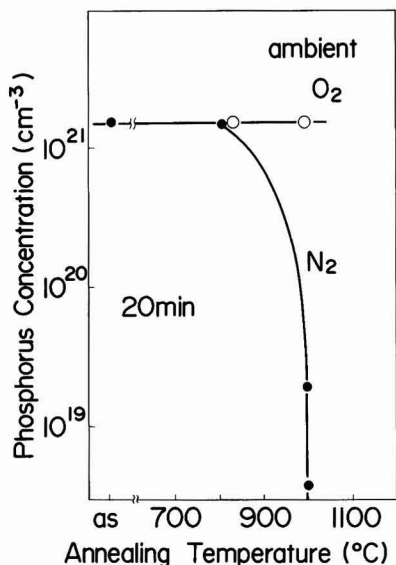


Fig. 13. Phosphorus concentration in the film after annealing in  $N_2$  and  $O_2$ .

doped polysilicon was deposited by CVD with  $PH_3$ ,  $SiH_4$ , and  $N_2$  gas at  $700^\circ C$ . The phosphorus film was evaporated on  $SiO_2$  from a red phosphorus source with a tungsten heater. The phosphorus spectra in as-deposited silicide film has a peak at  $129.5\text{ eV}$  ( $E_1$ ), as shown in Fig. 14. The peak value of phosphorus 2p in

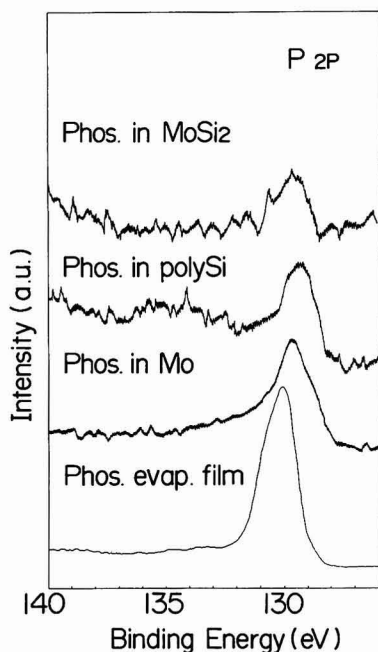


Fig. 14. X-ray photoelectron spectra of the phosphorus 2p electron core level in the doped molybdenum silicide film, doped polysilicon film, doped molybdenum film, and phosphorus evaporation film.

doped molybdenum film and doped polysilicon was observed to be the same. The peak value of phosphorus 2p in the evaporated phosphorus film is  $130.1\text{ eV}$  ( $E_2$ ), as shown in Fig. 14. This value is the same as that for red phosphorus as reported by Pelavin (15).

This chemical shift is not fully understood. The peak value of phosphorus in molybdenum film and in doped polysilicon is the same as in the doped silicide film, but is different from that of red phosphorus. Therefore, it is thought that the phosphorus in the film was incorporated interstitially, as in phosphorus implanted into  $SiO_2$  (16).

Figure 15 shows the phosphorus 2p spectra of the film before and after annealing. The film was annealed at  $1000^\circ C$  for 20 min in  $O_2$  and was etched off the thermally grown  $SiO_2$  on the silicide. The annealed film displays the two peaks such as  $E_1$  ( $129.5\text{ eV}$ ) and  $E_2$  ( $130.1\text{ eV}$ ).

The line shape of spectra  $E_2$  is corresponding to red phosphorus. This indicates that some phosphorus in the film may be gathered at the grain boundary after high temperature annealing because the film was crystallized. Then the phosphorus formed the metallic state of red phosphorus. These two peaks are tentatively interpreted as due to the interstitial state (corresponding to  $E_1$ ) and metallic state (corresponding to  $E_2$ ) of phosphorus.

#### Phosphorus Diffusion into Si Substrate

Phosphorus-doped molybdenum silicide was deposited on p-type (100) Si and the diffusions were performed in  $O_2$  at the nominal diffusion temperature. The thickness of the films was  $3000\text{ \AA}$ , the Mo/Si ratio was 0.45 (Mo:Si = 1:2.2), and the phosphorus concentration was  $1.5 \times 10^{21}\text{ cm}^{-3}$ . The phosphorus concentration profiles were determined by the incremental sheet resistivity method using the anodic oxidation technique. The profiles for various diffusion times at  $900^\circ C$  and various diffusion temperatures for 20 min are shown in Fig. 16 and 17, respectively.

These profiles are similar to those obtained from other diffusion sources such as doped polysilicon (17), or PSG. High surface concentrations are obtained with relatively low temperature diffusion. XPS and Auger analysis confirmed that sufficient phosphorus is always supplied at the silicide/Si interface and a high surface concentration is obtained. Therefore, this is a very attractive technique for fabricating MOS LSI's.

#### Ohmic Contact with Si Substrate

The major advantage of polysilicon gate technology is the excellent ohmic contact between the gate electrode and the Si substrate in a buried contact. The same advantage is required if silicide gate technology

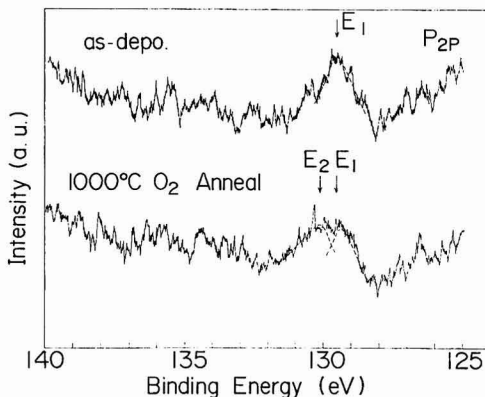


Fig. 15. X-ray photoelectron spectra of the phosphorus 2p electron core level in the films before and after annealing.

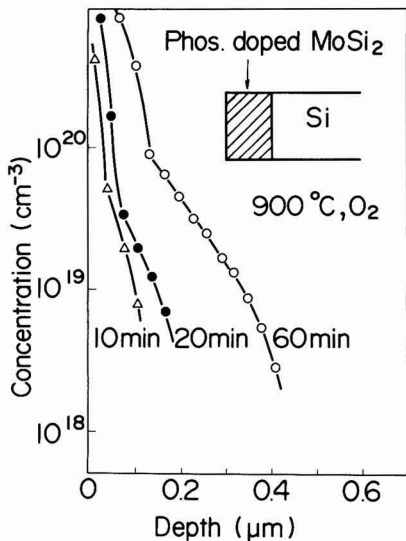


Fig. 16. Phosphorus depth profiles diffused from doped molybdenum silicide into Si substrate at 900°C for 10, 20, and 60 min in  $O_2$ .

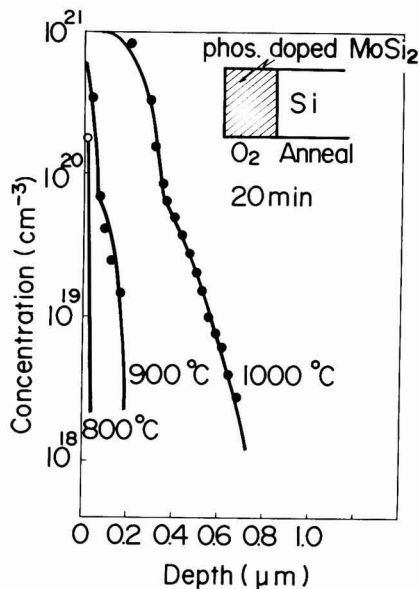


Fig. 17. Phosphorus depth profiles diffused from doped molybdenum silicide into Si substrate at 800°, 900°, and 1000°C for 20 min in  $O_2$ .

is to replace polysilicon technology. However, the contact resistance between the molybdenum silicide and Si often becomes high due to a highly resistive layer formed during annealing at the silicide/Si interface (12) or related to film deposition and stress (13).

The measured contact resistance between the silicide and silicon  $n^+$  layer is shown in Fig. 18 as a function of annealing temperature in  $O_2$ . The Mo/Si ratio in the film was 1:2.0 ( $MoSi_2$ ). The contact resistance was measured by a 1000 contact hole chain with a contact area of  $4 \times 4 \mu m^2$ . The contact resistance between

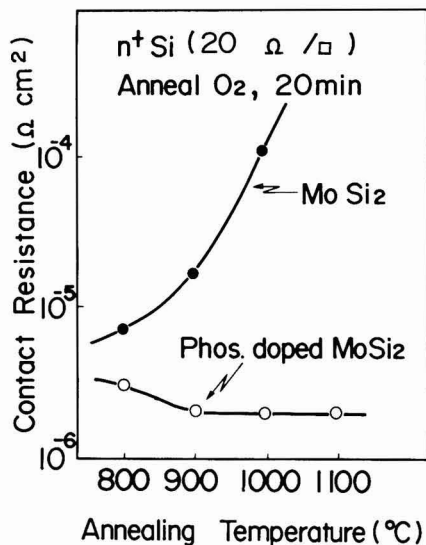


Fig. 18. Contact resistance between the molybdenum silicide and the  $n^+$  Si after annealing for 20 min in  $O_2$ .

nondoped silicide and the  $n^+$  Si layer increased with higher annealing temperatures, while the contact resistance of the doped silicide and the  $n^+$  Si layer was below  $2 \times 10^{-6} \Omega\text{-cm}$ , up to 1100°C. These results may be explained as follows. When the nondoped silicide/Si was annealed at high temperature, the donor impurity of the Si surface decreased and a highly resistive layer was formed at the silicide/Si interface. The presence of enough phosphorus in the doped silicide films prevented the formation of a high resistive layer, even after annealing at temperature up to 1100°C.

#### Resistivity

The effect of the Mo/Si ratio on film resistivity was evaluated. The resistivity of as-deposited films is quite high. As the annealing temperature increases, the resistivity decreased. The relation between the resistivity of annealed films and the Mo/Si ratio is shown in Fig. 19. The films were annealed for 20 min at 1000°C in  $N_2$ . The resistivity decreases as the Mo/Si increases. The resistivity of  $MoSi_2$  is  $7.5 \times 10^{-5} \Omega\text{-cm}$ . This value is lower than that of  $MoSi_2$  obtained from hot press targets. Because hot press targets have a significant level of impurities such as carbon, oxygen, and alkali ions, its impurities raise the film resistivity (18, 19).

Phosphorus concentration had no influence on the resistivity of the films.

#### MOS Device Characteristics

**$V_{FB}$  dependence on the Mo/Si ratio.**—Using various Mo/Si ratios for the gate electrodes, MOS diodes having a  $5 \times 10^{-3} \text{ cm}^2$  gate area were fabricated on thermally oxidized p-type (100) Si, with  $1 \times 10^{16} \text{ cm}^{-3}$  doping density. The gate oxide was 400 Å thick and was grown in dry  $O_2$  at 1000°C.

The samples were annealed at 1000°C in  $N_2$  for 20 min to reduce the resistivity and to crystallize the film, and then annealed at 450°C in forming gas (5%  $H_2$ , 95%  $N_2$ ) for 30 min to minimize surface states.

Capacitance was measured as a function of gate voltage at a frequency of 1 MHz. The flatband voltage,  $V_{FB}$ , was measured from the C-V plot. The  $V_{FB}$  of the silicide gate is shown in Fig. 20 as a function of the Mo/Si ratio. The figure also shows the  $V_{FB}$  of the molybdenum and  $n^+$  polysilicon gate. The  $V_{FB}$  of the MOS

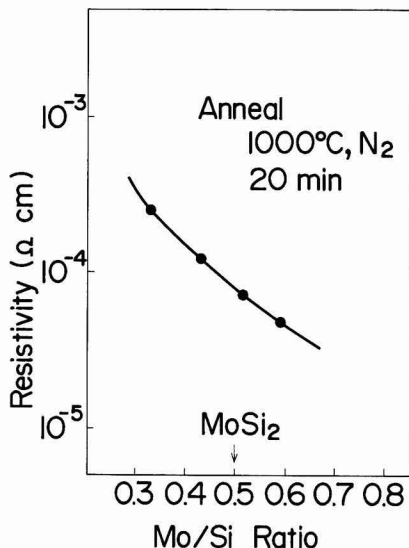


Fig. 19. Resistivity of the molybdenum silicide films as a function of the Mo/Si ratios. The films were deposited on  $\text{SiO}_2$  and annealed for 20 min at  $1000^\circ\text{C}$  in  $\text{N}_2$ .

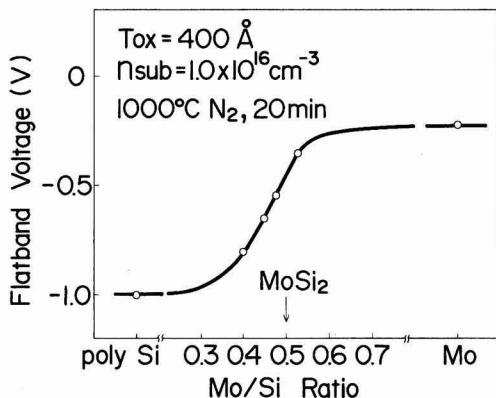


Fig. 20. Flatband voltage for various Mo/Si ratios after annealing for 20 min at  $1000^\circ\text{C}$  in  $\text{N}_2$ .

diode gradually increases from  $-1.0$  to  $-0.2\text{V}$  as the Mo/Si ratio increases. When the Mo/Si ratio decreases, the  $V_{\text{FB}}$  of the annealed silicide gate rises to the value for an  $n^+$  polysilicon gate. If the Mo/Si ratio increases,  $V_{\text{FB}}$  approaches the value for a molybdenum gate. The  $V_{\text{FB}}$  of the  $\text{MoSi}_2$  gate is  $-0.45\text{V}$ .

From measuring with the quasi static C-V method (20), the surface state density in the midgap was found to be below  $3 \times 10^{10} \text{ eV}^{-1} \text{ cm}^{-2}$  and was constant for various Mo/Si ratios. Further, the fixed charge in the oxide did not vary with different Mo/Si ratios. Thus, the  $V_{\text{FB}}$  shifts observed for the MOS diodes were mainly due to the difference of the effective work function for molybdenum silicide. As described in the previous section, the excess Si or Mo in the silicide films on the  $\text{SiO}_2$  moves toward the silicide/ $\text{SiO}_2$  interface and then forms an Si-rich or Mo-rich layer after high temperature annealing. It is confirmed that the effective work function of the silicide films is determined by the Mo/Si ratio at the silicide/ $\text{SiO}_2$  inter-

face, however, this phenomenon is not completely understood.

**Mobile ions.**—Mobile ions in the gate oxide were measured by the triangular voltage sweep (TVS) method with a temperature of  $230^\circ\text{C}$  and voltage sweep velocity of  $33 \text{ mV/sec}$  (21). The mobile ion density as a function of annealing temperature for nondoped and phosphorus-doped silicide gates is given in Fig. 21. The Mo/Si ratio in this test was 1:2.

Mobile ion density was about  $1 \times 10^{11} \text{ cm}^{-2}$  in the nondoped silicide gates annealed below  $900^\circ\text{C}$ , and density decreased to  $5 \times 10^{10} \text{ cm}^{-2}$  after  $1000^\circ\text{C}$  annealing. Mobile ion density of doped silicide gates annealed above  $900^\circ\text{C}$  in  $\text{O}_2$  were below the TVS sensitivity level ( $<10^9 \text{ cm}^{-2}$ ). After high temperature annealing, phosphorus diffuses slightly from the doped silicide to the  $\text{SiO}_2$  surface, and its oxide surface layer includes phosphorus and had a strong mobile ion gettering effect as in a phosphosilicate glass.

**Reliability of MOSFET's.**—MOSFET's were fabricated using doped silicide for the gate electrode. The Mo/Si ratio was 1:2 ( $\text{MoSi}_2$ ), a  $7 \text{ } \Omega\text{-cm}$  CZ p-type Si wafer was used as the substrate, and the gate oxide thickness was  $400\text{\AA}$ . The doped silicide film of  $3000\text{\AA}$  was deposited and patterned by plasma etching. Arsenic was ion-implanted in the source and drain regions, and CVD  $\text{SiO}_2$  film of  $8000\text{\AA}$  was deposited for surface passivation. The doped  $\text{MoSi}_2$  was annealed at  $1000^\circ\text{C}$  for 20 min together with activation of the source and drain implanted layers. Aluminum-containing silicon was metallized through contact holes and annealed at  $400^\circ\text{C}$  for 10 min in forming gas.

The current-voltage characteristics of the MOSFET's are shown in Fig. 22. Effective channel length and width are (a) 20 and  $100 \text{ } \mu\text{m}$ , and (b) 2 and  $19 \text{ } \mu\text{m}$ , respectively. Threshold voltage,  $V_{\text{th}}$ , for long channel ( $20 \text{ } \mu\text{m}$ ) is  $0.5\text{V}$  and for short channel ( $2 \text{ } \mu\text{m}$ ) is  $0.3\text{V}$ . Size effect of  $V_{\text{th}}$  is observed for channel lengths smaller than  $3.0 \text{ } \mu\text{m}$ .

The  $V_{\text{th}}$  shifts of the MOSFET after bias and temperature stress (BT stress) are listed in Fig. 23, where + and - indicate the gate bias polarities with respect to source, drain, and substrate. The test MOSFET had a channel length of  $20 \text{ } \mu\text{m}$  and width of  $100 \text{ } \mu\text{m}$ . The electric field was  $\pm 2.5 \text{ MV/cm}$  and the temperature was  $150^\circ\text{C}$ . After  $\pm\text{BT}$  stress for 1000 hr, shifts of  $V_{\text{th}}$  were within  $\pm 20 \text{ mV}$ . Nonionic  $V_{\text{th}}$  shifts were not observed under these stress conditions. Effective electron mobility was  $620 \text{ cm}^2/\text{V} \cdot \text{sec}$  and had no influence before and after BT stress. This indicates that the phosphorus-doped  $\text{MoSi}_2$  gate MOSFET is very stable, as in the polysilicon gate structure.

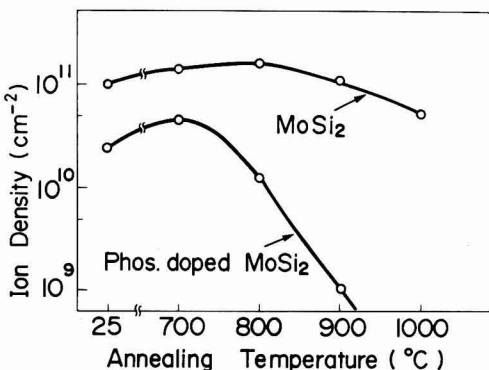


Fig. 21. Mobile ion density in the gate oxide films as a function of annealing temperatures.

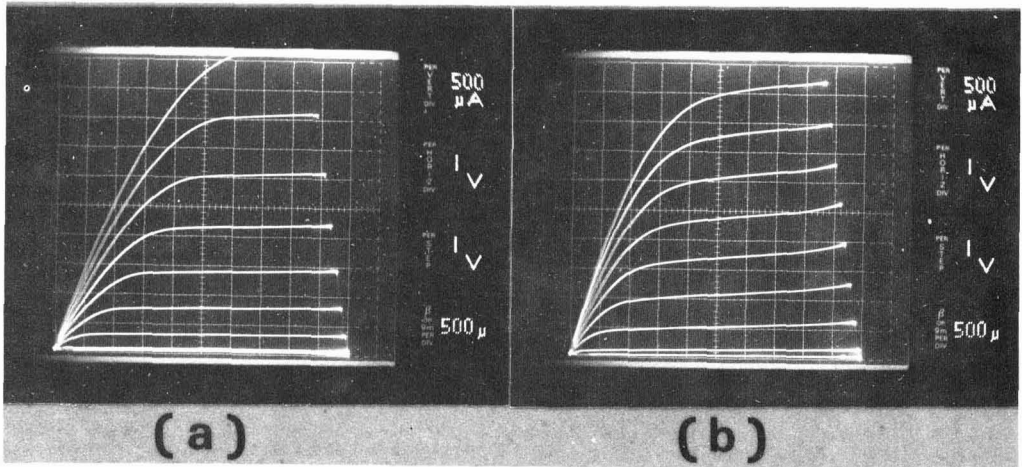


Fig. 22. Current-voltage characteristics of the phosphorus-doped molybdenum silicide gate MOSFET's. Effective channel length and width are (a) 20 and 100  $\mu\text{m}$ , (b) 2 and 19  $\mu\text{m}$ , respectively.

### Conclusion

Phosphorus-doped molybdenum silicide was deposited by co-sputtering Mo and Si in Ar containing  $\text{PH}_3$ .  $\text{PH}_3$  was decomposed to P and  $\text{H}_2$ , and the phosphorus combined with Mo and Si. As-deposited films ( $\text{Mo/Si} \leq 0.5$ ) exhibited amorphous structure and the resistivity was high. At high annealing temperatures the films became polycrystalline and resistivity was decreased. After annealing at 1000°C for 20 min, the resistivity of film with an Mo/Si ratio of 1:2 was  $7.5 \times 10^{-5} \Omega\text{-cm}$ . This value is one order of magnitude lower than that of polysilicon. As the proportion of Si increases in the film, the resistivity also increases.

After high temperature annealing, the excess Si in Si-rich silicide film on  $\text{SiO}_2$  and the excess Mo in Mo-rich silicide on  $\text{SiO}_2$  move to the surface and the silicide interface both. At these locations, Si-rich or Mo-rich silicide layers were formed.

The silicide films on Si with various Mo/Si ratios are changed in composition to a  $\text{MoSi}_2$  after high temperature annealing.

When the silicide is covered with  $\text{SiO}_2$ , phosphorus can diffuse from the films into the Si substrate as in doped polysilicon, so the contact region need not be doped prior to gate electrode deposition.

Good ohmic contact between the phosphorus-doped molybdenum silicide and Si substrate is maintained because the phosphorus prevents the formation of a highly resistive layer at the silicide/Si interface during high temperature annealing. Contact resistance

was below  $2 \times 10^{-6} \Omega\text{-cm}^2$  after annealing at temperatures up to 1100°C.

$V_{th}$  shifts are within  $\pm 20$  mV under stress conditions of  $\pm 2.5$  MV/cm for 1000 hr at 150°C and mobile ions in the film were no longer detectable after annealing. The reliability of phosphorus-doped molybdenum silicide gate technology is comparable to polysilicon gate technology.

These important advantages make doped molybdenum silicide material technology a viable alternative to polysilicon in LSI fabrication.

### Acknowledgments

The authors wish to thank Dr. T. Misugi, Dr. Y. Fukukawa, and H. Hashimoto for helpful discussion; S. Tatsuta for backscattering analysis; and M. Shiraki, T. Shinoki, T. Fukano, and H. Horie for help with measurement.

Manuscript submitted Nov. 14, 1980; revised manuscript received March 9, 1981.

Any discussion of this paper will appear in a Discussion Section to be published in the June 1982 JOURNAL. All discussions for the June 1982 Discussion Section should be submitted by Feb. 1, 1982.

Publication costs of this article were assisted by Fujitsu Laboratories Limited.

### REFERENCES

1. D. M. Brown, W. E. Engler, M. Garfinkel, and P. V. Gray, *Solid-State Electron*, **11**, 1105 (1968).
2. A. K. Sima, T. E. Smith, T. T. Shange, and N. N. Axelrod, *J. Vac. Sci. Technol.*, **10**, 436 (1973).
3. M. Kondo, T. Mano, H. Yanagawa, H. Kikuchi, T. Amazawa, K. Kiuchi, and H. Yoshimura, *ISSCC Dig. Tech. Papers*, 158 (1978).
4. M. Koyanaki, T. Hayashida, N. Yamamoto, and H. Hashimoto, Abstract 153, p. 409, The Electrochemical Society Extended Abstracts, Boston, Massachusetts, May 6-11, 1979.
5. F. Yanagawa, K. Kiuchi, T. Hosoya, T. Tsuchiya, T. Amazawa, and T. Mano, *Tech. Dig. IEDM*, 362 (1979).
6. H. Ishikawa, M. Yamamoto, H. Tokunaga, N. Toyokura, F. Yanagawa, K. Kiuchi, and M. Kondo, *IEEE Trans. Electron Devices*, **ed-27**, 1586 (1980).
7. T. Mochizuki, K. Shibata, T. Inoue, and K. Ohuchi, *Jpn. J. Appl. Phys.*, **17**, Suppl. 17-1, 37 (1978).
8. B. L. Crowder and S. Zirinsky, *IEEE J. Solid-State Circuits*, **sc-14**, 291 (1979).
9. S. P. Muraka, *Tech. Dig. IEDM*, 454 (1979).
10. K. C. Saraswat, F. Mohammadi, and J. D. Meindl, *ibid.*, 462 (1979).

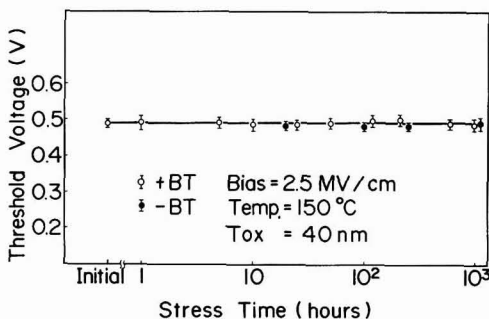


Fig. 23. Threshold voltage shifts of MOSFET's with effective channel length of 20  $\mu\text{m}$  after bias and temperature stress.

11. T. P. Chow, A. J. Steckl, M. E. Motamedi, and D. M. Brown, *ibid.*, 458 (1979).
12. T. Mochizuki, M. Kashiwagi, and Y. Nishi, 700 RNP, *This Journal*, 126, 457C (1979).
13. P. Shah, D. Laks, and A. Wilson, *Tech. Dig. IEDM*, 465 (1979).
14. K. Chow and L. G. Garrison, *This Journal*, 124, 113 (1979).
15. M. Pelavin, D. N. Hendrickson, J. M. Hollander, and W. Ljolly, *J. Phys. Chem.*, 74, 1116 (1970).
16. A. Saxena, in "Proceedings of International Topical Conference on SiO<sub>2</sub> and Its Interface," p. 195, Pergamon, New York (1978).
17. M. Takagi, K. Nakamura, C. Terada, and H. Kamioka, *Jpn. J. Appl. Phys.*, Suppl. 101 (1973).
18. C. Koburger, M. Ishag, and H. Geipel, Abstract 162, p. 428, The Electrochemical Society Extended Abstracts, St. Louis, Missouri, May 11-16, 1980.
19. R. S. Nowicki and J. F. Moulder, Abstract 163, p. 431, The Electrochemical Society Extended Abstracts, St. Louis, Missouri, May 11-16, 1980.
20. M. Kuhn, *Solid-State Electron.*, 13, 873 (1970).
21. M. Yamin, *IEEE Trans. Electron Devices*, ed-13, 79 (1966).

## Shaping of Bulk Semiconductor Samples by Photolithography and Chemical Etching

J. S. Blakemore, R. S. Mand,<sup>1</sup> and E. H. Wishnow

Oregon Graduate Center, Beaverton Oregon 97006

### ABSTRACT

Semiconductor bulk samples, suitable for characterization of electronic properties, have been made by simultaneous deep patterned mesa etching from opposing faces of polished wafers. Outlines of the samples to be produced were delineated by areas of hard-baked photoresist on those faces, with mirror-image masks aligned for the two opposing faces. Sample outlines thus created included the well-known "bridge-shaped" and "clover-shaped" forms used for electrical characterization. The etching action was quenched when canyons etched from the two faces met, releasing individual sample shapes. An H<sub>2</sub>SO<sub>4</sub>/H<sub>2</sub>O<sub>2</sub>/H<sub>2</sub>O etch was used in making GaAs samples, from polished wafers of (100), (110), (111), and (211) orientations; wafers of thickness in the range 0.2-0.5 mm could be used without excessive undercutting. Preliminary results are reported for silicon samples made by this method, using an HNO<sub>3</sub>/HF/H<sub>2</sub>O etch.

Numerous techniques have been developed for the characterization of (nominally homogeneously doped) bulk semiconductor materials (1). When the electrical resistivity is moderate (no more than a few hundred  $\Omega$  cm), some basic properties of isotropic monocrystalline materials can be assessed with reasonable accuracy from measurements on a bulk ingot or sliced complete wafer, using contactless or temporary probe methods. However, many characterization methods require a bulk sample of specific size and shape. There are special problems associated with the interpretation of data for an anisotropic solid (2, 3), for material with inhomogeneous doping (4), or for a porous ceramic sample (5). However, the concern of the present work was simply to arrive at desired sample shapes for isotropic monocrystalline semiconductors, with a primary interest in semi-insulating GaAs.

Intricate sample shapes can be produced, in principle, by mechanical, chemical, and electrochemical methods of attack. For the high resistivity GaAs of interest to us, electrochemical attack by spark erosion cutting was not possible. This method has been used for highly conducting semiconductors (6), though is more traditionally thought of as a method for shaping metallic samples (7).

Mechanical shaping techniques include use of a diamond cut-off wheel, string saw, airborne abrasive particle stream, and ultrasonic impact cutter head. For semiconductors which do not cleave excessively readily (such as Ge and Si), complex sample shapes have been made in many laboratories using a liquid slurry of abrasive particles, directed by an ultrasonic tool with a "cookie-cutter" impact head (8). Since a thin GaAs

wafer is prone to cleavage on {110} planes, impact cutting is much less attractive for that material, if the desired sample shape is to include arms with narrow necks. We have been able to use mechanical methods for making bulk GaAs samples in simple shapes such as a filamentary one without sidearms; but attempts to use impact cutting for shapes with narrow sidearms had relatively poor success.

At that point, we were encouraged (by Dr. P. K. Bhattacharya) to attempt sample shaping by unusually deep mesa etching, using photolithographic delineation for the areas to be protected from etching. A shallower version of this is, of course, a common procedure for electrical isolation of a thin conducting layer on a semi-insulating substrate (9), or one separated from the underlying material by a p-n junction.

This paper reports on a procedure we have found satisfactory for making GaAs samples, with simultaneous mesa etching from the opposing faces of a wafer of thickness up to approximately 0.5 mm. The etching action produced an array of "canyons" into the two faces. The etching action was quenched when the canyons from the opposing faces met, an event signalled by the release of individual sample shapes.

Some samples have similarly been made of silicon, and Fig. 7 and 8 will show the appearance of these. Whereas the procedure for GaAs has become a routine in this laboratory, that for silicon is preliminary and not optimized.

### Some Useful Sample Shapes

The simplest shape for measurements of the basic electronic transport parameters of a semiconductor (conductivity, Hall effect, etc.) is an elongated filamentary bar, of uniform cross section. If this cross section is rectangular, then the rectangular parallelepiped

<sup>1</sup> Present address: School of Applied Physics, University of Bradford, Bradford, England.

Key words: sample shape, mesa etching, gallium arsenide, silicon.



shape can be simply made with a series of cuts by a diamond wheel or string saw. That shape was used in Pearson and Bardeen's 1948 investigation (10) of carrier transport in doped silicon, with electroplated areas on ends and sides for current contacts and potential probes.

It is advantageous to have potential contacts removed from the region of current flow. This led to the adoption of more intricate sample shapes, often cut by impact grinding (8) through a parallel-faced wafer. Among these shapes one of the most useful has been the "bridge-shaped" one; a filamentary bar with sidearms. Those sidearms were "dumb-bell" shapes as utilized and illustrated by Pearson and Suhl (11) and by Debye and Conwell (12). Such dumb-bell shapes can provide large areas for minimization of contact resistance, though are not necessary if the contacting procedure provides an adequately small specific contact resistance, in  $\Omega\text{-cm}^2$ .

Figure 1 illustrates a bridge-shaped sample we have made by the procedure of photolithography and chemical etching described in the present paper. The sample shape of Fig. 1 uses simple rectangular sidearms; the shape analyzed by Jandl *et al.* (13) as a "double-cross." Jandl *et al.* showed that relatively short rectangular arms could permit adequate isolation of the contact pad areas from the current flow in the main bar. Thus current density and electric field strength are essentially constant throughout the volume being analyzed, for a bridge-shaped or double-cross sample of semiconductor material which is isotropic and uniformly doped.

In contrast, some other geometries cause the equipotential surfaces to be markedly nonplanar, and unequally spaced. That is not a problem for some semiconductor materials, particularly if measurements are to be made exclusively of low field transport in the dark. However, some semiconductors are less tolerant of field nonuniformity, especially if high electric fields and/or a photoconductive response is to be involved.

The sample shapes most commonly used for which the field pattern is markedly nonuniform are based on the theorem of van der Pauw (14, 15) for the resistance of a flat sample with peripheral contacts. These shapes include the simple rectangular slab with corner contacts (16), the "Greek cross" (17), and the "clover" shape<sup>2</sup> that van der Pauw proposed and illustrated

<sup>2</sup> This shape has attracted many names in the ensuing literature, including "iron cross," "papal cross," "Maltese cross," and others.

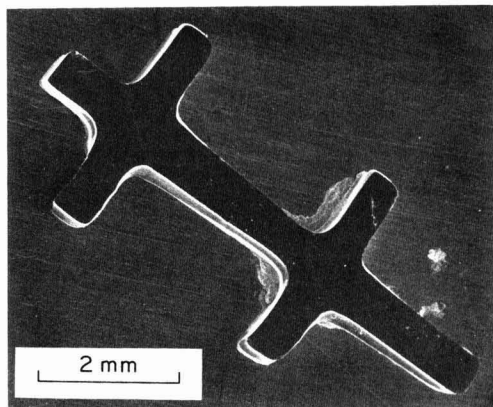


Fig. 1. A bridge-shaped sample of chromium-doped semi-insulating GaAs, created from a polished 0.45 mm thick wafer of (211) orientation, by etching inwards from both faces while the designated sample area was protected by photoresist. Etching was carried out in  $(2)\text{H}_2\text{SO}_4\text{-(1)H}_2\text{O}_2\text{-(1)H}_2\text{O}$  at  $80^\circ\text{C}$ .

(14, 15). Figure 2 illustrates a clover-shaped sample of GaAs, made by the method described in the present paper, and prior to the evaporation of Au:Ge contact areas in the outer corners.

### Experimental Procedures for GaAs Samples

As noted in the introduction, the procedure we evolved consisted of removal of unwanted bulk material surrounding designated sample outlines by chemical etching, this action proceeding from both faces of a wafer simultaneously. Meanwhile, the sample areas themselves were protected with hard-baked photoresist. This section describes the procedure as evolved for making GaAs bulk samples of satisfactory outline shape and profile.

Many factors determine the outcome when parts of a semiconductor wafer are protected by photoresist, and adjacent unprotected portions are chemically etched. Thus, etching may be carried out in a plasma chamber, or in a liquid. Our work as reported here used aqueous etches.

The etching rate in aqueous solution depends on the strength and freshness of the ingredients, on the solution temperature, and often on crystal orientation (18, 19). Highly preferential etching can sometimes be turned to advantage; thus, Otsubo *et al.* (20) used citric acid/peroxide etches into {100} GaAs to create flat-bottomed holes, and grooves of "tsuzumi" (hand-drum) profile. [An even more dramatic anisotropy of the etching rate has been demonstrated in the work of Kendall (21) with {110} silicon, using KOH-based etches to make deep narrow grooves.] However, our preference was for an etch that would work with more or less facility for GaAs wafers of various orientations.

The etch composition and strength that we have found particularly useful for the present purpose with GaAs of various orientations has been  $(2)\text{H}_2\text{SO}_4\text{-(1)H}_2\text{O}_2\text{-(1)H}_2\text{O}$ , used in the temperature range  $70^\circ\text{C}$ - $80^\circ\text{C}$ . Iida and Ito (22) showed that the  $\text{H}_2\text{SO}_4/\text{H}_2\text{O}_2/\text{H}_2\text{O}$  system includes some compositions that are highly selective, but found that the above-mentioned composition gave good polishing action for most low index planes of GaAs with, of course, an inferior response for the gallium (111A) plane. This has been our experience also. When the above-cited etch composition is used at  $80^\circ\text{C}$  for a (111) GaAs wafer, the attack rate on the (111A) plane is only about 30% slower than on

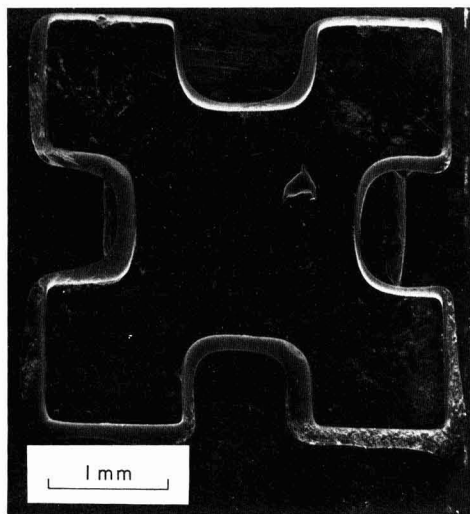


Fig. 2. A clover-shaped sample of semi-insulating GaAs, made by the same method as the sample of Fig. 1. The polished starting wafer here was of (100) orientation, 0.53 mm thick.

the (111B) plane ( $7 \mu\text{m}$  per min, compared with  $10 \mu\text{m}$  per min), but microscopic examination of a partly consumed wafer shows the attacked (111A) surface to be much more pitted than the opposite face.

Figure 3 illustrates the effect of various etching times on the total thickness reduction of wafers with orientations of (100), (110), (111), and (211), determined from microscopic measurement of the decrease of distance between bottoms of opposing etched canyons. These measurements, the consequences of using the above-cited etch at  $80^\circ\text{C}$ , correspond to an etching rate of some  $(10 \pm 1) \mu\text{m}/\text{min}$  for fresh etch acting on a GaAs surface with any orientation other than (111A). That rate, and the reduction of some 30% for (111A), is in general agreement with the findings of Iida and Ito (22) for etching rate vs. composition, orientation, and temperature. Figure 3, and similar results obtained with other wafers, shows no signs of any pre-etching induction period. Provided the etching solution is freshly prepared, and of large enough quantity so that reaction products do not slow the action, then etching reduces thickness at an essentially linear rate until sample separation occurs. For a wafer  $0.5 \text{ mm}$  thick, this requires about 25 min for most orientations, and perhaps 28–30 min for a {111} wafer.

The wording of the preceding paragraph was chosen to indicate that reliable etching at a constant rate was obtained when the etch (i) was used fresh, and (ii) was of volume sufficient to minimize the effects of dissolved etching products on the continuation of the process. Thus, for a part-wafer of area  $5 \text{ cm}^2$  and thickness  $0.5 \text{ mm}$ , one may need to etch away about  $0.75 \text{ g}$  of GaAs to separate out individual samples. It would be our practice not to attempt this with less than  $100 \text{ ml}$  of mixed etch, with vigorous stirring of the etch throughout to minimize the buildup of etch products near the surfaces under attack.

Since the procedure required that a wafer remain in the etch for a time of up to half an hour at a temperature of  $70^\circ\text{--}80^\circ\text{C}$ , it was extremely important that the photoresist over designated sample areas adhere as strongly as possible. That called for some changes from the photoresist procedures normally encountered in

the integrated circuit industry, where etch depths are typically no more than a few micrometers, and etch durations quite short.

Our objectives of etching completely through wafers up to a considerable thickness also placed requirements on the layout of any sample shape on the mask, that this allow for inevitable undercutting. Resist adhesion and undercutting are related, since any tendency of the resist to "lift off" around the edges will open up new territory for undercutting.

Figure 4 shows part of a (211) GaAs wafer bearing a repetitive array of hardened photoresist areas (each of the van der Pauw clover shape) after etching for 1 min. The unprotected areas have been etched to a depth of some  $10 \mu\text{m}$ . It will be observed that the resist has curled up from one corner, and is showing signs of doing so at two adjacent corners. That lack of adherence is unacceptable in view of the 20 or more minutes of additional etching time that would be necessary to complete separation of samples from each other.

The results of etching a wafer for a longer period of time are exemplified by the almost edge-on view shown in Fig. 5. The wafer here was of (100) orientation, patterned on both faces with photoresist, etched at  $80^\circ\text{C}$  for 7 min, and cleaved to permit study of the profiles of the canyons etched from the opposing faces. Note in Fig. 5 that (i) overhanging ledges of photoresist jut out above the canyon walls, (ii) the canyon

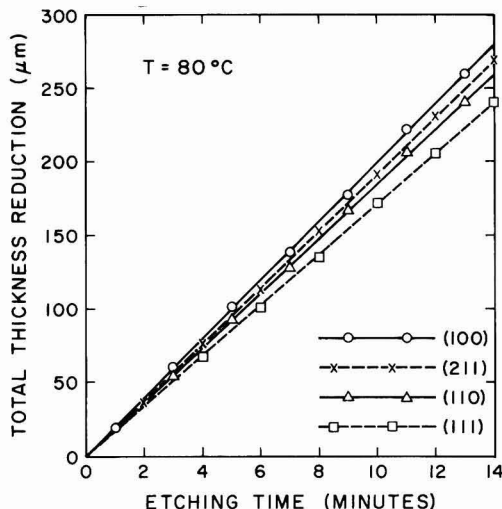


Fig. 3. Total reduction in wafer thickness (sum of amounts thinned from opposing sides) vs. etching time, for GaAs in  $(2)\text{H}_2\text{SO}_4\text{--}(1)\text{H}_2\text{O}_2\text{--}(1)\text{H}_2\text{O}$  at  $80^\circ\text{C}$ . These are representative data for wafers etched in large quantities of the etchant, with ample stirring, so that effects of etchant exhaustion and/or poisoning were minimized. The results for (100), (110), and (211) are all essentially the same. The total thinning rate is smaller for (111) wafers because of the slower attack rate for the (111A) face.

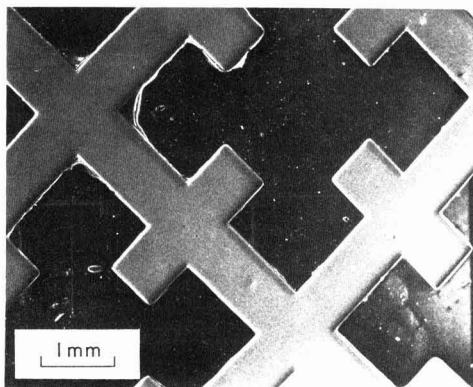


Fig. 4. Part of a repetitive pattern for making clover-shaped samples, as formed into hardened resist areas on the surface of a (211) GaAs wafer. One minute in the  $\text{H}_2\text{SO}_4/\text{H}_2\text{O}_2/\text{H}_2\text{O}$  etch has removed some  $10 \mu\text{m}$  of material from the unprotected areas. Note that poor adherence of the photoresist for this wafer has already led to curling back from some outer corners.

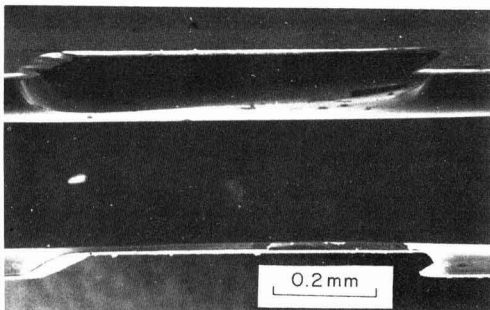


Fig. 5. An edge-on view of a  $400 \mu\text{m}$  thick (100) GaAs wafer, which had been (a) patterned with hardened resist so that resist edges would lie along  $\langle 011 \rangle$  directions, (b) etched at  $80^\circ\text{C}$  for 7 min, and then (c) cleaved to permit the edge-on view.

floors are essentially flat and parallel, and (iii) the canyon walls curve in a manner appropriate for complete nonselectivity of etching action. Somewhat to our surprise, we have found the canyon wall shapes to curve in essentially the same fashion for any (100) wafer (whether the edges of the resist are aligned with  $\langle 010 \rangle$  or  $\langle 011 \rangle$  types of orientation), and also for wafers of other orientations including (111).

The literature provides ample citations for etch pits produced in GaAs [and other zincblende structure solids such as InSb (23)] which show marked facets of preferential etching. Thus Iida and Ito (22) showed that slow action of an  $\text{H}_2\text{SO}_4/\text{H}_2\text{O}_2/\text{H}_2\text{O}$  etch on (100) could produce a flat-bottomed pit of trapezoidal cross section (overhanging canyon walls) when the edge of the resist-protected area was parallel to  $\langle 010 \rangle$  or  $\langle 001 \rangle$ . We have not observed this to happen with the relatively speedy etching action of the 2:1:1 composition at 80°C. With any orientation of the wafer and any alignment of the mask pattern, the canyon wall shows a curved profile such as that in Fig. 5. Incidentally, that figure shows undercutting to have proceeded by some 40  $\mu\text{m}$  at a stage when the canyon floor lies some 75  $\mu\text{m}$  below the original wafer surface plane.

Through the courtesy of M. Pope and M. Wright, photographic masks were made for us through which photoresist could be exposed. These masks had repetitive patterns for sample shapes (such as bridge-shape and clover-shape). It was necessary to have pairs of masks which were mirror images of each other, so that a matched pair placed to sandwich a prepared wafer would register the same pattern on both surfaces of that wafer. A simple mechanical fixture was constructed which enabled the pair of masks to be aligned with respect to each other, in respect of  $x$ ,  $y$ , and  $\theta$ .

Mask pairs of these kinds were made with opaque/transparent patternings suitable for use with positive resist, and additional pairs of the converse opacity for use with negative resist. Our first crude attempts at sample separation were made using a negative resist<sup>3</sup> on the wafer faces, and were (not surprisingly) accompanied by frequent failures owing to resist detachment during the lengthy etching. There can be little doubt that the procedure can be made to work perfectly well with negative resist applied and baked properly; but we have not persisted with this approach. For since it happened that we were successful rather soon in persuading positive resist<sup>4</sup> to stay in place until etching was complete, all our subsequent work has been based on the positive resist approach. Thus, for this we have been using masks with opaque areas where designated sample areas are to be protected from the etching action.

Photoresist as used in the integrated circuit industry is applied typically by spinning, with a resist layer thickness of perhaps 1  $\mu\text{m}$ , and an emphasis on the ability to create narrow linewidths (24). Our requirements were quite different. High spatial resolution was not important, but a tenacious and adherent resist layer on both faces was very important. These requirements were met most readily by dip coating of suitably prepared wafers, at a temperature ( $T \approx 20^\circ\text{C}$ ) and viscosity that would provide a hardened film thickness in the range 12-17  $\mu\text{m}$ .

Our wafer preparation now requires that both faces of the wafer be polished. That admittedly involves extra work, but we have found that undercutting progresses more slowly under photoresist that is firmly adherent to a polished face.

Thus the procedure as it has evolved comprises mechanical polishing of both faces, degreasing, baking dry at 90°C, cooling to room temperature, photoresist application by dip coating, a 1 hr "soft bake" at 90°C, cooling to 25°C, exposure to u.v. radiation through a

matched pair of facing masks, development in diluted (Shipley AZ-351) resist developer, water rinse, air dry, and then a 2 hr "hard bake" at 160°C. When cooled for handling, the wafer is then ready for etching.

Two physical arrangements have been used for etching. In one of these, the wafer (and its eventual daughter samples) is supported above a glass frit in the etching solution, while bubbled nitrogen gas is supplied from below to provide agitation. The other arrangement uses a magnetic stirrer within the beaker of etch on a hotplate. (The latter arrangement simplifies positive control of the temperature.) The clover-shaped sample of Fig. 2 happened to have been made using the first of these systems, while the bridge-shaped sample of Fig. 1 was made using the magnetic stirring system.

The clover-shaped sample of Fig. 2 came from a wafer 0.53 mm thick. Thus one might expect the periphery of the top and bottom sample surfaces to retreat by some 200-250  $\mu\text{m}$  if etching and undercutting were completely isotropic. A comparison of this sample with mask dimensions shows that the upper periphery has actually been cut back by  $(215 \pm 10)$   $\mu\text{m}$ . However, Fig. 6 shows a magnified edge-on view of one corner of this sample, and one may see that the cusped profile protrudes by only  $\sim 100$   $\mu\text{m}$ . This was obtained by allowing the etching to continue for some 30 sec after the first sample was seen to "calve" from the parent wafer. Now such a sample would normally have the resist stripped from top and bottom faces (with acetone and/or Shipley 1112A "photoresist stripper"), and then be etched over its entire surface prior to contacting, in order to remove the mechanical damage associated with the prior polishing procedures. That additional etching would further reduce the peripheral protuberance before the sample was ready for electrical measurements.

A clover-shaped sample with a protuberant profile as just described and illustrated is in technical violation of a requirement of van der Pauw's theorem (14, 15), that a sample be of constant thickness over its entire current-bearing area. However, a protuberance of the size described appears to involve an error in the analysis of van der Pauw resistivity and Hall measurements of less than 3% by direct measurement; an error in the (expected) sense of making the resistivity (using van der Pauw's expression) appear slightly low. That estimate of the error involved was obtained by first measuring a sample as resulting from

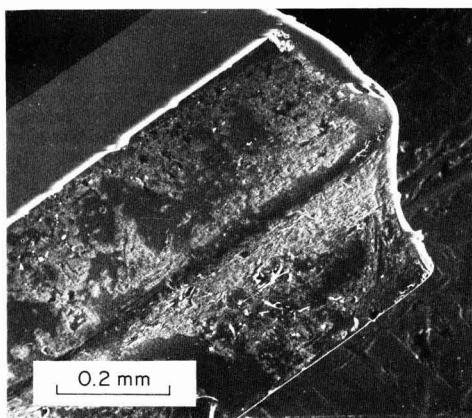


Fig. 6. A magnified edge-on view of one corner of the clover-shaped sample of Fig. 2. This shows details of the edge profile resulting from undercutting prior to sample separation, and the partial rounding off of this cusped protuberance during an additional 30 sec of etching after separation.

<sup>3</sup> MOS-Grade Negative Photoresist, available from KTI Chemicals, of Sunnyvale, California.

<sup>4</sup> AZ-1350J Positive Resist, available from the Shipley Company, of Newton, Massachusetts.

the photolithography/etching process, and then using an abrasive particle stream to "trim up" the re-entrant portions of the sample periphery.

The GaAs bridge-shaped sample of Fig. 1 shows similar imperfections of profile. In that case, these would be enough to require that the usual conversion [ $\sigma = (L/wt)(I/V)$ ] from resistance to bulk conductivity be modified to take account of the slightly non-rectangular cross section of the bar. Whereas the bridge sample of Fig. 1 has a thickness  $t = 0.45$  mm, we have usually resorted to thinner wafers when the desire was for Hall data with GaAs bridges of more nearly perfect geometry. Of course, a sample shape and profile such as that of Fig. 1 is perfectly adequate for photoconductive or various relative measurements.

Thus, for most of our purposes in measuring GaAs of resistivity up to the semi-insulating range, the procedure as described above needs little further optimization.

### Preliminary Results with Silicon Samples

A procedure for making silicon samples by simultaneous etching from both sides of a masked wafer has not been tested by us so far beyond the stage of crude feasibility. Results we obtained show that the etch we used, of (2)HNO<sub>3</sub>-(2)HF-(1)H<sub>2</sub>O composition (25), was not ideal for this purpose.

Figure 7 shows a clover-shaped silicon sample, made from a (100) wafer that had been polished on both faces, equipped with patterned photoresist as described in the previous section, and etched in the HNO<sub>3</sub>/HF/H<sub>2</sub>O solution until individual samples separated. With the etch brought to a temperature of 30°C prior to the introduction of the wafer, separation of individual samples from a wafer ~0.4 mm thick would occur in approximately 3 min. As is well known (19, 25), this is a fast-acting etch.

It will be apparent from Fig. 7 that the periphery of this sample (of 0.37 mm thickness) was undercut much more severely than for the GaAs samples previously illustrated. The extent of the undercutting is shown clearly in the enlarged edge-on view Fig. 8 provides of one corner of that sample. In this instance, etching action was quenched with water as soon as possible after the release of individual samples was spotted, thus the cusp tip was not appreciably eroded. However, note also in Fig. 8 that the edge of the sample blends toward the upper and lower surface faces in convex arcs. This shows that the etching action had preferentially attacked the wafer/photoresist interface.

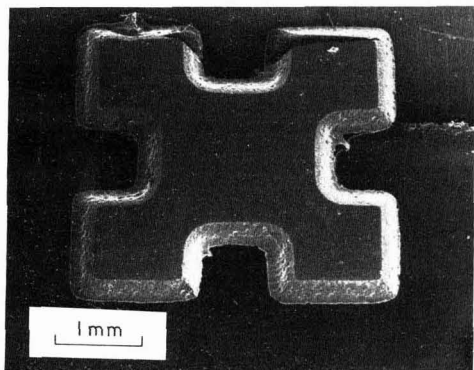


Fig. 7. A silicon clover-shaped sample, made by photomasking and chemical etching of a polished (100) wafer 370  $\mu$ m thick. Etching was carried out in (2)HNO<sub>3</sub>-(2)HF-(1)H<sub>2</sub>O at  $T \approx 30^\circ\text{C}$ , and sample separation occurred (with severe undercutting as may be seen) after etching from both faces simultaneously for 150 sec.

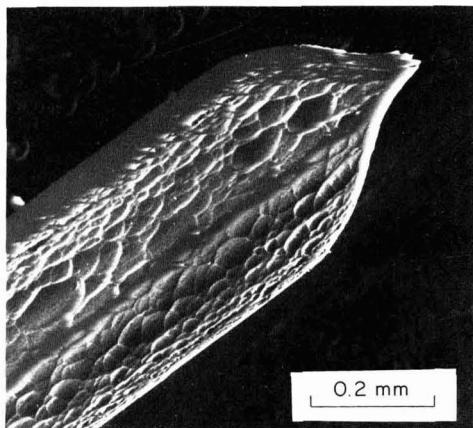


Fig. 8. An enlarged edge-on view of one corner of the silicon sample of Fig. 7. The convex curvature of the edge surface adjacent to the top and bottom faces indicates that the etch had preferentially attacked the (SiO<sub>2</sub>-rich) silicon surface under the edge of the resist layer.

That preferential attack is inherent in the mechanism by which an etch of the HNO<sub>3</sub>/HF/H<sub>2</sub>O family attacks silicon (19, 25), because the inevitable SiO<sub>2</sub> layer on the silicon surface is attacked by HF, the complexant in the mixture. That promotes undercutting, and lift-off of the photoresist shapes. When we have attempted to make silicon samples, but with the etch solution cooled, to slow down the reaction rate, the photoresist has always lifted off before the canyons from the two faces have had an opportunity to meet.

Thus one can envisage preferable etching approaches for making silicon samples. One possibility is that the wafer might first receive a quick dip in HF (to remove SiO<sub>2</sub> from the exposed areas), then be rinsed, and placed for an extended period in an etch (such as an alkaline one) that has a preference for dissolution of Si itself rather than SiO<sub>2</sub>.

### Acknowledgments

We wish to thank Morgan Pope and Mel Wright of Tektronix, Incorporated, for their splendid cooperation in making masks patterned to meet our various needs. We should also like to thank Pallab Bhattacharya and Robert Rugh for helpful discussions. This work has been supported in part by the National Science Foundation, through Grant DMR 79-16454.

Manuscript submitted Dec. 18, 1980; revised manuscript received May 7, 1981.

Any discussion of this paper will appear in a Discussion Section to be published in the June 1982 JOURNAL. All discussions for the June 1982 Discussion Section should be submitted by Feb. 1, 1982.

Publication costs of this article were assisted by the Oregon Graduate Center.

### REFERENCES

1. See, for example, W. R. Runyan, "Semiconductor Measurements and Instrumentation," Chap. 3, Texas Instruments, Inc., Dallas, TX (1975).
2. L. J. van der Pauw, *Philips Res. Rep.*, **16**, 187 (1961).
3. H. C. Montgomery, *J. Appl. Phys.*, **42**, 2971 (1971).
4. See, for example, R. T. Bate, in "Semiconductors and Semimetals, Vol. 4," R. K. Willardson and A. C. Beer, Editors, p. 459, Academic Press, New York (1968); also, J. S. Blakemore, *J. Appl. Phys.*, **52**, 840 (1981).
5. H. J. Juretschke, R. Landauer, and J. A. Swanson, *ibid.*, **27**, 838 (1956).



6. B. I. Stavitsky, *Elektron. Obra. Mater.*, **4**, 3 (1969).
7. R. H. Packwood and R. W. Smith, *J. Sci. Instrum.*, **44**, 1057 (1967).
8. W. L. Bond, *Phys. Rev.*, **78**, 646 (1950).
9. C. M. Wolfe, G. E. Stillman, and E. B. Owens, *This Journal*, **117**, 129 (1970).
10. G. L. Pearson and J. Bardeen, *Phys. Rev.*, **75**, 865 (1949).
11. G. L. Pearson and H. Suhl, *ibid.*, **83**, 768 (1951).
12. P. P. Debye and E. M. Conwell, *ibid.*, **93**, 693 (1954).
13. S. Jandl, K. D. Usadel, and G. Fischer, *Rev. Sci. Instrum.*, **45**, 1479 (1974).
14. L. J. van der Pauw, *Philips Res. Rep.*, **13**, 1 (1958).
15. L. J. van der Pauw, *Philips Tech. Rev.*, **20**, 220 (1958).
16. R. Chwang, B. J. Smith, and C. R. Crowell, *Solid-State Electron.*, **17**, 1217 (1974).
17. W. Versnell, *ibid.*, **22**, 911 (1979).
18. B. Tuck, *J. Mater. Sci.*, **10**, 321 (1975).
19. W. Kern, *RCA Rev.*, **39**, 278 (1978).
20. M. Otsubo, T. Oda, H. Kumabe, and H. Miki, *This Journal*, **123**, 676 (1976).
21. D. L. Kendall, *Appl. Phys. Lett.*, **26**, 195 (1975).
22. S. Iida and K. Ito, *This Journal*, **118**, 768 (1971).
23. H. C. Gatos and M. C. Lavine, *This Journal*, **107**, 433 (1960).
24. See, for example, A. B. Glaser and G. E. Subak-Sharpe, "Integrated Circuit Engineering," Section 5.10, Addison-Wesley, Reading, MA (1977).
25. H. Robbins and B. Schwartz, *This Journal*, **106**, 1020 (1959); B. Schwartz and H. Robbins, *ibid.*, **123**, 1903 (1976).

## Parameter Dependence of RIE Induced Radiation Damage in Silicon Dioxide

L. M. Ephrath,\* D. J. DiMaria, and F. L. Pesavento

IBM T. J. Watson Research Center, Yorktown Heights, New York 10598

### ABSTRACT

Radiation damage in silicon dioxide films exposed to reactive ion etching (RIE) in  $\text{CF}_4$  has been investigated. Capacitance-voltage (C-V) and photo-current-voltage (photo I-V) techniques were used to monitor charge trapping and location after the films were incorporated into MOS capacitors. Blanket etched films were used to study the trapping characteristics of bulk, neutral, radiation-induced traps as a function of position in the reactor, rf peak-to-peak voltage, and pre-RIE high temperature annealing. The trapping characteristics of films etched in a  $\text{CF}_4 + \text{H}_2$  mixture were also studied. Oxide films etched in  $\text{CF}_4 + \text{H}_2$  show reduced trapping when compared with oxides etched in  $\text{CF}_4$ . The ability of gate electrode materials to shield an underlying oxide during RIE was also tested. It was determined that aluminum and  $\text{n}^+$  polysilicon are effective in shielding oxide from RIE induced radiation damage.

Reactive ion etching (RIE) is a directional, dry etching technique that has been used in our laboratory to fabricate micron dimension FET logic and array chips (1, 2). RIE is used at several levels of processing including definition of recessed oxide isolation, polysilicon gate electrodes, and contact holes to polysilicon and diffused regions. Extensive use of RIE is required for the delineation of fine lines and openings with no undercut of the etch mask. RIE is, however, carried out in a radiation environment; substrates are subjected to bombardment by electrons, ions, and photons. For this reason, experiments have been carried out to determine the effect of RIE on the reliability of devices. RIE induced trapping was characterized by exposing a blanket oxide film to RIE, incorporating the etched oxide into an MOS device, and injecting charge into the conduction band of the oxide by avalanche injection. The numbers and cross sections of the traps, the density of trapped charge, and the centroid of the trapped charge distribution were determined by C-V and photo I-V techniques (3). Three distinct trapping sites were observed (4). The first was a buildup of positive charge at the silicon-silicon dioxide interface. These positive trapped charges present a coulombic capture cross section for electrons in the range of  $10^{-12}$  and  $10^{-13} \text{ cm}^2$  and have a density of about  $10^{12}$  positive charges/ $\text{cm}^2$ . These trapped positive charges are believed to be holes which were generated initially by ionization across the bandgap of the oxide. Some of the free positive charges in the silicon dioxide valence band are subsequently trapped at pre-existing sites

near the interfaces. The second type of trapping site is created by ion implantation damage within about 5 nm of the surface. These traps are observed only when a nonetching gas such as  $\text{O}_2$  is used to clean the surface. Presumably, an etching gas such as  $\text{CF}_4$  removes its damage as it is produced leaving only a residual when etching is stopped. The third type of trap is a neutral trapping center. These sites are distributed approximately uniformly throughout the bulk of the oxide. The electronic capture cross sections of these traps are between  $10^{-14}$  and  $10^{-17} \text{ cm}^2$  and their density is between  $10^{11}$  and  $10^{12} \text{ cm}^{-2}$ . These traps are very similar to those observed by Aitken, Young, Pan, and Ning (5-7) for oxides exposed to much higher energy radiation than in the present case (20-25 keV x-rays or electrons). In the comparatively low energy environment of RIE, the occurrence of trapping in the bulk suggests, by process of elimination, the involvement of photons which are sufficiently energetic to penetrate the oxide. Ion energies are not sufficient to penetrate the oxide, and energetic electrons would not reach the cathode because of its negative bias. High energy photons, though, would be created in the reactor when secondary electrons which are accelerated across the cathode dark space strike ground planes. Photons generated by secondary electrons in an rf sputtering configuration have been shown to degrade the stability of MOS devices (8). Secondary electrons vary in energy depending on when they are emitted during the rf cycle, but some may have energies corresponding to the full peak-to-peak voltage. Photon energies, then, could also approach this value. The trapped positive charge and the ion implantation damage were not studied beyond their initial characterization (Table I).

\* Electrochemical Society Active Member.

Key words: reactive ion etching, plasma etching, radiation damage.

Table I. Summary of trapping center data

Trapping center	Cross section (cm <sup>2</sup> )	Density (cm <sup>-2</sup> )	Source	Anneal T °C
Positive charge	10 <sup>-12</sup> -10 <sup>-13</sup>	10 <sup>12</sup>	Photons	400
Implantation damage	10 <sup>-14</sup> -10 <sup>-15</sup>	10 <sup>13</sup>	Ions	1000
Neutral center	10 <sup>-14</sup> -10 <sup>-17</sup>	10 <sup>11</sup> -10 <sup>12</sup>	Photons	600
Background	10 <sup>-17</sup>	10 <sup>12</sup>	—	—

The trapped positive charge is annealed at a low temperature of 400°C on the aluminum gated structures used in this study. The implantation damage can be eliminated by dip etching the oxide since the damage is confined to the surface or by avoiding the use of a nonetching gas. The neutral traps, however, are present throughout the bulk of the oxide and an anneal of 600°C or more is required for their removal. Thus, they must be avoided or annealed before aluminum metallurgy is in place.

In the present study, the RIE parameter dependence of the neutral traps was studied. The RIE parameters that were varied include position of substrate in the reactor, rf voltage, and composition of etching gas. Finally, the ability of gate electrode materials to shield an underlying oxide from RIE radiation damage was evaluated by etching oxide films masked with aluminum or n<sup>+</sup> polysilicon patterns.

### Experimental

**RIE system.**—The reactive ion etching system used in this work is shown in Fig. 1. The substrates were loaded onto an 18 cm diam aluminum plate. The aluminum plate was mechanically and electrically connected to the water-cooled copper rf cathode. A perforated anode plate which is attached to the grounded chamber was placed 3.3 cm from the cathode in order to prevent backspattering of aluminum sputtered from the substrate holder. A perforated anode plate was used so that wafers could be monitored visually during etching, and also to ensure an adequate and uniform supply of etchant in the vicinity of the wafers. The chamber was evacuated with a 6 in. oil diffusion pump and then backfilled with 40 sccm CF<sub>4</sub> to establish a dynamic pressure of 3.33 Pa (25 milli Torr). During etching, 0.25 W/cm<sup>2</sup> is delivered to the cathode. Under these conditions, the peak-to-peak voltage is 800V. The d-c voltage at the cathode is approximately one-half of the peak-to-peak voltage (9). The etch rate of silicon dioxide in CF<sub>4</sub> is about 50 nm/min.

**Sample preparation.**—Dry silicon dioxide films of 150 nm thickness were grown on boron-doped, <100> orientation, 0.1-0.5 Ω-cm resistivity p-type silicon substrates. The oxide films were then exposed to a CF<sub>4</sub> or CF<sub>4</sub> + H<sub>2</sub> plasma to etch approximately 50 nm of silicon dioxide. The wafers were then cleaned to remove metals and hydrocarbons from the surface of the oxide

in alkali and acid peroxide solutions using a procedure similar to that used by Irene (10), but without HF. Some wafers received a buffered HF dip at this point in order to remove ~10 nm from the surface of the oxide. After cleaning, some wafers were annealed in an N<sub>2</sub> ambient for 30 min. Annealing temperatures ranged from 600° to 1000°C. Circular aluminum dots, 13.5 nm in thickness and  $5.2 \times 10^{-3}$  cm<sup>2</sup> in area, were then evaporated in vacuum from resistively heated tantalum boats or rf heated crucibles. Finally, the backs of the wafers were stripped and metallized, and a forming gas anneal at 400°C for 20 min was carried out.

**Techniques.**—To investigate the enhanced electron trapping characteristics of silicon dioxide layers exposed to plasmas in an RIE system, avalanche injection (11, 12) and internal photoemission (13-15) techniques were used to inject electrons from the contacts of the MOS structures into the oxide. The experimental apparatus for avalanche injection (16) and internal photoemission (17) have been described in other publications. As the electrons traverse the film in the presence of an applied electric field, some of the carriers are trapped into sites created during RIE. This trapping is not particularly sensitive to the mode of carrier injection: avalanche injection from the silicon or internal photoemission from the aluminum or silicon. The trapping rate is not particularly sensitive to the average field in the oxide layer which is consistent with the weak field dependence of the capture process for radiation induced neutral traps recently reported by Ning (7). This weak field dependence is in contrast to the strong field dependence of electron capture on trapped holes (3, 7, 18).

The buildup of this trapped charge is sensed through the internal electric field it creates near the contacts by the capacitance-voltage (C-V) (19, 20) and photocurrent-voltage (photo I-V) (18, 21, 22) techniques which are well described in the literature. The voltage shifts between the C-V curves depend on the product  $\bar{x}Q$  where  $Q$  is the charge per unit area and  $\bar{x}$  is the centroid of trapped charge in the oxide layer measured with respect to the aluminum-oxide interface (19, 20). The voltage shifts between photo I-V data for both positive and negative polarity allow separate determination of  $\bar{x}$  and  $Q$  (18, 21). The combination of the C-V and photo I-V techniques can also be used to separate silicon-silicon dioxide interface trapping from bulk oxide trapping (18, 21, 22). Also by studying charge buildup as a function of time, electron capture cross sections  $\sigma_c$  and areal trap densities  $N_t$  can be determined (3). These quantities ( $\bar{x}$ ,  $Q$ ,  $\sigma_c$ , and  $N_t$ ) are used to characterize the different traps created by the exposure to RIE plasmas in the following sections. Only a very small amount of trapping was seen for the charging conditions used on samples fabricated in an identical manner, but not exposed to RIE (4). The results were reproducible for different locations within a sample, and for samples fabricated over a time span of several months.

### Results and Discussion

**RIE parameter dependence.**—It was suggested earlier that the neutral traps are created in the relatively low energy environment of RIE by photons. To substantiate this view, substrates were loaded onto the grounded perforated plate with the oxide film facing away from the cathode. In this way, the oxide film is no longer subjected to bombardment by energetic ions. The oxide film is also protected from secondary electrons from the cathode by the silicon substrate. The oxide film is, however, still exposed to photons that are created when secondary electrons strike the walls of the reactor. A plot of the volume density of trapped charge as a function of avalanche injection time (Fig. 2) shows that the oxide etched

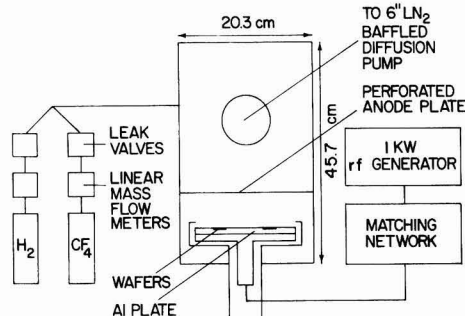


Fig. 1. Schematic of RIE reactor



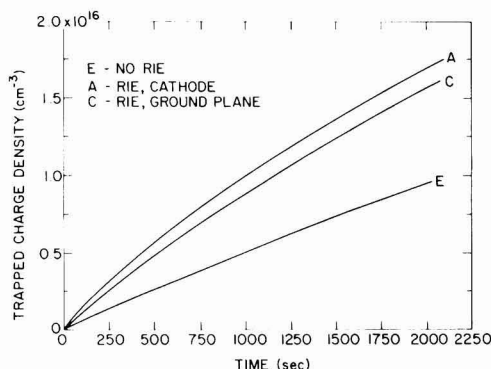


Fig. 2. Volume trapped charge density as a function of avalanche injection time for oxides exposed to RIE on the electrode and on a ground plane. Constant avalanche current =  $8 \times 10^{-9}$ A.

by RIE and the oxide exposed only to energetic photons show enhanced trapping relative to that measured in the control. Data points are taken at 44 sec intervals and so are represented by a solid line. The error bars included for data plotted against an expanded scale in Fig. 7 are representative of data shown in Fig. 2-6.

In the second experiment, the rf power was varied in order to vary the rf peak-to-peak voltage. Etch times were increased as voltage was decreased so that the amount of oxide removed was constant. The purpose of this experiment was to determine whether the introduction of traps exhibited a threshold in the regime of power and pressure that is appropriate for RIE. As can be seen in Fig. 3, enhanced trapping was observed for all oxides etched by RIE even though rf peak-to-peak voltage was reduced by more than a factor of two, from 730 to 330V. Thus, radiation damage is not avoided by etching for longer times at lower rf voltages. It is not possible to carry out RIE at lower voltages. RIE requires low pressures to maintain vertical etching and a low pressure discharge could not be sustained at voltages below 330V. It is possible, however, to reduce voltage if the requirement for directional etching is suspended. For the third experiment, pressure was increased to simulate plasma etching. Oxygen was added to  $CF_4$  so that a direct comparison could be made with oxides etched in a commercial barrel plasma etcher. The pressure of the  $CF_4$  +

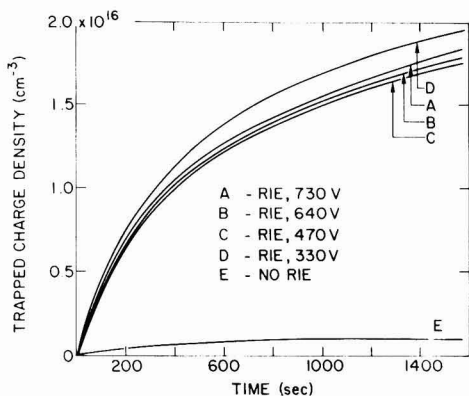


Fig. 3. Volume trapped charge density as a function of avalanche injection time for oxides exposed to RIE with rf peak-to-peak voltages between 730 and 330V. Constant avalanche current =  $2 \times 10^{-9}$ A.

20%  $O_2$  etching gas was increased to 0.5 Torr which results in an rf peak-to-peak voltage of 120V. The trapping data (Fig. 4) show that neutral traps are not created during plasma etching or during etching under plasma etching-like conditions in the RIE reactor. For completeness, an oxide was etched by low pressure RIE in the  $CF_4$  +  $O_2$  mixture to assure that the addition of  $O_2$  was not the significant factor. As expected, this oxide shows the presence of neutral traps with a trap density that is approximately equal to that of an oxide etched in  $CF_4$ .

The fourth and last experiment carried out with blanket etched oxide films was to add  $H_2$  to  $CF_4$ . This experiment was suggested by speculation that the neutral traps were created by breaking or relaxing bonds in the lattice of the oxide (6). If correct, the diffusion of atomic hydrogen into silicon dioxide might anneal neutral traps in a way that is analogous to the reduction in dangling bond density in amorphous silicon by atomic hydrogen (23). The data in Fig. 5 show that the addition of  $H_2$  does lead to a significant reduction in trapped charge when compared with an oxide etched in  $CF_4$  alone. A peak-to-peak voltage of 810V was measured. This value is slightly higher than that measured during RIE in  $CF_4$ . While the effect of adding  $H_2$  is reproducible and consistent with annealing of traps by atomic hydrogen, it was not possible to reduce trap density by introducing hydrogen in other ways. Trapping was not reduced by exposing oxides to a hydrogen plasma before or after RIE in  $CF_4$  or by annealing oxides in forming gas (90%  $N_2$ /10%  $H_2$ ) at 1000°C before RIE in  $CF_4$ .

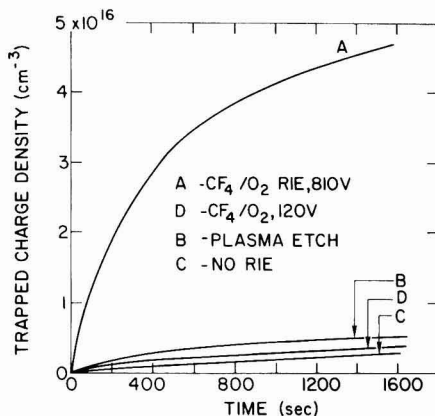


Fig. 4. Volume trapped charge density as a function of avalanche injection time for oxides exposed to RIE in  $CF_4$  +  $O_2$  and plasma etching in RIE and barrel-type plasma reactors. Constant avalanche current =  $2 \times 10^{-9}$ A.

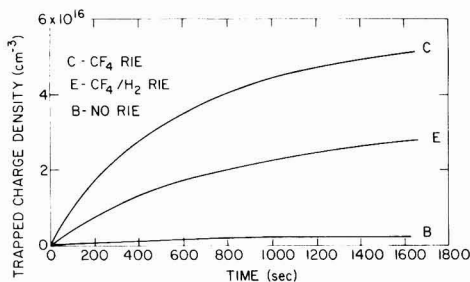


Fig. 5. Volume trapped charge density as a function of avalanche injection time for oxides exposed to RIE in  $CF_4$  and  $CF_4$  +  $H_2$ . Constant avalanche current =  $2 \times 10^{-9}$ A.

**Gate shielding.**—The purpose of experiments carried out with blanket oxide films is to understand the nature and parameter dependence of the neutral traps. During FET processing, however, the gate oxide is covered by the material that is used as a gate electrode. With this fact in mind, the ability of polysilicon and aluminum to shield an underlying gate oxide from the introduction of neutral traps was tested.

The procedure used to fabricate the samples begins with the same cleaning and oxidation steps described earlier. After the oxide was grown, a 350 nm thick film of silicon was deposited by chemical vapor deposition on some substrates and then doped  $n^+$  by the deposition and drive-in of  $\text{POCl}_3$ . The polysilicon plus 50 nm of oxide was etched using patterned photoresist to delineate 32 mil diam dots. On other oxidized substrates, 32 mil diam, 400 nm thick aluminum dots were evaporated by resistive heating. 50 nm of oxide was then etched by RIE. Appropriate control wafers were included to determine background trapping in the oxide, to provide a reference for the degree of shielding by the gate electrode, and to provide a comparison with wet etching of polysilicon. The data in Fig. 6 show that 400 nm of aluminum does shield the oxide. The shielded oxide exhibits the same increase in trapped charge density as the control, while the unshielded oxide again shows enhanced trapping. The trapping data for oxides covered by polysilicon plus resist during RIE also show that the oxide has been effectively shielded (Fig. 7). The trapped charge density for the reactive ion etched structure is shown on an expanded

scale with the trapped charge density obtained for a structure that was wet etched. The two samples show the same low density of trapped charge. In fact, the trapped charge density measured for both samples is approximately half that measured on similar structures with aluminum electrodes. This reduction is attributed to a decrease in background oxide trapping as a result of the high temperature deposition and doping of the polysilicon films. Other differences in plots of the trapped charge density as a function of the avalanche injection time on the Al-gated controls (compare Fig. 2 and 6 with Fig. 3, 4, and 5) are due to differences in the magnitude of the avalanche current used.

### Summary

The parameter dependence of neutral traps introduced during RIE has been investigated under worst case conditions of blanket etching and also with a gate electrode in place. During blanket RIE of silicon dioxide, neutral traps are created. These traps are removed by a 600°C anneal and so are of concern only if an RIE step occurs after aluminum metallurgy is in place. The trap density is reduced by adding  $\text{H}_2$  to the etching gas. Neutral traps were not introduced when the reactor was operated under plasma etching-like conditions. Finally, it is concluded that oxide is effectively shielded during RIE by a polysilicon or aluminum gate electrode.

### Acknowledgments

The authors wish to acknowledge the critical reading of this manuscript by J. M. Aitken, and the preparation of samples by the Silicon Process Studies Group. This research was supported in part by the Defense Advanced Research Projects Agency, and was monitored by the Deputy for Electronic Technology (RADCC) under contract number F19628-78-C-0225.

Manuscript submitted March 20, 1981; revised manuscript received June 4, 1981.

Any discussion of this paper will appear in a Discussion Section to be published in the June 1982 JOURNAL. All discussions for the June 1982 Discussion Section should be submitted by Feb. 1, 1982.

Publication costs of this article were assisted by IBM Corporation.

### REFERENCES

1. H. N. Yu, R. H. Dennard, T. H. P. Chang, C. M. Osburn, V. DiLonnardo, and H. E. Luhn, *J. Vac. Sci. Technol.*, **12**, 1197 (1975).
2. W. R. Hunter, L. M. Ephrath, W. D. Grobman, C. M. Osburn, B. L. Crowder, A. Cramer, and H. E. Luhn, *IEEE J. Solid-State Circuits*, **sc-14**, 275 (1979).
3. D. J. DiMaria, "The Physics of  $\text{SiO}_2$  and Its Interfaces," S. T. Pantelides, Editor, Pergamon Press, New York, p. 160 and references therein (1978).
4. D. J. DiMaria, L. M. Ephrath, and D. R. Young, *J. Appl. Phys.*, **50**, 4015 (1979).
5. J. M. Aitken and D. R. Young, *ibid.*, **47**, 1196 (1976).
6. J. M. Aitken, D. R. Young, and K. Pan, *ibid.*, **49**, 3386 (1978).
7. T. H. Ning, *ibid.*, **49**, 4077 (1978).
8. W. D. Ryden, E. F. Labuda, and J. T. Clemens, Abstract 55, p. 149, The Electrochemical Society Extended Abstracts, Washington, DC, May 2-7, 1976.
9. H. R. Koenig and L. I. Maisel, *IBM J. Res. Dev.*, **14**, 168 (1970).
10. E. A. Irene, *This Journal*, **121**, 1613 (1974).
11. A. Goetzberger and E. H. Nicollian, *J. Appl. Phys.*, **38**, 4582 (1967).
12. E. H. Nicollian and C. N. Berglund, *ibid.*, **41**, 3052 (1970).
13. R. Williams, *Phys. Rev.*, **140**, A569 (1965).
14. B. E. Deal, E. H. Snow, and C. A. Mead, *J. Phys. Chem. Solids*, **27**, 1873 (1966).
15. A. M. Goodman, *Phys. Rev.*, **144**, 588 (1966).
16. D. R. Young, D. J. DiMaria, and W. R. Hunter, *J. Electron. Mater.*, **6**, 569 (1977).
17. D. J. DiMaria and P. C. Arnett, *IBM J. Res. Dev.*, **21**, 227 (1977).

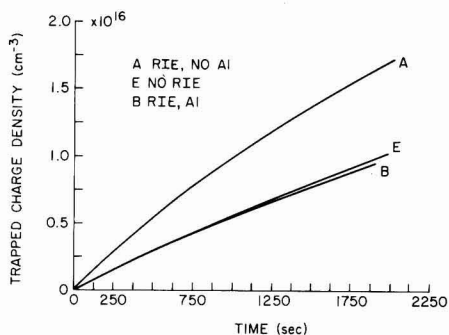


Fig. 6. Volume trapped charge density as a function of avalanche injection time for oxides exposed to RIE with and without an aluminum etch mask. Constant avalanche current =  $8 \times 10^{-9}$  A.

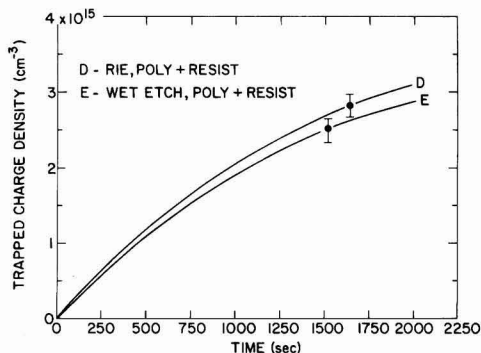


Fig. 7. Volume trapped charge density as a function of avalanche injection time for oxide after RIE of polysilicon electrode. Sample in which polysilicon was wet etched serves as a control. Constant avalanche current =  $8 \times 10^{-9}$  A.

18. D. J. DiMaria, Z. A. Weinberg, and J. M. Aitken, *J. Appl. Phys.*, **48**, 898 (1977), and references therein.
19. A. S. Grove, "Physics and Technology of Semiconductor Devices," Chap. 9, Wiley, New York (1967).
20. S. M. Sze, "Physics of Semiconductor Devices," Chap. 9, Wiley-Interscience, New York (1969).
21. D. J. DiMaria, *J. Appl. Phys.*, **47**, 4073 (1976).
22. R. J. Powell and C. N. Berglund, *ibid.*, **42**, 4390 (1971).
23. M. H. Brodsky, *Thin Solid Films*, **54**, 159 (1978).

## Ion Beam Analysis of Molecular Beam Epitaxy InAlAs/InGaAs Layer Structures

D. V. Morgan,<sup>1</sup> H. Ohno,<sup>2</sup> C. E. C. Wood, L. F. Eastman, and J. D. Berry

*School of Electrical Engineering and National Research and Resource Facility for Submicron Structure,  
Cornell University, Ithaca, New York 14853*

### ABSTRACT

In this paper the Rutherford backscattering technique combined with channeling is used to study the stoichiometry and perfection of molecular beam epitaxial layers of InAlAs and InGaAs. Corroborative evidence from SIMS and Auger profiling are used to supplement the RBS studies.

In recent years molecular beam epitaxy (MBE) has emerged as a valuable tool for the growth of electronic quality epitaxial layers of many compound semiconductors (1, 2). The improvement of layer quality depends critically on the development of analytical techniques with which to characterize the material properties. These include parameters such as mobility, conductivity, doping profile, deep level densities and energy levels, and crystal perfection. In this paper we consider the application of Rutherford backscattering (RBS) in evaluating the structure and quality of molecular beam epitaxial InGaAs and InAlAs layer structures. We also consider the use of ion beam channeling for the measurement of crystal perfection, with particular interest in the interfaces between heteroepitaxial MBE layers. RBS has many limitations in the present context including: (i) Poor sensitivity in the measurement of light elements such as aluminum in matrixes incorporating relatively heavy atoms such as indium; and (ii) the inability to resolve neighboring atoms in the periodic table (i.e., such as gallium and arsenic). In order to resolve any ambiguities arising from these limitations, complementary studies have been conducted with secondary ion mass spectrometry (SIMS) and sputter/auger profiling.

### Experimental Procedures

Lattice matched  $\text{In}_{0.53}\text{Ga}_{0.47}\text{As}$  layers were grown on (100) InP substrates by MBE. Substrates were heat cleaned *in situ* under stabilizing arsenic fluxes at 505°C for 2 min (3). A concentric double cell was used for gallium and indium to improve the spatial and depth composition uniformity of InGaAs layers, while separate aluminum and indium cells were used for growth of InAlAs alloys. Lattice mismatching to InP substrates measured by x-ray diffraction were  $\Delta a/a_0 < 1 \times 10^{-3}$  for InGaAs and  $\Delta a/a_0 < 2 \times 10^{-3}$  for InAlAs. Layers grown on GaAs substrates were not lattice matched. Typical substrate temperatures ( $T_s$ ) = 490°C for InGaAs and  $T_s = 510^\circ\text{C}$  for InAlAs. Low field electron mobilities of unintentionally doped InGaAs layers were as high as  $\mu_{300} = 8800 \text{ cm}^2/\text{Vsec}$  with  $n_{300} = 1 \times 10^{16} \text{ cm}^{-3}$  and  $\mu_{77} = 15,000 \text{ cm}^2/\text{Vsec}$  with  $n_{77} = 8.5 \times 10^{15} \text{ cm}^{-3}$ , while unintentionally doped InAlAs layers were of high resistance ( $\rho > 3 \times 10^{-3} \Omega \text{ cm}$ ). Single

crystal epitaxial aluminum layers were grown on some of the samples (below 120°C) without exposure to air to obtain Schottky barriers.

The basic principles underlying the RBS/channeling techniques have been discussed extensively in the literature (4-7) and consequently, only a brief summary will be provided here. A collimated beam of 2-2.5 MeV  $\text{He}^+$  ions is directed onto the crystal surface and the energy distribution of particles scattered through an angle  $\theta$  degrees is measured using a surface barrier nuclear particle detector. This energy spectrum of the backscattered ions yields information on the mass and depth distribution of the scattering ions (5). When the ion beam is incident in a random crystal direction, the near surface composition of the crystal may be deduced from the Rutherford scattering law (6). The relative concentration  $N_A$  and  $N_B$  of species A and B may be deduced from the respective yields  $Y$  using the approximate equation (5)

$$\frac{N_A}{N_B} = \frac{Y(A)}{Y(B)} \cdot \frac{[S]_A}{[S]_B} \left( \frac{Z_B}{Z_A} \right)^2 \quad [1]$$

where  $Z_A$  and  $Z_B$  are the atomic numbers for the atoms A and B and the  $[S]$  terms are the compound stopping powers in the crystal for scattering from the species A or B, respectively, given by the expression (5)

$$[S]_A = k_A^2 [S]_{\text{in}} + \frac{[S]_{\text{out}}}{\cos(\theta)} \quad [2]$$

$k_A^2$  is the kinematic factor for the atoms A (or B) and  $\theta$  is the scattering angle defined in the inset of Fig. 1. The stopping powers  $[S]_{\text{in}}$  and  $[S]_{\text{out}}$  correspond to the ingoing and scattered beam. For the compounds used in this work  $[S]$  was obtained from the stopping powers of the elements concerned by the use of the Bragg law (4, 8).

### Results and Discussion

The straightforward use of RBS in the measurement of the elemental composition (8) was of value to the present study. Figure 1 shows a spectrum obtained for random incidence from an  $\text{In}_x\text{Al}_{(1-x)}\text{As}$  layer 1.5  $\mu\text{m}$  thick ( $x = 0.4$ ) grown on GaAs. The random spectra were obtained by aligning the crystals to the  $\langle 100 \rangle$  axis and then carefully misaligning to find a random direction. In this figure we show both the compound (raw) RBS spectrum obtained by scatter-

<sup>1</sup> Permanent address: Department of Electrical and Electronic Engineering, University of Leeds, Leeds, England LS2 9JT.

<sup>2</sup> Permanent address: Sakaki Laboratory, Institute of Industrial Science, University of Tokyo, Tokyo, Japan.

Key words: channeling, MBE, RBS studies.

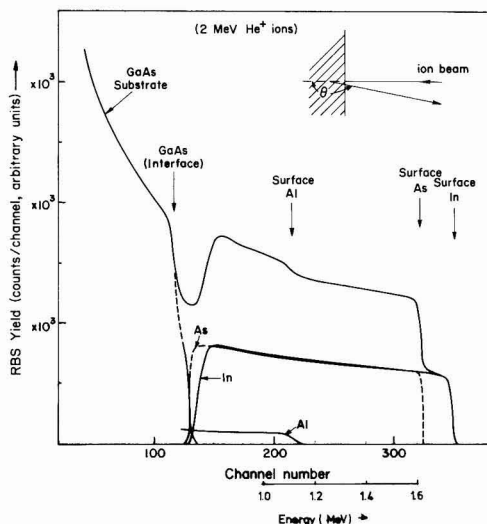


Fig. 1. Rutherford backscattering spectrum (RBS) obtained from an  $\text{In}_x\text{Al}_{1-x}\text{As}$  crystal ( $x = 0.4$ ) grown on a GaAs substrate. (Incident helium ion energy  $E_i = 2.0$  MeV scattering angle  $\theta = 168^\circ$ .) Both the composite spectrum and its component parts are shown.

ing 2 MeV  $\text{He}^+$  ions through  $168^\circ$ , together with the individual component spectra from the indium, arsenic, and aluminum and the substrate GaAs. In order to estimate the component spectra, a simple iterative procedure (9a) based upon the work of Ref. (9b) was used. For each component spectrum an increase in yield with depth was obtained by normalizing the surface yield of each of the spectra to unity and using the Rutherford scattering relationship [i.e., yield  $\propto (\text{energy})^{-2}$ ] to generate the depth dependence of the spectrum. In  $\text{InAlAs}$  grown on GaAs, for example, the GaAs substrate spectrum would be extracted first. The procedure described above would then be used for the In spectrum, followed by the As and finally the Al spectra. The heavier indium atoms give the clearest near-surface spectrum, while the much lighter aluminum spectrum superimposed on the relatively large background is more difficult to resolve and hence has the largest uncertainty. From this spectrum the value of  $x$  from the indium spectrum and  $(1-x)$  from the aluminum spectrum may readily be obtained.

RBS spectra have been obtained for a range of  $\text{In}_x\text{Al}_{1-x}\text{As}$  samples with  $x$  ranging between 0 and 1. The values of  $x$  and  $(1-x)$  and the arsenic concentration obtained from the corresponding RBS spectra are shown by the circular and triangular points in Fig. 2 as a function of the values predicted from the molecular beam cell fluxes. The full lines are the best straight lines through the experimental points. The arsenic concentration is stoichiometric (i.e., at 50%) in all the layers grown with  $x$  varied between 0 and 1. This is as expected from thermodynamic considerations. Observation of the indium concentration again confirms that the  $x$  values measured by RBS agree well with those estimated from the MBE flux monitor (3). The one departure from this behavior is that of a layer with  $x = 0.2$  (Fig. 3); here RBS estimates a value near to  $x = 0.1$ , which is confirmed by repeated measurements at different areas over the crystal surface. Another interesting feature of this spectrum is the appearance of a surface indium peak where the local  $x$  value rises to near the predicted  $x = 0.2$ . The reproducibility of the surface indium peak across the

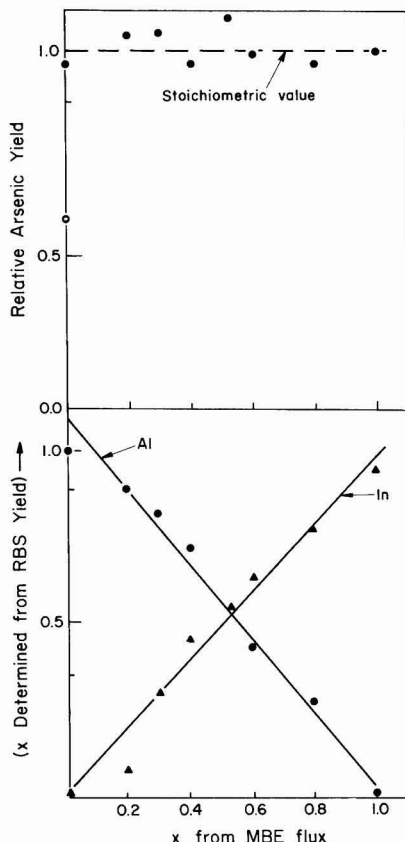


Fig. 2. A summary of the results obtained from a series of crystals grown with the value of  $x$  in  $\text{In}_x\text{Al}_{1-x}\text{As}$  varied from 0 to 1. The upper graph shows the normalized (stoichiometric value = 1.0) arsenic concentration as a function of  $x$ . In the lower graph the RBS values of  $x$  for indium and  $(1-x)$  for aluminum are plotted as a function of the predicted MBE flux values.

surface, confirms that it is not a local segregation of indium [as would be expected with spitting from the indium or aluminum source (10)]. The surface indium peak in this case arises from the surface accumulation of indium [or preferential incorporation of  $\text{Al}(\text{Ga})$ ] in the nucleation stages, during growth at high substrate temperatures or low  $\text{As}_4$  fluxes. Further confirmation comes from SIMS studies (Fig. 3 inset) where results show that the indium concentration falls by about 10% at about 0.5 micron inside the surface. The spatial uniformity of the surface indium accumulation was also confirmed by the SIMS studies. (Note that the very high arsenic yield near to the surface is an artifact of the present SIMS technique possibly associated with residual surface oxide persisting during the erosion process.) In comparison with the SIMS profiles, RBS spectra are relatively easy to interpret and they yield quantitative data. However, the problem of obtaining an aluminum profile from the spectrum shown in Fig. 3 is not tractable, making complementary SIMS profiles invaluable.

The ability of the backscattering technique to measure indium profiles is again indicated in Fig. 4(a) which shows an RBS spectrum of a  $1.5\text{ }\mu\text{m}$  lattice matched  $\text{InGaAs}$  crystal grown on an  $\text{InP}$  substrate. The indium profile extracted from this spectrum shows two regions of different composition, one at the surface

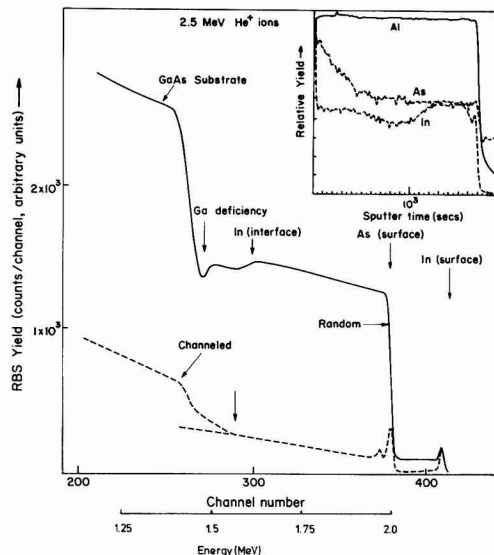


Fig. 3. RBS spectrum from an InAlAs crystal ( $x = 0.2$ ) grown on a GaAs substrate. In this case  $E_i = 2.5$  MeV and  $\theta = 170^\circ$ . Both the channelled  $\langle 100 \rangle$  and random spectra are shown. Also shown in the inset is the corresponding SIMS profile.

and a second peak approximately  $0.3 \mu\text{m}$  inside the crystal. This indium fluctuation was the result of indium surface segregation at the relatively high growth temperature ( $489^\circ\text{C}$ ). This was done to determine the upper temperature limit to the growth and to identify the growth problems that occur in this high temperature regime. We note that the surface indium concentrations indicate an almost 100% increase over the bulk indium value. Note also that the close proximity of the gallium and arsenic atomic masses makes it difficult for the profiles to be separated unambiguously from this spectrum. The reverse situation, namely a drop in indium concentration at the surface, was associated with an instability in the indium effusion cell temperature control and is clearly shown in Fig. 4(b) where the indium concentration in InAlAs falls from the value corresponding  $x = 0.8$  to  $x = 0.72$ . Note

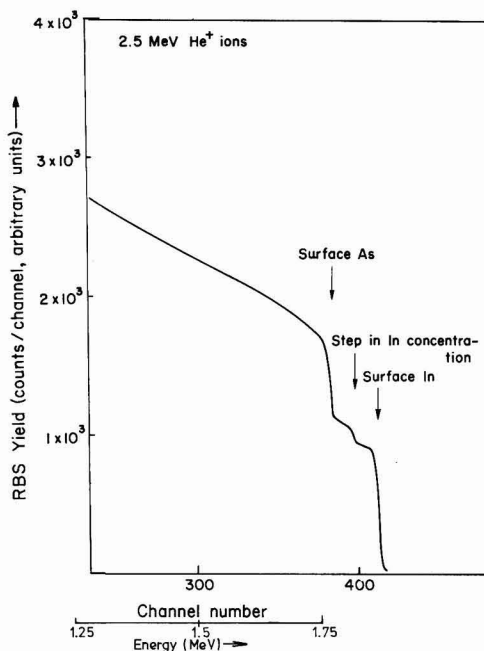


Fig. 4(b). RBS spectrum from an InAlAs crystal ( $x = 0.8$ ) grown on a GaAs substrate. ( $E_i = 2.5$  MeV,  $\theta = 170^\circ$ .)

also that it becomes more difficult to identify fluctuations unambiguously where the indium and arsenic spectra overlap.

In some potential device applications where the device active layer is of a composition that does not lattice match that of the substrate used, it is necessary to grade the ratio of the component elements to reduce mismatch strain and strain induced defects etc. (i.e.,  $x$  in  $\text{In}_x\text{Al}_{1-x}\text{As}$ ). Such structures provide good test vehicles for material characterization techniques. RBS alone can provide information on the compound composition and its depth dependence. When complemented by channeling measurement, however, information on crystal quality may also be obtained. This latter point is discussed later. The crystal analyzed in Fig. 5(a) is an  $\text{In}_x\text{Al}_{1-x}\text{As}$  sample where  $x$  was stepped down from 1.0 at the interface in 20% steps to 0 at the surface. To avoid oxidation of the AlAs surface region a thin InAs layer was deposited on the top surface. This is seen as the near surface peak at the high energy end of the spectrum of Fig. 5(a). From the main spectrum the indium yield is readily obtained by extracting the arsenic profile, which is known to be a constant from thermodynamic considerations and is also confirmed from sputter Auger and SIMS profiling studies. The indium profile lies close to that predicted by the growth parameters and is again confirmed by the Auger and SIMS results. The steps in the composition are apparent only for  $\text{In}_x$  ( $x$  stepped from 1.0 to 0.8) which is also confirmed by Auger sputtering profiles. The 20% steps from  $x = 0.8$  down to  $x = 0$  are reduced due to mismatch strain-induced interdiffusion at the high growth temperature ( $480^\circ\text{C}$ ). This strain becomes apparent in the channeling measurements discussed later in this paper. It is interesting to note that the Auger sputter profiling of the inverse layer structure (i.e., where  $x$  was stepped in 20% increments from 0 at the interface to 1.0 at the surface) grown at  $375^\circ\text{C}$  [inset shown in Fig. 5(b)] shows discrete steps, although this is not observed on the cor-

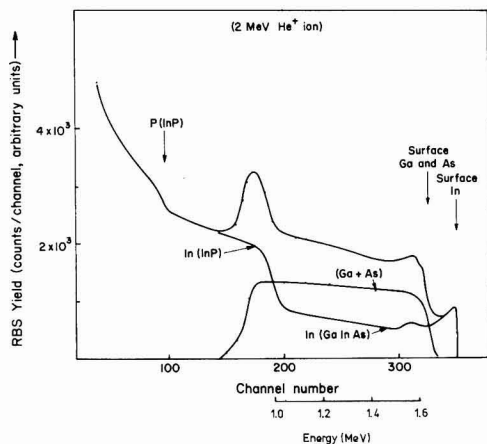


Fig. 4(a). RBS spectrum from an InGaAs crystal grown lattice matched to an InP substrate. ( $E_i = 2$  MeV (He ions)  $\theta = 168^\circ$ .)

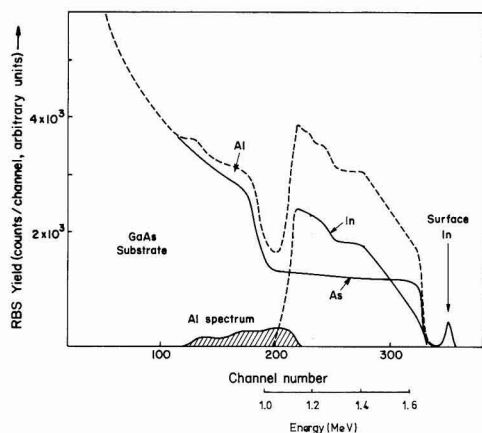


Fig. 5(a). RBS spectrum from an InAlAs crystal where the indium concentration  $x$  is varied from 1.0 at the interface in 20% steps to 0 at the surface. The AlAs surface is protected from oxidation by the growth of a thin InAs layer. [ $E_i = 2.0$  MeV (He) and  $\theta = 168^\circ$ .]

responding RBS spectrum as the ion beam energy and incident angle were not optimized for the best depth resolution. The RBS spectrum again illustrates the difficulty of extracting the aluminum profile. The extracted indium and aluminum signals are compared to the Auger profile results in Fig. 5(b) inset. Here both techniques confirm the relative integrity of the individual alloy layers and interface regions when grown at the lower temperature.

So far we have considered only the basic RBS technique. The following considers the use of the channeling process (6) to investigate bulk layer crystal quality and more importantly the crystalline perfection of interfaces. Figure 6 shows two RBS spectra obtained for aligned and random incidence from a multilayer structure consisting of an InGaAs (2500Å)/InAlAs (1000Å)/InP (substrate). Using the channeling technique there are two basic measures of crystal quality, the minimum yield  $x_{\min}$  and the dechanneling rate  $\alpha (= dx_{\min}/dz)$  where  $z$  is the depth of the penetration

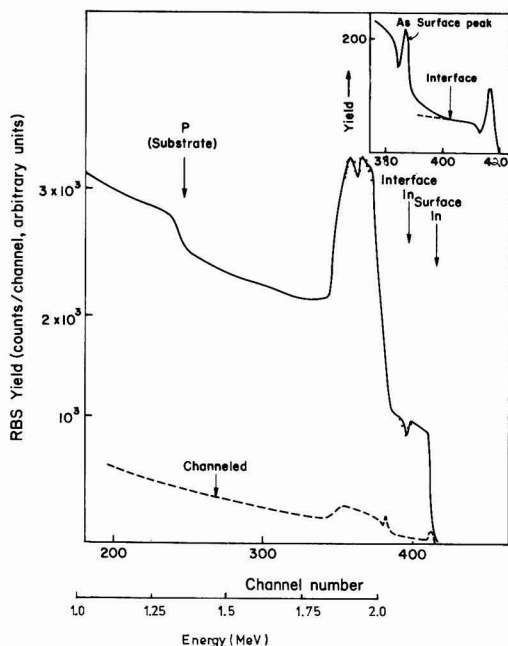


Fig. 6. The RBS spectrum for channeled and random incidence from an InGaAs/InAlAs/InP crystal, where the two epitaxial layers are grown lattice matched to the InP. [ $E_i = 2.5$  MeV (He ions),  $\theta = 170^\circ$ , axis for channeling  $\langle 100 \rangle$ .] The inset shows an enlarged version of the near surface channeled spectrum.

in the crystal (11). These parameters provide only a relative measure of crystal quality. In order, therefore, to provide a standard we note that for channeling along the  $\langle 100 \rangle$  axis in a good quality GaAs layer values of  $x_{\min} \approx 0.04$  and  $\alpha \approx 10^{-4} (\text{nm})^{-1}$  are typical. For the crystal shown in Fig. 6 (i.e., channeling along the  $\langle 100 \rangle$  axis) we obtain near surface values of  $x_{\min}(\text{In}) = 0.04$  and  $\alpha(\text{In}) = 5 \times 10^{-4} (\text{nm})^{-1}$ . The minimum yield shows excellent agreement with the best GaAs experimental results (12). In the case of the dechanneling rate  $\alpha$ , this result is a factor five larger than that typical of premium grade GaAs. However there are two reasons why this is reasonable. In the first instance dechanneling is a much more sensitive parameter than the minimum yield. Wood and Morgan (12), for example, have observed fourfold increases in  $\alpha$  in GaAs epitaxial layers at a growth interface. A second important consideration arises from the disparity in the atomic numbers of the component atoms—indium, arsenic, and aluminum. A large disparity gives rise to a much larger intrinsic dechanneling rate. In the case of planar channeling, computer simulation (13) results show that this factor alone could result in a 300% increase in going from GaAs to a material such as InAlAs. In view of these considerations it is concluded that the value of  $\alpha = 5 \times 10^{-4} (\text{nm})^{-1}$  is comparable to those obtained for high-grade epitaxial layers and indicates that the uppermost InAlAs layer exhibits a high degree of perfection, justifying the care in lattice matching to the substrate InP.

A second interesting feature of these spectra may be more clearly seen in the inset to Fig. 6, which shows an enlarged plot of the near surface indium peaks (i.e., the indium in the InAlAs and the InGaAs). At the interface between these two layers the indium channeling curve undergoes an abrupt transition resulting in a fourfold increase in the dechanneling parameter

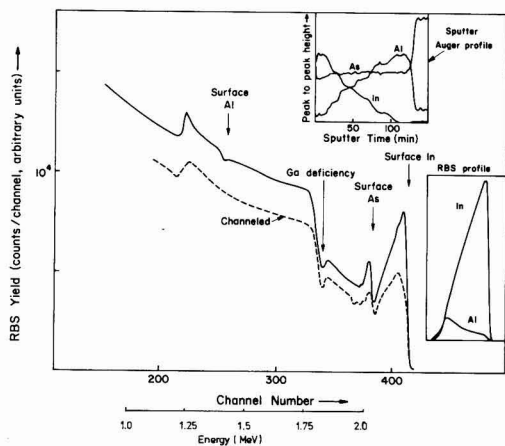


Fig. 5(b). The channeled ( $\langle 100 \rangle$  axis) and random spectra from an  $\text{In}_x\text{Al}_{1-x}\text{As}$  crystal where the indium concentration  $x$  is varied from 0 at the interface in 20% steps to 1.0 at the surface. [ $E_i = 2.5$  MeV (He ions),  $\theta = 170^\circ$ .] Also shown in the inset is the corresponding sputter Auger profile.



$\alpha(\text{In})$  (i.e.,  $\alpha$  increases from  $5 \times 10^{-4}$  to  $20 \times 10^{-4}$   $(\text{nm})^{-1}$ ). This indicates that the lattice structures are strained at the interface, presumably a result of imperfect matching, local segregation, or diffusion of group III elements within the alloy sublattice across the interface. It is clear that such strain can result in undesirable deep levels which could adversely affect the performance of FET's made from such layers. Further clarification of the interface strain may be gained from the random spectrum of Fig. 6. At the interface the indium yield decreases indicating that a deficiency of indium occurs during the transition from the growth of InGaAs to InAlAs. The indium deficiency at the interface is further evidence for accumulation of indium in these two ternary alloys growing under conditions of low As<sub>4</sub> fluxes or high temperature substrates. The total indium deficiency at the interface corresponds to a total equivalent of 1.5 monolayers of pure indium. Because of the limited depth resolution ( $\sim 200\text{\AA}$ ) it is not known how localized this deficiency is.

A third measure possible from a channeling spectrum is the area under the surface indium, gallium, and arsenic peaks (9). These peaks give the ratio of unscreened components in the surface disordered layer. From the  $\langle 100 \rangle$  channel spectrum shown in the inset of Fig. 1 we obtain a value of  $N(\text{In})/N(\text{Ga} + \text{As}) = 0.63$  which is significantly larger than the expected bulk value of 0.36. One of the difficulties of this measurement is that the Ga and As peaks cannot be separated and hence the source of the nonstoichiometry cannot be identified. Before leaving the topic of interfaces we note in the random spectrum in Fig. 3 that there exists a dip in the gallium yield when InAlAs is grown on a GaAs substrate which is explained by an Al/Ga exchange and redistribution reaction during growth of the first few atomic layers of any aluminum-containing alloy or compound on any gallium-containing alloy or compound. It is also observed that the dechanneling curve in Fig. 3 undergoes an abrupt increase as the interface between InAlAs and the GaAs substrate is approached. This is presumably a result of the interface strain expected since this interface is not lattice matched. The dechanneling results indicate that this strain extends some 2000Å into the epitaxial layer.

In order to further investigate the value of channeling measurements, studies have been carried out on the range of samples studied earlier (i.e., those with  $\text{In}_x\text{Al}_{1-x}\text{As}$  for  $x$  ranging from 0 to 1). The clear trend in these results is that the best channeling (i.e., lowest  $x_{\text{min}}$ ) was obtained in crystals with  $x \approx 0.5$  (i.e., the InP lattice matched system). We note also that layers grown on GaAs (not lattice matched) give poorer channeling. For example, in the case of  $x = 0.8$  [Fig. 4(b)] the crystal structure is so poor that it is very difficult to observe any channeling dips with any degree of certainty. The same conclusions may be drawn for other crystals with variable  $x$  [Fig. 5(b)], the near surface  $x_{\text{min}}(\text{In}) = 0.52$ , confirming that the crystallinity is very poor.

Another example of the value of this technique is shown in Fig. 7 in the spectrum from a lattice matched layer of InGaAs/InP. This layer exhibited a very low mobility compared to normal. The reason for this low mobility is apparent from the RBS spectra shown in Fig. 7. Consider first the random spectrum. This shows a series of peaks in the indium concentration culminating with a large surface accumulation (i.e., a 15–20% increase over the average bulk value). These oscillations occur and can be seen even when the indium and GaAs spectra overlap. Clearly any variation in indium concentration must be matched by a complementary change in the gallium. Of particular interest is the

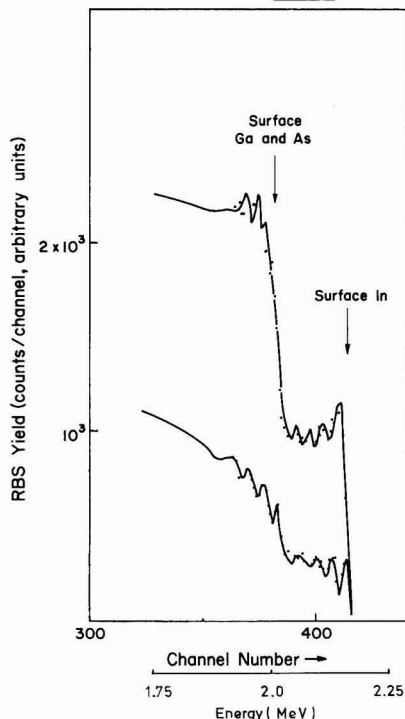


Fig. 7. RBS spectrum of an InAlAs grown on a GaAs substrate [ $E_i = 2.5$  MeV (He ions),  $\theta = 170^\circ$ ].

channeled spectrum; here the oscillations are greatly amplified (i.e., a maximum of 100% change). The reason for this greater sensitivity lies in the nature of the channeling process. The channeled component of the beam is screened from violent collisions. However, when the indium concentration increases, the channel becomes distorted and some channeled ions are no longer screened, resulting in the increased backscattering. In this way the effect of the indium fluctuations are amplified (i.e., 10% variation in the random RBS spectrum becomes a 100% change).

### Conclusions

Both random and channeling RBS have been used with complementary sputter Auger and SIMS techniques to study epitaxial InAlAs and InGaAs multilayer structures on (100) InP and GaAs substrates.

Results indicate that at higher temperatures or reduced arsenic fluxes indium accumulates on the surface during growth of both InGaAs and InAlAs alloys. The net effect is to leave an indium deficiency at near substrate layer interface regions. The effect was confirmed by observing depth fluctuations of the In/Ga ratio in layers grown with intentionally fluctuating arsenic fluxes. A further effect seen only by RBS was the preferential exchange of aluminum for gallium at the nucleation stage of InAlAs on GaAs substrates or on InGaAs layers.

### Acknowledgments

The authors are grateful to L. Rathbun for the sputter Auger data, to G. Morrison for SIMS data, and to Ms. Elma Weaver and Mrs. C. Edmondson for preparation of the typescript. We also acknowledge Dr. J. M. Poate (Bell Laboratories) and Professor G. Carter (University of Salford, UK) for the use of their RBS machines and the planning committee of NRRFSS for permission to use the MBE machine.

<sup>3</sup> The background correction procedure used to extract the surface peaks was that described by Morgan and Wood in Ref. (11).

Manuscript submitted Oct. 27, 1980; revised manuscript received April 23, 1981.

Any discussion of this paper will appear in a Discussion Section to be published in the June 1982 JOURNAL. All discussions for the June 1982 Discussion Section should be submitted by Feb. 1, 1982.

Publication costs of this article were assisted by Cornell University.

# REFERENCES

1. A. Y. Cho and J. R. Arthur, in "Progress in Solid State Chemistry," G. Somorjai and J. McCaldin, Editors, Pergamon, New York (1975).
2. C. E. C. Wood, in "Physics of Thin Films," Haff and Francombe, Editors, p. 35, Academic Press, New York (1980).
3. G. Davies, R. Heckingbottom, H. Ohno, C. E. C. Wood, and A. R. Calawa, *Appl. Phys. Lett.*, **37**, 290 (1980).
4. W. K. Chu, J. W. Mayer, M.-A. Nicolet, T. M. Buck, G. Amsel, and F. Eisen, *Thin Solid Films*, **17**, 1 (1973).
5. W. K. Chu, J. W. Mayer, and M.-A. Nicolet, "Backscattering Spectrometry," Academic Press, New York (1978).
6. D. V. Morgan, *Solid State Electron Devices*, **1**, 37 (1977).
7. D. V. Morgan, Editor, "Channeling: Theory Observation and Applications," Wiley-Interscience, London (1973).
8. P. Blood, K. L. Bye, and J. S. Roberts, *J. Appl. Phys.*, **51**, 1790 (1980).
9. (a) C. J. Madams, Ph.D. Thesis, University of Leeds (1978); (b) J. Zeigler and W. K. Chu, IBM Report No. R.C. 4288 (1973).
10. C. E. C. Wood, H. Ohno, D. Desimone, and L. F. Eastman, *J. Cryst. Growth*, Accepted for publication.
11. D. V. Morgan and D. R. Wood, *Proc. Roy. Soc. London, Ser. A*, **335**, 509 (1973).
12. D. R. Wood and D. V. Morgan, *Phys. Status Solidi A*, **17**, K143 (1973).
13. D. V. Morgan and D. P. Jackson, *Radiat. Eff.*, **29**, 99 (1976).

## Plasma Oxide FET Devices<sup>1</sup>

A. K. Ray\* and A. Reisman\*

IBM T. J. Watson Research Center, Yorktown Heights, New York 10598

# ABSTRACT

Plasma oxidation techniques described in this issue (1, 2) by the authors were employed alone, or in conjunction with thermal oxidation processes in the fabrication of n-channel polysilicon gate field effect transistors. Horizontal dimensions were delineated using optical lithography, and ranged from 2.5  $\mu$ m minimum dimensions up, to enable assessment of device parameters. The characteristics of 500°C plasma oxidized structures were compared to those fabricated in a conventional manner at 1000°C. Gate oxides were 35 nm thick and field planar oxide regions were 350 nm thick. Using wafers of a given resistivity, the thick and thin oxide thresholds of plasma oxide structures were higher than their thermal counterparts due, it is believed, to the absence of surface boron depletion in plasma oxidized regions. In line with this, threshold sensitivity to substrate bias (substrate sensitivity) was greater in plasma oxidized structures for a given starting background substrate doping level. Also because of the absence of impurity spreading, the sheet resistivity of  $n^+$  junctions was higher in plasma oxidized structures. Aside from doping level effects which can be advantageously accommodated for by appropriate device design, plasma oxidized devices are otherwise quite comparable to their thermal counterparts. They exhibit obvious device design and process control attributes due to shorter processing time at high temperatures, i.e., absence of oxidation induced stacking faults, confinement of junctions, and absence of surface impurity depletion. In n-channel devices, the absence of boron depletion during plasma oxidation has enabled the fabrication of surface and junction ion-implanted devices with lower boron doses and lower substrate sensitivity.

In the fabrication of micron or submicron device structures, there is an increasing interest in the use of lower processing temperatures to minimize impurity redistribution and defect generation effects. Oxidation is a key process in semiconductor device fabrication. High temperature oxidation is accompanied in addition to the problems mentioned above by surface depletion of impurities (3), oxidation enhanced diffusion (4), generation of stacking faults (4, 5), and so-called bird's beak generation (6). In Parts I and II the authors have described a low temperature plasma oxidation process (1, 2) in which uniform thickness oxides exhibiting excellent physical and electrical properties can be grown on 57 mm diam silicon wafers. In the process described, an oxygen plasma is generated at pressures above 10 mTorr in an electrodeless fused

silica reaction chamber using a 3 MHz rf generator and a 1 kW power output. The system is pumped continuously during oxidation and the oxygen pressure is varied by varying the oxygen flow rate. Silicon wafers are placed on either side of an rf coil, mounted perpendicular to the direction of gas flow, with the silicon surfaces to be oxidized facing away from the plasma. Oxide grows primarily on the silicon surfaces facing away from the plasma, while much thinner oxide grows on the silicon surfaces facing the plasma. The temperature of the wafers during plasma oxidation is about 500°C, and is measured by a Chromel-Alumel thermocouple placed adjacent to the wafers. The plasma oxides can be grown at rates less than, equal to, or greater than that obtainable via dry thermal oxidation processes at 1000°C, depending upon oxygen partial pressure, wafer position relative to the rf coil, temperature, and generator output power. The high-low thickness uniformity of the grown oxide was better than  $\pm 5\%$  and the standard deviation was of the order 1-3%. The etch rate and refractive index

\* Electrochemical Society Active Member.

<sup>1</sup> See Parts I and II prior to reading this paper: *This Journal*, **128**, 2460, 2466 (1981).

Key words: silicon, oxygen plasma, boron depletion, substrate sensitivity.

of the as-grown plasma oxides were comparable to thermal oxides grown at 1000°C. The as-grown oxides exhibited large negative flatband voltages with high interface trap density ( $3 \times 10^{12}/\text{cm}^2 \text{ eV}$ ). However, after a conventional low temperature postmetallization anneal (400°C, 20 min, forming gas), the interface charge and trap densities decrease to  $6 \times 10^{10}$ . The electrical breakdown strength (3-4 MV/cm) was somewhat lower than the thermal counterpart. However, after a postoxidation heat-treatment at 1000°C for 15 min in dry  $\text{O}_2$ , followed by 5 min in Ar, the breakdown strength improved to 7-8 MV/cm and the interface charge and trap densities dropped further to the  $2 \times 10^{10}$ . The properties of plasma grown oxides after a short anneal at 1000°C are thus comparable to the thermal oxides grown at 1000°C. The thickness change associated with this annealing treatment is less than 5 nm. In addition, boron depletion effects are absent, as are oxidation-induced stacking faults and bird's beak effects (2). Elimination of the bird's beak is due solely to the fact that an oxide pad is not required under the oxidation mask to avoid defect generation during the low temperature plasma oxidation. Based on these results, the present study was conducted to evaluate plasma oxides in terms of polycrystalline silicon insulated gate FET device characteristics.

### Experimental Techniques

Polysilicon gate FET devices were fabricated using optical lithographic techniques in conjunction with the plasma oxidation process alone, or in combination with thermal oxidation. For the present studies, plasma oxide growth rates considerably faster than 1000°C dry oxidation rates were employed. For example, 35 nm gate oxides were grown in 5 min and 350 nm field oxides were grown in 330 min. The comparable times for dry thermal oxidations at 1000°C would have been 38 and 1220 min, respectively. The plasma oxides were all grown at 500°C, 30 mTorr system partial pressure, 1 kW generator output power, and a generator frequency of 3 MHz. As mentioned, the growth of these plasma oxides occurs on the surfaces of the wafers facing away from the plasma which was described earlier (2). No external bias was applied to the wafers. There were three oxidation steps involved in the device fabrication; field isolation oxidation, gate insulator oxidation, and simultaneous source-drain: gate electrode oxidation. Four groups of wafers, two in each group, were employed in the experiments. These included: (A) wafers with plasma field, plasma gate insulator, and plasma source-drain: gate electrode oxidations, (B) wafers with plasma field, plasma gate insulator oxidations, and thermal gate electrode: source-drain oxidation, (C) wafers with plasma field oxidation, thermal gate insulator, and thermal gate electrode: source-drain oxidations, and (D) control wafers with thermal field, thermal gate insulator, and thermal source-drain: gate electrode oxidations. In order to keep the device fabrication process as simple as possible, no field or channel tailoring implants were employed in this first series of experiments, and source and drain regions were formed by diffusion. In addition, field regions were planar (as opposed to semi-ROX configurations). 0.5  $\Omega\text{-cm}$  p-type ( $B \sim 3.2 \times 10^{16}/\text{cm}^3$ ) Czochralski grown silicon wafers were used as substrates. About 350 nm of blanket field oxides were grown over the entire wafer using either plasma or thermal oxidation techniques as the starting point. Field regions were subsequently defined using standard photolithographic techniques. Gate oxides (35 nm) were then grown using plasma or thermal oxidation processes. Wafers with plasma gate insulators were given a postoxidation heat-treatment at 1000°C for 15 min in dry  $\text{O}_2$  followed by 5 min in Ar. As mentioned before, this heat-treatment reduces the interface traps and charge density, and improves the breakdown strength of

plasma oxides. During this postoxidation heat-treatment, as mentioned, about 5 nm of thermal  $\text{SiO}_2$  is grown in addition to the 30 nm of plasma gate oxide already present on the wafers. If the postoxidation annealing of the plasma oxides is conducted only in an inert atmosphere (argon), the interface electrical properties of the oxides are essentially equivalent to those obtained using the procedure described (2). The breakdown strength of the oxides following inert gas annealing does not improve however, although it is still adequate for device applications. Our normal procedure is to use the two-step annealing procedure so as to obtain the higher breakdown strength oxides. Wafers with conventional thermal oxides received a 1000°C, 5 min Ar postoxidation heat-treatment. After growing field and gate oxides, about 350 nm of undoped polysilicon films were deposited over the wafers and subsequently doped with phosphorus. Polysilicon gate electrodes, source, and drain regions were defined by photolithography. Source and drain were then formed by phosphorus diffusion. Following source-drain diffusion, 100 nm of oxides were grown over these regions using plasma or thermal oxidation processes. Subsequent device fabrication steps, e.g., CVD  $\text{SiO}_2$  deposition (250 nm), PSG formation, contact metallurgy, pre (500°C, 30 min, forming gas) and post (400°C, 20 min, forming gas) metallization anneals were common to all wafers.

### Results and Discussions

Threshold voltage comparisons of FET devices were made using a standard  $I$ - $V$  technique. Measurements were made on devices with a 10.8  $\mu\text{m}$  channel length and an 89.5  $\mu\text{m}$  channel width, unless otherwise specified. About ten devices on each wafer were measured to obtain the average threshold voltage. Figure 1 shows the  $I$ - $V$  characteristics of FET devices in wafer type A which were fabricated using only plasma oxidation steps. Threshold measurements were made with a source-substrate bias of  $-1\text{V}$  with the source grounded and 0.1V applied between the source and drain. The threshold voltage as determined from the straight line portion of the curves was  $0.88 \pm 0.07\text{V}$ . Figure 2 shows the  $I$ - $V$  characteristics of FET devices in control wafer, type D. The threshold voltage of FET devices made by conventional processes was  $0.74 \pm 0.065\text{V}$ . Comparing slopes of the straight lines in Fig. 1 and 2, it is seen that the channel transconductance of FET devices fabricated with plasma oxidation processes is essentially the same as those fabricated by conventional thermal techniques. The thermal oxide devices exhibited lower threshold voltages, but the spread in threshold voltages is essentially the same for the two types of wafers. This spread is quite

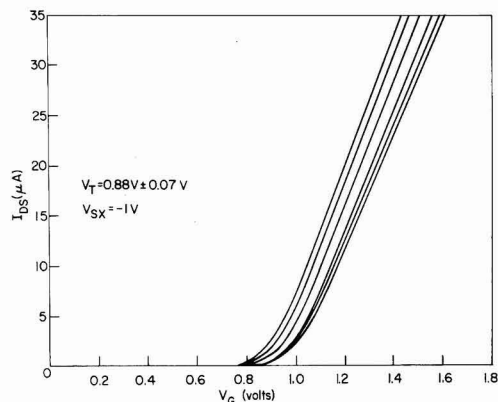


Fig. 1.  $I$ - $V$  characteristics of FET devices fabricated using only plasma oxidation steps.

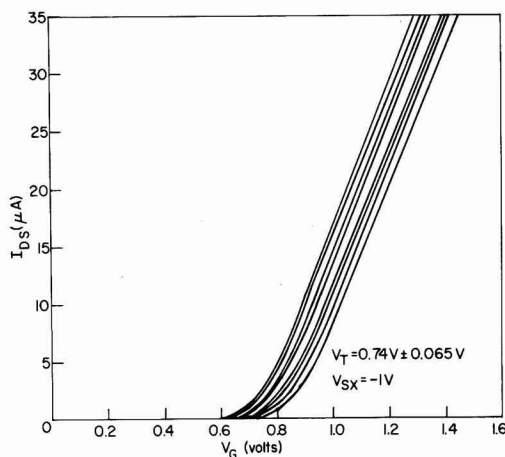


Fig. 2.  $I$ - $V$  characteristics of FET devices fabricated using only thermal oxidation steps.

common in devices which do not have channel implant tailoring and is due to bulk doping variations. Figure 3 shows the variation of the threshold voltage with channel mask length for the four types of wafers being examined. The effective channel length for each device size which would differ from the mask length by a value  $\Delta l$  could not be determined from the mask set employed, because the device width was different for each channel length. The channel etch tolerance for all devices should, however, be the same and the  $\Delta l$  value would depend then on junction diffusion spreading in each wafer type. Consequently, the comparison of similar devices in Fig. 3 is of less value than device-to-device comparison along each curve, and the relative position of one curve to the others. Devices on all the wafers showed the expected short channel effect below  $L = 3.5 \mu\text{m}$ . The straight line portions for the wafer types A and B may have a slight upward slope, because the large devices ( $L = 50.8 \mu\text{m}$ ,  $W = 508 \mu\text{m}$ ) in both wafer types A and B exhibit thresholds of 1.1-1.2V compared to values around 0.88V for somewhat smaller devices ( $L = 10.8 \mu\text{m}$ ,  $W = 89.5 \mu\text{m}$ ). Corresponding devices on wafer types C and D, both of which have thermal gate insulators show no such effect. If we now examine the curves for wafer types C and D of Fig. 3, it is seen that devices on wafer type D appear to show a lower threshold than corresponding devices on wafer type C. This is believed to be due to surface boron depletion (7) in wafer type D which underwent thermal field oxidation as compared to wafer type C which underwent plasma field oxidation. Since wafer types C and D both received a thermal gate insulator oxidation sequence, the relative threshold difference cannot

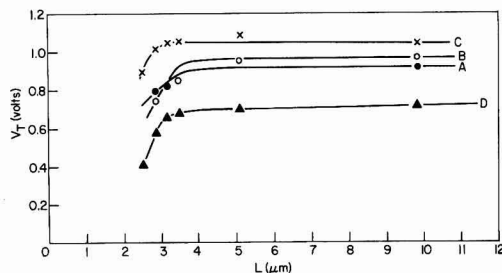


Fig. 3. Variation of thin oxide threshold voltage with channel mask length.

be due to gate insulator thickness difference between them. This was verified via C-V measurements on capacitor pads present on the device wafers on which flatband values were also determined to insure that the difference could not be attributed to difference in insulator charge levels. More definitive boron depletion experiments which confirmed the above are discussed more fully below.

Figure 4 shows the variation of thin oxide threshold voltage as a function of substrate bias voltage. It is seen that the control wafer D exhibits slightly lower substrate sensitivity than the plasma oxidized devices. This is also consistent with the existence of a boron depletion effect in the control wafers. The boron depletion effect is even more pronounced in the substrate sensitivity curves for Al gated thick oxide devices (Fig. 5). Thermal thick oxide devices (D) have much lower thresholds compared to plasma thick oxide devices (A, B, and C), again consistent with boron depletion effects in the former. The slight variation in thresholds of thick plasma oxide devices in wafer types A, B, and C is probably due to variation in oxide thickness (493, 507, and 509 nm, respectively) or bulk substrate doping level variations.

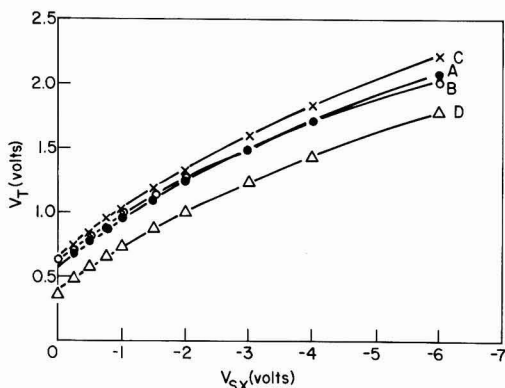


Fig. 4. Variation of thin oxide threshold voltage as a function of substrate bias voltage.

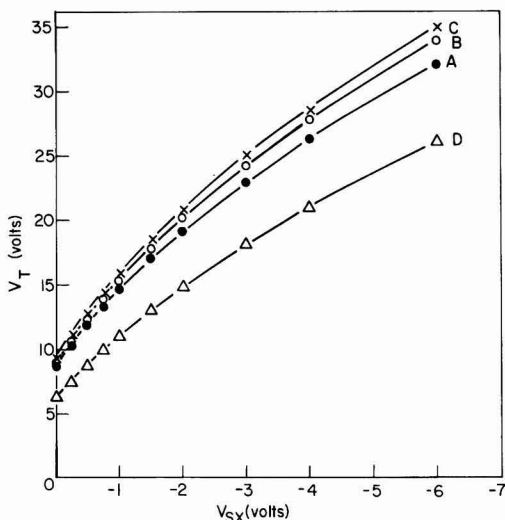


Fig. 5. Variation of thick oxide threshold voltage as a function of substrate bias voltage.

The absence of boron depletion effects during plasma oxidation was confirmed via pulsed C-V measurements on polysilicon gated capacitors in separate experiments. 350 nm of  $\text{SiO}_2$  was grown on 2  $\Omega$ -cm p-type ( $B \sim 8 \times 10^{15}/\text{cm}^3$ ) silicon wafers using either plasma oxidation at 500°C or thermal oxidation at 1000°C. These thick oxides were grown to enhance boron depletion effects, if present, as they would be in a conventional field oxidation. The thick oxides were then stripped off, and thin oxides (35 nm) were grown on the same wafers by plasma or thermal oxidation processes. Polysilicon gated capacitors were formed on this thin oxide, and the boron concentration profile near the Si-SiO<sub>2</sub> interface was determined via the pulsed C-V technique. Figure 6 shows the boron concentration profile near the Si-SiO<sub>2</sub> interface after plasma oxidation, indicating the absence of boron depletion effects. Figure 7 shows the boron concentration profile after thermal oxidation. The boron concentration gradually decreases from its bulk value as the Si-SiO<sub>2</sub> interface is approached. In Fig. 6 and 7 the profile is shown to within  $2L_D$  of the Si-SiO<sub>2</sub> interface, ( $L_D$  = Debye length), because at  $<2L_D$  the pulsed C-V data are not considered reliable. The sheet resistivity of  $n^+$  junctions for devices with thermal source-drain: gate electrode oxidation was lower ( $30 \Omega/\square$ ) than devices with plasma source-drain: gate electrode oxidation ( $41 \Omega/\square$ ). This is an indication of the formation of deeper junctions during the thermal source-drain: gate electrode oxidation step at the higher temperatures employed, since the same doping cycle was used for all the wafers during initial source-drain formation. The sheet resistivity of polysilicon gate electrodes ( $25 \Omega/\square$ ) was essentially the same for all wafers.

The results of the first device test run led to the fabrication of a second device test run to test semi-ROX plasma field oxides against thermal field oxides. Plasma oxidation was used only to grow field oxides in this test run with the gate oxides being grown ther-

mally at 800°C. During the gate oxide growth at 800°C, we would expect minimal surface boron depletion. The absence of boron depletion during plasma oxide growth should enable the fabrication of ion-implanted devices with lower boron field doses than that used in conventional processing. The use of lower boron doses in field ion implantation should also result in lower junction capacitance and lower substrate sensitivity. Field ion implantation conditions were chosen so as to obtain the same thick oxide thresholds for the plasma and thermal thick oxide devices with  $-0.75\text{V}$  on the substrate. For the plasma field oxides, boron implantation dosage was  $1.15 \times 10^{12}$  and 80 keV while that for thermal field oxides was  $7.5 \times 10^{12}$  and 65 keV. About 450 nm of semi-ROX plasma field oxides were grown on wafer type E at 550°C, 15 mTorr system pressure, and 1 kW generator output power in 6.5 hr. 200 nm of MgO on top of 5 nm of SiO<sub>2</sub> was used as an oxidation mask. About 450 nm of thermal field oxides were grown on wafer type F at 950°C. As mentioned above, gate oxides (22.5 nm) were grown on all wafers by thermal oxidation at 800°C. Channel tailoring ion implantation ( $B \sim 1.1 \times 10^{12}$ , 34 keV) was employed in this test run, and source-drain regions were formed via ion implantation. Other device fabrication steps were essentially the same as described before. Figure 8 shows the thick oxide thresholds for polysilicon gate plasma (wafer E) and thermal (wafer F) thick oxide devices as a function of substrate voltage. At  $-0.75\text{V}$  substrate bias voltage, the threshold for the thermal thick oxide devices is about 1V higher than the plasma oxide devices. It is seen from Fig. 8 that the plasma oxide devices have much lower substrate sensitivity compared to the thermal oxide devices because of the lower boron dosage required for field ion implantation. It is thus possible to obtain desired threshold voltage accompanied by lower substrate sensitivity in plasma oxide devices by adjusting ion implantation conditions, since no boron is lost to the grown oxide via a boron depletion effect.

Since the thin oxides in both types of wafers were grown thermally at 800°C, and same channel tailoring ion implantation was used, we expected the thin oxide threshold voltages to be the same for both wafers. Figure 9 shows the variation of thin oxide threshold voltage as a function of substrate bias voltage for the two types of wafers. Thin oxide devices have similar thresholds and substrate sensitivity. Threshold measurements were made on devices with nominal dimensions ( $L = 10.8 \mu\text{m}$ ,  $W = 89.5 \mu\text{m}$ ). Since plasma field oxides were grown at much lower temperature compared to thermal field oxides, there will be less

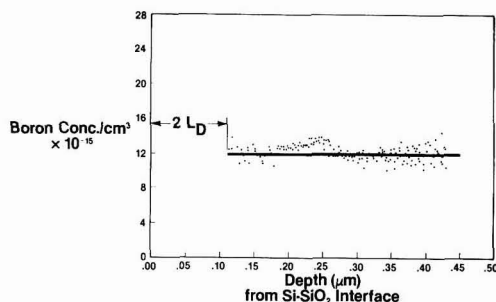


Fig. 6. Boron concentration in silicon as a function of depth from the Si-SiO<sub>2</sub> interface after plasma oxidation.

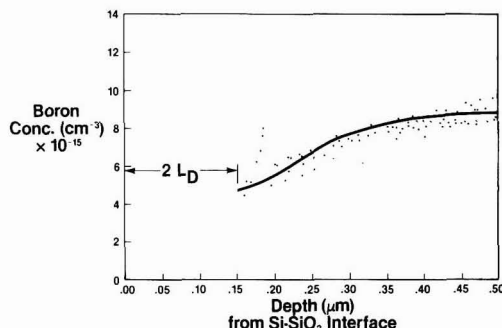


Fig. 7. Boron concentration in silicon as a function of depth from the Si-SiO<sub>2</sub> interface after thermal oxidation.

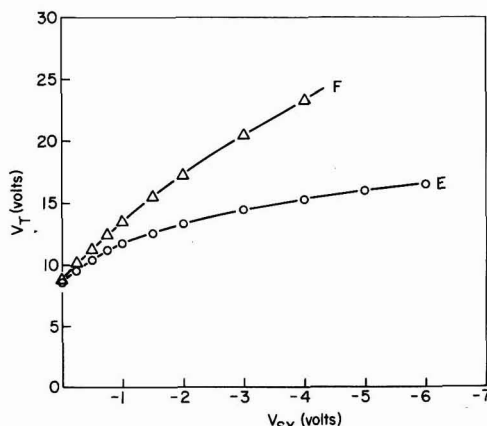


Fig. 8. Variation of plasma and thermal thick oxide threshold voltage as a function of substrate bias voltage.



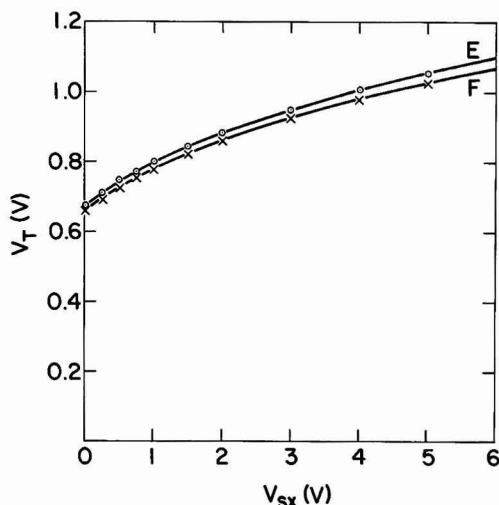


Fig. 9. Variation of thin oxide threshold voltage as a function of substrate bias voltage for plasma and thermal field oxide structures.

dopant redistribution in plasma oxidized structures and as a consequence, the boron concentration near the semi-ROX edges may be less for plasma field oxides compared to thermal field oxides. This could lead to leakage along the width of an FET channel often called "sidewalk leakage." This effect would be more pronounced for narrow width devices. In order to examine this phenomenon, the subthreshold characteristics of thin oxide FET devices with nominal dimensions  $L = 3.18 \mu\text{m}$  and  $W = 3.18 \mu\text{m}$  were determined. Figure 10 shows the subthreshold  $I$ - $V$  characteristics of FET devices with plasma (E) and thermal (F) field oxides. Both devices exhibit similar subthreshold behavior with no indication of abnormal leakage current, i.e., normal subthreshold conduction characteristics are observed.

### Conclusions

The characteristics of FET devices fabricated using plasma oxidation processes were found to be normal and comparable to devices fabricated in conventional manner. With a given starting substrate resistivity, the threshold voltages of plasma oxide devices are higher than thermal oxide devices because of the absence of boron depletion effects during plasma oxidation. A higher observed substrate sensitivity of plasma oxide devices is also consistent with the absence of the boron depletion effect. The higher sheet resistivity of  $n^+$  junctions in plasma oxide devices is presumably due to the formation of shallower junctions because of the lower source-drain:gate electrode oxidation temperature. The doping level employed during source-drain formation can be adjusted for desired junction sheet resistivity. It has been demonstrated

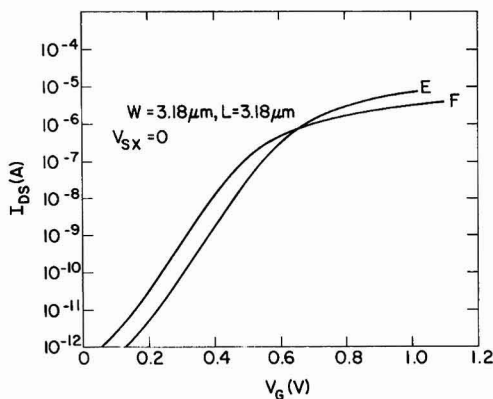


Fig. 10. Subthreshold  $I$ - $V$  characteristics of thin oxide FET devices with plasma and thermal field oxides.

that a required threshold voltage and lower substrate sensitivity in the field regions can be achieved in plasma oxide devices by using lower dosage implants, since no excess boron is lost to the grown oxide via a boron depletion effect. A similar but smaller effect would occur in the channel regions. In general, then, plasma oxide devices have advantages over thermal oxide devices in terms of lower processing temperatures, absence of defects, absence of surface dopant depletion and junction depth containment, as well as minimization of "bird's beak" phenomena.

### Acknowledgments

The authors are indebted to R. H. Dennard and C. M. Osburn for helpful discussions. The authors would like to thank G. Hu for impurity profile simulation and R. P. Havreluk for electrical measurements.

Manuscript submitted Jan. 30, 1981; revised manuscript received June 11, 1981. This was Paper 234 presented at the Minneapolis, Minnesota, Meeting of the Society, May 10-15, 1981.

Any discussion of this paper will appear in a Discussion Section to be published in the June 1982 JOURNAL. All discussions for the June 1982 Discussion Section should be submitted by Feb. 1, 1982.

Publication costs of this article were assisted by IBM Corporation.

### REFERENCES

1. A. K. Ray and A. Reisman, *This Journal*, **128**, 2460 (1981).
2. A. K. Ray and A. Reisman, *ibid.*, **128**, 2466 (1981).
3. B. E. Deal, A. S. Grove, E. H. Snow, and C. T. Sah, *ibid.*, **112**, 308 (1965).
4. S. M. Hu, *J. Appl. Phys.*, **45**, 1567 (1974).
5. S. P. Murarka, *ibid.*, **48**, 5020 (1977).
6. E. Bassous, H. N. Yu, and V. Maniscalco, *This Journal*, **123**, 1729 (1976).
7. D. L. Critchlow, R. H. Dennard, and S. E. Schuster, *IBM J. Res. Dev.*, **17**, 430 (1973).



# A Modified SEM Type EB Direct Writing System and Its Application on MOS LSI Fabrication

Y. Iida\* and K. Mori

Nippon Electric Company, Limited, Basic Technology Research Laboratories, Takatsu-ku, Kawasaki 213, Japan

## ABSTRACT

A modified SEM type electron beam exposure machine adopts an auto-registration function and it is converted to a direct writing purpose system. One-chip-one field and chip-by-chip registration scheme is adopted to increase the field size and to eliminate stage-related problems, such as laser interferometric control complexity and stage movement slowness. 2  $\mu\text{m}$  rule 64 k ROM, shrunk to 4/10 from the original design, is used as a device for testing the developed EB system capability. 0.8  $\mu\text{m}$  high, 2  $\mu\text{m}$  wide, L-shaped step made from bulk Si is used as registration marks and  $\pm 0.1 \mu\text{m}$  of 2 level overlay accuracy is achieved. Although no special optimization or device design modification is done on the shrinkage, the device fabricated by all EB direct writings and dry etching process shows no noticeable difference in electric functions from one made by photolithographic (DSW) processes. The system is stable without intensive maintenance jobs and overlay accuracy through the process (7 exposing levels) is better than  $\pm 0.25 \mu\text{m}$ , although the registration mark structure is changed by the fabrication processes. It becomes clear that this kind of direct writing machine is very useful for research of EB lithography and the LSI development.

Master mask fabrication using electron beam exposure has become usable on the factory level. A raster scanning machine is most popular for this purpose (1-3).

However, it is not clear yet which is the best system for direct writing and there is no commercial machine used for production. For a while the electron beam direct writing machine was used as an experimental or LSI development purpose tool, due to the small throughput from its serially exposing nature but quick turn around time. The system under these circumstances should have the following characteristics to compete with ever improving photolithographic machines (4): (i) Achievability of highly accurate re-registration, even though the wafer is distorted (5) and the registration mark is degraded by the fabrication processes; (ii) reasonable throughput to fabricate developing devices; (iii) high stability and high up-time ratio; and (iv) connection to computer aided design system is possible.

To satisfy (i), a vector scanning electron beam exposure is one of the best ways, because of its scheme to register the writing pattern on a chip by chip basis, using registration marks on each chip corner. If chip by chip registration is possible, necessary stage movement accuracy becomes less and reregistration could be realized even without laser interferometric control. It also reduces the EB system cost and complexity.

About (ii), a one-chip-one field strategy for large field would be one of the better choices, since it can reduce the stage movement time, which could be a large part of exposing time after the advent of high resolution high speed DAC for steering the electron beam. While this technique results in bigger writing field distortion, if all the exposure is accomplished by the same machine, there should not be any problem including overlaying.

To satisfy (iii), magnetic field scan and separation of main scan and correction for reregistration are important. About (iv), PG-3000 format<sup>1</sup> could be an interface.

The system developed in this research is a vector scanning type using prelens double deflection correc-

tion for registration and postlens main scanning. Field size is relatively large, 5 mm. It can accommodate various developing test devices like 64 K ROM, 4 k static RAM, 256 k bubble device, SAW device, etc. It could give important information for larger scale integration, which is often an ally of these devices (6). A testing tool selected for clarifying the system characteristics through its direct writing application is a 64 k ROM which simply reduced the conventional 5  $\mu\text{m}$  rule into the 2  $\mu\text{m}$  rule. Emphasis was placed on determining degradation in registration marks on the wafer by the process chosen to fabricate the 64 k ROM. The technologies used in the process were not only a direct writing, but reactive sputtering in combination with beam resists.

## System Description

A vector scan electron beam system<sup>2</sup> is modified for direct writing by the adoption of auto-registration system. A block diagram of the system is shown in Fig. 1. The electron beam column has a main postlens magnetic scanning coil and an additional small prelens double deflection coil for registration purposes. Main scan is achieved by a combination of positioning purpose high accuracy 16 bit DAC and fill-in mode high speed 12 bit DAC. Accelerating voltage is set at 20 kV, but is adjustable from 2.5 to 30 kV. A tungsten filament is used for its high stability. Also, a single crystal LaB<sub>6</sub> is used sometimes for tests. The modified machine is balanced to operate at an equivalent 0.5 MHz data rate with electron resist sensitivities of 5  $\mu\text{C}/\text{cm}^2$  for W filament and 30  $\mu\text{C}/\text{cm}^2$  for single crystal LaB<sub>6</sub>. The column can provide a minimum beam diameter less than 500 Å at 56 mm working distance. Typical probe size used for this work is 0.25-0.40  $\mu\text{m}$ . Beam blanking is electrostatic. A scintillator system is used to provide video signals for setup and registration. Registration has been accomplished in two stages.

First, the wafer is roughly registered in the stage movement direction and writing field, using large wafer registration mark. Next, the writing field is finely and automatically registered on a chip by chip basis using chip registration mark. Figures 2 and 3 show the wafer setting errors in shift and rotation, respectively, without preregistration to the cassette. Both errors

\* Electrochemical Society Active Member.

Key words: electron beam exposure, direct writing system, auto-registration, MOS LSI process, registration mark.

<sup>1</sup> A pattern data format, proposed by David W. Mann Company.

<sup>2</sup> LEBES, ETEC Corporation, Hayward, CA 94544.

## LEBES SYSTEM DIAGRAM

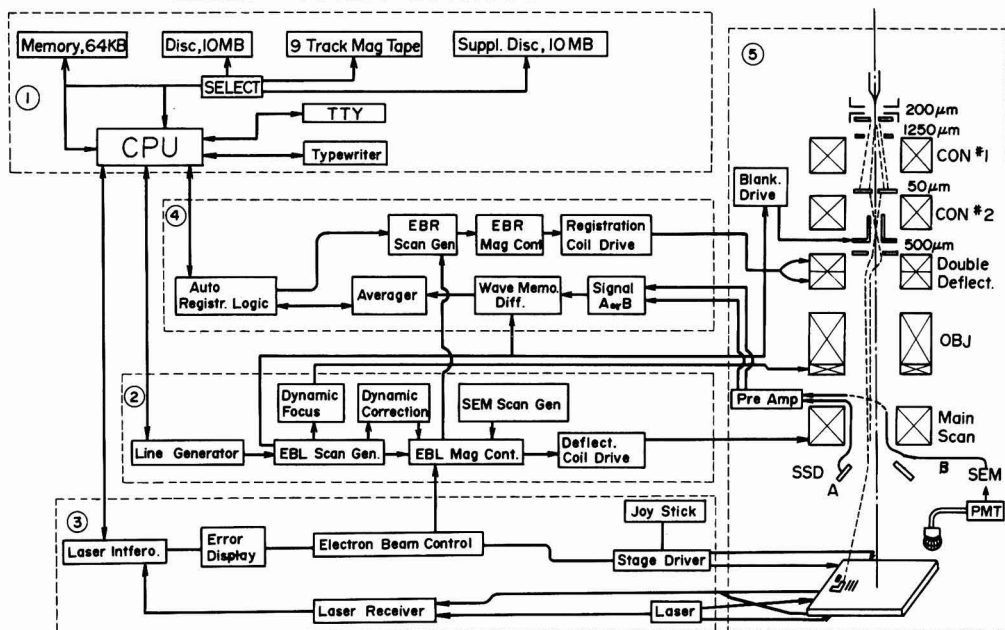


Fig. 1. LEBES system diagram

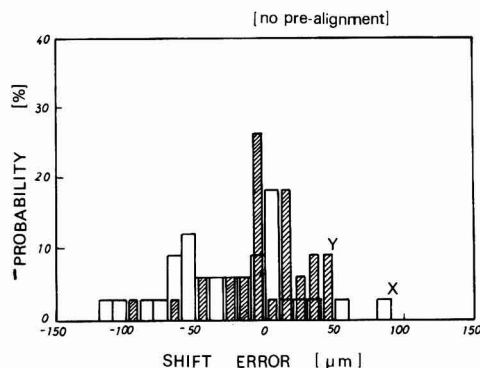


Fig. 2. Wafer setting error (shift); blank (X direction), shadowed (Y direction).

include that of wafer to cassette and that of cassette to column. They are fundamentally gaussian distribution. From the data, the auto-registration system correction range was designed to shift  $\pm 150 \mu\text{m}$  and rotate  $\pm 2.5^\circ$  at maximum. Field size is adjustable  $\pm 2\%$ . Any correction is accomplished by 12 bit multiplication DAC in X and Y directions, separately. Resolutions are  $0.073 \mu\text{m}$  in shift, and  $0.045$  and  $0.039 \mu\text{m}$  at the field corner in rotation and magnification, respectively. Drive amplifier for registration correction has high level response, close to  $10 \text{ MHz}$ . After registration pattern writing commences, the system can select a data file to expose, and multiple chip fabrication is possible aiming at small volume but quick fabrication.

Patterns are exposed in serpentine, rectangular, or raster format with pattern generation providing several primitive shapes such as rectangles, parallelograms, and triangles. Proximity correction has not been

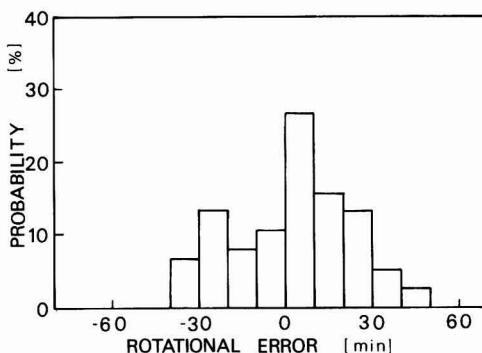


Fig. 3. Wafer setting error (rotation)

included, because of the relatively large design rule employed.

## Writing Method and Hysteresis

To minimize the settling time, jumping distance from one pattern to another is restricted through subfield sorting (7). For this method, a basketweave shift between subfields is the best (8). However, it causes a hysteresis error at the connection point of each subfield stripe. This error comes from magnetization of stage parts in the column by leakage field.

This problem is partially alleviated by shielding with Permalloy, as shown by the dotted line in Fig. 4. However, a system aiming at a large field, like the present one, cannot escape from the error completely. Stripe raster shift should be adopted. Using this method, the error is completely eliminated. A drawback is that longer settling time (typically 20 times the subfield jump time) is needed when the subfield is shifted from one corner to the other of a stripe. It is, however, only  $10 \text{ msec (field jump settling time)} \times 20$

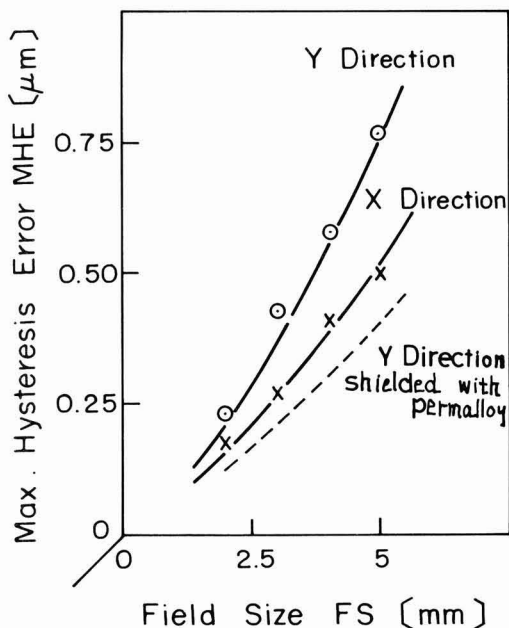


Fig. 4. Maximum hysteresis error as a function of field size

(number of stripes), making 200 msec. There is no problem compared with writing time, typically 3 min/strip for 64 k ROM.

#### Pattern Data Preparation

The pattern data are first created in an interactive computer aided design (CAD) system, and are output in PG-3000 format. The shapes are sorted to minimize long jumps between shapes using a large computer system (ACOS-700).

Consequently, pattern writing time will contain minimum overhead necessary for settling the deflection system. This is achieved by first sorting the chip data into subfields through which the writing will progress in a stripe raster fashion.

The typical size of a subfield is 1/20 of the field size. Within a subfield, the shapes are connected to compact the data. The resulting set of sorted records is then translated into code in the format required by the modified E-beam machine. Typical CPU time to treat 100 k data is about 10 min.

#### Resist Process

A key to this work is the resist system, which must provide high durability against reactive sputter etching and adequate sensitivity. Commercial availability of resists might be another important factor in order to make the fabrication process reliable. AZ-2400<sup>3</sup> was chosen as a positive electron resist (9) and NER-1 was chosen as a negative electron resist. The former is a well-known photoresist. The latter is made from narrow molecular weight dispersion polystyrene, which is easily available as molecular weight standard synthesized by living polymerization. Selection of negative resist molecular weight is important. The higher the molecular weight is, the greater the severity of the swelling problem and the "kissing" problem between lines, while soaking in the developer. A 4:1 tetrahydrofuran-ethanol mixture was selected as a low swelling developer. However, the smaller the molecular weight, the stronger the tensile stress and the more

Table I. Direct writing resist characteristics

RESIST	NER-1 (polystyrene)		AZ-2400
TYPE	NEGATIVE		POSITIVE
ETCHED MATERIAL	Si <sub>3</sub> N <sub>4</sub>	Poly-Si	Al
ETCHING GAS	CF <sub>4</sub> +H <sub>2</sub> 0.08 Torr	CCl <sub>4</sub> +F <sub>2</sub> 0.04 Torr	CCl <sub>4</sub> 0.35 Torr
ETCH RATIO (MATERIAL/RESIST)	4.3	2.1	6.5
TYPICAL PATTERN			

severe the distortion in the L-shaped pattern results. This is due to the polymer cross-linking by exposure and concomitant volume shrinkage.

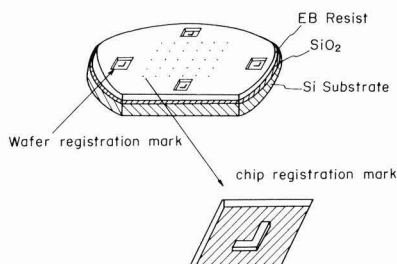
Relatively large 600 k molecular weight was chosen to optimize swelling and shrinking problems. It is called NER-1. Table I shows a summary of characteristics for both resists.

#### Linewidth Control and Registration Mark

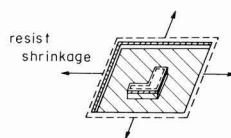
All EB direct writing process is practically usable when the device patterns are directly etched by EB resist mask; without metal mask transfer step the registration mark is compatible with the process. Delineation accuracy values, when using SiO<sub>2</sub>, Si<sub>3</sub>N<sub>4</sub>, poly-Si, and Al are  $\pm 0.15$ ,  $\pm 0.15$ ,  $\pm 0.15$ , and  $-0.25 \pm 0.15$   $\mu$ m, respectively. It is achieved by using reactive sputter etching (10) and highly durable EB resist against dry etching mentioned above.

For accurate registration, it is desirable to fabricate registration marks using electron beam exposure. The registration marks used in this work are 0.8  $\mu$ m high silicon pedestals, which are completely compatible with the silicon process. The fabrication process is illustrated in Fig. 5. There are several advantages to the process: (i) There is no foreign material like refractory metal, CVD poly-Si, etc.; (ii) the resist area for the registration mark is small and resist deformation caused by dry etching does not affect pattern accuracy.

#### 1. Electron Beam Exposure and Development



#### 2. Dry Etching of SiO<sub>2</sub> and Si



#### 3. Remove resist and wash out SiO<sub>2</sub>

Fig. 5. Si pedestal registration mark fabrication process with EB resist mask and dry etching.

<sup>3</sup> Shipley Company, Newton, MA.

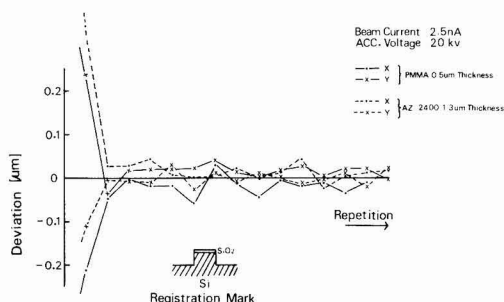


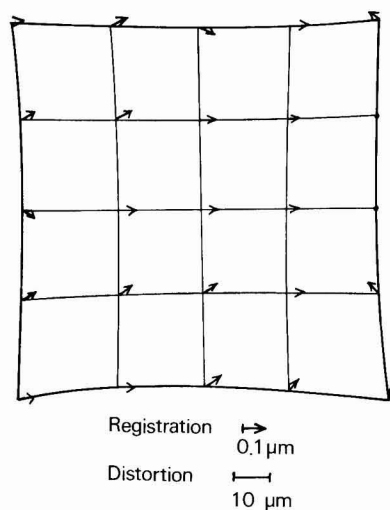
Fig. 6. Deviation in detected position from desired position

The larger the continuous resist area, the more critical the pattern deformation or positional shift. (iii) Device area; cleanliness is protected by the SiO<sub>2</sub> during the process. The SiO<sub>2</sub> is etched away after the process. Figure 6 shows the X direction and Y direction detection accuracy for the registration mark coated by different thickness resists. There is no notable difference between them. After two scans, the detection accuracy is better than 0.1 μm. Though the reason for relatively large error in the first scan is not clear, it could be because of resist deformation by the first beam scan. It is desirable to practice dummy scanning before the detection. Figure 7 shows an example of the two layer registration accuracy for the 5 mm field. Since the system has field distortion, the registration condition shown by the arrows is slightly different for different positions. They are, however, within ±0.1 μm.

#### Direct Writing Process and the Function of the Fabricated Device

The direct writing process is fundamentally an n-channel polysilicon MOS process. Figure 8 shows key steps in the etching process. Table II shows exposure and doping processes. After registration mark patterning, device areas were isolated by boron diffusion in the field and by the local oxidation of silicon (LOCOS). Threshold voltages for driver enhancement transistor and load depletion transistor are adjusted by boron ion and arsenic ion implantations, respectively. Gate insulator thickness was 400 Å; 5000 Å CVD polysilicon was used as gate metallization. The polysilicon was covered by 1600 Å CVD Si<sub>3</sub>N<sub>4</sub>. Arsenic ions were implanted to form the self-aligned source and drain. Wafers were annealed at 1000°C in a steam atmosphere to form the sidewall insulator of the polysilicon gate

#### 5mm Field OVERLAY ACCURACY



Exposure level	Shift (μm)		Rotation (min)
	X	Y	
1	-112.8	93.4	-12.9
2	27.6	-112.9	-25.2

Fig. 7. 5 mm field overlay accuracy

and thick silicon dioxide on the source and drain by heavily doped arsenic enhancing oxidation. After Si<sub>3</sub>N<sub>4</sub> removal, phosphorous was thermally diffused into the polysilicon. Double layers of phosphorous silicate glass and CVD SiO<sub>2</sub> were used as an insulator. PSG made it possible to topographically smooth the device surface, preventing discontinuing the Al metallization and thin SiO<sub>2</sub> eliminated the wetting and poor resist adhesion problems of PSG. Contact holes were etched into the double layer to write ROM information. Phosphorous-doped polysilicon 0.2 μm thick and 1.2 μm Al

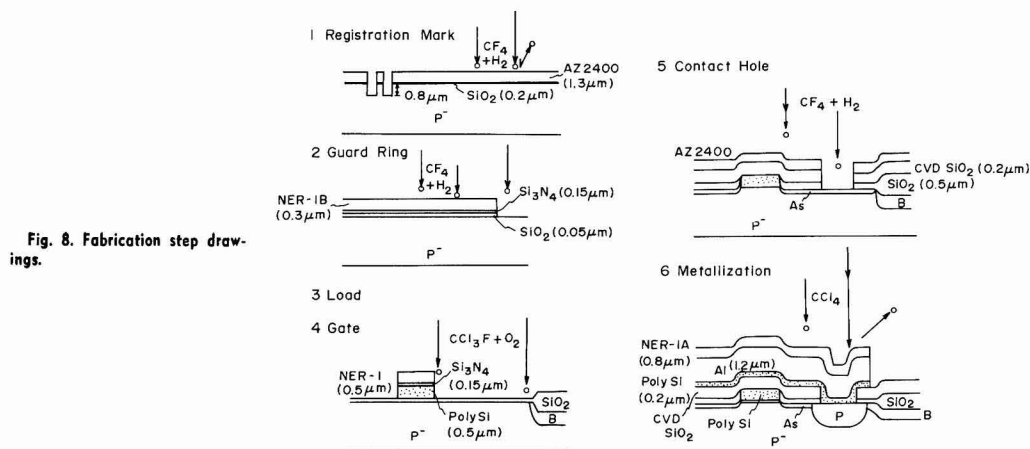


Fig. 8. Fabrication step drawings.

Table II. N-MOS process parameters used for the experiment

starting material	P-type, $50\Omega\cdot\text{cm}$ (511)
exposure [1]	registration mark ( $2\mu\text{m}$ )
exposure [2]	locos pattern ( $2\mu\text{m}$ )
field I/I	$^{11}\text{B}^+$ , 100 KeV, $2 \times 10^{13}\text{cm}^{-2}$
locos oxidation	$1000^\circ\text{C}$ , 4hr, $0.8\mu\text{m}$ $\text{SiO}_2$
gate oxidation	$950^\circ\text{C}$ , 85min dry $\text{O}_2$ , $400\text{\AA}$
channel I/I	$^{11}\text{B}^+$ , 150 KeV, $3 \times 10^{11}\text{cm}^{-2}$ $40\text{ KeV}$ , $5 \times 10^{11}\text{cm}^{-2}$
exposure [3]	Load pattern ( $5\mu\text{m}$ )
depletion Tr I/I	$^{75}\text{As}^+$ , 150 KeV, $2 \times 10^{12}\text{cm}^{-2}$
exposure [4]	Direct contact
exposure [5]	Gate pattern ( $2\mu\text{m}$ )
S/D I/I	$^{75}\text{As}^+$ , 150 KeV, $5 \times 10^{15}\text{cm}^{-2}$
exposure [6]	Contact pattern ( $2.5\mu\text{m}$ )
exposure [7]	Al pattern ( $2\mu\text{m}$ space)
exposure [8]	Pad pattern

were continuously deposited and etched as interconnectors. Annealings to remove the irradiation damage were carried out in  $\text{H}_2$  atmosphere at  $450^\circ\text{C}$ .

Figure 9 shows an overall view of the fabricated 64 k ROM and enlarged views. The  $2.5\mu\text{m}$  contact hole is centered in  $3\mu\text{m}$  width Al metallization. It is clear that the registration mark is kept well through the fabrication processes. Details are discussed in the following section.

Figure 10 shows a function of the device fabricated by all E-beam direct writing. As can be seen, the rise-time for the fall time of the signal are unbalanced. It was, however, assumed that the input and output buffer is not optimized, although high reduction (4/10) has been accomplished. The same design rule device, fabricated by photolithographic process (DSW), has shown very similar results (11).

### Overlay Accuracy

Table III shows an example of overlay accuracy through the process. The Vernier method was adopted to measure the accuracy. On the table, for example, GR-load shows overlay accuracy for load I/I pattern on the guard ring pattern.

The overlaid pattern always has little X and Y shift and distribution. The shift error origin is not clear, but the registration mark structure change caused by unbalanced resist or material coating of the mark are considered reasons. Similar phenomena are often discussed on Al metallization coverage.

Table III. Overlay accuracy through the all EB direct writing process

	X [ $\mu\text{m}$ ]		Y [ $\mu\text{m}$ ]	
	$\bar{X}$	$\sigma$	$\bar{Y}$	$\sigma$
GR- Load	-0.02	0.13	-0.05	0.13
GR- D.Contact	0.12	0.03	-0.04	0.12
GR- Gate	0.13	0.06	0.07	0.12
Gate- Contact	0.08	0.08	0.02	0.03
Contact- Al	0.07	0.07	0.09	0.06

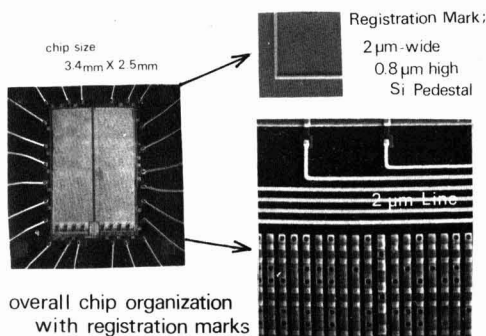


Fig. 9. Overall and magnified view of 64 k ROM

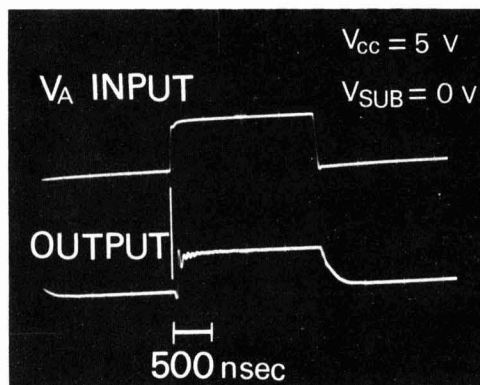


Fig. 10. An example of output waveform

Even considering shift and distribution, the results shows that the system well satisfied the required  $\pm 0.25\mu\text{m}$  overlay accuracy, using registration mark damaged by various coating and etching processes.

### Conclusion

The systems described here are a fundamentally modified SEM machine, not those machines which could be fabricated only by a huge company laboratory. The systems are easily modified to research fundamental electron optics and new strategy to write pattern, such as double deflection correction, hysteresis, and stripe scanning. It has, however, enough capability to fabricate LSI such as 64 k ROM by all direct writing process. The beam is focused into a small diameter area, less than  $500\text{\AA}$ .

The system could be used for quick fabrication of a wide variety of devices, like bubble memories, Josephson circuits, GaAs FET, etc. It is also used for new resist evaluation, research in physics related to electron beam damage, electron scattering, and delineation limitation.

### Acknowledgment

The authors wish to thank Drs. D. Shinoda and K. Muta for their encouragement. They would like to thank Messrs. S. Ishida, M. Tajima, and K. Kamimura for their technical assistance. They also thank Drs. Y. Okuto, Y. Ohnishi, and K. Suzuki, and Messrs. H. Mizumura, Y. Kurogi, M. Morimoto, and N. Endo for informative discussions.

Manuscript submitted Dec. 9, 1980; revised manuscript received May 13, 1981.

Any discussion of this paper will appear in a Discussion Section to be published in the June 1982 JOURNAL. All discussions for the June 1982 Discussion Section should be submitted by Feb. 1, 1982.

Publication costs of this article were assisted by Nippon Electric Company, Limited.

### REFERENCES

1. D. R. Herriott, *IEEE Trans. Electron Devices*, **ed-22**, 385 (1975).
2. N. C. Yew, *Solid State Technol.*, **20**, 86 (1977).
3. J. A. Doherty, *ibid.*, **20**, 83 (1977).
4. G. L. Resor, *Microelectron. J.*, **10**, 18 (1979).
5. L. D. Yau, *IEEE Trans. Electron Devices*, **ed-26**, 1299 (1979).
6. K. Suzuki, M. Morimoto, N. Endo, H. Ishiguro, K. Kurogi, Y. Iida, and K. Mori, in "Proceedings of

- 1980 Custom Integrated Circuits Conf.," p. 8, New York (1980).
7. T. H. P. Chang, A. J. Speth, C. H. Ting, R. Viswanathan, M. Parikh, and E. Munro, in "Electron and Ion Beam Science and Technology," R. Bakish, Editor, p. 377, The Electrochemical Society Soft-bound Proceedings Series, Princeton, NJ (1976).
8. W. D. Grobman, H. E. Luhn, T. P. Donohue, A. J. Speth, A. Wilson, M. Hatzakis, and T. H. P. Chang, *IEEE Trans. Electron Devices*, **ed-26**, 360 (1979).
9. M. Hatzakis and J. W. Shaw, in "Electron and Ion Beam Science and Technology," R. Bakish, Editor, p. 301, The Electrochemical Society Soft-bound Proceedings Series, Princeton, NJ (1978).
10. N. Endo and Y. Kurogi, *IEEE Trans. Electron Devices*, **ed-27**, 1376 (1980).
11. N. Endo, Private communication.

## MOS Device Fabrication Using X-Ray Lithography

K. Suzuki and J. Matsui

Nippon Electric Company, Limited, Basic Technology Research Laboratories, Takatsu-ku, Kawasaki 213, Japan

and T. Ono and Y. Saito

Nippon Telegraph and Telephone Public Corporation,  
Musashino Electrical Communication Laboratory, Musashino, Tokyo 180, Japan

### ABSTRACT

X-ray lithography has been applied to fabricate n-MOS devices such as transistor matrices, ring oscillators, and MOS capacitors. A propagation delay time as low as 200 psec/gate, and about 0.12 pJ power-delay product were obtained from the ring oscillator with 0.7  $\mu\text{m}$  effective gate length. From the threshold voltage measurements of the transistor matrices, it was found that the standard threshold voltage deviation in MOSFET's with 1.5  $\mu\text{m}$  effective gate length in a chip and the deviation in a wafer were as low as 5 and 7 mV, respectively.

X-ray lithography has been expected to be useful as a fine pattern replicating technique, because of its high resolution and productivity. Recently, a high power x-ray lithographic system using a water-cooled rotating Si anode for x-ray source and a beam vibration method for mask alignment has been developed and its performance was demonstrated (1, 2). An SiN/SiO<sub>2</sub>/SiN sandwich structure membrane mask (3) has also been developed and was applied to fabricate poly-Si gates in ring oscillators (2).

In this experiment, MOS devices have been fabricated using the above-mentioned x-ray lithographic system for four mask levels. The present paper describes the x-ray lithography process followed by dry etching, and also the device characteristics.

### X-Ray Lithography Process

The IC chips which have been fabricated in this experiment contain transistor matrices, ring oscillators, and MOS capacitors. Of the five lithographic steps, local oxidation of silicon (LOCOS) (4), gate, contact hole, and metallization were processed by x-ray lithography. Only the channel doping step was processed by photolithography. In order to examine the x-ray exposure influences on the devices, a few wafers in the lot were processed by photolithography through all lithographic processes.

A water-cooled rotating Si anode x-ray source was operated at 20 kW (20 kV, 1A) electron beam input power, which generates about  $6 \times 10^{-5}$  W/Sr SiK $\alpha$  x-ray radiation.

Key words: fine pattern, x-ray mask, dry etching, transistor matrices.

X-ray masks (3) consisting of an SiN (0.2  $\mu\text{m}$ )/SiO<sub>2</sub> (1.0  $\mu\text{m}$ )/SiN (0.2  $\mu\text{m}$ ) sandwich structure were prepared by CVD for SiN and by rf-sputtering for SiO<sub>2</sub>, respectively. The membranes have as high as 85% transparency for both the SiK $\alpha$  line and visible light. X-ray absorber patterns, consisting of a 0.8  $\mu\text{m}$  thick gold, were fabricated by a double lift-off method (5), in which 1.2  $\mu\text{m}$  thick polyimide spacer patterns are used for gold plating masks.

Details of the x-ray lithographic levels are shown in Table I. In three mask levels, i.e., LOCOS, gate, and metallization, negative resist SEL-N<sup>1</sup> has been used. Figure 1 shows a scanning electron micrograph of 2  $\mu\text{m}$  gate patterns exposed in a 0.8  $\mu\text{m}$  thick SEL-N. The SEL-N patterns show trapezoidal cross sections. This is caused by the swelling of SEL-N patterns in a developer followed by shrinking in rinsing solution and postbaking process. The swelling magnitude changes,

<sup>1</sup> SEL-N is produced by Somar Industry Corporation, in Japan.

Table I. X-ray lithographic levels

Level	Film	Resist	Etching method	Gas	Etch rate ratio (film/resist)
LOCOS	SiO <sub>2</sub>	SEL-N (0.7 $\mu\text{m}$ )	Wet etching	—	—
Gate	Poly-Si (0.4 $\mu\text{m}$ )	SEL-N (1.0 $\mu\text{m}$ )	Reactive sputter etching	CBrF <sub>3</sub>	3.5
Contact	PSG (0.8 $\mu\text{m}$ )	FBM (1.0 $\mu\text{m}$ )	Reactive sputter etching	C <sub>2</sub> F <sub>6</sub>	1.3
Metallization	Al (0.8 $\mu\text{m}$ )	SEL-N (1.5 $\mu\text{m}$ )	Plasma etching	CCl <sub>4</sub>	1.0



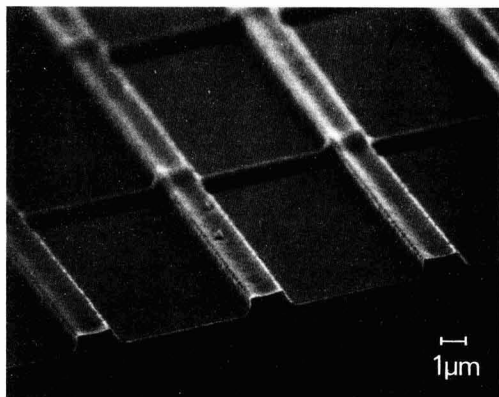


Fig. 1. Scanning electron micrograph of  $2\text{ }\mu\text{m}$  gate patterns exposed in a  $0.8\text{ }\mu\text{m}$  thick SEL-N.

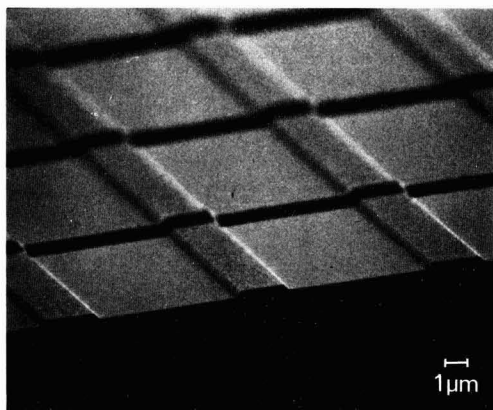


Fig. 3. Reactive sputter etched  $2\text{ }\mu\text{m}$  poly-Si gates

depending on the resist volume, and also on the kind of developer. In this experiment, methyl alcohol was used for developer, which resulted in rather small swelling. However, in contact hole level, negative resists, including SEL-N, are hard to use because of the large resist-covered area that leads to conspicuous swelling (narrowing or plugging up of the contact holes). In this level, therefore, a positive resist poly hexafluorobutyl metacrylate (FBM) (6) was used, which showed little swelling in the developer. A scanning electron micrograph of  $4\text{ }\mu\text{m}$  wide contact holes, exposed in a  $1.3\text{ }\mu\text{m}$  thick FBM, is shown in Fig. 2. FBM contact holes preserved squarish shoulders, and the side walls were inclined from the surface at  $75\text{ degrees}$ .

Dry etching has been employed for constructing gates, contact holes, and wiring. The etching method after each lithographic step is presented in Table I with gases used, and film to resist etch rate ratio. A scanning electron micrograph of  $2\text{ }\mu\text{m}$  poly-Si gates etched by reactive sputter etching (7) is shown in Fig. 3. Side walls of the poly-Si gates show  $45^\circ \sim 50^\circ$  tilts, which reflect SEL-N pattern profile used for etching mask. Figure 4 is an SEM photograph, which indicates good step coverage of the poly-Si gate at the  $0.5\text{ }\mu\text{m}$  guard ring projection.

Figure 5 shows the appearance of aluminum metallization in the transistor matrix after plasma etching. Although the etch resistance of SEL-N against plasma

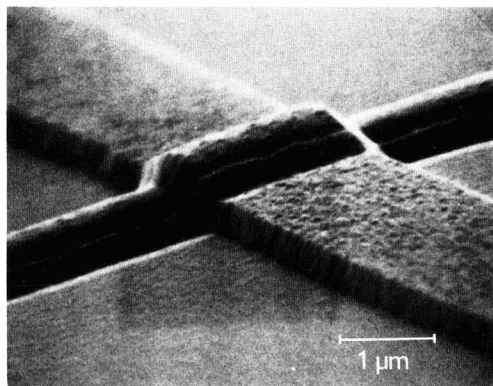


Fig. 4. Scanning electron micrograph showing good step coverage at the  $0.5\text{ }\mu\text{m}$  step.

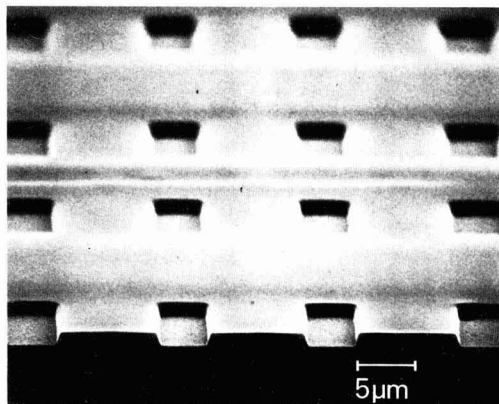


Fig. 2. Scanning electron micrograph of  $4\text{ }\mu\text{m}$  wide contact holes exposed in a  $1.3\text{ }\mu\text{m}$  thick FBM.

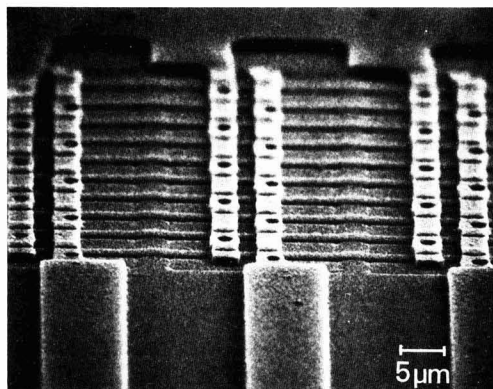


Fig. 5.  $3\text{ }\mu\text{m}$  wide aluminum metallization in a transistor matrix

etching using  $\text{CCl}_4$  is the same as that of aluminum, a considerably thick ( $\sim 1.5\text{ }\mu\text{m}$ ) SEL-N resist layer is required for x-ray exposure of the metallization level, because the decrease in the resist thickness at the shoulder of contact holes is significant. In this case,  $0.8\text{ }\mu\text{m}$  thick,  $3\text{ }\mu\text{m}$  wide,  $2\text{ }\mu\text{m}$  gap aluminum metallization is successfully fabricated, as shown in Fig. 5.

The x-ray masks were aligned to the wafer using the beam vibrating method (1,8). The alignment marks on the wafer were made by preferential etching using hydrazine solution. It was found that the S/N of this mark was not changed through the five lithographic processes. Therefore, the same mark was used for all lithographic processes without any protection. The total alignment error by the above-mentioned method was found to be less than  $0.3 \mu\text{m}$  ( $2\sigma$ ) in a 2 in. diam wafer, from measurements using vernier patterns which were made in each lithographic process.

### Device Characteristics

An example of the threshold voltage ( $V_{th}$ ) distribution for transistor matrixes with  $1.5 \mu\text{m}$  effective gate length is shown in Fig. 6. The upper numeral in each of the sixteen squares shows  $V_{th}$ , the average values of the  $V_{th}$  of 120 FET's in the transistor matrix. The lower numeral shows  $\sigma_0$ , the standard deviation in the  $V_{th}$ . The average value of  $\sigma_0$ , over all chips in the wafer, represented by  $\sigma_0$ , is  $5.0 \text{ mV}$ . The standard  $V_{th}$  deviation in the wafer,  $\sigma_1$  is  $6.7 \text{ mV}$ . Other wafers show a similar tendency. These results show highly uniform characteristics in devices made by x-ray lithography followed by dry etching.

Figure 7 is a photomicrograph of the ring oscillator fabricated by x-ray lithography. The ring oscillator is a 31-stage E/D mode unit with a fan-in and fan-out ratio of 1. Effective channel length is  $0.7 \mu\text{m}$  in the driver transistors, and  $2.3 \mu\text{m}$  in load transistors.

The output waveform for the ring oscillator at  $V_{dd} = 5 \text{ V}$  is shown in Fig. 8. The oscillation period is  $12.5 \text{ nsec}$ , which corresponds to  $202 \text{ psec/gate}$  propagation delay time. The power-delay product is about  $0.12 \text{ pJ/gate}$ .

The C-V curve for the MOS capacitor, fabricated using x-ray lithography for four mask levels and that by using photolithography for all mask levels, is shown in Fig. 9. Both MOS capacitors have the same design, and have been made in the same lot, except for the lithographic processes. There was no special annealing process after the x-ray lithographic process. Figure 9 shows that there is no x-ray radiation-induced damage in the MOS capacitor, when every standard process is over. It is reported, however, that the C-V curves from MOS capacitor irradiated by  $\text{AlK}\alpha$  ( $8.3\text{\AA}$ ) shift from the original state (9-11). It is considered that, in the

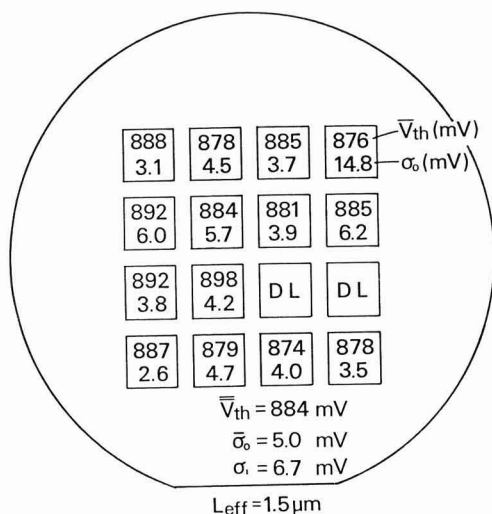


Fig. 6. An example of  $V_{th}$  distribution map in the wafer

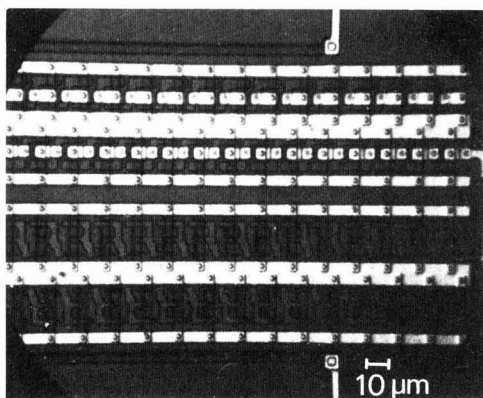


Fig. 7. Ring-oscillator fabricated by x-ray lithography

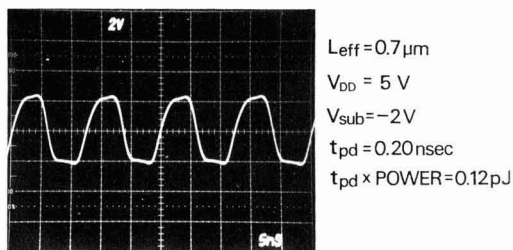


Fig. 8. Waveform of ring-oscillator fabricated by x-ray lithography.

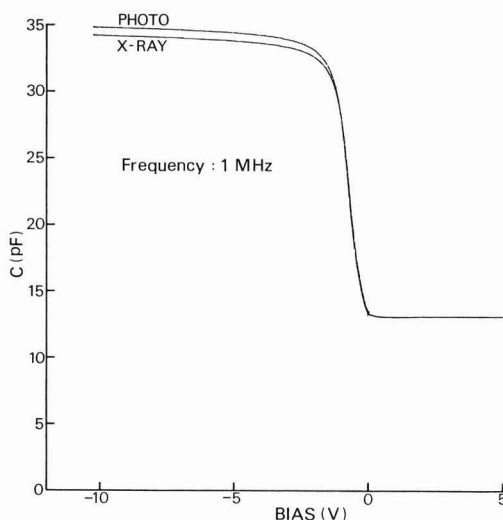


Fig. 9. C-V curve for MOS capacitor fabricated by x-ray lithography and that by photolithography.

present experiment, radiation-induced damage was annealed out at the high temperature processes, such as impurity diffusion, oxidation, and CVD.

### Conclusions

MOS devices, such as transistor matrixes with  $1.5 \mu\text{m}$  effective channel length, ring oscillators with  $0.7 \mu\text{m}$  effective channel length, and capacitors for C-V

measurements, have been fabricated using x-ray lithography, including automatic mask alignment.

Results obtained from the present study are as follows.

1. High contrast x-ray masks with 0.8  $\mu\text{m}$  thick gold patterns have been prepared on  $\text{SiN}/\text{SiO}_2/\text{SiN}$  membrane by double lift-off method.

2. Alignment marks made by preferential etching work well through all mask processes without any protection.

3. High registration accuracies, better than  $\pm 0.3 \mu\text{m}$  ( $2\sigma$ ) on 2 in. wafers, were realized.

4. Dry etching is successfully applied to fabricate poly-Si gates, PSG contact holes, and aluminum metalizations.

5. Standard deviation in  $V_{th}$  as low as 5 mV in a chip, about 6.7 mV in a wafer, was realized.

6. Propagation delay time reaching 202 psec/gate, and the power-delay product of 0.12 pJ/gate were obtained from the ring oscillator.

7. No x-ray exposure damage in devices has been observed from the C-V measurements, without any special annealing after the x-ray lithography processes.

#### Acknowledgment

The authors wish to thank Drs. S. Asanabe, D. Shinoda, and H. Muta of Basic Technology Research Laboratory, Nippon Electric Company, Limited, and Drs. S. Yamazaki and S. Nakayama of Musashino Electric Communication Laboratory, N.T.T. for their discussions and encouragement. The members of Polymer Section

of Electric Communication Laboratory, N.T.T. are also thanked for the supply of FBM resists.

Manuscript submitted Feb. 10, 1981; revised manuscript received April 17, 1981.

Any discussion of this paper will appear in a Discussion Section to be published in the June 1982 JOURNAL. All discussions for the June 1982 Discussion Section should be submitted by Feb. 1, 1982.

Publication costs of this article were assisted by Nippon Electric Company, Limited.

#### REFERENCES

1. S. Yamazaki, S. Nakayama, T. Hayasaka, and S. Ishihara, *J. Vac. Sci. Technol.*, **15**, 987 (1978).
2. S. Yamazaki and T. Hayasaka, *Jpn. J. Appl. Phys.*, **19**, Suppl. 19-1, 35 (1980).
3. K. Suzuki, J. Matsui, T. Kadota, and T. Ono, *Jpn. J. Appl. Phys.*, **17**, 447 (1978).
4. J. A. Appels, E. Kooi, M. M. Paffen, J. J. H. Schatorjé, and W. H. C. G. Varkuylen, *Philips Res. Rep.*, **25**, 118 (1970).
5. T. Ono and A. Ozawa, *Jpn. J. Appl. Phys.*, **19**, 2311 (1980).
6. M. Kakuchi, S. Sugawara, K. Murase, and K. Matsuyama, *This Journal*, **124**, 1648 (1977).
7. S. Matsuo, *Appl. Phys. Lett.*, **36**, 768 (1980).
8. S. Yamazaki, S. Nakayama, S. Ishihara, and S. Sasayama, *Bull. Jpn. Soc. Prec. Eng.*, **14**, 137 (1980).
9. S. E. Bernachi, Doctoral Thesis, Harvard University (1975).
10. H. L. Stover, F. L. Hause, and D. McGreevy, *Solid-State Technol.*, **Aug**, 95 (1979).
11. M. Peckerar, R. Fulton, and P. Blaise, *J. Vac. Sci. Technol.*, **16**, 1658 (1979).

## Measurement of the Diffusion Coefficient of Gallium in Molten Germanium

E. D. Bourret,<sup>1</sup> J. J. Favier, and O. Bourrel

Laboratoire d'Etude de la Solidification,  
Centre d'Etudes Nucleaires de Grenoble, 85X, 38041 Grenoble Cedex, France

#### ABSTRACT

The diffusion coefficient of  $^{72}\text{Ga}$  in molten germanium has been measured at  $T = 1219 \text{ K}$  using the shear-cell technique. The concentration profile was obtained from the intensity of the  $\gamma$ -emission detected in the range 0.740-0.900 MeV. The diffusion coefficient was found to be  $2.1 \times 10^{-8} \text{ m}^2\text{sec}^{-1}$  at this temperature.

The accurate determination of diffusion coefficients of solute in the liquid phase ( $D_L$ ) is becoming more and more important for the understanding of solidification in metallurgical processes as well as in crystal growth. Up to now, very few measurements of these coefficients have been made (1). In the germanium-gallium system, the lack of data for  $D_L$  has been pointed out by different authors (2, 3). In order to relate the diffusion phenomenon to the segregation during solidification, an accurate value of the diffusion coefficient near the solidus temperature is badly needed. This is of prime importance for determining the type of mass transport which took place during the growth of Ge-Ga crystal in a microgravity environment (2, 4). This paper reports the measurements of  $D_L$  at 1219 K.

The melting point of pure germanium is  $T_m = 1210.4 \text{ K}$ .

#### Experimental Procedure

Measurements were made using the shear-cell technique developed by Potard *et al.* (5). The shear-cell consists of several graphite disks mounted coaxially in which three off-center holes (1.5 mm diam) are drilled to form three capillaries when they are aligned. As shown in Fig. 1, solvent and solvent + solute metals were kept separate until an experiment was begun by aligning the upper and the lower capillaries in a vertical position. After diffusion, the disks were rotated so that the liquid columns were sheared. This last rotation of the disks avoids subsequent change of concentration due to solidification; thus there was no need for quenching the samples. Upper capillaries were filled with pure germanium and lower capillaries contained the dilute alloy germanium-gallium. Diffusion occurs from bottom to top for preventing additional

<sup>1</sup>Present address: Department of Materials Science and Engineering, Massachusetts Institute of Technology, Cambridge, Massachusetts 02139.

Key words: shear-cell technique, gallium, diffusion.

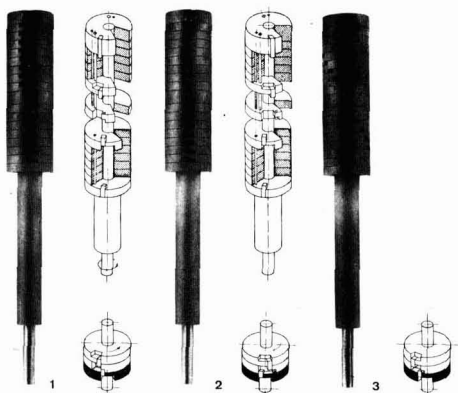


Fig. 1. The shear-cell: 1, filling; 2, diffusion; 3, shearing

effects due to segregation of gallium. Densities of gallium and germanium are, respectively, 5.91 and 5.32 g/cm<sup>3</sup>. In order to obtain a direct and precise concentration measurement of the samples, <sup>72</sup>Ga was used as a radioactive tracer. Under irradiation by thermal neutrons, gallium of normal isotopic composition, which contains 39.8% of <sup>71</sup>Ga, produces <sup>72</sup>Ga. <sup>72</sup>Ga emits  $\beta^-$  particles with a maximum energy of 2.54 MeV, followed by  $\gamma$ -emission with a maximum energy (96%) of 0.835 MeV. One gram of gallium was irradiated for 700 sec under a neutron flux of  $1.6 \times 10^{19} \text{ nm}^{-2} \text{ sec}^{-1}$ .

The active gallium was then melted with pure germanium to obtain a Ge-Ga alloy containing about 600 ppm of Ga.

Diffusion occurs at 1219 K, a "stabilizing" gradient of 100 K m<sup>-1</sup> being maintained between the bottom and the top of the cell to reduce convection.

### Results

A practical diffusion time was determined from theoretical considerations to be 20 min. A preliminary experiment, using nonactive gallium, confirmed that this time was correct. The gallium was found to diffuse over 4 disks. Concentration measurements which were made, in this case, by x-ray fluorescence cannot be used to evaluate the diffusion coefficient since, due to the small size of the samples, the surface of integration is very small and induces large experimental errors. In the shear-cell configuration, the boundary value problem is that of diffusion between a pair of semi-infinite solids. A solution of Fick's second law  $\left(\frac{\partial C}{\partial t} = D \frac{\partial^2 C}{\partial x^2}\right)$ , with the boundary conditions  $C = C_0$  at  $x > 0$  at  $t = 0$  and  $C = 0$  at  $x < 0$  at  $t = 0$  is given by

$$C(x,t) = \frac{C_0}{2} \left( 1 + \operatorname{erf} \frac{x}{2\sqrt{Dt}} \right)$$

Knowing  $x$ ,  $t$ , and  $C(x,t)$ ,  $D$  is given by

$$D = \frac{1}{4b^2t}$$

$b$  being the slope of

$$\operatorname{erf}^{-1} \left( \frac{2C}{C_0} - 1 \right) = \frac{x}{2\sqrt{Dt}}$$

The gallium concentration is proportional to the intensity of the  $\gamma$ -rays emitted with an energy in the range 0.740-0.900 MeV. Each measurement was corrected to account for the weight of the sample and the intensity of the <sup>72</sup>Ga peak as a function of time ( $t_{0.5} = 51,000 \text{ sec}$  for <sup>72</sup>Ga). If the intensity of the source at  $t$  is  $I_t$ , then at  $t + \Delta t$ , it will be

$$I_{t+\Delta t} = I_t \exp(-\lambda \Delta t) \quad [1]$$

$\lambda$  being the disintegration constant,  $\lambda = 0.693/t_{0.5}$ . The mean intensity during  $\Delta t$  is

$$\bar{I} = I_t \frac{1}{\Delta t} \int_0^{\Delta t} \exp(-\lambda t) dt \quad [2]$$

and then

$$I_t = \bar{I} \frac{0.693 \Delta t / t_{0.5}}{1 - \exp(-0.693 \Delta t / t_{0.5})} \quad [3]$$

The intensity represents the accumulated counts per time units. Every measurement is corrected using a reference time; in this case, the reference time is  $t = 0$  at the beginning of the countings.

Another correction is made to account for the dead time of the detector. To account for the dead time, an apparent half-life is determined using the decreasing curve of the activity of <sup>72</sup>Ga ( $\log N = -\lambda t$ ) (Fig. 2). This curve exhibits three different slopes corresponding to three apparent half-lives, as shown in Table I. The apparent half-lives are used to calculate the intensity of accumulated counts per time unit (Eq. [3]). The concept of apparent half-lives is used because the correlation (Table I) with straight lines is good enough so that specific corrections for each count rate according to Fig. 2 are not necessary and the corrective calculations are then simplified. Finally, the diffusion coefficient obtained from the measurements reported in Fig. 3 is  $D_L = 2.1 \times 10^{-8} \text{ m}^2 \text{ sec}^{-1}$  at  $T = 1219 \text{ K}$ . The coefficient of determination for the straight line is 0.999.

In earlier studies, Schmidt and Verhoeven (6) measured this diffusion coefficient at  $T = 1303 \text{ K}$ . The method used was the capillary-reservoir technique and led to the value of  $2.4 \times 10^{-8} \text{ m}^2 \text{ sec}^{-1}$ .

Considering an activation energy of 0.32 eV given by Kodera (3), this value, corrected to 1219 K, becomes  $2.0 \times 10^{-8} \text{ m}^2 \text{ sec}^{-1}$ , which is in good agreement with our direct measurements at this temperature.

The shear-cell technique is a very appropriate one for direct measurement of the interdiffusion coefficient in the vicinity of the liquidus temperature (less than 10 K above) and should be used before investigating

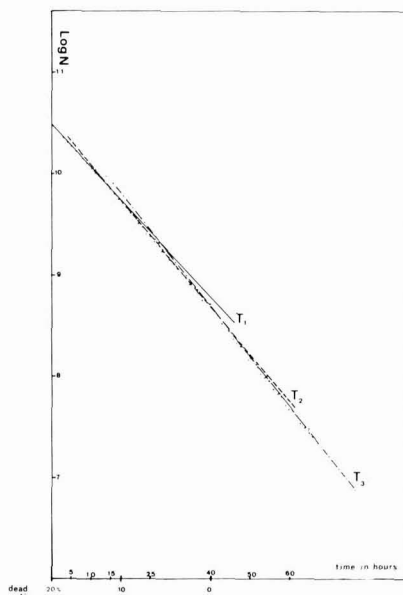


Fig. 2. Decreasing curve of the <sup>72</sup>Ga activity

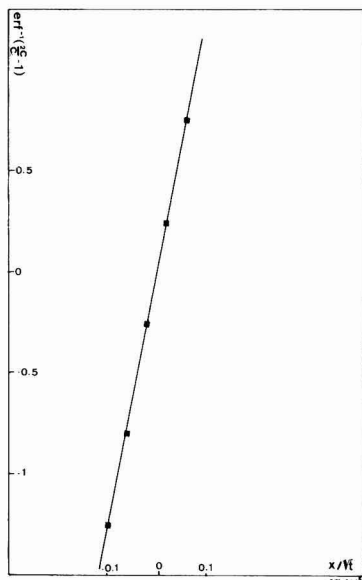


Fig. 3. Diffusion profile. Experimental data. Slope =  $34.68 = 1/2 \sqrt{D_L}$ ;  $T = 1219$  K.

solidification problems for which mass transport takes place partly by diffusion.

Table I. Correction due to the amount of dead time

Dead time	$\lambda$	Coefficient of determination	Apparent half-life (hr)
10-20%	0.0425	0.999	16.3
0-10%	0.0465	0.998	14.9
0	0.0491	1	14.1

### Acknowledgments

The authors are indebted to Dr. C. Potard for his advice about the shear-cell technique.

Manuscript submitted Jan. 26, 1981; revised manuscript received April 20, 1981.

Any discussion of this paper will appear in a Discussion Section to be published in the June 1982 JOURNAL. All discussions for the June 1982 Discussion Section should be submitted by Feb. 1, 1982.

Publication costs of this article were assisted by the Centre d'Etudes Nucleaires de Grenoble.

### REFERENCES

1. J. B. Edwards, E. E. Huckle, and J. J. Martin, *Met. Rev.*, **120**, Parts I and II (1968).
2. A. F. Witt, H. C. Gatos, M. Lichtensteiger, and J. C. Herman, *This Journal*, **125**, 1832 (1978).
3. H. Kodera, S. Iida, and S. Tauchi, *Jpn. J. Appl. Phys.*, **2**, 227 (1963).
4. J. J. Favier, *J. Cryst. Growth*, **49**, 373 (1980).
5. C. Potard, A. Teiller, and P. Dusserre, *Mater. Res. Bull.*, **7**, 583 (1972).
6. R. L. Schmidt and J. D. Verhoeven, *Trans. Met. Soc. AIME*, **239**, 148 (1967).

## A Mathematical Assessment of Chemical Diffusion Measurements in Transition Metal Oxides

François Morin\*

Institut de Recherche d'Hydro-Québec, Varennes, Québec, Canada J0L 2P0

### ABSTRACT

The relaxation method lends itself to the measurement of chemical diffusion coefficients in transition metal compounds. By means of various mathematical calculations, it is shown that the significance of experimental results can be greatly improved. A better insight into the interrelations between physical parameters like nonstoichiometry, defect mobility, and electrical conductivity should be gained by proper consideration of various experimental parameters. The effects of many parameters such as slow surface reaction, large departure from stoichiometry, and varying defect mobility, are reviewed. The electrical conductivity is perfectly equivalent to weight measurements when properly applied to relaxation experiments. Moreover, in some cases, it may contain some specific information regarding the interrelation between electronic and ionic defects.

Chemical diffusion in transition metal compounds is a common phenomenon. It has already been associated with various important physical processes like oxide growth and sintering of ceramics. There is also a renewal of interest in the search for new battery electrode materials. Various formalisms have already been developed in order to describe the basic mechanisms involved in the course of chemical diffusion (1-7), most of them largely based on C. Wagner's transport theory. Besides, most of our point defect theory originates

from Wagner and Schottky (8). Wagner *et al.* also applied the simple mass action law to point defects for several oxides (9-11). This last approach was considerably developed and also described with a convenient notation by Kröger and Vink (12-13). There are a few widely accepted examples, like CoO and Cu<sub>2</sub>O, where the diffusion and the point defect theories merge in a simple manner (14). Such a simple picture is also commonly transferred to other compounds.

Several controversial arguments were set forth in the recent years, regarding either coulombic interactions (15) or the prevalent existence of clustered de-

\* Electrochemical Society Active Member.  
Key words: defects, dielectrics, diffusion, kinetics.

fects (16-17) and nonrandom walk diffusion (18). In view of those complex considerations, the usual treatment of experimental data looks rather crude. Any comparison of experimental data with a more sophisticated theory would be faced with a crucial problem regarding the actual precision of those data. Thus, experimental diffusion phenomena would require a degree of accuracy that is neither intrinsically available for certain types of experiments nor has been completely evaluated in a peculiar experimental method.

The relaxation method might be one of the most suitable means for studying chemical diffusion with both a high precision and a simple procedure. The compound is first equilibrated with the outer atmosphere, whether pure oxygen or an oxidizing-reducing mixture. The compound must thus possess a nonnegligible electronic conductivity. The chemical activity of that atmosphere is suddenly changed from its original value to a different one and the evolution of the defect within the compound is normally recorded as a variation in weight or electrical conductivity *vs.* time. Dünwald and Wagner (19) also formulated the analytical solutions for various sample shapes such as plates, cylinders, and spheres. An equivalent solution has been described by Newman for brick-shaped samples (20). A few comprehensive reviews on the subject are available (21-23). The precision commonly reached with the relaxation method might suffice normally if the aim were simply to verify a largely accepted diffusion mechanism coupled with a very simple defect model. However, if one wants to make full use of this method, further consideration must be given to the various sources of error. Certain criteria have already been suggested by J. B. Wagner *et al.* (21, 23, 24) such as the equivalence between oxidation and reduction runs, the effect of graded sample sizes or diluted atmospheres for nonnegligible surface reactions, and also some preference for thermogravimetry instead of electrical conductivity. Such criteria deserve a complete mathematical analysis of all experimental parameters as has already been described (25). The basic simplicity of relaxation experiments is not an impairment of the significance of their results. Analysis of the relaxation method is considerably refined and more completely described here.

### The Relaxation Technique and Its Analytical Solution

The chemical diffusion coefficient  $\tilde{D}$  is unequivocally defined by Fick's first law

$$j_i = -\tilde{D} \cdot \frac{\partial c_i}{\partial x} \quad [1]$$

where  $c_i$  is the concentration of the chemical species, but can also sometimes be considered as a point defect concentration, and  $j_i$  is the flux of the same species. In the case of a transient concentration state, the preceding equation becomes, according to the mass conservation law

$$\frac{\partial c_i}{\partial t} = \frac{\partial}{\partial x} \left( \tilde{D} \cdot \frac{\partial c_i}{\partial x} \right) \quad [2]$$

which is equivalent to Fick's second law of diffusion.

If  $\tilde{D}$  is concentration independent, Eq. [2] then reads

$$\frac{\partial c_i}{\partial t} = \tilde{D} \cdot \frac{\partial^2 c_i}{\partial x^2} \quad [3]$$

The following set of time and boundary conditions fully describes the normally expected conditions for relaxation experiments

$$c_i(x, 0) = c_0 \quad \text{at } t = 0$$

$$c_i(0, t) = c_f \quad \text{at } t > 0$$

where  $c_0$  is the initial equilibrium concentration within the sample,  $c_f$  is the final equilibrium concentration,

and  $x$  is the length along the diffusion axis. Equation [3] can be extended to a three-dimensional case. According to Newman (20), the concentration  $c_i$  in a prism with overall dimensions equal to  $2a_1$ ,  $2a_2$ , and  $2a_3$  is expressed by the following relation

$$c_i(X, T) = c_0 \cdot f(X_1, T_1) \cdot f(X_2, T_2) \cdot f(X_3, T_3) \quad [4]$$

where

$$f(X, T) = \frac{2}{\pi} \sum_{n=0}^{\infty} \frac{(-1)^n}{n + \frac{1}{2}} \cdot \exp \{ -T(n + \frac{1}{2})^2 \pi^2 \} \cdot \cos \{ (n + \frac{1}{2}) \pi \cdot X \}$$

$$T = \frac{\tilde{D}t}{a^2}$$

$$X = x/a$$

The reduced coordinate  $X$  varies from zero to one while  $T$  varies from zero to infinity. The average concentration  $\bar{c}$  is a more readily accessible parameter than the local concentration  $c_i(X, T)$  so that

$$\bar{c} = c_f - (c_f - c_0) \int_0^1 \int_0^1 \int_0^1 f(X_1, T_1) \cdot f(X_2, T_2) \cdot f(X_3, T_3) \cdot dX_1 \cdot dX_2 \cdot dX_3 \quad [5]$$

Again,  $\bar{c}$  can be transformed to a dimensionless parameter

$$c_r = (c_f - \bar{c}) / (c_f - c_0) \quad [6]$$

By introducing Eq. [6] into Eq. [5] and integrating

$$c_r = g(T_1) \cdot g(T_2) \cdot g(T_3) \quad [7]$$

where

$$g(T) = \frac{2}{\pi^2} \sum_{n=0}^{\infty} \frac{1}{(n + \frac{1}{2})^2} \cdot \exp \{ -T \cdot (n + \frac{1}{2})^2 \cdot \pi^2 \}$$

For equilibration runs,  $c_r$  is usually interpreted in terms of weight or electrical conductivity variation *vs.* time. Therefore, both a relative weight  $W_r$  and a relative electrical conductivity have to be defined

$$\sigma_r = (\sigma_f - \bar{\sigma}) / (\sigma_f - \sigma_0) \quad [8]$$

$$W_r = (W_f - W) / (W_f - W_0) \quad [9]$$

In most cases,  $W_r$  can be shown to be strictly equivalent to  $c_r$ . But  $\sigma_r$  is identical to  $c_r$  only when a linear relationship between  $\sigma$  and  $c_i$  is obeyed and when the average conductivity is measured perpendicular to the diffusion axis. Any approximation of Eq. [7] or any actual departure from the ideal case should be assessed in comparison with that solution. A correction parameter,  $\Delta\tilde{D}/\tilde{D}$  is accordingly defined

$$(\Delta\tilde{D}/\tilde{D}) = (\tilde{D}_{\text{true}} - \tilde{D}_{\text{apparent}}) / \tilde{D}_{\text{apparent}} \quad [10]$$

so that

$$\tilde{D}_{\text{true}} = \tilde{D}_{\text{apparent}} [1 + (\Delta\tilde{D}/\tilde{D})]$$

The significance of  $\tilde{D}_{\text{true}}$  and  $\tilde{D}_{\text{apparent}}$  is two-fold. First, if all conditions are fulfilled for the exact application of Eq. [7],  $\tilde{D}_{\text{true}}$  is derived directly from that equation and  $\tilde{D}_{\text{apparent}}$  comes out from the approximations usually encountered with the same equation. Second, if any departure from the ideal relaxation case occurs,  $\tilde{D}_{\text{true}}$  is then derived from a more appropriate exact numerical solution. Then,  $\tilde{D}_{\text{apparent}}$  comes out from the normal analytical equation since that equation is often assumed to still correctly apply to the experimental case.



A Detailed Approach to Various Errors on  $\tilde{D}$

There are several potential error sources associated with the relaxation method. The precision of  $\tilde{D}$  and, consequently, its physical significance can be enhanced only if those error sources are properly identified and controlled. The most common ones are listed in Table I. Mathematical handling is straightforward for types one and two while numerical integration is required for the third type. It has been found convenient to illustrate each case numerically. Generally speaking,

values of  $\Delta\tilde{D}/\tilde{D}$  can be extrapolated readily up to about 10%. All errors do not add up necessarily, but the maximum uncertainty criterion may prove to be useful for type two. Not all the error sources mentioned in Table I lend themselves to a global statistical analysis based on the least squares fit. Some of those errors always behave in a systematic manner. Others would vary randomly from one relaxation run to another, but would systematically affect any single experiment.

The graphical representation of  $\tilde{D}$  vs.  $c_r$  bears much significance in finding potential error sources and also in evidencing unexpected phenomena.

Consequently, a normalized representation of  $\Delta\tilde{D}/\tilde{D}$  vs.  $c_r$  has been developed and is used throughout the present analysis.

**Mathematical approximations.**—The most common tendency when handling a large number of relaxation data within any single run, is to use a linearized graphical fit of these data and to measure the resulting slope. Equation [7] does not lend itself readily to that operation unless some approximation is made. In fact, the summation represented by  $g(T)$  rapidly reduces to its first term as  $c_r$  tends toward zero. Hence, a linear relationship between  $\ln c_r$  and  $T$  should work properly at low  $c_r$  values (19-21) and it also corresponds to the common practice. For the three-dimensional case

$$\tilde{D}t = \frac{\ln(512/\pi^6) - \ln(c_r)}{\frac{\pi^2}{4} \left( \frac{1}{a_1^2} + \frac{1}{a_2^2} + \frac{1}{a_3^2} \right)} \quad [11]$$

Analogous relationships can also be easily deduced for one- and two-dimensional processes. By comparing such equations with the reference analytical equation, one gets the results shown in Fig. 1. One-, two-, and three-dimensional approximations, such as in Eq. [11], are illustrated by means of specific examples. All corresponding curves were identified with their respective dimensional ratios. The worst approximation usually pertains to the three-dimensional equation. Under certain unfavorable geometrical conditions, Eq. [11] would even lose all of its original sense.

Another common approximation consists of neglecting either one or two diffusion axis out of the three possible ones. This is illustrated in Fig. 2. Equation

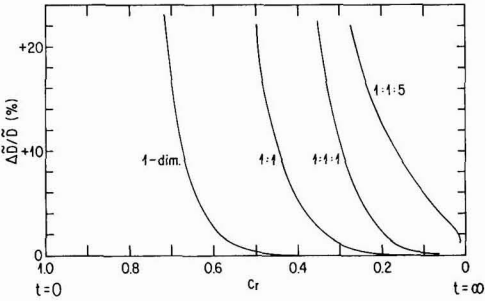


Fig. 1. Validity range for the use of a simple logarithmic relationship between  $c_r$  and  $T$ . One-, two-, and three-dimensional cases are considered.

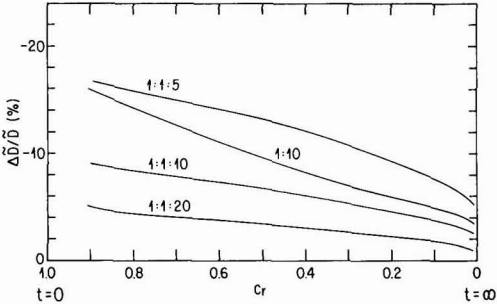


Fig. 2. Application of the full analytical equation, reduced to a two- or a one-dimensional diffusion process. The last figure, for any ratio, corresponds to the specifically neglected sample dimension.

[7] has been successively applied to the full and to the approximated sample geometries. The last figure appearing in any one ratio, corresponds actually to the neglected dimension. In contradistinction with Fig. 1, the correction factor  $\Delta\tilde{D}/\tilde{D}$  never completely disappears. Only for the most favorable cases does it remain within acceptable limits.

**Actual uncertainty on  $c_r$ .**—Most of the accuracy of  $\tilde{D}$  relies on a precise determination of  $c_r$  during the re-equilibration process. A crude estimate of the uncertainty of  $\tilde{D}$ , due to  $c_r$ , is a mathematical derivation of the reference equation and is shown in Fig. 3, mainly reflecting the mathematical behavior of Eq. [7]. Based on this behavior, it is often believed that the best pre-

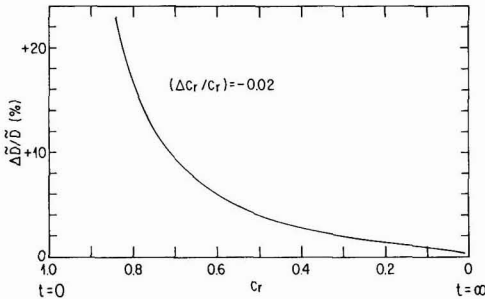


Fig. 3. Effect of the relative uncertainty  $\Delta c_r/c_r$  on the correction factor  $\Delta\tilde{D}/\tilde{D}$ , for a one-dimensional diffusion process.

Table I. Identification of most common error sources in relaxation experiments

Classification	Description
1. Mathematical approximations	Reduction to a two- or a one-dimensional diffusion process Reduction to a simple logarithmic equation
2. Experimental uncertainties	Uncertainties on $c_0$ , $c_r$ , and $\tilde{c}$ , respectively Uncertainties on time and dimensions Uncertainties on temperature and partial pressure
3. Nonanalytical conditions	Slow surface reaction Initial gas exchange period Large departure from stoichiometry; moving boundaries Concentration dependent mobility Temperature and pressure fluctuations during reequilibration

cision of  $\tilde{D}$  might be obtained for the lowest  $c_r$  values, i.e., the longest diffusion times. However, the overall uncertainty of  $c_r$  is normally not constant due to its definition given by Eq. [6]. In fact, the relative concentration  $c_r$  is the combination of three experimentally independent variables:  $c_0$ , the initial defect concentration,  $\bar{c}$ , the evolving average defect concentration and  $c_f$ , the final defect concentration. An optimum  $c_r$  range for the determination of  $\tilde{D}$  becomes evident when those three terms are dealt with separately as in Fig. 4. That range is more or less defined by the flattened portion of those three curves. It should vary somewhat from one experimental case to another but, roughly speaking, it will extend from about  $c_r = 0.55$  to  $c_r = 0.1$ . By averaging within such a region, the precision of  $\tilde{D}$  values will be increased.

**Other experimental parameters.**—In Eq. [7], the uncertainty of  $T$  is rather simply estimated more directly by considering  $\tilde{D}$ ,  $t$ , and  $a^2$  and adding the uncertainties for those terms together. A high degree of accuracy can be readily achieved on the measurement of time except for the absolute determination of the origin  $t = 0$  at the startup of the experiment. Mathematically speaking, that uncertainty is readily calculated. In practice, however, there is some risk that the lack of precision on  $t = 0$  be inadvertently used as a fitting parameter for the whole experimental curve. Slow pressure changes are more specifically dealt with later on. The expected uncertainty of  $\tilde{D}$  due to sample dimensions is very easily deduced for the simplest cases. For a one-dimensional diffusion process, it is equal to  $2(\Delta a/a)$ , and equal to  $6(\Delta a/a)$  for a perfectly cubic sample.  $\Delta a/a$  is the uncertainty on one single dimension. For any intermediate sample geometry,  $\Delta \tilde{D}/\tilde{D}$  would stand somewhere between the two former values.

Finally,  $\tilde{D}$  is also intrinsically influenced by temperature, and more occasionally, by partial pressure. With a perfect constancy of these two parameters during any single run, the uncertainty of  $\tilde{D}$  is limited to the lack of precision on temperature. It is rather insensitive to an exact absolute value of the partial pressure.

For example,  $\tilde{D}$  varies by about 0.9% for a 1°C variation in CoO at 1000°C. Much greater attention should be paid to the temperature or the partial pressure fluctuations during the course of a single reequilibration experiment;  $c_r$  is then appreciably affected through its experimentally fluctuating  $\bar{c}$  and  $c_f$  components. The surface concentration  $c_f$  is instantaneously modified

while  $\bar{c}$  is influenced more progressively. The true diffusion coefficient is only slightly affected compared

to the estimated  $\tilde{D}$ . That also explains why the usefulness of the experimental data become severely limited at  $c_r$  close to zero, i.e., at the largest values of  $t$ .

**Departure from the analytical solution.**—The third type of error, in Table I, is related to the occurrence of nonanalytical experimental conditions. Mathematical solutions for various specific sets of conditions can be developed by means of numerical analysis and, more precisely, with Crank-Nicholson's method (26). Little would normally be added to our present aims by dealing with two and three diffusion axes. Emphasis is placed on the one-dimensional process. Two- and three-dimensional diffusional processes are expected to behave in quite an analogous manner and this has been checked already for a few cases.

**Initial partial pressure modification.**—According to Eq. [7], the surface concentration must be abruptly modified at time  $t = 0$ , which is a condition difficult to achieve. The gas handling operation is a time-consuming process and slow surface reactions are also likely to occur. The use of pure oxygen appreciably simplifies the rapid establishment of new partial pressures, but limits the physically achievable partial pressure ranges. In many circumstances, gas mixtures must be employed, which implies either an additional gas flushing or gas sweeping operation. A specific example

is depicted in Fig. 5. The greatest effect on  $\Delta \tilde{D}/\tilde{D}$  appears immediately after emptying out the gas mixture. More explicitly, the value  $T = 0.0015$  is approximately equivalent to  $t = 10$  sec for a 1 mm thick CoO sample at 1000°C. For the quite common case where no flushing operation is used, the gas composition changes only very progressively, in a more or less logarithmic manner, even with a rapid switching between different mixtures. This process can be accelerated by faster sweep rates, but with an appreciable penalty on thermogravimetric measurement accuracy. Close attention to the initial partial pressure modification is especially important with faster reequilibrating compounds.

**Slow surface reaction.**—At the beginning of the relaxation process, the incoming defect flux in the first few layers of the solid sample is, theoretically, extremely large. The surface reaction may not be fast enough to accommodate such a flux, with the resultant occurrence of some deviation from the true surface equilibrium concentration. This departure from the ideal reequilibration process vanishes more or less rapidly as the relaxation process goes on, but the actual

determination of  $\tilde{D}$  remains affected for longer times. In the following somewhat simplified model, the surface reaction rate is assumed to be proportional to the surface concentration departure from equilibrium

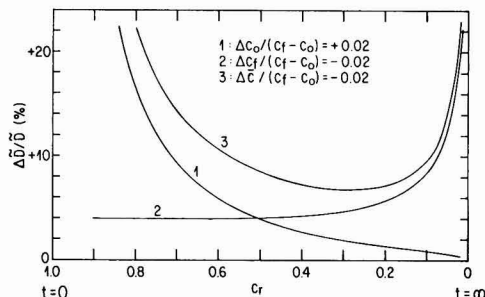


Fig. 4. Reconsideration of the uncertainty on  $c_r$  in view of its experimental components  $c_0$ ,  $c_f$ , and  $\bar{c}$  for a one-dimensional diffusion process.

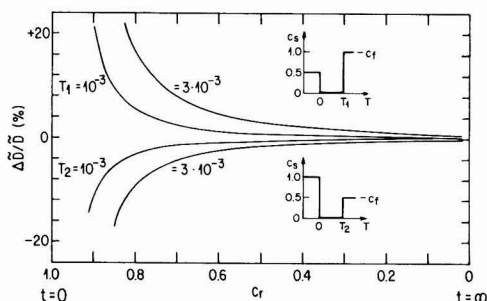


Fig. 5. Effect of a gas emptying operation for two distinct cases.  $c_s$  is the instantaneous surface concentration.

with the outer atmosphere. Hence

$$j(0, t) = A\{c_1(0, t) - c_r\} \quad [12]$$

By combining with Fick's first equation

$$\left(\frac{\partial c_1}{\partial x}\right)_{x=0} = B \cdot \{c_1(0, t) - c_r\} \quad [13a]$$

where  $C$  is defined as  $(c_1 - c_0)/(c_r - c_0)$ . Consequently

$$\left(\frac{\partial C}{\partial x}\right)_{x=0} = B\{1 - C(0, t)\} \quad [13b]$$

where  $j_1(0, t)$  is the flux at the gas-solid interface,  $A$  is a constant specific to the gas mixture, and  $B$  is equal to  $(A \cdot a/\tilde{D})$ . Equation [12] is analogous to the drying process already discussed by Newman (27) and the wustite surface reaction model used by Landler and Komarek (28) for a combined surface and volume rate-limited process. Other models have also been described and discussed at some length (29-31). But the main purpose of the present approach is to quantify the effect of a surface rate-limited reaction on the determination of  $\tilde{D}$  rather than identifying the exact surface mechanism responsible for that rate-limiting action. Equation [13b] has been introduced as a boundary condition for the numerical integration of Fick's second

law. The results for  $\Delta\tilde{D}/\tilde{D}$  are shown in Fig. 6. To scale up the phenomenon, various values were attributed to  $B$ , e.g.,  $B = 25$  leads to a limiting surface flux equal to the flux that would be theoretically observed at  $c_r = 0.976$  in the absence of a slow surface reaction. Since the individual curves uniquely depend on the magnitude of  $B$ , the present numerical solution is concentration independent. In contradistinction to Fig. 5, and to the error on the estimation of time at  $t = 0$ , there is a largely persistent effect of the surface reaction on  $\tilde{D}_{\text{apparent}}$ , even at very low  $c_r$  values.

Oxidizing-reducing mixtures like  $\text{H}_2/\text{H}_2\text{O}$  and  $\text{CO}/\text{CO}_2$  are quite susceptible to the kind of phenomenon presently discussed. Experimental results on wustite have been discussed at some length by J. B. Wagner *et al.* (24). Even pure oxygen should theoretically not be overlooked for a partly surface rate-limiting action.

**Large stoichiometric variations.**—Several compounds like  $\text{FeO}$ ,  $\text{MnO}$ , and  $\text{UO}_2$  exhibit large departures from stoichiometry. Large concentration variations have often been applied to those compounds for relaxation experiments. On fundamental grounds, the effect of a large stoichiometric variation within any single relaxation experiment is two-fold: (i) the outer crystal surface cannot be considered any more as a fixed boundary, in the case of a mobile cationic sublattice;

and (ii) there should be a stress-induced effect due to the concentration gradient. Case one must be numerically integrated. The apparent value of  $\sigma_r$  (see Eq. [8]), i.e., its value obtained without correcting the initial sample dimensions for the continuously advancing boundaries, departs from the actual value of  $\sigma_r$  or, else,  $c_r$ . It can be shown that

$$c_r = 1 - (a/a_f)[1 - (\sigma_r)_{\text{app}}] \quad [14]$$

where  $a$  is the instantaneous sample dimension and  $a_f$ , the final one. Weight and apparent conductivity variations vary in exactly the same way, so that a strictly equivalent equation also holds for  $W_r$ . The correction to be brought vs.  $c_r$ , to compensate for the departure from the true  $\tilde{D}$  value, is shown in Fig. 7. The other effect, concerning internal stresses in the course of diffusion, has been theoretically discussed at some length elsewhere (32-33). Practically speaking, there is no absolute need for large stoichiometric variations except for more sensitivity in a few thermogravimetric experimental procedures.

**Concentration-dependent diffusion coefficient.**—The eventual defect mobility variation, which has sometimes been reported for transition metal compounds (22, 34), is a rather controversial problem. That phenomenon is likely to be accompanied by either a change in the defect nature or by defect interactions. Taking

into account the sole effect of  $\tilde{D}$  variation and numerically integrating Fick's second law lead to the results shown in Fig. 8. In that solution,  $\tilde{D} = f(c_1)$  was defined as follows

$$\tilde{D}(c_1) = \tilde{D}_{\text{min}} + (\tilde{D}_{\text{max}} - \tilde{D}_{\text{min}}) \cdot (c_1/c_{\text{max}}) \quad [15]$$

Because  $\tilde{D}$  is concentration dependent and should likewise vary continuously during the course of the re-

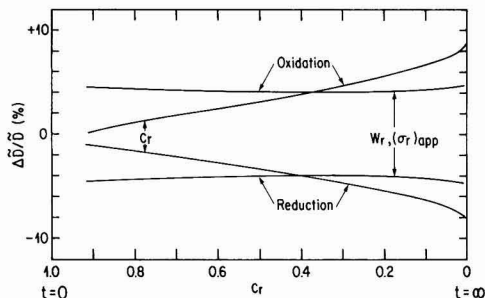


Fig. 7. Description of a large departure from stoichiometry in  $\text{MeO}_{1+y}$ . Here,  $y$  varies between 0 and 0.05.

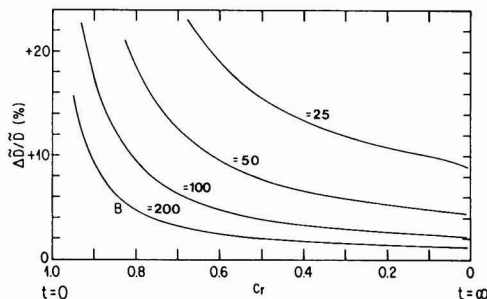


Fig. 6. Effect of a slow surface reaction on  $\Delta\tilde{D}/\tilde{D}$ .  $B$  is used here as a scaling parameter and it is proportional to the surface reaction rate constant.

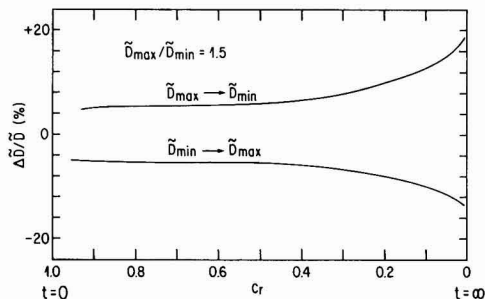


Fig. 8. Study of a chemical diffusion coefficient linearly dependent on concentration.

laxation process,  $\tilde{D}_{\text{true}}$  is arbitrarily taken as equal to its arithmetic mean,  $(\tilde{D}_{\text{max}} + \tilde{D}_{\text{min}})/2$ . Whenever the correction factor  $\Delta\tilde{D}/\tilde{D}$  is applied to the analytically calculated  $\tilde{D}$  values, the corrected  $\tilde{D}$  value becomes identical to the preceding arithmetic mean. From Fig. 8, the analytical  $\tilde{D}$  values should be slightly biased either positively or negatively depending on reequilibration being an oxidation or a reduction process. The expected analytical deviation during the course of a single experiment is somewhat smothered both by the actual diffusion process and by the use of the arithmetical average on  $\tilde{D}$ . A true  $\tilde{D}$  variation vs. concentration would consequently be more easily detected by several small successive concentration changes over a desired range, instead of a single large concentration variation.

### Thermogravimetric and Electrical Conductivity Measurements

One last and major point of interest in relaxation experiments is the physical means used in measuring the concentration evolution within the sample. Weight and electrical conductivity are the most suitable and the most widely used physical properties. The preference for either of these must be discussed on its respective merits. Theoretically speaking, one major advantage in using weight is that it always relates more directly to a chemical component activity than conductivity would, in agreement with a perfectly general thermodynamical formulation of diffusion. However, structural interpretation of defects is usually done currently, hence invalidating the preceding argument. Experimentally speaking, thermal noise, simple buoyancy, and gas flow effect limit the useful sensitivity of weight measurements. These factors can be quite well controlled in carefully designed experiments. An additional difficulty may come from the initial gas handling procedure associated with a rapid weight variation. The accuracy of thermogravimetric measurements depends on the magnitude of the absolute concentration change. Weight variations are thus easily recorded for large stoichiometric changes but at the same time, they become rather less sensitive at low defect concentrations.

For the counterpart, electrical measurements can intrinsically be made very precise so that their accuracy is usually limited by external factors like temperature and partial pressure control. The relative error made in conductivity measurements being generally constant, makes them very suitable for extended defect concentration ranges. The electrical conductivity is related to  $c_e$ , the free electron concentration or else the electron hole concentration in the following way

$$\sigma = \mu_e \cdot q_e \cdot c_e \quad [16]$$

where  $\mu_e$  is the electron mobility,  $q_e$  is the elementary charge, and the mobility  $\mu_e$  is normally considered to be constant. The mobility is quite often temperature dependent, but to a much lesser degree than the departure from stoichiometry. Four different conductivity types have been accordingly distinguished in Table II. The first two types, showing a linear relationship between electronic and ionic defects, are readily compatible with relaxation experiments. Type IV is the main exception to the use of electrical conductivity measurements. The conditions for types I and II do not need to be strictly obeyed to be used for relaxation experiments because the electrical conductivity is intimately related to defect concentration and to defect nature. In fact,  $\sigma$  only needs to be unequivocally related to the departure from stoichiometry. The effect of an eventual nonlinear relationship between  $\sigma_r$  and  $c_r$  can be readily evaluated by numerical integration of

Table II. Electrical conductivity in nonstoichiometric compounds in relation to the relaxation method

Conductivity type	Example	Ref.
I. Electrical conductivity is directly proportional to departure from stoichiometry; electronic mobility is temperature dependent	CoO	(36)
II. Electrical conductivity is directly proportional to departure from stoichiometry; electronic mobility is temperature independent	MnS	(36)
III. Electrical conductivity is dependent on nonstoichiometry; a mixed defect state prevails for a certain oxygen activity range.	MnO	(37)
IV. Electrical conductivity is identified with metallic conduction; it is independent of nonstoichiometry	NbO	(38)

that relationship. A power law between equilibrium values of  $\sigma$  and  $c_i$  is taken here as an example

$$\sigma = \text{constant} \cdot c_i^r \quad [17]$$

In this type of equation,  $c_i$  is normally dealt with as a defect concentration. The present treatment partly resembles that described by Campbell and O'Keefe (35), and  $r$  can either be thought of as an arbitrary exponent or it can be deduced from already existing experimental data on  $\sigma$  and  $c_i$ . For example,  $r = 3/4$  may also be interpreted in terms of  $n_g$  equal to 4 and  $n_x$  equal to 3. One other example is that of  $r$  equal to 0.5. Again, that may also correspond to  $n_g = 8$  and  $n_x = 4$  in  $\text{Me}_2\text{O}$ . Typical calculations, reported in Fig. 9 and 10, have been performed for various  $r$  and  $c_i/c_o$  ratios. Oxidation and reduction processes are identified by  $c_i/c_o$  greater or smaller than unity, respectively. These results can also be summarized as follows:

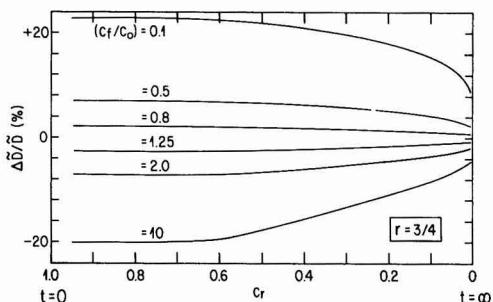


Fig. 9. Nonlinear dependency between electrical conductivity and concentration. The effect is shown for various concentration ratios, during both oxidation and reduction runs.

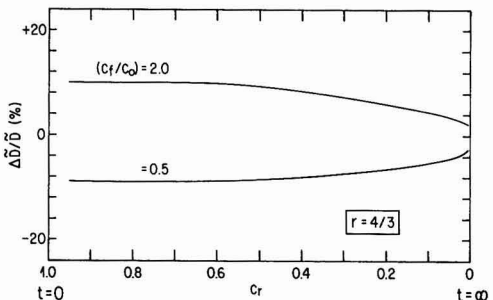


Fig. 10. Nonlinear dependency between electrical conductivity and concentration. Effect of an inverted power law coefficient on the correction factor  $\Delta\tilde{D}/\tilde{D}$ .

1. The effect on  $\Delta\tilde{D}/\tilde{D}$  is most important during about the first half of the relaxation run; it diminishes asymptotically at the very end of the experiment.

2. The greater the departure of  $r$  from unity, the greater the correction factor  $\Delta\tilde{D}/\tilde{D}$ ;  $\Delta\tilde{D}/\tilde{D}$  reverses sign when  $r$  goes from  $r < 1$  to  $r > 1$ .

3.  $\Delta\tilde{D}/\tilde{D}$  increases with increasing  $c_i/c_0$  departure from unity; that effect is symmetrical for low enough  $\Delta\tilde{D}/\tilde{D}$  values.

4. The nonlinearity effect on  $\tilde{D}$  tends to become negligible as  $r$  or  $c_i/c_0$  tend toward unity.

Other empirical relationships between  $\sigma$  and  $c_i$  have also been tested. The observations are quite analogous to those previously formulated. Therefore, the  $\Delta\tilde{D}/\tilde{D}$  behavior is not specifically tied to a peculiar relationship, but is generally dependent on (i) the degree of curvature between  $\sigma$  and  $c_i$ , combined with the magnitude of the concentration change and on (ii) the absolute sign of that curvature.

Finally, Fig. 11 is an exact representation of the most generally accepted defect model in cuprous oxide. Neutral cation vacancies are assumed to be the major defects and electrical conduction would come from the simultaneous and minor existence of electron holes and singly ionized cation vacancies (14). The present calculations provide the guidelines for correcting eventual relaxation experiments in  $\text{Cu}_2\text{O}$  or for probing the actual existence of the preceding model.

In brief, the effect of a nonlinear relationship between  $\sigma$  and  $c_i$  is predictable. The calculations involved in that process can either be used to correct diffusion coefficient measurements or, inversely, to detect the existence of a nonlinear relationship between those two fundamental parameters.

**Electrode configuration.**—The electric conductivity technique should normally be quite attractive. Nonetheless, there is a very common source of discrepancies which is directly related to the electrode configuration. For relaxation experiments, there should be two basic types of electrode configuration as illustrated in Fig. 12. According to type a, the electric current is perfectly parallel to the diffusion axis through the whole sample. Hence, the average conductivity is related to the average defect concentration by the following equation

$$\bar{\rho} = \text{constant} \cdot \int_0^a (1/c_i) \cdot dx \quad [18a]$$

or, since  $\bar{\sigma} = 1/\bar{\rho}$

$$\bar{\sigma} = \text{constant} / \int_0^a (1/c_i) \cdot dx \quad [18b]$$

where  $\bar{\rho}$  is the average sample resistivity. The electrode is simultaneously assumed to be perfectly porous and

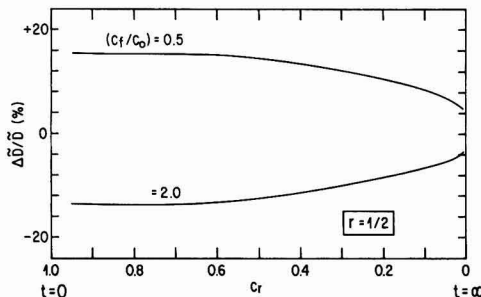


Fig. 11. Characterization of the cuprous oxide model behavior during relaxation runs with electrical conductivity.

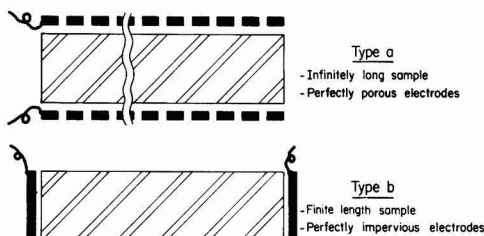


Fig. 12. Idealized electrode arrangements for relaxation runs

perfectly conducting. In type b, the current flow is strictly perpendicular to the diffusion axis and the electrodes are assumed to be completely impervious to diffusion. Hence

$$\bar{\sigma} = \text{constant} \cdot \int_0^a c_i \cdot dx \quad [19a]$$

or

$$\bar{\sigma} = \text{constant} \cdot \bar{c} \quad [19b]$$

The two preceding sets of equations represent a perfectly linear relationship between  $\sigma$  and  $c_i$ . The difference between Eq. [18b] and [19a] is obvious. Thus, directly substituting  $c_r$  for  $\sigma_r$  would lead to erroneous results in the first case. Regarding type a configuration, the assumption that the electrode layer is perfectly porous is hardly feasible. Type b is to be preferred. The use of electric conductivity measurements would thus be limited to one- and two-dimensional processes. Any intermediate configuration would lead to a nonohmic interpretation of the measurements. Wrapping the diffusion samples with electrode wires at a finite length from one another is one such case. It leads to at least partially incorrect results unless a full specific mathematical treatment is allowed for it. Such a treatment would be rather lengthy and cumbersome. The electrode configuration suggested here is simpler and more reliable.

### Final Comments

The relaxation method has been discussed here from the experimentalist's point of view. All calculations were based on a very few fundamental equations or else on very simple assumptions. These calculations were developed to let the relaxation method gain more potential regarding the study of defect diffusion and point defect behavior in transition metal compounds. The actual significance of  $\tilde{D}$  has not been discussed outside its basic definition given by Eq. [1]. That would naturally be the next important step in discussing present diffusion theories.

A graphical representation of  $\tilde{D}$  vs.  $c_i$  is suggested to give a better statistical weight to all data during any single experiment and to make use of all the information contained within any data set. Several numerical examples have been worked out in order to obtain more specific ideas about the actual effects of the most common error sources. Those examples were mostly done in dimensionless parameters so that they might be transferred to the practical design or assessment of experiment. Moreover, an optimum range for  $c_r$  that would lead to more accurate  $\tilde{D}$  values has been indicated.

The electrical conductivity measurements applied to the reequilibration method were thoroughly discussed. As long as there is a nonstoichiometric dependency of electrical conductivity, this measurement technique appears to be useful for all defect concentration ranges. Large concentration changes should generally be avoided. Nevertheless, the electrical conductivity may then, on the base of preceding calculations, be a useful

means of detecting some eventual nonlinear relationship between  $\sigma$  and  $c_i$ .

Finally, experimental papers on the relaxation method are still very representatively described by Childs *et al.* (23). Quite surprisingly, there is only a limited number of works in the field and there is ample room for further experimental development. The most useful aspect of the present mathematical analysis is in redesigning relaxation experiments so that not only more precise and reproducible data are made available, but also the experimental observations keep in pace with the constantly developing defect theory. In that sense, relaxation experiments have been performed recently on CoO and they are reported extensively elsewhere (39). Not only do we observe a clear tendency for  $\tilde{D}_{CoO}$  to vary with the oxygen activity but any discrepancy with previous assumptions on  $\tilde{D}_{CoO}$  is explained by the present analysis.

Manuscript submitted Dec. 18, 1980; revised manuscript received May 15, 1981. This was Paper 357 presented at the Hollywood, Florida, Meeting of the Society, Oct. 5-10, 1980.

Any discussion of this paper will appear in a Discussion Section to be published in the June 1982 JOURNAL. All discussions for the June 1982 Discussion Section should be submitted by Feb. 1, 1982.

Publication costs of this article were assisted by the Institut de Recherche d'Hydro-Québec.

#### REFERENCES

1. C. Wagner, *Z. Phys. Chem., Teil B*, **11**, 139 (1930).
2. C. Wagner, *ibid.*, **21**, 25 (1933).
3. C. Wagner, *ibid.*, **32**, 447 (1936).
4. L. S. Darken, *Trans. AIME*, **175**, 184 (1948).
5. C. Wagner, *Adv. Electrochem. Electrochem. Eng.*, **4**, 1 (1966).
6. D. E. Coates and A. D. Dalvi, *Oxid. Met.*, **2**, 331 (1970).
7. W. Weppner and R. A. Huggins, *This Journal*, **124**, 1569 (1977).
8. W. Schottky and C. Wagner, *Z. Phys. Chem., Teil B*, **11**, 163 (1930).
9. H. Dünwald and C. Wagner, *ibid.*, **22**, 212 (1933).
10. H. V. Baumbach and C. Wagner, *ibid.*, **24**, 59 (1934).
11. C. Wagner and H. Hammen, *ibid.*, **40**, 197 (1938).
12. F. A. Kröger and H. J. Vink, *Solid State Phys.*, **3**, 307 (1956).
13. F. A. Kröger, "The Chemistry of Imperfect Crystals," p. 313, North-Holland Publishing Co., Amsterdam (1966).
14. P. Kofstad, "Nonstoichiometry, Diffusion, and Electrical Conductivity in Binary Metal Oxides," pp. 138, 328 ff., Wiley-Interscience, New York (1972).
15. C. Wagner, *Prog. Solid State Chem.*, **10**, 3 (1975).
16. M. S. Seltzer and R. I. Jaffee, Editors, "Defects and Transport in Oxides," Battelle Institute Materials Science Colloquia, Columbus (1973), Published by Plenum Press, New York (1974).
17. C. R. A. Catlow, W. C. Mackrodt, M. J. Norgett, and A. M. Stoneham, *Philos. Mag. A*, **40**, 161 (1979).
18. R. A. McKee, *Phys. Rev. B*, **21**, 4269 (1980).
19. H. Dünwald and C. Wagner, *Z. Phys. Chem., Teil B*, **24**, 53 (1934).
20. A. B. Newman, *Trans. AICHE*, **27**, 310 (1931).
21. J. B. Wagner, in "Mass Transport in Oxides," NBS Special Publication No. 296, p. 65, Washington, DC (1968).
22. P. E. Childs and J. B. Wagner, in "Heterogeneous Kinetics at Elevated Temperatures," G. R. Belton and W. L. Worrell, Editors, pp. 269-342, Plenum Press, New York (1970).
23. P. E. Childs, L. W. Laub, and J. B. Wagner, *Proc. Br. Ceram. Soc.*, **19**, 29 (1971).
24. L. W. Laub and J. B. Wagner, *Oxid. Met.*, **7**, 1 (1973).
25. F. Morin, *Can. Met. Quart.*, **14**, 97 (1975).
26. J. Crank, "Mathematics of Diffusion," p. 186, Clarendon Press, Oxford (1956).
27. A. B. Newman, *Trans. AICHE*, **27**, 203 (1931).
28. P. F. J. Landler and K. L. Komarek, *Trans. AIME*, **236**, 138 (1966).
29. S. Stotz, *Ber. Bunsenges. Phys. Chem.*, **70**, 769 (1966).
30. C. Wagner, *ibid.*, **70**, 775 (1966).
31. H. J. Grabke, K. J. Best, and A. Gala, *Werkst. Korros.*, **21**, 911 (1970).
32. J. C. M. Li, R. A. Oriani, and L. S. Darken, *Z. Phys. Chem.*, **49**, 271 (1966).
33. R. H. Campbell, Ph.D. Thesis, Arizona State University (1969).
34. F. Morin, *Can. Met. Quart.*, **14**, 105 (1975).
35. R. H. Campbell, W. J. Kass, and M. O'Keeffe, in "Mass Transport in Oxides," NBS Special Publication No. 296, p. 173, Washington, DC (1968).
36. J. P. Delmaire and H. LeBrusq, *C.R. Acad. Sci. Paris, Series C*, **284**, 635 (1977).
37. J. P. Bocquet, M. Kawahara, and P. Lacombe, *C.R. Acad. Sci. Paris*, **265**, 1318 (1967).
38. J. A. Roberson and R. A. Rapp, *J. Phys. Chem. Solids*, **30**, 1119 (1969).
39. F. Morin and R. Dieckmann, Paper submitted to *Z. Phys. Chem.*



# Comparison Between C.V.T. of Titanium Diboride by Different Transport Agents: Experimental Results and Application of Two Thermodynamic Models

C. Bernard\*

Laboratoire de Thermodynamique et Physico-Chimie Métallurgiques,  
E.N.S.E.E.G., B.P. 44, 38401 Saint Martin d'Heres, France

and G. Constant\* and R. Feurer

Laboratoire de Chimie Minérale et Cristallographie,  
E.N.S.C.T., 118, Route de Narbonne, 31077 Toulouse, Cedex, France

## ABSTRACT

In order to explain the differences experimentally observed in the chemical vapor transport of titanium diboride by various transporting agents we have used thermodynamics to model the process. Two different calculating methods have been undertaken. The first one is based upon the consideration of the transport process as two successive thermodynamic equilibria whose chemical compositions have been obtained by minimization of the Helmholtz free energy. The second one refers to the Richardson and Nöläng model and accounts for the mass transport by calculating the flux functions of the vapor phase constituents. The comparison between experiments and results of each calculating method shows that the two models give fuller information, contribute to a satisfactory explanation of the experiments, and allow one to choose available transporting agents.

In order to grow titanium diboride single crystals of a relatively large size (about a few millimeters), we have undertaken a set of chemical vapor transport experiments in sealed tubes using a great variety of transport agents:<sup>1</sup> halogens, hydrogen halides, titanium and boron halides, tellurium tetrachloride. While doing these long-lasting experiments we could reveal very different behaviors for each transport agent (1, 2). This is the set of results we use to test predictive models based upon thermodynamic considerations. Two different types of approaches are tested in this way. As both use the minimization of a thermodynamic function of the system, their simultaneous implementation is very easy. The comparative study of their respective pros and cons points out how pertinent a simultaneous use of both models is in predicting the transport phenomenon in closed tubes.

## Experimental

Experiments have been carried out in silica sealed tubes (6 mm diam 100 mm long, and 12 mm diam 100 mm long). The starting materials are industrial titanium diboride powder (> 99%), halogen, and halides. The quantities are about 300 mg of  $\text{TiB}_2$  (an excess) and  $6 \times 10^{-4}$  mol of t.a. per 10  $\text{cm}^3$ . The tube is air evacuated to  $10^{-5}$  Torr for 6 hr then sealed under low pressure transport agent. The ampuls are heated by electric horizontal furnaces in temperature gradient of 10 deg.  $\text{cm}^{-1}$  for one month.

Experiments have been carried out for nine transport agents and transport was observed except in the case of  $\text{TiI}_4$ . The transport occurs from the cold to the hot end of the tube with some t.a., from the hot to the cold end with the others. Table I gives the experimental observations with an average evaluation of the amount transported in each case.

Chemical analyses have been made by spectrophotometric measurements on the transported crystals.

\* Electrochemical Society Active Member.

Key words: chemical vapor transport, flux function, thermodynamic model, titanium diboride, transport agent.

<sup>1</sup> t.a. in the following text.

They show a variation in the boron-titanium ratio when changing the transport agent.

After cooling of the ampul, in most cases the tube was unpolished showing an etching of silica at the source end. Gaseous or liquid halides remain on the tube and except in the case of tellurium halides no solid compound other than  $\text{TiB}_2$  appears at the sink end.

## First Thermodynamic Model: Equilibria in Closed Tubes

The model consists in decomposing the transport process into two successive equilibria. The first one is at the source end of the tube at temperature  $T_1$  taking into account the powdery titanium diboride, the transport agent, and the silica of the tube. The composition of this system at equilibrium is determined by minimization of the Helmholtz free energy.<sup>2</sup> The gas phase of this equilibrium causes the transport.

The second equilibrium system consists of the gas phase taken at the sink end of the tube together with silica at  $T_2$  temperature. A second minimization of the Helmholtz free energy gives the composition of the sink system at equilibrium.

<sup>2</sup> The computer program used for the minimization is a slightly modified version of the one used for the minimization of the Gibbs free energy (3).

Table I. Data and results for  $\text{TiB}_2$  transported from  $T_1$  to  $T_2$

t.a.	$T_1$ (K)	$T_2$ (K)	$\text{TiB}_2$ transported (mg/month)
$T_1$ $\text{I}_2$	1125	1225	50
$\wedge$ $\text{Br}_2$	1050	1200	50
$\wedge$ $\text{HCl}$	1075	1225	10
$T_2$ $\text{TeCl}_4$	1255	1125	150
$\wedge$ $\text{TeBr}_4$	1255	1125	150
$\wedge$ $\text{BBr}_3$	1235	1105	150
$\wedge$ $\text{Cl}_2$	1270	1125	20
$T_2$ $\text{TiBr}_4$	1320	1270	10
$\text{TiCl}_4$	1300	1190	0

Such systems are of great complexity because of the number of chemical reactions which are feasible between halogen, titanium, boron, silicon, and oxygen but the number of constituents is not limited in the calculation method. The only limit is the knowledge of the thermodynamic values of all the compounds. All the values used in the calculations are reported at the end of the text in the Appendix.

The Helmholtz free energy is minimized; that is, the very one which falls to a minimum at equilibrium in a sealed tube (under constant  $V$  and  $T$ ). Let us consider a system involving  $\Gamma$  phases, each phase itself involving  $N_\gamma$  constituents. The Helmholtz free energy is

$$F = G - PV$$

after the Euler's theorem

$$G = \sum_{i=1}^{N_\gamma} n_i \bar{G}_i$$

with  $\bar{G}_i = \left( \frac{\partial G}{\partial n_i} \right)_{P,T} = \mu_{i\gamma}^0 + RT \ln P_i$  (for one gaseous species for example

$$\frac{F}{RT} = \sum_{\gamma=1}^{\Gamma} \sum_{i=1}^{N_\gamma} n_{i\gamma} \left[ \frac{\mu_{i\gamma}^0}{RT} + \phi_\gamma \ln P_i + (1 - \phi_\gamma) \ln a_{i\gamma} \right] - \frac{1}{RT} \sum_{\gamma=1}^{\Gamma} \sum_{i=1}^{N_\gamma} \phi_\gamma n_{i\gamma} RT$$

$$\frac{F}{RT} = \sum_{\gamma=1}^{\Gamma} \sum_{i=1}^{N_\gamma} n_{i\gamma} \left[ \frac{\mu_{i\gamma}^0}{RT} + \phi_\gamma \left( \ln \frac{RT}{V} + \ln n_{i\gamma} - 1 \right) + (1 - \phi_\gamma) \ln a_{i\gamma} \right]$$

with  $n_{i\gamma}$  = mols of the  $i$ th species in  $\gamma$ th phase;  $\mu_{i\gamma}^0$  = standard chemical potential of the  $i$ th species in the  $\gamma$ th phase;  $\phi_\gamma = 1$  if a gaseous phase;  $\phi_\gamma = 0$  if nongaseous phase;  $a_{i\gamma}$  = activity of the  $i$ th species in the  $\gamma$ th nongaseous phase; and  $V$  = volume of the tube.

The nongaseous phases are assumed to be pure, their activity is taken equal to 1, and the chemical potential gradients are contingent on the temperature. The gaseous compounds are assumed to follow the ideal gas law.

The compositions of the two equilibria have been calculated for the following conditions: temperature gradient 1200-1300 K (or vice versa), transport agent  $6 \times 10^{-4}$  mol, volume of the tube 10 cm<sup>3</sup> and with five series of transport agents: (i) halogen Cl<sub>2</sub>, Br<sub>2</sub>, I<sub>2</sub>; (ii) hydrogen halides HCl, HBr; (iii) tellurium halides TeCl<sub>4</sub>; (iv) titanium halides TiCl<sub>4</sub>, TiBr<sub>4</sub>, TiI<sub>4</sub>; (v) boron halides BCl<sub>3</sub>, BBr<sub>3</sub>, BI<sub>3</sub>.

The set of calculations provides a number of indications. The whole set of numerical results gives too many tables, so we have limited the presentation to one series of transporting agents, the boron halides for example (Table II). This table shows the complexity of the vapor phase and the non-negligible role of silica; as to the presence of titanium diboride at the sink it means the suitability of the chosen temperature gradient (if the gradient is not in the good direction we do not obtain TiB<sub>2</sub> at the sink).

In the order to determine the amount of TiB<sub>2</sub> expected at the sink when the equilibrium state has been reached, we have reported in Table III the calculated values which indicate the tendency of the system to transport TiB<sub>2</sub>, together with experimental results when obtained. The poor agreement between the two sets of results is obvious. So, while TiCl<sub>4</sub> is

Table II. Compositions in mols of source and sink equilibria by minimization of the Helmholtz free energy for BCl<sub>3</sub>, BBr<sub>3</sub>, and BI<sub>3</sub> as transport agents

Source 1<TiB <sub>2</sub> > + 1<SiO <sub>2</sub> > + 60.10 <sup>-4</sup> Bx <sub>3</sub> T <sub>1</sub> = 1300 K (mol)			Sink Gas phase of the 1 <sup>st</sup> equilibrium + 1<SiO <sub>2</sub> > T <sub>2</sub> = 1200 K (mol)		
BCl <sub>3</sub>					
TiCl <sub>4</sub>	1.77	× 10 <sup>-6</sup>	TiCl <sub>4</sub>	6.9	× 10 <sup>-7</sup>
TiCl <sub>3</sub>	1.4	× 10 <sup>-7</sup>	TiCl <sub>3</sub>	3	× 10 <sup>-8</sup>
BCl <sub>3</sub>	2.2791	× 10 <sup>-4</sup>	BCl <sub>3</sub>	2.0082	× 10 <sup>-4</sup>
BCl <sub>2</sub>	3	× 10 <sup>-8</sup>	SiCl <sub>4</sub>	2.9327	× 10 <sup>-4</sup>
BClO	3	× 10 <sup>-8</sup>	SiCl <sub>3</sub>	7.11	× 10 <sup>-8</sup>
SiCl <sub>4</sub>	2.6630	× 10 <sup>-4</sup>	SiCl <sub>3</sub>	1.3	× 10 <sup>-7</sup>
SiCl <sub>3</sub>	1.815	× 10 <sup>-8</sup>	<SiO <sub>2</sub> >	9.9998144	× 10 <sup>-1</sup>
SiCl <sub>2</sub>	5.0	× 10 <sup>-7</sup>	<B <sub>2</sub> O <sub>3</sub> >	1.238	× 10 <sup>-8</sup>
<TiB <sub>2</sub> >	9.9999805	× 10 <sup>-1</sup>	<TiB <sub>2</sub> >	1.19	× 10 <sup>-8</sup>
<SiO <sub>2</sub> >	9.9971803	× 10 <sup>-1</sup>			
<B <sub>2</sub> O <sub>3</sub> >	1.8796	× 10 <sup>-4</sup>			
P = 5.46 atm			P = 4.95 atm		
Source T <sub>1</sub> = 1300 K (mol)			Sink T <sub>2</sub> = 1200 K (mol)		
BBr <sub>3</sub>					
Br	2	× 10 <sup>-8</sup>	Br	1	× 10 <sup>-8</sup>
TiBr <sub>4</sub>	4.3	× 10 <sup>-7</sup>	TiBr <sub>4</sub>	3.7	× 10 <sup>-7</sup>
TiBr <sub>3</sub>	6	× 10 <sup>-8</sup>	TiBr <sub>3</sub>	3	× 10 <sup>-8</sup>
BBr <sub>3</sub>	6.362	× 10 <sup>-8</sup>	BBr <sub>3</sub>	4.790	× 10 <sup>-8</sup>
BBrO	2	× 10 <sup>-8</sup>	BBr <sub>2</sub>	1	× 10 <sup>-8</sup>
SiBr <sub>4</sub>	4.0141	× 10 <sup>-4</sup>	SiBr <sub>4</sub>	4.1358	× 10 <sup>-4</sup>
SiBr <sub>3</sub>	7.7	× 10 <sup>-7</sup>	SiBr <sub>2</sub>	1.6	× 10 <sup>-7</sup>
<TiB <sub>2</sub> >	9.9999948	× 10 <sup>-1</sup>	<SiO <sub>2</sub> >	9.9998841	× 10 <sup>-1</sup>
<SiO <sub>2</sub> >	9.9959781	× 10 <sup>-1</sup>	<B <sub>2</sub> O <sub>3</sub> >	7.7	× 10 <sup>-8</sup>
<B <sub>2</sub> O <sub>3</sub> >	2.6610	× 10 <sup>-4</sup>	<TiB <sub>2</sub> >	9	× 10 <sup>-8</sup>
P = 4.98 atm			P = 4.55 atm		
Source T <sub>1</sub> = 1300 K (mol)			Sink T <sub>2</sub> = 1300 K (mol)		
BI <sub>3</sub>					
I <sub>2</sub>	1.291	× 10 <sup>-8</sup>	I <sub>2</sub>	1.439	× 10 <sup>-8</sup>
I	9.17	× 10 <sup>-8</sup>	I	1.692	× 10 <sup>-8</sup>
TiI <sub>4</sub>	2.08	× 10 <sup>-8</sup>	TiI <sub>4</sub>	2.02	× 10 <sup>-8</sup>
BI <sub>3</sub>	1.6	× 10 <sup>-7</sup>	TI <sub>3</sub>	2	× 10 <sup>-8</sup>
SiI <sub>4</sub>	4.3852	× 10 <sup>-4</sup>	BI <sub>3</sub>	1.3	× 10 <sup>-7</sup>
SiI <sub>3</sub>	1.04	× 10 <sup>-8</sup>	SiI <sub>4</sub>	4.3327	× 10 <sup>-4</sup>
<TiB <sub>2</sub> >	9.9999787	× 10 <sup>-1</sup>	SiI <sub>2</sub>	6.30	× 10 <sup>-8</sup>
<SiO <sub>2</sub> >	9.9958041	× 10 <sup>-1</sup>	<SiO <sub>2</sub> >	1	
<B <sub>2</sub> O <sub>3</sub> >	2.9305	× 10 <sup>-4</sup>	<B <sub>2</sub> O <sub>3</sub> >	0	
P = 4.57 atm			<TiB <sub>2</sub> >	2	× 10 <sup>-8</sup>
			P = 5.05 atm		

Table III. Number of mols of TiB<sub>2</sub> "deposited" at sink when gas is first equilibrated with TiB<sub>2</sub> at source and experimentally transported amounts (after one month)

Transport agent	Calculated values (mol)	Experimental (mg TiB <sub>2</sub> )
HBr	$7.0 \times 10^{-6}$	—
TiCl <sub>4</sub>	$2.0 \times 10^{-6}$	0
HCl	$1.7 \times 10^{-6}$	10
TiBr <sub>4</sub>	$1.5 \times 10^{-6}$	10
BCl <sub>3</sub>	$1.2 \times 10^{-6}$	—
TeCl <sub>4</sub>	$1.1 \times 10^{-6}$	150
Cl <sub>2</sub>	$6.6 \times 10^{-7}$	20
BBr <sub>3</sub>	$9 \times 10^{-8}$	150
Br <sub>2</sub>	$4 \times 10^{-8}$	—
BI <sub>3</sub>	$2 \times 10^{-8}$	50
I <sub>2</sub>	$2 \times 10^{-8}$	50

Table IV. Percentages of silicon halides in the source vapor phase

Σ SiXn		Σ SiXn	
t.a.	Σ N	t.a.	Σ N
BI <sub>3</sub>	0.95	TeCl <sub>4</sub>	0.30
BBr <sub>3</sub>	0.86	4Br	0.128
BCl <sub>3</sub>	0.55	HCl	0.08
I <sub>2</sub>	0.54	TiBr <sub>4</sub>	0.013
Br <sub>2</sub>	0.51	TiCl <sub>4</sub>	0.004
Cl <sub>2</sub>	0.30		

Σ SiXn: number of mols of all silicon halides.  
Σ N: total mol number of the gaseous phase.

expected to work a hundred times better than  $\text{BI}_3$ , it is the latter which produces experimental transport.

In Table IV the relative importance of the silicon halides in the vapor phase is reported. These values represent maximum limits of silica etching never reached in facts because of the passivation of the tubes.

So this first model gives the appropriate transport direction, accounts for the silica etching, but does not enable us to anticipate the importance of mass transport. In such experiments in which weak transport occurs (few milligrams a month), it seems interesting to implement a method which optimizes, or at least provides indications about the speed of transport; that is the reason why we refer to the Richardson and Nöläng model.

### Second Model

In his thesis (6) Richardson has demonstrated (4, 5) the influence on the transport rate of all the vapor species, even when they had very low partial pressures. Moreover, when studying the transport of  $\text{SnO}_2$  by iodine and sulfur (4), he points out the competition between two tin halides that constitutes a case similar to ours in which the titanium is present in the gas phase as  $\text{TiX}_3$  and  $\text{TiX}_4$ , both responsible for the transport of  $\text{TiB}_2$  (in a few cases  $\text{TiX}_2$  also appears).

We have applied this model to our systems to predict the rate of chemical transport. The principal assumptions are that the gaseous diffusion follows the laminar flow model, that the system has reached a

steady state, and that the total pressure is equal to the average value of the pressures at sink and source calculated by the first method. Then, the reactions of the walls of the ampul are assumed infinitely kinetically hindered so that the fluxes are position independent. It is therefore necessary to neglect all the products of reactions with silica. The Gibbs free energy of the systems  $\text{TiB}_2/\text{t.a.}$  is minimized at the assumed pressure successively at source and sink temperature. The results of these minimizations for a number of transport agents experimentally tested are reported in Tables V-XII, the compositions of the equilibria are given as partial pressures (atm) for the gaseous species and number of moles for the solid ones. These partial pressure values allow us to obtain the flux functions of the various species.

In the approximation of the experimental model the flux function of a species can be written as

$$\phi_i = \frac{1}{RT} \left( \frac{P_0}{P} \right) \left( \frac{\bar{T}}{T_0} \right)^\alpha \left[ \bar{P}_i \left( \sum_i \lambda_{ir} \frac{\Delta P_i}{\Delta T} \right) / \sum_i \lambda_{ir} \bar{P}_i - \frac{\Delta P_i}{\Delta T} \right] = \frac{1}{RT} \left( \frac{P_0}{P} \right) \left( \frac{\bar{T}}{T_0} \right)^\alpha [f(i)]$$

with

$$\bar{P}_i = \frac{P_{i1} + P_{i2}}{2}$$

Table V.  $\text{I}_2$   $6 \times 10^{-4}$  mol,  $\langle \text{TiB}_2 \rangle$  1 mol,  $T_1 = 1200$  K,  $T_2 = 1300$  K,  $P = 3.3$  atm

Compositions of source (1) and sink (2) equilibria			$\frac{P_{i2} - P_{i1}}{T_2 - T_1}$	$\bar{P}_i$
Gas phase	$P_{i1}$ (atm)	$P_{i2}$ (atm)		
$\text{TiI}_4$	1.1878	1.1874	$-6.204 \times 10^{-3}$	1.477
$\text{TiI}_3$	$2.325 \times 10^{-3}$	$4.471 \times 10^{-3}$	$2.146 \times 10^{-5}$	$3.4 \times 10^{-3}$
$\text{BI}_3$	$4.628 \times 10^{-3}$	$5.602 \times 10^{-3}$	$9.97 \times 10^{-5}$	$5.11 \times 10^{-3}$
$\text{I}_2$	1.1876	1.5066	$3.19 \times 10^{-3}$	1.347
$\text{I}$	$2.759 \times 10^{-1}$	$5.655 \times 10^{-1}$	$2.89 \times 10^{-3}$	$4.21 \times 10^{-1}$
Solid phases	$n_{i1}$ (mol)	$n_{i2}$ (mol)		
$\langle \text{TiB}_2 \rangle$	$9.9978 \times 10^{-1}$	$9.9983 \times 10^{-1}$	$\frac{\sum \lambda_{ir} (P_{i2} - P_{i1})}{T_2 - T_1} = -1.65 \times 10^{-3}$	
$\langle \text{B} \rangle$	$4.26 \times 10^{-1}$	$3.25 \times 10^{-1}$	$\sum \lambda_{ir} \bar{P}_i$	

Table VI.  $\text{Cl}_2$   $6 \times 10^{-4}$  mol,  $\langle \text{TiB}_2 \rangle$  1 mol,  $T_1 = 1300$  K,  $T_2 = 1200$  K,  $P = 3.4$  atm

Compositions of source (1) and sink (2) equilibria			$\frac{P_{i2} - P_{i1}}{T_2 - T_1}$	$\bar{P}_i$
Gas phase	$P_{i1}$ (atm)	$P_{i2}$ (atm)		
$\text{TiCl}_4$	1.07333	1.10326	$-2.993 \times 10^{-4}$	1.0883
$\text{TiCl}_3$	$5.996 \times 10^{-3}$	$3.10 \times 10^{-3}$	$2.986 \times 10^{-4}$	$4.5 \times 10^{-3}$
$\text{BCl}_3$	2.26641	2.26656	$-1.6 \times 10^{-5}$	2.2665
Solid phases	$n_{i1}$ (mol)	$n_{i2}$ (mol)		
$\langle \text{TiB}_2 \rangle$	$9.99879 \times 10^{-1}$	$9.99880 \times 10^{-1}$	$\frac{\sum \lambda_{ir} (P_{i2} - P_{i1})}{T_2 - T_1} = -2.72 \times 10^{-3}$	
			$\sum \lambda_{ir} \bar{P}_i$	

Table VII.  $\text{HCl}$   $6 \times 10^{-4}$  mol,  $\langle \text{TiB}_2 \rangle$  1 mol,  $T_1 = 1200$  K,  $T_2 = 1300$  K,  $P = 5$  atm

Compositions of source (1) and sink (2) equilibria			$\frac{P_{i2} - P_{i1}}{T_2 - T_1}$	$\bar{P}_i$
Gas phase	$P_{i1}$ (atm)	$P_{i2}$ (atm)		
$\text{TiCl}_4$	$4.8217 \times 10^{-1}$	$4.3795 \times 10^{-1}$	$-4.42 \times 10^{-4}$	$4.60 \times 10^{-1}$
$\text{TiCl}_3$	$1.729 \times 10^{-2}$	$3.271 \times 10^{-3}$	$1.54 \times 10^{-4}$	$2.500 \times 10^{-2}$
$\text{BCl}_3$	$8.9738 \times 10^{-1}$	$8.3116 \times 10^{-1}$	$-6.62 \times 10^{-4}$	$8.64 \times 10^{-1}$
$\text{HCl}$	1.1144	1.3613	$2.469 \times 10^{-3}$	1.2379
$\text{BHCl}_2$	$1.0154 \times 10^{-1}$	$1.099 \times 10^{-1}$	$8.45 \times 10^{-5}$	$1.058 \times 10^{-1}$
Solid phases	$n_{i1}$ (mol)	$n_{i2}$ (mol)		
$\langle \text{TiB}_2 \rangle$	$9.99949 \times 10^{-1}$	$9.99952 \times 10^{-1}$	$\frac{\sum \lambda_{ir} (P_{i2} - P_{i1})}{T_2 - T_1} = -1.06 \times 10^{-4}$	
			$\sum \lambda_{ir} \bar{P}_i$	

Table VIII.  $\text{TeCl}_4$   $6 \times 10^{-4}$  mol,  $\langle \text{TiB}_2 \rangle$  1 mol,  $T_1 = 1300$  K,  $T_2 = 1200$  K,  $P = 7$  atm

Compositions of source (1) and sink (2) equilibria			$\frac{P_{t_2} - P_{t_1}}{T_2 - T_1}$	$\bar{P}_t$ (atm)
Gas phase	$P_{t_1}$ (atm)	$P_{t_2}$ (atm)		
$\text{TiCl}_4$	1.9860	2.2538	$-2.378 \times 10^{-3}$	2.065
$\text{TiCl}_3$	$9.158 \times 10^{-3}$	$4.893 \times 10^{-3}$	$4.265 \times 10^{-4}$	$7.02 \times 10^{-3}$
$\text{BCl}_3$	4.1151	4.5056	$-3.905 \times 10^{-3}$	4.3103
$\text{TeCl}_2$	$2.52 \times 10^{-3}$	$8.80 \times 10^{-4}$	$1.64 \times 10^{-5}$	$1.71 \times 10^{-3}$
Solid phases	$n_{t_1}$ (mol)	$n_{t_2}$ (mol)		
$\langle \text{TiB}_2 \rangle$	$9.997589 \times 10^{-1}$	9.997595	$\Sigma \lambda_{tr} \frac{P_{t_2} - P_{t_1}}{T_2 - T_1}$	
$\langle \text{Te} \rangle$	$4.069 \times 10^{-4}$	$5.486 \times 10^{-4}$	$\frac{\Sigma \lambda_{tr} P_t}{T_2 - T_1} = -9.26 \times 10^{-4}$	

Table IX.  $\text{TiCl}_4$   $6 \times 10^{-4}$  mol,  $\langle \text{TiB}_2 \rangle$  1 mol,  $T_1 = 1300$  K,  $T_2 = 1200$  K,  $P = 6$  atm

Compositions of source (1) and sink (2) equilibria			$\frac{P_{t_2} - P_{t_1}}{T_2 - T_1}$	$\bar{P}_t$
Gas phase	$P_{t_1}$ (atm)	$P_{t_2}$ (atm)		
$\text{TiCl}_4$	5.4203	5.6685	$-2.48 \times 10^{-3}$	5.5444
$\text{TiCl}_3$	$4.830 \times 10^{-1}$	$2.762 \times 10^{-1}$	$2.07 \times 10^{-3}$	$3.796 \times 10^{-1}$
$\text{BCl}_3$	$9.664 \times 10^{-3}$	$5.525 \times 10^{-3}$	$4.14 \times 10^{-4}$	$7.59 \times 10^{-3}$
Solid phases	$n_{t_1}$ (mol)	$n_{t_2}$ (mol)		
$\langle \text{TiB}_2 \rangle$	$9.99995 \times 10^{-1}$	$9.99997 \times 10^{-1}$	$\Sigma \lambda_{tr} \frac{P_{t_2} - P_{t_1}}{T_2 - T_1}$	
			$\frac{\Sigma \lambda_{tr} \bar{P}_t}{T_2 - T_1} = -1.06 \times 10^{-4}$	

Table X.  $\text{TiBr}_4$   $6 \times 10^{-4}$  mol,  $\langle \text{TiB}_2 \rangle$  1 mol,  $T_1 = 1300$  K,  $T_2 = 1200$  K,  $P = 6$  atm

Compositions of source (1) and sink (2) equilibria			$\frac{P_{t_2} - P_{t_1}}{T_2 - T_1}$	$\bar{P}_t$
Gas phase	$P_{t_1}$ (atm)	$P_{t_2}$ (atm)		
$\text{TiBr}_4$	5.3474	5.6560	$-3.086 \times 10^{-3}$	5.502
$\text{TiBr}_3$	$5.4136 \times 10^{-1}$	$2.8612 \times 10^{-1}$	$2.55 \times 10^{-3}$	$4.14 \times 10^{-1}$
$\text{TiBr}_2$	$1.925 \times 10^{-3}$	$4.46 \times 10^{-4}$	$1.48 \times 10^{-5}$	$1.18 \times 10^{-3}$
$\text{BBr}_3$	$1.0894 \times 10^{-1}$	$5.737 \times 10^{-2}$	$5.15 \times 10^{-4}$	$8.31 \times 10^{-2}$
Solid phases	$n_{t_1}$ (mol)	$n_{t_2}$ (mol)		
$\langle \text{TiB}_2 \rangle$	$9.99994 \times 10^{-1}$	$9.99997 \times 10^{-1}$	$\Sigma \lambda_{tr} \frac{P_{t_2} - P_{t_1}}{T_2 - T_1}$	
			$\frac{\Sigma \lambda_{tr} \bar{P}_t}{T_2 - T_1} = -1.32 \times 10^{-4}$	

Table XI.  $\text{Bi}_3$   $6 \times 10^{-4}$  mol,  $\langle \text{TiB}_2 \rangle$  1 mol,  $T_1 = 1200$  K,  $T_2 = 1300$  K,  $P = 4.7$  atm

Compositions of source (1) and sink (2) equilibria			$\frac{P_{t_2} - P_{t_1}}{T_2 - T_1}$	$\bar{P}_t$
Gas phase	$P_{t_1}$ (atm)	$P_{t_2}$ (atm)		
$\text{TiI}_4$	2.8663	2.0252	$-8.41 \times 10^{-3}$	2.4457
$\text{TiI}_3$	$3.323 \times 10^{-3}$	$6.772 \times 10^{-3}$	$3.45 \times 10^{-5}$	$5.05 \times 10^{-3}$
$\text{BiI}_3$	$6.595 \times 10^{-2}$	$8.468 \times 10^{-2}$	$1.87 \times 10^{-4}$	$7.53 \times 10^{-2}$
$\text{I}_2$	1.5038	1.9843	$4.80 \times 10^{-3}$	1.744
$\text{I}$	$3.1051 \times 10^{-1}$	$6.490 \times 10^{-1}$	$3.38 \times 10^{-3}$	$4.80 \times 10^{-1}$
Solid phases	$n_{t_1}$ (mol)	$n_{t_2}$ (mol)		
$\langle \text{TiB}_2 \rangle$	$9.99655 \times 10^{-1}$	$9.9972 \times 10^{-1}$	$\Sigma \lambda_{tr} \frac{P_{t_2} - P_{t_1}}{T_2 - T_1}$	
$\langle \text{B} \rangle$	$1.281 \times 10^{-2}$	$1.151 \times 10^{-3}$	$\frac{\Sigma \lambda_{tr} \bar{P}_t}{T_2 - T_1} = -1.43 \times 10^{-3}$	

Table XII.  $\text{BBr}_3$   $6 \times 10^{-4}$  mol,  $\langle \text{TiB}_2 \rangle$  1 mol,  $T_1 = 1300$  K,  $T_2 = 1200$  K,  $P = 5$  atm

Compositions of source (1) and sink (2) equilibria			$\frac{P_{t_2} - P_{t_1}}{T_2 - T_1}$	$\bar{P}_t$
Gas phase	$P_{t_1}$ (atm)	$P_{t_2}$ (atm)		
$\text{TiBr}_4$	$6.407 \times 10^{-2}$	$6.107 \times 10^{-2}$	$3.0 \times 10^{-5}$	$6.26 \times 10^{-2}$
$\text{TiBr}_3$	$4.694 \times 10^{-3}$	$1.999 \times 10^{-3}$	$2.69 \times 10^{-5}$	$3.34 \times 10^{-3}$
$\text{BBr}_3$	4.9305	4.9367	$-6.24 \times 10^{-5}$	4.934
$\text{Br}$	$4.67 \times 10^{-4}$	$9.5 \times 10^{-5}$	$3.7 \times 10^{-6}$	$2.81 \times 10^{-4}$
Solid phases	$n_{t_1}$ (mol)	$n_{t_2}$ (mol)		
$\langle \text{TiB}_2 \rangle$	$9.99991 \times 10^{-1}$	$9.99992 \times 10^{-1}$	$\Sigma \lambda_{tr} \frac{P_{t_2} - P_{t_1}}{T_2 - T_1}$	
$\langle \text{B} \rangle$	$2.72 \times 10^{-5}$	$2.50 \times 10^{-5}$	$\frac{\Sigma \lambda_{tr} \bar{P}_t}{T_2 - T_1} = 1.14 \times 10^{-5}$	

mean partial pressure value between the two equilibria

$$\frac{\Delta P_t}{\Delta T} = \frac{P_{t_2} - P_{t_1}}{T_2 - T_1}$$

$$\bar{T} = \frac{T_1 + T_2}{2}$$

$\alpha$  is a constant used in the relationship  $\bar{D} = \bar{D}_0 (P_0/P)$

$(T/T_0)^\alpha$  to describe the temperature and total pressure variation of the diffusion coefficient. Its value lies between 1.5 and 2.

$\lambda_{ir}$  is the stoichiometric coefficient of the  $r$ th element in the  $i$  species where  $r$  is present only in the vapor phase (here  $r$  is the halogen). The relation between  $\phi_i$  and the flux of the  $i$  species is

$$J_i = \bar{D}_0 \phi_i \frac{\Delta T}{\Delta x}$$

in which  $\Delta x$  is the length of the tube and  $\bar{D}_0$  the mean diffusion coefficient; this single average value replaces the diffusion coefficients  $D_0$ .

Richardson and Nöling (4, 5) wished to optimize the flux function, in this paper we shall only compare the values of this function for different transport agents.

The transport of  $\text{TiB}_2$ , for the titanium part, being due to  $\text{TiX}_3$  and  $\text{TiX}_4$ , we can write

$$\begin{aligned} \phi[\text{TiB}_2] &= \phi[\text{TiX}_3] + \phi[\text{TiX}_4] \\ &= \frac{1}{RT} \left( \frac{P_0}{P} \right) \left( \frac{T}{T_0} \right)^\alpha [f(\text{TiX}_4) + f(\text{TiX}_3)] \end{aligned}$$

The different values obtained (Table XIII) show that, with the exception of  $\text{BBr}_3$ , the functions  $\phi$  of the halides have opposite signs. Therefore, there is a competition between them and only one is responsible for the transport.

A means of comparison of the transport agents in spite of the different values of  $\bar{P}$  and  $D_0$  is the consideration of the ratio

$$R = - \frac{\text{flux of the transporting halide}}{\text{flux of the second halide}}$$

When the ratio tends toward 1 (equal fluxes), infinitely slow transport is expected. The values of  $R$  for the various transport agents are reported in Table XIII against the amounts experimentally transported. There is now a very good agreement between the two series of results except for  $\text{TeCl}_4$  and  $\text{Cl}_2$ .

These two transport agents will be studied together with  $\text{TiBr}_4$  and  $\text{TiCl}_4$ , all of them producing an  $R$  value close to 1. Let us consider the case of  $\text{Cl}_2$ : For that carrier, just like for  $\text{TiCl}_4$  and  $\text{TeCl}_4$ , there appears neither boron (unlike the cases of  $\text{BI}_3$ ,  $\text{BBr}_3$ , and  $\text{I}_2$ ) nor  $\text{BHCl}_2$  (unlike the case of  $\text{HCl}$ ) and, as  $\text{Cl}_2$  acts only as a solvent and is completely consumed, the relation between the partial pressures results in

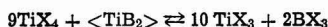
$$P_{[\text{TiCl}_3]} + P_{[\text{TiCl}_4]} = \frac{1}{2} P_{[\text{BCl}_3]}$$

and

$$P_{[\text{BCl}_3]} = \frac{2}{3} P_{\text{total}}$$

The model assumes the same pressure at source and sink and, in the absence of chemical potential gra-

dient, transport becomes impossible. The same phenomenon occurs in the case of  $\text{TeCl}_4$  (with transport of tellurium in the process). In the cases of  $\text{TiBr}_4$  and  $\text{TiCl}_4$ , transport can be described by the equation



and as we started from  $\text{TiX}_4$ , we necessarily have

$$P_{[\text{TiX}_3]} = 5P_{[\text{BX}_3]}$$

which gives for the flux functions

$$\phi_{[\text{TiX}_3]} = 5\phi_{[\text{BX}_3]}$$

now

$$\phi_{[\text{TiB}_2]} = \phi_{[\text{TiX}_3]} + \phi_{[\text{TiX}_4]} + \frac{1}{2} \phi_{[\text{BX}_3]}$$

In the absence of solid boron we shall have

$$\phi_{[\text{TiX}_4]} = -4.5 \phi_{[\text{BX}_3]}$$

and

$$\frac{\phi_{[\text{TiX}_3]}}{\phi_{[\text{TiX}_4]}} = \frac{5}{4.5} = -1.11 \quad (\text{cf., Table XIII})$$

These few equations explain why the Richardson model predicts no transport in these cases. To understand why two of these transport agents still give experimental transport, it is necessary to come back to the first model and to consider Table IV showing the side reactions with silica of the tube. In the case of  $\text{TiCl}_4$  and  $\text{TiBr}_4$ , there is almost no attack so that the restraints on the partial pressures remain and, as predicted, there is no transport. On the contrary, in the case of  $\text{Cl}_2$  and  $\text{TeCl}_4$ , silicon halides are formed by attack of the tube, and the restraints fall down, and the transport becomes possible.

### Conclusion

The application of thermodynamics and flux functions, while pointing out their limitations, provides a useful insight into investigating transport system.

The grouping of the two submitted models brings an approach of the complicated chemical processes which occurs. From that approach we deduce the transport direction and the importance of the wall etching as well as its influence on the transport. Lastly, it allows one to make *a priori* choice between the different transport agents.

Manuscript submitted Nov. 7, 1980; revised manuscript received April 6, 1981. This was Paper 425 presented at the Los Angeles, California, Meeting of the Society, Oct. 14-19, 1979.

Any discussion of this paper will appear in a Discussion Section to be published in the June 1982 JOURNAL. All discussions for the June 1982 Discussion Section should be submitted by Feb. 1, 1982.

Publication costs of this article were assisted by the École Nationale Supérieure de Chimie.

Table XIII. Results of calculations after the Richardson model

t.a.	$\text{BBr}_3$	$\text{BI}_3$	$\text{I}_2$	$\text{HCl}$	$\text{TiBr}_4$	$\text{TiCl}_4$	$\text{TeCl}_4$	$\text{Cl}_2$
$f(\text{TiX}_4)$	$-3 \times 10^{-5}$	$4.9 \times 10^{-3}$	$3.8 \times 10^{-3}$	$3.9 \times 10^{-4}$	$2.3 \times 10^{-3}$	$1.9 \times 10^{-3}$	$4.5 \times 10^{-4}$	$2.7 \times 10^{-4}$
$f(\text{TiX}_3)$	$-2.7 \times 10^{-5}$	$-3.4 \times 10^{-5}$	$-2.7 \times 10^{-5}$	$-1.6 \times 10^{-4}$	$-2.60 \times 10^{-3}$	$-2.1 \times 10^{-3}$	$-4.9 \times 10^{-4}$	$-3.0 \times 10^{-4}$
t.h.*	$\text{TiBr}_3 + \text{TiBr}_4$	$\text{TiI}_4$	$\text{TiI}_4$	$\text{TiCl}_4$	$\text{TiBr}_3^{**}$	$\text{TiCl}_4$	$\text{TiCl}_4$	$\text{TiCl}_4$
R***		142	138	2.25	1.11	1.11	1.1	1.1
exp. (mg)	150	50	50	<10	<10	0	150	20

\* t.h. = halide effective in the transport.  
 \*\* =  $+ \text{TiBr}_2$  with  $f(\text{TiBr}_2) = -1.5 \times 10^{-5}$ .  
 \*\*\* = defined in the text as:  $f(\text{TiX}_4)/f(\text{TiX}_3)$ .

## APPENDIX

The various constituents taken into account in equilibria calculations are:

Cl	(a)	Br	(a)	<Te>	(e)	<TiH <sub>2</sub> >	(a)
Cl <sub>2</sub>	(a)	Br <sub>2</sub>	(a)	Te	(e)	<TiB <sub>2</sub> >	(a)
TiCl	(a)	BBr	(a)	Te <sub>2</sub>	(e)	<TiB>	(a)
TiCl <sub>2</sub>	(a)	BBr <sub>2</sub>	(a)	TeCl <sub>2</sub>	(e)	<Ti>	(a)
TiCl <sub>3</sub>	(a)	BBr <sub>3</sub>	(a)	TeCl <sub>4</sub>	(d)	Ti	(a)
TiCl <sub>4</sub>	(a)	TiBr	(a)	<TiTe <sub>2</sub> >	(f)	TiO	(c)
<TiCl <sub>2</sub> >	(a)	TiBr <sub>2</sub>	(a)	TiTe	(e)	TiO <sub>2</sub>	(c)
BCl <sub>3</sub>	(a)	TiBr <sub>3</sub>	(a)	TeO	(e)	<Ti <sub>2</sub> O <sub>3</sub> >	(c)
BCl	(a)	TiBr <sub>4</sub>	(a)	TeO <sub>2</sub>	(e)	<Ti <sub>3</sub> O <sub>5</sub> >	(c)
SiCl <sub>4</sub>	(b)	<TiBr <sub>2</sub> >	(a)	Te <sub>2</sub> O <sub>2</sub>	(e)		
SiCl <sub>3</sub>	(a)	SiBr <sub>4</sub>	(d)			<SiO <sub>2</sub> >	(a)
						(cristobalite)	
SiCl <sub>2</sub>	(b)	SiBr <sub>2</sub>	(d)	<B>	(a)	<Si <sub>3</sub> Ti <sub>5</sub> >	(d)
SiCl	(a)	BBrO	(a)	BO <sub>2</sub>	(a)	SiO <sub>2</sub>	(a)
BClO	(a)	HBr	(a)	B <sub>2</sub> O <sub>2</sub>	(a)	SiO	(a)
TiClO	(a)	BHBr <sub>2</sub>	(a)	B <sub>2</sub> O <sub>3</sub>	(a)	<Si>	(a)
TiCl <sub>2</sub> O	(a)			(B <sub>2</sub> O <sub>3</sub> )	(a)	Si	(a)
ClH	(a)	I	(a)	H <sub>2</sub>	(a)	O <sub>2</sub>	(a)
ClH <sub>2</sub> HSi	(a)	I <sub>2</sub>	(a)	H	(a)	H <sub>4</sub> Si	(a)
Cl <sub>2</sub> H <sub>2</sub> Si	(a)	BI	(a)	BH <sub>2</sub>	(a)	H <sub>2</sub> O	(a)
ClH <sub>3</sub> Si	(a)	BI <sub>2</sub>	(a)	BH <sub>3</sub>	(a)		
ClHO	(a)	BI <sub>3</sub>	(a)	B <sub>2</sub> H <sub>6</sub>	(a)		
BHCl <sub>2</sub>	(a)	TiI	(a)	B <sub>10</sub> H <sub>14</sub>	(a)		
		TiI <sub>2</sub>	(a)	BH <sub>3</sub> O <sub>3</sub>	(a)		
		TiI <sub>3</sub>	(a)	B <sub>3</sub> H <sub>3</sub> O <sub>3</sub>	(a)		
		TiI <sub>4</sub>	(a)	BH <sub>2</sub> O <sub>2</sub>	(a)		
		<TiI <sub>2</sub> >	(a)	BHO	(a)		
		SiI <sub>2</sub>	(d)				
		SiI <sub>4</sub>	(d)				

(a) JANAF thermochemical tables, U.S. Department of Commerce, N.B.S., 2nd ed., Dow Chemical Co, Midland, MI (1971).

(b) JANAF thermochemical tables, U.S. Department of Commerce, N.B.S., supplement (1974).

(c) JANAF thermochemical tables, U.S. Department of Commerce, N.B.S., supplement (1975).

(d) I. Barin, O. Knacke, and O. Kubaschewski, "Thermochemical Properties of Inorganic Substances," Springer Verlag, Berlin, Heidelberg, New York, supplement (1977).

(e) K. C. Mills, "Thermodynamic Data for Inorganic Sulfides, Selenides and Tellurides," Butterworths, London (1974).

(f) For <TiTe<sub>2</sub>> the following thermodynamic values have been used:  $\Delta f_{298}^\circ = -50900 \text{ cal mol}^{-1}$ , after Mills (e),  $S_{298}^\circ = 28 \text{ cal. deg.}^{-1} \text{ mol}^{-1}$ , estimated by the Latimer's method (e), the function  $G_T - H_{298}/T$  has been estimated to  $35.1 \text{ cal. deg.}^{-1}$  at 800 K (e) and the approximations of the method being taken of, it has been considered as a linear function of the temperature:  $G_T - H_{298} = 23.785 - 0.01414T$ .

## REFERENCES

1. R. Feurer, C. Bernard, and G. Constant, *C.R. Acad. Sci. Paris*, **282**, 1117 (1976).
2. R. Feurer, G. Constant, and C. Bernard, *J. Less-Common Met.*, **67**, 107 (1979).
3. C. Bernard, Y. Deniel, A. Jacquot, P. Way, and M. Ducarroir, *ibid.*, **40**, 165 (1975).
4. B. I. Nöläng and M. W. Richardson, *J. Cryst. Growth*, **34**, 198 (1976).
5. B. I. Nöläng and M. W. Richardson, *ibid.*, **34**, 205 (1976).
6. M. W. Richardson, *Acta Univ. Upsaliensis*, **464** (1978).



# Vacuum Plasma Electron Beam Melting of Reactive and Refractory Metals and Their Alloys

## One Step Melting of Low Oxygen Content Titanium Scrap by Using VPEB

S. Kashu, K. Watanabe, M. Nagase, and C. Hayashi

*Vacuum Metallurgical Company, Limited, P.O. Box 11, Yachimata, Inba-gun, Chiba 289-11, Japan*

and Y. Yoneda

*ULVAC Corporation, 2500, Hagizono, Chigasaki-shi, Japan 253*

### ABSTRACT

Vacuum plasma electron beam (VPEB) melting with a hot hollow cathode gives satisfactory results for recovery of low oxygen content titanium scraps and Zircaloy-2 scraps. The yield of relatively high vapor pressure elements, such as Cr, can be controlled easily to meet with the tolerance. The VPEB has a high energy density and purification effect which is similar to that of high voltage electron beam melting. Power input of the VPEB to a target of a molten pool is by far more stable and the yield of materials throughout the melting of reactive and refractory metals and their alloys is quite satisfactory compared to those of high voltage EB or the vacuum arc melting process. The VPEB process is also safer, easier to operate, and suitable for automation. Three examples of VPEB application at VMC-ULVAC are described in this paper.

A simple recycle process of reactive metal and alloy scrap to sound ingots is aimed at. Low oxygen content, loose-shape titanium scraps (Fig. 1), the chemical composition of which is shown in Table I, are melted by using VPEB. Oxygen content of the VPEB melted ingots satisfied the high quality level of JIS Grade-1 specification. One-step melting of high purity reactive metal scrap by using VPEB is feasible both technologically and economically.

Figure 2 illustrates a VPEB one-step recycle furnace. A schematic drawing of the furnace is shown in Fig. 3. By using a 200 mm diam water-cooled copper crucible and an ingot pulling mechanism, a 1m length of titanium ingot (weight 130 kg) is produced. Melt stocks of titanium scraps, which are represented in Table II, are charged to a material feeding chamber and moved over the lip of the crucible. An 18 in. gate valve is attached to the furnace for semicontinuous feeding of the melt stock. A 20 in., 8 m<sup>3</sup>/sec oil ejector pump, a 1 m<sup>3</sup>/sec mechanical booster pump, and a rotary piston pump with a capacity of 7 m<sup>3</sup>/min are equipped in series. A d-c power supply of 100V and 3 kA maximum output is used as the VPEB power source.

Figure 4 illustrates the melting operation. An example of operating parameters are represented in

Key words: VPEB, titanium, metals.

Table I. JIS\* chemical composition of Ti in ppm

	H	O	N	Fe
Grade 1	<150	<1500	<500	<2000
Grade 2	<150	<2000	<500	<2500
Grade 3	<150	<3000	<700	<3000

\* JIS H 4670.

Table III. Figure 5 illustrates the surface of the one-step melted titanium ingot. Table IV represents the

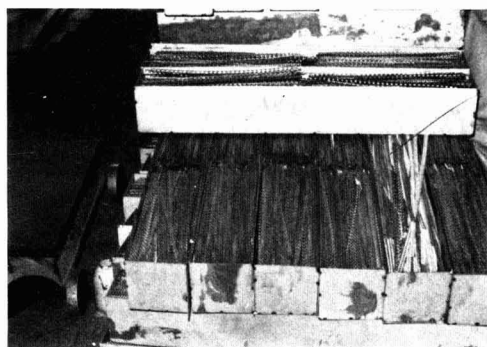


Fig. 1. Loose shape titanium recycle scraps

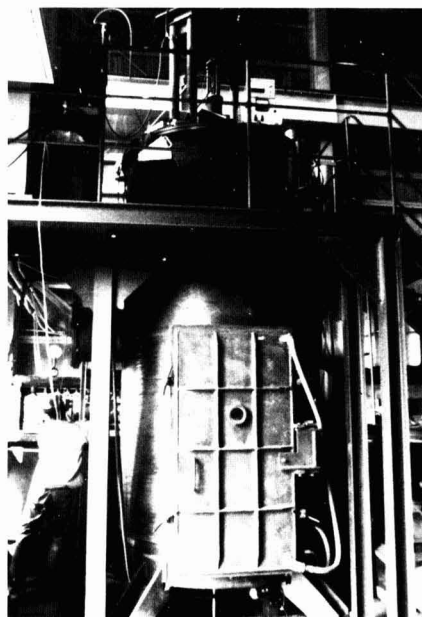


Fig. 2. Overall view of the VPEB one-step recycle furnace

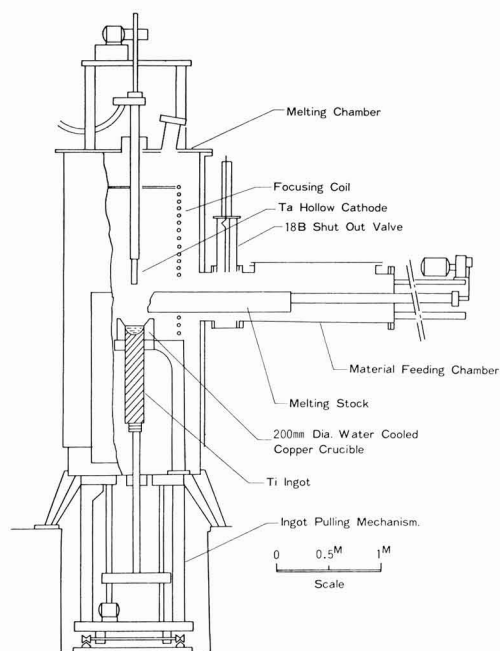


Fig. 3. Schematic drawing of VPEB one-step recycle furnace

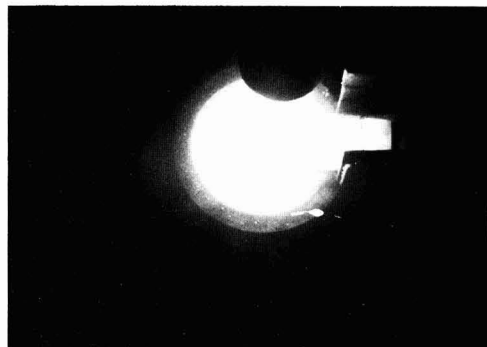


Fig. 4. Molten pool of titanium is bombarded by means of VPEB

results of the oxygen level of the recycled ingot. Table V represents the results of the chemical analysis of the 3 mm diam titanium wire which is forged and drawn from an ingot made by the VPEB process. A standard chemical analysis value of a commercially used high

Table II. Typical value of oxygen content

Ti scraps	O (ppm)
No. 1	630
No. 2	750
No. 3	790
No. 4	830
No. 5	500

Table III. Operating parameter of VPEB for Ti scrap melting

Operating pressure (Pa)	6.7 ~ 9.3
VPEB out put Voltage (V)	80 ~ 85
Current (kA)	1.8 ~ 2.0
Wattage (kW)	140 ~ 170
Melting rate (kg/hr)	23

Table IV. Typical value of oxygen content

Ingot No.	Material	O <sub>2</sub> content (ppm)	
		Material	Ingot*
11	650	T	750
		B	1070
12	580	T	710
		B	950
13	670	T	750
		B	1040
14	750	T	770
		B	1030
15	580	T	610
		B	680

\* T: Top of the ingot. B: Bottom of ingot.

Table Va. Chemical analysis of 3 mm od Ti wire

Lot No.	Impurity content (ppm)		
	O	Fe	C
W-1	750	490	130
W-2	710	300	110
W-3	690	410	93
W-4	730	430	140
W-5	670	360	770
Average value	710	400	110

Table Vb. Impurity level of JIS Grade-1 Ti wire

	Impurity content (ppm)		
	O	Fe	C
Lower limit	400	200	50
Average	650	450	100
Upper limit	850	600	150

Table VI. Chemical composition of Zircaloy-2

Sn	Fe	Cr	Ni
1.20-1.70	0.07-0.20	0.05-0.15	0.03-0.08

Table VII. Preliminary test of VPEB melt

	I	II	III	VI	Raw material
Operating pressure (Ar Pa)	1.2	1.1	1.2	5.3	
Melting time (min)	7	0.5	2	2	
VPEB melting power (kW)	50.4	51.6	52.8	51.4	
Charged weight (g)	1049	1466	1322	1458	
Weight loss (g)	2	2	1	<1	
Chemical analysis (%)					
Sn	1.27	1.38	1.35	1.39	1.40
Ni	0.052	0.053	0.054	0.054	0.057
Cr	0.023	0.060	0.018	0.058	0.097
Fe	0.104	0.120	0.117	0.124	0.139

Table VIII. Operating parameter of VPEB

Operating pressure	Ar 1.9-2.0 Pa
Voltage	44-50 (V)
Current	1500-1700 (A)
Melting power	70-80 (kW)
Melting speed	Approx. 1.6 (kg/min)
Hearth size	w 125 × D 135 × L 1650 (mm)

Table IX. Operating parameter of VAR

Operating pressure	0.7-1.3 Pa
Voltage	32 (V)
Current	5700 (A)
Melting power	182.4 (kW)
Melting speed	5.2-5.8 (kg/min)
Crucible size	ID 250 (mm)

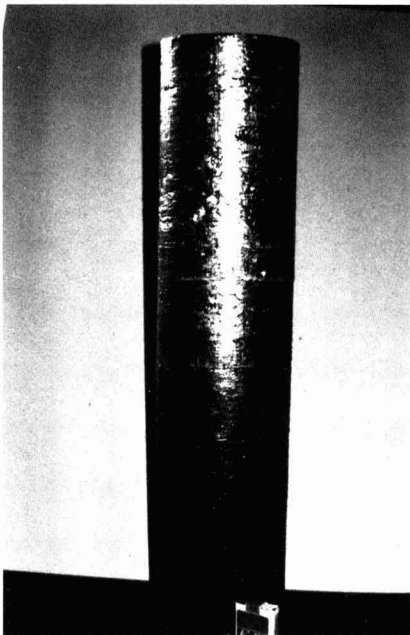


Fig. 5. One-step melted titanium ingot

purity grade titanium wire is also shown as the reference.

A low oxygen content 200 mm diam titanium ingot can be produced by VPEB one-step melting. Results are shown as follows: (i) The increase of the oxygen content level by one-step melting is less than 100 ppm. (ii) The melting rate of titanium one-step melting is 0.2 kg/kA · min. This value is acceptable in practical application. (iii) Variations of pressure, voltage, and current are very small so that extremely stable operation continues throughout melting. (iv) Argon gas consumption for VPEB discharge is small and can be neglected. It is, however, possible to recycle the argon, if required. (v) Operating experience has proved that the VPEB process is economically advantageous.

Direct Recovery of Zircaloy-2 Scrap by Using VPEB

Zircalloy (Table VI) scraps are conventionally shipped back to a chemical processing plant. In this

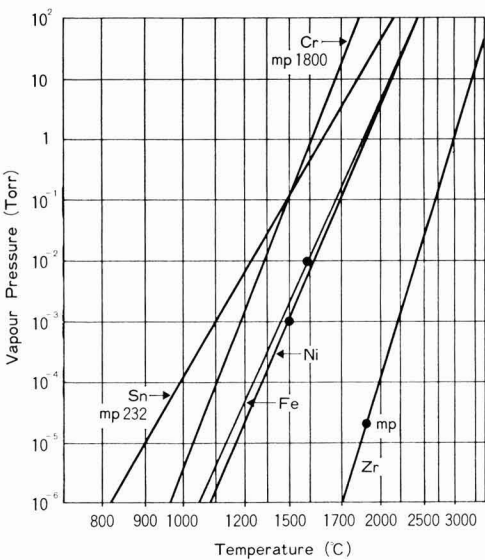


Fig. 6. Vapor pressure of additional elements of Zircaloy-2



Fig. 7. General view of the VPEB scrap recycle furnace

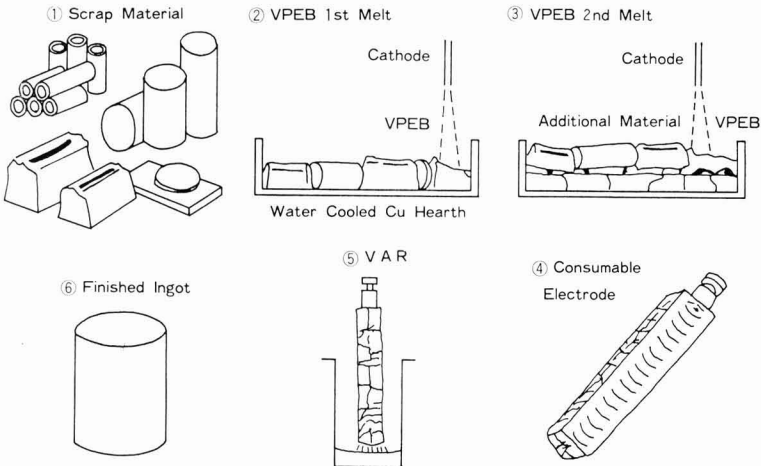
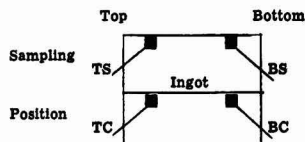


Fig. 8. Process of direct recovery of Zircaloy scrap.

Table X. Chemical analysis of finished ingot (%)

	ASTM B-350	Sn 1.20-1.70	Fe 0.07-0.20	Ni 0.03-0.08	Cr 0.06-0.15	Rate of Cr addition
Ingot 1	Raw material*	1.49	0.139	0.051	0.082	
	TC-1	1.59	0.149	0.060	0.122	0.059
	TS-1	1.35	0.142	0.053	0.124	0.059
	BC-1	1.52	0.136	0.049	0.120	0.059
	BS-1	1.48	0.141	0.046	0.123	0.059
Ingot 2	Average	1.53	0.142	0.051	0.122	0.059
	TC-2	1.67	0.149	0.060	0.151	0.061
	TS-2	1.59	0.140	0.054	0.142	0.061
	BC-2	1.50	0.116	0.046	0.134	0.061
	BS-2	1.48	0.106	0.043	0.125	0.061
Ingot 3	Average	1.56	0.127	0.051	0.138	0.061
	TC-3	1.52	0.144	0.054	0.102	0.025
	TS-3	1.49	0.138	0.052	0.098	0.025
	BC-3	1.46	0.125	0.047	0.091	0.025
	BS-3	1.45	0.110	0.045	0.100	0.025
Ingot 4	Average	1.48	0.129	0.049	0.098	0.025
	TC-4	1.69	0.127	0.060	0.087	0
	TS-4	1.66	0.123	0.059	0.087	0
	BC-4	1.54	0.098	0.047	0.073	0
	BS-4	1.53	0.095	0.047	0.072	0
	Average	1.60	0.110	0.054	0.080	0

\* Average value of 10 sampling.



paper, however, a new process for direct recovery of Zircaloy scrap is proposed. Surface-cleaned Zircaloy

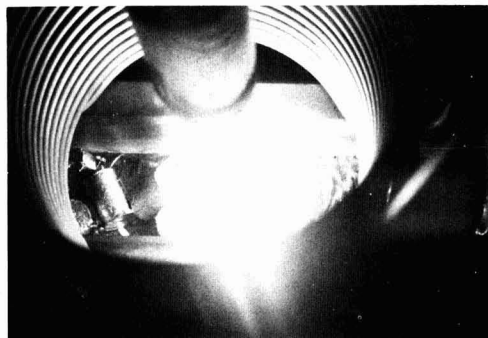
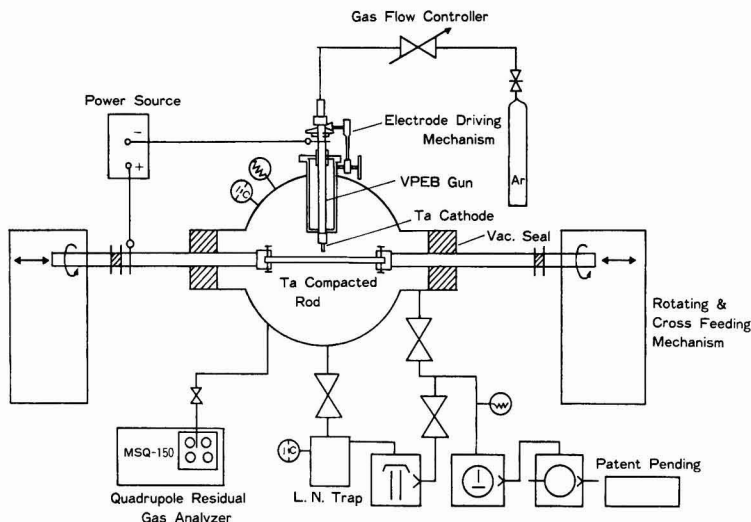


Fig. 9. VPEB melting of Zircaloy scrap for electrode

scraps are converted in a specially designed vacuum plasma electron beam furnace to an electrode for vacuum arc remelting which is a part of a conventional process. Sufficient mechanical strength and electrical conductivity are the two factors required with the VPEB processed electrode, while compensation for chromium loss (Fig. 6) during the melting was considered. The result of the development work is satisfactory and the new process can be a big improvement.

Figure 7 illustrates the specially designed VPEB scrap recovery furnace. Scraps are laid on a water-cooled copper hearth which has dimensions suitable for electrode to successive VAR. The hearth is movable back and forth in the vacuum chamber while VPEB bombards the surface of the scraps. A simple scanning mechanism is equipped for the VPEB gun. A chromium charging mechanism feeds the necessary addition of chromium granules following the first melt down. A larger charging mechanism feeds Zircaloy scraps over the first melt for additional second melting as is illustrated in Fig. 8. VPEB melting in this ap-

Fig. 10. Schematic drawing of the VPEB melting equipment.



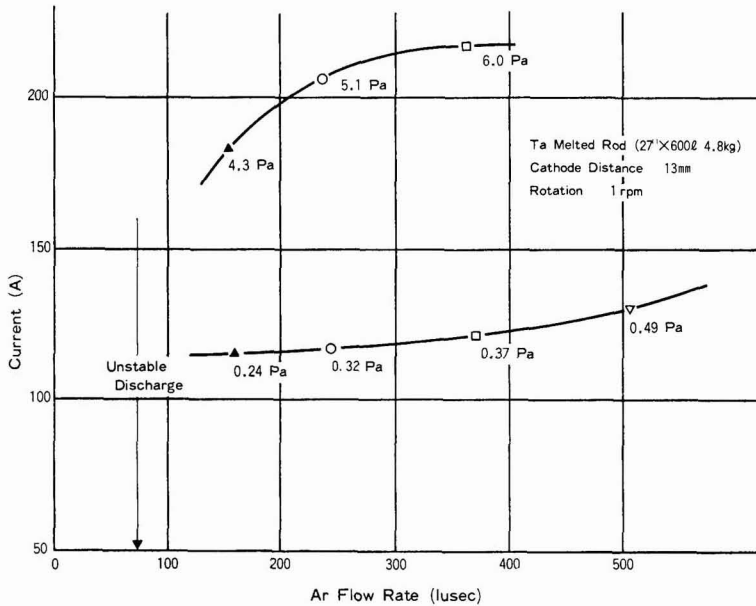


Fig. 11. Minimum current for Ta melting.

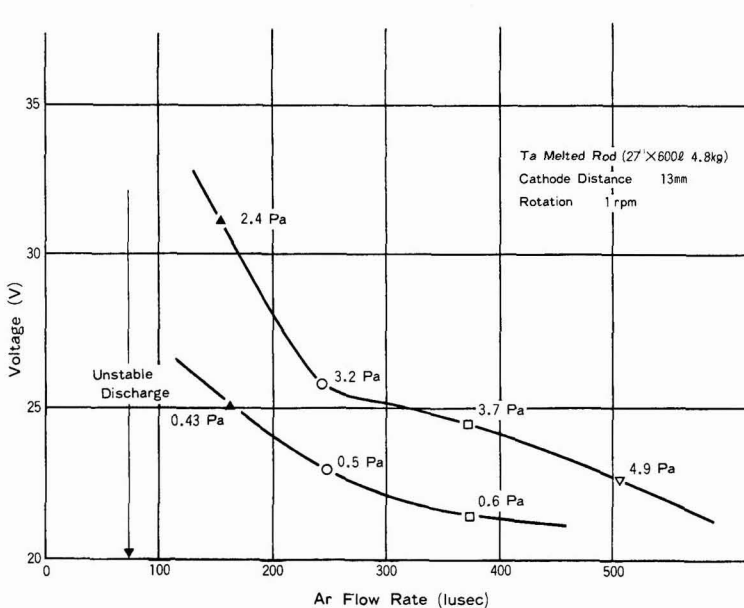


Fig. 12. Corresponding voltage for Ta melting.

plication is aimed at joining scraps to a satisfactory electrode, so a complete melt down of the charge is not required. Figure 9 illustrates melting operation. An example of the operating parameters are represented in Tables VII and VIII. Table IX represents the parameters for successive VAR operation. Table X represents the results of chemical analysis of the finished ingot.

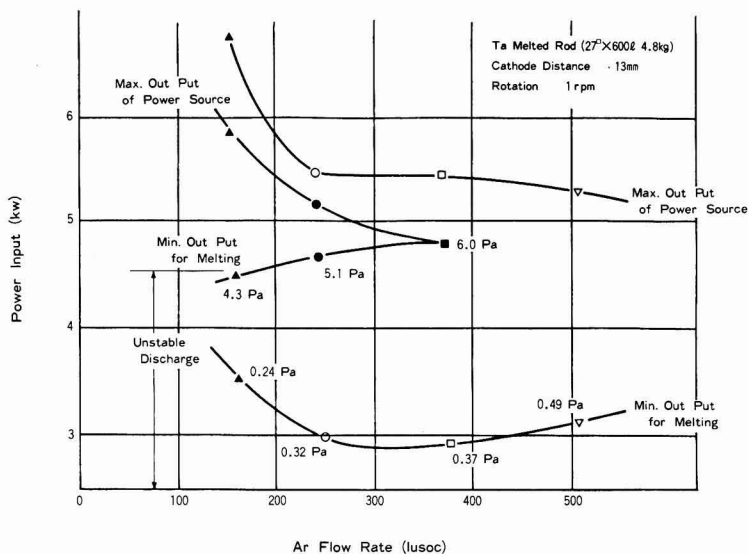
The addition of chromium is not required at least for several recyclings. This is a favorable result for actual production. Chromium loss as a whole is kept small because of the relatively short thermal history of the electrode. However, it will be required to add chromium if, for example, all scraps charged are of chips and thin sheets.

The VPEB is considered to be the ideal heat source for the direct recovery of Zircaloy scraps. VPEB is operable at low voltage and medium to high vacuum. There is no danger of damage to the water crucible with sufficient power density to melt down refractory metals. Power input can be controllable and maintained constant for as much time as is required. Practically any shape of raw stock can be charged.

#### Melting Tantalum by Using VPEB

Tantalum ingot is conventionally produced by using either a vacuum arc (VA) furnace or high voltage electron beam (HVEB) furnace. A vacuum sintering (VS) furnace has been an alternative for producing smaller rod shapes. An example of VPEB melting,

Fig. 13. Electrical power input vs. operating flow rate.



which is new, economical, versatile, easy for maintenance and operation, and produces a similar grade of purification to that of HVEB, is presented in this paper.

Figure 10 illustrates a schematic of the equipment. Melting and purification of a tantalum rod or ingot by using the VPEB is aimed at. A mechanical drive gives rotation and push-pull transfer motion to the tantalum rod through vacuum-tight seals while VPEB melts the surface. A quadrupole residual gas analyzer (RGA) is used for dual purpose: monitoring the purity of background environment and gaseous or vapor composition degassed during the melting. Partial pressure of any active gases or vapors which may react with hot tantalum must be kept below a certain level. Argon pressure to keep VPEB is roughly between  $3 \times 10^{-1}$  and 10 Pa measured in the vacuum chamber. Figures

11 and 12 illustrate the minimum current and corresponding voltages required for melting the tantalum surface, respectively. Shift of operating pressure was made by changing pumping speed and argon flow rate.

Figure 13 represents electrical power input vs. operating flow rate. Table XI summarizes a comparison of operating parameters at the two typical conditions. Details of basic experiment and data were published elsewhere (1, 2). Table XII represents some of the purification effects obtained for surface melting of powder compacts  $22 \text{ mm } \phi \times 500 \text{ mm L}$ , 76% density made by hydrostatic compaction of 100 mesh Ta. Carbon powder was additionally mixed for the No. 02 series in order to promote oxygen removal by CO reaction. The result indicates that partial pressure of  $\text{H}_2\text{O}$  and the total pressure played a major role in this case. Figures 14 and 15 represent monitored gas composition during the processing.

A new product, SMTR (3) (surface melted tantalum rod) is an example of optimized use of VPEB. The SMTR has pure, dense, and sound surface made by VPEB melting while the inside (central portion) of the rod is composed of sintered smaller density tantalum. Figure 16 represents an example of the process flow. Figure 17 illustrates the purification effect at the surface. Figure 18 illustrates radial density variation from the surface to the center. Average density before and after surface melting is 76% and 88%, respectively. The fabricated square rod  $5 \times 5 \text{ mm}$  cross section and annealed at  $1200^\circ\text{C}$  1 hr showed mechanical properties represented in Table XIII, which is, by far, over the specification JIS H4701. Similar surface treat-

Table XI. VPEB operating parameters

Ta melted rod ( $22\phi \times 500 \text{ L}$  3.15 kg)

Ar flow rate (lusc)	Pressure (Pa)	Power Input	Pool depth (mm)	Pool diameter (mm)
250	4.3	220A (5.15 kW)	1.2-1.5	3-4
250	0.27	220A (5.45 kW)	5.0-7.0	15-17

Cathode: Ta  $7\phi \times 8\phi \times 55 \text{ L}$ . Cathode distance: 13 mm. Rotating speed: 1 rpm.

Table XII. Surface purification effect of SMTR

Sample No.	Surface before melting O <sub>2</sub> ppm C ppm	Surface after melting O <sub>2</sub> ppm C ppm	Surface hardness after melting Hv (1 kg)	Pressure (Pa)	P <sub>H<sub>2</sub>O</sub> (Pa) before melting ↓ melting	P <sub>O<sub>2</sub></sub> (Pa) before melting ↓ melting
01-5	810	490	172	5.1	0.05	$7 \times 10^{-4}$
02-1	47	8	172	5.1	0.13	$7 \times 10^{-4}$
	920	420	175	5.1	0.05	
01-7	410	30	175	5.1	0.13	$5 \times 10^{-6}$
	870	111	86	0.33	0.009	
02-3	42	6	86	0.33	0.01	$4 \times 10^{-4}$
	940	142	82	0.33	0.008	$8 \times 10^{-6}$
	530	24	82	0.33	0.01	$4 \times 10^{-4}$



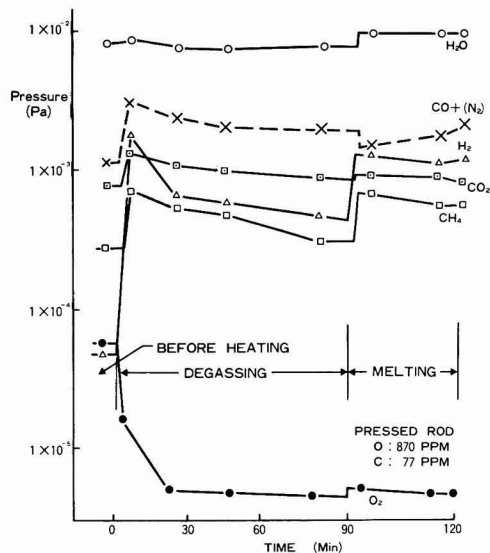


Fig. 14. Gas composition during Ta melting (1)

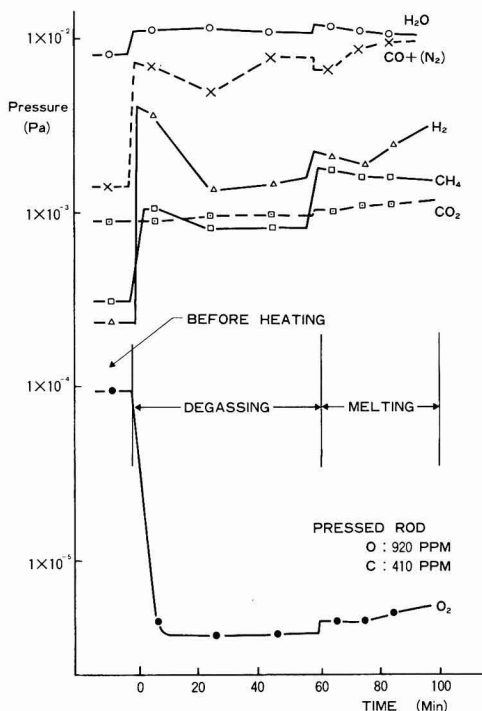


Fig. 15. Gas composition during Ta melting (2)

ment applied for VA melted ingot eliminates surface machining and results in more utilization of the precious metal. A few percent of evaporation loss which is unavailable in the case of HVEB purification is not necessarily the case for SMTR. That is also valuable for saving tantalum metal.

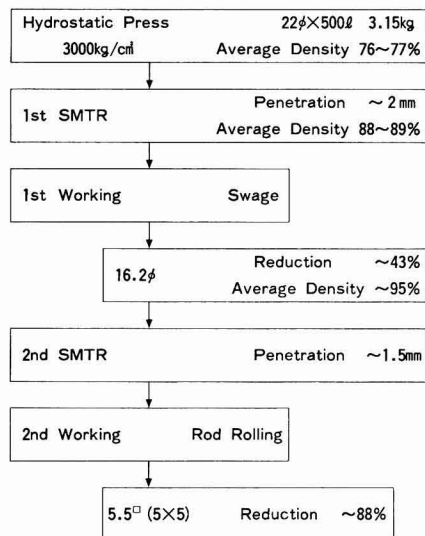


Fig. 16. Process of SMTR

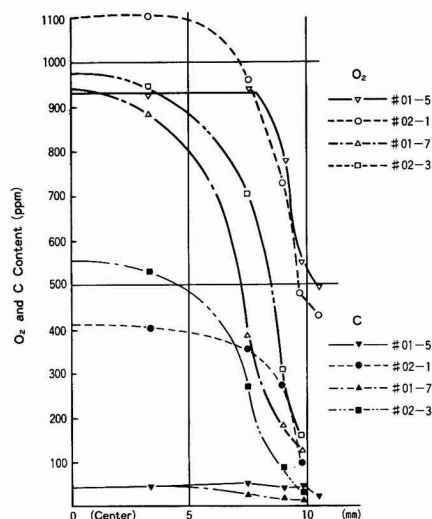


Fig. 17. Purification effect at the surface of the SMTR

Major operating parameters to be considered in the VPEB are listed as follows: (i) voltage, (ii) current, (iii) cathode to target distance, (iv) flow rate of operating gas, (v) vacuum pressure of operating gas, and (vi) impurity levels of residual gases. Geometrical configurations of structures inside the vacuum cham-

Table XIII. Mechanical properties of SMTR processed Ta rod\*

Tensile strength (kg/mm <sup>2</sup> )		Elongation (%)	
46.4	Average	57	Average
46.9	46.7	53	47
46.8		31	

\* Size: 5 × 5 mm. Heat-treatment: 1200°C × 1 hr. JIS specifications: JIS H4701: Tap-0, tensile strength (kg/mm<sup>2</sup>) >25; elongation (%) >25; and Tap-1/4 H, tensile strength (kg/mm<sup>2</sup>) >35; elongation (%) >20.

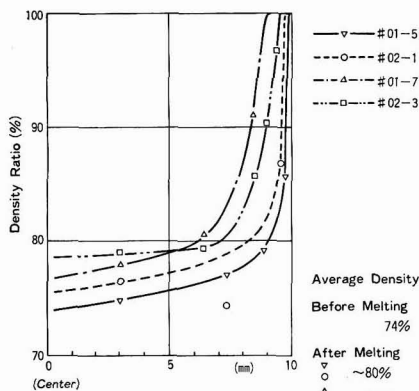


Fig. 18. Radial density variation of SMTR

ber should be paid due consideration with respect to gas flow pattern and electrical field distribution. Magnetic confinement can improve concentration of the plasma, with additional expense.

In summary, application of VPEB requires careful design of system. Operation of VPEB, however, has big advantages in reliability (stability) and safety over VA or HVEB. VPEB is usable for producing both large ingots and small diameter rods starting from

powder compact, sponges, or any shape of raw stock. It is also usable for controlled heating which verifies application in a variety of heat-treatments. Energy density at a target surface can be as high as  $10^4$  kW/cm<sup>2</sup>, which is sufficient for surface melting of refractory metals and alloys. VPEB can often be an alternative short-cut process of an existing production line; valuable for rationalization or saving labor, energy, and thus cost.

#### Acknowledgments

The authors are indebted to Mr. H. Takei and his group, ULVAC Corporation, for the design and manufacture of the VPEB scrap recycle furnace. Mr. K. Yoshida, Vacuum Metallurgical Corporation, gave helpful advice throughout this study.

Manuscript received May 7, 1980. This was Paper 300 presented at the St. Louis, Missouri, Meeting of the Society, May 11-16, 1980.

Any discussion of this paper will appear in a Discussion Section to be published in the June 1982 JOURNAL. All discussions for the June 1982 Discussion Section should be submitted by Feb. 1, 1982.

Publication costs of this article were assisted by the Vacuum Metallurgical Company, Limited.

#### REFERENCES

1. S. Kashu, S. Nishino, and C. Hayashi, in Trans. 10th Vac. Met. Conf., pp. 771-798 (1967).
2. S. Kashu, S. Nishino, and C. Hayashi, in Trans. 3rd Intern. Conf. Electron and Ion Beam Science and Technology, pp. 221-235 (1968).
3. Patent pending.

## The Formation of SiO<sub>2</sub> in an RF Generated Oxygen Plasma

### I. The Pressure Range Below 10 mTorr

A. K. Ray\* and A. Reisman\*

IBM Thomas J. Watson Research Center, Yorktown Height, New York 10598

#### ABSTRACT

This paper deals with the formation of SiO<sub>2</sub> on silicon in an rf generated oxygen plasma in the pressure range below 10 mTorr. A companion paper describes the behavior of the oxide growth process in the pressure range above 10 mTorr. The oxide was formed in an open-tube pumped fused silica system without substrate biasing. Oxide formation rate was studied as a function of substrate temperature, conductivity type, resistivity, distance from the end of the plasma generating coil, oxygen pressure, and generator power output. Based on the results obtained on masked substrates, using the silicon-mask interface as a marker, it was determined that within the limits of experimental error, all the oxide formed in the pressure range studied was deposited on the surface and not a result of oxidation. The rate of deposition increased with increasing power, decreasing pressure, and decreasing wafer to plasma generation zone distance. This rate was temperature independent and was unaffected by substrate parameters. Excellent uniformity was obtained over 56 mm diam wafers,  $\pm 3-5\%$ . The properties of the oxide deposited at 600°C and above are only slightly poorer than thermal oxides grown at 1000°-1100°C. They exhibit somewhat higher fixed charge and interface state density while the breakdown strength, etch rate, and refractive index are essentially the same as thermal oxides. A key observation of the plasma process conducted at pressures below 10 mTorr is that the oxide always forms on the silicon surface facing the plasma. This is opposite to the results obtained at higher pressures described in Part II of this study.

It is to be anticipated that as semiconductor devices are scaled to smaller dimensions, i.e., less than 1  $\mu$ m ground rules, currently employed chip processing tem-

peratures will tend to become incompatible with desired device designs, because impurities present in shallow junctions and/or in surface threshold adjusting layers will tend to redistribute. The problem will be compounded further by surface depletion of im-

\* Electrochemical Society Active Member.  
Key words: silicon, plasma, oxidation, SEM.

purities during oxidation (1), oxidation enhanced diffusion effects (2), and the generation of substrate defects (2, 3). Two of the primary high temperature processes to be contended with are oxidation, and ion implantation damage annealing and activation.

As a first step in evolving a lower temperature processing sequence, the authors have focused on the oxidation process. One might assume, initially, that the lower the temperature at which one can conduct an oxidation process, the better. This is not necessarily true from a stress point of view. If, for example, the intrinsic stress at the oxide formation temperature tends toward zero, then any temperature excursions above this temperature will force the oxide into tension, making it susceptible to cracking at mask opening corners. To minimize this problem, oxidation processes should be conducted at the highest possible temperature consistent with impurity redistribution, surface depletion, and defect generation constraints.

High pressure and plasma oxidation processes both offer potential for use at lower temperatures. The high pressure approach (4, 5) is in current use, but for large areas (5) is conducted only in wet oxygen ambient atmospheres, and at moderate pressures, up to 25 atm. In dry oxygen, pressures in excess of 100 atm would be required (4) to achieve oxidation rates comparable to wet oxidation. Such a pressure-temperature combination is not achieved readily on a practical basis for a variety of technical reasons which will be discussed by us at a later time. Very high oxidation rates have, however, been reported using plasma anodization approaches (6-15) at temperatures as low as 170°C (12). Two general problems encountered in using plasma approaches have been the difficulty in achieving uniform growth over areas greater than 1-2 cm<sup>2</sup> (6, 7) and the generally poor electrical and defect characteristics of the oxides (7, 12). Partial resputtering of the grown oxides has been considered by Kraitchman (8) and others (12, 13), but none of the reports considered seriously the possibility of sputtering from the walls of the reaction chamber onto the wafer surface as an effect to be contended with. In addition, using presumably similar experimental techniques, different workers have obtained significantly different results. Lingenza (6) reported power and temperature dependencies, but no substrate bias voltage dependency on oxidation rate. He also found parabolic growth behavior for biased oxidations and non-parabolic growth in unbiased oxidations. Skelt and Howells (7) and Kraitchman (8), however, saw no temperature dependency, and Kraitchman implied that there was no power dependency. Furthermore, Kraitchman found parabolic growth behavior for both biased and unbiased oxidations, even when constant current biasing (as opposed to constant voltage) was employed. Pulfrey and Reche (12), on the other hand, observed linear kinetics in constant current anodizations.

The present study was prompted by the noted discrepancies among the reported results and by a desire to see if uniform growth could be achieved over large areas. In addition, it was desired to operate in an electrodeless system to avoid possible electrode sputtering contamination effects. It was felt also that the plasma and sample temperatures should be independently controllable to a degree at least, by separating the plasma generation and oxidation zones, and that the effects of temperature and power on both oxide quality and growth kinetics required better understanding. Independent temperature control was accomplished by separating the plasma generation and oxidation zones, with the sample being placed at predetermined distances from the plasma generation zone in a resistance-heated portion of a reaction chamber. Excited species drift from the plasma generation region to the oxidation zone at the drift velocity of the low pressure flowing gas.

This paper deals with the pressure regime below 10 mTorr while a companion paper, Part II, is concerned with the pressure regime > 10 mTorr for reasons which will become obvious.

### Experimental Techniques

The experimental setup for plasma oxidation in the pressure regime below 10 mTorr is shown schematically in Fig. 1. Ultrahigh purity bottled oxygen (99.999%) was purified further by heating to 1000°C in a quartz chip bed to decompose any hydrocarbons present to  $\text{CO}_2$  and  $\text{H}_2\text{O}$ . These contaminants were removed subsequently in a liquid nitrogen trap. The liquid nitrogen trap could be used to remove  $\text{CO}_2$  and  $\text{H}_2\text{O}$  without liquefying the oxygen because the oxygen pressures employed (2-100 mTorr) were less than the vapor pressure of oxygen at the boiling point of nitrogen. The vapor pressures of  $\text{CO}_2$  and  $\text{H}_2\text{O}$  at liquid nitrogen temperature are estimated to be of the order of  $10^{-5}$  and  $10^{-8}$  mTorr, respectively. For an operating pressure of 10 mTorr, this corresponds to maximum values of 1 ppm of  $\text{CO}_2$  and 1 ppb of  $\text{H}_2\text{O}$  in oxygen, assuming equilibrium obtains. The purified oxygen was used to generate an oxygen plasma in the 80 mm ID, 100 cm long fused silica reaction chamber by a variable frequency (0.5-8 MHz) rf generator. All experiments were conducted at 0.5 MHz unless otherwise specified. Electrical coupling to the system was effected by a six turn coil of 0.25 in. OD Cu tubing placed around the reactor tube and connected to the rf generator by appropriate cables. In our experimental system, only the generator output power was known. An estimate of the power input to the plasma could not be made. Hence, a variation of the generator output power was considered as a variation of the power input to the plasma. The coupling mechanism was assumed not to change with power and pressure variations. The system was pumped continuously during the experiments, and the pressure in the chamber was controlled by regulating the oxygen mass flow into the reaction chamber using a mass flow controller. The pressure in the reaction chamber was measured by a thermocouple gauge located at the exit end of the reaction tube. In order to avoid coupling to the rf field, the thermocouple gauge was placed remote to the plasma generating region. Most of the silicon wafers used were 56 mm diam p-type with a nominal resistivity of 10  $\Omega$  cm. The wafers were cleaned prior to an experiment by a process described elsewhere (16). A wafer was placed, on a quartz sample holder, perpendicular to the direction of gas flow. The temperature of the wafer was, as mentioned above, varied and controlled by an external resistance heated furnace. The temperature of the wafer was measured by a Chromel-Alumel thermocouple placed adjacent to it.  $\text{SiO}_2$  film thickness was measured using an IBM 7840 Film Thickness Analyzer (17). The IBM 7840 F.T.A. measures combined reflectance of the films and substrate in the wavelength range of 380-750 nm and computes the thickness of the film from the optical constants of

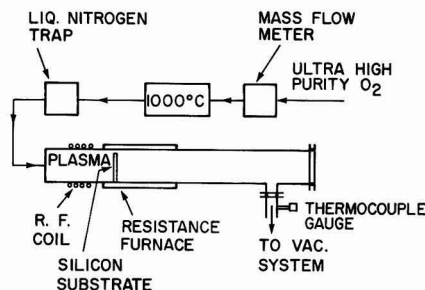


Fig. 1. Schematic diagram of the experimental plasma oxidation system.

the film and substrate. The film thicknesses measured by the F.T.A. were checked with the values obtained ellipsometrically and found to agree to better than  $\pm 5\%$ . Since the IBM 7840 F.T.A. can be programmed to measure oxide thickness automatically at 21 predetermined locations over the entire wafer, and is much more rapid in use than the ellipsometric measurement available to us, it was used to gather the uniformity data. The electrical properties of plasma  $\text{SiO}_2$  were determined by measurements of fixed charge density, surface-state density, and electrical breakdown strength in conventional fashion, i.e., C-V measurements and ramp voltage breakdown measurements.

### Results and Discussions

In an initial experiment, a silicon wafer was placed perpendicular to the direction of gas flow 20 cm downstream from the end of the rf induction coil. The temperature of the wafer was maintained at  $650^\circ\text{C}$ . An oxygen plasma was generated at 5 mTorr and a generator output power of 4.5 kW at 0.5 MHz. About 50 nm of  $\text{SiO}_2$  was formed in 4 hr on the surface of the wafer facing the plasma. No  $\text{SiO}_2$  was formed on the other side of the wafer. Thickness uniformity of the  $\text{SiO}_2$  film formed was better than  $\pm 5\%$ . Under the same conditions, but with increasing pressure in the chamber, the thickness of  $\text{SiO}_2$  formed decreased significantly. Consequently, to study the effect of pressure on oxide formation, the generator output power was subsequently increased to 7 kW to increase oxide thickness to reasonable values. Figure 2 shows the thickness of  $\text{SiO}_2$  formed in 4 hr as a function of system oxygen pressure at 7 kW. The pressure was changed simply by changing the rate of oxygen input to the system. Since pressure was found to vary linearly with oxygen input rate in the pressure range studied, the flow rate and, therefore, the linear gas stream velocity were constant. The oxygen flow rate was  $2.1 \text{ scm}^3/\text{min}$  at 30 mTorr pressure, and the linear gas stream velocity was 20 cm/sec. As seen in Fig. 2, the oxide thickness obtained after 4 hr shows two distinct regimes when plotted in log-log fashion. The oxide thickness decreases from 350 nm in 4 hr at 1.5 mTorr to 40 nm in 4 hr at 7 mTorr with approximately a 1.4 power dependency on pressure. Above 7 mTorr, the rate decreases much more slowly, i.e., to the 0.1 power. Even with the high (7 kW) output power employed, the  $\text{SiO}_2$  thickness at 30 mTorr is only 34 nm in 4 hr. If one wants rapid growth, it is evident from Fig. 2 that the operating pressure should be as low as possible in the experimental configuration described. An operating pressure of 2.5 mTorr was then chosen for the low pressure studies, because below 2.5 mTorr

it was difficult to ignite and maintain an oxygen plasma. The behavior at this pressure is representative of the range up to about 10 mTorr. The variation of oxide thickness with position of the silicon wafer outside the confines of the rf coil was studied at  $650^\circ\text{C}$ , 2.5 mTorr and 4.5 kW generator output power. Figure 3 shows the data obtained in a 2 hr series of growth experiments. The oxide thickness decreases sharply with increasing distance up to 12 cm. At distances greater than 12 cm, the oxide thickness remains more or less constant. As the thickness uniformity was found to vary more in the region from 7-12 cm than in the region greater than 12 cm, a distance of 20 cm from the end of the rf coil was then chosen for most of the experiments. Experiments were also conducted with the wafer in a horizontal position. The rate of  $\text{SiO}_2$  formation was greatly reduced compared to vertical mounting, and a significant  $\text{SiO}_2$  thickness gradient was generated across the axial direction of the wafer.

The effect of generator output power on the thickness of oxide formed in 1 hr was studied at  $650^\circ\text{C}$  and 2.5 mTorr, the wafer being placed vertically at a distance of 20 cm from the end of the rf coil. With increasing power, the oxide thickness increases linearly with power up to 6 kW and above 6 kW, the oxide thickness increases as  $(\text{power})^{4.5}$ , Fig. 4, but as might be expected from the large slope of the curve, the thickness uniformity of the  $\text{SiO}_2$  formed was poor at the higher power. An output power of 4.5 kW yields a reasonable oxide formation rate and good thickness uniformity. With the preceding as a basis for choosing a usable set of experimental conditions, the kinetics of  $\text{SiO}_2$  formation were studied at 2.5 mTorr  $\text{O}_2$  pressure, 4.5 kW of generator output power, and the silicon wafer placed vertically at a distance of 20 cm from the end of rf coil. Figure 5 shows the thickness of  $\text{SiO}_2$  formed at  $600^\circ\text{C}$  as a function of time. It is seen from Fig. 5 that the oxide thickness varies linearly with time in the entire oxide thickness range up to 160 nm. Thermal oxidation of silicon at high temperatures in dry oxygen, of course, follows linear parabolic kinetics to a first approximation. The proposed model of a conventional thermal oxidation process (18) is that there are three basic steps: (i) the transfer of oxidant from the gas phase to  $\text{SiO}_2$  at the gas- $\text{SiO}_2$  interface; (ii) the transport of oxidant through the  $\text{SiO}_2$  to the Si- $\text{SiO}_2$  interface and (iii) the reaction of oxidant with Si to form  $\text{SiO}_2$  at the Si- $\text{SiO}_2$  interface. In a film growth process, the step (i), depending on the temperature, linear gas stream velocity, and the film thickness, may or may not be rate limiting (19). In a conventional thermal oxidation process, step (i)

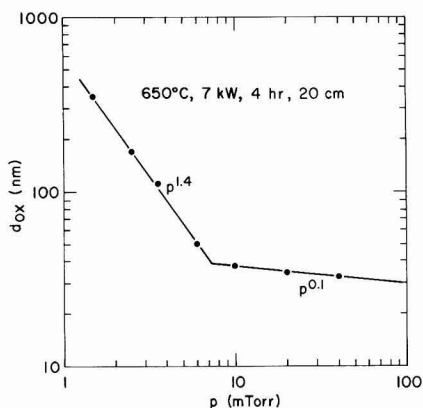


Fig. 2. Thickness of  $\text{SiO}_2$  formed at  $650^\circ\text{C}$  in 4 hr as a function of system oxygen pressures.

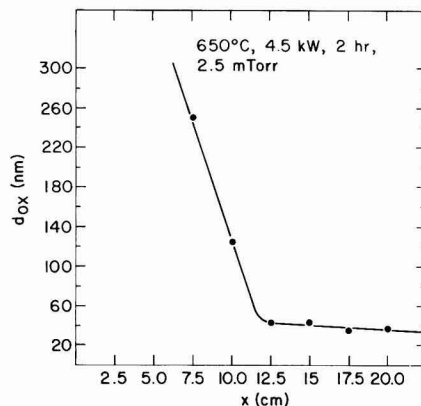


Fig. 3. Thickness of  $\text{SiO}_2$  formed at  $650^\circ\text{C}$  in 2 hr as a function of distance of the wafer from the end of rf coil.

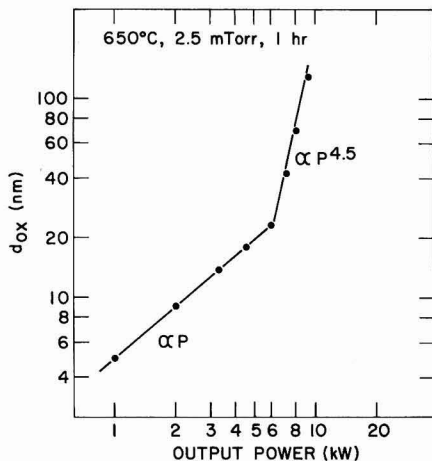


Fig. 4. Thickness of  $\text{SiO}_2$  formed at 650°C in 1 hr as a function of generator output power.

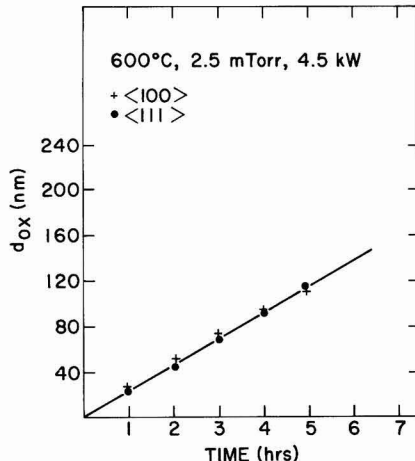


Fig. 6. Thickness of  $\text{SiO}_2$  formed at 600°C as a function of time for <111> and <100> oriented silicon wafers.

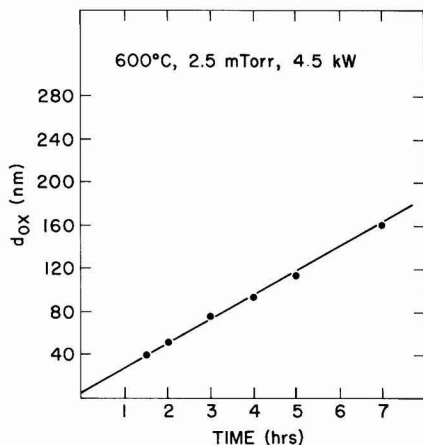


Fig. 5. Thickness of  $\text{SiO}_2$  formed at 600°C as a function of time

is usually not rate limiting. The step (ii), if it is a diffusion-controlled process, follows parabolic kinetics. The third step determines the oxidation rate and follows linear kinetics. If step (iii) alone determines the rate of oxidation, then the rate of oxidation should depend on the temperature, the orientation, and the doping level of silicon wafers and should not depend on oxide thickness.

Figure 6 shows the thickness of  $\text{SiO}_2$  formed at 600°C as a function of time for <111> and <100> orientated Si wafers. The rate of  $\text{SiO}_2$  formation on <111> surfaces is seen to be the same as that on <100> Si wafers while both are seen to be linear with time. Oxide formation was found not to depend on silicon dopant concentration either. Figure 7 shows the thickness of oxide formed in 3 hr at 600°C for both p- and n-type wafers of different resistivities. Oxide formation rate was found to be independent of temperatures also. Figure 8 shows the thickness of  $\text{SiO}_2$  formed as a function of time for three different temperatures. In another series of experiments, about 307.5 nm of dry thermal  $\text{SiO}_2$  were first grown at 1000°C on Si wafers, and these wafers were then used as substrates for subsequent plasma experiments. Figure 9 shows the oxide thickness of these wafers as a function of time of ex-

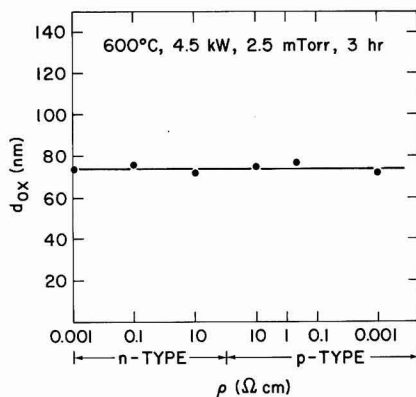


Fig. 7. Thickness of  $\text{SiO}_2$  formed at 600°C in 3 hr for wafers of different resistivities.

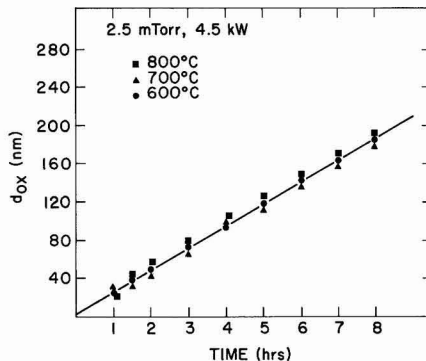


Fig. 8. Thickness of  $\text{SiO}_2$  formed as a function of time at 600°C, 700°C, and 800°C.

posure to the oxygen plasma. The oxide thickness still increases linearly with time, and the rate of increase is the same as that observed for bare silicon wafers. The data for bare silicon wafers is taken from Fig. 8. From

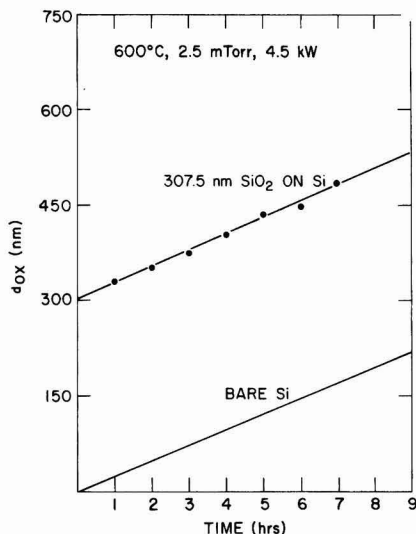


Fig. 9. Thickness of SiO<sub>2</sub> formed at 600°C as a function of time for starting silicon wafers with 307.5 nm of dry thermal SiO<sub>2</sub>.

the above experimental results, it would appear that the second process does not determine the rate of formation of SiO<sub>2</sub> under the growth conditions studied. Furthermore, the temperature, wafer orientation, and resistivity independence of oxide formation rate made questionable the possibility that the linear kinetics observed are due to a combination of steps (i) and (iii) and raised the possibility that the oxide formed in our experiments was not the result of a reaction between silicon and oxygen, but was due to a deposition of SiO<sub>2</sub> in the fused silica reaction chamber at the high rf generator output power and low operating pressure employed. The possibility existed that SiO<sub>2</sub> or a silicon oxygen species, e.g., SiO sputtered from the wall of the reaction chamber, could react with oxygen and deposit SiO<sub>2</sub> on the silicon wafers. In order to test this hypothesis, a silicon wafer was partially masked with Al (400 nm thick) and then exposed to the plasma under the standard set of conditions described. After about 800 nm of SiO<sub>2</sub> was formed, the wafer was cleaved, the Al was etched in dilute HCl, and the cross section was examined in an SEM. It is clear from the

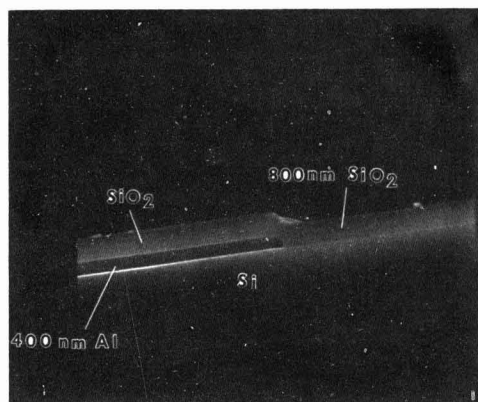


Fig. 10. SEM micrograph of the cross section of a silicon wafer after SiO<sub>2</sub> formation.

SEM micrograph (Fig. 10) that SiO<sub>2</sub> formed on both the exposed Si surface as well as over the Al, indicating that the SiO<sub>2</sub> is deposited oxide. Using the silicon-aluminum interface as a marker, it appears that very little, if any, silicon is oxidized during this process. Whether SiO<sub>2</sub> molecules are sputtered as such, and then deposited, or whether a species such as SiO is sputtered which reacts with oxygen homogeneously or at the silicon surface to form SiO<sub>2</sub> could not be determined. We consider the direct sputtering of SiO<sub>2</sub> to be unlikely since the properties of the deposited SiO<sub>2</sub> are quite different from those of conventionally sputtered silica (20). The refractive index of oxides deposited at 600°C and at lower temperatures was measured by ellipsometry at 632.8 nm and was in the range 1.461-1.465. The etch rate of the plasma deposited SiO<sub>2</sub> was comparable to that of dry thermal SiO<sub>2</sub> grown at 1000°C. The etch rates were compared by etching simultaneously the thermal and plasma oxides in 1:9 (49% HF:40% NH<sub>4</sub>F) solution at room temperature. The etch rate was determined by measuring the change in oxide thickness during etching. The etch rates at room temperature were in the range of 74-76 nm/min. In order to evaluate the electrical properties of the plasma-deposited SiO<sub>2</sub>, about 75 nm of plasma deposited was formed on 2 Ω cm p-type <100> oriented Si wafers at 600°C. No other high temperature heat-treatment was given to the oxide. Aluminum dots 32 mil in diameter were evaporated on the oxide through a metal mask. Aluminum was also evaporated on the back side of the wafers for electrical contact. A post-metallization anneal in forming gas at 400°C for 20 min was given to the capacitors. Figure 11 shows the high frequency C-V curve of these capacitors. The high frequency C-V curve was obtained at 1 MHz with a voltage ramping rate of 0.2 V/sec. Well-defined inversion and accumulation regions were obtained. The hysteresis effect observed between the inversion and accumulation regions may be due to the presence of a large number of surface states. Surface-state density measured by the quasi-state technique was about 10<sup>12</sup>/cm<sup>2</sup> eV at midgap. With surface-state density so high, the expression for V<sub>FB</sub> in terms of fixed positive charge becomes complicated. So effective charge density (Q<sub>f</sub>) was calculated from the flatband voltage (V<sub>FB</sub>) determined via the high frequency C-V curve according to the formula

$$V_{FB} = \phi_{ms} - \frac{Q_f}{C_{ox}}$$

where  $\phi_{ms}$  = work function difference between Al and the semiconductor, taken as -0.7V for 2 Ω cm p-type silicon,  $C_{ox}$  = oxide capacitance per unit area, and  $Q_f$  = effective charge per unit area.

The calculated effective charge density from the V<sub>FB</sub> is  $1.3 \times 10^{-3}$  C/m<sup>2</sup> which is equivalent to  $8 \times 10^{11}$ /cm<sup>2</sup> singly charged centers. A high temperature (1000°C) postoxidation heat-treatment was given to some wafers, but this did not reduce effective charge density appreciably. Electrical breakdown strength was measured on one hundred Al-SiO<sub>2</sub>-Si capacitors in accumulation. Figure 12 is a histogram showing the

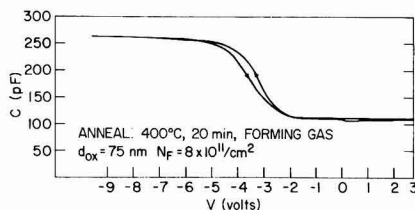


Fig. 11. High frequency C-V curve of plasma deposited SiO<sub>2</sub> capacitors after postmetallization anneal in forming gas at 400°C for 20 min.



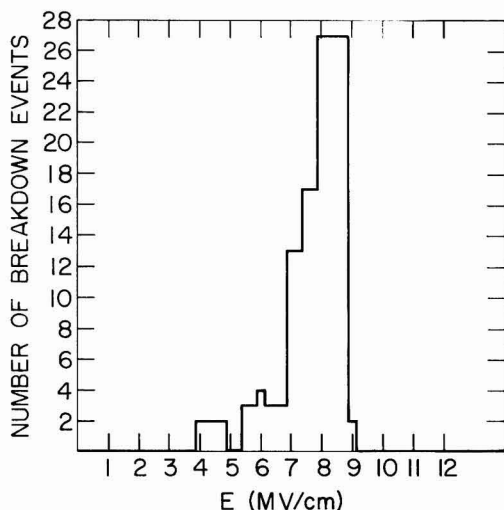


Fig. 12. Histogram showing the number of breakdown events at different breakdown strengths for one hundred plasma SiO<sub>2</sub> capacitors.

number of breakdown events at different breakdown strengths. The breakdown strength is high and there are few low field breakdown events.

### Conclusions

From our experimental results, it can be concluded that the SiO<sub>2</sub> formed on the surface of a silicon wafer facing the plasma in a low pressure (<10 mTorr) oxygen plasma is deposited oxide. The deposited oxide is believed to be sputtered material from the wall of the quartz reaction plasma. The exact mechanism (sputtering or reactive sputtering) of SiO<sub>2</sub> formation is not clear. Since the properties of the deposited oxide bear more of a resemblance to thermal oxides grown at 1000°C than sputtered oxide, we believe that reactive sputtering is the mechanism of oxide formation. The rate of oxide deposition increases with increasing power input to the plasma and decreasing pressure and distance of the wafer from the plasma. The increase of oxide formation rate with decreasing pressure is due to the fact that at pressures less than 10 mTorr, wall sputter deposition appears to be the primary mechanism of oxide formation. The sputtering phenomenon leading to deposition rather than oxidation is a function of pressure only and does not depend on the distance of the wafer from the plasma generating zone. Clearly, however, the rate of deposition in such a process will depend on the distance. Very uniform deposits are obtained only under certain experimental conditions. The use of high power or positioning the wafer

too close to the plasma results in less uniform deposits. The properties of the deposited oxide are probably related to the purity of the quartz reaction chamber. Refractive index, etch rate, and electrical breakdown strength of the oxides deposited at 600°C are comparable to those of thermal SiO<sub>2</sub> grown at 1000°C. Fixed charge and surface state densities are higher. Limited results indicate that the oxides deposited at lower temperatures have properties similar to those deposited at 600°C. This technique thus may have potential for forming passivation layers for interconnections where conventional high temperature CVD methods cannot be used. The companion paper that follows describes the plasma system behavior at pressures greater than 10 mTorr which is dramatically different from that described here.

Manuscript submitted Dec. 18, 1980; revised manuscript received April 27, 1981. This was Paper 167 presented at the St. Louis, Missouri, Meeting of the Society, May 11-16, 1981.

Any discussion of this paper will appear in a Discussion Section to be published in the June 1982 JOURNAL. All discussions for the June 1982 Discussion Section should be submitted by Feb. 1, 1982.

Publication costs of this article were assisted by IBM Corporation.

### REFERENCES

1. B. E. Deal, A. S. Grove, E. H. Snow, and C. T. Sah, *This Journal*, **112**, 308 (1965).
2. S. M. Hu, *J. Appl. Phys.*, **45**, 1567 (1974).
3. S. P. Murarka, *ibid.*, **48**, 5020 (1977).
4. R. J. Zeto, C. G. Thornton, E. Hryckowian, and C. D. Bosco, *This Journal*, **122**, 1409 (1975).
5. H. Mioshi, N. Tsubouchi, and A. Nishimoto, *ibid.*, **125**, 1824 (1978).
6. J. R. Ligenza, *J. Appl. Phys.*, **36**, 2703 (1965).
7. E. R. Skelt and G. M. Howells, *Surf. Sci.*, **7**, 490 (1967).
8. J. Kraitchman, *J. Appl. Phys.*, **38**, 4323 (1967).
9. J. R. Ligenza and M. Kuhn, *Solid State Technol.*, **b33** (December 1970).
10. M. A. Copeland and R. Pappu, *Appl. Phys. Lett.*, **19**, 199 (1971).
11. D. L. Pulfrey, F. G. M. Hathorn, and L. Young, *This Journal*, **120**, 1529 (1973).
12. D. L. Pulfrey and J. H. Reche, *Solid State Electron.*, **17**, 627 (1974).
13. R. Dragila, L. Bardos, and G. Loncar, *Thin Solid Films*, **34**, 115 (1976).
14. L. Bardos, G. Loncar, I. Stoll, J. Musil, and F. Zacek, *J. Phys. D. Appl. Phys.*, **8**, L195 (1975).
15. J. Musil, F. Zacek, L. Bardos, G. Loncar, and R. Dragila, *ibid.*, **12**, L61 (1979).
16. E. A. Irene, *This Journal*, **121**, 1613 (1974).
17. IBM 7840 Film Thickness Analyzer, Product Information.
18. B. E. Deal and A. S. Grove, *J. Appl. Phys.*, **36**, 3770 (1965).
19. A. Reisman and M. Berkenblit, *This Journal*, **113**, 146 (1966).
20. W. A. Pliskin, P. D. Davidse, H. S. Lehman, and L. I. Maissel, *IBM J. Res. Dev.*, **11**, 4, 461 (1967).

# The Formation of $\text{SiO}_2$ in an RF Generated Oxygen Plasma

## II. The Pressure Range Above 10 mTorr

A. K. Ray\* and A. Reisman\*

IBM Thomas J. Watson Research Center, Yorktown Heights, New York 10598

### ABSTRACT

This paper describes the formation of  $\text{SiO}_2$  in an rf generated oxygen plasma in the pressure range above 10 mTorr. The experimental setup used for this study is the same as that described in Part I of this study. Using the silicon-mask interface as a marker and examining the cross section of silicon wafers after oxide formation, it was concluded that the mechanism of oxide formation in the pressure range 10-100 mTorr is growth of  $\text{SiO}_2$ . A unique and unexpected result of the plasma process conducted at pressures greater than 10 mTorr is that oxide growth occurs primarily on the surface of the wafer facing away from the plasma, in sharp distinction to the observations made at pressures less than 10 mTorr where the oxide forms only on the surface facing the plasma. A key experimental parameter is the confinement of the plasma by the wafer which was observed only at pressures greater than 10 mTorr and at generator frequencies from 0.5 to 3 MHz. Oxide growth rate was studied as a function of pressure, power, frequency of the applied field, and substrate parameters to determine the optimum growth conditions. The etch rate, refractive index, stress, fixed charge, interface states, and breakdown strength of plasma oxides grown at  $500^\circ\text{C}$  compare very favorably to thermal oxides grown at  $1100^\circ\text{C}$ .

In Part I of this study (1), it was concluded that the  $\text{SiO}_2$  formed in a low pressure oxygen plasma is a deposited oxide. The deposited oxide is believed to result from the sputtering of  $\text{SiO}_2$  or an oxygen-silicon species from the wall of the fused silica reaction chamber. Because of the long mean free path at low pressures, it is possible for the sputtered material to deposit on a wafer placed as far as 20 cm from the plasma generating region. The sputter yield is therefore expected to be minimized with increasing pressure and decreasing power input to the plasma. In this paper, we describe the *in situ* oxidation of Si at higher pressures and lower power in the plasma system. The results are unique in that at elevated pressures, not only does deposition cease, but oxidation occurs primarily on the silicon surface facing away from the plasma.

### Process and Kinetic Studies

When the operating pressure was increased to 30 mTorr and power output from the generator was reduced to 1 kW, no detectable  $\text{SiO}_2$  was formed on a silicon wafer placed at a distance of 20 cm from the end of the rf coil. Consequently, for experiments in the high pressure regime ( $>10$  mTorr), the wafer was placed closer (2 cm) to the coil. Under this condition, surprisingly, the plasma was confined by the wafer and the bulk of the  $\text{SiO}_2$  was formed on the surface of the wafer facing away from the plasma (the wafer back side) while a much thinner oxide was formed on the surface facing the plasma (the wafer front side). The high-low thickness uniformity of the oxide formed on the back side was better than  $\pm 5\%$  and the standard deviation was of the order of 1-3%. The thin oxide formed on the front surface was much less uniform. For example, on a 56 mm diam silicon wafer, there is a region around the wafer periphery where oxide thickness is considerably greater than in the central area. This region of greater oxide thickness increases with increasing oxidation time. After about 5 hr of oxidation at  $540^\circ\text{C}$ , there was a region 6 mm wide around the periphery where oxide thickness was about 200 nm as

compared to an average oxide thickness of about 65 nm in the central area. During the same oxidation time, about 300 nm of  $\text{SiO}_2$  was formed on the back side. An initial explanation for this observation that came to mind was that the oxide formed in equal amounts on both surfaces, but that the  $\text{SiO}_2$  formed on the surface facing the plasma was resputtered. In addition, it was to be determined whether the oxide films formed were wall-sputtered oxides, as was the case at low pressures, grown oxides, or combinations of the two with resputtering complicating the picture. To resolve these questions, the results required analysis according to the schematic representation depicted in Fig. 1. In Fig. 1, the expected wafer cross section is depicted for the possible cases, *in situ* growth only,

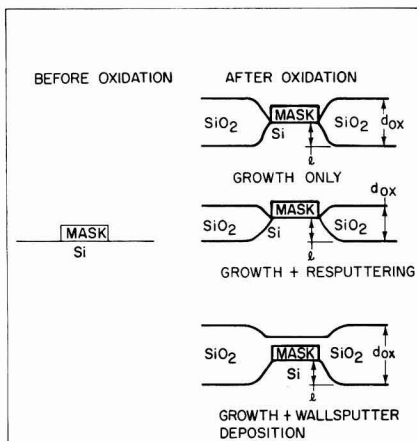


Fig. 1. Schematic representation of the cross section of a silicon wafer for the possible cases, growth only, growth + resputtering, and growth + wall-sputter deposition.

\* Electrochemical Society Active Member.  
Key words: silicon, plasma, oxidation, SEM.

growth plus resputtering, and growth plus wall-sputter deposition. On the left-hand side of Fig. 1 the situation before oxide formation is shown where part of the silicon area is masked against oxide formation. Using the silicon-mask interface as a marker, it is possible to distinguish among the possible cases mentioned earlier. If the  $\text{Si-SiO}_2$  interface is below the original silicon surface (silicon-mask interface), then clearly some of the  $\text{SiO}_2$  at least is being formed by a growth mechanism because silicon is consumed from the substrate during the oxide formation process. The thickness of  $\text{SiO}_2$  would be approximately twice the distance ( $l$ ) of the  $\text{Si-SiO}_2$  interface below the silicon-mask interface. This value should equal the measured oxide thickness ( $d_{ox}$ ) if resputtering and deposition are both absent. If growth and resputtering take place simultaneously and the rate of resputtering is less than the rate of growth, then for the same amount of oxidation, as in the case above, the  $\text{Si-SiO}_2$  boundary will be at the same distance ( $l$ ) from the  $\text{Si-mask}$  interface, but the measured oxide thickness ( $d_{ox}$ ) will be less than  $2(l)$  and there will be thickness asymmetry relative to the marker. If growth and wall-sputtering take place simultaneously, then oxide would form over the mask as well as on the silicon substrate. As a result, the apparent thickness of the masking layer would change after oxide formation, and the  $\text{SiO}_2$  boundary would again be unsymmetrical with respect to the silicon-mask interface. If the resputtering rate is greater than the growth rate, no oxide would be detected and the unmasked silicon surface would drop below the silicon-mask interface. Finally, if all processes occur simultaneously, e.g., deposition, oxidation, and resputtering, mask thickness would increase, and asymmetry around the mask level would result except in the unlikely event that the resputtering rate and deposition rate are identical. 200 nm thick  $\text{MgO}$  was used as a mask to examine these possibilities. The reason for selecting  $\text{MgO}$  as a mask is discussed later. Figure 2 is an SEM micrograph of the cross section of a silicon wafer after oxide formation on the  $\text{MgO}$  masked silicon surface which faces away from the plasma. It is evident from the picture that oxide formed on this surface is grown oxide and not deposited oxide. There is also no evidence of resputtering or wall-sputtering. Figure 3 shows the cross section of the wafer after oxide formation on the  $\text{MgO}$  masked silicon wafer surface which faces the plasma. Even though the oxidation was carried out for the same length of time as for the back side, the distance of the  $\text{Si-SiO}_2$  interface from the original silicon surface is much less compared to that in Fig. 2, indicating that oxidation has taken place to a much lesser extent on the front surface. However, the oxide is symmetrical around the original silicon surface. Consequently, it may be concluded that the thinner oxide grown on the front surface is due to a reduced oxidation rate, and not due to growth plus simultaneous resputtering of oxide. Further, there is no evidence of deposition on either surface of the wafer. The difference in oxidation rate, for the back side and front side oxidations is believed to be due to self-biasing of the wafer in the plasma. This phenomenon is being examined currently and will be discussed when our experiments are completed. Further interesting observations are as follows.

When two silicon wafers are placed one behind the other, greater than 5 mm apart, the oxide thickness on the back side of the wafer closest to the plasma is uniform and significantly greater than that on the back side of the second wafer. For separation distances less than 5 mm, the oxide thickness uniformity on the first wafer degrades significantly. When the two wafers are placed in direct contact with each other, the back side of the second wafer only is oxidized. The design of the wafer holder was found to be critical for obtaining uniform oxide growth. In order to get uniform growth over an entire wafer, the wafer has to be mounted vertically and supported only at its base. Other mount-

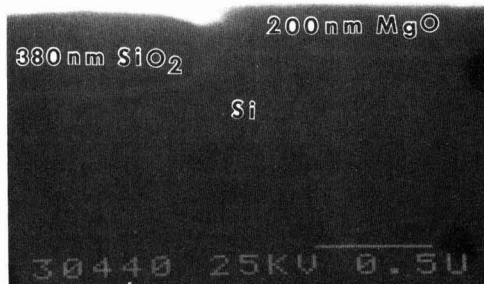


Fig. 2. SEM micrograph of the cross section of a silicon wafer after  $\text{SiO}_2$  formation on an  $\text{MgO}$  masked silicon surface which faces away from the plasma.

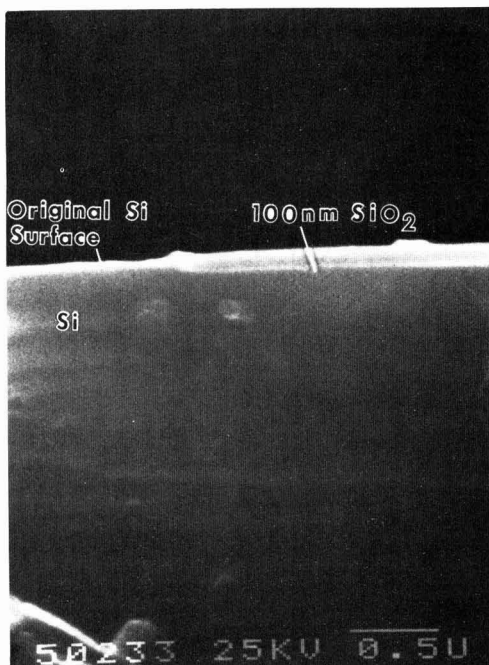


Fig. 3. SEM micrograph of the cross section of a silicon wafer after oxide formation of an  $\text{MgO}$  masked silicon surface which faces the plasma.

ing configurations, e.g., horizontal placement, wafer support on its bottom and edges, etc. lead to nonuniform growth.

Our process of plasma oxidation involves placing the silicon wafer vertically perpendicular to the direction of the gas flow with the surface to be oxidized facing away from the plasma. This is true for a wafer located on either side of the rf induction coil. Thus, two wafers can be oxidized simultaneously using this plasma oxidation technique. The rate of oxidation is a strong function of the position of the wafer relative to the edge of the coil, decreasing sharply with increasing distance. For the experimental results to be discussed below, the wafer(s) was placed at a distance of 2 cm from the end of the rf coil. Since the wafer lies adjacent to the plasma generation region, the temperature of the wafer is determined to some extent by plasma heating. It takes about 15 min for the temperature of the wafer to stabilize when the plasma is ignited. To study the kinetics of oxidation at a particular temperature, the wafer was brought to an initial temperature using the resistance heat furnace and then a helium plasma was struck at the desired pressure. When the wafer temperature stabilized, the gas input was changed over to oxygen. The latter step takes about a minute. A control wafer was heated in a helium plasma for 30 min to determine whether any oxide is formed during the preheating stage due to contaminants. No detectable amount of  $\text{SiO}_2$  formed. The temperature of the resistance heated furnace was varied to obtain the desired oxidation temperature, independent of the power used to generate the plasma. To study the kinetics of oxide formation on two surfaces of a wafer simultaneously, wafers polished on both sides were oxidized for different lengths of time. As mentioned before, the oxide thickness on the front side is less uniform. The average oxide thickness on the front side was computed from the thickness measurements on a 4 cm diam central area of the wafer. Figure 4 shows the thickness of oxide grown at 540°C on the back and front sides of a wafer as a function of time. Oxide thickness on the back side was about 4-5 times the oxide thickness on the front side. In order to analyze the kinetics of oxidation, the data was plotted as  $\log d$  vs.  $\log t$  (Fig. 5). Both curves follow essentially the same behavior. The oxide thickness appears to increase as  $t$  in the initial oxidation phase and as  $t^{1/2}$  for longer oxidation times. It is interesting to note that for the back side of the wafer, the  $t^{1/2}$  law is obeyed at an oxide thickness of 150 nm whereas for the front side, the  $t^{1/2}$  law prevails at an oxide thickness of 40 nm. If neutral species are responsible for oxidation, then the onset of

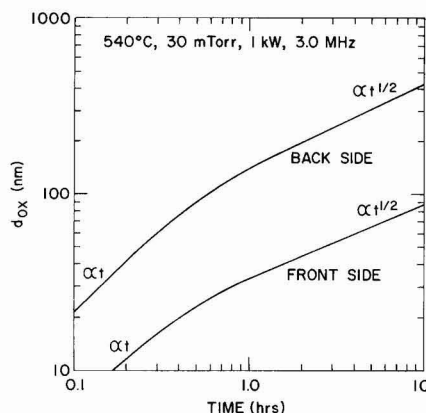


Fig. 5. Thickness vs. time for the data shown in Fig. 4 plotted as  $\log d$  vs.  $\log t$ .

a parabolic law for two different oxide thicknesses would imply that oxidation on the two surfaces is due to different species being responsible for oxidation on each side of the wafer. If we assume that plasma oxidation follows linear-parabolic kinetics (2), then in the parabolic regime  $d_{ox} \propto C_0^{1/2}$  and in the linear regime  $d_{ox} \propto C_0$  where  $d_{ox}$  is the oxide thickness grown in a fixed time and  $C_0$  is the concentration of oxidizing species in the gas phase. The two lines in Fig. 5 are more or less parallel indicating that the difference in the oxidation behavior of the two surfaces cannot be explained on the basis of different concentrations of oxidizing species present on either side of the silicon wafer. However, if the oxidizing species is charged, then in addition to the oxidizing species itself, the electric field ( $V/d_{ox}$ ) would affect the rate of oxidation and the onset of parabolic behavior (3).  $V$  is the applied or built in potential difference across the oxide. Studies are in progress to examine such built in potentials and the role they play in the plasma oxidation mechanism.

Figure 6 shows the thickness of the oxide grown on the back side of a wafer in 1 hr at 425°C as a function of oxygen pressure in the reaction chamber. Below 10 mTorr, the oxide thickness is seen to increase sharply with increasing pressure while above 10 mTorr,

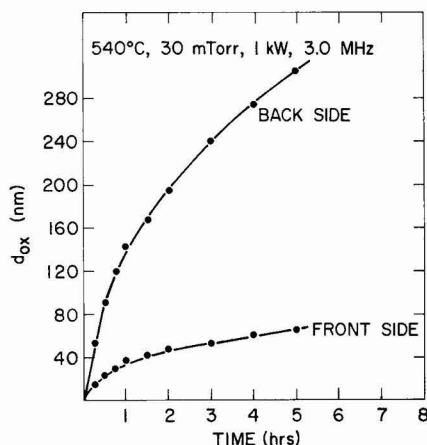


Fig. 4. Thickness of  $\text{SiO}_2$  grown at 540°C on the back and front sides of a wafer as a function of time.

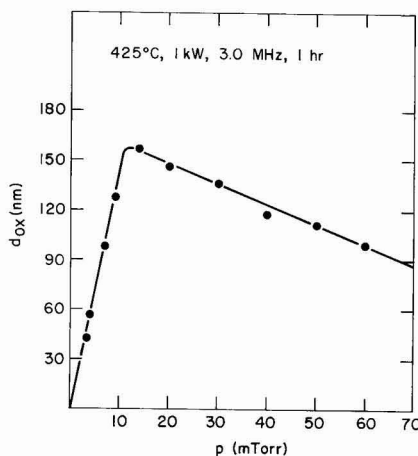


Fig. 6. Thickness of  $\text{SiO}_2$  grown at 425°C as a function of oxygen pressure in the reaction chamber.

it decreases slowly with increasing pressure. The effect below 10 mTorr may be explained by the increase in concentration of the oxidizing species with increasing pressure and the effect above 10 mTorr may be explained by the loss of oxidizing species due to an increase in recombination rate with increasing pressure. It is to be recalled from the previous paper that at pressures less than 10 mTorr, when wall-sputtering is the primary mechanism for oxide formation, the rate of oxide formation on the front side of a wafer decreases with increasing pressure. This is a completely different phenomenon than that shown in Fig. 6, which refers only to the process of oxidation taking place on the back side of a wafer. Concomitant with the process of oxidation shown in Fig. 6, at pressures below 10 mTorr, deposition of oxide is taking place on the front side of a wafer in accordance with the discussion in Part 1. If an experiment is conducted, however, at pressures in excess of 10 mTorr, the front side deposition ceases and, of course, the process described in Fig. 6 continues to occur. One other point with respect to Fig. 6 which describes back-side oxidation is that the experiments were conducted at generator output powers in which the front-side deposition rate was very small compared to the rate of oxidation. This point is important because in the experiments to be described at a later date, it will be shown that the back-side oxidation rate is affected by the thickness of an oxide on the front side. One other important aspect of the pressure effect is at pressures less than 10 mTorr, the plasma is not well confined by the silicon wafer, while at pressures greater than 10 mTorr, the visible plasma is totally confined by the wafer. This confinement phenomenon which is striking to observe depends not only on the pressure but also on the frequency of the applied field. The confinement is readily obtained from 0.5 to 3 MHz and very difficult to obtain at 13.6 MHz. When confinement is not obtained, the back-side oxidation rate is dramatically decreased. Figure 7 shows the thickness of oxide grown as a function of time for two generator output powers. Since with increasing power from 1 to 2 kW, there is only a small increase in oxide thickness, most of our experiments were carried out with 1 kW power. The effect of the frequency of the applied field on the thickness of the grown oxide as a function of time is shown in Fig. 8. With increase in frequency from 0.5 to 3 MHz, there is about a 20% increase in oxide thickness. The higher frequency was used in most experiments to obtain higher growth rates. As shown in Fig. 9, the thickness of oxide grown in a fixed time experiment was found

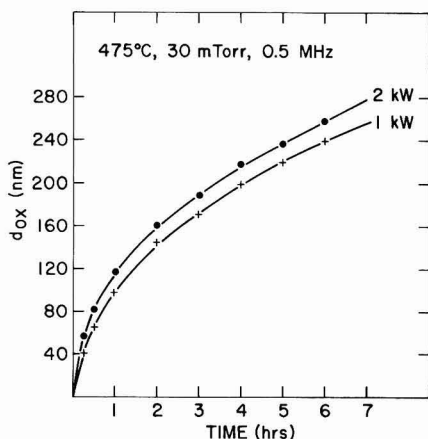


Fig. 7. Thickness of  $\text{SiO}_2$  grown at  $475^\circ\text{C}$  as a function of time for 1 and 2 kW generator output powers.

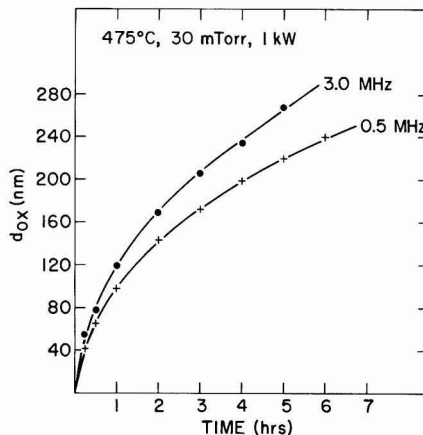


Fig. 8. Thickness of  $\text{SiO}_2$  grown at  $475^\circ\text{C}$  as a function of time for applied field frequencies of 0.5 and 3 MHz.

not to depend on the resistivity of a silicon wafer. At these low oxidation temperatures, dopants are practically immobile and they are not expected to play a role in the oxidation rate. Oxide thickness as a function of time for  $\langle 111 \rangle$  and  $\langle 100 \rangle$  orientation silicon wafers is shown in Fig. 10. Oxide thickness was found to be independent of silicon orientation also, supporting the rate data which indicate a mass transport limited growth process. Since the linear regime, if at all present in our experiments, was probably confined to times less than 10 min, no distinction between the two silicon orientations was possible for the initial stage of the growth process. The effect of temperature on the thickness of oxide grown as a function of time is shown in Fig. 11. Temperature has more of an effect in the parabolic regime than in the initial regime. If we define a parabolic rate constant  $K_p$  as  $d_{ox}^2 = K_p t$  for the parabolic regime, then the activation energy of  $K_p$  is found to be 0.16 eV compared to 1.3–2.3 eV (4, 5) observed for the thermal oxidation of silicon. This is, of course, expected in view of the low temperatures at which we are able to effect oxidation. It should be noted, based on the above, that at  $540^\circ\text{C}$ , growth rates comparable to dry thermal oxidation at  $1100^\circ\text{C}$  can be achieved by plasma oxidation, but the oxidation rate is strongly limited by the wafer distance from the plasma zone.

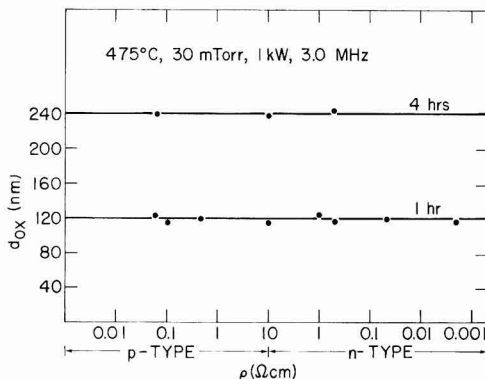


Fig. 9. Thickness of  $\text{SiO}_2$  grown at  $475^\circ\text{C}$  for silicon wafers of different resistivities.

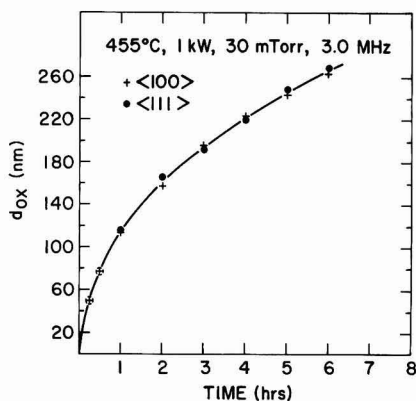


Fig. 10. Thickness of  $\text{SiO}_2$  grown at  $455^\circ\text{C}$  as a function of time for  $\langle 111 \rangle$  and  $\langle 100 \rangle$  oriented silicon wafers.

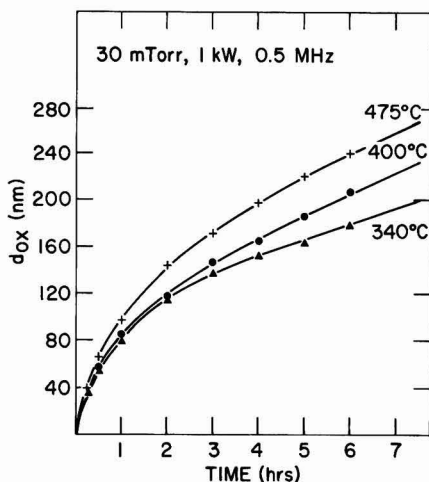


Fig. 11. Thickness of  $\text{SiO}_2$  grown as a function of time at  $340^\circ$ ,  $400^\circ$ , and  $475^\circ\text{C}$ .

### Masking Studies

Some interesting observations were also made when a mask material was used. Ligenza (6) reported using Al as an oxidation mask. However, in our case, Al oxidized preferentially to Si and the rate of silicon oxidation, when 50% of the wafer was uniformly masked with Al, was a factor of approximately three less than that of an unmasked silicon wafer. This behavior indicates a large sticking coefficient on the Al of the oxidizing species and is reminiscent of epitaxial growth behavior on Ge and ZnO reported previously by one of the authors (7-9). However, when MgO was used as a mask material, exposed Si areas oxidized at the same rate as that of a blanket silicon wafer.  $\text{Si}_3\text{N}_4$  was also found to be an effective oxidation mask material and like MgO did not affect growth rate on unmasked surfaces. However, difficulty was encountered in etching  $\text{Si}_3\text{N}_4$  preferentially to  $\text{SiO}_2$  after plasma oxidation using this masking material. SIMS studies indicated that the surface of the  $\text{Si}_3\text{N}_4$  is oxidized, probably to  $\text{SiO}_x\text{N}_y$  during plasma oxidation. The bird's beak effect described by Bassous *et al.* (10) was examined using 200 nm of MgO as a mask. After about 380 nm of plasma oxide was grown, the MgO was dissolved in a saturated ammonium oxalate solution at

room temperature, and the Si-SiO<sub>2</sub> interface was examined using SEM. It is evident from Fig. 12 that the bird's beak effect is apparently absent in plasma oxidation.  $\text{Si}_3\text{N}_4$  directly on top of silicon surface may minimize the bird's beak effect in conventional oxidation but the stress at the  $\text{Si}_3\text{N}_4$ -Si interface damages the underlying silicon at high temperatures. In order to avoid the generation of dislocations and other defects, a pad oxide must be used between the  $\text{Si}_3\text{N}_4$  and the silicon surface. This pad oxide provides a diffusion path for oxidation and gives rise to a bird's beak. The ability to plasma oxidize silicon at lower temperatures enables one to place the oxidation mask in direct contact with silicon and thereby eliminate bird's beak formation.

### Properties of Plasma Grown $\text{SiO}_2$

The properties of plasma  $\text{SiO}_2$  grown at  $500^\circ\text{C}$  were studied and were compared to thermal  $\text{SiO}_2$  grown at  $1100^\circ\text{C}$ . The results are summarized in Table I. The refractive indexes were determined at 632.8 nm using ellipsometry. The etch rates of plasma and thermal  $\text{SiO}_2$  were compared by etching simultaneously the two types of oxide in 1:9 (40% HF:49%  $\text{NH}_4\text{F}$ ) solution at room temperature. The stress ( $\sigma_f$ ) at the Si-SiO<sub>2</sub> interface was calculated knowing the film thickness ( $t_f$ ), substrate thickness ( $t_s$ ), and the radius of curvature of the silicon substrate ( $R$ ), using the formula

$$\sigma_f = \frac{E_s}{6(1 - \gamma_s)} \frac{t_s^2}{t_f} \cdot \frac{1}{R}$$

where  $E_s$  = Young's modulus of the silicon substrate and  $\gamma_s$  = Poisson's ratio.

In order to get an accurate measurement of the radius of curvature, 7 mil thick wafers polished on both sides were used. About 450 nm of  $\text{SiO}_2$  were grown by plasma oxidation or by thermal oxidation at  $1100^\circ\text{C}$ . Oxide was then etched from one surface of the wafers. The compressive stress in  $\text{SiO}_2$  results in elas-

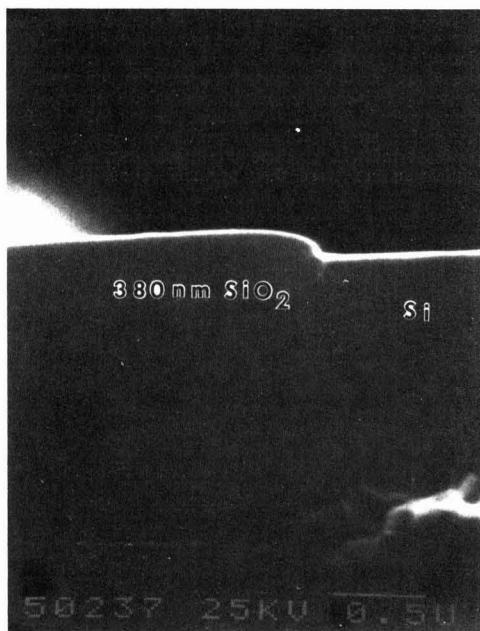


Fig. 12. SEM micrograph of the cross section of a silicon wafer after oxide growth showing the apparent absence of bird's beak effect.



Table I. Properties of plasma SiO<sub>2</sub> grown at 500°C compared to thermal SiO<sub>2</sub> grown at 1100°C

Properties	Plasma SiO <sub>2</sub> 500°C growth temperature	Thermal SiO <sub>2</sub> 1100°C growth temperature
Etch rate in 1:9 BHF (nm/min)	74-76	75
Refractive index	1.461-1.465	1.462
Stress (dynes/cm <sup>2</sup> )	1.5-1.6 × 10 <sup>9</sup>	3.1-3.4 × 10 <sup>9</sup>
Fixed charge (No./cm <sup>2</sup> )	2-6 × 10 <sup>10</sup>	2 × 10 <sup>10</sup>
Interface states (No./cm <sup>2</sup> eV)	2-6 × 10 <sup>10</sup>	2 × 10 <sup>10</sup>
Retention time (sec)	~100	>500
Breakdown strength (MV/cm)	4-8	10
Boron depletion	Absent	Present
Bird's beak effect	Absent	Present
Oxidation-induced defects	Absent	Present

tic bending of the wafer. The radius of curvature of the silicon wafer was determined by an automatic x-ray diffraction technique described by Segmüller *et al.* (11). The stress for plasma oxide was determined to be  $1.5-1.6 \times 10^9$  dynes/cm<sup>2</sup> and that of thermal oxide was  $3.1-3.4 \times 10^9$  dynes/cm<sup>2</sup>. The difference in stress can be explained by the different growth temperatures and the subsequent cooling to room temperature. If we assume that strain at the Si-SiO<sub>2</sub> interface is proportional to the difference in thermal contraction of Si and SiO<sub>2</sub> during cooling from the growth temperature, and that the intrinsic stress at the growth temperature is negligible, then we can write strain  $\propto (\alpha_{\text{Si}} - \alpha_{\text{SiO}_2}) \Delta T$  where  $\alpha_{\text{Si}}$  and  $\alpha_{\text{SiO}_2}$  are the coefficients of expansion of Si and SiO<sub>2</sub>, respectively, and  $\Delta T$  is the difference between the growth temperature and room temperature. Thus, the ratio of stress in plasma oxide (500°C) and thermal oxide (1100°C) is expected to be  $(1100 - 23)/(500 - 23) = 2.27$ , close to 2.1, the ratio of the experimentally determined stress values. Since the deformation in silicon is elastic in nature as evidenced by the absence of slip in the oxidized wafers, the rate of cooling from the growth temperature to room temperature is not important.

Fixed charge and interface-state density for oxides grown on <100> Si wafers were determined using high frequency and quasi-static C-V techniques. As-grown oxides exhibited large negative flatband voltages and high surface-state density ( $3 \times 10^{12}$ /cm<sup>2</sup> eV). Figure 13 shows high frequency (solid line) and quasi-static (dotted line) C-V curves of Al-SiO<sub>2</sub>-Si capacitors with only a standard postmetal anneal (400°C, 20 min, forming gas). No high temperature postoxidation heat-treatment was given to these capacitors prior to metallization nor were they premetal annealed at a

lower temperature. The postmetal anneal fixed charge density calculated from the flatband voltage was  $6 \times 10^{10}$ /cm<sup>2</sup>, and the surface-state density at midgap was found to be  $6 \times 10^{10}$ /cm<sup>2</sup> eV. When, in addition to the standard postmetallization anneal, a postoxidation heat-treatment (1000°C, 20 min, Ar) was given, both the fixed charge and surface-state density values dropped to  $2 \times 10^{10}$ . Another postoxidation heat-treatment at 1000°C for 15 min in dry O<sub>2</sub> followed by 5 min in Ar also reduced the fixed charge and surface-state density to the same value. However, the postoxidation heat-treatment in dry O<sub>2</sub> also improved the breakdown strength of plasma oxides considerably. A breakdown strength histogram on one hundred capacitors with different postoxidation heat-treatments is shown in Fig. 14. Plasma oxides without any postoxidation heat-treatment exhibited breakdown strengths of 3-4 MV/cm. The postoxidation heat-treatment at 1000°C in Ar did not change this breakdown histogram. However, after postoxidation heat-treatment in oxygen, the breakdown strength increased to 7-8 MV/cm. During the heat-treatment in oxygen, another 5 nm of thermal SiO<sub>2</sub> were formed in addition to the 35 nm of plasma oxide already present on the wafer. The improvement in breakdown strength cannot be accounted for by this additional 5 nm of thermal SiO<sub>2</sub>. The improvement is also not due to the densification of SiO<sub>2</sub> at high temperature since the argon anneal at the same temperature did not improve breakdown characteristics. It is possible that some kind of stoichiometric change in plasma oxide takes place during annealing in oxygen. One aspect of our experimental technique which is suspect is the use of liquid nitrogen baffled mechanical pumping to maintain desired pressures during oxidation. This is accompanied unavoidably by oil back streaming which may incorporate carbon into the oxide films. The oxygen treatment may remove these defects.

In order to establish the presence or absence of oxidation-induced stacking faults and other defects, about 400 nm of plasma SiO<sub>2</sub> were grown on a silicon wafer, the oxide was subsequently stripped in BHF and the silicon surface was etched in Wright etch for 40 sec. The etched silicon surface was then examined using optical microscopy. No oxidation-induced stacking faults or other defects were observed. Plasma oxidation thus has definite advantages over thermal oxidation from the defect and bird's beak elimination point of view, both of which advantages arise because of the lower oxidation temperatures employed.

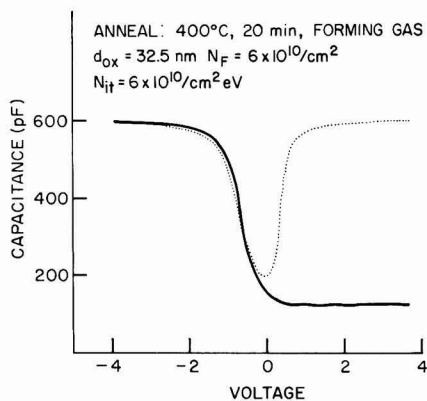


Fig. 13. High frequency and quasi-static C-V curves of plasma SiO<sub>2</sub> capacitor after postmetallization anneal in forming gas at 400°C for 20 min.

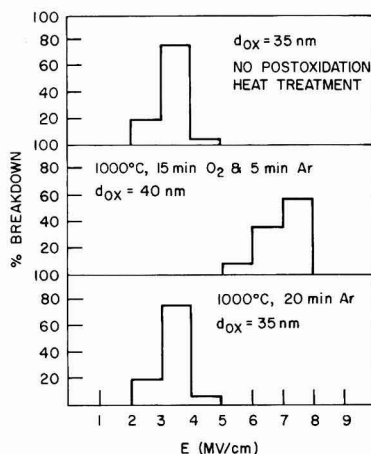


Fig. 14. Breakdown histogram of plasma SiO<sub>2</sub> capacitors with different postoxidation heat-treatments.

### Conclusions

From the experimental results described in this paper, we can conclude that oxide formation in an oxygen plasma in the pressure range above 10 mTorr is solely due to silicon oxidation. The process of oxidation involves placing the wafer surface to be oxidized facing away from the plasma, close to the plasma generation region, and perpendicular to the direction of gas flow. The oxide thickness grown in a fixed time experiment increases with increasing power, temperature, frequency of the applied field, and decreases with increasing pressure and distance of the wafer from the plasma. Oxide thickness was found to be independent of the resistivity and crystallographic orientation of the wafer. The growth rate and properties of  $\text{SiO}_2$  grown in an oxygen plasma at  $500^\circ\text{C}$  were comparable to thermal  $\text{SiO}_2$  grown at  $1000^\circ\text{--}1100^\circ\text{C}$ . Low fixed charge and interface-state densities were obtained following only a low temperature postmetallization anneal. Following a short postoxidation anneal in argon or oxygen, these values improved further by a factor of three. Breakdown strength improved considerably following a brief postoxidation heat-treatment at  $1000^\circ\text{C}$  in dry  $\text{O}_2$ , but not in argon. Bird's beak and oxidation-induced defects were both found to be absent in plasma grown oxides.

Manuscript submitted Dec. 18, 1980; revised manuscript received April 27, 1981. This was Paper 167 pre-

sented at the St. Louis, Missouri, Meeting of the Society, May 11-16, 1980.

Any discussion of this paper will appear in a Discussion Section to be published in the June 1982 JOURNAL. All discussions for the June 1982 Discussion Section should be submitted by Feb. 1, 1982.

Publication costs of this article were assisted by IBM Corporation.

### REFERENCES

1. A. K. Ray and A. Reiman, *This Journal*, **128**, 2460 (1981).
2. B. E. Deal and A. S. Grove, *J. Appl. Phys.*, **36**, 3770 (1965).
3. U. R. Evans, "The Corrosion and Oxidation of Metals," p. 823, Edward Arnold, Publisher, London (1960).
4. E. A. Irene and Y. J. Vander Meulen, *This Journal*, **123**, 1380 (1976).
5. E. A. Irene and D. W. Dong, *ibid.*, **125**, 1146 (1978).
6. J. R. Ligenza, *J. Appl. Phys.*, **36**, 2703 (1965).
7. A. Reisman, M. Berkenblit, S. A. Chan, and J. Angilello, *J. Electronic Mater.*, **2**, 177 (1973).
8. M. Berkenblit and A. Reisman, *Met. Trans.*, **2**, 803 (1971).
9. V. J. Silvestri and T. O. Sedgwick, *This Journal*, **117**, 198 (1970).
10. E. Bassous, H. N. Yu, and V. Maniscalco, *ibid.*, **123**, 1729 (1976).
11. A. Segmuller, J. Angilello, and S. J. LaPlaca, *J. Appl. Phys.*, **51**, 6224 (1980).

## Preparation and Electrical Properties of $\text{V}_2\text{O}_3$ Single Crystals of Controlled Stoichiometry

S. A. Shivashankar,<sup>1</sup> R. Aragón,<sup>2</sup> H. R. Harrison, C. J. Sandberg, and J. M. Honig

Purdue University, West Lafayette, Indiana 47907

### ABSTRACT

$\text{V}_2\text{O}_3$  crystals have been grown by the skull-melting technique and subsequently annealed in  $\text{CO}_2/\text{CO}$  atmosphere to produce crystals of controlled stoichiometry. Crystals were characterized by x-ray Laue back-reflection photography, lattice parameter refinement, polarized reflected light microscopy, neutron and gamma ray diffraction, and thermogravimetric analysis. Deviations from strict stoichiometry,  $\text{V}_{2-x}\text{O}_3$ , were found to follow the relation  $y \sim f_0 y^{3/4}$  in the dependence on oxygen fugacity. The dependence of electrical resistivity on temperature was measured for two different samples, and the variation of the temperature of metal-insulator transition with sample composition was determined.

As is by now well recognized,  $\text{V}_2\text{O}_3$  and its dilute alloys with other transition metal sesquioxides undergo a variety of spectacular metal-insulator transitions, which can be drastically altered by small changes in sample composition. Approximately 400 publications have been catalogued by us which deal with various aspects of this problem. It has also been known for some time that small departures from the 3/2 ratio of oxygen/vanadium considerably affect the physical properties of  $\text{V}_2\text{O}_3$  or its alloys. While there is general agreement concerning the overall effects, various workers in the field differ from each other in their detailed findings. This points up the need for a method that permits precise control to be achieved over the exact oxygen stoichiometry. The object of the present publication is to report on progress in this particular area.

<sup>1</sup> Present address: IBM Thomas J. Watson Research Center, Yorktown Heights, New York 10598.

<sup>2</sup> Present address: Departamento de Física, Universidad Nacional de La Plata, La Plata, Pcia. de Buenos Aires, Argentina.

Key words: electrical properties of  $\text{V}_2\text{O}_3$ , preparation of  $\text{V}_2\text{O}_3$  single crystals, annealing procedures for  $\text{V}_2\text{O}_3$ .

A variety of techniques have been used to obtain samples of nonstoichiometric vanadium sesquioxides; these may be briefly summarized as follows: For polycrystalline samples, treatment of  $\text{V}_2\text{O}_5$  or of other vanadium oxides in  $\text{CO}_2/\text{H}_2$  or  $\text{CO}_2/\text{CO}$  mixtures at high temperatures (1-3), generation of ceramic sintered bodies by reaction of  $\text{V}_2\text{O}_3$  with a small quantity of  $\text{V}_2\text{O}_5$  or of VO in evacuated quartz ampuls (4-8), reduction of  $\text{VO}_2$  whiskers under a variety of low partial pressures of oxygen at  $1500^\circ\text{C}$  (9); for growth of single crystals, use of  $\text{TeCl}_4$  or  $\text{HCl}$  as a chemical transport agent in a gradient furnace (5, 8, 10-12), and growth of bulk single crystals by the Verneuil flame-fusion technique (13, 14), utilizing different  $\text{H}_2/\text{O}_2$  ratios, and by the Reed tri-arc technique (15, 16).

Physical investigations carried out on the resulting ceramic specimens include phase equilibria studies (1, 3, 4, 15, 17), heat capacity measurements at ordinary temperatures (9) and in the cryogenic temperature range (10), lattice parameter determinations by x-ray diffraction techniques (2, 5, 8, 11), magnetic susceptibility investigations (2, 4, 6, 8, 14), electrical resistivity

measurements (4, 5, 8, 11-14), Seebeck coefficient studies (13), optical measurements (9), electron microscope imaging (12), NMR and Mössbauer techniques (7, 8), and inelastic neutron spin-flip scattering investigations (7).

### Growth of Single Crystals

The common deficiency in most of the techniques for growing single crystals is the lack of adequate control over the ambient. This is manifested in a recent investigation on V<sub>2</sub>O<sub>3</sub> single crystals grown in this laboratory either by the Reed tri-arc technique (15, 16) or by CVT, using TeCl<sub>4</sub> as the transporting agent (16). With the aid of polarized reflected light microscopy Aragón (18) has demonstrated the occasional presence of higher oxide phase domains in these V<sub>2</sub>O<sub>3</sub> single crystals, even though they appear to be single phase and homogeneous in x-ray diffraction patterns. To remedy this problem, and to obtain a homogeneous sample of precisely defined stoichiometry, thin slices cut from single crystalline boules were annealed in a variety of different CO<sub>2</sub>/CO buffering atmospheres. By altering the CO<sub>2</sub>/CO ratio one may precisely control the equilibrium fugacity of oxygen,  $f_{O_2}$ , and thereby achieve the variations in oxygen stoichiometry discussed below.

Single crystals of V<sub>2</sub>O<sub>3</sub> were grown in a skull-melting apparatus; the principles, techniques, and operating procedures have been repeatedly described elsewhere (19-26). Provision was made for operation in a vacuum/gas chamber (volume ~ 125 liters) for control of the ambient (25, 26). The charge for each skull-melter run consisted of approximately 500g of V<sub>2</sub>O<sub>3</sub> powder obtained by reducing 99.9% Cerac/Pure V<sub>2</sub>O<sub>5</sub> (placed in alumina boats) in flowing hydrogen at 1000°C for 10 hr. Traces of water present in the hydrogen used for reduction were removed by passing the gas over copper mesh at 0°C. A susceptor is required to initiate the melting of the V<sub>2</sub>O<sub>3</sub> powder in the skull melter; it was found that a relatively small polycrystalline piece (10-20g) of previously produced V<sub>2</sub>O<sub>3</sub> served this purpose very well. Two separate runs with CO<sub>2</sub>/CO mixtures in the ratio of 25/75 were carried out, employing gas flow rates in the range 5-10 l/min at different stages of the melting process. Although these experiments had to be terminated early because of technical difficulties arising from the high electrical conductivity of V<sub>2</sub>O<sub>3</sub> at elevated temperatures, single crystals as large as 10 × 6 × 5 mm<sup>3</sup> were nevertheless obtained in the center of the boules. These crystals were singularly free of voids and cracks that often blemish V<sub>2</sub>O<sub>3</sub> crystals grown by the tri-arc (Czochralski) technique. This material then served as the starting point for the annealing process described below.

### Subsolidus Annealing Procedures

Specimens grown by the above process were annealed under controlled CO<sub>2</sub>/CO atmospheres at temperatures below their melting point. Figure 1 provides information on the stability range of the various vanadium oxides; the upper part of this phase diagram is taken from the compilation by Okinaka *et al.* (27) of experimental results published by Katsura and co-workers (1, 3). The V<sub>2</sub>O<sub>3</sub>/VO/V boundaries were calculated by us from data on the free energies of formation collected by Reed (28). As the data incorporated in the phase diagram (Fig. 1) are taken from different sources, the phase boundaries as indicated are not considered to be precise. Included in this diagram is a set of well-calibrated  $f_{O_2}$  values corresponding to a variety of different CO<sub>2</sub>/CO mixtures, as specified by Deines *et al.* (29). It is seen that as one lowers the ratio  $r \equiv CO_2/(CO_2 + CO)$ , the volume percentage of CO<sub>2</sub> in the mixture, from approximately 90% to about 5%, one should be able to generate V<sub>2</sub>O<sub>3</sub> compositions bordering from the most oxygen-rich to the most oxygen-poor.

Most of the annealing runs were carried out at 1200°C in a horizontal resistance furnace 60 cm in length, under a typical gas flow of 20-50 cm/min. Provision was made for rapid quenching of the specimens at the end of the run in the controlled atmosphere. Gas flow was carefully regulated by utilizing two-stage regulators on the gas cylinders. The desired CO<sub>2</sub>/CO ratio and mixing of the gases was achieved with a Matheson 7372 gas proportioner equipped with precision NRS flow-control valves. V<sub>2</sub>O<sub>3</sub> single crystals, cut into thin plates by use of a low-speed diamond wheel saw, were placed in a silica tube plugged loosely with silica wool. Silica wool by its baffling action aids the equilibration of the sample with the flowing gas mixture. Calculations (30) based on estimated cation diffusion rate constants for Al<sub>2</sub>O<sub>3</sub>, Cr<sub>2</sub>O<sub>3</sub>, and Fe<sub>2</sub>O<sub>3</sub> (31) showed that annealing times of ~75-100 hr should suffice to generate a uniform oxygen stoichiometry in plates of 300 micron thickness of V<sub>2</sub>O<sub>3</sub> at 1200°C. Annealing times of 75 hr were generally used.

A few runs were also carried out in a vertical resistance furnace at 1400°C; however, because of large temperature gradients and fluctuations the annealing conditions could not be regulated as closely.

Several annealing experiments were also carried out with solid buffers: VO/V<sub>2</sub>O<sub>3</sub>, Fe/FeO, FeO/Fe<sub>3</sub>O<sub>4</sub>, and Ni/NiO, corresponding to values of log  $f_{O_2}$  (atm) = -21.4, -14.8, -12.3, and -10.1, respectively at 1000°C (32). Specimens to be annealed were cut into plates approximately 250 microns in thickness and placed in a silica tube with roughly five times their weight of the solid buffer mixture. The tube was then evacuated, sealed, and placed in a furnace at 1000°C for 100 hr, and finally quenched to room temperature.

### Characterization

Samples were characterized by several different techniques.

**X-ray Laue back-reflection photography.**—Laue photography was used primarily to confirm that the dominant phase present in the annealed single crystals was the corundum V<sub>2</sub>O<sub>3</sub> phase. At 1200°C the corundum phase covers the range  $-7.7 \geq \log f_{O_2} \geq -14.7$  (nominal).

**X-ray lattice parameter refinement.**—Lattice parameters of annealed single crystals were determined and refined with an ENRAF NONIUS CAD-4 diffractometer, controlled by a PDP-8/e minicomputer. Molybdenum K $\alpha_1$  and K $\alpha_2$  radiation was used, with a graphite monochromator in the detector arm. Within the detection limit of roughly 2-5%, no extraneous phases were found in single crystals annealed under the conditions specified above.

**Polarized reflected light microscopy.**—Annealed single crystals were examined by polarized reflected light microscopy which is a sensitive technique for detecting extraneous phases. Samples annealed in the solid-solid buffer mixtures mentioned above showed evidence of phase segregation. By contrast, samples annealed under CO<sub>2</sub>/CO proved to be consistently monophasic in the range  $-7.7 \geq \log f_{O_2} \geq -14.7$  (nominal, 1200°C). All electrical measurements were carried out on single crystals annealed in these gaseous buffered atmospheres.

**Neutron and gamma ray diffraction.**—Skull-melter V<sub>2</sub>O<sub>3</sub> crystals annealed in CO<sub>2</sub>/CO have recently been examined by neutron and gamma ray diffraction (33). Compared to unannealed V<sub>2</sub>O<sub>3</sub> grown by the tri-arc technique, these samples showed very much narrower and taller diffraction peaks. The annealed samples also proved to be of very homogeneous composition.

**Thermogravimetric analysis.**—The oxygen content of the samples annealed at various oxygen partial pressures was determined by thermogravimetric tech-

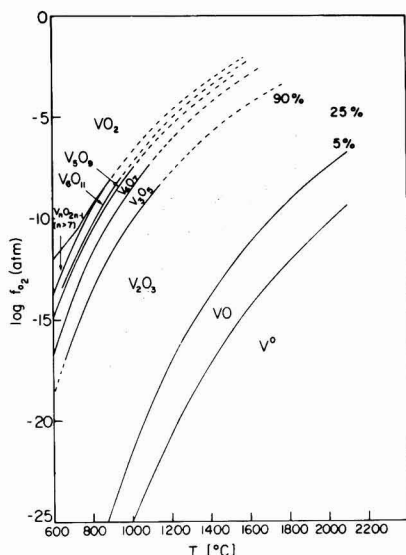
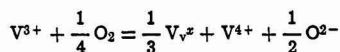


Fig. 1. Stability diagram of part of the V-O system in  $\log f_{O_2}$ -temperature representation. Solid lines (with dashed extrapolations) are phase boundaries; dotted lines,  $CO_2/CO$  gas mixtures; numbers are volume percentages of  $CO_2$ , i.e.,  $CO_2/(CO + CO_2)$ . Note melting point of  $V_2O_3 = 1967^\circ C$ .

niques. A single crystal weighing approximately 200 mg was annealed at a series of different  $f_{O_2}$  in the range  $-8.0 \geq \log f_{O_2} \geq -12.0$  at  $1200^\circ C$  for 80 hr, quenched at the end of each annealing run, and weighed with a precision of  $\pm 1 \mu g$ . As a final step, the sample was annealed at a value of  $\log f_{O_2} = -11.0$  at  $1200^\circ C$  and reweighed; this is thought to correspond to the condition required to achieve stoichiometry (1). The sample was then oxidized in pure oxygen to  $V_2O_5$  at  $670^\circ C$  in a du Pont 951 Thermogravimetric Analyzer. This instrument is capable of 0.4% accuracy in differential weight measurements. It was thus determined for the sample annealed at  $\log f_{O_2} = -11.0$  at  $1200^\circ C$  that the final composition was given by  $V_{2-y}O_3$ , with  $y < 0.001$ . From the mass determinations at the different  $f_{O_2}$  values it was possible to establish a correspondence between composition and equilibrium oxygen fugacity at a given temperature.

The results so obtained are shown in Fig. 2 as a plot of  $\log y$  (in  $V_{2-y}O_3$ ) vs.  $\log f_{O_2}$  (oxygen fugacity) at  $1200^\circ C$ ; least-squares fitting of the data yields a straight line with a slope of 0.74. This power law may be understood in terms of the simple point defect scheme (34)



where, in the Kröger-Vink notation,  $V_v^{\bullet}$  denotes a neutral vanadium vacancy. This scheme predicts an equilibrium vacancy concentration

$$[V_v^{\bullet}] = K(T) \frac{[V^{3+}]}{[V^{4+}]} f_{O_2}^{3/4}$$

where  $K(T)$  is the equilibrium constant and concentrations are taken to be equivalent to the corresponding

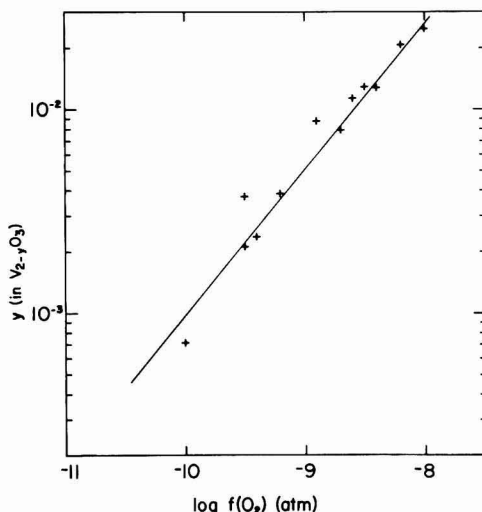


Fig. 2. Deviation from stoichiometry ( $y$  in  $V_{2-y}O_3$ ) as a function of  $\log f_{O_2}$  for  $V_2O_3$  at  $1200^\circ C$ .

activities. This is equivalent to the observed relation  $y \sim f_{O_2}^{3/4}$  (34, 35).

### Electrical Measurements

We conclude with a brief report on the variation of the electrical properties of  $V_{2-y}O_3$  with increasing  $y$ , prepared as described above. Figure 3 shows the variation of the electrical resistivity  $\rho$  with temperature  $T$  for samples with  $y = 0.0$  and  $0.017$ , displaying the sharp, first-order transition from metallic (M) to the antiferromagnetic insulating (AFI) phase. While the progressive lowering of the transition temperature ( $T_t$ ) in  $V_{2-y}O_3$  with increasing  $y$  has been previously reported (4, 8), new features emerge from the present investigation. Transition temperatures as low as 14 K have been observed, in contrast to the previously lowest transition temperature of  $\sim 50$  K reported earlier

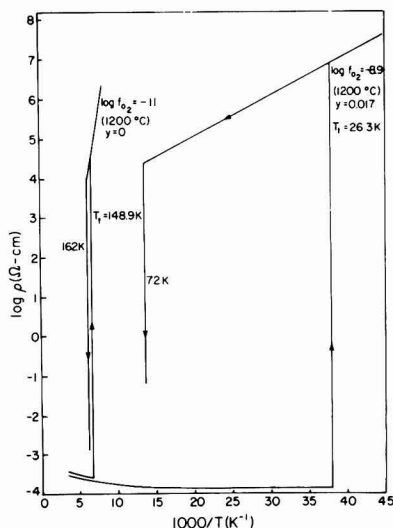


Fig. 3. Metal-insulator transition in  $V_{2-y}O_3$  for single crystals of widely different stoichiometry,  $\log \rho$  vs.  $1/T$ . (a)  $y = 0.0$ ,  $T_t = 152$  K; (b)  $y = 0.017$ ;  $T_t = 26$  K.

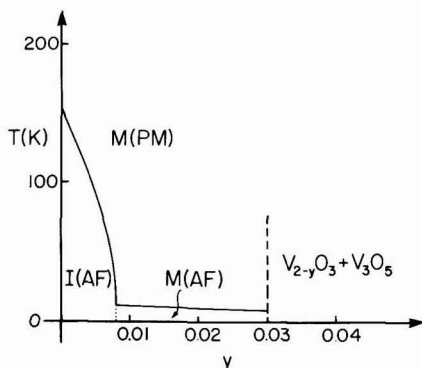


Fig. 4. Phase diagram for  $V_{2-y}O_3$ ,  $T_t$  vs.  $y$ . M(PM) = metal (paramagnetic), M(AF) = metal (antiferromagnetic), I(AF) = insulator (antiferromagnetic).

(8). The resistivity discontinuity remains large for all  $y$ ; indeed  $\Delta\rho$  increases from about  $10^8$   $\Omega$ -cm at  $y = 0$  ( $T_t = 152$  K) to about  $10^{12}$   $\Omega$ -cm at  $y \approx 0.017$  ( $T_t = 14.0$  K). At the same time the hysteresis in the transition temperature ( $\Delta T_t$ ) increases from 12 to 63 K. Earlier studies showed constant values of  $\Delta\rho$  and  $\Delta T_t$  independent of the deviation from stoichiometry (8).

Figure 4 shows a phase diagram for  $V_{2-y}O_3$  based on electrical resistivity measurements. This provides a modification of the phase diagram given by Ueda *et al.* (8), by extending the M-AFI boundary to  $\sim 11$  K for  $y \approx 0.017$ .  $T_t$  declines at first rather slowly with increasing  $y$ , until a range approaching  $y \approx 0.014$  is reached; there is then a precipitous decline in  $T_t$  with further departures from strict stoichiometry. The M-AFI transition disappears altogether at a critical value of  $y \approx 0.018$ ; for greater departures from the 3/2 ratio of O/V, the material remains metallic at all temperatures and undergoes antiferromagnetic ordering below 11 K. This AF ordering, investigated earlier by Ueda *et al.* (6) through Mössbauer studies, was confirmed in our present studies by the observations of anomalous behavior of electrical resistivity near the magnetic ordering temperature. A more detailed discussion of these findings will be provided elsewhere.

### Acknowledgments

The authors wish to thank Mr. S. Chen and Professor R. W. Robinson for their x-ray characterization of several samples. This work was supported by NSF-MRL Grant DMR77-23798.

Manuscript submitted Dec. 1, 1980; revised manuscript received ca. June 4, 1981.

Any discussion of this paper will appear in a Discussion Section to be published in the June 1982 JOURNAL. All discussions for the June 1982 Discussion Section should be submitted by Feb. 1, 1982.

Publication costs of this article were assisted by Purdue University.

### REFERENCES

1. T. Katsura and M. Hasegawa, *Bull. Chem. Soc. Jpn.*, **40**, 561 (1967).
2. M. Nakahira, S. Horiuchi, and H. Ooshima, *J. Appl. Phys.*, **41**, 836 (1970).
3. M. Nakahira and T. Katsura, *Metall. Trans.*, **1**, 369 (1970).
4. D. B. McWhan, A. Menth, and J. P. Remeika, *J. Phys. (Paris)*, **32**, C-1079 (1971).
5. K. Nagasawa, Y. Bando, and T. Takada, *J. Cryst. Growth*, **17**, 143 (1972).
6. Y. Ueda, K. Kosuge, S. Kachi, S. Shinjo, and T. Takada, *Mater. Res. Bull.*, **12**, 87 (1977).
7. Y. Ueda, K. Kosuge, S. Kachi, H. Yasuoka, H. Nishihara, and A. Heidemann, *J. Phys. Chem. Solids*, **39**, 1281 (1978).
8. Y. Ueda, K. Kosuge, and S. Kachi, *J. Solid State Chem.*, **31**, 171 (1980).
9. N. Kimizuka, M. Ishii, M. Saeki, M. Nakano, and M. Nakahira, *Solid State Commun.*, **12**, 43 (1973).
10. D. B. McWhan, J. P. Remeika, J. P. Maita, H. Okinaka, K. Kosuge, and S. Kachi, *Phys. Rev. B*, **7**, 326 (1973).
11. M. Pouchard and J.-C. Launay, *Mater. Res. Bull.*, **8**, 95 (1973).
12. J.-C. Launay, M. Pouchard, and R. Ayroles, *J. Cryst. Growth*, **36**, 297 (1976).
13. V. N. Novikov, B. A. Tellerchik, E. I. Gindin, and V. G. Prokhorov, *Soviet Phys. Solid State*, **12**, 2061 (1971).
14. V. G. Zubkov, J. I. Matveenko, B. A. Tellerchik, and P. V. Gel'd, *ibid.*, **13**, 2885 (1972).
15. J. C. C. Fan and T. B. Reed, *Mater. Res. Bull.*, **7**, 1403 (1972).
16. H. Kuwamoto, Thesis, Purdue University, May 1978, unpublished.
17. J. Springer, *J. Less-Common Metals*, **1**, 14 (1965).
18. R. Aragón, Tech. Rept. "Status Report on the Growth and Characterization of Some Oxide Crystals from the Melt," Purdue University, January 1979, unpublished.
19. D. Michel, *Rev. Int. Hautes Temp. Refract.*, **9**, 225 (1972).
20. V. I. Aleksandrov, V. V. Osiko, A. M. Prokhorov, and V. M. Tatarintsev, *Vest. Akad. Nauk SSSR*, No. 12, 29 (1973).
21. J. F. Wencus, M. L. Cohen, A. G. Emslie, W. P. Menashi, and P. F. Strong, Tech. Rept. AFCRL-TR-75-0213 (1975).
22. V. I. Aleksandrov, V. V. Osiko, A. M. Prokhorov and V. M. Tatarintsev, in "Current Topics in Materials Science," Vol. 1, E. Kaldis, Editor, pp. 421-480, North-Holland, Amsterdam (1978).
23. D. Michel, M. Perez y Jorba, and R. Collongues, *J. Cryst. Growth*, **43**, 546 (1978).
24. J. E. Keem, H. R. Harrison, S. P. Faile, H. Sato, and J. M. Honig, *Am. Ceram. Soc. Bull.*, **56**, 1022 (1977).
25. H. R. Harrison and R. Aragón, *Mater. Res. Bull.*, **13**, 1097 (1978).
26. H. R. Harrison, R. Aragón, and C. J. Sandberg, *ibid.*, **15**, 571 (1980).
27. H. Okinaka, K. Kosuge, and S. Kachi, *Jpn. J. Appl. Phys.*, **9**, 224 (1970).
28. T. B. Reed, "Free Energy of Formation of Binary Compounds: An Atlas of Charts for High-Temperature Chemical Calculations," MIT Press, Cambridge, MA (1971).
29. P. Deines, R. H. Nafzinger, G. C. Ulmer, and E. Woerman, "Temperature-Oxygen Fugacity Tables for Selected Gas Mixtures in the System C-H-O at One Atmosphere Total Pressure," Bulletin of the Earth and Mineral Science Experiment Station No. 88, The Pennsylvania State University, University Station, PA (1974).
30. J. Crank, "The Mathematics of Diffusion," 2nd ed., p. 50, Clarendon Press, Oxford (1975).
31. C. E. Birchenall, in "Mass Transport in Oxides," N.B.S. Special Publication **296**, pp. 119-127 (1968).
32. J. S. Huebner, in "Research Techniques for High Pressure and High Temperature," G. C. Ulmer, Editor, pp. 123-177, Springer Verlag, New York (1971).
33. S. A. Werner, Personal communication.
34. P. Kofstad, "Non-stoichiometry, Diffusion and Electrical Conductivity in Binary Metal Oxides," pp. 177-178 and 27-46, Wiley-Interscience, New York (1972).
35. M. Wakihara and T. Katsura, *Metall. Trans.*, **1**, 363 (1970).



# p-Type NiO as a Photoelectrolysis Cathode

F. P. Koffyberg\* and F. A. Benko

Department of Physics, Brock University, St. Catharines, Ontario L2S 3A1, Canada

## ABSTRACT

From an experimental study of p-type  $\text{Ni}_{0.98}\text{Li}_{0.02}\text{O}$  as a cathode for the photoelectrolysis of water, we have determined its flatband potential [ $+0.1\text{V}$  (SCE) at a pH of 9.2] and its bandgap (3.47 eV, indirect). The electron affinity of NiO is only 1.4 eV, which is unusually small compared to most other oxides; this is due to the valence band being mainly nickel-3d type instead of the usual oxygen-2p type. The relevance of 3d valence bands to the performance of semiconducting photoelectrodes is discussed.

The photoelectrolysis of water using semiconducting electrodes has been the subject of intensive research recently (1, 2). For solar applications, electrode materials must have the following properties (apart from being good conductors): (i) A bandgap larger than 1.23 eV but smaller than 3 eV; (ii) a flatband potential which is sufficiently negative (for n-type photoanodes) or positive (for p-type photocathodes) so that a depletion layer of the proper sign is formed without the need for an external bias, and (iii) excellent chemical stability, both in the dark and under illumination. The last requirement limits the field of possible materials to oxide semiconductors. Nearly all oxide materials investigated so far have been n-type.

Stoichiometric NiO is an insulator, but it can be doped with lithium to give a good conducting p-type material. The conductivity mechanism has been a subject of some controversy, but an exhaustive review (3) of experimental data shows that the free holes move, with low mobility, in a narrow valence band made up mainly of 3d-type wavefunctions originating from the  $\text{Ni}^{2+}$  ions. Because of the low mobility, heavy doping is necessary to achieve acceptable conductivity; this, in turn, will produce narrow depletion layer widths so that the efficiency of an NiO photocathode is expected (and found) to be low. However, since both flatband potential (4) and bandgap data (5) are available, we thought it worthwhile to measure the properties of NiO as a photocathode.

In this paper we report the photocurrent-potential characteristics and the spectral quantum efficiency of  $\text{Ni}_{0.98}\text{Li}_{0.02}\text{O}$ . From the data we obtain the flatband potential and bandgap, which are in good agreement with the literature values. We then calculate the electron affinity of NiO, which is much smaller than the values reported for most other oxides; we propose that this is due to the d-type valence band. Finally, the implications of our results for the search for suitable solar photoanodes are discussed.

## Experimental

Polycrystalline samples of  $\text{Ni}_{0.98}\text{Li}_{0.02}\text{O}$  and  $\text{Ni}_{0.95}\text{Li}_{0.05}\text{O}$  were prepared by thoroughly grinding NiO powder (Fischer Reagent Grade) moistened with the appropriate quantity of  $\text{LiNO}_3$  solution. After drying, disks (area  $1.2\text{ cm}^2$ , thickness  $0.1\text{ cm}$ ) were pressed and subsequently fired at  $1000^\circ\text{C}$  for 12 hr in air. The disks were then reground, re-pressed, and finally fired for 24 hr at  $1450^\circ\text{C}$ , during the final firing the disks were embedded in  $\text{NiO}(\text{Li})$  powder to prevent lithium loss by evaporation. Disks so prepared had reproducible and stable photoelectrolytic properties. If the final firing was done at a lower temperature, then photocurrents slowly decreased in time; we ascribe this to lithium leaching. Qualitatively

the polycrystalline samples with 2 and 5% Li, and a single crystal sample with 0.2% Li, showed the same behavior; the 2% Li samples (with a resistivity of  $9 \pm 1\text{ }\Omega\text{cm}$ ) showed the largest photocurrents, and all data reported are for this composition.

Experiments were performed in a one-compartment cell; solutions (from reagent-grade materials) were flushed continuously with hydrogen or oxygen. The counterelectrode was  $7\text{ cm}^2$  of platinized Pt. All potentials are with respect to SCE; measurements were made potentiostatically. Photocurrent measurements were made with pulsed light from a 150W xenon arc ( $0.81\text{ W/cm}^2$  intensity at the sample); the time dependence was recorded with a digital storage oscilloscope. For the quantum efficiency ( $\eta$ ) measurements the monochromatic light pulses were shaped such that only the instantaneous photocurrents were measured with a lock-in amplifier. For a given sample the  $\eta$  values were reproducible to  $\pm 3\%$ , but variations of  $\pm 20\%$  were found between different samples.

## Results

On exposing the sample, in hydrogen-flushed 0.1M  $\text{Na}_2\text{HPO}_4$  solution, pH = 9.2, to "white" xenon arc light the cell current increased within one msec to a maximum value; it then decayed relatively slowly to a smaller steady-state value. We define (Fig. 1)  $i_m$  as the instantaneous photocurrent and  $i_s$  as the steady-state photocurrent, both corrected for the dark current  $i_d$ . These currents are shown in Fig. 2 as a function of sample potential. This general behavior was observed in 0.1M phosphate solutions ranging in pH from 1 to 12, in 0.2M solutions of  $\text{Na}_2\text{SO}_4$ ,  $\text{Na}_2\text{HPO}_4$ ,  $\text{Na}_2\text{CO}_3$ , and in 0.01M KOH. Changing the counter-

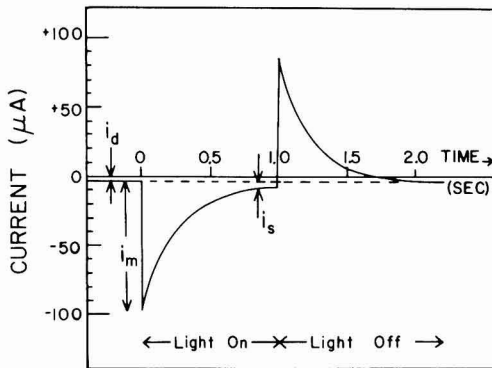


Fig. 1. The current response of  $\text{Ni}_{0.98}\text{Li}_{0.02}\text{O}$  to a light pulse. Electrolyte: 0.1M  $\text{Na}_2\text{HPO}_4$ , pH = 9.2,  $\text{H}_2$  flushed. Sample potential  $-0.45\text{V}$  (SCE).

\* Electrochemical Society Active Member.

Key words: semiconductor, electrode, photoelectricity, electrolysis.



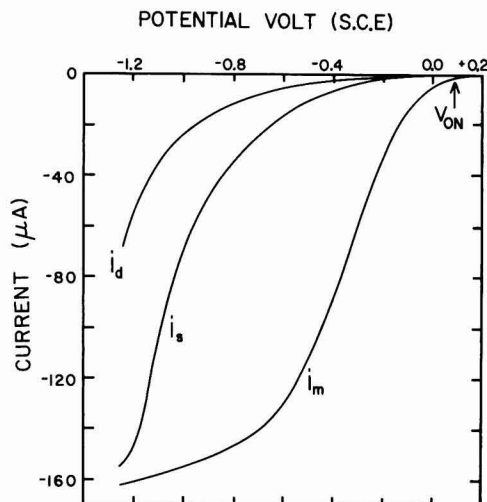


Fig. 2. The instantaneous photocurrent  $i_m$ , the steady-state photocurrent  $i_s$ , and the dark current  $i_d$  of  $\text{Ni}_{0.98}\text{Li}_{0.02}\text{O}$  as a function of sample potential  $V(\text{SCE})$ . Electrolyte: 0.1M  $\text{Na}_2\text{HPO}_4$ , pH = 9.2,  $\text{H}_2$  flushed.

electrode from Pt to metallic  $\text{La}_{0.9}\text{Sr}_{0.1}\text{CoO}_3$  made no difference. Only in 0.01M KOH solutions flushed with oxygen was  $i_s$  much larger, approximately 90% of  $i_m$  in the potential range of 0 to  $-1.0\text{V}$ . In phosphate solutions the onset potential  $V_{\text{ON}}$ , defined where  $i_m$  equals  $1\text{ }\mu\text{A}$  (Fig. 2) was equal to  $+0.07 \pm 0.05\text{V}$  (SCE) at pH = 9.2; it shifted regularly  $0.056 \pm 0.005\text{V/pH}$  unit more positive with decreasing pH. The quantum efficiency  $\eta$  (defined as the ratio of the instantaneous photocurrent density and the incident photon flux) is shown as a function of the photon energy ( $h\nu$ ) in Fig. 3.  $\eta$  is proportional to the optical absorption coefficient  $\alpha$  if the depletion layer width and the minority carrier diffusion length are both

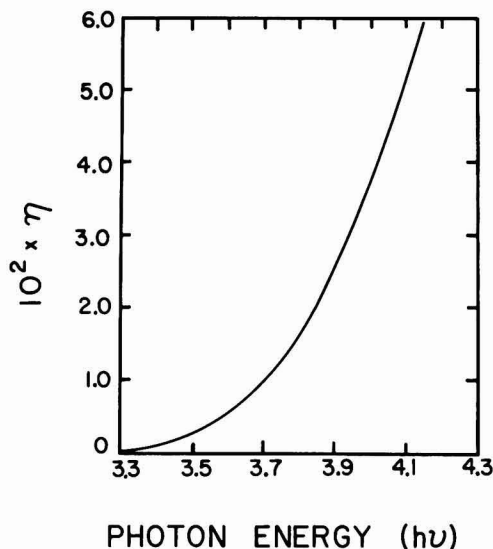


Fig. 3. The quantum efficiency  $\eta$  as a function of photon energy  $h\nu$ , at an electrode potential of  $-0.7\text{V}$  (SCE).

smaller than  $\alpha^{-1}$  (6); these conditions are met in our heavily doped samples. Then the bandgap  $E_g$  can be determined from a linear plot of  $(\eta h\nu)^{1/2}$  vs.  $(h\nu)$ ; the most linear plot was obtained with  $n = 2$  (Fig. 4), indicating that the optical transition from the valence to the conduction band is indirectly allowed.  $E_g$  was found to be equal to  $3.47 \pm 0.04\text{ eV}$  (average for five samples).

### Discussion

The value of the bandgap for NiO found by us is at the lower end of the range (3.4–3.7 eV) of values determined from absorption measurements (5). The spread in the reported values for  $E_g$  is probably due to the existence of strong crystal field absorption and lithium-induced optical absorption in the visible, which overlaps the bandgap absorption (7). These complications are unimportant for the photoelectrolysis experiment, which is sensitive only to that part of the overall absorption spectrum in which electron-hole pairs are produced by photon absorption.

At least two reactions are possible at the NiO cathode: hydrogen generation by photoelectrolysis and reduction of NiO according to  $\text{NiO} + \text{H}_2\text{O} + 2e^- \rightarrow \text{Ni} + 2\text{OH}^-$ . The decomposition potential for the latter reaction is  $-0.62\text{V}$  (SCE) at pH = 9.2; the rapid rise in the dark current  $i_d$  for sample potentials less than  $-0.9\text{V}$  (Fig. 2) suggest that there the NiO reduction contributes substantially to the cell current. However, in the potential range  $-0.9$  to  $+0.1\text{V}$  the instantaneous photocurrent  $i_m$  is large with respect to  $i_d$ ; we assume that here the dominant reaction is photoelectrolysis.

The rapid rise in the photocurrent, on exposing the sample to light, and its subsequent slow decay to a lower steady-state value have been observed previously for the n-type photoanodes  $\text{TiO}_2$  and  $\text{Fe}_2\text{O}_3$ . Hardee and Bard (8) have proposed the following explanation for this behavior: On exposure to light an intermediate electrolysis product is formed by a fast forward (cathodic) reaction; this intermediate is unstable at the applied electrode potential and is subsequently re-oxidized in a slower back-reaction. The back-reaction slows down with increasing cathodic potential, so that at sufficiently negative potential  $i_s$  will be equal to  $i_m$ . This explanation may be valid for p-type NiO as well, but our experimental

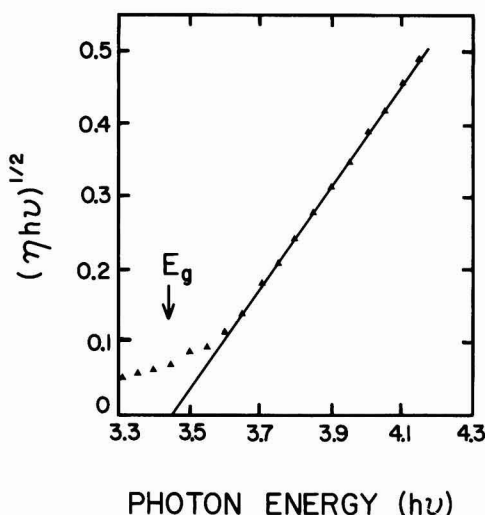


Fig. 4. Determination of the bandgap  $E_g$  for  $\text{Ni}_{0.98}\text{Li}_{0.02}\text{O}$  from a plot of  $(\eta h\nu)^{1/2}$  vs.  $h\nu$ .

results give no indication of the nature of the intermediate species. However, the  $i_m$  vs.  $V$  curve (Fig. 2) has the characteristic shape of a photoelectrolysis curve, and we take the flatband potential  $V_{FB}$  of NiO equal to or slightly more positive than the onset potential  $V_{ON}$ . At pH = 9.2,  $V_{FB}$  is therefore  $+0.1 \pm 0.05V$  (SCE).

A possible objection can be raised against this identification of  $V_{FB}$  with  $V_{ON}$ , since in some p-type materials [LuRhO<sub>3</sub> (9), GaP (10)]  $V_{ON}$  is not identical to  $V_{FB}$ . The clearest case is p-GaP, where  $V_{ON}$  is 0.7V more negative than the  $V_{FB}$  determined from a Mott-Schottky plot of the differential capacitance. This is due to the presence of an active electron-hole recombination center situated 0.7 eV above the valence band; evidence for this is a small maximum in the quantum efficiency spectrum at a photon energy 0.7 eV less than the bandgap energy. We consider it very improbable that a similar situation exists for NiO, for the following reasons. First, a careful search for a small maximum in  $\eta$  at photon energies less than  $E_g$  was a failure. Secondly, our  $V_{FB}$  value, extrapolated from pH = 9.2 to pH = 1 by 0.059 mV/pH unit, is  $+0.58V$ ; this is very close to the value ( $+0.64V$  SCE) found previously (4) from a Mott-Schottky plot. Therefore we take  $V_{FB} = +0.1V$  at pH = 9.2.

We can now calculate the electron affinity EA of NiO from the relation (10)

$$EA = eV_{FB} - E_g + e\Delta E_F + eV_H + 4.74 \quad [1]$$

Here  $\Delta E_F$  is the energy difference between the Fermi level and the top of the valence band, and  $V_H$  is the potential drop in the Helmholtz layer due to absorbed  $H^+/OH^-$  ions; we take the SCE level 4.74 eV below vacuum (Fig. 5).  $\Delta E_F$ , calculated (3) from the hole concentration and the hole effective mass ( $6 m_0$ ) is less than 0.1 eV for our samples, and can be neglected. In general  $V_H$  is pH dependent according to  $V_H = 0.059 (pH - P_0)$  where  $P_0$  is the pH of zero charge for the NiO-solution interface. From electrophoresis experiments (11)  $P_0$  has been estimated as 10.2 for NiO, with a probable accuracy of one pH unit. At pH = 9.2,  $V_H$  is therefore unlikely to be larger than 0.1V, and it can be neglected as well. Taking all uncertainties into account, we find therefore  $EA = 1.4 \pm 0.2$  eV (Fig. 5).

In NiO the valence band is therefore located 4.9 eV below the vacuum level; for most other oxides the valence band lies 7.0-7.5 eV below vacuum (12, 13). This is due to the fact that in NiO the valence band is made up mainly from Ni-3d type wave functions (3), instead of O-2p wave functions as for

most other oxides. Photoemission experiments (14) indeed show a p-bandedge approximately 2 eV below the d-bandedge. The O-2p band is therefore at its usual position of 7 eV below vacuum, but it is not the valence band in NiO.

Butler and Ginley (15) have proposed a scheme to calculate both  $P_0$  and EA for a compound from the electronegativities of the constituent atoms. For NiO such a calculation leads to a predicted  $P_0$  of 8.5 (in fairly good agreement with the experimental value of 10.2), and an EA of 4.01 eV, (in contrast with the experimental value of 1.4 eV) which would place the valence band at 7.5 eV below the vacuum level. This is very close to the position of the O-2p band, and it suggests strongly that the predictions from the Butler and Ginley scheme will be correct for oxides with O-2p valence bands, but will be incorrect for materials with d-type valence bands.

It is clear from our results that p-type NiO is not a good photocathode for solar photoelectrolysis; although the spontaneous band bending is sufficiently large (0.8V), its large bandgap and the back-reaction render it unsuitable. However, materials which, like NiO, have  $EA + E_g \approx 5.0$  eV could be good photoanodes if they had n-type conductivity. For the presently known n-type oxide photoanodes the sum of EA and  $E_g$  seems to be 7-7.5 eV (12), so that materials with suitably small  $E_g$  do not operate spontaneously, but need an external bias to form the depletion layer. Our results show that n-type oxides with a 3d valence band could have the desirable combination of both small  $E_g$  and small EA, if the 3d valence band lies at least 2 eV above the O-2p band. Regrettably we cannot test this prediction with NiO, since it cannot be doped n-type.

From the review (2) of the data presently available, it is already clear that not all 3d semiconducting oxides will have suitable valence bands; for example, the oxides containing  $Fe^{3+}$  (3d<sup>5</sup>) and  $Zn^{2+}$  (3d<sup>10</sup>) ions have a valence band approximately 7 eV below vacuum. However, photoemission data for Cu<sub>2</sub>O (3d<sup>10</sup>) indicate a valence band 5.3 eV below vacuum (16); this value is confirmed by photoelectrolysis experiments on Cu<sub>2</sub>O (17). Preliminary experiments by us on CuO (3d<sup>9</sup>) also indicate a valence band at approximately 5 eV. Therefore, as a speculation, we suggest that oxides based on Cu<sup>+</sup>, Cu<sup>2+</sup>, Ni<sup>2+</sup>, and possibly Co<sup>2+</sup>, if they can be made n-type, may be promising materials for bias-free solar photoanodes.

### Summary

The flatband potential of p-type NiO, determined from the potential dependence of the instantaneous photocurrent of an NiO/electrolyte/Pt cell, is  $+0.1V$  (SCE), in good agreement with the literature value; the NiO bandgap, determined from spectral quantum efficiency data, is 3.47 eV. Taken together, these two parameters indicate that the conduction band in NiO lies unusually high, only 1.4 eV below the vacuum level. This, in turn, is due to the fact that the valence band is made up of mainly 3d-type wavefunctions, instead of oxygen-2p type wavefunctions as is the case for the majority of oxides investigated so far. If materials with 3d valence bands can be made n-type, then they offer the possibility of constructing solar photoelectrolysis cells which would operate without an externally applied bias.

### Acknowledgment

We are grateful to the National Science and Engineering Research Council of Canada for financial support of this research.

Manuscript received March 9, 1981.

Any discussion of this paper will appear in a Discussion Section to be published in the June 1982 JOURNAL.

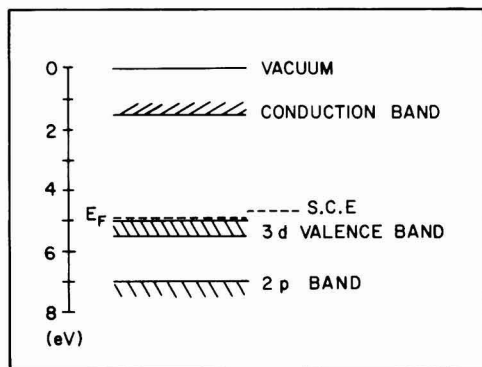


Fig. 5. Energy band scheme for NiO. The width of the 3d valence band is uncertain [Ref. (3)].

All discussions for the June 1982 Discussion Section should be submitted by Feb. 1, 1982.

Publication costs of this article were assisted by Brock University.

## REFERENCES

1. A. Nozik, *Ann. Rev. Phys. Chem.*, **29**, 189 (1978).
2. L. A. Harris and R. H. Wilson, *Ann. Rev. Mater. Sci.*, **8**, 99 (1978).
3. A. J. Bosman and H. J. van Daal, *Adv. Phys.*, **19**, 1 (1970).
4. T. O. Rouse and J. L. Weininger, *This Journal*, **113**, 184 (1966).
5. J. B. Goodenough, in "Progress in Solid State Chemistry," H. Reiss, Editor, Vol. 5, p. 272, Pergamon Press, Oxford (1971).
6. F. P. Koffyberg, K. Dwight, and A. Wold, *Solid State Commun.*, **30**, 433 (1979).
7. R. Newman and R. M. Chrenko, *Phys. Rev.*, **114**, 1507 (1959).
8. K. L. Hardee and A. J. Bard, *This Journal*, **124**, 215 (1977).
9. H. S. Jarrett, A. W. Sleight, H. H. Kung, and J. L. Gillson, *J. Appl. Phys.*, **51**, 3916 (1980).
10. M. A. Butler and D. S. Ginley, *This Journal*, **127**, 1273 (1980).
11. G. A. Parks, *Chem. Rev.*, **65**, 177 (1965).
12. H. P. Maruska and A. K. Ghosh, *Solar Energy Mater.*, **1**, 411 (1979).
13. D. E. Scaife, *Solar Energy*, **25**, 41 (1980).
14. D. E. Eastman and J. L. Freeouf, *Phys. Rev. Lett.*, **34**, 395 (1975).
15. M. A. Butler and D. S. Ginley, *This Journal*, **125**, 228 (1978).
16. J. A. Assimos and D. Trivich, *Phys. Status Solidi A*, **26**, 477 (1974).
17. J. F. Kos, Private communication.

# Investigations into the Electrochromism of Lutetium and Ytterbium Diphthalocyanines

David Walton, Brian Ely, and George Elliott

Marconi Research Laboratories, Great Baddow, Chelmsford, Essex, England

## ABSTRACT

A comparison was made between the infrared, electronic, and electron spin resonance spectroscopic properties of lutetium and ytterbium diphthalocyanines, in the solid state as analytically pure powders, and after vacuum sublimation as thin deposited films. No significant differences were observed. Spectroscopic analysis of the sublimed films during electrochromic changes showed that the lutetium and ytterbium complexes behaved in a similar manner. Both gave identical variations in their electronic spectra with potential. Electron spin resonance data demonstrated that the oxidative color change is not associated with a change in paramagnetism, although the shape of the signal from the lutetium complex was altered upon oxidation. The ytterbium complex displayed no ESR signal before or after electro-oxidation.

Diphthalocyanine complexes of rare-earth elements are of interest in view of their electrochromic properties (1-3). The lutetium complex displays four colors (orange, green, blue, and purple), when an applied potential is varied between  $\sim \pm 1.5V$  (vs. aqueous Ag/AgCl reference) in a suitable electrolytic system. Similar results are obtained whether the complex is deposited as a thin film on an electrode surface (3) or in solution in dimethylformamide (4).

Recent investigations into the electrochromic changes of the Lu complex have concerned the variation in ESR spectrum of solutions in dimethylformamide (4), the charge transport phenomena during oxidation (5-7) and attempts to isolate the oxidized species (8). In this paper we wish to report the results of some electrochemical and spectroscopic studies made on lutetium and ytterbium diphthalocyanines. Comparisons are made between the infrared, visible, and electron spin resonance spectra of the analytically pure solids and sublimed films of the complexes deposited on to conducting glass for electro-optical devices. The voltammetry and the changes in the visible and electron spin resonance spectra of the deposited films during the electrochromic transformations are also investigated.

## Experimental

**Preparation.**—The complexes are prepared by the reaction of the rare-earth acetate salt with excess of phthalonitrile, according to the method of McKay (9).

**Key words:** electrochromism, rare-earth diphthalocyanines, electronic spectra, electron spin resonance spectra.

The required product was isolated from the mix by extraction into chloroform. Solvent evaporation gave a green powder which was carefully washed with organic solvents (acetic anhydride, methanol, acetone) to remove traces of a persistent impurity.

The residual deep-green powder gave elemental analyses for the empirical formula  $M\text{Pc}_2\text{H}$  where  $M = \text{Lu, Yb}$ , and  $\text{Pc} = \text{C}_{32}\text{H}_{16}\text{N}_8$ . Thus:

LuPc <sub>2</sub> H theoretical	C, 64.00; H, 2.77; N, 18.65%
found	C, 64.15; H, 2.79; N, 18.57%
YbPc <sub>2</sub> H theoretical	C, 64.10; H, 2.77; N, 18.69%
found	C, 64.01; H, 2.79; N, 18.85%
Yields 30-40%.	

This procedure is advantageous since no lengthy chromatographic purification is employed, and the product is obtained in an unsolvated condition. The empirical formula is in agreement with the results of a recent x-ray structural analysis on neodymium diphthalocyanine (10) though the presence of the unique proton has not been established unequivocally, and its role in the bonding of the molecule is not clear.

**Film deposition.**—15 mg of the powdered diphthalocyanine complex was placed in a silica crucible, 15 cm above which a 50 cm<sup>2</sup> square of commercially available tin-oxide coated conducting glass was positioned. The conducting glass was a standard commercial product,

Nesa glass, of 80-100  $\Omega$ /square, supplied by PPG Industries Incorporated, Pittsburgh. The apparatus was evacuated to  $\sim 10^{-5}$  Torr and the crucible heated indirectly to  $\sim 450^\circ\text{C}$ . Sublimation of the complex occurred, giving a uniform film, pale green in color, of thickness  $\sim 2000\text{\AA}$ .

**Apparatus.**—Infrared spectra were recorded on Pye-Unicam Model SP3-100 spectrometer, and visible spectra on a Hitachi Perkin-Elmer Model 204, all recorded at room temperature. ESR spectra were recorded on a Varian Model E3 spectrometer. Film thicknesses were measured by the interference fringe method on a Reichert Zetopan research microscope.

Electrolyses were performed using a laboratory-built solid-state potentiostat, based on operational amplifier circuits, and operating in a conventional three-electrode mode. The working electrode comprised a slide of tin-oxide coated conducting glass with a working area  $2 \times 1\text{ cm}$ , upon which the diphthalocyanine complex had been deposited by sublimation. This was suspended in an aqueous electrolyte, containing either 5%  $\text{Na}_2\text{SO}_4$  or 5%  $\text{KCl}$ , at pH 6-7, degassed with argon. An EIL standard aqueous silver/silver chloride reference electrode was employed in all instances. A suitable counterelectrode was a  $1\text{ cm}^2$  piece of platinum foil.

For cyclic voltammetry, the potential sweep was driven by a Commodore PET personal computer employing a Hewlett Packard 59303A digital to analogue converter working on an IEEE 488 bus through the external input of the potentiostat. Scans could be initiated at any intermediate potential between the preset positive and negative limits, and the potential could be varied linearly between the limits starting in either initial sweep direction. Current/potential curves were recorded on a Philips PM8131 X-Y recorder. Potentials were monitored on a Fluke series 8600A digital multimeter.

**Electrolysis procedure.**—The duration of electrolysis and the potential required varied with thickness of the diphthalocyanine film. Electrolyses were continued until the color change was complete. Similar results were obtained whether the potential was stepped directly to the final value or progressively varied to this value over a period of several seconds. Typically at  $+1.5\text{V}$  the initially green-colored film became orange over a period of a few seconds, with the passage of an electric current. The orange species was air stable over several hours. The slide could be removed from the electrolysis cell, washed with distilled water, dried in a stream of nitrogen gas, and placed in a spectrometer. By this means the ESR spectra of the oxidized species were recorded. By returning the slide to the electrolysis cell and maintaining a potential of  $\sim 0\text{V}$ , the green coloration returned. Reduction at  $\sim -0.8\text{V}$  gave a blue species. This was not air stable and returned uniformly to green over a period of a few minutes on removing from the cell. Further reduction at  $\sim -1.3\text{V}$  resulted in the formation of a deep purple coating. This also was unstable in air, and on removal from the cell it reverted uniformly to blue over a period of a few seconds, and then to green in a few minutes. The purple and blue species could also be converted to green within the electrolysis cell, in the absence of air, by the application of a small positive potential. To obtain the visible spectra of the reduced species, the electrolysis was performed in an especially adapted cell with windows of optical glass, placed directly in the beam.

All reagents and chemicals were of analytical grade, purified by conventional methods.

## Results

**Spectral properties of thin films of diphthalocyanine complexes.**—The infrared, visible, and electron spin resonance spectra of sublimed films of the diphthalocyanine complexes were compared with the corresponding spectra of the solid powders and no significant differences were observed.

The infrared spectrum of a lutetium diphthalocyanine film sublimed directly onto a potassium bromide disk is given in Fig. 1. The ytterbium complex gives an almost identical spectrum. The characteristic peaks at  $1320\text{ cm}^{-1}$ ,  $1112\text{ cm}^{-1}$ , and  $724\text{ cm}^{-1}$  are observed in the nujol mulls of the powder samples. [The presence of absorptions at  $2220\text{ cm}^{-1}$ ,  $1515\text{ cm}^{-1}$ ,  $1361\text{ cm}^{-1}$ ,  $760\text{ cm}^{-1}$ , and  $631\text{ cm}^{-1}$  (sharp) in the crude product, obtained directly from chloroform extraction, shows the presence of a persistent impurity, removed by careful solvent washings.]

Comparison with other published infrared spectra shows a very close correspondence in the prominent lines for other rare earth complexes, as shown in Table I, which lists the results of MacKay *et al.* (9), Kirin *et al.* (11), Kirin *et al.* (12), Moskalev and Kirin (13), and Misumi and Kasuga (14). There are some discrepancies, for example, we do not find a line in the region of  $1070\text{--}1078\text{ cm}^{-1}$ , and it is possible that this only appears in the blue form of the rare-earth complex. Some of the other workers have listed several other minor peaks, which we did not detect in our analysis. It is possible that some of the spectra could indicate the presence of impurities; a particular example is the spectrum published by Corker *et al.* (4), which would indicate a high proportion of the colorless persistent by-product which we found in our crude preparation, and also reported by MacKay *et al.* (9).

The visible spectrum of a green sublimed ytterbium diphthalocyanine film on conducting glass slide is shown in Fig. 2, curve (a), and displays a broad main peak at  $668\text{ nm}$ , the half peak width being  $55\text{ nm}$ , and a distinctive weak and broad peak at  $463\text{ nm}$ . The shape of this spectrum is very similar to that of green solutions of the complex as powder dissolved in a range of organic solvents, though the peaks are narrower in solution. Thus, in chloroform: lutetium complex main peak  $660.5\text{ nm}$  ( $\epsilon = 1.71 \times 10^5$ ), half peak width  $19\text{ nm}$ , and weak broad peak at  $458\text{ nm}$ ; ytterbium complex,  $661\text{ nm}$  ( $\epsilon = 1.59 \times 10^5$ ) half peak width  $19\text{ nm}$ ,  $457\text{ nm}$  (weak). Solvatochromic effects do not appear to be pronounced in the visible spectra of the green complexes, and the wavelengths of maximum absorption,  $\lambda_{\text{max}}$ , of the lutetium (ytterbium) complex in methanol solution is  $657\text{ nm}$  ( $658\text{ nm}$ ), and in dimethylsulfoxide solution is  $661\text{ nm}$  ( $661.5\text{ nm}$ ).

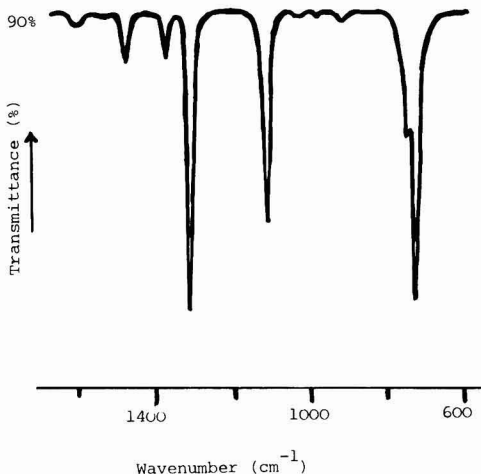


Fig. 1. Infrared spectrum of lutetium diphthalocyanine, as sublimed film on potassium bromide disk.

Table I. Prominent infrared lines ( $\text{cm}^{-1}$ )

This paper LuPc:H	Ref. (9) GdPc:H	Ref. (11) NdPc:H	Ref. (12) NdPc:	Ref. (13)			Ref. (14). Only "metal sensitive" lines listed					
				NdPc:H	YPc:H	ErPc:H	LaPc:H	CePc:H	NdPc:H	EuPc:H	ErPc:H	YbPc:H
724	725	726	725	726	728	729						
740	741	740	740	738	743	743						
778	778	772	771	768	780	783						
882	881	878	880	874	883	884						
1060	1054	1060	1060	1056	1052	1057	880	884	881	885	886	887
	1070	1075	1075				1059	1050	1056	1062	1063	1064
1112	1110	1112	1114	1106	1110	1113	1084	1070	1072	1077	1075	1078
1320	1314		1326	1321	1321	1327						
1370	—		1360									
1450	1440		1448									
1600	1600		1604									

These solvents span a wide range of dielectric constants (Table II). These results suggest the ground and excited states of the transition to be similar in polarity, unlike, *e.g.*, merocyanine dyes where a change of dielectric produces a considerable shift in wavelength of maximum absorption (20).

The electron spin resonance spectrum of solid, analytically pure, lutetium diphthalocyanine powder at room temperature displays a single resonance at 3390G, the half peak width being 9.7G. This is slightly sharpened by cooling to liquid nitrogen temperatures, but no structure is observed. Similar structureless signals are obtained in chloroform and purified dimethylformamide solutions. The sharp single line at  $g \sim 2$  indicates that the unpaired electron is located on the porphyrin ring and not on the metal.

When a sublimed film of lutetium diphthalocyanine on tin-oxide coated glass is suspended in the beam, the same signal is observed, though broader, the half peak width being 22.0G.

Ytterbium diphthalocyanine shows no ESR signal at all, whether in the solid state, in solution, or as a sublimed film.

**Electrochemical transformations using cyclic voltammetry.**—Figure 3 shows the current/potential curve for a sublimed film of lutetium diphthalocyanine on conducting glass, suspended in 5% aqueous sodium sulfate solution. Potentials are referred to aqueous silver/silver chloride, and the sweep rate was 10 mV/sec.

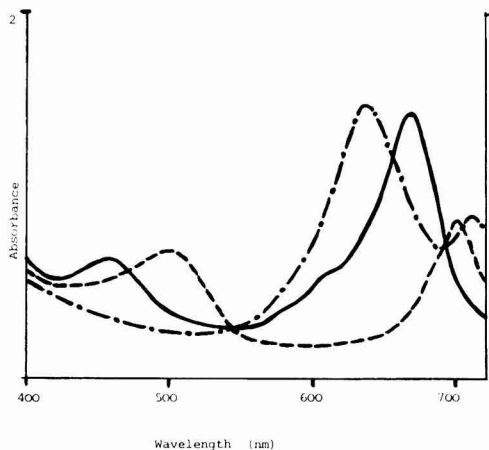


Fig. 2. Electronic spectrum of ytterbium diphthalocyanine as sublimed film on conducting glass. Variation with electrode potential. (a) — green form ( $\sim 0\text{V}$ ); (b) --- electro-oxidized orange species ( $\sim +1.5\text{V}$ ); (c) —●— electro-reduced blue species ( $\sim -0.8\text{V}$ ). (Electrolyte 5% aqueous KCl, potentials w.r.t. aqueous Ag/AgCl reference film thickness  $\sim 2000\text{\AA}$ ).

Table II.

Solvent	Dielectric constant $\epsilon$	Dipole moment $\mu$	Absorption max LuPc:H (nm)	Absorption max YbPc:H (nm)
$\text{CHCl}_3$	4.81	1.15	660.5	661
$\text{CH}_3\text{OH}$	32.7	2.87	657	658
$(\text{CH}_3)_2\text{SO}$	46.7	3.9	661	661.5

Curve (a) shows the first full oxidation/reduction cycle, starting with an initially green film at 0V. At  $+1.5\text{V}$  the color becomes orange and an oxidation current is passed. No reduction current is observed in this region upon scan reversal and the potential is swept to  $-0.2\text{V}$  before the green color reappears and a reduction current is observed. The shape and definition of these waves depend very much upon the sweep rate, and faster scan rates are unsatisfactory. The green/orange change is color reversible but the difference of  $\sim 1.7\text{V}$  between the oxidative and reductive reactions suggests that chemical processes are associated with the electron transfer reactions. Further reduction to  $-1.0\text{V}$  produces a blue coloration with the passage of a reduction current. Scan reversal produces an oxidation wave at  $-0.2\text{V}$  with the reappearance of the green color. These results are reproducible over several cycles.

Curve (b) displays the first blue/green reductive cycle, limiting the voltage sweep between 0 and  $-1.6\text{V}$ , starting from green at 0V, and demonstrates that this change is independent of the orange/green transformation. It is less sensitive to scan rates and good peaks of similar "quasi-reversible" shape are obtained at 140 mV/sec. There is a linear rise of current with scan rate, and a close to linear increase in the peak separation potential within the range of scan rates 10 mV/sec  $\rightarrow$  140 mV/sec.

Further reduction at potentials beyond  $-1.6\text{V}$  results in a purple coloration in the film, but an ill-

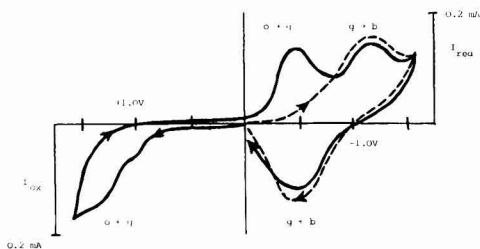


Fig. 3. Lutetium diphthalocyanine as sublimed film on conducting glass. Cyclic voltammetry in 5% aqueous KCl vs. aqueous Ag/AgCl reference, film thickness 2000 $\text{\AA}$ , slide area  $\sim 2\text{ cm}^2$ . Scan rate 10 mV/sec, 1st cycle. Letters refer to color changes, g = green, o = orange, b = blue. (a) — full oxidation/reduction cycle: start 0V, initial sweep anodic. (b) --- reduction cycle only: start 0V, initial sweep cathodic.



defined wave is observed together with current due to solvent breakdown and is not shown in the figure.

The above results are for a film thickness  $\sim 2000\text{\AA}$ . Variations in the film thickness affect the voltammetry, particularly of the green/orange transformation.

**Electronic spectra.**—Figure 2 shows the visible spectrum of a single film of ytterbium diphthalocyanine sublimed on to conducting glass in (a) the initial green, (b) the oxidized orange, and (c) the reduced blue forms. All spectra were recorded *in situ* in an electrochemical cell fitted with optical glass sides, and the potentials employed were 0V, +1.5V, -0.8V, respectively (vs. aqueous Ag/AgCl reference, 5% aqueous KCl electrolyte). The results from the lutetium complex are very similar and the sets of data from both complexes are given in Table III.

These spectral changes are of a similar form to those obtained from electrochemical transformations of a solution of lutetium diphthalocyanine in carefully purified dimethylformamide (4). Purification of the solvent is necessary because green solutions of lutetium and ytterbium diphthalocyanines in dimethylformamide gradually become blue on standing in the absence of an electrode potential. The mechanism of this change is not clear though it has been reported that green solutions of gadolinium diphthalocyanine became blue upon the addition of base (9), and that Russian workers have added hydrazine to solutions of lutetium diphthalocyanine in DMF to improve solubility, giving deep blue solutions (8, 15, 16).

We have established that the addition of triethylamine to green solutions of lutetium and ytterbium diphthalocyanines in dimethylsulfoxide, methanol, acetone, and freshly purified dimethylformamide (vacuum distilled from anhydrous  $\text{CuSO}_4$ ), produces an immediate blue coloration. It has not been shown with certainty that this base-produced blue color is due to the same species as that produced by electrochemical reduction. There are similarities in the electronic spectra of both species. The spectrum of the electroreduced blue species is given in curve (c) of Fig. 2. A distinctive twin peak is observed, that at shorter wavelength being more intense than that at long wavelength. A similar shape is observed in basified solutions though in these instances there is some distortion in the shape of the long wavelength peak, and also a weak "shoulder" at  $\sim 560\text{ nm}$  that is not present in the spectrum of the electrochemically reduced form. Comparative data for blue species in methanol, acetone, dimethylsulfoxide, and dimethylformamide solutions, compared to the electroreduced blue species as a thin film are given in Table IV. Blue solutions in the above solvents are air stable. Solutions in dimethylformamide have retained their color over several months, and evaporation yields dark crystals which are solvated (12). The electrochemically produced blue coloration in thin solid films is unstable in air, and returns to the green form over a period of a few minutes.

Color changes which parallel the electrochemical color changes can be induced by chemical oxidants

Table III. Electronic spectra of lutetium and ytterbium diphthalocyanines as sublimed films on conducting glass. Variation with electrode potential

Potential <sup>a</sup> (V)	Color	Metal complex	Characteristic absorptions, $\lambda_{\text{nm}}$ (absorbance <sup>b</sup> )
0	Green	Lu	668 nm (1.32) 463 (weak, broad)
0	Green	Yb	668 nm (1.46) 465 (weak, broad)
+1.5	Orange	Lu	698 nm (0.56) 493 (broad, 0.43)
+1.5	Orange	Yb	700 nm (0.60) 496 (broad, 0.48)
-0.8	Blue	Lu	634 nm (1.30) 714 (0.60)
-0.8	Blue	Yb	637 nm (1.42) 713 (0.66)

<sup>a</sup> Potentials vs. aqueous Ag/AgCl reference, 5% aqueous KCl electrolyte.

<sup>b</sup> Both films  $\sim 2000\text{\AA}$  in thickness.

Table IV. Electronic spectra of blue forms of lutetium and ytterbium diphthalocyanines

Medium	Metal complex	$\lambda_1$	$\lambda_2^b$	Abs ( $\lambda_1$ )	Abs ( $\lambda_2$ )
Solution in DMF <sup>a</sup>	Lu	614	693	1.91	
	Yb	616	688	1.95	
Solution in MeOH <sup>a</sup>	Lu	617	696	1.89	
	Yb	619	689	2.06	
Solution in Acetone <sup>a</sup>	Lu	609	691	1.90	
	Yb	611	687	1.94	
Solution in DMSO <sup>a</sup>	Lu	617	692	1.91	
	Yb	619	690	1.93	
Thin film in aqueous $\text{Na}_2\text{S}_2\text{O}_4$ (2%) / $\text{Na}_2\text{SO}_3$ (2%)	Lu	635	705	1.70	
	Yb	637	703	1.43	
Thin film at -0.8V electroreduced (5% KCl)	Lu	634	714	1.88	
	Yb	637	713	1.82	

<sup>a</sup> Solutions were prepared by dissolving the green solid complex in the required solvent and were converted to blue by the addition of a trace of  $\text{Et}_3\text{N}$ .

<sup>b</sup> This peak is somewhat misshapen on the spectra of solutions prepared as above. Sharper definition is observed in the spectrum of a DMF solution that has been eluted from a chromatographic column packed with neutral alumina [see Ref. (17)].

and reductants. Figure 4 displays the visible spectra of a film of lutetium diphthalocyanine on a glass slide in (a) initially green form, (b) oxidized to orange after  $\sim 1\text{ min}$  in 4% (w/v) aqueous acidified ceric sulfate solution, (c) reduced to blue after  $\sim 1\text{ min}$  in a mixture of 2% sodium dithionite/2% sodium sulfite solution, (d) purple after 2 min in 4% aqueous sodium dithionite solution. The orange species is air stable but the blue and purple forms revert to green on removal from solution. The spectra were recorded in a cell with optical glass sides using a Grubb-Parsons experimental spectrometer based on a D2 monochromator unit. The data from the chemically reduced blue species are included in Table IV for comparison. The difficulty in arresting the reduction process at the blue stage reflects the difference between chemical reduction and electrochemical reduction, where a precise potential can be applied to achieve maximum effect in a system where species can exist in several oxidation states.

**Electron spin resonance.**—In the green form lutetium diphthalocyanine has a single ESR absorption [Fig. 5, curve (a) for a thin film on conducting glass]. Upon electro-oxidation at +1.8V in 5% aqueous sodium sulfate (w.r.t. aqueous Ag/AgCl reference) for several minutes, the absorption remains of similar amplitude but has become much sharper [Fig. 5, curve (b)]. The

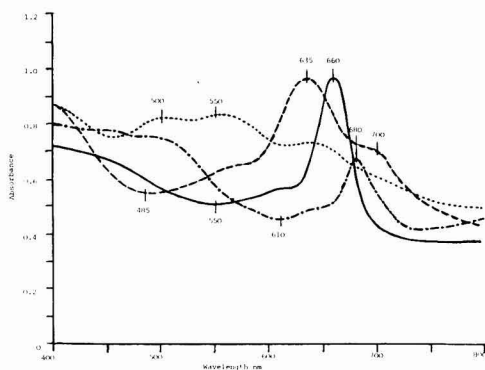


Fig. 4. Electronic spectrum of lutetium diphthalocyanine as sublimed film on glass. Color changes induced by chemical oxidants/reductants. (a) — initial green form; (b) —●— orange after  $\sim 1\text{ min}$  in 4% aqueous ceric sulfate solution; (c) - - - blue after  $\sim 1\text{ min}$  in aqueous mixture of 2% sodium sulfite + 2% sodium dithionite; (d) - · - · purple after  $\sim 5\text{ min}$  in 4% aqueous sodium dithionite solution.



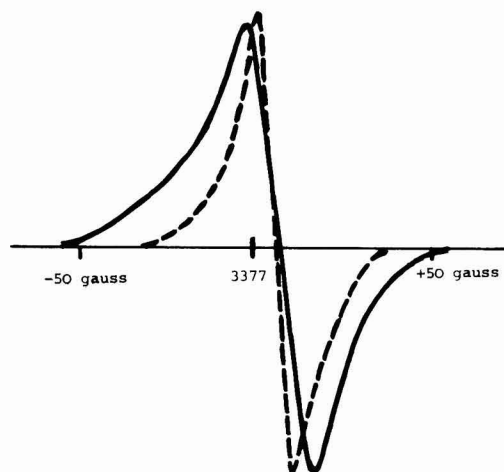


Fig. 5. Lutetium diphthalocyanine as sublimed film on conducting glass. Change of electron spin resonance spectrum with oxidation potential. (a) — green form ( $\sim 0V$ ); (b) - - - orange form ( $\sim +1.5V$ ). (Electrolyte 5% aqueous  $Na_2SO_4$ , potentials vs. aqueous  $Ag/AgCl$  reference. Instrumental conditions: room temperature, modulation amplitude 5G, power 2 mW).

color of the film is orange. The color change is, therefore, not associated with a loss of paramagnetism in the system. If electro-oxidation is continued for 1 hr, a 30% loss in intensity of the sharp signal is observed, but on returning to the green form at 0V, the broader absorption reappears at its full intensity. The slide was removed from the electrochemical cell, washed, and dried before placing in the cavity of the spectrometer at room temperature.

In 5% aqueous KCl electrolyte a more rapid narrowing of the signal is observed, concomitant with the rapid appearance of the orange coloration. Further electrolysis for  $\sim \frac{1}{2}$  hr results in the total loss of the sharp signal, but, on returning to the green form at 0V the full intensity of the initial broad absorption is restored.

It seems that exhaustive electrolysis results in a total loss of signal. We have confirmed that this occurs in solutions of lutetium diphthalocyanine that are electro-oxidized in DMF/0.1M tetrabutylammonium tetrafluoroborate, as has been recorded (4), but the color change from green to orange is associated with a sharpening of the signal, not a loss of paramagnetism. This result is supported by the behavior of films of ytterbium diphthalocyanine. This complex is ESR inactive in the green form. It remains inactive after electro-oxidation to orange at  $+1.8V$  even after  $\sim 1$  hr of electrolysis, though the color change occurs in less than 1 min. No change of paramagnetism occurs in this system.

Some comparative, but less detailed measurements were made on holmium and europium diphthalocyanines. Solid samples showed ESR signals that, compared with lutetium, were only 0.01 times the value in the case of holmium and 0.1 times the value in the case of europium; the ytterbium signal was virtually zero. Thin films of Ho and Eu did not show sufficiently large signals to enable differences to be observed between the green and orange forms of the complex, the glass substrate giving a small residual signal which masked the small responses due to the rare earth compounds.

### Discussion

The observation of ESR signals from both the initially green and the electro-oxidized orange forms of

lutetium diphthalocyanine is in accord with the evidence of Nicholson and Pizzarello (5, 6) who measured an approximately two-electron change from charge-transport data during electro-oxidation, employing aqueous sodium sulfate and potassium chloride electrolytes. These results do not necessarily conflict with those of Corker *et al.* (4) who reported that in dimethylformamide solution with tetrabutylammonium tetrafluoroborate support electrolyte, the electro-oxidation to a "yellow-red" species was concomitant with a loss of ESR signal and the removal of one electron, since the experimental conditions were different in this latter instance.

If the electro-oxidation is a multi-stage reaction in which the color change and modification of the ESR signal are distinct from the eventual loss of the ESR signal, then the relative rates of these processes may differ in solution compared to a solid film, particularly if ionic migration (5, 6) as well as electron transfer is important during the transformation. Furthermore, the behavior of lutetium diphthalocyanine in dimethylformamide solution appears to be complicated, and the nature of all species that may be present is not certain. Analytical data published by Kirin *et al.* (12) suggests that a blue product obtained from dimethylformamide solution may have the composition  $R_2Pc_3 \cdot 3DMF$ , where R is the rare-earth atom.

The difference in behavior of the ESR signal in sodium sulfate solution as compared to potassium chloride solution is paralleled by the observations of Nicholson and Pizzarello (18) who also noticed a difference between these electrolytes. They showed that the propagation of the anodic reaction boundary in a thin film of lutetium diphthalocyanine depended on the nature of the ambient gas, and that the boundary ceased to move in sodium sulfate electrolyte if oxygen was excluded, but this was not true in potassium chloride electrolyte. It was concluded that oxygen was bound in the red form of the diphthalocyanine prepared in sodium sulfate electrolyte. Raynor *et al.* (19) have studied the origin of ESR signals in diamagnetic phthalocyanines of Zn, Ni, Pd, and Pt and have suggested that oxygen is the cause of a substantial part of the signal, but is not present as a simple radical with the unpaired electron localized on the oxygen. We conclude that the difference in ESR behavior of the lutetium complex in aqueous sodium sulfate and potassium chloride electrolytes may represent the differential uptake of oxygen following an initial two-electron change to the orange species. However, the existence of the original ESR signals in the green lutetium complex, and the much lower ESR responses from the holmium, europium, and particularly ytterbium complex are not easily explained by this simple model, and further work is required to elucidate the structure of these species.

### Acknowledgments

This paper is published by permission of the Technical Director, GEC-Marconi Electronics Limited.

We wish to thank Professor G. R. Luckhurst and the Southampton University Chemistry Department for performing the electron spin resonance measurements; the Chelmsford College Science Department for the use of their u.v./visible spectrometer, and Mr. I. Forster for producing a program for the PET computer to perform voltammetry.

Manuscript submitted Feb. 2, 1981; revised manuscript received May 12, 1981.

Any discussion of this paper will appear in a Discussion Section to be published in the June 1982 JOURNAL. All discussions for the June 1982 Discussion Section should be submitted by Feb. 1, 1982.

### REFERENCES

1. P. N. Moskalev and I. S. Kirin, *Opt. Spectrosc.*, **29**, 220 (1970).

2. P. N. Moskalev and I. S. Kirin, *Russ. J. Phys. Chem.*, **46**, 1019 (1972).
3. M. M. Nicholson and R. V. Galiardi, Final Report Contract N 62269-76-C-0574-AD-A039596; *Chem. Abstr.*, **87**, 144073V (1977).
4. G. A. Corker, B. Grant, and N. J. Clecak, *This Journal*, **126**, 1339 (1979).
5. M. M. Nicholson and F. A. Pizzarello, *ibid.*, **126**, 1490 (1979).
6. F. A. Pizzarello and M. M. Nicholson, *J. Electron. Mater.*, **9**, 231 (1980).
7. M. M. Nicholson and F. A. Pizzarello, *This Journal*, **127**, 821 (1980).
8. P. N. Moskalev, G. N. Shapkin, and A. N. Darovskikh, *Russ. J. Inorg. Chem.*, **24**, 188 (1979).
9. A. G. MacKay, J. F. Boas, and G. J. Troup, *Aust. J. Chem.*, **27**, 955 (1974).
10. K. Kasuga, M. Tsutsui, R. C. Petterson, K. Tatsumi, N. VanOpdenbosch, G. Pepe, and E. F. Mayer, Jr., *J. Am. Chem. Soc.*, **102**, 4835 (1980).
11. I. S. Kirin, P. N. Moskalev, and Yu. A. Makashev, *Russ. J. Inorg. Chem.*, **12**, 369 (1967).
12. I. S. Kirin, P. N. Moskalev, and N. V. Ivannikova, *ibid.*, **12**, 497 (1967).
13. P. N. Moskalev and I. S. Kirin, *ibid.*, **15**, 7 (1970).
14. S. Misumi and K. Kasuga, *Nippon Kagaku Zasshi*, **92**, 335 (1971).
15. P. N. Moskalev, G. N. Shapkin, and Yu. S. Misko, *Radiokhimiya*, **20**, 343 (1978).
16. P. N. Moskalev and G. N. Shapkin, *Elektrokhimiya*, **14**, 574 (1978).
17. I. S. Kirin, P. N. Moskalev, and Yu. A. Makashev, *Russ. J. Inorg. Chem.*, **10**, 1065 (1965).
18. M. M. Nicholson and F. A. Pizzarello, *This Journal*, **127**, 2617 (1980).
19. J. B. Raynor, M. Robson and A. S. M. Torrens-Burton, *J. Chem. Soc. Dalton Trans.*, **23**, 2360 (1977).
20. L. G. S. Brooker, G. H. Keyes, and D. W. Haseltine, *J. Am. Chem. Soc.*, **73**, 5350 (1951).

## Technical Note



### Excitation into Charge Transfer Band of $\text{Y}_2\text{O}_3\text{S:Eu}$

Lyuji Ozawa\*

Matsushita Electric Industrial Company, Limited, Central Research Laboratories, Moriguchi, Osaka, Japan

This note describes the mode of excitation into the charge transfer band of  $\text{Y}_2\text{O}_3\text{S:Eu}$  phosphor. In general, the radiative transition impurities (i.e., activator ions) in crystals can be optically excited in three ways; by (i) direct excitation into absorption of the ions (direct), (ii) excitation into associated activator-host absorption (i.e., charge transfer band, CTB), and (iii) indirect excitation via absorption of host lattice (host), i.e., radiative recombination of mobile electron-hole pairs (radiation-induced carriers) at activator ions. This can be seen comprehensively in excitation spectrum giving rise to luminescence. Figure 1 shows, for instance, the excitation spectrum of the  $\text{Eu}^{+3}$  luminescence line at 627 nm ( $^5\text{D}_0 \rightarrow ^7\text{F}_2$  transition) of  $\text{Y}_2\text{O}_3\text{S:Eu}$ ; the spectrum consists of the small and narrow direct excitation lines ( $4f^6$  transition), and a broad and strong CTB overlapped partially with a host band (shadowed). It has been believed that the CTB excitation belongs to the host excitation (1) because the CTB partially overlaps with the host absorption band and the hole photoconductivity has been suggested in  $\text{Y}_2\text{O}_3\text{S:Eu}$  under the CTB radiation (2). It has then been said that the CTB is an essential necessity to obtain the efficient cathodoluminescence phosphors (3). A question is raised as to whether the CTB belongs to the host excitation.

An experimental difficulty in determining the excitation mode of the CTB is that by either way of the photoexcitations, the activator ions emit the same characteristic activator luminescence even though the excitation mechanisms involved are quite different. Thus, the ambiguity always remains in the discussion of the CTB excitation if the study has been made with the measurements of the luminescence or excita-

tion spectra alone. It has recently been shown that the concentration dependence (CD) curve of activator luminescence provides us with a powerful tool to clarify the excitation mode of activator ions (4). There are two excitation modes to be considered for the luminescence study in the first-order approximation: (i) direct excitation and (ii) indirect excitation through mobile carriers. The mode of the excitations can be clearly distinguished if the measurements of the CD curves are made on powdered phosphor

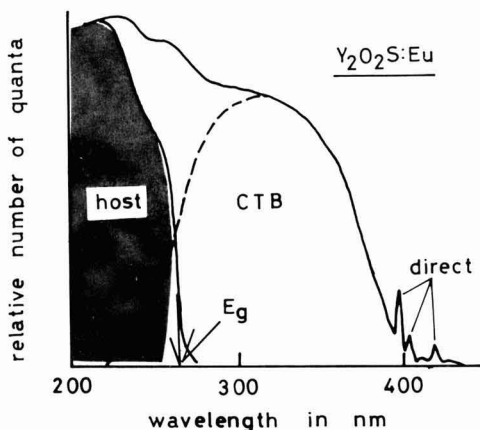


Fig. 1. Excitation spectrum of  $\text{Y}_2\text{O}_3\text{S:Eu}$  (0.01) giving rise to luminescence line at 627 nm ( $^5\text{D}_0 \rightarrow ^7\text{F}_2$  transition). The spectrum consists of host absorption band (host), charge transfer band (CTB), and direct excitation lines of  $\text{Eu}^{+3}$  (direct).

\* Electrochemical Society Active Member.

Key words: luminescence, phosphor.

screens. For direct excitation of activator ions, the time-averaged luminescence intensities from phosphor screen, obtained under constant intensity, has a linear dependence on activator concentration " $C$ " in the concentration region where the concentration quenching mechanisms are neglected, and the normalized CD curve exhibits no crystal size effect (5). When the activator luminescence is due to the radiative recombination of the mobile carriers (created by host lattice absorption) at activator ions, the CD curve has two slopes, depending on  $C$ , in which  $C^*$  at the discontinuity (i.e., inflection of the curve) shows the crystal size effect due to the mobile carriers;  $C^*$  decreases as the crystal size increases (4-6). We use this distinguishable different appearance in the CD curves to clarify the mode of the CTB excitation of  $Y_2O_3S:Eu$ .

Figure 2 shows the CD curves of the  $Eu^{+3}$  luminescence line at 627 nm of  $Y_2O_3S:Eu$  under irradiation of electron beam (CL), host-photoexcitation using the 200 nm radiation (PL-host), CTB excitation by the 320 nm radiation (PL-CTB), and direct photoexcitation using the 417 nm radiation (PL-direct). We used the 200 nm radiation for the PL-host to keep away from the entanglement of the CTB in the excitation. It can be seen that the CD curve of the PL-host is almost identical with that of CL, because the activator ions in both cases are predominantly excited through the mobile carriers created in the crystal (6). Both curves have two slopes and the value of  $C^*$  shows the crystal size effect. The normalized curve for the PL-direct fits in with the theoretical curve of  $C(1-C)^{12}$  (unity slope below  $C = 1 \times 10^{-2}$  and optimum  $C = 8 \times 10^{-2}$ ) (5) and the curve exhibits no crystal size effect.

Referring the CD curves of the PL-host and PL-direct, it has been revealed that the mode of the CTB excitation actually belongs to the direct excitation. The CD curve for the CTB has unity slope, instead of two slopes, in the region below  $C = 3 \times 10^{-3}$  and exhibits no crystal size effect. There is no evidence to show that the luminescence process at the  $Eu^{+3}$  is determined by the mobile carriers. The curve obtained clearly indicates that the CTB excitation falls under the category of direct excitation by incident radiation rather than the category through host-lattice excitation.

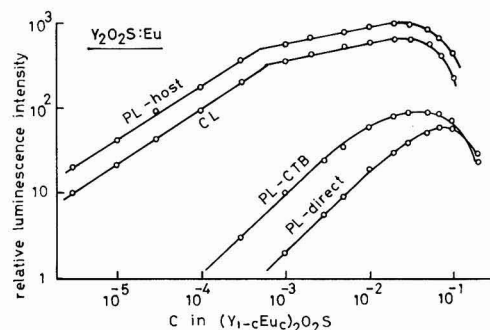


Fig. 2. Concentration dependence curves of  $Eu^{+3}$  luminescence of  $Y_2O_3S:Eu$  under irradiation of various excitation modes: electron beam (CL), host photoexcitation using 200 nm radiation (PL-host), charge transfer photoexcitation with 320 nm radiation (PL-CTB), and direct photoexcitation using 417 nm radiation (PL-direct).

Irradiation of the CTB radiation of  $Y_2O_3S:Eu$  probably creates an  $Eu^{+2}$  and a hole as a consequence of the electron (charge) transfer from anion ( $O^{2-}$  or  $S^{2-}$ ) to  $Eu^{+3}$ . Since hole photoconductivity has been suggested in  $Y_2O_3S:Eu$  under irradiation of the CTB radiation (2), the  $Eu^{+2}$  may be stable at room temperature and does not release the electron; the luminescence may occur as the  $Eu^{+2}$  captures the free hole (4). Because  $Eu$  ions in the crystal never move out from their occupied lattice sites during the luminescence process, the absorption (and subsequent luminescence) is definitely limited in the volume where the CTB radiation has been penetrated. In other words, the place at which the luminescence occurs is not determined by the free holes which move out from the location created. The penetration of the CTB radiation into the powdered phosphor screen is determined by  $(\alpha + \beta)^{-1}$  where  $\alpha$  and  $\beta$  are absorption and scattering coefficients, respectively. The value of  $\alpha$  changes with  $C$ ; i.e.,  $\alpha = kC$  where  $k$  is expressed in  $cm^{-1}$  and depends only on the oscillator strength of the absorption. When the activator concentration is below  $3 \times 10^{-3}$ ,  $\alpha \ll \beta$ , and the penetration volume is determined by  $\beta^{-1}$  and the cross section of the radiation beam; both are constant, resulting in the linear dependence of luminescence intensities on  $C$  (5). The penetration depth is decreased with increasing activator concentrations beyond  $3 \times 10^{-3}$  ( $\alpha \gtrsim \beta$ ); subsequently, the apparent optimum activator concentration moves to  $C = 5 \times 10^{-2}$  (5).

The results of the CD curves suggest that the CTB and host absorption bands possibly occur at different levels, and the partial overlap in the excitation spectrum (Fig. 1) is not real; they are apparently overlapped. If it is so, the band model may be inadequate to explain the luminescence process of the  $Eu^{+3}$  in  $Y_2O_3S:Eu$  which has been considered (1, 3).

In conclusion, it has been shown that the excitation into the charge transfer band falls under the category of the direct excitation by the incident radiation, which the excitation is restricted in the penetration volume of the incident radiation. Therefore, it can be said that the presence of the charge transfer band is not essential to obtain the efficient cathodoluminescence phosphors. The efficient activator cathodoluminescence is predominantly due to the radiative recombination of the mobile electron-hole pairs at the activator ions, and the number of the electron-hole pairs created in the penetration volume would be about 100 times the number of the direct excitation of the activator ions by the incident electrons.

Manuscript received May 26, 1981.

Any discussion of this paper will appear in a Discussion Section to be published in the June 1982 JOURNAL. All discussions for the June 1982 Discussion Section should be submitted by Feb. 1, 1982.

Publication costs of this article were assisted by Matsushita Electric Industrial Company, Limited.

#### REFERENCES

1. C. W. Struck and W. H. Fonger, *Phys. Rev. B*, **4**, 22 (1971).
2. W. I. Dobrov and R. A. Buchanan, *Appl. Phys. Lett.*, **21**, 201 (1972).
3. D. J. Robbins, B. Cockayne, J. L. Glasper, and B. Lent, *This Journal*, **126**, 1222 (1979); H. Yamamoto and T. Kano, *ibid.*, **126**, 305 (1979).
4. L. Ozawa, *ibid.*, **128**, 140 (1981).
5. L. Ozawa, *ibid.*, **126**, 106 (1979).
6. L. Ozawa and H. N. Hersh, *Phys. Rev. Lett.*, **36**, 683 (1976).

## Erratum

### Concentration Profiles in Electrowinning Circuits

#### I. Current Efficiency

F. M. KIMMERLE, R. L. LeROY, and O. VITTORI

(This Journal, Vol. 128, No. 9, pp. 1864-1869)

Due to the Canadian postal disruptions, proofs of this article were not received in time for correction. Figure 2 was mislabelled, and should be replaced by the following

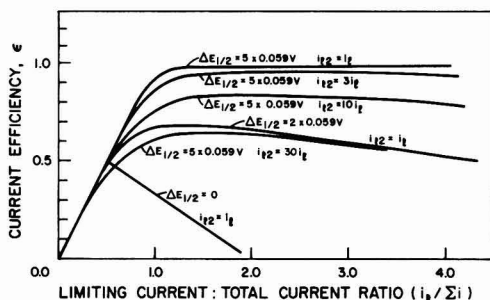


Fig. 2. Current efficiency variation for kinetic parameters characteristic of metal deposition in competition with hydrogen evolution,  $(\alpha n)_1 = 2.0$  and  $(\alpha n)_2 = 0.5$ .

In the discussion of Fig. 1 and 2, case 1 should have stated that efficiency approaches the asymptotic value  $\epsilon_\infty = 1$  when the current density is *much less than* the limiting current density, in situations where the transfer coefficient for metal deposition is less than that for the competing reaction.

Before Eq. [3], the requirement for a function describing current density should have read that it must vary in a monotonic fashion from case 1 to case 2, and that

$$\lim_{C \rightarrow \infty} \epsilon = \epsilon_\infty \quad \text{and} \quad \lim_{C \rightarrow 0} \epsilon = 0$$

In the discussion of Fig. 5, the statement concerning the dependence of current efficiency on  $i_l/\Sigma i$  should have noted that it can be approximated by two straight-line portions at concentrations above 0.01M.



# Determination of the Measurable Low $P_{O_2}$ Limits of Oxygen Ion-Conducting Solid Electrolytes

**T. A. Ramanarayanan\***

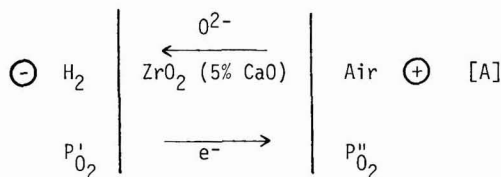
Exxon Research and Engineering Company, Corporate Research-Science Laboratories, Linden, New Jersey 07036

Oxygen ion-conducting solid electrolytes based on  $ZrO_2$  and  $ThO_2$  are widely used for the measurement of oxygen chemical potentials in high temperature gaseous environments, melts and solid phases (1). These electrolytes have also applications in determining the kinetics of diffusion-controlled processes (2) and the rates of surface reactions (3).

In most applications of oxygen-conducting solid electrolytes, the ionic transference number of the electrolyte,  $t_{ion}$ , must be unity. At extremely low  $P_{O_2}$  values, the ionic transference number of the electrolyte is decreased by the introduction of excess electronic conduction. Thus, especially for low oxygen partial pressure measurements, there is a need to establish the low  $P_{O_2}$  limits (above which  $t_{ion} > 0.99$ ) as a function of temperature. Since these low  $P_{O_2}$  limits are extremely sensitive to the presence of minute impurity levels in the electrolyte (4), the measurable low  $P_{O_2}$  limits can vary between two electrolytes of nearly identical chemical composition.

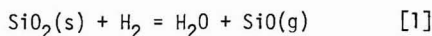
In the present communication, a simple experiment for the determination of the low  $P_{O_2}$  limits of an oxide-ion conducting electrolyte is discussed. The technique has been used for establishing the low  $P_{O_2}$  limits of  $ZrO_2$  ( $\sim 5\%$   $CaO$ ) solid electrolyte tube purchased from Degussa.

The electrochemical cell used in the present experiments may be represented as:



in which the left hand electrode is extremely pure hydrogen. It would be nearly impossible

experimentally to obtain a  $P_{O_2} = 0$  in the hydrogen electrode. For one thing, even the best purification ensures only a finite extremely low  $P_{O_2}$  level. Secondly, a reaction between the  $H_2$  gas and the quartz tube in which the electrochemical cell was placed is possible in principle:



At a temperature of 1100°K, which is in the middle of the temperature range used in the current study, the equilibrium constant,  $K_1$ , for reaction [1] equals  $2.05 \times 10^{-16}$ . Assuming that both  $H_2O$  and  $SiO$  are generated by reaction [1] only, one can assume that  $PH_{2O} \approx P_{SiO}$ . With this assumption, one calculates at 1100°K a  $PH_{2O}$  value of  $1.43 \times 10^{-8}$  atm. This amount of water vapor in  $H_2$  would correspond to a  $P_{O_2}$  of  $3.6 \times 10^{-34}$  atm, which is extremely low. It is not suggested here that the reaction [1] proceeds to equilibrium, but only that even if it did, the  $P_{O_2}$  in the hydrogen stream would be very low.

According to Schmalzried (5,6), the Emf of cell A under these conditions is given by,

$$E = \frac{nRT}{4F} \ln \left[ \frac{p_{\theta}^{1/n+p'_1} p_{O_2}^{1/n}}{p_{\theta}^{1/n+p''_1} p_{O_2}^{1/n}} + \frac{p_{\theta}^{1/n+p'_2} p_{O_2}^{1/n}}{p_{\theta}^{1/n+p''_2} p_{O_2}^{1/n}} \right] \quad [2]$$

where  $n = 4$  for a stabilized zirconia electrolyte,  $P_0$  and  $P_0$  refer to the  $P_{O_2}$  values at which the ionic conductivity of the electrolyte equals the positive hole conductivity and excess electronic conductivity respectively. As discussed by Schmalzried (5,6), for  $P_0 \gg P_{O_2} \gg P_0$ , equation [2] reduces to

$$P_{\theta} = P_{O_2}'' \exp (-4 EF/RT) \quad [3]$$

Equation [3] applies to cell [A] and the  $P_0$  values can be determined from the measured open circuit Emf values as a function of

temperature. From the  $P_0$  values, the limiting low  $P_{O_2}$  values which can be measured using a  $ZrO_2$  (~5% CaO) Degussa electrolyte can be calculated as follows.

The excess electronic transference number,  $t_e$ , of the electrolyte at low oxygen partial pressures is given by,

$$t_e = \frac{\sigma_e}{\sigma_e + \sigma_{ion}} \quad [4]$$

where  $\sigma_e$  and  $\sigma_{ion}$  are the excess electronic conductivity and ionic conductivity, respectively. For stabilized zirconia electrolytes, at a given temperature,  $\sigma_{ion}$  is a constant and  $\sigma_e = \sigma_e^0 P_{O_2}^{-1/4}$  where  $\sigma_e^0$  is a constant (1). Thus, Eq. [4] can be rewritten in the form,

$$\frac{1}{t_e} = 1 + k P_{O_2}^{1/4} \quad [5]$$

where  $k = \sigma_{ion}/\sigma_e^0$ . By definition,  $P_{O_2} = P_0$ , when  $t_e = 0.5$ . Upon substitution into Eq. [5],

$$k = (P_0)^{-1/4} \quad [6]$$

hence

$$\frac{1}{t_e} = 1 + \left( \frac{P_{O_2}}{P_0} \right)^{1/4} \quad [7]$$

If the lowest  $P_{O_2}$  value measurable with the  $ZrO_2$ -based electrolyte is denoted by  $P_{O_2}^L$ , then,

$$t_e = 0.01 \text{ for } P_{O_2} = P_{O_2}^L \quad [8]$$

Equation (8) corresponds to the generally agreed ionic transference number of >0.99 for an acceptable solid electrolyte. Upon substitution of Eq. [8] in Eq. [7],

$$P_{O_2}^L = 99^4 P_0 \quad [9]$$

The experimental cell arrangement used in the present study is shown in Fig. (1). A degussa  $ZrO_2$  (~5% CaO) solid electrolyte tube (3/8" O.D. x 1/4" I.D.) was platinized over a 1" length on the inside and outside using platinum paste (Engelhard #6082). The paste was thinned with xylene and brushed on to the cleaned solid electrolyte surface. The coated portion was heated gradually to 800°C in a furnace, held at this temperature for one

hour and furnace-cooled to room temperature. A series of four coatings was applied in this manner. Platinum lead wires were used to contact the inside and outside Pt paste. A slow stream of dry air was circulated through the inside of the electrolyte tube using a small alumina tube. The electrolyte tube was surrounded by an outer quartz tube. The outer surface of the electrolyte tube was exposed to a stream of high purity hydrogen. High purity hydrogen gas from a gas cylinder was further purified by passing through an Engelhard platinum catalyst (for conversion of any  $O_2$  to  $H_2O$ ); the water vapor was subsequently absorbed in a series of magnesium perchlorate towers.

The electrochemical cell was heated in a non-inductively wound tube furnace. A grounded Inconel tube was used around the quartz tube to eliminate stray Emfs. The cell was initially heated to a temperature of 750°C ( $\pm 1^\circ C$ ). The open circuit Emf developed across the cell was measured using a Hewlett Packard electronic voltmeter. The cell Emfs were observed to increase slightly with the flowrate of  $H_2$ ; the flowrate dependence vanished beyond a certain flowrate. The actual flowrate where this occurred was not measured since no flowmeter was placed in the system. The flowrate independent Emf was taken to be the correct Emf value. An Emf reading was considered steady if the random variation over a two hour period was within  $\pm 1$  mV. Emf readings were taken at 50°C intervals up to 950°C.

The experimentally measured Emf values are shown as a function of temperature in Fig. 2. Shown in Fig. 3 are the  $P_0$  values calculated using Eq. [3]. The temperature dependence of  $P_0$  follows the expression:

$$\log P_0 = 4.77 - \frac{35,130}{T} \quad [10]$$

Fig. 3 also contains the  $P_0$  values reported by Patterson (7) and by Schmalzried (6) for the  $ZrO_2$  (7 1/2% CaO) electrolyte. In Fig. 4, the limiting low  $P_{O_2}$  values,  $P_{O_2}^L$ , obtained using Eq. [9] have been plotted as a function of temperature. The temperature dependence of  $P_{O_2}^L$  can be expressed by the relation:

$$\log P_{O_2}^L = 12.75 - \frac{35,130}{T} \quad [11]$$

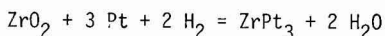
Also shown in Fig. 4 are the limiting  $P_{O_2}$  values of the  $ZrO_2$  (7 1/2% CaO) electrolyte according to Patterson (7). In Fig. 4 are



also shown the coexistence  $P_{O_2}$  values of two commonly used metal-metal oxide reference electrodes, the Fe-FeO electrode and the Cr-Cr<sub>2</sub>O<sub>3</sub> electrode. It is readily seen that the Degussa ZrO<sub>2</sub> (5% CaO) electrolyte can accurately measure the  $P_{O_2}$  of the Fe-FeO electrode, but not the Cr-Cr<sub>2</sub>O<sub>3</sub> electrode.

There are a few points which must be mentioned in connection with measurements involving cells of the type A. First of all, since the electrolyte exhibits some electronic conduction under conditions involved in measurements with cell A, even under open circuit conditions, there is electronic transport through the electrolyte from the low  $P_{O_2}$  side to the high  $P_{O_2}$  side. Such transport is accompanied by oxygen ion transport in the opposite direction. It is conceivable that the oxygen arriving at the left hand electrode of cell A by transport through the electrolyte raises the  $P_{O_2}$  at the left hand electrode/electrolyte interface locally. This effect should be more serious at low flow rates; at the higher flow rates, the oxygen is rapidly carried away in the hydrogen stream. This would in principle explain why the cell Emf would increase with flow rate in a certain range.

Another effect to be concerned about is the possibility of a chemical reaction between ZrO<sub>2</sub> and Pt at the left hand electrode where conditions are reducing. Meschter and Worrell (8) have determined the Gibbs' energy of formation of the intermetallic compound ZrPt<sub>3</sub> using electrochemical measurements involving a ThO<sub>2</sub>-Y<sub>2</sub>O<sub>3</sub> electrolyte. They have estimated that the reaction,



is possible at 800°C at  $P_{O_2}$  values below  $\sim 10^{-25}$  atm. No ZrPt<sub>3</sub> could be detected by X-ray diffraction on the platinized surface of the electrolyte tube after completion of experiments with cell A.

Shores and Rapp (9) have reported on the possibility of proton conduction in ThO<sub>2</sub> base electrolytes in the presence of H<sub>2</sub>-H<sub>2</sub>O environments. However, no such conduction has been reported for ZrO<sub>2</sub> based electrolytes. Wagner (10) found the solubility of water vapor in ZrO<sub>2</sub> containing 8 or 17% Y<sub>2</sub>O<sub>3</sub> in the temperature range, 900°C-1000°C to be extremely small, of the order of 13-30 ppm. Thus, it is assumed in the present study that there is no significant proton conduction in the ZrO<sub>2</sub> (5% CaO) electrolyte.

## ACKNOWLEDGEMENTS

The author expresses his appreciation to Professor R. Rapp for helpful suggestions.

## REFERENCES

- (1) R. A. Rapp and D. A. Shores, "Solid Electrolyte Galvanic Cells," Chapter in "Physicochemical Measurements in Metals Research," Part 2, ed. by R. A. Rapp, Interscience Publishers, 1970, p. 123.
- (2) T. A. Ramanarayanan and R. A. Rapp, *Met. Trans.*, **3**, 1972, 3239.
- (3) V. B. Tare and H. Schmalzried, *Trans. Met. Soc. AIME*, **236**, 1966, 444.
- (4) T. A. Ramanarayanan and W. L. Worrell, *Canad. Met. Quart.*, **13**, 1974, 325.
- (5) H. Schmalzried, *Z. Physik. Chem. (N.F.)*, **38**, 1963, 87.
- (6) H. Schmalzried, *Z. Elektrochem.*, **66**, 1962, 572.
- (7) J. W. Patterson, *J. Electrochem. Soc.*, **118**, 1971, 1033.
- (8) P. J. Meschter and W. L. Worrell, *Met. Trans.*, **7A**, 1976, 299.
- (9) D. A. Shores and R. A. Rapp, *J. Electrochem. Soc.*, **119**, 1972, 300.
- (10) C. Wagner, *Ber. Bunsenges. Phys. Chem.*, **72**, 1968, 778.

Manuscript submitted Nov. 5, 1980;  
revised manuscript received March 24, 1981.

Publication costs of this article were assisted by Exxon Research and Engineering Company.

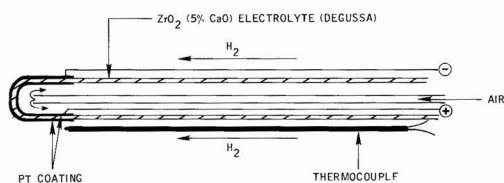


Fig. 1. Experimental cell arrangement for the determination of low  $P_{O_2}$  limits of oxygen ion conducting solid electrolytes.

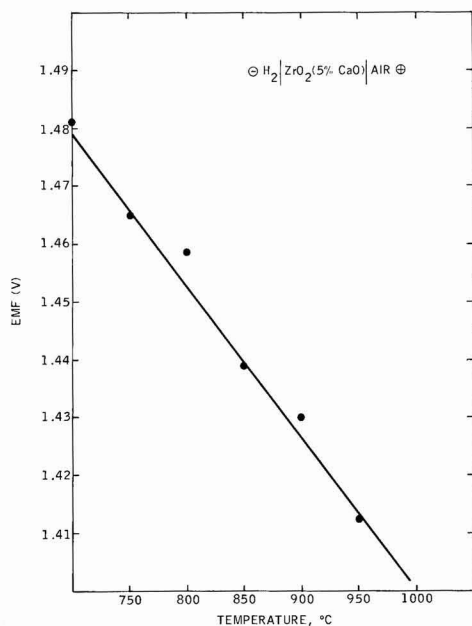


Fig. 2. The open circuit Emf of cell A as a function of temperature.

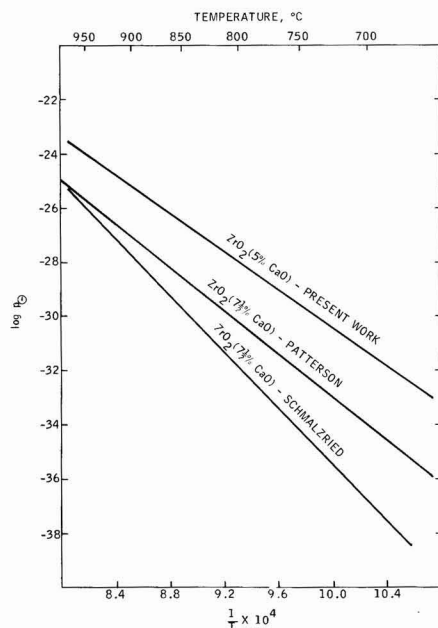


Fig. 3.  $P_{O_2}$  values as a function of temperature.

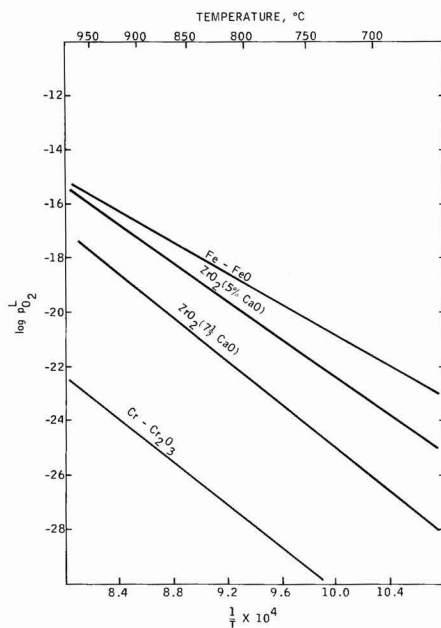


Fig. 4. Limiting  $P_{O_2}$  values as a function of temperature.

# Direct Observation of Surface States at the $\text{TiO}_2$ Electrolyte Interface

Withana Siripala and Micha Tomkiewicz\*

Department of Physics, Brooklyn College of CUNY, Brooklyn, New York 11210

Relaxation Spectrum Analysis was suggested<sup>(1)</sup> as a general technique for measurements of charge accumulation modes and their corresponding relaxation times at the space charge layer of a semiconductor with strong emphasis on semiconductor liquid junction interfaces. Among all the reported results<sup>(2-4)</sup>, none was, as yet, confirmed by an independent technique.

We wish to report here, evaluation of parameters of surface states that were observed on the surface of single crystal  $\text{TiO}_2$  in contact with an aqueous electrolyte, using the Relaxation Spectrum Analysis technique and subband gap spectral response.

Fig. 1 shows the impedance spectrum of single crystal  $\text{TiO}_2$  in contact with phosphate buffer. For detailed explanation of the experimental technique, the reader is referred to reference (1).

The equivalent circuit was found to consist of two parallel passive capacitive elements with distinctive relaxation times. The dependence of the capacitive elements on the electrode potential is shown in fig. 2. The space charge capacitance  $C_{sc}$ , obeys the Mott-Schottky

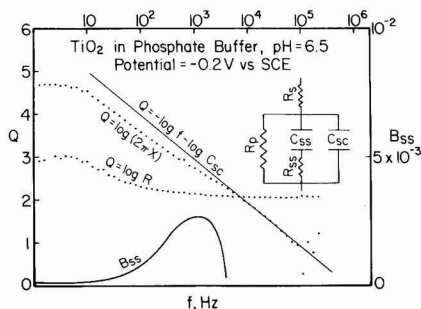


Fig. 1. Impedance response curves for n-type  $\text{TiO}_2$  in 0.33 M phosphate buffer. On the right-hand corner is the equivalent circuit constructed from the curves in the manner explained on ref. (1). Area =  $0.07 \text{ cm}^2$ .

relation over an extended range of potentials, from which the flatband potential and the doping level of the crystal were evaluated. The dependence of  $C_{ss}$  on the electrode potential, also shown in fig. 2., is more complex. It is dominated by a single gaussian distribution, centered around 0 V vs SCE. Similar behavior was found with surface states that were introduced on purpose by chemical modification of  $\text{TiO}_2$ <sup>(5-6)</sup> and by unmodified  $\text{TiO}_2$  under certain surface preparation conditions<sup>2</sup>. The difference between the states observed here and those that were previously reported is that the relaxation times of the surface states in the previously reported examples were all fast and limited by the series resistance of the electrolyte. This resulted in our inability to distinguish the surface state capacitance from the space charge layer capacitance. The surface state capacitance in those reports was evaluated from the deviations of the observed capacitance from the expected Mott-Schottky behavior. In the present case the states are much slower and their relaxation time clearly distinguishable from that of the space charge layer. The possible origin of the gaussian distribution of the surface states was previously reported<sup>(5-6)</sup>. From the maximum amplitude of the gaussian distribution coverage of  $1.8 \times 10^{13} / \text{cm}^2$  was

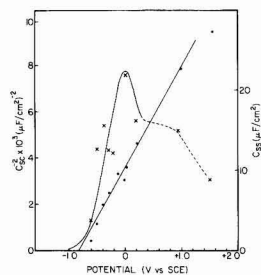


Fig. 2. Mott-Schottky plot of  $C_{sc}$  (left scale) and the variation of  $C_{ss}$  with potential (right scale). o -  $C_{sc}$ , X -  $C_{ss}$ . The solid lines are theoretically based on linear behavior of the Mott-Schottky plot and gaussian lineshape for  $C_{ss}$ .

\* Electrochemical Society Active Member

estimated. From the potential of the maximum of the gaussian distribution and from the intercept of the Mott-Schottky plot, we can infer that the surface states are located around 0.8 eV from the bottom of the conduction band, or approximately 2.2 eV above the top of the valence band.

The influence of the surface states on the band gap light induced current voltage behavior will be discussed in the full manuscript which will follow this letter. Fig. 3 shows the spectral response of subband gap illumination with a clearly distinctive peak at 550 nm which is equivalent to photon energy of 2.2 eV. This can only be due to light induced electron ejection from the top of the valence band to the surface states. From fig. 1, it is observed that the states are relatively fast states with relaxation times in the millisecond range and can efficiently communicate with the bulk of the semiconductor.

Full analysis of these results, their implication on the photoelectrochemical behavior of  $\text{TiO}_2$  and the relation between the surface states reported here and those that were reported in the literature will be discussed in subsequent publications.

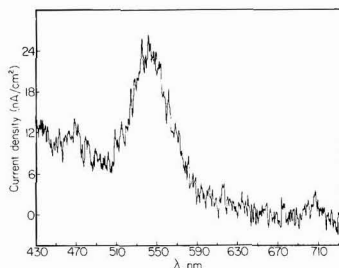


Fig. 3. Subband gap spectral response of the same crystal as in fig. 1 and 2.

#### REFERENCES

- (1) M.Tomkiewicz: J. Electroch. Soc. 126, 2220 (1979).
- (2) M.Tomkiewicz: J. Electroch. Soc. 126, 1505 (1979).
- (3) M.Tomkiewicz, in "Semiconductor Liquid Junction Solar Cells", A.Heller, ed. p. 92, The Electrochemical Society Softbound Proceedings Series, Princeton, N.J. (1977).

(4) M.Tomkiewicz, J.K.Lyden, R.P.Silberstein and F.H.Pollak: Proc. of the ACS Symposium on "Photoeffects at Semiconductor Electrolyte Interfaces", A.J.Nozik, ed. 146, 267 (1981)

(5) M.Tomkiewicz: J. Electroch. Soc. 127, 1518 (1980).

(6) M.Tomkiewicz: Surf. Sci. 101, 286 (1980).

#### ACKNOWLEDGMENT:

This work was supported by NASA Grant# NAG1-44.

Manuscript submitted May 1, 1981; revised manuscript received July 10, 1981.

Publication costs of this article were assisted by Brooklyn College of CUNY.



## Abstracts of Recent News Papers

Presented at the Denver, Colorado, Meeting of the Society, October 11-16, 1981

622 RNP

### Measurement of the Near-Surface Crystallinity of Silicon-on-Sapphire by U.V. Reflectance

M. T. Duffy, J. F. Corboy, R. T. Smith, and G. W. Cullen, RCA Laboratories, Princeton, NJ 08540, G. Harbeke and J. R. Sandercock, Laboratories RCA Ltd., Zurich, Switzerland, and M. Blumenfeld, RCA Solid State Div., Palm Beach Gardens, FL 33403

In semiconductor technology there is a need for a fast, nondestructive quality control method for determining the quality of semiconductor materials entering the product line, and also for research purposes. The work described in this paper provides a basis for the rapid quantitative characterization of semiconductor surfaces by specular reflectance measurements. The method used is fast, nondestructive, requires no contact to the sample surface, and is suitable for in-line quality control and research purposes. The work described is concerned with determining the crystalline quality of heteroepitaxial silicon films on sapphire, but the method is applicable to other systems.

623 RNP

### Improved Resistivity Measurement of Epitaxial Silicon from Hg Probe Data

V. Sils, C. A. Levi, and C. Peterson, Alpha Industries, Inc., Woburn, MA 01801

Hg probe measurements are subject to uncertainty at low bias voltages due to variations in the Hg-oxide-Si contact potential. A new Hg probe design featuring a clear fused quartz orifice reduces stray capacitance, leakage, and variation of contact area. Extrapolation of the resulting C-V measurements yields the true contact potential, which is used in a modified ASTM method to calculate resistivity and depletion depths. Results show improved reproducibility of resistivity measurements, independent of surface treatment.

624 RNP

### Autodoping Phenomena in Epitaxial Silicon

G. K. Ackermann, Technische Fachhochschule Berlin, D-1000 Berlin 65, Germany and E. Ebert, IBM Laboratories, D-703 Boeblingen, Germany

Autodoping experiments were performed using an AMC 7600 epitaxial reactor, <100>-n-doped silicon wafers, arsenic-doped buried layers of total implanted or diffused dose of  $7 \times 10^{14} \text{ cm}^{-2}$  up to  $3 \times 10^{16} \text{ cm}^{-2}$ , and buried layer areas between 10 and 100% wafer area. Intentionally undoped epitaxial layers of  $1.4 \mu\text{m}$  thickness were grown.

The lateral autodoping was found to be extremely uniform. Autodoping follows a square root law with respect to buried layer area, and an almost linear relationship due to subcollector doping. An analysis of the buried layer doping profile identifies the diffusional source with electrically inactive arsenic.

### Deposition of $\text{SiO}_2$ Thin Films in Strong Acids

M. A. Smith, Union Carbide Corp., Technical Center, South Charleston, WV 25303, and L. L. Levenson, Dept. of Physics, University of Colorado at Colorado Springs, Colorado Springs, CO 80907

We have observed deposition of  $\text{SiO}_2$  films on surfaces in 1-8M nitric acid between approx. 80° and 100°C. Scanning electron microscopy shows the films are composed of closely packed spheres approx. 100Å in diameter. Chemical identification is made with Auger electron spectroscopy. Materials on which films form are Ta, Au, Si, Nb, and  $\text{Al}_2\text{O}_3$ . Deposition occurs inside a sealed vessel made entirely of Pyrex-type glass. Attack of the vessel provides the sole source of  $\text{SiO}_2$ .

This work was performed at the Graduate Center of Materials Research, University of Missouri-Rolla, Rolla, MO 65401.

626 RNP

### Role of Particulate Contamination in MOS Oxide Failures

J. R. Monkowski, Dept. of Electrical Engineering, The Pennsylvania State University, University Park, PA 16802

During oxidation, particulate contamination present on the wafer reacts with the growing  $\text{SiO}_2$  producing microscopic regions high in ionic contamination. These regions, typically  $1 \mu\text{m}$  or less in diameter, have been correlated with sites of breakdown failures in MOS capacitors. The temperature dependence of these failures supports a mechanism of thermal breakdown in these microscopic regions. Since the particulate contamination is not soluble in water or many of the chemicals used in wafer cleaning, this is a major source of contamination. Breakdown statistics show that low particulate chemicals have a significant effect in reducing this premature breakdown.

627 RNP

### Contamination-Free High Temperature Treatments of Silicon

P. F. Schmidt, Bell Laboratories, Allentown, PA 18103

The deleterious effects of contamination of silicon devices with transition group metals is well known. Minority carrier lifetime and junction leakage currents are degraded by the contamination, which preponderantly stems from high temperature furnace treatments when these metals diffuse from the outside through the walls of the quartz furnace tube and into the silicon being heat-treated. The addition of a few percent HCl to dry oxygen will prevent this contamination. However, HCl cannot be permitted to contact the silicon surface in many high temperature steps, and addition of HCl to steam provides no protection against contaminant of the silicon. A simple way to apply the HCl-dry  $\text{O}_2$  protection to other high temperature treatments is to employ a double-wall quartz tube, with the customary HCl-dry  $\text{O}_2$  mixture flowing in the space between inner

and outer tube only. Complete protection during steam oxidation at 1000°C for 1 hr was observed over a three week period, with a 1% HCl-99%  $\text{O}_2$  mixture flowing in the annulus only. At 1100°C, a slight contamination with Cu, Ni, and Co was observed, indicating that either the flow rate or the concentration of HCl should be increased at 1100°C.

628 RNP

### Electrical Properties of Oxides Grown on Polysilicide/Polysilicon Sandwich Layers

D. A. Baglee and J. W. McPherson, Houston Process Development Laboratory, Texas Instruments Inc., Houston, TX 77001

Polysilicide/polysilicon sandwich (polysilicide) layers are a possible low sheet resistance replacement for polysilicon in VLSI structures. We have investigated the insulating properties of their thermally grown oxides and have found abnormally high leakage ( $10^{-8} \text{ A}$ ) at low fields (0.3 mV/cm), differing significantly from the expected Fowler-Nordheim characteristics. Breakdown strengths were approximately 3 mV/cm, similar to polysilicon oxides. The effects of oxidation conditions and annealing are presented together with a possible conduction mechanism.

629 RNP

### Properties of High Temperature LPCVD Oxide Films

Y. Avigal, Intel Corp., Santa Clara, CA 95051

Oxide growth rate and properties such as etch rate, refractive index, pinhole density, adhesion, and breakdown voltage were studied as a function of temperature, pressure, and reactant flow rates. In addition, film integrity was studied, and specifically pinhole density, particulates and blistering were addressed. At least partial solutions were found for these problems, and are presented in this paper.

630 RNP

### Process Technology for Two Micron CMOS/SOS VLSI Circuits

K. Verma, D. Gorton, and D. Kinell, Lockheed Microelectronics Center, Sunnyvale, CA 94086

Very large integrated circuits (VLSI) for space system command and communication network must meet the criteria of: 1. Speed power performance from weight and size considerations, and 2. high tolerance to hostile radiation environment at high and low temperature extremes. The selection of an appropriate process technology depends on many factors such as performance, process maturity for the LSI/VLSI circuits, and availability of the starting substrate wafers in standard sizes. Silicon-on-sapphire (SOS) has demonstrated these qualities.

This paper presents the process technology of 2 micron channel length CMOS/SOS which has been developed in our laboratory for gate-array based LSI circuits. The paper focuses on the following key processing areas:

2 micron lift-off/dry etching process; channel implant matrix study with  $V_T$  and doping profiles; optimum siox reflow process for excellent metal coverage; backfill low temperature oxide for the planarity and radiation; thin gate oxide characterization.

## 631 RNP

### Shallow Bipolar Transistors with Polysilicon Contacts

S. F. Chu and H. C. Hamel, IBM General Technology Div., East Fishkill Facility, Hopewell Junction, NY 12533

NPN transistors with 100 nm emitter depth diffused from an arsenic-implanted polysilicon layer have been investigated. The emitters were contacted through the  $N^+$  polysilicon layer whose top portion had been converted to PtSi. The low current d-c gain of these transistors was in the range of 70-100 as long as the unreacted polysilicon film thickness was at least 30 nm. If less than 30 nm of polysilicon was left after PtSi formation, current gain dropped by as much as 50%. The forward transit time was found to be independent of polysilicon film thickness.

## 632 RNP

### A New Type of Device Structure for Bipolar Logic IC's with Polysilicon Emitter Regions

X.-L. Jiang (Present address: Dept. of Physics, Tufts University, Medford, MA 02155) Beijing Semiconductor Device Research Institute, Beijing (Peking), China

An experimental TTL circuit with a new type of device structure, different from double-diffusion transistors, was realized by using polysilicon-silicon interface-contacted n-p junctions, formed by CVD of a heavily phosphorus-doped polysilicon layer onto p-type single crystal base regions at low temperatures, as the emitter-base junctions of the circuit transistors. The experimental results showed that the transistors with polysilicon emitter regions (PER) had proper d-c characteristics and good high frequency performance. For PER transistors, the conventional n-p diffusion (or implantation and post-implantation annealing) of the emitter regions is avoided. This development is of great importance for raising the yield of npn circuit transistors with very narrow width base regions. Hence, very high  $f_T$  values will result if fine patterning is used. Therefore, the PER technology will provide a promising new approach to the fabrication of high-speed bipolar digital LSI and VLSI circuits with relatively low cost.

## 633 RNP

### Formation of Low Resistance Vias in a Polyimide Multilevel Metallization Process

S. J. Rhodes, Plessey Research (Caswell) Ltd., Allen Clark Research Centre, Caswell, Towcester, Northants, England

Polyimide is becoming accepted as the insulating dielectric in multi-level metallization processes. One of the most difficult techniques involved is the formation of a low resistance contact between two levels of metallization. By using titanium during the second metal deposition we have shown that the native aluminum oxide on the underlying metal can be nullified. We have also found that, using this technique, the silyz preparation and titanium thickness were critical. This method, however, has been developed into a high yielding process suitable for VLSI applications.

## 634 RNP

### Improvement of Coverage over Steep Topography for Aluminum Alloy Films Sputtered Under RF Bias in the Dual RF Diode-D-C Magnetron Mode

R. S. Nowick (Present affiliation: Exxon Enterprises), E. V. English, L. E. Gulbrandsen, A. J. Learn, and K. W. Schuette, Perkin-Elmer Corp., Physical Electronics Div., Mt. View, CA 94043 and Intel Corp., Santa Clara, CA 95051

A practical method for high rate sputter deposition of aluminum alloys over steep topography is described. In this technique, aluminum or aluminum alloys are sputtered via d-c magnetron in a rotating substrate table configuration, and the alloy constituent, e.g., copper, silicon, etc., is sputtered by rf diode with rf substrate bias. The resultant multi-layered films are shown to exhibit 50% + coverage over vertical topography of one + micron in height. Nonbiased depositions typically yield ca. 25% coverage over the same topography, even with 300°C substrate heating.

## 635 RNP

### Mask Pattern Effect on the Diffused Resistance in Silicon

T. Suganuma, T. Sakai, S. Nakao, and Y. Komatsu, Nippon Electric Co., Ltd., Semiconductor Div., 1753 Shimonumabe, Nakahara-ku, Kawasaki, 211 Japan

Sheet resistance of selective diffused region was found to depend on both diffused area dimensions and masking film area dimensions; either predeposition is from gas sources or solid sources. The mask pattern effect strongly correlates with masking materials and predeposition conditions. By the effect, device characteristics vary and distribute broadly even in a chip in a wafer, however excellent the uniformity of sheet resistances across an unpatterned wafer is.

## 636 RNP

### Chemical Etching—An Analytical Tool for Laser Crystallization of Amorphous Silicon

M. Akulfi and R. Ogden, Naval Ocean Systems Center, Code: 9251, San Diego, CA 92152

The differential effects of chemical etching on the different morphologies of silicon were investigated in order to develop them into an analytical tool for evaluating the crystallization of silicon. Etch rates were measured for amorphous and (100) oriented single crystal silicon. Several etchants were found to etch these benchmark morphologies at significantly different rates while substantially enhancing the grain boundaries of polycrystalline silicon. The application of these differential effects has proven to be useful in analyzing the phenomenon of laser crystallization of amorphous silicon. Experimental results are presented.

## 637 RNP

### Structure and Composition of Electrochromic Iridium Oxide Films

J. D. E. McIntyre, Bell Laboratories, Murray Hill, NJ 07974

The structure and composition of anodically formed, electrochromic iridium oxide (IROX) films, colored (oxidized) and bleached (reduced) in both aqueous and nonaqueous electrolytes, have been investigated using combined Rutherford backscattering and nuclear reaction microanalysis techniques. The composition of the colored film was found to vary from fully hydrated ( $\sim \text{IrO}_2 \cdot 2\text{H}_2\text{O}$ ) near the outer surface to almost anhydrous ( $\sim \text{IrO}_2$ ) near the metal-oxide interface. Protons and small metal cations ( $\text{Li}^+$ ,  $\text{Na}^+$ ) were found to be the primary charge compensating species inserted into the IROX film during reduction to preserve electroneutrality.

## 638 RNP

### MOCVD Growth of a Superlattice Solar Cell Structure

M. W. Wanlass and A. E. Blakeslee, Solar Energy Research Institute, Golden, CO 80401

This paper reports progress toward realization of a new cascade solar cell structure whose chief advantages over other present concepts are: use of silicon for the substrate and low bandgap cell; avoidance of the necessity of lattice matching; and incorporation of a GaAs/GaP superlattice to eliminate misfit dislocations and thus enhance efficiency. Details of the design, construction, and operation of an automated MOCVD system for growing this structure are presented. Early results pertaining to layer growth and uniformity as well as electrical and optical properties are reported.

## 639 RNP

### Ohmic Contact Formation to p-Type InP Using Zn-Ag Metallization

B. Molnar and I. P. Isaacson, Naval Research Laboratory, Washington, DC 20375

An evaporated Ag-Zn (15% by weight Zn) alloy has been used to form ohmic contact to lightly doped p-type InP (Zn). Ohmic behavior was observed for substrate dopings of  $10^{-5}$  to  $10^{-7} \text{ cm}^{-3}$ . The evaporated thin layer of Ag-Zn was alloyed at 380-400°C subsequent to deposition. The contact resistance was determined by applying the procedure of Cox and Strack, to measurements made between varying contact size. The contact resistance measured for this metallization varied with the substrate doping. It was  $5 \times 10^{-3} \Omega \text{ cm}^2$  for  $2 \times 10^{-5} \text{ cm}^{-3}$  material and  $2 \times 10^{-4} \Omega \text{ cm}^2$  for  $5 \times 10^{-7} \text{ cm}^{-3}$  material. In conclusion, we have found that the Zn-Ag metallization can be used to produce low contact resistance to lightly doped, p-type InP.

This work was supported by the Naval Electronic Systems Command.

## 640 RNP

### Epitaxial Growth Studies of InP: Addition of Hydrogen Chloride to Mixing Zone

T. E. Erstfeld and K. P. Quinlan, RADC/ESM, Hanscom AFB, MA 01731

The effect of the addition of hydrogen chloride to the mixing zone in a three zone reactor for the preparation of InP epitaxial structures by the vertical growth method was investigated. Various flow rates of HCl in the mixing zone were investigated as a function of phosphine flow rate and mixing zone temperature. These variables are discussed in relation to the growth rate of the epitaxial structures, carrier concentrations and mobilities are reported.

## 641 RNP

### Properties of Ion-Implanted P-N Junction in InP

H. B. Dietrich, T. H. Weng, and M. L. Bark, Naval Research Laboratory, Washington, DC 20375

A study has been made of ion-implanted p-n junctions in InP. P-N and N-P junctions have been fabricated by the respective implantation of Be into bulk n-type material and Si into bulk p-type material. In addition, all ion-implanted P-N junctions have been made in S.I. material by the successive implantation of Si and Be. Measured diode characteristics (n-factor breakdown voltage, reverse leakage currents) are presented and discussed in the context of substrate doping and processing. Ohmic contacting of the p-type implanted layer is also discussed.

## 642 RNP

### Double Layer Modeling of Impurity Redistribution in Sulfur-Implanted GaAs

C. Paz de Araujo and R. Y. Kwor, Dept. of Electrical Engineering, University of Notre Dame, Notre Dame, IN 46556



Sulfur-implanted GaAs is modeled as a double-layered medium of dissimilar diffusion characteristics to account for the severe nongaussian redistribution of the implanted profile during annealing. Two effective diffusion coefficients are found for each energy, dose, and annealing temperature combination. LSS, Pearson IV, and SIMS data for as-implanted S-profiles in doses ranging from  $10^{15}$  to  $10^{17}$  cm $^{-2}$  are used as initial conditions. Postannealing profiles generated by this model are in good agreement with the corresponding SIMS data.

643 RNP

### The Reduction in Degradation of GaAs LED's by Ru $^{+}$ Treatment

J. R. Shealy, General Electric Co., Electronics Park, Syracuse, NY 13201 and School of Electrical Engineering, Cornell University, Ithaca, NY 14853 and J. M. Woodall, IBM Thomas J. Watson Research Center, Yorktown Heights, NY 10598

One mechanism of degradation in performance of light emitting diodes (LED's) involves a surface change in the p-n junction region which is reversible with a brief etch. Therefore it was suspected that this degradation might be due to photocorrosion. To test this idea, GaAs LED's were treated with Ru $^{+}$  using the procedure to passivate GaAs photoelectrochemical solar cells (1). Forward bias stressing for 1000 hr showed that the Ru $^{+}$  treatment reduced the failure rate by a factor of less than 1/3.

I. B. A. Parkinson, A. Heller, and B. Miller, *This Journal*, 126, 954 (1979).

644 RNP

### An LPE Growth of InGaAsP/InP DH Laser Structures on V- and U-grooved Substrates

Y. Nishitani, T. Tanahashi, I. Umebu, H. Ishikawa, and K. Akita, Fujitsu Laboratories, Ltd., 1015 Kamikodanaka, Nakahara-ku, Kawasaki, Japan

V- and U-grooves were etched along  $\langle 110 \rangle$  direction on (100) InP substrates by HCl-H $_2$ O $_2$  and HCl-H $_2$ SO $_4$ , respectively, under the limited compositions. In the growth on V-groove, the active layer could be isolated in the groove by controlling the amount of supercooling of growth melts, growth time, and depth of the groove. However, in the case of U-groove, the active layer could not be isolated under the conditions examined. Typical cw threshold current of laser with isolated active layer was 20 mA at 25°C.

645 RNP

### Teflon-Sprayed Nickel Electrodes for Alkaline Electrolyzers

O. Teschke, F. Gallemebeck, and C. P. D. Évora, Physics and Chemistry Institute, Energy Group, UNICAMP, 13100, Campinas, S.P. Brazil

During operation of water electrolyzers, gas bubbles migrate from the electrode surfaces to the bulk of the electrolyte, increasing the solution IR drop. Bubbles adhering to the electrode are responsible for overvoltage increases due to raised actual current density. These adverse effects of gas bubbles are decreased by changing the electrode wetting characteristics. This is done by partially covering the electrode surface with Teflon. Teflon-covered areas act as gas collector sites, leaving free metal in contact with solution thus allowing for rapid bubble growth and release.

646 RNP

### The Study of Reaction Process in Si Dry Etching

J. Nishizawa and N. Hayasaka, Research Institute of Electrical Communication, Tohoku University, Sendai 980, Japan

IR spectroscopy has been used as in situ observation of fluorocarbon plasma during the dry etching of Si. The decompositions of molecules like CF $_4$   $\rightarrow$  CF $_3$  + F are mainly considered by many workers in the reaction processes of Si dry etching by fluorocarbon plasma. The decomposed molecules like CF $_3$  and CF $_2$  have not been found in CF $_4$  plasma by IR spectroscopic measurements, and C $_2$ F $_6$ , C $_2$ F $_4$ , and SiF $_4$  which are the etching products, have been detected. The possible reaction processes which explain the results of IR spectroscopic and etching rate measurements have been expected, which have been constructed only by the detected species in IR and emission spectroscopic measurements.

647 RNP

### Surface Composition and Etching of III-V Semiconductors in Cl $_2$ Ion Beams

R. A. Barker, T. M. Mayer, and R. H. Burton, Bell Laboratories, Murray Hill, NJ 07974

Surface composition of InP, GaP, and GaAs before and after etching in Cl $_2$  ion beams was investigated. In situ analysis of the substrate using Auger electron spectroscopy (AES) demonstrated selective removal of phosphorus from InP leaving a thin ( $\leq 50$  Å) surface layer enriched with In after etching at room temperature with a 500 eV Cl $_2^+$ /Cl $_2$  beam. GaP and GaAs do not show selective removal of the group V element, resulting in no significant change in surface composition after etching. These results reflect the involatility of the indium chlorides at room temperature. Etch rate results indicate that at low ion energy (200 eV) or high neutral reactant flux, removal of the group III chloride from the surface is rate limiting. At high ion energy (500 eV) and low neutral flux, supply of reactant to the surface is rate limiting.

648 RNP

### An Anisotropic Plasma Etching Process for Polysilicon

H. Kalter, A. Meyer, and R. A. M. Wolters, Philips Research Laboratories, Eindhoven, The Netherlands

An anisotropic etching process for polysilicon has been developed using a chlorine-based gas mixture. Etching with mixtures of CCl $_4$  + Cl $_2$  generally does not cause undercutting of the mask and has a good stop against SiO $_2$  with a selectivity of typically 15. The etching rate of photoresist relative to that of polysilicon depends on the rf frequency. For H.P.R. 204 and n $^+$  poly the ratio is 0.8 to 1.0 at a few hundred kHz and about 1.8 at 13.56 MHz. With this etching process 2  $\mu$ m pattern details can easily be achieved with good reproducibility and uniformity.

649 RNP

### Selectivity Aspects in Aluminum Plasma Etching

R. A. M. Wolters, Philips Research Laboratories, Eindhoven, The Netherlands

Selectivity of photoresist, SiO $_2$ , and Si (contact windows) in an aluminum etching process using CCl $_4$  + Cl $_2$  were investigated. The process is in general anisotropic. The erosion products of the photoresist participate in the chemical process of the aluminum etching. The etch rate of the underlying oxide was found to be strongly dependent on the composition of the gas mixture used. The selectivity to silicon is poor. To have full benefit of the plasma process a good stop against contact windows is necessary. For this purpose silicides were investigated.

650 RNP

### Anisotropic and Selective Etching with Chlorinated Plasmas

K. Nishioka, H. Itakura, M. Yoneda, H. Abe, and H. Nakata, Computer Development Laboratories Ltd. and LSI R&D Laboratories, Mitsubishi Electric Corp., 4-1, Mizuhara, Itama, Hyogo, Japan

The anisotropic property and selectivity of poly-Si, Si $_3$ N $_4$ , and SiO $_2$  etched with chlorinated plasmas (CCl $_4$ , CCl $_3$  + O $_2$ , C $_2$ ClF $_5$ , etc.) were investigated as a function of oxygen concentration, gas flow rate, rf-coupling method, and rf-frequency. The anisotropic profile of the etched poly-Si pattern could be obtained with good etch selectivity to SiO $_2$ , Si $_3$ N $_4$ , and photoresist, by controlling the above-mentioned plasma etching conditions. Oxygen additions to CCl $_4$  showed different effects on the etching characteristics from that of CF $_4$ .

651 RNP

### Chemical Vapor Deposition (CVD) and Plasma Processing Deposition (PPD) in Coatings with Refractory Materials

R. Avni, U. Carmi, and A. Inspektor, Div. of Chemistry, Nuclear Research Center, Beer-Sheva, Israel

The deposition of pyrolytic carbon, silicon, silicon nitride, boron nitride, and carbide on a solid substrate in a high temperature reactor and in inductive radio frequency (rf) low pressure plasmas is compared. In the high temperature reactor (CVD) and in the rf plasma (PPD), hydrocarbons, diborane, or silane gas mixture with argon were used. In both CVD and PPD processes two regions are considered namely (i) reactions in the gaseous phase and (ii) in the region near the solid substrate (gas-solid). The differences in the rate of deposition between CVD and PPD are discussed.

652 RNP

### The Effects of Ion Transport and Oxide Electric Field on Plasma Oxidation of Silicon

R. P. H. Chang, Bell Laboratories, Murray Hill, NJ 07974, J. Siejka and J. Perrière, Groupe de Physique des Solides, de l'Ecole Normale Supérieure, Paris, France, and M. Croset, Thomson CSF, Laboratoire Central de Recherche, Orsay, France

Recent studies on plasma oxidation of silicon have shown that it is a potential process for the VLSI technology. The study of plasma oxidation kinetics can, in general, be divided into three parts: (a) Plasma-oxide surface reaction—the surface formation of negative oxygen species; (b) the transport of charged species across the oxide—mainly via electric fields at low temperatures; and (c) interfacial reaction kinetics—the formation of SiO $_2$  from oxygen reacting with Si at the SiO $_2$ -Si interface. In this paper, we present experimental results which show that both the oxide electric field and the ion conduction play a significant role in the transport of negative oxygen species across the SiO $_2$ . The experiments were carried out in the Bell Laboratories' multipurpose plasma machine. The experimental conditions were similar to earlier experiments (1). Samples of plain silicon, as well as samples of silicon covered by thin ( $\approx 200$  Å) ion conducting (electron resistive) oxides, e.g., ZrO $_2$ , ZrO $_2$  (with dopant), and Nb $_2$ O $_5$  with large (compared to that of SiO $_2$ ) dielectric constants were used. For the case of plain silicon, the current through the SiO $_2$  is mainly composed of electrons, while those currents through SiO $_2$  with dielectric overlays consist of large fractions of O $_2^-$  species. The function of the thin dielectric overlay on SiO $_2$  is to increase the ion to electron ratio in the current which flows from the SiO $_2$  to SiO $_2$  and at the same time allowing an increase in the electric field across the SiO $_2$ . Oxidation current efficiencies have been found to vary from a fraction of a percent (for plain silicon) to as high as 20% (for ZrO $_2$  (a)).

1. R. P. H. Chang, Thin Solid Films, 56, 89 (1979).

## 653 RNP

**CCl<sub>4</sub> Plasma Etching of InP**

R. A. Gottscho, G. Smolinsky, and  
R. H. Burton, Bell Laboratories,  
Murray Hill, NJ 07974

Measurements of CCl<sub>4</sub> plasma etch rates of InP as a function of substrate temperature, time, and rf power indicate a complex reaction mechanism. Etch rates at fixed power, pressure, flow, frequency, and etch time exhibit a non-Arrhenius temperature dependence implying the presence of multiple and competing reaction pathways. Etch rates as a function of time provide evidence for at least three etching reactions and one etch-inhibiting reaction. Qualitatively, all of these data can be understood in terms of two competitive rate-limiting steps: product desorption and reactant adsorption.

## 654 RNP

**Phosphorus Pentafluoride and Sulfuryl Fluoride Applied to Etch SiO<sub>2</sub> in Search for Higher Selectivities**

K. M. Eisele, Institute for Applied  
Solid States Physics,  
D7800 Freiburg, Germany

Realistic selectivities for etching SiO<sub>2</sub> over Si are about 15:1. All processes available operate on the edge of forming polymers. It is therefore indicated to search for etch gases with an inherent selectivity for SiO<sub>2</sub> with reasonable etch rates and without the risk of depositing polymers. Sulfuryl fluoride has been chosen for its property to etch SiO<sub>2</sub> at elevated temperatures. Phosphorus pentafluoride is known to cleave easily the silicon-oxygen bond in siloxanes and to form SiF<sub>4</sub> and POF<sub>3</sub>. However, these gases have not filled the expectations. They etch Si, SiO<sub>2</sub>, and Si<sub>3</sub>N<sub>4</sub> with lower rates than can be obtained with the more common etch gases. Ion mass spectroscopy is employed to find reasons for the low etch rates and poor selectivity.

## 655 RNP

**A Thin Film Monitor for Measuring In Situ the Etch Rate of Silicon**

H. J. Trumpp and J. Greschner, IBM  
Deutschland GmbH, EF Component  
Technology, D/3196, 7030 Boeblingen,  
Germany

A thin monocrystalline silicon film allows in situ the measurement of the silicon dry etch rate by laser interference or by spectrum analysis with a film thickness probe. This paper outlines the process for the production of thin film monitors (TFM). Modifications to insure equal etch rate of TFM and product are discussed and also ways to detect the etch end point. Examples of application are given for the etching of silicon trenches and for etch processes with silicon as etch stop.

## 656 RNP

**Reactive Ion Etching of Submicron Silicon Grooves for Electron Beam Transmission Masks**

J. Greschner and H. J. Trumpp, IBM  
Deutschland GmbH, 7032 Sindelfingen,  
Germany

In a newly developed fabrication process self-supporting masks with submicron structures are generated in a thin crystalline silicon membrane. These silicon transmission masks are required for future electron and ion beam lithography methods. The most important fabrication steps are two reactive ion etching processes for the etching of SiO<sub>2</sub> and Si with very high etch rate ratios and a zero etch bias. They allow the etching of silicon trenches smaller than 0.5 μm and as deep as 6 μm. The fabrication process of the silicon transmission masks is described and results of the deep trench etching are shown which indicate the limits of this etching method.

## 657 RNP

**Etching of Aluminum and Polysilicon in Parallel Plate Reactors in Cl-Based Plasmas**

F. Schmidt and N. Hoffmann, VALVO  
Röhren- und Halbleiterwerke der Philips  
GmbH Stressemannallee 101, 2000  
Hamburg 54, Germany

Based on results reported in St. Louis we developed process and equipment further and introduced the etching of both aluminum and poly-Si into production. The processes are based on CCl<sub>4</sub>/Cl<sub>2</sub>-mixtures, mainly used in a two-step sequence. We describe aluminum and poly-Si etching in the same equipment and give results of selectivities and uniformities received in large scale production. The main tool of process control is pressure monitoring, which also is used for automatic endpoint detection.

## 658 RNP

**Charge Stability in Sealed Lead Acid Aircraft Batteries**

S. Warrell, Chloride Technical Ltd.,  
Swinton, Manchester, England

One of the major disadvantages of nickel cadmium or lead acid batteries currently used in aircraft is their regular maintenance requirement. A sealed "recombining" battery would offer several intrinsic advantages for use as an aircraft main battery. However, in service aircraft batteries are subjected to demands on their stability, often under conditions of prolonged constant potential charge at elevated temperatures. The improved stability of a sealed recombining lead acid aircraft battery is discussed in relation to the heating effects occurring during overcharge and the influence of lead alloy composition and aging.

## 659 RNP

**Characterization of Selenium Implantation for GaAs Integrated Circuits**

P. A. Leigh, C. J. Allen, and J. A. Bowie,  
British Telecom Research Labs,  
Martlesham Heath, Ipswich,  
IP5 7RE, Suffolk, England

Using an automatic electrochemical Hall profiling apparatus the limitations of ambient temperature selenium implantation have been explored. The effects of dose, energy, substrate temperature, and anneal temperature have been studied with emphasis on doses between  $1.5 \times 10^{12}$  ions cm<sup>-2</sup>. A diffusion effect due to elevated substrate temperature, independent of annealing was found for low doses. The fall in activation for doses less than  $3 \times 10^{12}$  cm<sup>-2</sup> was related to a constant factor.

## 661 RNP

**Fe, Cr, and Co Doping of Liquid Phase Epitaxial and Bulk-Grown InP**

R. L. Messham and A. Majerfeld,  
Dept. of Electrical Engineering,  
University of Colorado, Boulder, CO  
80309, and K. J. Bachmann, Dept. of  
Chemistry, North Carolina State  
University, Raleigh, NC 27650

The incorporation of Fe, Cr, and Co in InP LPE layers and, also, bulk-grown InP crystals lightly doped with Fe were studied. The solubility of Fe in In increases from 0.07 to 0.4 atomic percent over the range 700°-900°C. However, the solubility of In in In-P solutions is greatly reduced. The Fe, Cr, and Co-doped LPE layers and the Fe-doped bulk-grown crystals are all n-type. A 0.68 eV electron trap is observed in Fe-doped crystals.

## 662 RNP

**High Energy Density Zinc-Air Primary Cells for Navigational Aids**

R. Varbev, Bulgarian Academy of  
Sciences, Central Laboratory of  
Electrochemical Power Sources,  
Sofia 1040, Bulgaria

Two types of high energy density zinc-air primary cells (500 and 3000 A-hr) developed for navigational buoy light powering are presented. The performance characteristics and the design and construction differences of both are discussed. The results from the operation of 500 A-hr cells in buoys on the Baltic Sea and some investigations connected with water balance are reported. Initial performance data of 3000 A-hr buoy light battery tests are given.

## 663 RNP

**Laser Enhanced Gold Plating on Bulk Metal Samples**

R. J. von Gutfeld, M. H. Gelchinsky, and  
L. T. Romankiw, IBM Thomas J.  
Watson Research Center, Yorktown  
Heights, NY 10598

For the purpose of saving precious metals, we have investigated laser-enhanced gold plating on a variety of bulk metal samples, using a focused argon laser to define the localized plated area. We describe experimental conditions and results for plating on bulk copper, nickel, and stainless steel. Mill sized gold spots and mill wide lines up to a mil in thickness have been fabricated. Under appropriate conditions to be described, the resulting gold patterns are formed without any background plating. A thin background coating can also be achieved when described.

## 664 RNP

**Metallic Glass Alloy Coatings**

D. S. Lashmore and A. W. Ruff,  
National Bureau of Standards, Center  
for Materials Science, Washington, DC  
20234

It is shown that it is possible to produce amorphous nickel phosphorus alloys with phosphorus contents controllable from 10 to about 50 atomic percent. At least two distinct atomic configurations have been identified which can be selected through the deposition parameters. The microhardness of one of the configurations is shown to be uniformly higher than the others. The dry sliding wear performance of the plated alloy, produced by pulsed electrodeposition, exceeds the wear performance of the direct plated alloy. After heat-treating (400°C, 30 min) the dry sliding wear performance is comparable to hard chromium.

## 665 RNP

**Selected Transport Properties of Electroless Copper Plating Baths**

R. Y. Ying, L. C. Frazer, and F. M.  
Donahue, Dept. of Chemical  
Engineering, University of Michigan,  
Ann Arbor, MI 48109

In order to analyze kinetic data where mass transport is important, certain transport properties are required. This paper presents data and correlating equations for the viscosity and density of baths with EDTA and Quadrol as the ligands and reports diffusivities calculated from rotating disk studies in EDTA baths.

## 666 RNP

**Density and Growth of Dendritic Elements in Electrodeposition**

J.-H. Shyu and U. Landau, Dept. of  
Chemical Engineering, Case Western  
Reserve University, Cleveland OH 44106

Analytical models for initiation and propagation of dendritic elements in electrodeposition have recently been derived and presented at previous meetings. The propagation model takes into account only a single dendritic element. The present work extends this analysis by considering the interaction among neighboring dendrites thereby providing the optimal density of propagating dendrite assembly. The density is found to be a strong function of the diffusion layer thickness. The higher the flow the more closely packed the roughness elements are. The model provides good agreement with experimental results.

## SECTION NEWS

### European Section

The European Local Section held its first business meeting on July 15, 1981 at the C.N.R.S. Laboratories in Bellevue, France. Following the business meeting, a two day scientific meeting was held on July 16 and 17, attended by about 100 scientists from 13 countries. Twenty-six papers were presented on various topics in luminescence including luminescence in II-VI compounds, luminescent devices and materials, and new techniques for advanced research in luminescence. The local section plans to hold a second luminescence meeting at the University of Dublin in 1983. Meetings on other topics will be held as interest develops. Those interested in obtaining additional information on the European Local Section should contact either R. Heindl or P. Caro, C.N.R.S. Laboratories, 1 Place Aristide Briand, 92190 Meudon-Bellevue, France.

## NEW MEMBERS

It is a pleasure to announce the following new members of The Electrochemical Society as recommended by the Admissions Committee and approved by the Board of Directors in September 1981.

### Active Members

Albery, W. J., London, England  
Amsterdam, M. F., Scottsdale, AZ  
Baum, T. A., Dallas, TX  
Burkhart, M. F., Dallas, TX  
Chan, T., Mountain View, CA  
Chang, T., San Jose, CA  
Cheema, J. S., Rexdale, Ont., Canada  
Chen, Y.-N., Sunnyvale, CA  
Cheng, K. W., Palo Alto, CA  
Devaud, G., Boulder, CO  
Dorwichter, K. D., Broomfield, CO  
Emili, W., Reutlingen, West Germany  
Fonstad, C. G., Cambridge, MA  
Frens, G., Eindhoven, The Netherlands  
Henry, P. M., Chicago, IL  
Kawakami, N., Tokyo, Japan  
Kerns, R. C., Golden, CO  
Krongelb, J. A., Sudbury, MA  
Kuan, T. S., Calabasas, CA  
Lichtenberger, J. A., Dayton, OH  
Milgram, A. A., Palo Alto, CA  
Moriarty, W. L., South Meriden, CT  
Morley, R. M., Colorado Springs, CO  
Patel, P. J., Milwaukee, WI  
Rauscher, A., Szeged, Hungary  
Ravishanker, P. S., Linden, NJ  
Rhodes, R. K., Madison, WI  
Schertenleib, K., Colorado Springs, CO  
Scribner, L. L., Jr., Charlottesville, VA  
Semones, D. E., Mentor, OH  
Skibba, M. J., Denver, CO  
Stoffel, E. J., Manhattan Beach, CA  
Strebe, J. A., Milwaukee, WI  
Trischman, G. M., Milwaukee, WI  
Uibrecht, A. G., Wyckoff, NJ  
Wang, T. E., Milpitas, CA  
Wollam, J. S., Acton, MA

### Student Members

Christian, K. D., Amsterdam, NY  
DeCosta, M. A., Bethlehem, PA  
Frydrych, D. J., Philadelphia, PA  
Griffin, A. T., Durham, NC  
Guanti, R. J., Baltimore, MD  
Henry, W. P., Lincoln, NE  
Krisht, M. H., Tucson, AZ  
Leatherman, G. L., Troy, NY  
Lee, U. R., Gainesville, FL  
Parus, S., West Lafayette, IN  
Sinha, S., Princeton, NJ  
Sundaram, L. M. G., Troy, NY  
Terry, F. L., Jr., Brookline, MA  
Van Nijie, W. A. M., Heverlee, Belgium  
Wright, J. C., Stanford, CA

## NEWS ITEMS

### Gordon Research Conferences

The Winter Gordon Research Conferences will be held January 11-February 19, 1982 at the Holiday Inn of Ventura (On the Beach), Ventura, California.

Topics for this conference include: polymers, orientational disorder in crystals, electrochemistry, composites, peptides, sensory transduction in microorganisms, metals in biology, angiotensin, alcohol, and biology of aging.

For further information, contact Dr. Alexander M. Cruickshank, Director, Gordon Research Conferences, Pastore Chemical Laboratory, University of Rhode Island, Kingston, RI 02881, telephone 401-783-4011 or 401-783-3372.

### International Symposium on Adhesive Joints

An "International Symposium on Adhesive Joints: Their Formation, Characteristics and Testing" will be held at the American Chemical Society Meeting in Kansas City, Missouri, on September 12-17, 1982.

For further information, contact Dr. K. L. Mittal, Symposium Chairman, Bldg. 300-40E, IBM Corporation, Hopewell Junction, NY 12533, telephone 914-897-6630.

### "Polyimides: Synthesis, Characterization, and Applications"

The First Technical Conference on Polyimides: Synthesis, Characterization, and Applications, sponsored by the Mid-Hudson Section of the Society of Plastics Engineers, will be held at the Nevele Country Club in Ellenville, New York, on November 10-12, 1982.

For further information, contact Dr. K. L. Mittal, Program Chairman, IBM Corporation, D/49F, B/300-40E, Hopewell Junction, NY 12533, telephone 914-897-6630.

# Manager, Chemical Vapor Deposition

Battelle, a world leader in R&D, is looking for a highly qualified person with extensive CVD experience to manage and direct a group of 22 scientists and technicians engaged in basic and applied research and pilot plant development. Activities of the group include:

- Solar grade silicon
- Fluidized bed coatings
- Hard faced coatings
- Sensor coatings
- Laser and plasma assisted CVD
- Electronic and optical thin films
- Oxidation resistant coatings
- Component fabrication

Battelle's Columbus Laboratories, located in Columbus, Ohio, has received world-wide recognition as a pioneer in CVD, the group originally being established in 1935. The selected individual will be expected to increase Battelle's business while improving the group's reputation in the technical community. Excellent comprehensive benefits, salary commensurate with experience. Send resume in confidence to: **Box #B-84, The Electrochemical Society, Inc., 10 South Main St., Pennington, NJ 08534.**



**Battelle** Columbus  
Laboratories  
An Equal Opportunity Employer

### Notice to Authors for Montreal, Canada, Meeting

The 75-word abstracts for the Montreal, Canada, Meeting of the Society, May 9-14, 1982, must be received by Society Headquarters on or before December 1, 1981. Extended abstracts are due on or before January 1, 1982. These deadlines must be adhered to in order for a paper to be considered for inclusion in the meeting program. Further details appear in the Call for Papers, pages 503C-508C of this Journal.

## ECS Membership Statistics

The following three tables give a breakdown of membership as of Oct. 1, 1981.

Table I. ECS Membership by Sections

Section	October 1				
	1977	1978	1979	1980	1981
Boston	287	291	374	394	412
Chicago	214	237	265	284	262
Cleveland	140	144	154	156	152
Columbus	84	82	91	82	85
Detroit	127	113	138	138	134
European	—	—	—	3	42
Indianapolis	39	33	30	28	33
Metropolitan New York	667	639	687	697	705
Midland	28	29	34	34	27
National Capital Area	182	167	175	180	170
Niagara Falls	79	84	151	161	136
North Texas	149	147	178	226	238
Ontario-Quebec	187	158	163	165	171
Oregon	—	—	—	6	17
Pacific Northwest	67	93	102	91	82
Philadelphia	222	217	229	243	248
Pittsburgh	132	122	149	136	119
Rocky Mountain	67	89	106	125	147
San Francisco	391	425	495	567	640
South Texas	69	56	45	35	28
Southern California-Nevada	286	279	304	340	346
Twin Cities	—	—	—	9	100
Non-Section	882	1199	1028	1151	1196
Subtotal—In Good Standing—All Classes	4299	4604	4898	5251	5490
Delinquents (Active and Student)	325	323	362	467	511
TOTAL	4624	4927	5260	5718	6001

Table II. ECS Membership by Divisions\*

Division	October 1				
	1977	1978	1979	1980	1981
Battery	1317	1370	1478	1550	1606
Corrosion	1287	1311	1309	1341	1386
Dielectrics and Insulation	962	1020	1025	1106	1178
Electrodeposition	1179	1177	1161	1167	1179
Electronics	2398	2375	2363	2731	2931
General Materials and Processes	1548	1523	1394	1388	1471
Semiconductors	1777	1788	1948	2244	2434
Luminescence	554	511	460	477	480
Electrothermics and Metallurgy	863	873	804	769	789
Industrial Electrolytic	693	698	712	682	685
Organic and Biological Electrochemistry	599	625	613	632	689
Physical Electrochemistry	1550	1618	1647	1712	1827
Energy Technology Group	—	205	813	1293	1363

\* A member may be included in the count of several Divisions.

Table III. ECS Membership by Grade

	October 1					1981/1980
	1977	1978	1979	1980	1981	
Active	3701	3958	4208	4458	4690	5.20
Member Reps. of Contributing Companies	135	127	142	148	134	(9.46)
Emeritus	114	116	117	125	127	1.60
Life	47	49	51	53	53	—
Honorary	9	13	14	14	16	14.29
Subtotal Active in Good Standing	4006	4263	4532	4798	5020	4.63
Delinquent	258	267	312	413	420	1.69
Total Active on Record	4264	4530	4844	5211	5440	4.39
Students	293	341	366	453	470	3.75
Delinquent	67	56	50	54	91	68.52
Total Students	360	397	416	507	561	10.65
Total Individual Members	4624	4927	5260	5718	6001	4.95

## POSITION AVAILABLE

**Electrochemists - Engineers - Metallurgists**  
—Considering a career change for the right opportunity? We are confidential executive recruiting and placement specialists serving the electrochemical industry. We have a variety of positions available, which range from entry level through management. Client companies pay all fees. Write or call in strict confidence to D. Rocky Bradley, SHS of Allentown, 1401 N. Cedar Crest Blvd., Suite 56, Allentown, PA 18104 (215) 437-5551.

## POSITIONS WANTED

Please address replies to the box number shown, c/o The Electrochemical Society, Inc., 10 South Main Street, Pennington, N.J. 08534-2896.

**Materials Scientist/Electrochemist—Ph.D.** Extensive practical and theoretical experience in anodic oxide films, etching, capacitor technology, and thin film devices. Strong background in electrochemistry, materials science, and metallurgy, with main emphasis in process development and optimization. Versatile and innovative with several patents and publications. Seeking responsible position. Reply Box C-232.

**Electrochemist/Electrochemical Engineer — Ph.D.** Seeks challenging research position. Background in solid-state batteries and electrolyzers, theory and practice. Catalysis experience. Expertise in electrode reaction studies. Publications. Reply Box C-233.

Abstracts of Recent News Papers—  
Denver, Colorado, Meeting 485C-488C

Section News ..... 489C

New Members ..... 489C

Notice to Authors ..... 489C

ECS Membership Statistics ..... 490C

Position Available ..... 490C

Positions Wanted ..... 490C

Nominations for ECS Award in  
Solid State Science and  
Technology ..... 491C

Announcement of the David C.  
Grahame Award ..... 491C

New Books ..... 491C-494C

ECS Summer Fellowship Awards to  
be Granted ..... 492C

Call for Papers—First Symposium on  
Very Large Scale Integration Science  
and Technology ..... 495C

Call for Papers—Montreal, Canada  
Meeting ..... 503C-508C

## Nominations Solicited for the Sixth Electrochemical Society Award in Solid State Science and Technology

Nominations are solicited by the Honors and Awards Committee for the Solid State Science and Technology Award. Since establishment of the biennial award in 1972, the recipients have been the following:

1973 William G. Pfann

1977 Robert N. Hall

1975 Harry C. Gatos

1979 Morton B. Panish

1981 Gerald L. Pearson

The next award will be presented at the Spring 1983 Meeting of the Society.

The recipient of this Award must have made distinguished contributions to the field of solid state science. He need not be a member of the Society, and there are no restrictions regarding age, sex, race, citizenship, or place of origin.

The Award consists of a silver medal together with a bronze replica and the sum of \$1500. The recipient will deliver an address to the Society on a subject related to the contributions for which the Award is presented.

This is one of the Society's most prestigious awards, and we urge all members of the Society to give serious consideration to possible candidates. Please send nominations, with supporting documents, to E. H. Nicollian, Bell Laboratories, 600 Mountain Ave., Murray Hill, N.J. 07974. The supporting documents need not be lengthy, and may consist of a half-page description of the contributions made, a half-page biography, and a list of publications of the candidate. If the paper titles are not included in the publication list, please identify the most outstanding papers. If the Committee needs more information, the nominator will be contacted. If possible, please submit the nominations by March 1, 1982 to facilitate consideration by the Committee. Nominations close at the opening of the Spring 1982 Meeting.

## NEW BOOKS

### U.V. Curing in Screen Printing for Printed Circuits and the Graphic Arts, edited by S. G. Wentink and S. D. Koch.

1981, Technology Marketing Corp., 17 Park St., Norwalk, CT 06851. 209 pages, bound. \$72.00.

Chapter 1 offers a brief explanation of u.v. curing and the principles behind it. Chapters 2 and 3 provide the reader with an explanation of the different types of u.v.-curable inks and coatings and their components. Chapter 4 and 5 focus on the selection and the proper maintenance of u.v. curing equipment. Since u.v. curing has deeply penetrated the printed circuits technology, an entire chapter is devoted to this topic. Chapter 6 thus examines the application of u.v. curing in printed circuits by discussing specifications and requirements, property evaluations, operating requirements, and economic factors that are unique to the printed circuits industry. Chapters 7 and 8 focus primarily on production. Toxicity and safety of the inks, coatings, and the curing equipment are important issues that are addressed, in great detail, in chapter 9. Chapter 10 provides a detailed summary of the equipment selection process leading to an extensive coverage of economic justification for u.v. curing.

## Announcement of the New David C. Grahame Award of the Physical Electrochemistry Division of The Electrochemical Society, Inc. and Call for Nominations

Nominations are solicited for the David C. Grahame Award, to be presented for the first time in the Spring of 1983.

The Physical Electrochemistry Division has established this new Award in order to encourage excellence in Physical Electrochemistry Research and to stimulate publication of high quality research papers in the *Journal of The Electrochemical Society*. This encouragement is provided by bringing recognition to Active Members of the Society who have made outstanding contributions to the field of Physical Electrochemistry and who have enhanced the scientific stature of the Society by the presentation of well-recognized papers in the *Journal* and at Society Meetings. For the purpose of this Award, Physical Electrochemistry is defined as that area of Electrochemistry traditionally represented by the Physical Electrochemistry Division in the *Journal* and at Society Meetings.

The "David C. Grahame Award" shall be granted to a currently Active Member of the Society for some recent outstanding scientific contribution to Physical Electrochemistry. For the purpose of the Award, "currently active" is to be measured by publication of more than one paper in the *Journal* and attendance at more than one Society Meeting, as a member of the Society, within the previous five years.

The Award will be made biennially at the Society Spring Meeting, with the first Award to be presented in May 1983.

The recipient will receive a certificate, a stipend of \$500 and, if required, financial assistance toward travel expenses to the Society Meeting at which the Award is made. The recipient is required to attend the Society Meeting at which the Award is given and to present an Award lecture in the General Session of or in a Symposium sponsored by the Physical Electrochemistry Division at that Meeting. In the event that the Award is made jointly to two or more co-recipients, the Award to each of the co-recipients will comprise a certificate and a check for an amount to be decided by the Physical Electrochemistry Division Executive Committee. The Award is financed from the income of a "Physical Electrochemistry Division Award Fund," specifically established for this purpose by contributions from the Physical Electrochemistry Division and the General Electric Company.

To be considered for the Award, nominations must be accompanied by supporting documents, such as a biography, list of publications, professional activities, and a brief summary of the recent outstanding contribution on which the Award is to be based. Letters of support by scientists well recognized in the area of Physical Electrochemistry will also be taken into account. Nomination documents in 6 copies should be submitted to the Award Chairman, Dr. J. D. E. McIntyre, Bell Laboratories, 1D-354, Murray Hill, NJ 07974. Deadline for receipt of nominations by the Award Committee Chairman is December 31, 1981.



### Chromates Symposium 80 Focus of a Standard, Proceedings, Rockville, Maryland, September 16-18, 1980.

1981, Industrial Health Foundation Inc., 5231 Centre Ave., Pittsburgh, PA 15232. 370 pages, paper. \$25.00.

The first group of papers is concerned mainly with toxicity of chromium and its compounds. The second group of papers includes subjects such as electroplating, pigments, paints, welding, wood preservation, and tanning. The last section is largely concerned with monitoring exposure to chrome particularly in the metallurgical industries.

### Electrochemie und Elektronik, October 23-24, 1980, by Deutsche gesellschaft für chemisches apparatewesen.

1981, Verlag Chemie, Deuchema, Deutsche Gesellschaft, Frankfurt/Main 97 01 46 6000 Frankfurt. 289 pages, paper.

The conference was organized by the Fachgruppe Angewandte Elektrochemie of the Society. Sessions were held on: Measurement techniques; displays, sensors, modules; power sources; semiconductor-electrodes; and process control. Papers are in German, with English summaries.

### Tribology in Metal Working—New Developments.

1980, Institute of Mechanical Engineers, distributed by Society of Automotive Engineers, 400 Commonwealth Dr., Warrendale, PA 15086. 63 pages, paper. \$28.00.

The titles of the papers presented at the conference are: Recent developments in the analysis and applications of hydrostatic lubrication in sheet metal forming; selected lubrication by electrochemical deposition for sheet and bulk forming operations; the treatment of metal-working tools by ion implantation; hot strip mill roll gap lubrication; surface coatings for cutting and forming tools;

### Summer Fellowship Award Program of The Electrochemical Society

The Board of Directors of The Electrochemical Society has voted to allocate \$4,500 for summer fellowships in 1982. The Award subcommittee shall have the discretion of deciding the number of recipients and the amount granted to each, within the limits of the appropriation.

The purpose of the award is to assist a student in continuing his/her graduate work during the summer months in a field of interest to The Electrochemical Society. According to the rules for the Society Summer Fellowship Program, if one award is given, it shall be called the Edward G. Weston Fellowship Award; if two awards are given, the second one shall be designated the Colin Garfield Fink Fellowship Award; if more than two are given, the third award shall be called the Joseph W. Richards Fellowship Award.

Candidate's qualifications: "The award shall be made without regard to sex, citizenship, race, or financial need. It shall be made to a graduate student pursuing work between the degree of B.S. and Ph.D., in a college or university in the United States or Canada, and who will continue their studies after the summer period. A previous holder of an award is eligible for reappointment."

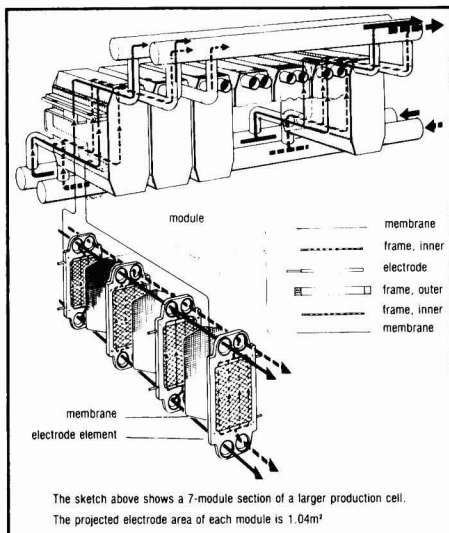
Qualified graduate students are invited to apply for these fellowship awards. Applicants must complete an application form and supply the following information:

1. A brief statement of educational objectives.
2. A brief statement of the thesis research problem including objectives, work already accomplished, and work planned for the summer of 1982.
3. A transcript of undergraduate and graduate academic work.
4. Two letters of recommendation, one of which should be from the applicant's research adviser.
5. Successful recipients of fellowships shall agree not to hold other appointments or other fellowships during the summer of 1982.

Application forms are available from the Chairman of the Fellowship Awards Subcommittee, to whom completed applications and letters of recommendation should be sent: Dr. Stanley Bruckenstein, SUNY, Department of Chemistry, Buffalo, New York 14214.

Deadline for receipt of completed applications will be January 1, 1982 and award winners will be announced on May 1, 1982.

# Electro Syn Cell



A new monopolar membrane cell of modular design is now available for synthesis of organic and inorganic chemicals. Start with a laboratory unit (0.04m<sup>2</sup>), and when ready expand this to a pilot scale module (1.04m<sup>2</sup>), and then to a production plant of several modules. Cell parts are available in a wide variety of materials. Further advantages: leakproof, uniform hydrodynamics, narrow inter-electrode gap, injection molded frames.

**THE ELECTROSYNTHESIS CO.**

P.O. Box 16, E. Amherst, N.Y. 14051 Tel.: (716) 684-0513



the non-embedded abrasive compound is a tool for saving time and money in the manufacture and overhaul of parts and machinery; new oil mist lubrication concepts for higher efficiency and better environment; and tribology in metal working, developments in perspective.

**Primary Electrochemical Cell Technology Advances since 1977**, edited by R. W. Graham.

1981, Noyes Data Corp., Noyes Bldg., Park Ridge, NJ 07656. 388 pages, bound, \$48.00.

This book describes over 200 processes relating to the worldwide development for primary battery chemistry, design, manufacture, and applications technology. Those processes, representative of the recent patent literature of the U.S., also encompass the newer technology development in Japan, Europe, and other countries. There are chapters on alkaline zinc dry cells; lithium batteries; metal-air and zinc-silver oxide batteries; seawater, reserve, and thermal batteries; batteries for photographic applications; pacemaker battery technology. There are indexes by inventor, patent number, and companies.

**Leiterplattenfertigung Heute: Fertigung, Qualität, Probleme und Problemlösungen, Tagung Dusseldorf, 1980. (VDI Berichte No. 387) (English Transfection. Production of Circuit Boards Today) Germany, September 29-30, 1980**, by Verein Deutscher Ingenieure.

1980, VDI Verlag GmbH, Postfach 1139 D-4000 Dusseldorf 1, Germany. 112 pages, paper.

Papers include: Layout for automatic assembly of printed circuits; possibilities of semi-automatic data control for printed circuits; semiadditive process in printed circuit manufacture and its practical applications; thin film laminate—an alternative to the semiadditive process; alternatives of gliding printed circuits; production of printed circuits plated with copper; flexible printed circuits—production problems and their solutions; and computer-aided manufacturing of multi-layers.

**Laser and Electron-Beam Solid Interactions and Materials Processing**, edited by J. F. Gibbons et al.

1981, Elsevier North-Holland, 52 Vanderbilt Ave., New York, NY 10017 and P.O. Box 211, 1000 AE Amsterdam, The Netherlands. 629 pages, bound, \$70.00.

The book is divided into the following parts: Fundamental mechanisms; elemental semiconductors; compound semiconductors; device applications; deposited films and silicon on insulators; silicides and metals. Some of the specific topics discussed in the papers: Threshold energy density for pulsed laser annealing of silicon; convection in pulsed laser formed melts; adsorption of oxygen in laser-induced amorphous silicon; transient and furnace annealing of ion-implanted gallium arsenide; laser processing of silicon for advanced microelectronic devices and circuits; beam processing; laser epitaxy over buried layers; laser growth of thin silicon crystals in patterned structures; silicide formation using laser and electron beams; laser quenched metal-silicon alloys; pulsed laser annealing of aluminum; high power effects on unimplanted and implanted aluminum single crystals.

**International Congress on Surface Technology, Proceedings**, edited by G. Rohrbach.

1981, VDI Verlag GmbH, 4 Dusseldorf 10, Postfach 10-250, Germany. 613 pages, paper.

Sessions covered: Survey presentations; technologies for the treatment of surfaces, surface quality, construction; technologies for measuring and analyzing surfaces; preparation of metal and synthetic surfaces; processes for metallic and ceramic coating; protection by means of modern organic coatings; electrodeposition and chemical treatment of surfaces in engineering; thermic and thermochemical processes for treatment of surfaces; special properties of surfaces; and information and documentation regarding surface technology.

# Senior Plating Engineers

The growth and development of our plating requirements have created openings for Senior Process Engineers with broad expertise in electrochemistry. The successful candidates will be responsible for insuring that our plating and printing processes continue to produce quality front panels and precision components for our instruments. We manufacture tightly toleranced parts ( $\pm 0.0002$ ) and utilize class 10,000 clean rooms on our chemical etch lines. Our rack and barrel plating lines plate both metal and plastic parts and are capable of producing a variety of surface finishes and textures. Expertise needed for these areas are as follows:

## Lead Engineer

The Lead Engineer will be responsible for the technical direction of eight other professionals in the areas of general plating, anodizing and printing and chemical etching. This will require a solid background in electrochemistry, plus experience in the production of parts using chemical etching with U.V. photo resists on metal and plastic substrates. A Ph.D. in Chemistry or Chemical Engineering plus two to four years' experience as a Lead or Project Engineer is required.

## Senior Engineer

The Senior Engineer will investigate, verify and maintain all of our metal and plastic plating and engineering processes. Familiarity with Ni, Zn, Cd, Au, Ag, Cu, Brass, Sn, Electroless Ni-Cu and Albaloy plating is desired. Knowledge of anodizing and printing with U.V. ink is also helpful. This position will require a Ph. D. or Master's level education in Chemistry or Chemical Engineering, as well as three to five years' diverse experience with metal and plastic parts.

Tektronix, Inc. develops, manufactures and markets internationally recognized precision electronic measurement instruments, computer peripherals and related electronic instrumentation. Headquartered near Portland, Oregon and supported by sales and service personnel throughout the U.S., we are within a two-hour drive of the Cascade Mountains and ocean beaches. The close-by natural playgrounds and the City of Portland provide a variety of recreational and cultural interests.

Salary is \$25,000 - \$45,000 depending on experience. Benefits include educational support, insurance and profit sharing programs, and relocation assistance.

If you feel that you are qualified for either of these positions, please send a detailed resume and salary history to Gene Lambird, M.S. Y6-010, Tektronix, Inc., P.O. Box 500, H75, Beaverton, Oregon, 97077 or call 800-547-1164 for more information.

An equal opportunity employer m/f/h.

**Tektronix**  
COMMITTED TO EXCELLENCE

### Electrodes of Conductive Metallic Oxides, edited by S. Trasatti.

1981, Elsevier North-Holland, 52 Vanderbilt Ave., New York, NY 10017 and P.O. Box 211, 1000 AE Amsterdam, The Netherlands. 336 pages, bound. \$63.00.

Part B is mainly devoted to the kinetic aspects of reactions at oxide electrodes. The first chapter deals, however, with the surface chemistry of oxides. The second chapter provides a critical review of organic reactions at and with oxide films in the low and high potential ranges. Chlorine and oxygen evolution are the anodic reactions that have been studied in most detail at oxide electrodes. A critical survey of the literature is provided in the third chapter. The last chapter has been compiled by an expert from the technological field who has long been involved in the research and development programs of an industry that pioneered the use of oxide anodes in chlor-alkali cells. This chapter is devoted to the scientific aspects of the matter, and points out the problems encountered in the practical use of the materials with special emphasis on long-term performances that constitute the major technological requirement.

### Langmuir-Blodgett Films, edited by W. A. Barlow.

1980, Elsevier Scientific Publishing Co., Molenwerf 1, 1014 AG Amsterdam, The Netherlands and 52 Vanderbilt Ave., New York, NY 10017. 288 pages, bound. \$75.50.

### Electron Microscopy Society of America 38th Annual Meeting, Proceedings, edited by G. W. Bailey.

1981, Claitors Publishing Div., 3165 S. Acadian at 1-10, P.O. Box 3333, Baton Rouge, LA 70821. 665 pages, bound. \$35.00.

Except where noted, these books have been prepared by the staff of The Engineering Societies Library, and were selected for inclusion in the *Journal* by Dr. Daniel Cubicciotti of Stanford Research Institute. The Electrochemical Society does not have copies available for sale or loan. Orders for the books should be forwarded directly to the publishers.

## ADVERTISERS' INDEX

Battelle .....	489C
ECO Instruments .....	499C
Electrosynthesis Co. ....	492C
Princeton Applied Research Corp. ....	498C
Solartron .....	496C
Stonehart Associates .....	497C
Tektronix .....	493C

## OUT-OF-PRINT SOCIETY VOLUMES

The following volumes sponsored or published by The Electrochemical Society, Inc. are now out-of-print. Xerographic copies\* or reprints† of these volumes are available.

- \* **Vapor Plating.** C. F. Powell, I. E. Campbell, and B. W. Gonser, Editors. A 1955 symposium. 158 pages.
- \* **The Structure of Electrolytic Solutions.** W. J. Hamer, Editor. A 1957 symposium. 441 pages.
- \* **Technology of Columbium (Niobium).** B. W. Gonser and E. M. Sherwood, Editors. A 1958 symposium. 120 pages.
- \* **Surface Chemistry of Metals and Semiconductors.** H. C. Gatos, J. W. Faust, Jr., and W. J. La Fleur, Editors. A 1959 symposium. 526 pages.
- \* **Electrode Processes, First Conference.** E. Yeager, Editor. A 1959 symposium. 374 pages.
- \* **Mechanical Properties of Intermetallic Compounds.** J. H. Westbrook, Editor. A 1959 symposium. 435 pages.
- \* **Zirconium and Its Alloys.** J. P. Pemsler, E. C. W. Perryman, and W. W. Smeltzer, Editors. A 1965 symposium. 205 pages.
- † **Measurement Techniques for Thin Films.** B. Schwartz and N. Schwartz, Editors. 1965 and 1966 symposia. 347 pages.
- † **Electrode Processes, Second Conference.** E. Yeager, H. Hoffman, and E. Eisenmann, Editors. A 1966 symposium. 190 pages.
- \* **Electrolytic Rectification and Conduction Mechanisms in Anodic Oxide Films.** P. F. Schmidt and D. M. Smyth, Editors. A 1967 symposium. 230 pages.
- \* **Electrets and Related Electrostatic Charge Storage Phenomena.** L. M. Baxt and M. M. Perlman, Editors. A 1967 symposium. 150 pages.
- \* **Dielectrophoretic and Electrophoretic Deposition.** E. F. Pickard and H. A. Pohl, Editors. A 1967 symposium. 138 pages.
- \* **Electron and Ion Beam Science and Technology, Third International Conference.** R. Bakish, Editor. A 1968 symposium. 725 pages.
- \* **Optical Properties of Dielectric Films.** N. Axelrod, Editor. A 1968 symposium. 325 pages.
- \* **Thin Film Dielectrics.** F. Vratny, Editor. A 1968 symposium. 680 pages.
- \* **Ohmic Contacts to Semiconductors.** B. Schwartz, Editor. A 1968 symposium. 356 pages.
- \* **Semiconductor Silicon.** R. R. Haberecht and E. L. Kern, Editors. A 1969 symposium. 750 pages.
- \* **Chemical Vapor Deposition, Second International Conference.** J. M. Blocher, Jr. and J. C. Withers, Editors. A 1970 symposium. 872 pages.
- \* **Marine Electrochemistry.** J. B. Berkowitz, M. Banus, M. J. Pryor, R. Horne, P. L. Howard, G. C. Whitnack, and H. V. Weiss, Editors. A 1972 symposium. 416 pages.

\* Order from University Microfilms, Inc., 300 North Zeeb Street, Ann Arbor, Mich. 48103. Specify an Electrochemical Society volume.

† Order from Johnson Reprint Co., 355 Chestnut St., Norwood, N.J. 07648. Specify an Electrochemical Society volume.

- \* **Semiconductor Silicon 1973.** H. R. Huff and R. R. Burgess, Editors. A 1973 symposium. 936 pages.
- \* **High Temperature Oxidation of Metals.** By P. Kofstad. The Corrosion Monograph Series. 340 pages.
- \* **Chemical Vapor Deposition, Fourth International Conference.** G. F. Wakefield and J. M. Blocher, Jr., Editors. A 1973 symposium. 595 pages.
- \* **Electrets, Charge Storage and Transport in Dielectrics.** M. M. Perlman, Editor. A 1973 symposium. 675 pages.
- \* **Fine Particles.** W. E. Kuhn and J. Ehrhrtmann, Editors. A 1974 symposium. 352 pages.
- \* **Corrosion Problems in Energy Conversion and Generation.** C. S. Tedmon, Editor. A 1974 symposium. 484 pages.
- \* **Electrocatalysis.** M. W. Breiter, Editor. A 1974 symposium. 378 pages.
- \* **Electron and Ion Beam Science and Technology, Sixth International Conference.** R. Bakish, Editor. A 1974 symposium. 594 pages.
- \* **Energy Storage.** H. P. Silverman and J. B. Berkowitz, Editors. A 1975 symposium. 258 pages.
- \* **Chemical Vapor Deposition, Fifth International Conference.** J. M. Blocher, Jr., H. E. Hintermann, and L. H. Hall, Editors. A 1975 symposium. 848 pages.
- \* **Etching.** H. G. Hughes and M. J. Rand, Editors. A 1976 symposium. 203 pages.
- \* **Electrode Materials and Processes for Energy Conversion and Storage.** J. D. E. McIntyre, S. Srinivasan, and F. G. Will, Editors. A 1977 symposium. 340 pages.
- \* **Electron and Ion Beam Science and Technology, Eighth International Conference.** R. Bakish, Editor. A 1978 symposium. 297 pages.
- \* **International Symposium on Solar Energy.** J. B. Berkowitz and I. A. Lesk, Editors. A 1976 symposium. 372 pages.
- \* **High-Temperature Metallic Corrosion of Sulfur and Its Compounds.** Z. A. Foroulis, Editor. A 1969 symposium. 276 pages.
- \* **Properties of Electrodeposits—Their Measurement and Significance.** R. Sard, H. Leidheiser, Jr., and F. Ogburn, Editors. A 1974 symposium. 430 pages.
- \* **Chemical Vapor Deposition, Sixth International Conference.** L. F. Donaghey, P. Rai-Choudhury, and R. N. Tauber, Editors. A 1977 symposium. 596 pages.
- \* **Battery Design and Optimization.** S. Gross, Editor. A 1978 symposium. 486 pages.



# CALL FOR PAPERS

## FIRST INTERNATIONAL SYMPOSIUM ON VERY LARGE SCALE INTEGRATION SCIENCE AND TECHNOLOGY OCTOBER 17-22, 1982—DETROIT, MICHIGAN

The First International Symposium on Very Large Scale Integration Science and Technology, co-sponsored by the Electronics and the Dielectrics & Insulation Divisions, will be held as a part of the 160th Meeting of The Electrochemical Society in Detroit, Michigan, October 17-22, 1982.

The symposium will include a wide range of topics in high density, high performance device manufacturing science and technology. The emphasis will be on those processes and technologies that are unique to VLSI requirements. Publication of a proceedings volume is planned.

Topics to be considered in the symposium include the following: 1. **Device** fundamentals, design, modeling, and characterization; device and process scaling, and ultimate limits. 2. **Process and Materials** fundamentals, modeling, and characterization, and their relation to device performance. 3. **Integrated Circuit Fabrication Technology** for high speed, high density, and high reliability; prediction and control of yield and performance limitations from processes, materials, and defects; integrated circuit factory automation and control.

### DEVICE SCIENCE AND TECHNOLOGY (Co-Chairmen—C. J. Dell'Oca and A. J. Reisman)

- Basic device fundamentals related to very small geometries and high performance. Device scaling and limits.
- Effect of parasitics and their reduction through device design and process optimization.
- Device modeling in relation to processes or process modeling.
- Device advances such as thin gate insulators or  $\text{Si}_3\text{N}_4$  gate dielectrics, silicide gates, shallow emitters, heterojunction devices, and other advances in bipolar and MOS devices.

### PROCESSES AND MATERIALS FOR VLSI (Co-Chairmen—D. A. Doane, H. Geipel, and H. R. Huff)

- Science and technology of low temperature processes required to achieve high performance VLSI, such as LPCVD, plasma CVD, high pressure oxidation, and ion implantation.
- Fine line definition and dry etching science and technology, selectivity, surface profile control.
- Process modeling, one and two dimensional, for diffusion and surface profiles.
- Lithographic aspects, such as applications, problems and limits of optical, x-ray, and electron beam exposure systems and resist materials.
- Properties and preparation of materials such as thermal  $\text{Si}_3\text{N}_4$ , thin gate oxide, polycides, silicides, thin epitaxial layers, insulators, etc.
- Contact and gate technology: fabrication and properties; use of silicides; and polycides.
- Novel processes for VLSI, such as beam annealing.

### INTEGRATED CIRCUIT FABRICATION SCIENCE AND TECHNOLOGY

(Co-Chairmen—N. Goldsmith and C. M. Osburn)

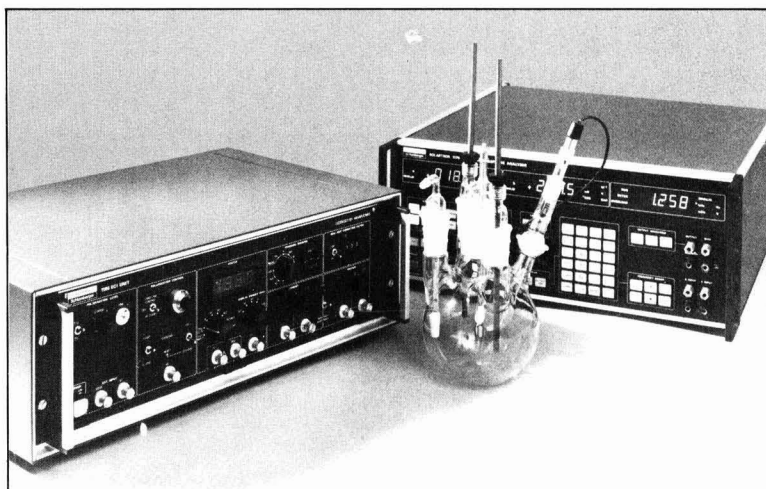
- Approaches to achieving high density, high performance bipolar and MOS technologies.
- Methods and properties of device isolation for high density integrated circuits.
- Multilevel interconnect technologies: fabrication and reliability.
- Process or residual impurity-induced defects: formation, understanding, and control.
- Yield analysis and prediction: factory automation and control.
- Reliability.

Authors must submit five copies of a 500 word, or longer, abstract specifically stating the contribution that the paper makes to the field. These abstracts will be used solely to select papers for presentation at the symposium. In-depth review papers which give wide coverage of a field are also sought, and those eminent in the fields of devices, materials, and advanced IC process technologies are invited to submit abstracts. The abstracts should be submitted by **January 15, 1982**, to either the Chairman, Conrad J. Dell'Oca, LSI Logic Corp., 1601 McCarthy Blvd., Milpitas, CA 95035; or to the Vice-Chairman, W. Murray Bullis, Fairchild Camera and Instrument Corp., 4001 Miranda Ave., Palo Alto, CA 94304. Authors submitting abstracts will be notified if their papers have been accepted for presentation and will be given specific instructions for subsequent manuscript preparation for the proceedings. Authors of accepted papers will also be required to submit a 75-word abstract (deadline—May 1, 1982) and a 500-1000 word extended abstract (deadline—June 1, 1982) to The Electrochemical Society, Inc., 10 South Main Street, Pennington, NJ 08534.

# Solartron

INSTRUMENTATION GROUP

## Frequency Response Analysis for the Electrochemist



The Solartron 1186 Electrochemical Interface Unit has been designed to provide the interfacing requirements for the control and measurement of cell characteristics using the Solartron 1170 series Frequency Response Analysers, by superimposing its sine wave output as an internally generated polarisation voltage. In addition to its role as an interface the unit contains all the features necessary to make it a general purpose potentiostat enabling both ac and dc impedance measurements to be undertaken.

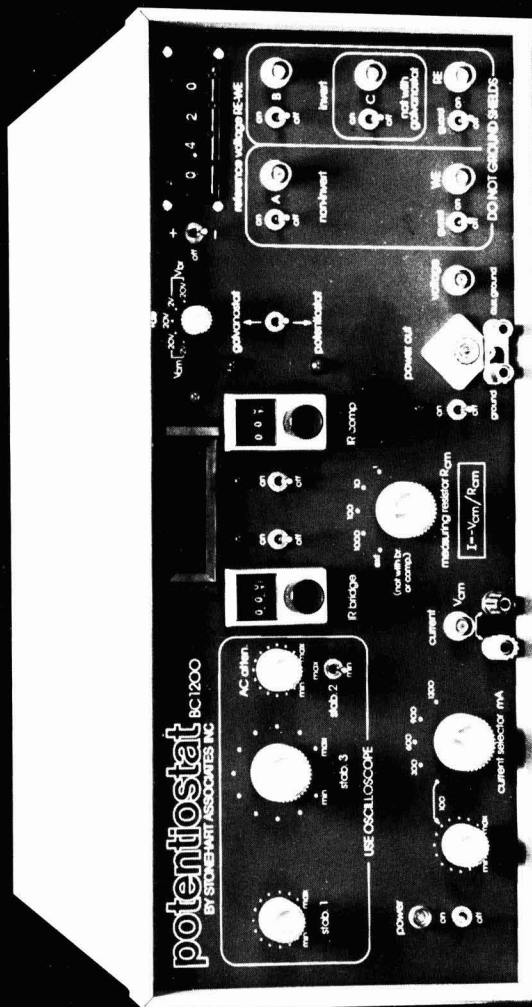
These features enable the majority of electrochemical analyses to be implemented, including:

- Corrosion
- Battery testing
- Biological measurements
- Photo-electric effects
- Education.

Solartron Instrumentation Group, Data Systems Division of Sangamo Weston Inc.  
17972 Sky Park Circle, Suite F, Irvine, CA 92714 Tel: (714) 641-7137

SANGAMO WESTON  
**Schlumberger**

The most powerful CPU around.  
Think about it.



The BC1200 High Performance Potentiostat is widely regarded as the most advanced machine commercially available. Areas of application range from ring and disc at sub-microampere levels to 1.2 ampere, and wide-band impedance.

- Up to  $\pm 9.999V$  bias set digitally.
- 3 independent programming inputs with signal mixing.
- Programmable in both potentiostatic & galvanostatic modes.
- $3\frac{1}{2}$  digit DVM with range select.
- Precision IR correction and compensation using a wide-band bridge.
- Slew rates better than 6V/microsec and 4A/microsec.

# stonehart associates

Post Office Box 1220, Madison, Connecticut 06443 Telephone Area Code 203 245-7507



# Uncompromising Instrumentation... for Controlled Potential Coulometry

**The Technique**—Known throughout the electrochemical community, controlled potential coulometry (CPC) is a high precision, high accuracy analytical technique. Since coulometry is a "primary" method, it is often employed for absolute purity determinations as well as general electrochemical investigations.

For years, CPC has been used in the atomic energy industry where remote, high accuracy metals analysis is required. A variety of precious metals are conveniently handled by CPC and recently, Harrar<sup>1</sup> has demonstrated its use in precious metal plating bath analyses. Of course many anions and organics are also amenable to this technique.

**The System**—The EG&G PARC Model 380 System for CPC consists of a research quality potentiostat (Model 173), a stable digital coulometer (Model 179), and an electrolysis cell of convenient design (Model 377A). Together these components provide a highly practical and effective system for a variety of electrochemical work including CPC.

**The Potentiostat**—Since the Model 173 offers very accurate potential control, highly selective electrolyses can be carried out. An impressive combination of other performance specs such as 3  $\mu$ s response time,  $\pm 1$  A current capability and  $\pm 100$  V compliance voltage, makes the Model 173 mainframe ideal for CPC work.

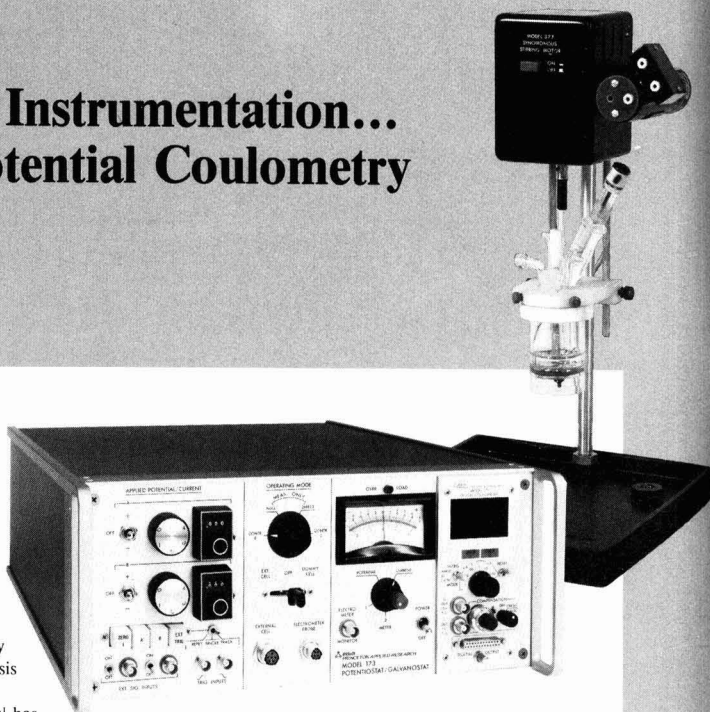
**The Coulometer**—The Model 179 Digital Coulometer plugs into the 173 Potentiostat and is used to integrate the electrolysis current. It provides a digital display of


accumulated charge which autoranges over seven decades of charge. Features such as current polarity discrimination, background subtraction and digital output of coulombs greatly simplify the CPC measurement.

**The Electrolysis Cell**—The Model 377A is a carefully designed package for coulometry requiring only the addition of mercury or the optional platinum electrode kit. The 377A incorporates an efficient stirring system for rapid electrolyses and minimum analysis times.

**Applications Back-Up**—For more information on how the Model 380 Controlled Potential Coulometry System can be used in your work, contact the Electrochemistry Product Group, EG&G PRINCETON APPLIED RESEARCH, P. O. Box 2565, Princeton, NJ 08540; 609/452-2111.

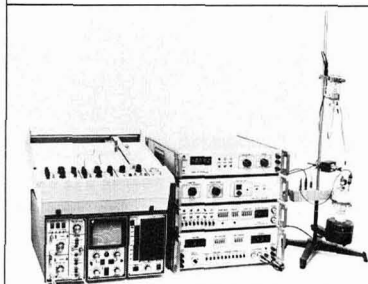
<sup>1</sup>Jackson E. Harrar and Miles C. Waggoner, "Precious Metal Analysis By Controlled Potential Coulometry," *Plating and Surface Finishing*, January 1981, pp. 41-45.



 **EG&G PRINCETON APPLIED RESEARCH**



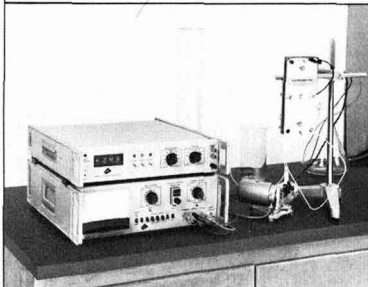
# Instrumentation for Electrochemistry and Chemistry Research



## ELECTROCHEMOSCOPE I

A complete line of versatile instruments for the electrochemist includes the unique ELECTROCHEMOSCOPE I which makes available for the first time . . .

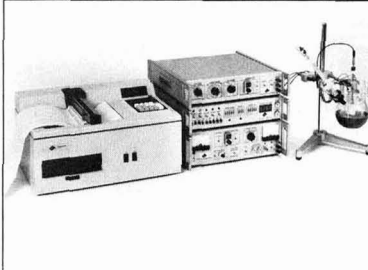
- All digital circuitry • Real time CRT display plus X-Y Recorder
- Floppy disc storage of 16 plots • Scale expansion and background subtraction of stored data • Computer interface
- Digital display of current, voltage and coulombs.



## ELECTROPREP™ SYSTEM

A complete system for preparative electrosynthesis and coulometry is based on the unique ELECTROPREP cell which offers a wide choice of easily interchanged electrodes, optimized cell geometry and choice of interchangeable separators. Optimally matched components of the system provide . . .

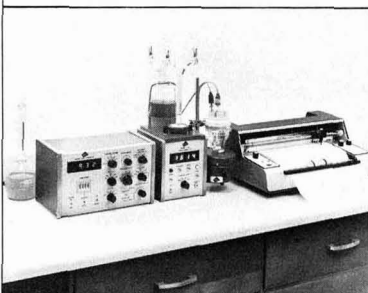
- Production of up to 200 millimoles per hour
- Completely automated operation
- Controlled voltage and constant current operation.



## COMPUTER-AIDED CORROSION MEASUREMENTS

Included in the wide choice of instruments for corrosion research from ECO INSTRUMENTS, the CMS-10 Computer-Aided Electrochemical Corrosion Measurement System introduces the advantages of data processing including . . .

- Raw data stored on floppy discs for instant retrieval
- Standard corrosion calculations done automatically, displayed digitally and/or printed out
- User programmable for new and non-standard calculations
- Sample testing time reduced to a few minutes.



## TITRISTAT™ II

The TITRISTAT II offers a unique combination of capabilities and conveniences, such as . . .

- First derivative plots plus  $\frac{\Delta E}{\Delta V}$  providing true equivalence point
- Potentiometric, amperometric, Karl Fischer and both direct and incremental thermometric titrations
- Automatic end-point search, pH Stat, and preset end-point search
- Two digital displays — ml's added and actual parameter sensed
- Computer compatible outputs for both displays.

**ECO INSTRUMENTS**  
Division of Sea Data Corporation

153 California Street - Newton, Mass. 02158, U.S.A.  
Tel. (617) 661-8080 - Telex: 951107 - Cable: Seadata New



## Instructions to Authors

The **JOURNAL OF THE ELECTROCHEMICAL SOCIETY** is the official monthly journal of the Society. It contains three sections: Electrochemical Science and Technology, Solid-State Science and Technology, and Reviews and News. Technical Papers, Technical Notes, and Accelerated Brief Communications are published in the first two sections and Review Papers in the third. All manuscripts submitted are considered for publication, with the understanding that they have not been submitted, accepted for publication, or published elsewhere. A wide range of subject matter is acceptable. Manuscripts can be handled promptly and efficiently if these instructions are followed.

**Technical Papers** describe fundamental or applied studies in depth. They contain new data and/or new interpretations of existing data. Abstracts summarizing the results are required.

### TYPES OF PAPERS

**Technical Notes** report briefly on limited research or development that is not being pursued further. No abstracts are required.

**Accelerated Brief Communications** present, in camera-ready format of limited length, scientific or technological information warranting rapid dissemination. No abstracts are required.

**Review Papers** furnish critical analyses of topical subjects. Abstracts are required.

Submit three complete, clear copies of each manuscript and the originals of all figures and illustrations to:

### SUBMISSION

Editorial Office

The Electrochemical Society, Inc.

10 South Main Street

Pennington, New Jersey 08534-2896

A letter accompanying the manuscript should give (a) the name and mailing address of the author to whom correspondence should be sent, (b) reference to any presentation of the work at a meeting of The Electrochemical Society, (c) the Division or Group of the Society or the Divisional or Group Editor (both are listed in the front of each issue of the Journal) whose interests are most closely related to the work being discussed, (d) the section of the Journal in which the work should appear, and (e) the names and addresses of people able to act as reviewers.

Following receipt by the Editorial Office, each manuscript is sent to a Divisional or Group Editor with knowledge of the subject matter. This editor arranges for review of the manuscript and communicates with the author(s) regarding revisions. Final acceptance or rejection of a manuscript is determined by the Editor.

### EDITORIAL PRACTICES

Accelerated Brief Communications are handled as rapidly as possible, ordinarily with a response to the author(s) from the Divisional Editor, the Group Editor, or the Editor within three weeks of their arrival at Pennington. Response to the authors of other manuscripts usually takes place within six weeks. Following acceptance, authors are notified of the Journal issue in which publication is scheduled; about one month before publication, page proofs and an order blank for reprints are provided. Proofs must be promptly corrected and returned. Extensive alterations by the author may delay publication; their cost will be billed to the author(s).

To help meet publication costs, a payment of \$65.00 per printed page is requested for the publication of technical material. If at least one author is a Society member or an employee of a Patron or Sustaining member, a 10% reduction is allowed. Acceptance of manuscripts for publication is, however, based on merit and is in no way dependent on such payment, which may be waived in individual cases upon request.

### PUBLICATION CHARGE

Organization and clarity are essential elements of successful written communication. Identify the subject matter in the title, using words useful in indexing. State the purpose of

the work early in the text. Avoid introductory and explanatory material that is overly familiar to those in the field. Present the work and the arguments in an order that leads naturally to clearly specified conclusions. Provide enough information for the work to be reproduced and the logic behind it to be understood. Identify and justify any assumptions that are made; avoid tacit assumptions. Omit details that are generally known or that can be covered by reference to other publications. Give the magnitude and define the significance of experimental errors. Use headings and subheadings as appropriate. Avoid proprietary and trade names, but capitalize them where their use is necessary. Define unusual technical terms and abbreviations. Where symbols are used extensively, list them with their definitions at the end of the paper. Avoid repetition in the text and duplication of material in figures and tables. Be brief but clear.

Edit and proofread the manuscript carefully; these are not the responsibilities of the editors or reviewers.

To aid in indexing, authors must supply standard key-descriptors, preferably four of them, from a list with instructions published annually in the December issue of the Journal and available from the Editorial Office. These key-descriptors must appear at the bottom of the first page of the manuscript.

### KEY- DESCRIPTORS

Accelerated Brief Communications must be typewritten or printed on standard forms obtained, with detailed instructions for their use, from the Pennington Editorial Office.

### MANUSCRIPT PREPARATION

All other manuscripts must be typewritten or printed, double-spaced throughout, on one side only of white 21.6 x 27.0 cm paper, with 2.5-3.8 cm margins. Do not use single spacing anywhere, in title, abstract, text, references, tables, or figure captions.

For general matters of style and format, see papers in recent issues of the **Journal** and consult a style manual such as that of the American Chemical Society or that of the American Institute of Physics. These also provide lists of common abbreviations and units. The following specific items should be noted:

(a) **Système Internationale (SI)** units are to be used; a description may be found in NBS Special Publication 330 or ASTM Metric Practice Guide E-380-72.

(b) The signs of cell and electrode potentials are to follow the IUPAC conventions of 1953.

(c) **Mathematical equations** should be written on a single line, if possible, using parentheses, brackets, the solidus, negative exponents, etc.

(d) **References** are to be listed separately at the end of the paper in the order they are cited in the text, being sure that each listed reference is cited. Authors' initials must be given, and Chemical Abstracts abbreviations must be used. Citations of other than the generally available literature should be avoided if possible.

(e) **Tables** are to be presented on individual sheets, with both captions and body double-spaced.

(f) **Figure captions** and numbers are to be included on a separate sheet and must not appear in the body of any figure or illustration.

(g) **Drawings and graphs** will ordinarily be reduced to column width (8.3 cm) and after such reduction should have lettering at least 0.15 cm high. Lettering must be of letter-guide quality. Originals in India ink on tracing cloth or paper are preferred, but India ink on coordinate paper with blue ruling is acceptable. When several curves are shown, each may be lettered and identified in the caption. The Editorial Office will not make corrections or additions to figures.

(h) **Photographs** should be used sparingly. The originals supplied must be glossy prints and should be protected against bending. Micrographs must have a labeled unit length within the body of the picture; reduction for printing makes magnifications meaningless.

Printed in the United States of America

# APPLICATION FOR ADMISSION

TO

**The Electrochemical Society, Inc.**

Return completed application to:

**Secretary**

**The Electrochemical Society, Inc.**

**10 South Main Street, Pennington, New Jersey 08534-2896  
609-737-1902**

To the Board of Directors of The Electrochemical Society, Inc:

**For office use only**

Date Rec'd. \_\_\_\_\_ \$ \_\_\_\_\_

Notice of Ackn. \_\_\_\_\_

Checked: \_\_\_\_\_

Approved: \_\_\_\_\_

Please print complete name and address as it should appear on mailings.

Name: \_\_\_\_\_

Address: \_\_\_\_\_

\_\_\_\_\_

\_\_\_\_\_

\_\_\_\_\_

\_\_\_\_\_

Business Telephone: (include area code) \_\_\_\_\_

I hereby make application for admission to The Electrochemical Society, Inc., as a \_\_\_\_\_ member, and enclose the amount of \$ \_\_\_\_\_ covering the first year's dues. (Please see reverse side for proper class of membership and dues applying thereto, noting the options with regard to the date of election and active life membership and the credit available for nonmember meeting registration.)

1. Date of Birth: \_\_\_\_\_ (month) \_\_\_\_\_ (day) \_\_\_\_\_ (year)

2. Please check LOCAL SECTION with which you wish to affiliate:

- |   |   |  |   |   |
|---|---|--|---|---|
| <input type="checkbox"/> Boston (05)    | <input type="checkbox"/> European (27)          | <input type="checkbox"/> Natl. Capital Area (45) | <input type="checkbox"/> Pacific Northwest (65) | <input type="checkbox"/> San Francisco (85)     |
| <input type="checkbox"/> Chicago (10)   | <input type="checkbox"/> Indianapolis (30)      | <input type="checkbox"/> North Texas (55)        | <input type="checkbox"/> Philadelphia (70)      | <input type="checkbox"/> So. Calif.-Nevada (90) |
| <input type="checkbox"/> Cleveland (15) | <input type="checkbox"/> Metropolitan N.Y. (35) | <input type="checkbox"/> Ontario-Quebec (60)     | <input type="checkbox"/> Pittsburgh (75)        | <input type="checkbox"/> Twin Cities (96)       |
| <input type="checkbox"/> Columbus (20)  | <input type="checkbox"/> Midland (Mich.) (40)   | <input type="checkbox"/> Oregon (62)             | <input type="checkbox"/> Rocky Mountain (80)    | <input type="checkbox"/> None (99)              |
| <input type="checkbox"/> Detroit (25)   |   |  |   |   |

3. Please indicate your DIVISIONAL and GROUP interests, noting your primary interest(s) with the number 1 and secondary interest(s) with the number 2.

- |  |  |  |
|--|--|--|
| <input type="checkbox"/> Battery (AO)                    | <input type="checkbox"/> Electronics (EO)                    | <input type="checkbox"/> Industrial Electrolytic (IO)            |
| <input type="checkbox"/> Corrosion (BO)                  | <input type="checkbox"/> New Electronic Technologies (E1)    | <input type="checkbox"/> Luminescence and Display Materials (KO) |
| <input type="checkbox"/> Dielectrics and Insulation (CO) | <input type="checkbox"/> Semiconductors (E3)                 | <input type="checkbox"/> Organic and Biological                  |
| <input type="checkbox"/> Electrodeposition (DO)          | <input type="checkbox"/> Electrothermics and Metallurgy (HO) | <input type="checkbox"/> Electrochemistry (FO)                   |
|  | <input type="checkbox"/> Energy Technology (GO)              | <input type="checkbox"/> Physical Electrochemistry (JO)          |

4. Education:

Institution	Dates Attended	Major Subject	Degree Earned
-------------	----------------	---------------	---------------

_____	_____	_____	_____
_____	_____	_____	_____
_____	_____	_____	_____

5. Work Experience:

Name of Employer (current, followed by previous)	Dates	Position
--	-------	----------

_____	_____	_____
_____	_____	_____
_____	_____	_____

6. The Society's Constitution provides that two Active Members of the Society (who can substantiate the above record) must recommend you for admission to membership. It will facilitate the handling of your application if you are able to have your references sign this application form; if this is not convenient, please list their names and addresses. On a student application, only a single faculty member recommendation with signature (including title and institution) is required.

Name (please print)	Signature	Address
---------------------	-----------	---------

Name (please print)	Signature	Address
---------------------	-----------	---------

The undersigned certifies that the above statements are correct and agrees, if elected to the Society, to be governed by its Constitution and Bylaws and to promote the objects of the Society as stated in its Constitution.

Date \_\_\_\_\_ 19 \_\_\_\_\_ (Signature) \_\_\_\_\_

# EXTRACTS FROM THE CONSTITUTION AND BYLAWS

## CONSTITUTION—Article II

### Membership

Section 1. The individual membership shall consist of Active, Honorary and Emeritus Members. The Board of Directors may from time to time authorize other classifications of membership as defined in the Bylaws of the Society.

(Active Member—Annual Dues \$50.00)

Active Member  
Section 2. An Active Member shall be interested in electrochemistry or allied subjects and possess a Bachelor's degree, or its equivalent, in engineering or natural science. In lieu of a Bachelor's degree, or its equivalent, any combination of years of undergraduate study and years of relevant work experience in electrochemistry or allied subjects adding to at least seven years shall be required. Election to Active Membership shall require the recommendation of two Active Members in good standing.

## BYLAWS—Article II

### Non-Voting Membership

(Student Member—Annual Dues \$10.00)

Student Member  
Section 1. Student Member. A Student Member shall be a full-time undergraduate or graduate student registered for a degree in natural science or engineering. The applicant for Student Membership shall be recommended by a member of the faculty of the school. Upon graduation with a Bachelor's degree or equivalent in natural science or engineering, the Student Member may apply for Active Membership. The application shall be approved by two Active Members of the Society in good standing. If the Student Member enters graduate school as a full-time student, the person may choose to apply for Active Membership or remain a Student Member.

## BYLAWS—Article XXI

### Dues and Fees

Dues  
Section 1. The annual dues for Active Members shall be fifty dollars. The annual dues for Student Members shall be ten dollars. Each member shall receive the JOURNAL OF THE ELECTROCHEMICAL SOCIETY.

Date of Election  
Section 2. When individuals are elected to membership, they must elect to initiate their membership as of January 1 or July 1 of the year of election; or, if elected during the last quarter, January 1 of the year following election. In the case of a July 1 election for starting membership, dues will be prorated.

Active Life Membership  
Section 3. Any Active Member who shall pay in one lump sum the amount equivalent to two-thirds of the remaining dues to age sixty-five at the time of payment, but not less than an amount of 5 years of full dues, shall be exempt from payment of any further dues and shall be considered an Active Member during the remainder of his or her life.

## BOARD OF DIRECTORS ACTION OF OCTOBER 9, 1960

Nonmember Meeting Registration Credit  
If application for new membership is received within four months of the payment of nonmember registration at a Society Meeting by the applicant, the difference between the nonmember and member registration fees shall be credited toward the first year's dues.

## CONSTITUTION—Article III

### Admission and Dismissal of Members

Section 1. Application for individual membership shall be in writing on a form adopted by the Board of Directors.

Section 2. The Admissions Committee shall be a rotating committee consisting of three members. One member shall be appointed each year by the President with the approval of the Board of Directors for a term of three years to replace the outgoing member. This Committee shall receive from the Secretary all properly executed and properly recommended applications for admission which he has received from persons desirous of becoming members of the Society. It shall be the duty of this Committee, after examining the credentials of applicants, to make appropriate recommendation to the Board as to approval or rejection of the applications. Unanimous approval of an applicant by this Committee shall be required before the candidate's name may be submitted to the Board of Directors for election. The election to membership shall be by a mail vote of the Board of Directors. The candidate shall be considered elected two weeks after the date the proposed membership list is mailed to the Board if no negative votes have been received by the Secretary. If a candidate receives one negative vote, his application shall then be considered and voted upon at the next meeting of the Board of Directors. Two negative votes cast at this meeting shall exclude a candidate. The Board of Directors may refuse to elect a candidate who, in its opinion, is not qualified for membership. The names of those elected shall be announced to the Society. Duly elected candidates shall have all the rights and privileges of membership as soon as their entrance fee, if any, and dues for the current year have been paid.

Section 3. A member desiring to resign shall send a written resignation to the Office of the Society.

Section 4. Upon the written request of ten or more Active Members that, for cause stated therein, a member be dismissed, the Board of Directors shall consider the matter and, if there appears to be sufficient reason, shall advise the accused of the charges against him. He shall then have the right to present a written defense, and to appear in person before a meeting of the Board of Directors, of which meeting he shall receive notice at least twenty days in advance. Not less than two months after such meeting the Board of Directors shall finally consider the case and, if in the opinion of the majority of the Board of Directors a satisfactory defense has not been made and the accused member has not in the meantime tendered his resignation he shall be dismissed from the Society.

Section 7. The entrance fee, if any, annual dues and any other payments to be made by the members of the Society shall be paid in accordance with regulations set forth in the Bylaws.

Section 8. Any member delinquent in dues after April 1 shall not receive the Society's publications and will not be allowed to vote in any Society election until such dues are paid. All members in arrears for one year after April 1 shall lose their membership status and can be reinstated only by action of the Board of Directors.

# **Call for Papers**

## **161st Meeting, Montreal Canada, May 9-14, 1982**

Divisions which have scheduled sessions are listed on the overleaf, along with the symposium topics.

### **1. Symposium Papers.**

Authors desiring to contribute papers to a symposium listed on the overleaf should check first with the symposium chairman to ascertain appropriateness of the topic.

### **2. General Session Papers.**

Each of the Society Divisions or Group which will meet in Montreal, Canada, can plan a general session. If your paper does not fit readily into a planned symposium, you should specify "General Session."

### **3. To Submit a Meeting Paper.**

Each author who submits a paper for presentation at a Society Meeting must do three things:

A—Submit one original 75-word abstract of the paper on the attached form or a facsimile thereof. **Deadline for receipt of 75-word abstract is December 1, 1981.**

B—Submit original and one copy of an Extended Abstract of the paper. **Deadline for receipt of Extended Abstract is January 1, 1982.** See (6) below for details.

C—Determine whether the meeting paper is to be submitted to the Society Journal for publication. See (7) below for details.

**Send all material to The Electrochemical Society, Inc., 10 South Main Street, Pennington, NJ 08534.**

Unless the 75-word and required Extended Abstracts are received at Society Headquarters by stated deadlines, the papers will not be considered for inclusion in the program.

### **4. To Submit a Recent News Paper.**

Recent News Papers and Extended Recent News Papers are invited for this meeting. Each author must submit one of the following items to the Session Chairman:

A—Triplicate copies of a 75-word abstract of a Recent News Paper, for a 10-minute presentation. **Deadline for receipt is March 24, 1982.**

B—Triplicate copies of a 75-word abstract and, also, a 200-300 word abstract of an Extended Recent News Paper, for a 20-minute presentation. **Deadline for receipt is March 14, 1982.**

Send all material to the appropriate Session Chairman listed, for Recent News Papers only.

### **5. Meeting Paper Acceptance.**

Notification of acceptance for meeting presentation, along with scheduled time, will be mailed to authors with general instructions no earlier than two months before the meeting. Those authors who require more prompt notification are requested to submit with their abstracts a self-addressed postal card with full author-title listing on the reverse.

### **6. Extended Abstract Volume Publication.**

All scheduled papers will be published in the EXTENDED ABSTRACTS volume of the meeting. The volume is published by photo-offset directly from typewritten copy submitted by the author. Please note that the EXTENDED ABSTRACTS will be in a new double column format. Please follow the NEW instructions listed below.

A—Abstracts are to be from 500 to 1000 words in length. The abstract should contain to whatever extent practical all significant data to be presented during oral delivery.

B—Abstracts are to be typed single spaced on the special double column typing forms which are sent to each author after the submission of a short abstract. The entire abstract, including tables and figures, must not exceed four (4) columns in length. The maximum size of four columns has been established as formal operating policy to maintain reasonable publication costs, and papers exceeding this limit may be returned or rejected.

C—Title of paper is to be in capital letters centered. Author(s) name, affiliation, and address is typed immediately below in capital and lower case letters centered.

D—All tables and figures must be securely mounted on the special typing guides within the margins; rubber cement is recommended for this purpose. What is submitted will be reproduced photographically exactly as it is sent. However, it will be reduced so that graphs and tables will be half their original size. Keep the lettering large enough to be legible when later reduced to half size. Place references and figures after the text.

E—Mail original and one copy of the abstract to: The Electrochemical Society, Inc., 10 South Main St., Pennington, NJ 08534.

### **7. Manuscript Publication in Society Journal.**

All meeting papers upon presentation become the property of The Electrochemical Society, Inc. However, presentation incurs no obligation to publish. If publication in *Journal* is desired, papers should be submitted as promptly as possible in full manuscript form in order to be considered. If publication elsewhere after presentation is desired, written permission from Society Headquarters is required.



# Montreal, Canada, Meeting Symposia Plans—Spring 1982

## May 9-14, 1982

- a.) For receipt no later than December 1, 1981, submit a 75-word abstract of the paper to be delivered on the attached overleaf.  
 b.) For receipt no later than January 1, 1982, submit two copies of an extended abstract, 500-1000 words.  
 c.) Send all abstracts to The Electrochemical Society, Inc., 10 South Main Street, Pennington, NJ 08534, with the exception of Recent News Papers. For Recent News Papers see preceding page.

### CORROSION

#### General Session

Papers on all aspects of low and high temperature corrosion and associated phenomena will be considered. Experimental techniques for the study of corrosion processes and corrosion products are also of interest. Suggestions and inquiries should be sent to the Session Chairman: R. P. Frankenthal, Bell Laboratories, Room 1D-352, Murray Hill, NJ 07974.

#### CORROSION/ENERGY TECHNOLOGY/ DIELECTRICS AND INSULATION/ ELECTROTHERMICS AND METALLURGY

##### Corrosion Problems in Nuclear and Fusion Technologies

This symposium will discuss material degradation problems related to nuclear and fusion technologies. In the nuclear fusion area papers related to corrosion problems in LWR, LFMBR, and HTGR reactors are solicited. Corrosion in aqueous and molten sodium heat transfer fluids will be discussed. Other suitable topics are fusion product interactions with fuel cladding, decarburization of steel in molten sodium, and nuclear safety related corrosion problems. In the fusion area papers related to corrosion problems in the reactor first wall and blankets are solicited. Suitable topics would be hydrogen embrittlement of the first wall, liquid lithium, and molten salt corrosion in blanket systems.

Suggestions and inquiries should be sent to the Symposium Co-Chairmen: J. H. De Van, Oak Ridge National Laboratory, Post Office Box X, Oak Ridge, TN 37830; or J. McGreer, Brookhaven National Laboratory, Dept. of Energy and Environment, Bldg. 801, Upton, NY 11973.

#### DIELECTRICS AND INSULATION/ CORROSION/ELECTRONICS/ ELECTROTHERMICS AND METALLURGY/ ENERGY TECHNOLOGY

##### Materials and New Processing Technologies for Photovoltaics

This symposium will deal with novel aspects of materials processing and characterization of photovoltaic devices. Papers are especially solicited on low cost silicon for photovoltaics, low cost recrystallization processes, techniques for increasing cell efficiency, novel thin film cell materials and processes, and new packaging concepts. Papers on concentrator and on flat panel systems, and on low cost assembly and automation will be welcome.

A proceedings volume for this symposium is being considered. Papers for this volume must be provided in camera-ready copy form at the time of presentation.

Suggestions and inquiries should be sent to the Symposium Co-Chairmen: J. Dismukes, Exxon Research and Engineering Co., Post Office Box 8, Linden, NJ 07036; P. Rai-Choudhury, Westinghouse Electric Co., Research Laboratories, Pittsburgh, PA 15235; or E. Sirt, Heliotronic GmbH, Postfach 1129, D-8263, Burghausen, Germany.

#### DIELECTRICS AND INSULATION/ ELECTRONICS/AMERICAN CERAMICS SOCIETY

##### Applications of Glasses and Ceramics in Device Technology

Papers are solicited from all areas relative to the preparation, properties, and use of glasses and ceramics in device technology and packaging. Emphasis is placed on the relationship of chemical and physical prop-

erties with the intended application. This includes composition, formulation, and technique of application. Of particular interest are fritted glass and ceramic compositions used, for example, in passivation and isolation, spin-on glasses and ceramics used in diffusion, passivation, or active circuit components and conventionally formulated solder glasses or ceramics now extensively employed in the electronics industry as sealing, dielectric, capacitor, and substrate materials. Also of interest are CVD and evaporative glasses and ceramics other than silicon dioxide used in the industry.

Suggested topics include passivation and planarization techniques using glasses and ceramics in VLSI technology; composition, properties, and use of glasses in fiber optics; protection of memory devices in a hostile environment with chemically durable glasses and ceramics; characterization of evaporated glass and ceramic materials suitable for construction of capacitors for high-speed semiconductor devices; sintering packages composed of ceramic or glass to protect highly conductive and corrosive metallurgies; fabrication of thick and thin films of metallized ceramics; and methods of producing bubble-free films of reflowed glasses. Other topics include: The effect of compositions on physical properties such as sealing temperature, coefficient of expansion, hardness, ductility, and chemical stability in wafer processing and device packaging. Also included are electronic properties such as dielectric breakdown, polarization phenomena, charge character under bias, conductivity, and surface leakage.

Suggestions and inquiries should be sent to the Symposium Co-Chairmen: J. L. Powell, IBM Corp., GTE, Dept. 249, Bldg. 300-40E, East Fishkill Industrial Junction, NY 12533; R. C. Buchanan, University of Illinois, 204 Ceramics Bldg., Urbana, IL 61801; or D. L. Flowers, Motorola Inc., Bldg. 356, 5005 East McDowell Rd., Phoenix, AZ 85008.

#### DIELECTRICS AND INSULATION/ ELECTRONICS/NEW TECHNOLOGY SUBCOMMITTEE

##### Inorganic Resist Systems

Recent advances involving inorganic resist systems have opened the way to the use of these materials for patterning micron and submicron geometries using photolithography, as well as electron beam and ion beam lithographies. This symposium will address the chemistry, physics, and materials science of these resists. Topics of specific interest will include the chalcogenide glass/silver compound systems, the structure, physics, and chemistry of the chalcogenide glass and silver compounds that form the resists; the wet and dry processing of the inorganic resists; and the fundamental physical and chemical processes taking place during exposure and subsequent processing.

Suggestions and inquiries should be sent to the Symposium Co-Chairmen: A. Heller, Bell Laboratories, Rm. 6D-321, Murray Hill, NJ 07974; or D. A. Doane, Bell Laboratories, Rm. 7B-530, Murray Hill, NJ 07974.

#### ELECTRONICS Semiconductors

##### Micromachining and Micromechanics

New ideas, developments, and technologies for micromechanical structures are to be explored in this symposium, with the purpose of gaining a greater understanding of the mechanics of semiconductor materials and structures as well as the advanced processing techniques which are required to fully realize the potential of micromechanical structures. Specific topics of interest for this symposium include: Fundamental aspects and practical applications of wet and dry isotropic and anisotropic etching; fabrication methods and applications of thin semiconductor, insulating or metallic membranes,

cantilever beams, and other structures; epitaxial growth of semiconductors to form islands or to refill etched grooves; thermal, electrical, or photoinduced migration of "wires" in semiconductors; composite mechanical structures involving semiconductor/semiconductor or semiconductor/glass bonding; mechanical applications of semiconductors including ink-jet components, print heads, optical-bench assemblies and laser structures, gas analysis devices and fluid-flow structures; pressure, strain, and acceleration transducers; novel three-dimensional electronic device structures; as well as other processes, structures, and devices related to semiconductor micromachining and micromechanics.

Suggestions and inquiries should be sent to the Symposium Chairman: K. Petersen, IBM Corp., K43/281, 5600 Cottle Rd., San Jose, CA 95193.

#### Molecular Beam Epitaxy

Papers dealing with all aspects of MBE semiconductor film deposition are solicited for this symposium. Areas that further the science, technology, or understanding of the following will be emphasized: 1. Dopant sources and incorporation; 2. ternary and quaternary heterojunctions and alloy growth; 3. quantum well and modulation-doped devices; 4. long wavelength source and detector materials/devices; 5. metal/semiconductor and semiconductor/insulator structures; and 6. novel techniques, new materials, and device results.

Publication of a proceedings volume is being considered. Late news papers are encouraged, as well as those to be presented by student authors.

Suggestions and inquiries should be sent to the Symposium Chairman: C. E. C. Wood, Dept. of Electrical Engineering, Cornell University, Phillips Hall, Ithaca, NY 14853.

#### Luminescence

##### Luminescence in Amorphous Materials

This symposium is to provide a forum for those interested in luminescence as it manifests inhomogeneities in the environment of the emitting center. Papers are invited on glasses, liquids, polymers, liquid crystals; topics are site-selection spectroscopy, inhomogeneous broadening, energy transfer among nonequivalent sites, correlation of luminescence with composition or with structure, etc.

Suggestions and inquiries should be sent to the Symposium Co-Chairmen: L. A. Riseberg or C. W. Struck, GTE Laboratories, 40 Sylvan Rd., Waltham, MA 02254.

#### Phosphor Depreciation

This symposium will emphasize the measurement and characterization of the explanation for, and the means of dealing with phosphor depreciation and luminescent material degradation; this will include all types of phosphor materials in all applications. Of particular interest will be papers concerning the fundamental understanding of and explanation for phosphor depreciation. Experimental and theoretical papers are solicited covering the following suggested topics: 1. Identification, measurement, and characterization techniques; 2. photochemical phenomenon; 3. color center formation and related effects; 4. electron burn; 5. mercury interaction; 6. ion bombardment; 7. study of material surface, e.g., SEM, ESCA (XPS), SIMS, AES, etc.; and 8. theoretical depreciation models.

Suggestions and inquiries should be sent to the Symposium Chairman: C. F. Chenot, GTE Products Corp., Chemicals/Metals Div., Hawes St., Towanda, PA 18848.

#### Phosphor Screening

This symposium will emphasize properties of phosphors which relate to the performance or fabrication of phosphor-containing products, such as fluorescent lamps, CRT's, and



flat panels. Examples of subjects for papers include: 1. Optical properties of phosphors as they relate to product performance; 2. phosphor efficiencies as a function of excitation density; 3. surface properties of phosphor to optimize screen application; and 4. phosphor degradation during excitation.

Suggestions and inquiries should be sent to the Symposium Chairman: H. Forest, Zenith Radio Corp., Rauland Tube Div., 2407 West North Ave., Melrose Park, IL 60160.

### General Session

Papers concerning any aspect of luminescence or display materials are invited. Groups of papers will be organized wherever possible in such topics as:

Luminescence: General synthesis and properties of: lamp, cathode-ray tube, and x-ray phosphors; organic and organo-metallic phosphors; electroluminescence; thermoluminescence; and chemiluminescence; ultraviolet phosphors and lamps; special properties and uses of luminescent materials; and luminescence theory.

Displays: General preparation and properties of display materials and devices, including light emitting diodes; thin films, electroluminescent devices; chromics; liquid crystal devices; plasma display; injection lasers; and fiber optics.

Twenty-five minutes will be allotted for each paper, including discussions. Review or survey papers requiring a longer time will also be considered.

Suggestions and inquiries should be sent to the Session Chairman: G. R. Gillooly, General Electric Co., 1099 Ivanhoe Rd., Cleveland, OH 44110.

## ELECTRONICS/DIELECTRICS AND INSULATION

### Growth of Single Crystals on Amorphous Substrates

The intention of this symposium is to provide a forum for the presentation and discussion on a wide range of topics concerned with the growth of single crystals on foreign amorphous substrate. Papers from the following general areas are solicited: Beam-induced recrystallization of deposited films; lateral CVD epitaxial overgrowth; graphoeptitax; solid phase zone growth; and growth from liquid, vapor, and MBE techniques.

Although most recent research is concentrated on growth of silicon on amorphous insulator and on growth of GaAs on amorphous insulator, papers on the growth of other materials are welcomed. Of particular interest are experimental works on crystal growth, research on growth and nucleation theory, the characterization of the microstructure of the crystalline material and the interface between the crystalline and amorphous materials, and work on device application such as SOI, solar cells, and electro-optical devices.

Suggestions and inquiries should be sent to the Symposium Co-Chairmen: H. W. Lam, Texas Instruments Inc., Post Office Box 26221, MS 944, Dallas, TX 75265; or J. Monkowski, Dept. of Electrical Engineering, Pennsylvania State University, University Park, PA 16802.

### Tutorial on Semiconductor Technology

This symposium is a new venture and will be held to review some major aspects of semiconductor technology. Topics to be addressed by invited speakers include chemical and dry etching, lithography and resist technology, film deposition techniques, ion implantation and diffusion, and oxidation and compound semiconductors. Emphasis will be placed on basic principles as well as on the latest developments in processes and technologies. The symposium will be oriented toward those who are new to the current technologies in semiconductor device fabrication.

Some selected contributed papers may be included. A proceedings volume is being considered and will, hopefully, be available at the time the symposium is held. Manuscripts for both invited and contributed papers will be due October 1, 1981.

Suggestions and inquiries should be sent to the Symposium Co-Chairmen: D. A. Doane, Bell Laboratories, Murray Hill, NJ 07974; B. Fraser, Bell Laboratories, Murray Hill, NJ 07974; or D. W. Hess, Dept. of Chemical Engineering, University of California, Berkeley, CA 94720.

### Joint General Session

Papers which deal with all aspects of materials of interest for electronic devices in-

cluding their preparation, characterization, interactions, and device applications and whose subject matter is not covered by the special symposia are invited to be submitted to this session. Also invited are papers on the basic chemistry and physics of materials processing, computer control of materials processing, and computer modeling of the formation and of the characterization of materials and devices. Of particular interest are new materials and processes.

Suggestions and inquiries should be sent to the Session Co-Chairmen: E. H. Nicollian, Bell Laboratories, Murray Hill, NJ 07974; F. N. Schmittmann, Hewlett Packard Laboratories, 3500 Deer Creek Rd., Palo Alto, CA 94304; or G. Schwartz, IBM Corp., Dept. 206, Bldg. 300-48A, Hopewell Junction, NY 12533.

### Joint Recent News Papers Session

Recent News Papers and Extended Recent News Papers consisting of topics covered by the symposia and sessions being sponsored or co-sponsored by the Electronics and Dielectrics and Insulation Division are invited for presentation.

Suggestions and inquiries should be sent to the Session Chairman: W. A. Pliskin, IBM Corp., Dept. 108, Internal Zip 48A, Hopewell Junction, NY 12533. A special call for Recent News Papers will appear in the January, February, and March 1982 issues of the JOURNAL.

## ELECTROTHERMICS AND METALLURGY

### Electrochemistry of Pyrometallurgical Processes

Papers are solicited on the fundamentals or applied aspects of electrowinning and electrorefining of metals in molten salt electrolysis.

Suggestions and inquiries should be sent to the Symposium Chairman: D. Piron, Dept. de Genie Metallurgique, Universite de Montreal, Ecole Polytechnique, Montreal, Quebec, Canada H3C 3A7.

### Transport Phenomena in Metals

The main theme of this symposium will be concerned with diffusional transport in metals and alloys and will emphasize both experimental and theoretical (including analytical modeling) approaches to the subject. Diffusional phenomena associated with transport along defects (e.g., grain boundaries) will be considered along with lattice diffusion. It is recognized that insight into metal and alloy diffusion may be obtained from studies of intermetallic phases and compounds of metals and nonmetals; a limited number of such papers pertinent to the theme of the symposium will be included in the program.

Suggestions and inquiries should be sent to the Symposium Co-Chairmen: R. W. Heckel, Dept. of Metallurgical Engineering, Michigan Technological University, Houghton, MI 49931; or R. A. Rapp, Dept. of Metallurgical Engineering, Ohio State University, 116 West 19th Ave., Columbus, OH 43210.

## ELECTROTHERMICS AND METALLURGY/CORROSION

### Electrochemical Techniques for High Temperature Corrosion Studies

This symposium will focus on electrochemical techniques for the study of high temperature corrosion processes involving molten salt electrolytes. Both theoretical and experimental papers are solicited. Suitable topics will include: 1. The use of emf cells to measure fundamental data relevant to corrosion processes; 2. New or novel high temperature reference electrodes; 3. use of emf cells to measure or control (by coulometric titration) high temperature corrosive environments; 4. use of polarization or transient electrochemical techniques to study corrosion reactions or to measure corrosion rates; 5. use of a.c. impedance techniques to investigate electrode reactions; 6. molten salt galvanic corrosion; and 7. use of electrochemical techniques to infer corrosion mechanisms.

Suggestions and inquiries should be sent to the Symposium Co-Chairmen: D. A. Shores, General Electric Co., Research and Development Center, Bldg. K-1, Rm. 3A46, Post Office Box 8, Schenectady, NY 12301; or R. A. Rapp, Dept. of Metallurgical Engineering, Ohio State University, 116 West 19th Ave., Columbus, OH 43210.

## ELECTROTHERMICS AND METALLURGY/DIELECTRICS AND INSULATION/ELECTRONICS

### Tenth International Conference on Electron and Ion Beam Science and Technology

Papers on the following subjects are solicited: 1. Electron beam technology—papers covering fundamentals of equipment ranging from electron sources through electron beam microfabrication systems; 2. ion beam technology—papers covering the spectrum from ion sources through ion beam microfabrication systems and ion implantation systems; 3. interaction mechanisms—papers on all aspects of beam-materials interaction including physics of the processes, material-range kinetics, radiation effects, radiation damage, annealing, and proximity effects; 4. advance devices—papers on devices that are products of modern microfabrication techniques, with emphasis on high resolution structures and outstanding performance; 5. microphotographic processes—papers dealing with electron and x-ray resists and all aspects of exposure-processing and pattern-forming techniques; 6. etching technology—papers related to microdevices, specifically on ion and plasma techniques; 7. electron beam recording—papers dealing with techniques for recording and information storage, and systems for this task; 8. device-failure diagnostics and instrumentation for the purpose—papers on the broadening of sub-miniature device technology which is placing new demands upon those concerned with production and application of these devices, as well as papers dealing with all aspects of device diagnostics and failure analysis; and 9. high energy beams and applications—papers on all aspects and processes related to evaporation, materials purification, welding, and melting.

Suggestions and inquiries should be sent to the Conference Chairman: R. Bakish, Bakish Materials Corp., Post Office Box 148, Englewood, NJ 07631.

## ENERGY TECHNOLOGY

### Ion Insertion Phenomena

The aim of the symposium is to bring together researchers in all fields in which ion insertion phenomena are relevant. Examples include experimental and theoretical studies of ion insertion in energy storage (e.g., lithium batteries, electrodes, hydrides) and electrochromic materials; areas of electrocatalysis and photoelectrochemistry in which ion insertion is believed to play a role. Topics include: ionic (cationic and anionic) and atomic diffusion, electron transport, thermodynamics, electronic states, optical properties, ion ordering, insertion overpotential, reversibility, and aging. Studies of the influence on these processes of materials properties (structure, stoichiometry, composition, etc.) as determined by methods of fabrication are welcomed.

Suggestions and inquiries should be sent to the Symposium Co-Chairmen: G. Beni, Bell Laboratories, Crawford Corner Rd., Holmdel, NJ 07733; or W. C. Dautremont-Smith, Bell Laboratories, Murray Hill, NJ 07974.

### Photobiological Energy Conversion and Storage Processes

This symposium will cover the following topics: 1. The primary photoacts and the secondary redox reactions of photosynthesis (including biological photovoltaics and electrochemical phenomena); 2. developmental and genetic aspects of photosynthetic apparatus; and 3. fuels and energy-intensive chemicals from photosynthesis in vivo and in vitro. Papers on both theoretical and practical aspects of these topics are solicited.

Suggestions and inquiries should be sent to the Symposium Co-Chairmen: S. Lien, Solar Energy Research Institute, 1617 Cole Blvd., Golden, CO 80401; J. Arntzen, Michigan State University, MSU-DOE Plant Research Laboratory, East Lansing, MI 48824; or P. A. Loach, Dept. of Biochemistry and Molecular Biology, Northwestern University, Evanston, IL 60201.

### General Session

Papers are solicited in areas of energy technology not covered by current symposia. Of particular interest are electrochemical aspects of energy conversion, distribution, and storage.

Suggestions and inquiries should be sent to the Session Co-Chairmen: H. J. Hovel, IBM Corp., Thomas J. Watson Research Center, P.O. Box 218, Yorktown Heights, NY 10593; or A. J. Nozik, Solar Energy Research Institute, 1617 Cole Blvd., Boulder, CO 80401.

## ENERGY TECHNOLOGY/BATTERY

### Energy Systems for Developing Countries

This symposium covers energy systems applicable to developing countries, emphasizing electrochemical storage and generation coupled to new and renewable energy technologies. Energy sources such as solar (electric and thermal), geothermal, wind, hydro, power (including small hydro), biomass, oil shale, and tar sands, ocean energy, peat, are considered in this symposium.

The symposium will consist of a few invited papers in key areas and contributed papers.

Suggestions and inquiries should be sent to the Symposium Co-Chairmen: H. L. Chum, Solar Energy Research Institute, 1617 Cole Blvd., Golden, CO 80401; or E. G. Gagnon, General Motors Corp., Research Laboratories, Dept. 37, 12 Mile and Mound Roads, Warren, MI 48090.

## ENERGY TECHNOLOGY/BATTERY/ PHYSICAL ELECTROCHEMISTRY

### Platinum Electrocatalysts: Efficient Utilization and Alternatives

Platinum is used as a catalyst material in many electrochemical systems. Because of the cost and availability considerations, a more efficient utilization of platinum in these systems is important. The search for a total or partial substitute of platinum is an ongoing pursuit. This symposium provides a forum for discussion of these aspects.

Papers are solicited from all fields, including batteries, fuel cells, electrolysis cells, and electro-organic syntheses. Of interest are the papers on the following topics: 1. Theoretical and experimental studies to investigate and quantify inefficiencies leading to a poor platinum utilization, deactivation mechanisms, and others; 2. efficient Pt utilization via better catalyst preparation techniques, electrode structure design, catalyst stabilization, and catalyst support; and 3. platinum substitutes including alloys, non-noble metals, and amorphous materials.

Suggestions and inquiries should be sent to the Symposium Co-Chairmen: E. Yeager, Electrochemical Laboratory, Case Western Reserve University, University Circle, Cleveland, OH 44106; H. C. Maru, Energy Research Corp., 3 Great Pasture Rd., Danbury, CT 06810; or J. P. Hoare, 26065 Dover, Detroit, MI 48239.

### Molten Carbonate Fuel Cell Technology

Papers are solicited on all aspects of molten carbonate fuel cell chemistry and electrochemistry, materials, and systems technology. It is intended that this symposium should summarize the state-of-the-art and underline the growing interest in the molten carbonate fuel cell as potentially the highest efficiency and most cost effective topping cycle for electricity generation from coal in central station power plants, as well as in smaller dispersed cogeneration applications.

Appropriate subjects of papers include: 1. Electrochemistry and electrocatalysis of anode and cathode processes; 2. cation effects on reaction rates; 3. effect of impurity species on cell performance; 4. transport effects: melt physical chemistry including vapor pressure; 5. porous electrode structures; 6. optimized operational parameters for cells; 7. cell and stack design—component design requirements—cost-effective approaches to cell modeling and cell construction; 8. alternative materials for cell components; 9. systems and systems analysis for cogeneration applications; and 10. systems and systems analysis of power plant designs.

Suggestions and inquiries should be sent to the Symposium Co-Chairmen: J. R. Selman, Dept. of Chemical Engineering, Illinois Institute of Technology, IIT Center, Chicago, IL 60616; or T. D. Claar, Institute of Gas Technology, 3424 South State St., Chicago, IL 60616.

## INDUSTRIAL ELECTROLYTIC

### Electrochemical Process and Plant Design

The symposium will focus on design methodology used in electrochemical processes and plants. Papers are solicited both on electrochemical engineering aspects of applied problems as well as on underlying principles upon which design techniques are based. Papers are solicited in such areas as: 1. Experience in scale-up at the beaker, bench, pilot, and full-scale; 2. evaluation of candidate processes and alternatives; 3. economic evaluation; 4. identification of critical design variables; 5. cell and flow-sheet optimization; 6. instrumentation and process control; 7. computer-aided design techniques; 8. mathematical models of electrolyzers; and 9. physical property data.

A proceedings volume is planned and papers are to be submitted by April 1, 1982. Suggestions and inquiries should be sent to the Symposium Co-Chairmen: R. C. Alkire, University of Illinois, 1209 West California St., Urbana, IL 61801; R. Varian, Dow Chemical Co., Central Research, Midland, MI 48649; or T. Beck, Electrochemical Technology Corp., 3936 Leary Way NW, Seattle, WA 98107.

## INDUSTRIAL ELECTROLYTIC/BATTERY/ ENERGY TECHNOLOGY

### Transport Processes in Electrochemical Systems

This symposium is concerned with all fundamental and applied aspects of transport processes in electrochemical systems. Papers are solicited on the following topics: 1. transport in aqueous and nonaqueous electrolytes; 2. transport in porous electrodes; 3. transport in membranes and micro-porous separators; 4. transport in liquid membranes; 5. transport in molten salts; and 6. novel methods for characterizing transport properties.

Suggestions and inquiries should be sent to the Symposium Co-Chairmen: T. Katan, Lockheed Palo Alto Research Laboratory, Dept. 52-35, Bldg. 204, 3251 Hanover St., Palo Alto, CA 94304; R. S. Yeo, The Continental Group, Energy Systems Laboratory, 10432 North Tantau Ave., Cupertino, CA 95014; or D.-T. Chin, Dept. of Chemical Engineering, Clarkson College of Technology, Potsdam, NY 13676.

## INDUSTRIAL ELECTROLYTIC/ ENERGY TECHNOLOGY

### Hydrogen Production and Storage

This symposium will consider all aspects of hydrogen production and storage, with emphasis on electrochemical methods. The results of experimental, theoretical, and applications-oriented work will be included.

Papers are solicited on the following or related topics: 1. Electrolytic hydrogen production; 2. future prospects and economics of hydrogen production/use; 3. hydride and other storage methods; 4. hydrogen recovery in the electrochemical process industry; 5. new technologies for both production and storage; and 6. materials problems in hydrogen systems.

Suggestions and inquiries should be sent to the Symposium Chairman: D. E. Hall, INCO Research and Development Center, Inc., Sterling Forest, Suffern, NY 10901.

## ORGANIC AND BIOLOGICAL ELECTROCHEMISTRY

### Electrochemistry for the Study and Control of Cell and Tissue Growth and Repair

This multidisciplinary symposium covers topics dealing with ionic control of cell and tissue function. Specific areas with range from potential dependent membrane processes involved in the delivery and maintenance of intracellular ionic concentrations via impedance and flux studies and the use of electrochemically transduced weak periodic current for the study and manipulation of cell regulation. Discussion areas will include electrochemical factors which control cell proliferation and development with potential therapeutic applications.

Suggestions and inquiries should be sent to the Symposium Chairman: A. A. Pilla, Bioelectrochemistry Laboratories, Columbia University, 630 West 168th St., New York, NY 10032.

## Redox Mechanisms and Interfacial Properties of Molecules of Biological Importance

This symposium will present papers dealing with the applications of electrochemical and related methodologies to elucidate the redox mechanisms and interfacial properties of naturally occurring biomolecules and related model systems. In addition, papers will be presented and are solicited concerned with newly emerging techniques, such as chemically modified electrodes and multiple-technique approaches (e.g., spectro-electrochemistry) which have been or would be employed to help obtain mechanistic information concerning the redox and interfacial behaviors of biomolecules.

Both invited and contributed papers are planned.

Suggestions and inquiries should be sent to the Symposium Chairman: G. Dryhurst, Dept. of Chemistry, University of Oklahoma, Norman, OK 73019.

## General Session

Suggestions and inquiries should be sent to the Session Chairman: J. H. Wagenknecht, Monsanto Co., 800 North Lindbergh Blvd., St. Louis, MO 63166.

## ORGANIC AND BIOLOGICAL ELECTROCHEMISTRY/INDUSTRIAL ELECTROLYTIC

### Industrial Electro-Organic Chemistry

This symposium will focus on the application of electro-organic synthesis to the production of commercially desirable compounds. Papers are solicited describing such syntheses on a laboratory, pilot plant, or full commercial scale. Examples of "indirect" electro-organic syntheses, via electrochemically generated inorganic redox reagents, will be accepted. Descriptions of engineering studies, economic analyses, and comparisons with competing chemical processes are encouraged. Papers will not be limited to those which describe commercially successful syntheses.

Suggestions and inquiries should be sent to the Symposium Co-Chairmen: J. P. Coleman, Monsanto Co. Corporate Research Laboratories, 800 North Lindbergh Blvd., St. Louis, MO 63166; or C. Oloman, Dept. of Chemical Engineering, University of British Columbia, Vancouver, British Columbia, Canada V6T 1W5.

## ORGANIC AND BIOLOGICAL ELECTROCHEMISTRY/PHYSICAL ELECTROCHEMISTRY/DIELECTRICS AND INSULATION

### Polymer Film Electrodes

This symposium will be concerned with the recent progress in the applications and study of polymer film electrodes. Most welcome are experimental and theoretical papers that deal with the preparation and study of these films. Of particular interest are the areas which include: 1. Preparation of electroactive polymer films by, e.g., dip-coating, spin-coating, plasma, and electrochemical polymerization; 2. electron transfer and ion transport in the films; 3. electrochemical characteristics and electrode applications of the polymer films; 4. semiconductor surface corrosion inhibition; 5. electrocatalysis; 6. electrochemical selectivity; and 7. electrode characteristics of highly conducting polymers.

A symposium volume is being considered. Suggestions and inquiries should be sent to the Symposium Co-Chairmen: A. F. Diaz, IBM Corp., Research Laboratories, P32/281, 5600 Cottle Rd., San Jose, CA 95133; or L. R. Faulkner, Dept. of Chemistry, University of Illinois, 1209 West California St., Urbana, IL 61801.

## PHYSICAL ELECTROCHEMISTRY

### Double Layer Phenomena

This symposium will focus on the structure of charged interfaces. The theory of that part of the interface which is domi-

nated by the long-range ionic interactions is well developed. However, the theory of the contributions of the solvent molecules and of the role of short-range noncoulombic interactions is much less well developed. Papers dealing with theoretical and experimental aspects of the double layer will be welcome. The papers are to be presented so as to enhance a dialogue between experimentalists and theorists. Topics of particular interest for this symposium include: 1. To what extent can the solvent near the electrode be considered to be a monolayer; 2. is interfacial water different than bulk water; 3. spectroscopic studies of the interfacial region; 4. theory and simulation of charged interfaces. Both invited and contributed papers are planned.

Suggestions and inquiries should be sent to the Symposium Chairman: D. Henderson, IBM Corp., Research Laboratory, K33/281, 5700 Cottle Rd., San Jose, CA 95193.

### General Session

Papers concerning any aspect of physical electrochemistry not included in the topic areas of the symposia are welcome.

Suggestions and inquiries should be sent to the Session Chairman: E. J. Cairns, Lawrence Berkeley Laboratory, Energy and Environment Div., 90-3026, University of California, Berkeley, CA 94720.

### PHYSICAL ELECTROCHEMISTRY/ BATTERY/ENERGY TECHNOLOGY

#### Solid Electrolytes

Two primary topics will be addressed in this symposium: General solid electrolyte research and technology, and the more specific area of  $\beta/\beta'$ -alumina ceramic degradation

in battery applications. Appropriate topics for the general session include new solid electrolytes, fundamental properties of solid electrolytes, ionic and ionic/electron conductors, applications of solid electrolytes, and methods of fabrication of solid electrolytes. The session on degradation of  $\beta/\beta'$ -alumina will discuss materials degradation problems related to the electrolyte in sodium-sulfur batteries.

Suggestions and inquiries on the session on general solid electrolyte research and technology should be sent to G. C. Farrington, Dept. of Materials Science, University of Pennsylvania, 3231 Walnut St., Philadelphia, PA 19104; or J. B. Wagner, Jr., Center for Solid State Sciences, Arizona State University, Tempe, AZ 85281. Suggestions and inquiries on the session on degradation of  $\beta/\beta'$ -alumina should be sent to A. Virkar, Dept. of Materials Science, University of Utah, Salt Lake City, UT 84112.

- 
- a.) For receipt no later than December 1, 1981, submit a 75-word abstract of the paper to be delivered on the attached overleaf.  
b.) For receipt no later than January 1, 1982, submit two copies of an extended abstract, 500-1000 words.  
c.) Send all abstracts to The Electrochemical Society, Inc., 10 South Main Street, Pennington, NJ 08534, with the exception of Recent News Papers. For Recent News Papers see preceding pages.
- 

Use overleaf in submitting your abstract for  
The 1982 Spring Meeting  
of  
The Electrochemical Society, Inc.  
to be held at the  
Queen Elizabeth Hotel  
Montreal, Canada  
May 9-14, 1982

# 75-Word Abstract Form

(Deadline for receipt—December 1, 1981)

## MONTREAL, CANADA, MEETING—MAY 9-14, 1982

Submit to: The Electrochemical Society, Inc.  
10 South Main Street, Pennington, NJ 08534

Schedule for \_\_\_\_\_ of \_\_\_\_\_  
Symposium ECS Division

Abstract No. \_\_\_\_\_  
(do not write in this space)

(Title of paper) \_\_\_\_\_

(Authors) (Underline name of author presenting paper) \_\_\_\_\_

(Business Affiliation and Address) \_\_\_\_\_

(ZIP Code)

(Tel. No.)

(Type abstract in this area—double spaced.)

Do you require any audiovisual equipment?

☐ 35 mm (2 x 2 in.) slide projector

☐ Vu-Graph

☐ other (specify)

Is a full length paper on this work to be  
submitted for Society Journal publication?

☐ Yes

☐ No

Papers presented before a Society technical meeting become the property of the Society and may not be published elsewhere without written permission of the Society. Papers presented at Society technical meetings must be authored by a member or sponsored by an active member.

Insert name of Society member author or sponsor



# The Electrochemical Society, Inc.

10 SOUTH MAIN STREET  
PENNINGTON, NEW JERSEY 08534

Telephone: 609-737-1902

## SOME QUESTIONS AND ANSWERS ABOUT THE ELECTROCHEMICAL SOCIETY BUILDING FUND

*Q. Why did The Electrochemical Society buy a headquarters building?*

A. As the Society approached the end of the ten year lease it held on its headquarters space near Princeton, it undertook a careful evaluation of the possible alternatives for housing its operations and concluded that the purchase of an existing building would be the most economical and efficient way of meeting its needs. The cost of continuing to lease was expected to double before very long, and the investment required for new construction was considered to involve too great a commitment of Society resources. Fortunately, a building well suited to the Society's needs became available in the right time frame, and effective August 1, 1980, the Society purchased the property and moved to 10 South Main Street in Pennington, New Jersey.

*Q. How was the purchase of the building financed?*

A. The Society utilized \$48,750 of the existing surplus in the Society's General Operating Fund to pay 25% of the \$195,000 purchase price. The remainder, \$146,250, was covered by a mortgage at 12% interest, written for a period of five years but payable on a ten year mortgage schedule. As of August 1, 1985, when the mortgage will have to be refinanced, the balance will be \$94,327.68.

*Q. What is the purpose of The Electrochemical Society Building Fund?*

A. The Electrochemical Society Building Fund was set up by the Society's Board of Directors to receive and record contributions from Society members and friends that will be used first to repay the monies taken from the General Operating Fund for the building purchase and then to reduce the mortgage balance.

*Q. Why does the Society need contributions to its building fund?*

A. The Electrochemical Society has traditionally sought permanent funding for long range commitments so as to maximize the use of current income in the current technical activities that benefit its members. In purchasing a headquarters building, the Society has entered into an undertaking that will ultimately limit the growth of its housing costs and reduce its need for additional income. Contributions to the building fund will speed the completion of this undertaking and help the Society deal with its increasing publication and technical program costs.

*Q. Are contributions to the building fund tax deductible?*

A. Yes. The Electrochemical Society is classified as a 501(c)(3) non-profit charitable organization by the Internal Revenue Service.

-----

TO: The Electrochemical Society, Inc.

Enclosed is my contribution of \$\_\_\_\_\_ to the Building Fund.

\_\_\_\_\_  
Signature



## THE ELECTROCHEMICAL SOCIETY PATRON MEMBERS

### **Bell Laboratories**

Murray Hill, NJ

### **Dow Chemical Co.**

Inorganic Chemicals Dept.  
Midland, MI

### **Exxon Research and Engineering Co.**

Corporate Research  
Advanced Energy Systems Laboratory,  
Solid State Sciences Laboratory,  
Linden, NJ

Engineering Technology Div.  
Florham Park, NJ

### **General Electric Co.**

Battery Business Dept., Gainesville, FL  
Chemical Laboratory, Knolls Atomic Power Laboratory,  
Schenectady, NY  
Lamp Div., Cleveland, OH  
Materials & Process Laboratory, Large Steam  
Turbine-Generator Dept., Schenectady, NY

### **General Electric Co. (continued)**

Research and Development Center,  
Chemical Systems & Technology  
Laboratory & Physical Chemistry Laboratory,  
Signal Processing & Communication Laboratory,  
Schenectady, NY  
Semiconductor Products Dept.,  
Syracuse, NY

### **International Business Machines Corp.**

New York, NY

### **INCO Research and Development Center**

Suffern, NY

### **Olin Corp.**

Chemicals Div.  
Charleston Technology Center  
Charleston, TN

### **Philips Research Laboratories**

Eindhoven, The Netherlands

### **Westinghouse Electric Corp.**

Electronic Tube Div., Elmira, NY  
Lamp Div., Bloomfield, NJ  
Semiconductor Div., Youngwood, PA  
Research Laboratories, Pittsburgh, PA

## THE ELECTROCHEMICAL SOCIETY SUSTAINING MEMBERS

### **The Aerospace Corp.**

Los Angeles, CA

### **Airco Industrial Gases**

Murray Hill, NJ

### **Airco Speer Carbon Graphite**

St. Marys, PA

### **Allied Chemical Corp.**

Industrial Chemicals Div.  
Solvay, NY

### **Aluminum Co. of America**

New Kensington, PA

### **Aluminum Co. of Canada, Ltd.**

Montreal, Que., Canada

### **AMAX Inc.**

Greenwich, CT

### **AMP Inc.**

Harrisburg, PA

### **Analog Devices, Inc.**

Norwood, MA

### **Applied Materials, Inc.**

Santa Clara, CA

### **Asahi Chemical Industry Canada, Ltd.**

Toronto, Ont., Canada

### **ASARCO, Inc.**

South Plainfield, NJ

### **Battelle Memorial Institute**

Columbus, OH

### **Battery Technology Co.**

A Division of Duracell International  
Tarrytown, NY (2 memberships)

### **Bell-Northern Research**

Ottawa, Ont., Canada

### **Boeing Co.**

Seattle, WA

### **The Borg-Warner Corp.**

Roy C. Ingersoll Research Center  
Des Plaines, IL

### **BP Research Centre**

Middlesex, England

### **Brown, Boveri & Co., Ltd.**

Research Center  
Baden, Switzerland

### **Canadian Industries Ltd.**

Montreal, Que., Canada

### **Cominco Ltd.**

Trail, B.C., Canada

### **The Continental Group, Inc.**

Energy Systems Laboratory  
Cupertino, CA

### **Corning Glass Works**

Corning, NY

### **Crawford & Russell Inc.**

Stamford, CT

### **Diamond Shamrock Corp.**

Painesville, OH

### **Duro-Test Corp.**

North Bergen, NJ

### **Eagle-Picher Industries, Inc.**

Electronics Div.  
Joplin, MO

### **Eastman Kodak Co.**

Rochester, NY

### **EG&G Princeton Applied Research Corp.**

Princeton, NJ

### **Electric Power Research Institute**

Palo Alto, CA

### **Electrochemical Technology Corp.**

Seattle, WA

### **Electrode Corp.**

Chardon, OH

### **Eltra Corp.**

Prestolite Div., Toledo, OH  
C&D Batteries, Conshohocken, PA

### **Energy Development Associates**

A Gulf and Western Co.  
Madison Heights, MI

## SUSTAINING MEMBERS (CONTINUED)

- Ever Ready Co. (Holdings) Ltd.**  
Whetstone, London, England
- Exmet Corp.**  
Bridgeport, CT
- Fairchild Camera & Instrument Corp.**  
Research & Development Laboratory  
Palo Alto, CA
- FMC Corp.**  
Inorganic Chemicals Div.  
Buffalo, NY
- Ford Motor Co.**  
Dearborn, MI
- The Gates Rubber Co.**  
Denver, CO
- General Motors Corp.**  
Delco-Remy Div., Anderson, IN  
Research Laboratories Div.  
Warren, MI
- Gould Inc.**  
Gould Laboratories—  
Energy Research  
Rolling Meadows, IL  
Gould Information Center  
Cleveland, OH
- Great Lakes Carbon Corp.**  
New York, NY
- GTE Laboratories**  
Waltham, MA
- GTE Sylvania Inc.**  
Chemical & Metallurgical Div.  
Towanda, PA
- The Harshaw Chemical Co.**  
Cleveland, OH
- Heliotronic GmbH**  
Burghausen, Germany
- Hewlett Packard Co.**  
Loveland, CO
- Hewlett Packard Laboratories**  
Palo Alto, CA
- Hill Cross Co., Inc.**  
West New York, NJ
- Hoechst-Uhde Corp.**  
Englewood Cliffs, NJ
- Honeywell, Inc.**  
Power Sources Center  
Horsham, PA
- Hooker Chemical Corp.**  
Niagara Falls, NY (2 memberships)
- Hughes Research Laboratories**  
Div. of Hughes Aircraft Co.  
Malibu, CA
- IMI Marston Limited**  
Wolverhampton, England
- INCO ElectroEnergy Corp.**  
Engineering & Development Center  
Ray-O-Vac Corp.  
Madison, WI  
Engineering & Development Center  
Exide Corp.  
Yardley, PA
- International Lead Zinc Research Organization, Inc.**  
New York, NY
- International Minerals and Chemical Corp.**  
Electrochemical Div.  
Orrington, ME
- Johnson Controls, Inc.**  
Milwaukee, WI
- Kaiser Aluminum & Chemical Corp.**  
Pleasanton, CA
- Kawecki Berylo Industries, Inc.**  
a subsidiary of Cabot Corp.  
Boyertown, PA
- KW Battery Co.**  
Skokie, IL
- Arthur D. Little, Inc.**  
Cambridge, MA
- Lockheed Missiles & Space Co., Inc.**  
Research Laboratory  
Palo Alto, CA
- Marathon Battery Co.**  
Waco, TX
- Matsushita Electric Industrial Co., Ltd.**  
Osaka, Japan
- Mead Advanced Systems Research and Development Laboratories**  
Dayton, OH
- Medtronic Energy Technology**  
Minneapolis, MN
- Mepco/Electra, Inc.**  
Columbia, SC
- Microwave Associates, Inc.**  
Burlington, MA
- Molycorp, Inc.**  
New York, NY
- Monsanto Co.**  
St. Louis, MO
- Motorola Inc.**  
Phoenix, AZ
- M&T Chemicals Inc.**  
Detroit, MI
- NIFE Jungner AB**  
Oskarshamn, Sweden
- Noranda Research Centre**  
Pointe Claire, Que., Canada
- Occidental Research Corp.**  
La Verne, CA
- Olin Corp.**  
Metals Research Laboratories  
New Haven, CT
- Owens-Illinois Inc.**  
Toledo, OH
- Oxy Metal Industries Corp.**  
Warren, MI
- Perkin-Elmer Corp.**  
Norwalk, CT
- Phelps Dodge Refining Corp.**  
Maspeth, NY
- Philips Laboratories, Inc.**  
Briarcliff Manor, NY
- PPG Industries, Inc.**  
Chemical Div.  
Pittsburgh, PA
- Prototech Co.**  
Newton Highlands, MA
- RCA Corp.**  
Color Picture Tube Div.  
Lancaster, PA
- Reynolds Metals Co.**  
Reduction Research Div.  
Sheffield, AL
- Rockwell International**  
El Segundo, CA
- Sandia Laboratories**  
Albuquerque, NM
- J. C. Schumacher Co.**  
Oceanside, CA
- Shipley Company, Inc.**  
Newton, MA
- Siemens Aktiengesellschaft**  
Munich, Germany
- Signetics Corp.**  
Sunnyvale, CA
- Siltec Corp.**  
Menlo Park, CA
- Sperry Research Center**  
Sudbury, MA
- Sprague Electric Co.**  
North Adams, MA
- The Stackpole Corp.**  
St. Marys, PA
- Standard Telecommunication Laboratories Ltd.**  
Essex, England
- Stauffer Chemical Co.**  
Dobbs Ferry, NY
- St. Joe Minerals Corp.**  
Monaca, PA
- Tektronix, Inc.**  
Beaverton, OR
- Teletype Corp.**  
Skokie, IL
- Texas Instruments Inc.**  
Attleboro, MA  
Dallas, TX
- Tokyo Shibaura Electric Co., Ltd.**  
Toshiba Research and Development Center  
Kawasaki, Japan
- Toyota Central Research and Development Labs, Inc.**  
Nagoya, Japan
- Union Carbide Corp.**  
Battery Products Div.,  
Corporate Research Dept.  
New York, NY
- United States Steel Corp.**  
Research Laboratory  
Monroeville, PA
- Varian Associates**  
Palo Alto, CA
- Wacker Chemitronic**  
Burghausen, Germany
- Western Electric**  
Princeton, NJ
- Xerox Corp.**  
Webster Research Center  
Rochester, NY
- Yardney Electric Corp.**  
Pawcatuck, CT
- Yuasa Battery Co., Ltd.**  
Osaka, Japan

-A 2012551  
1982